

ABSTRACTS BOOK

UN'INIZIATIVA DI CON IL PATROCINIO DI GRAZIE A

Organizzatori, Patrocini e Sponsorizzazioni

Il XXI Congresso della Società Italiana di Scienze Planetarie è organizzato dalla **SISP-AC** in collaborazione con l'Istituto Nazionale di Astrofisica, con il Dipartimento di Scienze e Metodi dell'Ingegneria (DISMI) dell'Università di Modena e Reggio Emilia (UniMoRE)

Con il Patrocinio di

Con il supporto di

Scientific Organising Committee

Davide Grassi (INAF - IAPS) Co-Chair

Manuel Iori (Dipartimento di Scienze e Metodi dell'Ingegneria – UniMORE) Co-Chair

Roberto Orosei (INAF - IRA) Co-Chair

Maria Teresa Brunetti (CNR – IRPI)

Fabrizio Capaccioni (INAF – IAPS)

Giacomo Filippo Carrozzo (INAF - IAPS)

Giuliano Liuzzi (Dipartimento di Ingegneria - Università della Basilicata)

Andrea Longobardo (INAF - IAPS)

Luca Maggioni (INAF – IAPS)

Matteo Massironi (Dipartimento di Geoscienze – Università di Padova)

Giuseppe Mitri (Dipartimento di Ingegneria e Geologia - Università di Chieti Pescara)

Marco Morelli (MISP – Museo Italiano di Scienze Planetarie)

Giacomo Nodjoumi (Space Science Data Centre – ASI)

Giovanni Pratesi (Dipartimento di Scienze della Terra - Università di Firenze)

Veronica Roccatagliata (Dipartimento di Fisica e Astronomia – Università di Bologna)

Gene Walter Schmidt (INAF – IAPS)

Gianni Strazzulla (INAF – OaCt)

Natalia Amanda Vergara Sassarini (INAF - Osservatorio Astronomico di Padova)

Local Organising Committee

Manuel Iori	**(DISMI – UniMORE) Chair**
Davide Grassi	**(INAF-IAPS) Co-Chair**
Roberto Orosei	**(INAF -IRA) Co-Chair**
Federico Tosi	**(INAF – IAPS) Co-Chair**
Fabrizio Capaccioni	(INAF – IAPS)
Alberto Avallone	(DISMI – UniMORE)
Filippo Bonafé	(DISMI – UniMORE)
Giulia Caselli	(DISMI – UniMORE)
Mirko Cavecchia	(DISMI – UniMORE)
Giulia Dotti	(DISMI – UniMORE)
Benedetta Ferrari	(DISMI – UniMORE)
Pietro Girardis	(DISMI – UniMORE)
Alberto Locatelli	(DISMI – UniMORE)
Mirko Mucciarini	(DISMI – UniMORE)
Francesco Sala	(DISMI – UNIMORE)

Lunedì 2 Febbraio 2026
Palazzo Dossetti - Aula Magna “Manodori”

	09:00	13:00	Mattinata dedicata alle scuole			
	13:00	14:00	Iscrizione e Accoglienza, affissione posters			
	14:00	14:40	Apertura del Congresso e Saluti istituzionali – Interverranno: **Prof.ssa Rita Cucchiara**, Rettrice della UNIMORE **Prof.ssa Elena Degoli**, Direttrice Dipartimento di Scienze e Metodi dell'Ingengeria **Dott. Lanfranco de Franco**, ViceSindaco della cittòà di Reggio Emilia **Dott. Francesco Petracchini**, Direttore Dipartimento DSTTA CNR (remoto) **Dott. Andrea Argan**, Coordinatore Unità Scientifica Progetti dallo Spazio INAF (remoto)			
	14:40	14:45	Informazioni Logistiche - Annunci			
	14:45	15:30	PREMI SISP 2025 Consegna Premi e Relazioni ad Invito dei vincitori Premio Giovane Ricercatore I Edizione – 2025 **Assegnato a Giovanni Poggiali** Premio Miglior Articolo da Tesi di Dottorato I Edizione – 2025 **Assegnato a Christian Magliano**			
	15:30	16:00	Coffee Break			
Sessione - Pianeti e Satelliti - Mars						
	Chair	**Jeremy Brossier**				
	16:00	16:12	Oxia Planum, Mars: characterizing clay-rich regions	Francesca Altieri	INAF-IAPS	pag 16
	16:12	16:24	The Geology of East Tempe Terra, Mars	Alessandro Frigeri	INAF-IAPS	pag 18
	16:24	16:36	Wind streaks in the EXOMars 2028 landing site	Simone Silvestro	INAF-OaCN	pag 20
	16:36	16:48	Numerical modelization as a way to infer water content in martian landslides	Agnese Caramanico	Università di Urbino	pag 22
	16:48	17:00	Study of compositional variability of Phobos and Deimos surfaces using TGO/CASSIS images.	Joel Beccarelli	Università di Padova CISAS	pag 24
	17:00	17:12	Preparation for MIRS investigation on Phobos and Deimos in the framework of the MMX sample return mission	Giovanni Poggiali	INAF-OAA	pag 26
	17:12	17:30	**Discussione**			
		17:30	**Fine Giorno 1**			

Martedì 3 Febbraio 2026
Palazzo Dossetti - Aula Magna “Manodori”

Sessioni Mattutine

Astrobiologia e Astrochimica - Sessione Habitability					
	Chair	**Daniele Fulvio**			
	09:00	09:12	Analysis of solar radiation effects on icy moons surfaces using GEANT4 tool	Mattia Sesso - Uni Trieste	pag 29
	09:12	09:24	The reactions of atomic oxygen with aromatic compounds and implications for the evolution of extraterrestrial carbonaceous material	Marco Parriani - Uni Perugia	pag 31
	09:24	09:36	Insights into the habitability of other worlds through laboratory simulations using cyanobacteria capable of far-red photosynthesis	Daniela Billi - Uni Roma Tor Vergata	pag 33
	09:36	09:48	The prebiotic production of oligonucleotide sequences from 3',5' cyclic nucleotide precursors: what we have learned from field experiments	Giovanna Costanzo CNR-IBPM	pag 34
	09:48	10:00	The role of convection in sustaining putative ecosystems in the subsurface oceans of icy moons	Silvia Pagnoscin Uni Firenze	pag 36
	10:00	10:15	**Discussione**		
Sessione Dinamica dei corpi celesti naturali ed artificiali					
	Chair	**Stefano Palmiotto**			
	10:15	10:27	Potential interaction of 99942 Apophis with the high Earth orbit population during the 2029 close approach	Giulia Schettino CNR-IFAC	pag 39
	10:27	10:39	Estimating the steady-state number of Earth's coorbital bodies derived from lunar ejecta	Elisa Maria Alessi CNR-IMATI	pag 41
	10:39	10:45	**Discussione**		
	10:45	11:15	Coffee Break		
Sessione In ricordo di Riccardo Pozzobon					
	Chair	**Matteo Massironi**			
	11:15	11:20	Introduzione	Matteo Massironi UniPd	
	11:20	11:30	Planetary caves: looking below the surface	Francesco Sauro UniPd	
	11:30	11:40	Da PANGEA a DaedalusCAM	Javier Suarez UniPd	
	11:40	11:50	Dalla superficie al sottosuolo: cartografia e analisi dei siti di allunaggio	Giacomo Melchiori UniPd	
	11:50	12:00	Mapping the Dream: The Quantitative Reality of Mars Landing sites	Maurizio Pajola INAF-OAPd	
	12:00	12:15	Exploring Below the Surface: a Journey Across Worlds	Alice Lucchetti/ Barbara de Toffoli UniPd INAF	
Sessione Divulgazione, Didattica e Comunicazione					
	Chair	**Luca Tonietti**			
	12:15	12:27	A role-playing game for the dissemination of Planetary Defence	Maddalena Mochi Uni Pisa	pag 43
	12:27	12:39	AsteroidAlert Escape Room: SISP–AC Outreach Call 2024	Andrea Farina Uni Padova	pag 45
	12:39	12:45	**Discussione**		

Martedì 3 Febbraio 2026
Palazzo Dossetti - Aula Magna “Manodori”

Sessioni Pomeridiane

Sessione Piccoli Corpi - Comete				
Chair		**Elena Mazzotta Epifani**		
14:15	14:27	Early CN Outgassing and Production Rates of C/2024 E1 (Wierzchos) at 4 AU	Alessandra Mura INAF-OaPd	pag 48
14:27	14:39	Comet 3I/Atlas through the CASSIS stereo camera onboard EXOMars/TGO	Gabriele Cremonese INAF-OaPd	pag 50
14:39	14:51	Statistical Analysis of Cometary Ices: Inheritance or Chemical Reset?	Manuela Lippi INAF-OAA	pag 51
14:51	15:00	**Discussione**		
Planetologia sperimentale e di laboratorio - Sessione "Traces of Life"				
Chair		**Giovanna Maria Costanzo**		
15:00	15:12	Bacteria, salts and brine mixtures : infrared spectral mapping of a laboratory analogue for habitability on icy moons.	Stefano Rubino INAF-IAPS	pag 54
15:12	15:24	The impact of different cations in sulfates on the photostability of Uracil under martian-like UV irradiation	Cristina García-Florentino INAF-OAA	pag 56
15:24	15:36	Investigating the stability of 9-methylanthracene in magnesium and calcium sulfates under UV irradiation to assist detection of organics on Mars	Francesco Renzi INAF-OAA	pag 58
15:36	15:48	Dielectric Characterization of Perchlorate Solutions as Analogues of Martian Subglacial Liquid Water	Gabriele Turchetti, Uni Roma Tre	pag 60
15:48	16:00	Ion irradiation of ices on organic refractories is a source of CO_2 and CO on TNOs	Massimo Germanà INAF-OACt / Uni Catania	pag 62
16:00	16:15	**Discussione**		
16:15	16:45	Coffee Break		
Focus S1 - Water in the Inner Solar System: Past Activity and Climatic Evolution				
Chair		**Giacomo Carrozzo**		
16:45	16:57	Esker-like Ridges in the South Polar Ice-cap on Mars: Possible Evidence of Ice Melting	Luca Guallini INAF-IRA	pag 65
16:57	17:09	Evidence of recent warm-based glaciation and meltwater drainage from eskers at Deuteronilus Mensae, Mars	Giovanni Munaretto INAF-OaPd	pag 67
17:09	17:21	Are Carbonates Hiding Among Martian Clays?	Jeremy Brossier INAF-IAPS	pag 69
17:21	17:33	Alkaline vs Acidic Aqueous Weathering on Mars – a comparative study from Earth analogs.	Enrico Bruschini INAF-IAPS	pag 71
17:33	17:45	**Discussione**		
Focus S5 - Planet formation and evolution in solar system analogues				
Chair		**Veronica Roccatagliata**		
17:45	17:57	A change of paradigm in planet formation: Outflow cavity walls as hidden factories for large dust grains	Giovanni Sabatini INAF-OAA	pag 74
17:57	18:09	Exoplanet observations at Osservatorio Polifunzionale del Chianti: its role in global research networks	Marianna Michelagnoli OPC - Uni Firenze	pag 75
18:09	18:15	**Discussione**		
20:00		**Cena Sociale ristorante "La terra del tuono"**	https://www.terradeltuono.it/	

Mercoledì 4 Febbraio 2026
Palazzo Dossetti - Aula Magna “Manodori”

Sessioni Mattutine

Focus S7 - From Orbital Data to Scalable Landing-Site Frameworks				
Chair		**Giacomo Nodjoumi / Veronica Camplone**		
09:00	09:12	The Space Science Data Center (SSDC) Science Computing Hub (SciComHub): a centralized platform for data access, processing, analysis, and software development.	G. Nodjoumi ASI	pag 78
09:12	09:24	MATISSE: integrating planetary data for advanced and targeted analysis	Veronica Camplone ASI	pag 80
09:24	09:30	**Discussione**		
Focus S2 - The meteorites and impactites collections in Italy				
Chair		**Marco Morelli / Daniela Faggi**		
09:30	09:42	The meteorite and impactite collection of the italian Museum of Planetary Sciences: scientific and cultural significance	Daniela Faggi MISP-Fondazione PARSEC	pag 83
09:42	09:54	The Vatican Meteorite Collection at the Vatican Observatory	Robert Macke, Vatican Observatory	pag 85
09:54	10:06	Potential of imaging spectroscopy and SEM-EDS to map the surface mineralogical composition of NWA 4966 and NWA 6726 carbonaceous chondrites	Simone Pascucci CNR-IMAA	pag 87
10:06	10:18	Scalea, a new italian meteorite: description and characterization	Vanni Moggi Cecchi Uni Firenze	pag 89
10:18	10:30	**Discussione**		
10:30	11:00	Coffee Break		
Meteore, Meteoriti e Polvere interplanetaria				
Chair		**Maximilian Vovk**		
11:00	11:12	Uncontaminated Cosmic Dust from the Upper Stratosphere: DUSTER Collections and Multi-Analytical Characterization of micron and sub-micron particles	Luca Tonietti Uni Parthenope	pag 92
11:12	11:24	Spectroscopic and geochemical characterization of lunar breccia NWA 11421: insights into the lunar crust–mantle composition and implication for moon exploration.	Andrew Alberini INAF - OAA	pag 94
11:24	11:36	Evidence for a new CR-like carbonaceous (CX) grouplet	Tiberio Cuppone Uni Firenze	pag 96
11:36	11:48	A new micrometeorite from Mount Gariglione unveils new insights about the origin of extraterrestrial (Al,Cu)-alloys.	Giovanna Agrosì Uni Bari	pag 98
11:48	12:00	Revealing impact signatures in Ureilite diamonds and graphite through nanoscale analysis	Anna Barbaro Uni Padova	pag 100
12:00	12:12	Coated impact melt bombs from the Wabar Craters (Saudi Arabia)	Luigi Folco Uni Pisa	pag 101
12:12	12:30	**Discussione**		

Mercoledì 4 Febbraio 2026
Palazzo Dossetti - Aula Magna “Manodori”

Sessioni Pomeridiane

Sessione Piccoli Corpi - Asteroidi					
	Chair	**Filippo Tusberti**			
	14:00	14:12	Dynamics and origin of the NEA pair 2021 PH27 and 2025 GN1	Albino Carbognani INAF-OAS	pag 104
	14:12	14:24	NEOPOPS – The NEO Physical Observations and Properties Simulation	Elisabetta Dotto INAF-OAR	pag 106
	14:24	14:36	NEOVST: A mini 4-SDSS-colors Survey of newly-discovered Near-Earth Objects through the VLT Survey Telescope.	Pedro H. Hasselmann INAF-OAR	pag 107
	14:36	14:48	Dust dynamics and plasma simulations in support of planetary defense missions such as Hera and Ramses.	Stavro Ivanoski INAF - OaTs	pag 109
	14:48	15:00	Ramses mission update: preparing for Apophis' 2029 close approach to Earth	M. Lazzarin Uni Padova	pag 110
	15:00	15:15	**Discussione**		
Astrobiologia e Astrochimica - Sessione Mars					
	Chair	**Andrew Alberini**			
	15:15	15:27	Organics detection on Mars by the MARS2020 Perseverance rover	Teresa Fornaro INAF-OAA	pag 113
	15:27	15:39	Project Anoxymars: studying the detectability of anoxygenic microorganisms ahead of the EXOMars mission.	Mariano Battistuzzi INAF-OAA	pag 115
	15:39	15:51	Microbial Community Divergence and pH-Driven Biomineralization in Two Terrestrial Analogs to Mars	Agnese Piacentini Uni Roma La Sapienza	pag 116
	15:51	16:03	Assessing the viability of Antarctic cryptoendolithic communities exposed to Mars-like conditions	Carmen del Franco UniTus	pag 118
	16:03	16:15	Microbially influenced evaporitic textures and microbiota of the Makgadikgadi Pan (Botswana): analogues for Martian biosignature formation	Alice Tarozzi Uni Bologna	pag 120
	16:15	16:27	Functional ecology of bacteria in Antarctic cryptoendolithic communities from dry and cold conditions analogous to Mars environments	Ricardo Belmonte-Lopes Uni Tuscia	pag 121
	16:27	16:45	**Discussione**		
	16:45	17:00	Sessione EUROPLANET		
	17:00	17:30	Coffee Break + Sessione Parmigiano Reggiano		
	17:30	19:30	Sessione Poster		
	19:00	21:00	**AperiPoster**		

Giovedì 5 Febbraio 2026
Palazzo Dossetti - Aula Magna “Manodori”

Sessioni Mattutine

Sessione Planetologia sperimentale e di laboratorio					
	Chair	**Francesca Furnari**			
	09:00	09:12	Preliminary tests to combine X-ray microtomography and dielectric measurements to assess the radar properties of pure ice	Flavia Cimbolli Spagnesi, Uni Roma Tre	pag 124
	09:12	09:24	Laboratory investigation of ice analogs including O2, to constrain the surface composition of Solar System icy moons	Alessandra Migliorini INAF-IAPS	pag 126
	09:24	09:36	Mafic Mineralogy in the VNIR, support of synthetic or peculiar composition to the mineralogical analysis of remote sensed surfaces	Cristian Carli INAF-IAPS	pag 128
	09:36	09:48	Martian Simulants for Gusev and Gale craters igneous products: rheological, mineralogical and spectral characterization.	Alessandro Pisello Uni Perugia	pag 130
	09:48	10:00	Characterization of an ExoMars mission reference gypsum sample using payload-analog techniques	Sole Biancalani INAF-OAA	pag 132
	10:00	10:12	MA_MISS spectroscopic measurements on the ExoMars/RFM mission reference samples	Marco Ferrari INAF-IAPS	pag 134
	10:12	10:24	Identifying Earth rock analogs of Oxia Planum in preparation for the Rosalind Franklin Mission	Monica Rasmussen INAF-IAPS	pag 136
	10:24	10:45	**Discussione**		
	10:45	11:15	Coffee Break		
Focus S6 - Advanced image processing and Artificial Intelligence/Machine Learning for planetary exploration					
	Chair	**Natalia Amanda Vergara Sassarini / Stavro Ivanoski**			
	11:15	11:27	Unsupervised machine learning of FTIR spectra from two Hayabusa2' Ryugu particles reveals stratified regolith evolution	Marianna Angrisani INAF-IAPS	pag 139
	11:27	11:39	Mercury’s surface classification through Graph Attention Networks	Lorenzo Spina INAF-OaPd	pag 141
	11:39	11:51	Terraced craters on Mars: analysis in arcadia planitia and detection in additional regions via deep learning	Maddalena Faletti CISAS/INAF-OaPd	pag 143
	11:51	12:03	Three-dimensional imaging of subsurface structures within martian south polar layered deposits using MARSIS radar data	Alessio Margheri Uni Trento	pag 145
	12:03	12:15	**Discussione**		

Giovedì 5 Febbraio 2026
Palazzo Dossetti - Aula Magna “Manodori”

Sessioni Pomeridiane

Focus S3 - Atmospheric Observation and Spectral Modeling in Planetary Science				
Chair		**Giuliano Liuzzi**		
14:00	14:12	Advanced σ Radiative Transfer Model: Enhancing Atmospheric Remote Sensing for Earth and Planetary Exploration	Guido Masiello Uni Basilicata	pag 148
14:12	14:24	New laboratory measurements of the CO2-H2 Collision-Induced Absorption in the [4000, 4750] cm-1 spectral range from 240 K to 500 K	Francesca Vitali INAF-IAPS	pag 149
14:24	14:36	Infrared Spectral Diagnostics of Jupiter's Moon-Induced Auroral Footprints	Chiara Castagnoli INAF-IAPS	pag 151
14:36	14:48	JUICE-MAJIS Earth Gravity Assist data overview and comparison with PRISMA	Giuseppe Piccioni INAF-IAPS	pag 153
14:48	15:00	**Discussione**		
Pianeti e Satelliti - Outer Solar System				
Chair		**Chiara Castagnoli**		
15:00	15:12	Photometrically corrected maps of Saturn mid-sized icy moons from Cassini-VIMS observations	Marjorie Galinier INAF-IAPS	pag 155
15:12	15:24	ESA's L4 mission: a new voyage to the ocean world Enceladus	Alice Lucchetti INAF-OaPd	pag 157
15:24	15:36	Synchronized eruptions on Io	Alessandro Mura INAF-IAPS	pag 159
15:36	15:45	**Discussione**		
15:45	16:15	Coffee Break		
Pianeti e Satelliti - Moon and Mercury				
Chair		**Beatrice Baschetti**		
16:15	16:27	Global thermophysical characterization of Mercury's diurnal temperature cycle: thermal amplitudes, gradients, and stress indices in support of BepiColombo SIMBIO-SYS	Pamela Cambianica INAF-OaPd	pag 161
16:27	16:39	High-resolution observations of the Earth-Moon system with the JANUS instrument during the JUICE LEGA flyby	Pasquale Palumbo INAF-IAPS	pag 163
16:39	16:51	OH/H_2O formation and stability in the lunar mid-latitudes: insights from the Mairan crater region	Federico Colaiuta Uni Roma Sapienza / INAF-IAPS	pag 165
16:51	17:03	The MoonSWA project: integrated spectral and laboratory analysis of lunar space weathering	Francesca Zambon INAF-IAPS	pag 167
17:03	17:15	**Discussione**		
17:30	19:00	Assemblea Plenaria Società Italiana di Scienze Planetarie - Angioletta Coradini		

Venerdì 6 Febbraio 2026
Palazzo Dossetti - Aula Magna “Manodori”

Focus S4 Volatile and refractory material emissions in planetary environments: a modeling perspective					
	Chair	**Luca Maggioni**			
	09:00	09:12	When shape meets temperature: morphological and thermophysical interactions in Mercury's permanently shadowed craters	Silvia Bertoli INAF_OaPd	pag 170
	09:12	09:24	Solar activity effects on lunar surface and impact	Lorenzo Calderone INAF-OaTs	pag 172
	09:24	09:36	Impact-induced sulfur melting on Mars: a potential source of native sulfur detected by the Nasa's Curiosity rover	Luca Maggioni INAF-IAPS	pag 173
	09:36	09:48	An exogenic contribution to lunar water ice: a cometary post-impact plume through smoothed particle hydrodynamics	Gianfranco Magni INAF-IAPS	pag 175
	09:48	10:00	**Discussione**		
Sessione Sviluppo di Strumentazione					
	Chair	**Marianna Angrisani**			
	10:00	10:12	Development of quartz crystal microbalances for Enceladus applic	Andrea Longobardo INAF-IAPS	pag 178
	10:12	10:24	HISCAL, the new Hyperspectral Imaging Spectrometers CALibration Facility in INAF-IAPS	Stefania Stefani INAF-IAPS	pag 179
	10:24	10:36	ASI-SSDC: towards a new role supporting innovation and space missions	Angelo Zinzi ASI	pag 181
	10:36	10:45	**Discussione**		
	10:45	11:15	Coffee Break		
Focus S8 - Beyond the visible: Uncovering interior composition and processes through tectonic and geodynamic lenses					
	Chair	**Gene Walter Schmidt / Salvatore Buoninfante**			
	11:15	11:27	Structural analysis of Ariel's surface	Susanna Tonoian Uni Padova	pag 184
	11:27	11:39	Possible local subduction and spreading processes in Vinmara Planitia, Venus: geological and geophysical constraints	Davide Sulcanese Uni Pescara	pag 186
	11:39	11:51	Coronal repaving of Venus's surface	Nicholas Montiel Uni Padova	pag 187
	11:51	12:00	**Discussione**		
	12:00	13:00	Consegna Premi del Congresso: • Premio al Miglior Contributo Poster • Premio al Miglior Contributo Orale		
		13:00	**FINE CONGRESSO**		

SESSIONE POSTER

Astrobiologia e Astrochimica			
1	Carbon chain diversity in L1544 and IRAS 16293-2422: an astrochemical pathfinder study for the SKAO	Lisa Giani	pag 189
2	The Oxygenic Photosynthetic Habitability of M-stars acquaplanets	Michele Maris	pag 191
3	Laboratory experiments on the origin and evolution of extraterrestrial ozone from ion irradiated ices and icy mixtures	Daniele Fulvio	pag 193
4	Investigation into the origins and detection of biomolecule homochirality in early Earth/Mars environment	Rukiah Mitri	pag 194
5	The Fantastic Four: Tc, Re, Th, and U in geobiological processes.	Gloria Giacchino	pag 196
Dinamica dei corpi celesti naturali ed artificiali			
6	Orbit determination study of artificial satellites using observational data from the Schmidt and Copernico telescopes at the Mount Ekar observing station	Luca Cortese	pag 197
7	Astrometry of near-earth asteroids and resident space objects with the TANDEM system	Stefano Palmiotto	pag 198
8	Secular Effects in small bodies impact frequencies	Aldo Dell'Oro	pag 200
Meteore, Meteoriti e Polvere interplanetaria			
9	Toward the First Meteor Detections on Mars: Predicting Brightness and Altitude Using the Erosion–Fragmentation Model	Maximilian Vovk	pag 201
10	Iron oxidation state and coordination environment in brazilian tektites	Gabriele Giuli	pag 202
11	Evidence for Mixed-Redox Dust Aggregation in an EL3 Enstatite Chondrite EET90992	Paola Manzari	pag 203
12	Micrometeoroids flux and impacts vaporization at the Moon	Patrizia Borin	pag 204
13	3D porosity of lunar meteorite Tisserlitine 006	Alice Macente	pag 205
14	A new italian meteorite from Monte Bondone(Trento). Description and preliminary data.	Marco Morelli	pag 207
15	Mineralogical characterization of the fusion crust of the Cavezzo L5 anomalous chondrite and first find of Ni2S sulphide.	Marianglona Rondinelli	pag 208
16	Cosmic Dust Flux During the Quaternary: Size Distribution of Scoriaceous and Unmelted Micrometeorites from the Transantarctic Mountains Collection	Samuele Ottaviani	pag 210
17	A petrological approach to the study of chondrites	Simone Borghetti	pag 211
18	Synthesis of a new lunar regolith based on the microchemical and mineralogical characterization of lunar meteorites	Valeria De Santis	pag 212
19	Physical properties of L and L/LL ordinary chondrites as Didymos-Dimorphos analogue	Edoardo Rossi	pag 214
20	Unveiling the composition of EET87746 antarctic meteorite by a non-destructive approach	Giovanni Fanelli	pag 216
21	The meteorites and impactites collections at the Department of physics and geology of Perugia University	Paola Comodi	pag 218
Pianeti e Satelliti - Outer Planets			
22	Interpreting Io's Thermal Emission: Constraints From Juno/Jiram M-Band Observations	Federico Tosi	pag 220
23	Analysis of Io's tidal response as a function of the properties of the partially molten layer	Matteo Paris	pag 222
24	Cassini states and librations of the Galilean satellites: a numerical approach in Euler angles	Giulio Macrì	pag 224
25	Investigating the composition of Jupiter's energetic ion environment	Christina Plainaki	pag 226
26	Improved treatment of stray light in the JIRAM-JUNO spectrometer: application to Jupiter auroral observations	Davide Grassi	pag 228
27	Modeling thermal convection within Europa's icy layer: constraints on shell thickness	Michelangelo Formisano	pag 230
28	Strike-slip or extensional deformation on Ganymede? Kinematic modeling of the south polar ice shell	Gianluca Frasca	pag 232
29	Serendipitous Lightning Spectroscopy with MAJIS during JUICE Earth Gravity Assist	Emiliano D'Aversa	pag 233

Pianeti e Satelliti - Moon			
30	An updated mapping of the orientale basin (Moon) using newly developed color vision deficiency-friendly color scales	Yelena Caddeo	pag 234
31	Evaluation of the Moon Mineralogy Mapper reliability in lunar shadowed regions	Giuseppe Massa	pag 236
32	EMM project: SELENE (Simulated Environment for Lunar Exploration and Natural dynamics Experi-ments) for lunar dust mobilization experiments.	Carmen Porto	pag 238
Pianeti e Satelliti - Mercury and Venus			
33	Core and mantle evolution of a reduced Mercury.	Giuseppe Mitri	pag 240
34	First results from a study of the photometric properties of Mercury's surface using MESSENGER-MDIS data	Beatrice Baschetti	pag 241
35	Geologic mapping of the Beethoven quadrangle (H07), Mercury.	Laura Guzzetta	pag 243
36	Why are infilled craters so diverse on Mercury?: constraints from calculated infill and crustal thicknesses	Gene W. Schmidt	pag 245
37	Assessing the crustal density of Mercury through gravity data modelling	Salvatore Buoninfante	pag 247
38	Structural and topographic evidence for a hidden multiring basin in Mercury's Discovery quadrangle (H-11)	Antonio Sepe	pag 249
39	A New View Of Mercury: Improving Global Messenger Mosaics with GSA Pansharpening	Adriano Tullo	pag 251
40	Optimisation of the STC Colour Target Acquisition of the Surface of Mercury	Francesco Sala	pag 253
41	Surface and Subsurface Morphometric Evidence for Lava Tubes on Venus	Barbara De Toffoli	pag 255
Pianeti e Satelliti - Mars			
42	Martian dust properties in Mars Years 34 to 38: TGO/NOMAD UVIS-LNO nadir data preliminary results.	Fabrizio Oliva	pag 257
43	Geomorphological evidence of ice activity on Mars surface at mid-latitude	Marco Moro	pag 258
44	Analyis and mitigation of interferences in MARSIS radargrams: a computer vision approach	Alessandro Piombini	pag 260
45	MOSTO: a 3D virtual reality hyperspectral analysis application for CRISM MTRDR data	Marco Baroni	pag 262
46	Predict-then-optimize stochastic planning for MARSIS raw data acquisition	Alberto Avallone	pag 264
47	The application of s-FORUM radiative transfer code to the Martian atmosphere	Lorenzo Buriola	pag 266
Pianeti e Satelliti			
48	Towards a three-dimensional interior model inversion framework	Antonio Genova	pag 268
49	CAn we REly on Our Network? Uncovering human-factor signatures in boulder mapping with the CARE-ON project	Sandro Rossato	pag 270
50	Plumes with Smoothed Particle Hydrodynamics: from Enceladus to Europa and beyond	Matteo Teodori	pag 271
52	New parametrizations of non-LTE effects for atmospheric studies and applications to satellite IR observations	Lorenzo Cassini	pag 273
Pianeti e Sistemi planetari extrasolari			
53	A comprehensive picture about jovian clouds and hazes from Juno/JIRAM infrared spectral data	Francesco Biagiotti	pag 276
54	Integration of Exomercat 2.0 into ExoplAn3T for Extended Exoclimate Simulations	Francesca Manni	pag 278

Piccoli Corpi			
55	Spectroscopy results from the near-earth objects physical observations and properties simulations (NEOPOPS) program: what we have learned so far	Simone Ieva	pag 280
56	Roughness of planetary surfaces: statistical multi-facet approach combining hapke and fractal theories	Andrea Raponi	pag 282
57	The evolving activity of the hyperbolic comet C/2024 e1 (Wierzchos): a "proxy target" for the ESA Comet Interceptor space mission	Aelena Mazzotta Epifani	pag 284
58	New insights into the Didymos surface: geological map using both Dart/Draco and unexplored Liciacube/Luke images	Filippo Tusberti	pag 286
59	NEOPOPS - How to characterize a potential threat with ground-based observations ?	Jules Bourdelle de Micas	pag 288
60	NEAs Global Boulder Size Frequency Distribution: what to Expect for (99942) Apophis?	Maurizio Pajola	pag 290
61	First year of NEAs Spectroscopic Observations within the NEOPOPS Project at Asiago Observatory	Fiorangela La Forgia	pag 292
62	3D Reconstruction of DART Ejecta at Dimorphos Highlights An Anisotropic, Filamentary Structure	Prasanna Deshapriya Jasinghege Don	pag 294
Planetologia sperimentale e di laboratorio			
63	Spectroscopic measurements of Hexahydrite relevant for the jovian icy moons	Francesca Fumari	pag 296
64	EMM project: The PLATA laboratory facility for the martian boundary layer research	Gabriele Franzese	pag 298
65	Experimental petrology approaches to lunar volcanism: the case study of Lunar Sinuous Rilles (LSR)	Gabriele Scognamiglio	pag 300
66	INSIGHTS ON MERCURY'S CRUSTAL COMPOSITIONS BY COMBINING THERMODYNAMIC MODELLING AND SPECTRAL ANALYSES OF GLINKA CRATER	Camilla Cioria	pag 302
67	Quantifying Ammonium in Two-Component Mineral Mixtures Using IR Reflectance: Influence of Ma-trix Albedo	Eliana La Francesca	pag 303
68	The Arcetri Astrobiology Laboratory: exploring the Solar System within international space agencies programs, looking for traces of life and potential sign of astrobiological processes.	John Robert Brucato	pag 305
69	PVRG rocks spectra catalogue: insights into natural volcanic rocks in the effect of the crystalline-amorphous ratio on the VNIR and MIR spectra.	Maximiliano Fastelli	pag 307
70	Laboratory IR Spectroscopic Study of Asteroid (269) Justitia Analogues for EMA Mission	Simone De angelis	pag 309
Sviluppo di strumentazione			
71	VENOM: Venture the ExtractioN of Organic Molecules – Mainframe Design and Subsystem Reconfiguration.	Tommaso Troise	pag 311
72	In situ planetary exploration: from Titan (Huygens-HASI), to Mars (ExoMars-Amelia/Dreams) and back to the outer solar system	Francesca Ferri	pag 313
73	Developing a NEO-Radar Capability in Europe: Upgrade Proposal for DSS-63	Giuseppe Pupillo	pag 315
74	Thermophysical modeling in the SSDC solar system exploration framework: towards future missions and planetary defense	Edoardo Rognini	pag 317
75	Exploring the lunar South Polar regions with MOONIS, the italian spectrometer on Rashid 3 rover	Maria Cristina De Sanctis	pag 319
76	Radiometric performance model for a notional imaging spectrometer as part of the "Uranus Flagship" mission	Beatrice Gorga	pag 322
77	The Lunar Earth Temperature Observatory (LETO) instruments on the Moon: Extending FORUM Cli-mate Datasets with Disk-Integrated Far-Infrared Observations	Simone Menci	pag 324
78	Observation strategy and performance analysis of MIST-A onboard the Emirates Mission to the Asteroid belt	Mauro Ciarniello	pag 326
79	A Multiband Imaging Camera for the Exploration of the Uranian Planetary System: Design and Expected Performance	Pietro Fraccaroli	pag 328
80	Spatial sampling in geologic investigations with GPR in planetary exploration.	Caterina Rossi	pag 330
81	Development of an additively manufactured temperature sensor for martian atmospheric measurements	Elisabetta Dolejsi	pag 332
82	Simulation, Planning and Visualization of MoonIS Operations	Lorenzo Rossi	pag 334
83	DAEDALUSCAM: measuring lava tubes to compare the effectiveness of robotic exploration	Javier Eduardo Suarez Valencia	pag 336
84	A feasibility study for an optical-IR spectrometer for a future Uranus mission: the atmospheric science case	Cfrancesco Camilloni	pag 338

XXI Congresso Nazionale di Scienze Planetarie

Sessione Pianeti e Satelliti
Marte

OXIA PLANUM, MARS: CHARACTERIZING CLAY-RICH REGIONS. F. Altieri[1], M. Rasmussen [1], J. Brossier[1], A. Frigeri[1], J. Trisic Ponce[1], M.C. De Sanctis[1], E. Bruschini[1], S. De Angelis[1], M. Ferrari[1], M. Formisano[1], L. Rossi[1], E. Ammannito[2], [1]INAF/IAPS, Via del Fosso del Cavaliere 100, 00133, Rome, Italy (francesca.altieri@inaf.it), [2]ASI, Via del Politecnico snc, 00133 Rome, Italy.

Introduction: Oxia Planum (Figure 1) is a region of Mars located on the margin between the old, heavily cratered highlands of Arabia Terra (Noachian-aged) and the younger, smoother lowlands of Chryse Planitia (Hesperian-aged). From orbit it shows several geomorphological records of past widespread water–rock interactions, including fractured, layered, clay-bearing deposits with high astrobiological potential [1, 2, 3]. For this reason, Oxia Planum has been selected as the landing site for the ESA Rosalind Franklin Mission (RFM). The main goal of the RFM is to search for past (and/or present) traces of life, particularly in the Martian shallow subsurface where material of astrobiological interest is better preserved. To achieve this, the RFM rover is equipped with a drill capable of collecting, for the first time for a mission on Mars, samples down to a depth of 2 meters, and with a suite of instruments designed to discriminate biosignatures in both the samples and their environment [4].

Here we focus on Regions of Interest (ROIs) within Oxia Planum that, according to remote sensing data, show the highest ferromagnesian clay content. Our aim is to systematically investigate correlations with geological units [5], fractures [6], and stratigraphy (from DTM, Digital Terrain Model), to better understand formation processes at Oxia and to contribute to strategies for selecting drilling sites once on Mars.

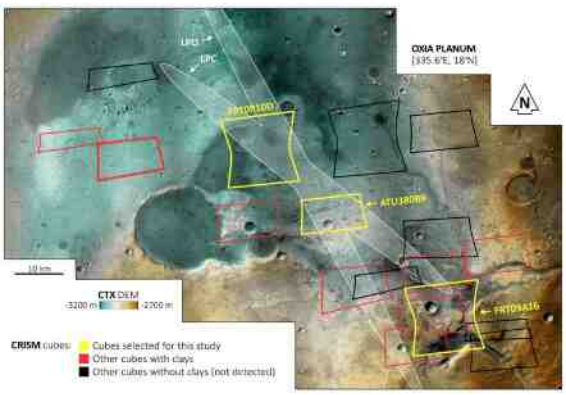


Figure 1 – Oxia Planum with CRISM data coverage. The CRISM data used in this study are shown in yellow footprints; red data also show clay deposits, while black data show no clay detections.

Dataset and Method: Clays on Oxia have been detected and mapped thanks to the OMEGA imaging spectrometer on ESA mission MEX (Mars Express), global coverage with mean spatial sampling of about 1 km/pixel, and the imaging spectrometer CRISM on board the NASA mission MRO (Mars Reconnaissance Orbiter), able to target smaller area with spatial sampling of about 20 m/pixel.

Geological units [5] have been classified using the data from the cameras that from orbit are still studying Mars: CTX (spatial sampling of about 5 m/pixel) and HiRISE (0.25 m/pixel) on MRO, and CaSSIS on TGO (Trace Gas Orbiter, ESA mission, 4 m/pixel).

In this work we are selecting ROIs from three CRISM hyperspectral cubes (Figure 1), based on the areas with the strongest spectral features diagnostic for ferromagnesian clay detection:
- northern part, CRISM cube c1: FRT0810D, Oct. 2007, where several clay deposits were detected;
- central part, CRISM cube c2: FRT09A16, Jan. 2008, closer to the landing site ellipse center;
- southern part, CRISM cube c3: ATU380B9, Sept. 2015, closer to the remains of a delta.

Figure 2 shows the ROIs we have targeted in CRISM cube c1.

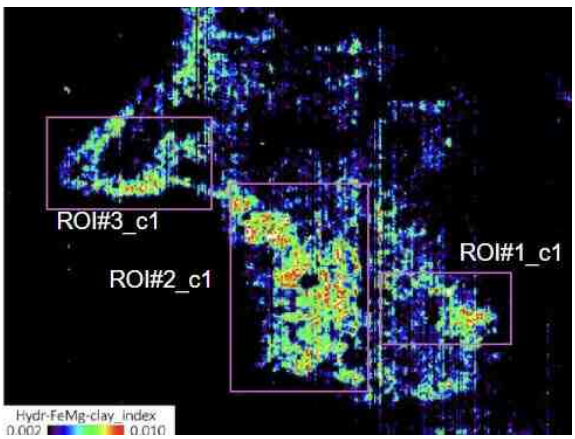


Figure 2 – Location of the three ROIs identified on CRISM cube c1 (not projected). ROIs are overlain on the map of a CRISM spectral parameter used to identify clay. Modified from [3].

Preliminary Discussion: Data analysis on ROI#1 from c1 confirms that on areas with the highest clay content fractured terrains exhibit more tightly spaced (1-5m) fractures and low relief relative to surrounding areas. We are studying the correlations with geological units mapped in [5], Figure 3. The background image in grey scale in Figure 3 is from HiRISE (spatial sampling about 25 cm/pixel) and the superimposed colored map is the spectral parameter "D2300" [7] from the CRISM dataset (spatial sampling about 18 m/pixel) used to map the presence of

clay (dark: low abundance, yellow: higher relative abundance).

Stereo pairs from CTX and HiRISE imagery can also be used to retrieve topographic profiles. To better understand and constrain water-related processes that may have occurred at Oxia and define the stratigraphic relationships of clay-rich deposits in the region, require reliable topographic profiles. DEM improvement is now in progress.



Figure 3 - Example of a ROI from FTR0810D (c1).

Conclusions: Once RFM is at Oxia, drilling sites will be carefully identified to maximize the scientific return of the mission and to optimize rover operation. Drilling to depths below 0.5 meters will need significant resources from the rover, and the sample collection sites shall be thoughtfully evaluated for selection. Our approach aims to support strategies for selecting potential drilling sites by providing a more comprehensive perspective of the clay-rich deposits based on orbital observations.

References:

[1] Mandon L. et al., 2021, *Astrobiology*, *21*(4), 464–480. https://doi.org/10.1089/ast.2020.2292.
[2] Quantin-Nataf, C., et al., 2021, *Astrobiology*, *21*(3), 345–366. https://doi.org/10.1089/ast.2019.2191.
[3] Brossier, J., et al., 2022, Icarus, 386, 115114. https://doi.org/10.1016/j.icarus.2022.115114.
[4] Vago, J., et al., 2017, *Astrobiology*, *17*(6–7), 471–510. https://doi.org/10.1089/ast.2016.1533
[5] Fawdon, P., et al., 2024, Maps 20 (1), 2302361, https://doi.org/10.1080/17445647.2024.2302361
[6] Apuzzo A. et al., 2025, Planetary and Space Science, Volume 267, 2025, 106169, https://doi.org/10.1016/j.pss.2025.106169
[7] Viviano-Beck, C. E., et al., 2014, *Journal of Geophysical Research: Planets*, *119*(6), 1403–1431. https://doi.org/10.1002/2014JE004627.

Acknowledgments: This activity is founded in the framework of the Accordo ASI – INAF n. n. 2023-3-HH.0.

THE GEOLOGY OF EAST TEMPE TERRA, MARS Alessandro Frigeri[1], Monica Rasmussen[1], Francesca Altieri[1], Jeremy Brossier[1], Janko Trisic-Ponce[1] and Maria Cristina De Sanctis[1]; [1]Istituto di Astrofisica e Planetologia Spaziali (IAPS), Istituto Nazionale di Astrofisica (INAF), Roma, Italy (alessandro.frigeri@inaf.it)

Introduction Tempe Terra is a region situated on the northern hemisphere of Mars at the northeast edge of the Tharsis Rise volcano-tectonic province, considered key for our understanding of Mars's geological evolution [1].

East Tempe Terra on Mars sits on the transition between Mars's ancient southern highlands and the low northern plains. The Martian dichotomy has always attracted the interest of science. Looking at the Martian global topography, the elevated cratered regions of the southern hemisphere contrast with the relatively smooth terrain north of the dichotomy. At the global scale, the transition between the southern highlands and northern lowland plains occurs on a sinuous boundary where topographic elevations drop 2000 to 4000 meters in a few hundred kilometers, with regional slopes of about 1 degree, two orders of magnitude larger than the southern and northern hemispheres alone [2].

Here we report our study of the geology of the East of Tempe Terra region and its relevance as a context for specific studies in spectroscopy. Through geologic mapping [3], we traced the elements for the description of the evolution of the area, from morphologic features to the definition of geologic units with their stratigraphic relationships and absolute ages.

Geographic and Physiographic setting Our 200 by 300 km study area is located between the Syntiskaya crater and Tempe Fossae (42.5-47.5 °N, 300.0-305.0 °E). The topography dips towards the northeast, with a total elevation decrease of about 2000 meters. Plateaus constitute the general morphology of the area with their flat, slightly dipping surfaces set at different elevations. A set of parallel elongated valleys oriented NNE-SSW shows mounds, pitted terrain, and fan deltas. The action of erosion is evident in the lower plateau unit, where we found evidence for inverted morphologies of old channels and craters, as specifically reported by [4] and what was documented eastward by [5].

The main morpho-tectonic features of the area are wrinkle ridges and linear fractures. Linear fractures are oriented ENE-WSW, similar to the general trend of the Tempe Terra fault system. Crater floors and ejecta show a wide range of deposits, mostly interpreted as the product of impact on a volatile-rich underground.

Among the others, the area contains a series of 0.5 to 2 km wide fresh craters. One of these craters was studied by spectral analysis [6], highlighting an anomalously large abundance of seasonal water ice on the ejecta, providing new insights into ice variation in the Martian ground. In our companion work [7], we classified the craters on the bases of their ejecta morphology and described pattern in their spatial distribution.

Geology The region preserves a superposition of volcanic surfaces, compressional structures, Tharsis-related grabens, fluvial channels, erosional scarps, and ice-related landforms. These features provide a traceable record of the interplay between volcanism, tectonism, climate-driven water activity, and long-term erosion from the late Noachian through the Amazonian. The area also contains clear indicators of past ground-ice mobilization and episodes of surface water flow.

The oldest unit (P1) was laid down as a volcanic surface with a wrinkle ridges still visible. The surface of P1 unit was then marked by impacts.

A second major resurfacing event emplaced the P2 plateau, interpreted to be volcanic in nature, burying parts of P1 and armoring many older features under new material. The P2 unit shows the action of a first generation of erosion by water, forming valleys cutting P2, in some cases carved all the way down into P1, creating the first generation of valleys. A massive erosional event removed portions of the P2 unit, exposing P1 and producing the multi-level plateau

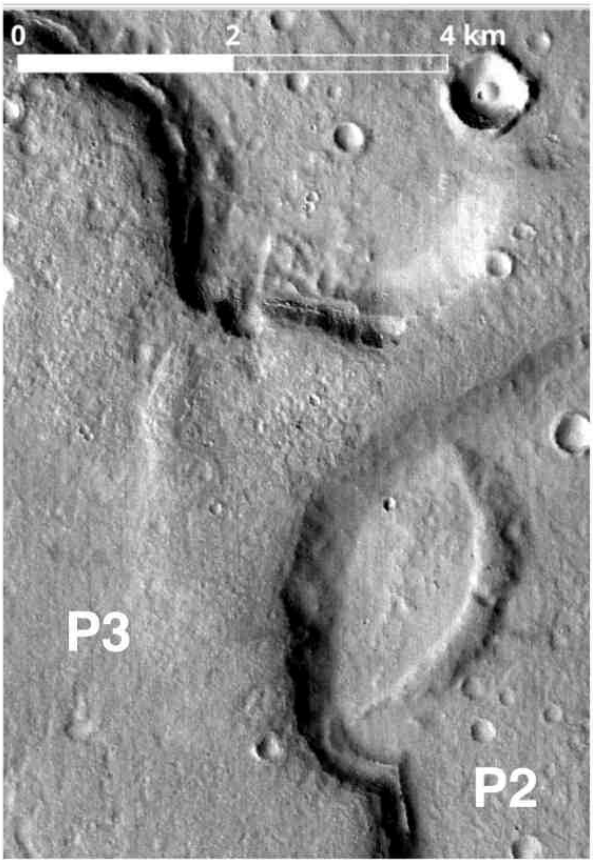


Figure 1: Stratigraphic contact of plateau unit P3 over P2, MRO/CTX image mosaic data (center is 43.008°N, 57.216°W).

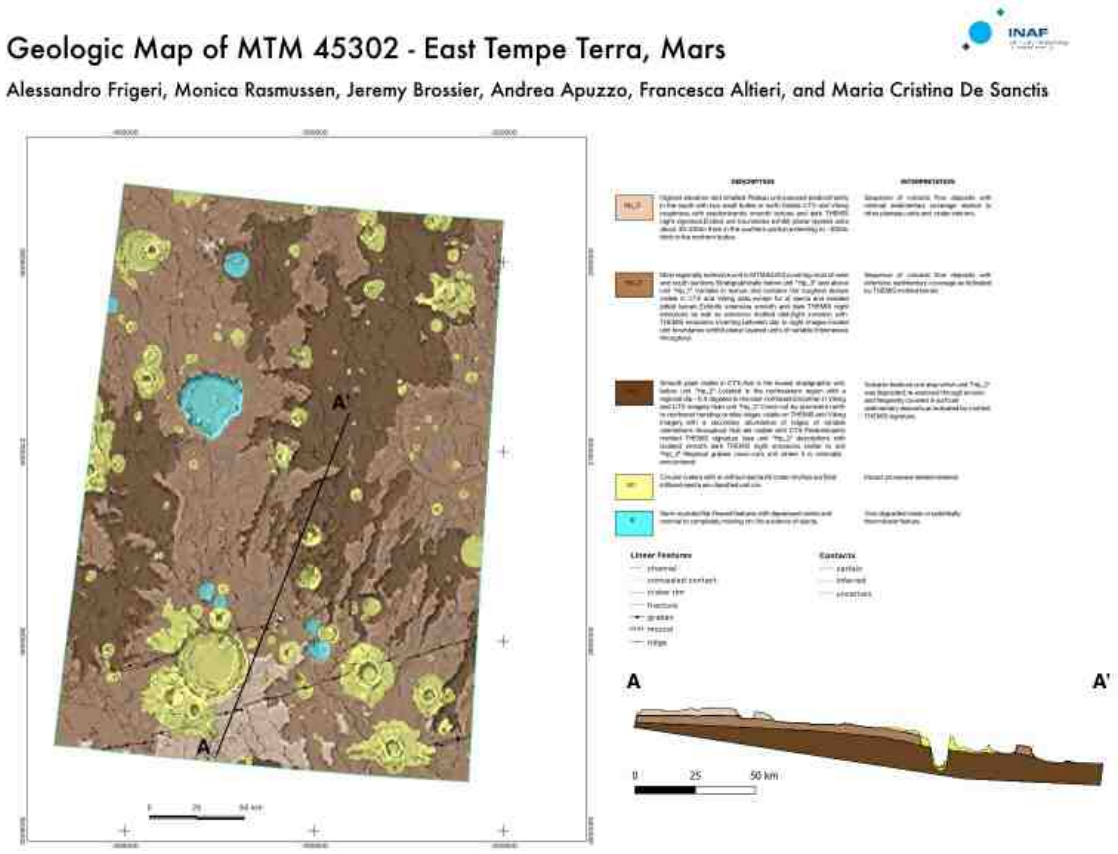


Figure 2: The draft of the 1:1M geologic map of East Tempe Terra [3]. Main map units P1, P2, P3 described in the taxt are reported in shades of brown. The geologic cross-section A-A' on the right refers to the black segment in the main map.

structure. This stripping also re-exposed older channels and inverted ridges, preserving a snapshot of the different erosion phases. Unit P3 emplaced over P2 (see Figure1) with a process analogous to the emplacement of P2, and then the Tempe Terra ENE-trending grabens sliced the southern sector of the study area. These fractures cut through earlier channels and wrinkle ridges, showing that tectonic processes were still active after the surface had already seen water and erosion.

In the final stages of modification, melting ground ice created small collapses, scalloped scarps, seep-like alcoves, and occasional viscous-flow deposits. These ice-related features overprint the older tectonic and fluvial landscape, with the distinctive etched and highly reworked appearance we see today. The geologic map we are developing and reported Figure 2, synthesize the evolution and current setting of the area.

Conclusions and Future Work Our study describes the geologic history of the area from the emplacement of the units to their modification by cratering, fluvial, and ice-related processes. We are finalizing the geologic mapping, specifically the extraction of absolute unit ages from crater size frequency-distribution. East Tempe Terra is an archive of Mars's structural, climatic, and erosional history, with direct implications for understanding planetary evolution and planning future exploration. Our study is serving as context for spectroscopic [6] and geomorphologic studies [7] which in turn, will improve our knowledge on the geologic evolution of the area.

Acknowledgements: This work is supported by ASI-INAF contract n.2023-3-HH.0 *Esplorazione di Marte*

References: **[1]** C. J. Orlov et al. In: *Journal of Geophysical Research: Planets* 127.11 (2022), e2022JE007407. **[2]** M. T. Zuber et al. In: *Journal of Geophysical Research: Planets* 97.E5 (May 25, 1992), pp. 7781–7797. **[3]** A. Frigeri et al. In: *Geological Society of America Abstracts, Vol. 57, No. 6*. 2025. **[4]** Z. Liu et al. In: *Earth and Planetary Science Letters* 562 (2021), p. 116854. **[5]** J. Brossier et al. In: *Planetary and Space Science* 247 (2024), p. 105924. **[6]** F. Furnari et al. In: *Congresso di Scienze Planetarie abstract book*. 2024. **[7]** M. Rasmussen et al. In: *Geological Society of America Abstracts, Vol. 57, No. 6*. 2025.

WIND STREAKS IN THE EXOMARS 2028 LANDING SITE. S. Silvestro[1,2], D.A. Vaz[3],1, F.M. Grasso[4], D. Tirsch[5], E. Favaro[6], Y. Caddeo[7], F. Salese[7], C.I. Popa[1], G. Franzese[1], G. Mongelluzzo[1], C. Porto[1], M. Pajola[8], F. Esposito[1]. [1]INAF, Osservatorio Astronomico di Capodimonte, Napoli, Italy (simone.silvestro@inaf.it). [2]SETI Institute, Mountain View, CA, USA. [3]CITEUC, University of Coimbra, Portugal. [4]CNR ISAC Lecce, Italy. [5]Inst. Planetary Res., DLR, Berlin, Germany. [6]ESA/ESTEC, Noordwijk, the Netherlands. [7]IRSPS, Università G. d'Annunzio, Chieti-Pescara, Italy, [8]INAF, Osservatorio Astronomico di Padova, Italy.

Introduction: The ESA ExoMars mission will land at Oxia Planum to search for signs of life on Mars [1, 2] (Fig. 1a). Aeolian processes play a significant role in shaping the landing surface, evidenced by documented features like dust devil tracks, bright bedforms (transverse aeolian ridges [TARs]), and erosive wind-formed ridges (periodic bedrock ridges [PBRs]) [3-6]. However, little attention has been paid to wind streaks, which are abundant in the landing site and provide valuable insights into recent climatic conditions. These features are the focus of our attention (Fig. 1).

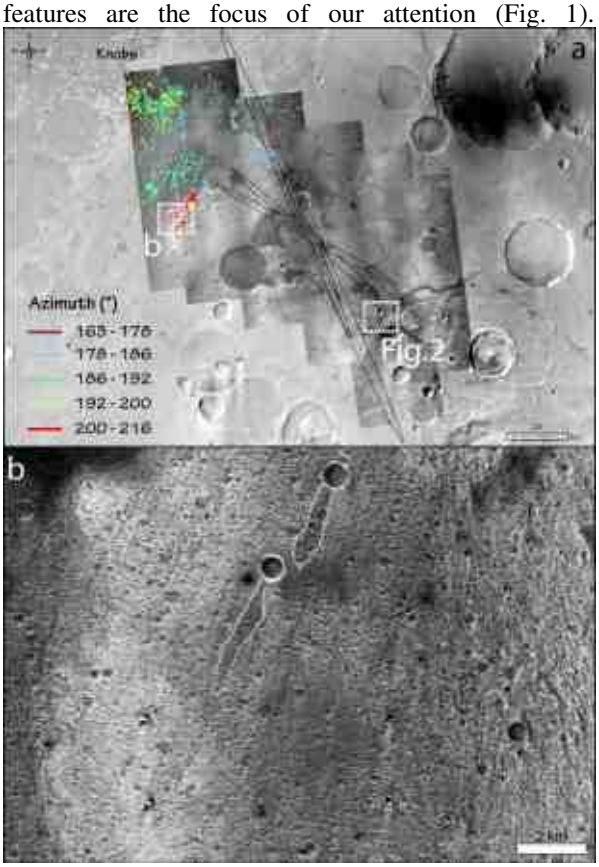


Fig. 1: Mapped wind streaks and stripes (n = 954) in Oxia Planum. **a)** The study area is limited by the Context Camera (CTX) mosaic, which was used for mapping the streaks and integrated with CaSSIS data. Wind streaks are colored by their azimuth (°). **b)** Dark, elongated stripes are better preserved in the lee of impact craters and were formed by winds coming from the NE.

Methods: A total of 954 wind streaks were manually mapped in the study area within a GIS environment (Fig. 1). Mapping was performed by leveraging the broad coverage of CaSSIS (4 m/pixel) and CTX (6 m/pixel) mosaics, with details validated using high-resolution HiRISE images (50-25 cm/pixel). Because the main focus of this report is the wind streak orientation, data were projected using a Lambert Conformal Conic (LCC) projection centered in Oxia Planum to minimize directional distortion. The vast majority (n = 784) of the mapped features are bright-toned, while n = 170 are dark-toned, elongated streaks or *stripes*.

Results: Previous studies have documented the presence of differently oriented dust devil tracks in the landing area [4, 5]. In this work, we report the presence in the study area of different types of linear features that we interpret having an aeolian origin (Fig. 1).

Bright-toned wind streaks, oriented towards the SSW (mean azimuth 189°) and indicating winds originating from the NNW–NNE, are especially abundant in the NW sector of the study area (Fig. 1a). This spatial arrangement is likely due to the high number of local topographic obstacles (craters and knobs) in this sector, which favor the nucleation and preservation of these features (Fig. 1a). Analysis of the orientation distribution reveals slight variations, allowing us to distinguish two to three distinct sub-populations that are interpreted as being controlled by the regional topography.

Dark-toned stripes: We refer to these features as 'dark-toned stripes' to distinguish them from the classic dark wind streaks associated with topographic obstacles [8]. These stripes form a dark-toned 'streaky' pattern with a main NE-SW trend (red lines in Fig. 1b). At the HiRISE scale, they consist of elongated dark patches covering the bright, clay-enriched unit, which is the main scientific target of the mission [2]. Furthermore, the presence of small scarps suggests a degree of consolidation or cementation, similar to the 'dark patches' previously reported [9]. Interestingly, these stripes are better preserved in the lee of some ~ 600-m-large impact craters (white dashed line in Fig. 1b), suggesting formative winds blowing consistently from the NE to the SW. The resulting orientations of the dark stripes thus significantly differ from the nearby bright streaks (red/blue lines in Fig. 1a). Further analysis (Fig. 2) details the SSE-oriented dark stripes (3) found in close association with a ~2-km-large impact crater. Both

CaSSIS and HiRISE data confirm that these dark-toned stripes (3) are formed by a smooth, dark-toned ejecta blanket (2) that has been preferentially preserved along the southern rim of the crater, directly overlying the bright clay-enriched bedrock (1). The stripes exhibit fracturing and small impact craters, suggesting a degree of induration (cementation or consolidation). Their orientation is slightly divergent but similar to the bright wind streaks in this sector, suggesting control by the current regional wind regime. Crucially, a distinct dark-toned wind streak (4), likely depositional, is also observed emanating from the same crater. This streak appears as a blue sandy halo in the HiRISE color composite (Fig. 2b), underscoring the difference between these mobile, eolian features (4) and the more consolidated, ejecta-controlled dark stripes (3).

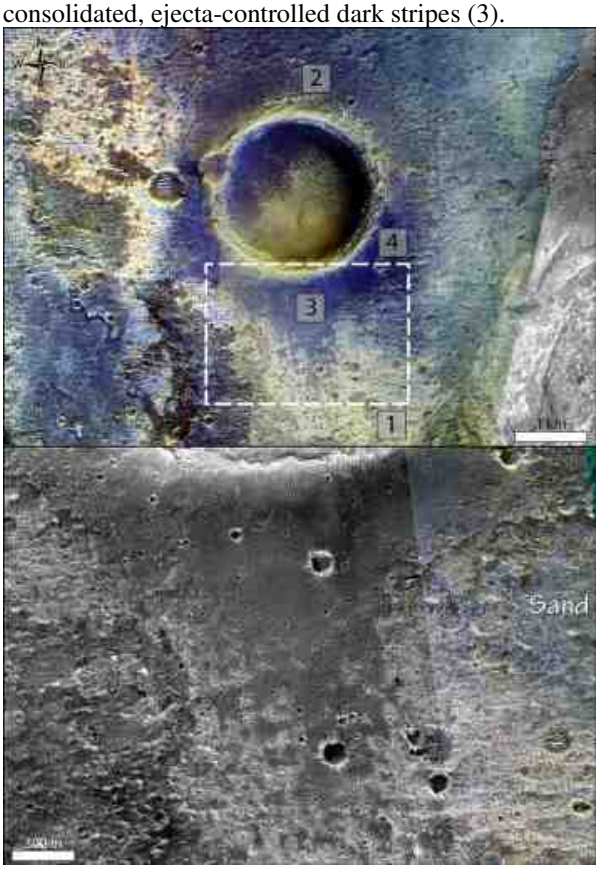


Fig. 2: a) Dark stripes (3) found in the lee of a ~ 2-km-large impact crater (**see Fig. 1a for location**). Key features labeled are: (1) Bright Noachian bedrock, (2) Crater ejecta, and (4) a dark depositional streak (Type 2 in [8]). CaSSIS NPB MY34_005012_018_2. **b)** Detail of the stripes (3), which are formed by the same smooth (at the HiRISE scale) crater ejecta blanket (2). Note the bluish area on the right, which is interpreted as a thin sand mantle and corresponds to the dark streak (4). HiRISE PSP_007019_1980 (RED & IRB).

Discussion: Our findings suggest the presence of a new class of Martian aeolian feature. Unlike all previously described wind streaks, which consist of loose material (sand, dust, or frost) [8, 10-12], the features presented here appear to be composed of consolidated material. Specifically, the dark stripes in the lee of the crater in Fig. 2 can be interpreted as an *'aeolian preservation streak'*. This feature arises from the differential erosion of a consolidated unit (crater ejecta blanket) by winds from the N-NNW, thereby preserving the ejecta in the erosional shadow of the crater rim while exposing the underlying Noachian bedrock. The orientation of this feature is consistent with the bright wind streaks in the same area, suggesting the N-NNW wind regime has been dominant in shaping the landscape over geological timescales. An alternative explanation, currently under evaluation, is the asymmetrical distribution of ejecta due to a high-angle impact. The stripes shown in Fig. 1b, particularly where they cluster behind topographic obstacles (dashed in Fig. 1b), can also be interpreted as preservation streaks. Although their degree of consolidation remains to be definitively determined (a question the ExoMars Rover might address), their orientation differs slightly from the bright streaks. This divergence suggests either a different formation timeline (if consolidated, only long-term winds could shape them) or a stronger local topographic control on the wind regime.

Conclusion: Our results show two distinct populations of streaks and suggest the presence of a new type of feature (the *'aeolian preservation streak'*) composed of consolidated material, indicating the dominance of northerly winds over geological timescales; this novel hypothesis requires crucial validation by the ESA Rosalind Franklin rover.

References: [1] Vago J. et al. (2017). Astrobiology, 17. [2] Quantin et al. (2021), Astrobiology, 21. [3] Balme M. et al. (2017), PSS, 153, 39-53. [4] Silvestro S. et al. (2021), GRL, 48. [5] Favaro E. et al. (2021), JGR, 126. [6] Favaro E. et al. (2024), EPSL, 626. [7] Greeley R. et al. (1978), Icarus, 34. [8] Thomas P. et al. (1981), Icarus, 45. [9] Fawdon P. et al. (2024), Journal of Maps, 20. [10] Silvestro et al. (2014), 8th Int. Conf. on Mars, abst#1193. [11] Fenton et al. (2015). Aeol. Res.,16. [12] Silvestro et al. (2015), JGR, 120, 4. **Acknowledgement:** The results reported here were obtained in the context of the Earth-Moon-Mars (EMM) project, led by INAF in partnership with ASI & CNR, funded under the National Recovery and Resilience Plan, Mission 4, Component 2, Investment 3.1: “Fund for the realisation of an integrated system of research and innovation infrastructures" Action 3.1.1 funded by the EU, NextGenerationEU.

NUMERICAL MODELIZATION AS A WAY TO INFER WATER CONTENT IN MARTIAN LANDSLIDES. A. Caramanico[1], L. Lanci[1], M. I. Herreros[2], M. Francioni[1] and P. Stocchi[1], [1]Dipartimento di Scienze Pure e Applicate, Università di Urbino "Carlo Bo" (first author e-mail address: a.caramanico1@campus.uniurb.it), [2]Centro de Astrobiologìa (CAB) CSIC-INTA, Madrid.

Introduction: Mass wasting is a geological process reported in almost every rocky body of our solar system [1], although the debate regarding the dynamics and the presence of water in martian landslides is still ongoing. The low percentage of well characterized landslides on Mars (especially from the mechanical point of view) contributes to the general lack of useful data to solve the issue. For this reason, we propose a combination of geomorphological analyses and numerical modeling performed on two different models to prove the mechanical properties of a minor landslide (volumes < 10^{10} m^3) and estimate the water content involved in the landslide's dynamics. Crater counting technique was also used to give an age to the landslide and temporally constrain its rheological properties (and environmental conditions) to a certain period of Mars history.

Methodologies: The dataset used in this research combines CTX (Context Camera, 5,99 m/px) dataset with a single HRSC (High Resolution Stereo Camera) derived DEM (Digital Elevation Model, up to 10m/px of vertical accuracy) covering the entire impact crater. This data combination allowed us to perform detailed measurements on DEM file (total runout distance "ΔL", total drop height "H", width of the deposits "W", levee height "h"), to estimate the volume of the deposits in the accumulation zone (useful for balancing the topographic reconstructions and ensuring mass conservation during simulations), and to make accurate observations regarding the morphologies and surface features of the landslide. Some of these physical measurements were used for calculating parameters to use in simulations [2, 3].

Topographic profiles of the basal and pre-event topography were reconstructed and used as input for the numerical simulations. For the sake of objectivity, we performed simulations with two differend models: our in-house model [3, 4, 5] and the commertial software MADflow [6]. The aim was to obtain a good match between the simulation results and the observed extension, shape and thickness of the actual landslide. In this way, we may infer the dynamics of failure and the water content involved in such a mass movement.

The modeling phase consisted of a systematic parametric analysis. The range of the parameters used in the simulations was extracted from experimental studies [7, 8] and bibliography [8].

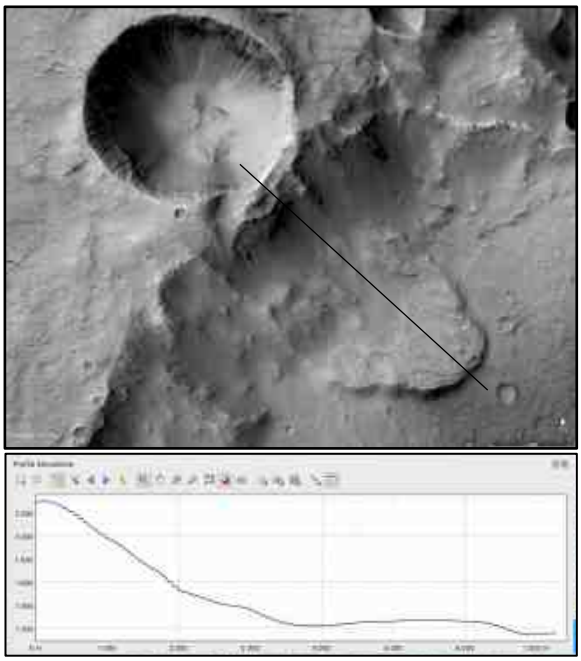


Figure 1*: A close-up view to the landslide studied in this work and, below, its longitudinal profile; on CTX resolution (~ 6 m/px), it is easy to trace the boundaries of the lobate front, different sections (erosion, transport and accumulation zone), the surface texture and the lateral extension; on top of the scar, a secondary crater shows seepages on its walls. (source: Google Mars)*

Case study: We chose to apply these methods to a martian landslide located in an unnamed impact crater of the Noachian highlands, close to the basin of Utopia Planitia (**Fig.1**). Among the reasons that drew our selection to this specific site, the most important are (i) the characteristic long runout and (ii) the lobate front of the landslide's deposits, some geomorphological clues that may favor a possibly visco-cohesive material (i.e. suggesting water involvment). Moreover, in the surrounding of the crater, there are outcrops of clay minerals and a secondary impact with evindences of seasonal seepages (RSL) on top of the landslide's scar. This may be a good candidate on which to test our hypothesis through numerical simulations and rheologies that include both frictional and cohesive parameters.

Results: The best match obtained with our in-house model corresponds to a Bingham material, whereas with MADflow the best match is obtained for a Coulomb-viscous fluid. It is worth noting that, despite the differences in the model formulations, both seem to favor the hypothesis of a visco-cohesive

material, suggesting the possible presence of water in the interstitial pore space. The shape of the deposits, as well as their thickness and lateral extent, is in good accordance with the observations, with tolerable discrepancies. The values of density, viscosity and yield stress used in the simulations allow us to estimate the water content in the mixture.

The numerical results, combined with geomorphological features of the landslide and the surrounding environment, suggest that water may have been involved in this geological process.

Crater counting results gave an age of approximately 220 Ma, highlighting the recent nature of the studied landslide and subsequently the hypothesized presence of water in this site in a recent martian time (Late Amazonian).

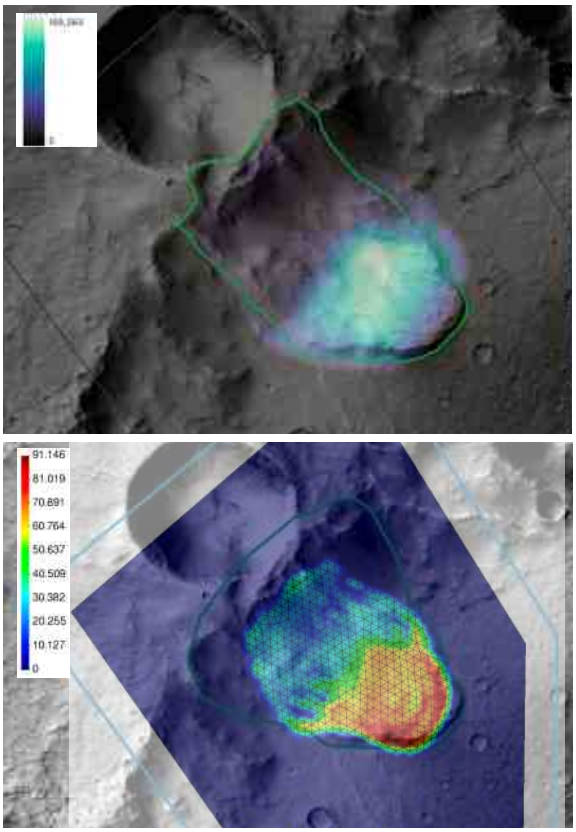


Figure 2*: Graphic visualization of results from simulations with ourin-house model (on bottom) and MADflow (on top), in QGIS environment; there are some discrepancies between real data and simulated output, but both the models seem to reproduce well the shape and thickness of landslide's deposits for a viscous-cohesive material.*

References: [1] Brunetti M. and Peruccacci S. (2023) *Oxford Res. Enciclopedya of Planet. Sci.,* https://doi.org/10.1093/acrfore/9780190647926.013.254. [2] Guimpier A. et al. (2021) *Planet. & Space Sci., 206,* 105303. [3] Quecedo, Pastor, Herrero et al., (2004) Int. J. Numer. Meth. Eng., 59, 755–79. [4] Pastor, Herreros et al. (2009). Engineering Geology, 109 (1–2), 124–134. [5] Herreros, Molina et al. (2021), EPSC2021-116, https://doi.org/10.5194/epsc2021-116. [6] Chen J. H. and Lee C. F. (2007) *International Forum on Landslide Disaster Management*, ISBN 978-962-7619-30-7. [7] Maciel F. G. et al. (2008) *J. Braz. Soc. Mech. Sci. & Eng. Vol. 31 no.1,* https://doi.org/10.1590/S167858782009000100 010. [8] Leyva de-la-cruz B. et al (2016) *Ing. Mech. Vol. 19 no.3, pag.143-149.* [9] Delage P. et al. (2022) *XX International Conf. on Soil Mech. & Geotech. Eng.*

STUDY OF COMPOSITIONAL VARIABILITY OF PHOBOS AND DEIMOS SURFACES USING TGO/CASSIS IMAGES. J. Beccarelli,[1,2], G. Munaretto[2], M. Pajola[2], A. Lucchetti[2], G. Cremonese[2], N. Thomas[3], G. Poggiali[4], A. Valantinas[5] ,F. Tusberti[2], L. Penasa[2], C. Rossi[2], L.L. Tornabene[6,7], M. Almeida[3], M. Read[8], K. Mason-Piercy[3], M.R. Patel[8]; **1)**Centro di Ateneo di Studi e Attività Spaziali - "Giuseppe Colombo (CISAS/UniPD), Via Venezia 1, 35131, Padova (PD), Italy, e-mail: joel.beccarelli@studenti.unipd.it; e-mail: joel.beccarelli@inaf.it; **2)**Istituto Nazionale di Astrofisica, Osservatorio Astronomico di Padova (INAF/OAPD), Vicolo dell'Osservatorio, 5, 35122, Padova (PD), Italy; **3)**Physikalisches Institut, Sidlerstr. 5, University of Bern, CH-3012 Bern, Switzerland; **4)**INAF Osservatorio Astronomico di Arcetri, largo E. Fermi n.5, I-50125 Firenze, Italy; **5)**Brown University, Department of Earth, Environmental and Planetary Sciences, 180 Thayer St, Providence, RI 02912, USA; **6)**Institute for Earth and Space Exploration, University of Western Ontario, Dept. of Earth Sciences, 1151 Richmond Street, London, Onatrio, N6A 5B7, Canada; **7)**The SETI Institute, 339 Bernardo Ave, Suite 200, Mountain View, CA 94043, United States; **8)**School of Physical Sciences, The Open University, Walton Hall, Milton Keynes, UK.

Introduction: The Martian system comprises Mars and two natural satellites, i.e., Phobos and Deimos. Although their origins remain uncertain, two theories seek to explain their physical and orbital parameters: the gravitational capture of a carbonaceous and primitive asteroid **[1]** and the giant impact between Mars and another body **[2-4]**. Ref. **[5]** has firstly divided Phobos' surface into two main spectral units, based on the different Vis/NIR spectral ratio. While the blue unit exhibits a higher albedo in the visible, and it is associated with the biggest Phobos crater Stickney (9 km in diameter), the red unit gets redder with increasing wavelength and dominates the rest of the surface. A third unit has been observed, called *transitional*, which originated from the mixing between the two units **[5,11]**. Although the two moons revealed a featureless spectrum, a band at 650 nm has been detected by analyzing MRO/CRISM **[13]** data in both red units **[6].** Such a feature has been attributed to either desiccated nontronite or to the presence of Fe nanoparticles created by the action of the space weathering (SW) and/or by micrometeorite impacts **[7-8]**. On the contrary, a feature in VIS-NIR linked to a mafic mineralogy has been reported close to 1000 nm in Phobos red unit by **[9-10]**, and in MeX/OMEGA data **[12]** only in the blue unit by **[11]**. In late 2026, the Japanese space agency JAXA is scheduled to launch the Martian Moons eXploration (MMX) mission, whose primary objective is to shed light on the origin of the Martian system **[24]**.

In this work, we analyze five Colour and Stereo Surface Imaging System (CaSSIS **[14]**) cubes, a stereocamera on board the ESA/Trace Gas Orbiter (TGO), intended for image acquisition at four different wavelengths: 499.9 nm (BLU), 675.0 nm (PAN), 836.2 nm (RED), and 936.7 nm (NIR). Such camera has been proven to be very sensitive in distinguishing ferric and ferrous mineralogy **[15].** In particular, ferrous minerals show a distinctive band at about 1000 nm due to the electronic transition of the Fe^{2+}, and are typically found in olivine and pyroxene, thus indicating a mafic composition **[16]**. Conversely, ferric minerals show specific features between 500 nm and 700 nm due to the Fe^{3+} transitions occurring in minerals such as hematite and goethite **[16]**. As shown by **[15],** these different mineralogies can be identified using specific CaSSIS band ratio, where high values of PAN/BLU and RED/PAN are associated with a ferric composition, while a high value of PAN/NIR and RED/NIR to a ferrous one.

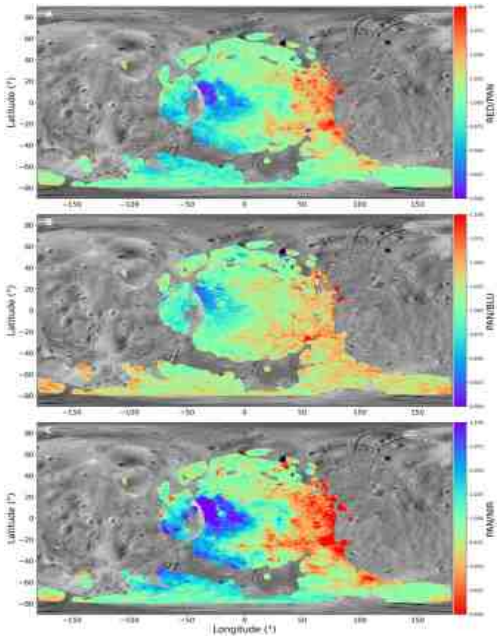


Figure 1. Equirectangular maps of RED/PAN (A), PAN/BLU (B), and PAN/NIR (C) on Phobos' surface.

Methods: We selected four sets of CaSSIS images for Phobos and one for Deimos. For each set, we computed a map of geometrical parameters, including local incidence, emission, and phase angles as well as equirectangular longitude and latitude, using the NAIF SPICE Kernel toolkit **[17]** via the *Spiceypy* library **[18]**. Since the position of the target in different CaSSIS filter acquisitions is not constant and the illumination angle maps are not perfectly aligned due to inaccuracies in SPICE Kernels, we apply an alignment pipeline using the *Elastix* Python library **[19].** We then photometrically correct each image with the *Lommel-Seeliger Disk-Function* (LS)*,* suitable for dark surfaces such as Phobos and Deimos **[20-21]**. From each cube, we compute the band ratios following the procedure described by **[15]** to trace the presence

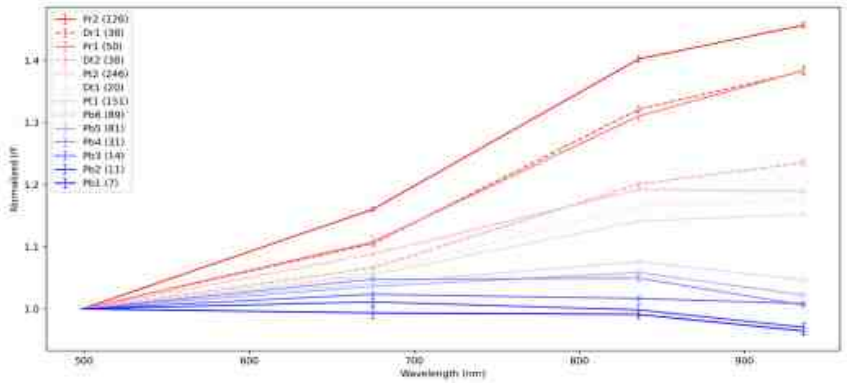


Figure 2. Mean spectra normalized to the BLU filter and with associated standard errors. The number of pixels belonging to each ROI is reported in the legend. The notation is as follows: P=Phobos, D=Deimos, "b", "r", and "t" are respectively blue, red, and transitional units.

of ferrous and ferric minerals on the surface of Phobos and Deimos. Finally, we identified *Regions of Interest* (ROIs) focusing on the PAN/NIR across the whole surface and extracted mean spectra to study the spectral variability of the two moons.

Results and Conclusions: As shown in **Fig. 1. A-B**, the RED/PAN and PAN/BLU ratios are higher for the red unit of Phobos, consistent with the presence of ferric minerals. In contrast, the blue unit exhibits a higher PAN/NIR spectral ratio (**Fig. 1.C**), indicative of the 1000 nm absorption band, and therefore, of the presence of ferrous minerals such as olivine and pyroxene. The normalized mean spectra of the Phobos blue unit (Pb1-6 in **Fig. 2**) consistently show a decrease of the I/F toward the 1000 nm wavelength, whereas the red unit spectra (Pr1-2 in **Fig. 2**) do not show such a decrease and instead become redder at longer wavelength. A subtle decrease in the PAN filters for the Phobos red unit spectra may be an indication of a band in the range 500-700 nm, consistent with the presence of Fe nanoparticle agglomerates originated from intense SW or micrometeorite impacts **[6]**. This supports the hypothesis that the red unit represents an older material relative to the blue unit. The observed correlations between the two units and the band ratios further suggest distinct mineralogies and, hence, potentially different origins. Phobos' bulk material may consist of material similar to the red unit, whereas the blue unit may have originated from an exogenous source, i.e., non-indigenous to Phobos, also in agreement with recent studies, e.g., **[23]**. From **Fig. 3,** a similarity between Deimos' surface and Phobos' red unit can be inferred. In particular, most of the regolith is associated with high RED/PAN or low PAN/NIR. However, blue bright spots can be identified (see white arrows in **Fig. 3A**), which correlate with higher values of PAN/NIR (e.g., **Fig. 3D**). This kind of behaviour is consistent with recent works published on MeX/HRSC data **[22]** and may indicate the possibility that the same material that forms Phobos blue unit, also reached Deimos. However, the spectra of Deimos do not show a decrease toward 1000 nm, which mayimply a higher mixing factor between blue and bulk material. In particular, the spectra obtained from the blue bright spot ROIs are consistent with a transitional Phobos unit (see Dt1 and Dt2 in **Fig. 2**), while the rest of the surface is compatible with the red unit (Dr1).

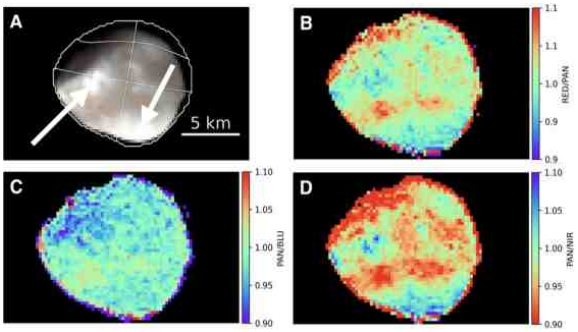


Fig 3. A) RGB (R = RED, G =PAN, B=BLU) color composite of the Deimos cube with latitude and longitude grid; B) RED/PAN (normalized to 1.1327); C) PAN/BLU (normalized to 1.0899); D) PAN/NIR (normalized to 0.8683).

References: **[1]** Hansen, B. M. S. 2018, *MNRAS*, 475, 2452–2466; **[2]** Craddock, R. A. 2011, *Icarus*, 211, 1150; **[3]** Rosenblatt, P. & Charnoz, S. 2012, *Icarus*, 221, 806; **[4]** Hyodo, R. et al., 2018, *APJ*, 860, 150; **[5]** Murchie, S. L. et al. 1991, *JGR*, 96, 5925; **[6]** Fraeman, A. et al. 2014, *Icarus*, 229, 196; **[7]** Pieters, C. M. et al. 2000, *Meteor. & Planet. Sci.*, 35, 1101; **[8]** Sasaki, S. et al. 2001, *Nature*, 410, 555; **[9]** Murchie, S. & Erard, S. 1996, Icarus, 123, 63; **[10]** Gendrin, A. et al. 2005, *JGR*, 110; **[11]** Pajola et al. 2025, *A&A,* A56; **[12]** Bibring, J.-P. et al. 1989, *Nature*, 341, 591; **[13]** Murchie, S. et al. 2007, *JGR*, 112; **[14]** Thomas, N. et al. 2017, *Sp. Sci. Rev*, 212, 1897; **[15]** Tornabene, L. L. et al. 2018, *Sp. Sci. Rev.*, 214, 1; **[16]** Clark, R. N. 2004, *Mineralogical Association of Canada*, 17–55; **[17]** Acton Jr, C. H. 1996, *Planet. Sp. Sci.*, 44, 65; **[18]** Annex, A.M. et al. 2020, *JOSS*, 5, 2050; **[19]** Klein, S. et al. 2009, *IEEE transactions on medical imaging*, 29, 196; **[20]** Pajola, M. et al. 2018, *Planet. Sp. Sci.*, 154, 63; **[21]** Fornasier, S. et al. 2024, *A&A*, 686, A203; **[22]** Wargnier, A. , et al. 2025, *A&A*, 694, A304; **[23]** Munaretto, G. et al. 2025, *A&A*, 700, L1; **[24]** Kuramoto, K. et al. 2022, *Earth, Planet. Sp.*, 74, 12.

PREPARATION FOR MIRS INVESTIGATION ON PHOBOS AND DEIMOS IN THE FRAMEWORK OF THE MMX SAMPLE RETURN MISSION. G. Poggiali[1], J. R. Brucato[1], A. Alberini[1], M. Pajola[2], J. Beccarelli[3,2], L. Ruiz Lozano[4], A. Wargnier[5,6], K. Yumoto[5], S. Fornasier[5], M. A. Barucci[5] 1 INAF-Astrophysical Observatory of Arcetri, l.go E. Fermi n.5, 50125 Firenze, Italy (giovanni.poggiali@inaf.it); 2 INAF-Astronomical Observatory of Padova, Padova, Italy;3 Centro di Ateneo di Studi e Attività Spaziali - "Giuseppe Colombo (CISAS/UniPD), Padova, Italy; 4 Royal Observatory of Belgium (ROB), Brussels, Belgium; 5 LIRA, Observatoire de Paris, Universités PSL, Sorbonne, Paris Cité, CY Cergy Paris, CNRS, Meudon, France; 6 ISAS JAXA, Sagamihara, Japan

Introduction: Martian Moon eXploration (MMX) mission [1], set to be launched in autumn 2026, will reach the Martian system to start a detailed investigation of the two moons of the Red Planet, Phobos and Deimos, and bring back a sample from Phobos, the biggest moon, in 2031. The primarly mission objective is to shed a light on the puzzling origin of the two moons of Mars to clarify if they formed after a giant impact on Mars [2] as suggested by the modeled orbital parameters, or if they are two captured primitive dark asteroids [3], as inferred by remote sensing observation. Among all the payload instruments, the MMX InfraRed Spectrometer (MIRS) [4] will be critical to characterize the surface of the Martian moons (Figure 1). This instrument will be pivotal to investigate the mineralogical composition of the surface and the possible presence of volatiles and organics.

In the growing interest of the scientific community around Phobos and Mars in preparation of MMX mission, it is essential to increase the laboratory work using analog samples, exploiting all the data we possess to prepare and support the future exploration. The ESA Mars Express (MEx) mission hosting OMEGA and PSF spectrometers as well as the HRSC multifilter camera represents the most suitable tool to built an essential dataset for the study of the two martian moons.

In parallel, laboratory is the main tool to interpret the effect of physical properties such as grain size, composition, porosity and space weathering on the remote sensing data using simulant, and analog materials (either minerals or meteorites).

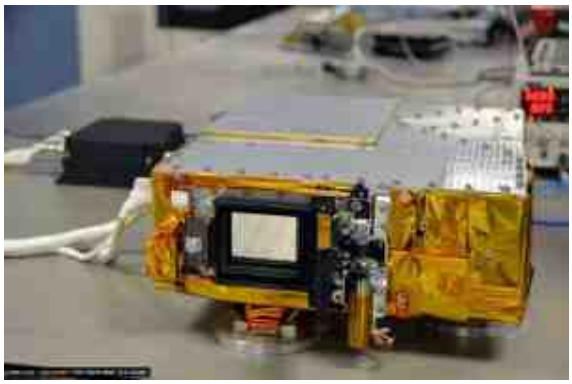


Figure 1. MIRS flight model at LIRA laboratory before shipping to MELCO for integration on MMX spacecraft (credit: LIRA/MIRS team/S. Cnudde)

The synergy between remote sensing and laboratory approaches can open the door to more complex and meaningful interpretation of the remote sensing observations and Phobos investigation by MMX represent one of the best opportunity.

Moreover, the community's interest in Phobos and Deimos science was confirmed by the decision of ESA to allow a fly-by of the moon Deimos with ESA's Hera spacecraft during its journey to the binary asteroid Didymos-Dimorphos. The probe acquired several images of the moon and Mars with its instruments, including the Hyperscout spectrophotometer and the TIRI thermal camera.

Methods: In this study we will show the importance of a close synergy between complex laboratory analysis and the interpretation of remote sensing data. The presentation will go through the reanalysis and interpretation of archive data from the ESA Planetary Science Archives in particular of the MEx mission. We will show data from OMEGA [5] and cameras, to fully exploit the potential derived from decades-long observations of moons and the planet Mars. These instruments, along with PFS and TES thermal spectrometer (the latter on board Mars Global Surveyor), offer a unique point of view on the Martian moons allowing to investigate the mineralogical nature of the surface (Figure 2). Morevoer, new data from TGO-NOMAD [6] on the 2.7 micron region will be showed and analyzed using laboratory analogs (Figure 3).

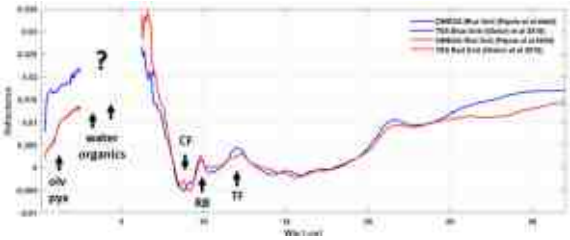


Figure 2. The current knowledge of the infrared spectrum of Phobos red and blue units, the two main geological units on the surface, joining OMEGA and TES observations. The position of important infrared features linked with major components to be search in Mars moons are highlighted with black arrows.

On the other side, the effect of grain size and composition will be showed in combination to identify a key factor in understanding the physical pro-

cesses and characteristics of the Phobos and Deimos surfaces. In detail, we will show how selected range of grain size (i.e. < 100 µm or 100-200 µm) affects some of the main features of the infrared spectrum (slope, 2.7 µm band and Christiansen features, Reststrahlen bands and Transparency features in the mid-infrared range). Moreover, we will prove how a realistic grain size distribution derived from boulder and regolith size frequency can change the final outcome of the spectrum. These physical properties will also be studied through their link with composition mixing two or more components (Figure 4). Special attention will be given to identify which variable most influences the resulting spectrum and whether different environmental conditions (vacuum, temperature, irradiance...) can affect the final result.

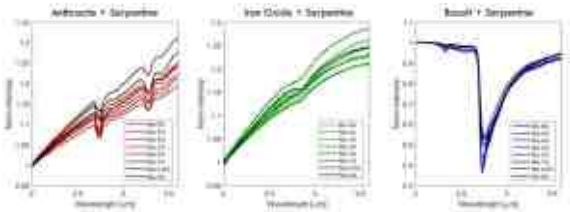


Figure 3. Mixture of hydrated phyllosilicate (serpentine) in several dark albedo materials (anthracite, iron oxide and basaltic rock) with increasing percentages to identify a limit of detection for the 2.7 micron band in Phobos and Deimos surfaces.

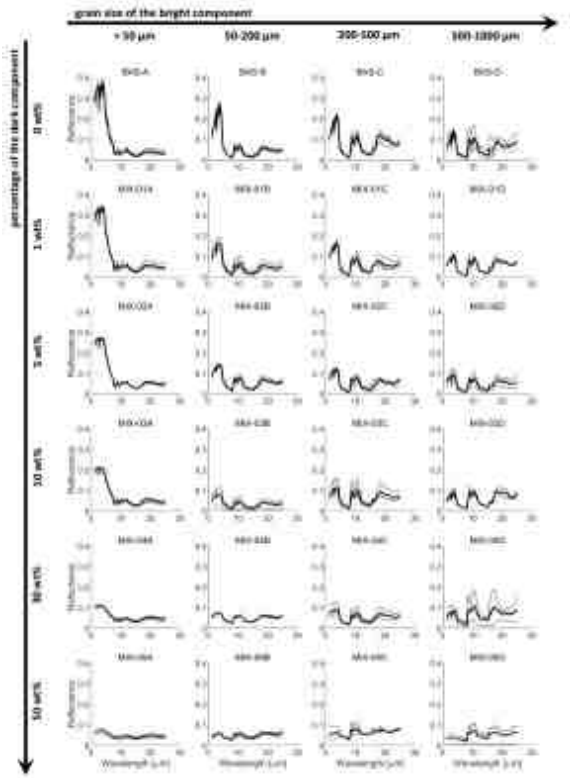


Figure 4. IR spectra of several mixture samples between dark and bright albedo components with different grain size (x axis) and different percentage of dark compenent (y axis). Spectra are shown at the same scale for reflectance.

Results and conclusion: Results of laboratory analysis in support of remote sensing interpretation will be showed, focusing on albedo, NIR slope and on the 2.7 µm absorption band, originated from stretching of the OH hydroxil group. Moreover, these laboratory data will be used for the interpretation of recently published observations from various missions such as Mex/OMEGA [5] and TGO/NOMAD [6]. Moreover, additional MEx mission data from the ESA PSA [7] archive will be shown and compared with previous observations and laboratory data focusing on unpublished data from recent years.

The goal of this work is to show the deep link that exists between remote sensing interpretation and laboratory measurements and how new advances can be achieved through the reanalysis of archival data. In the renewed interest in Martian moons we believe that a step forward on laboratory analogs can be made, leading to a more confident comparison with real surfaces. Therefore, only if the remote sensing data are combined with laboratory experiments on minerals and meteorites we can aim to obtain a basic knowledge for any future analysis aiming to interpret the nature of these enigmatic and elusive objects.

References: [1] Kuramoto K. et al. (2022), *Earth Planets Space, 74*, 12 [2] Higuchi A. and Ida S. (2017). AJ, 153, 155 [3] Hyodo R. et al. (2018). ApJ, 860, 150 [4] Barucci M. A. et al. (2021), *Earth Planets Space, 73*, 211 [5] Pajola M. et al. 2025. A&A, 697, A56 [6] Ruiz Lozano L. et al. (2025). JGR Planets (submitted) [7] Besse S. et al. 2018. PSS, 150, 131-140

Acknowledgment: G.P. work on remote sensing data was supported by ESA Archival Research Visitor Programme. G.P, J.R.B., M.P. participation in MMX mission is supported by INAF. MIRS was funded by CNES and developed by LIRA laboratory in collaboration with several laboratories in France and Japan.

XXI Congresso Nazionale di Scienze Planetarie

Sessione Astrobiologia

Habitability

ANALYSIS OF SOLAR RADIATION EFFECTS ON ICY MOONS SURFACES USING GEANT4 TOOLKIT.

Mattia Sesso[1], Federico Dogo[1,2], Lorenzo Biasiotti[2], Stavro Ivanovski[2,1], Lorenzo Calderone[2], Sergio Monai[2], Paolo Simonetti[2] and Giovanni Vladilo[2].
[1]Università degli Studi di Trieste (mattia.sesso@studenti.units.it),
[2]INAF-Osservatorio Astronomico di Trieste

Introduction: In planetary sciences, the use of simulations to describe radiation–matter interactions is gaining increasing attention. One notable example is the Geant4 toolkit, which has become one of the most widely used Monte Carlo simulation tools thanks to its flexibility and its ability to model complex geometries and a broad range of physical processes across an extensive energy spectrum [1–3]. For these reasons, Geant4 is considered a benchmark in computational geophysics and astrobiology, as it enables (i) investigation of the effects of cosmic radiation on living organisms [4], (ii) assessment of microorganism survival under extraterrestrial conditions [5], and (iii) analysis of the protection offered by various natural [5] and artificial shields [7].

Despite these capabilities, icy moons remain an underexplored target for Geant4 simulations, even though their geological peculiarities and astrobiological potential make them ideal for studying interactions between these bodies and their surrounding radiation environment. In particular, plumes observed on Europa and Enceladus provide a direct link between their possible subsurface oceans [8]—which, according to some hypotheses, may contain organic material [9,10]—and outer space.

Therefore, this work focuses on the effects of radiation on the surface and plumes of icy moons, as well as their potential biological content, using Geant4 simulations.

Methods: Defining the system's geometry is one of main Geant4's requirements. In this study, Europa and Enceladus were modeled as spherical bodies composed of ice and water, with a superficial layer 10 cm thick. The emission of water vapor plumes—containing traces of CO_2, CH_4, NH_3, and H_2—from fractures near the South Pole was represented in the simulation as a truncated cone, with an altitude of 200 km for Europa [11] and 500 km for Enceladus [12], a total opening angle of 90°, and a density that decreases toward outer space. The surface layer was divided into latitude–longitude bins, each capable of recording the absorbed radiation dose, and a corresponding latitude–longitude map of absorbed dose was produced.

The dynamics of particles ejected from the plumes of Europa and Enceladus were modeled using a spherical ballistic approach, which estimates the horizontal landing distance relative to the point of origin. This model assumes that particles are emitted from the surface with a known initial velocity and an inclination angle relative to the vertical. This approach enables identification, on the absorbed dose map, of regions where the presence of cellular life is most likely.

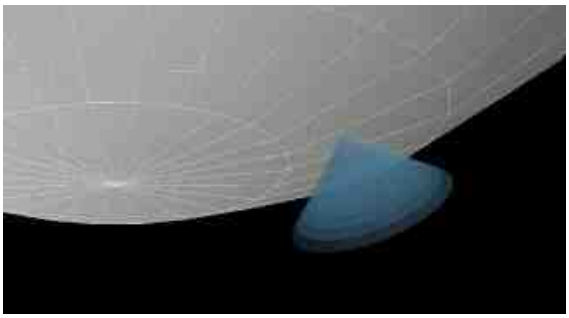


Figure 1. Representation of the geometry of Europa with a plume near the South Pole.

Another fundamental point in Geant4 regards the definition and characterization of radiation source. In this study protons and electrons were selected as a primary source. Specifically, the electron/proton flux spectra observed by Cassini [13] were used. The source was set to strike the two bodies equatorially, simulating the position of the Sun over one of their rotation periods.

Results: The preliminary results show that, as expected from the almost negligible inclination of Enceladus and Europa, the equatorial region is the most exposed to radiation, while the polar regions show lower dose values. The presence of plumes, however, appears to have no effect on the dose distribution: in fact, being located at very low latitudes in both cases (−79° on Enceladus and −70° on Europa) and having a conical shape with the apex pointing toward the surface, the area shielded by their presence is very small. Consequently, any microbial life forms possibly present on the surface around the plume's emission point would not gain any additional advantage from its presence, at least in the case under consideration in which the plume has a conical shape and the radiation source strikes the body equatorially.

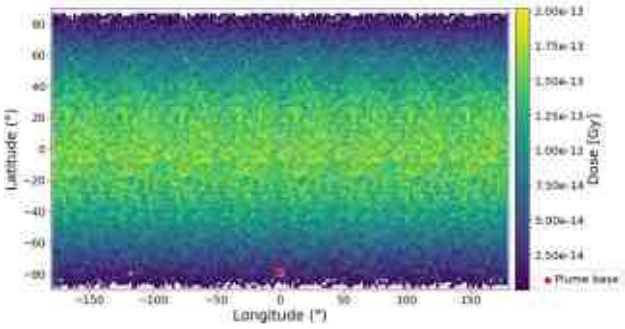


Figure 2. Latitude–longitude map of the dose absorbed by the 10 cm-thick soil layer of Enceladus, using an electron source.

Conclusions: Future work will focus on improving the representation of plume shape and distribution on the surface to better reproduce observations suggested by Lyman-α and O I 130.4 nm emissions reported in [4]. Additionally, the radiation source model will be refined to account for the fact that radiation striking bodies such as Europa and Enceladus does not originate exclusively from the Sun; particles trapped in the magnetospheres of Jupiter and Saturn can follow planetary magnetic field lines and impact their satellites from non-equatorial directions. Another factor to consider is the contribution of cosmic rays.

References:

[1] Agostinelli S., et al. (2003) *NIMA, 506, 3*.
[2] Allison J., et al. (2006) *IEEE Transactions on Nuclear Science, 53, 1*.
[3] Allison J., at al. (2016) *NIMA, 835*.
[4] Paschalis P., et al. (2014) *New Astronomy, 33.*
[5] Chen J., et al. (2022) *Nuclear Science and Techniques, 33, 11.*
[6] Guo J., et al. (2017) *Life Sciences in Space Research, 14*.
[7] Dartnell L.R., et al. (2007) *Geophysical Research Letters, 34, 2.*
[8] Roth L., et al. (2014) *Nature, 451, 7179.*
[9] Porco C., et al. (2017) *Astrobiology, 17, 9.*
[10] Perera L. and Cockell C. (2023) *Astrobiology, 23, 3.*
[11] Lorenz R. (2016) *Icarus, 267.*
[12] Porco C., et al. (2006) *Science, 311, 5766.*
[13] Andersen A., et al. (2025) *JGR Space Physics, 130, 3.*

THE REACTIONS OF ATOMIC OXYGEN WITH AROMATIC COMPOUNDS AND IMPLICATIONS FOR THE EVOLUTION OF EXTRATERRESTRIAL CARBONACEOUS MATERIAL

M. Parriani[1], G. Pannacci[1], G.Vanuzzo[1], P. Casavecchia[1] and N.Balucani[1]
[1]DCBB, Università degli Studi di Perugia, Via Elce di Sotto 8, 06123 Perugia, IT
e-mail: marco.parriani@unipg.it

Abstract:

Refractory carbonaceous matter found across the Solar System is dominated by complex structures including aliphatic chains, small and large aromatic rings, functionalized aromatics, and heteroaromatic structures embedded within a kerogen-like macromolecular matrix. These materials have been detected in a wide variety of environments, including comets, meteorites, asteroids, and interplanetary dust particles [1-3]. Remarkably, refractory carbonaceous matter with a similar structure is also spread throughout the interstellar medium, as revealed by the spectroscopic signatures of aromatic and aliphatic compounds [3]. Polycyclic aromatic hydrocarbons (PAHs) as individual molecules are also widespread in space; the identification of molecular species as large as cyanopyrene in the Taurus Molecular Cloud has highlighted how aromatic compounds can form in very diverse environments, from the very low temperatures of dark clouds (10 K) to the high temperatures of photon-dominated regions. A very interesting question concerns the origin of the carbonaceous material. Is there a relationship between the refractory carbonaceous compounds of the interstellar medium and those of small bodies of the Solar System, or did the carbonaceous compounds of small Solar System bodies form independently? Based on current knowledge, interstellar carbonaceous material is much less rich in oxygen and nitrogen than that found in meteorites, asteroids, and comets. Carbonaceous material in interplanetary dust is even richer in oxygen and carbon. Is this sufficient to rule out a relationship, or are there processes that can explain the enrichment of nitrogen and oxygen? Aromatic compounds have also been identified in Martian sediments upon thermal decomposition of solid samples by the SAM instrument on the NASA Curiosity rover [4,5]. Molecules such as chlorobenzene, dichlorobenzene, and thiophene reflect structural components or fragments of a more complex organic matrix. This observation aligns with the findings that Martian organics, when present, are typically embedded within mineral matrices or protected within sedimentary structures, forming macromolecular material resembling the kerogen-like refractory organics observed in meteorites and cometary dust. Understanding the chemical evolution of these extraterrestrial organic reservoirs requires detailed knowledge of the fundamental reactivity of small aromatic and heteroaromatic units with abundant reactive species. Among these, atomic oxygen (AO) plays a central role in multiple planetary settings. On Mars—as in other tenuous, oxidizing atmospheres—AO can be chemically, and photochemically, produced [6]. The photodissociation of H_2O, CO, and CO_2 produces AO in comets when they are exposed to the sunlight. In kerogen-like carbonaceous materials found in different Solar System reservoirs, oxygen is generally present in peripheral or intermolecular positions rather than incorporated within aromatic rings. In the diffuse interstellar medium, mid-IR constraints show that free hydroxyl, carbonyl, or carboxyl groups are extremely limited, implying that when oxygen is present, it occurs mainly as ether-like linkages or minor substituents connecting or decorating larger aromatic–aliphatic domains rather than forming stable O-heterocycles [3]. In contrast, the insoluble organic matter of carbonaceous chondrites contains a broader variety of oxygen functionalities, including ethers, carbonyls, hydroxyl groups, and cross-linking O-bearing bridges, consistent with more extensive parent-body processing. Cometary refractory organics lie between these extremes: CHON particles show significant oxygen content but without evidence for oxygen directly embedded within aromatic rings, suggesting predominance of bridging or substituent oxygen associated with disordered polyaromatic units. Across these environments, oxygen therefore appears primarily in linking, substituent, or peripheral functional groups, with intra-ring oxygen playing at most a minor role [3]. Investigating the oxygen reactivity with representative aromatic fragments provides key insights into how complex carbonaceous solids are modified or degraded in the extraterrestrial environments. To probe these reactions, we performed a systematic series of experiments using the crossed-molecular-beam (CMB) technique [7] with mass spectrometric detection. In a CMB experiment, two supersonic beams—one containing atomic oxygen, the other the target hydrocarbon—are made to collide under single-collision conditions. Reaction products are detected by a rotatable mass spectrometer equipped with time-of-flight analysis, allowing measurement of laboratory angular and velocity distributions for selected mass-to-charge ratios. From these, primary reaction channels, branching fractions, and the nature of key intermediates can be directly inferred. This approach yields a picture of the reaction mechanism, including the role of intersystem crossing (ISC), which is often involved in the competition between adiabatic and spin-forbidden pathways in oxygen–aromatic reactions. A coherent understanding has emerged from CMB investigations of AO reactivity with benzene, toluene, pyridine, and acrylonitrile [8,9]. In benzene,

the reaction is characterized by the formation of phenoxy radicals and CO-forming channels resulting from ring contraction or cleavage, with a significant contribution from ISC-enabled pathways [8]. Toluene exhibits a dominant CH_3-elimination channel, accompanied by hydrogen-loss and CO-forming reactions; a sizable fraction of the reactive flux proceeds through nonadiabatic transitions [9]. Heteroaromatic molecules such as pyridine introduce additional complexity: nitrogen alters the position and accessibility of triplet–singlet crossings, modifies the stability of oxygenated intermediates, and leads to characteristic N-containing products alongside CO formation [10]. These comparative studies show that small structural changes—substitution patterns, heteroatom inclusion, ring size—can have substantial impact on the oxidative pathways of aromatic frameworks. Within this systematic effort, we have extended our technique to reactions with thiophene, ethylbenzene, phenol, and naphthalene. Our preliminary results indicate that the $O(^3P)$ attack on thiophene predominantly leads to ring cleavage, with the formation of thioacrolein and CO, implying the loss of both aromaticity and cyclic structure in a single reactive event. This behavior parallels the efficient ring-contraction mechanism observed in the AO reaction with pyridine, although the sulfur substitution introduces its own mechanistic features. Our data suggest that heteroatom-containing aromatic units—whether nitrogen- or sulfur-bearing—tend to be especially susceptible to ISC-mediated pathways that facilitate deep fragmentation. In the case of the reaction of AO with toluene (methylbenzene) and ethylbenzene, our data exhibit similarities (as expected since they are the smallest alkyl-substituted benzenes) but also differences with the ipso attack favored in the case of AO + methylbenzene and the ortho attack favored in the case of AO + ethylbenzene. Finally, significant differences have been observed between benzene and naphthalene. According to our preliminary data and their analysis, the formation of the adduct seems to be dominant in the AO + naphthalene reaction. In contrast, in the AO reaction with benzene, it accounted for only 2%. These results point to a much greater resilience of PAHs compared to monocyclic aromatics. The implications of these results extend across planetary science, astrochemistry, and the interpretation of sample-return datasets. Aromatic and heteroaromatic molecules represent fundamental sub-units within the macromolecular material of comets [1], carbonaceous asteroids [2], meteorites [11], and interstellar dust [3]. Their reactivity with AO appears to influence the chemical evolution of these systems, directing pathways toward partial oxidation, ring contraction, side-chain cleavage, or complete breakdown into small volatile species such as CO. On Mars, where organics detected to date appear embedded in sediments and released only upon the breakdown of these mudstones, oxygen-driven degradation may contribute to the scarcity of accessible organic molecules at the surface. In more protected environments—subsurface niches, organic-rich fine grains, or ice-rich matrices—similar reactions may proceed more slowly, allowing partial preservation of kerogen-like networks whose aromatic sub-units resemble the model systems investigated in the laboratory. Overall, the expanding CMB dataset on benzene, toluene, pyridine, acrylonitrile, thiophene, and related species provides a mechanistic foundation for interpreting how aromatic fragments behave under planetary and astrophysical conditions. By revealing the dominant reaction channels and fragmentation patterns, these studies offer a molecular-level framework of the transformation, survival, and chemical evolution of carbonaceous matter throughout the Solar System—linking laboratory dynamics to the organic inventories detected on comets, asteroids, meteorites, and planets.

References:

[1] Hänni, N. et al. Nat. Commun. (2022).
[2] Naraoka, H. et al. Science 379, eabn9033 (2023).
[3] Pendleton, Y. J., & Allamandola, L. J. ApJS 138, 75 (2002).
[4] Millan, M. et al. JGR: Planets 127, e2021JE007107 (2022).
[5] J. Lasne et al. (2016) Astrobiology, 16, 977.
[6] D. Viúdez-Moreiras et al. (2020) Icarus, 336, 113458
[7] P. Casavecchia P. et al. (2015) Int. Rev. Phys. Chem., 34, 161–204.
[8] Vanuzzo, G. et al. J. Phys. Chem. A 125, 8434–8453 (2021).
[9] Balucani, N. et al. Faraday Discuss. 251, 523–549 (2024).
[10] Recio P. et al. (2022) Nat. Chem., 14, 1405 1412.
[11] Eigenbrode, J. L. et al. Science 360, 1096 1101 (2018).

Acknowledgments:

Support from the Italian MUR PRIN2020 (2020AFB3FX-Astrochemistry beyond the second period elements), the Italian Space Agency (Bando ASI Prot. n. DC-DSRUVS-2022-231, Grant no. 2023-10-U.0 MIGLIORA) and Università degli Studi di Perugia (Fondo Ricerca di Ateneo 2022, COLONIZE Indagini preliminari su risposte biologiche, materiali cementizi alternativi e nuove fonti energetiche per affrontare la colonizzazione infrastrutturale dello Spazio) is acknowledged.

INSIGHTS INTO THE HABITABILITY OF OTHER WORLDS THROUGH LABORATORY SIMULATIONS USING CYANOBACTERIA CAPABLE OF FAR-RED PHOTOSYNTHESIS. Daniela Billi[1], Giorgia di Stefano[1], Costanza Maria Martella[1], Mickael Baqué[2], Beatrice Boccia[3], Maria Grazia Albanese[4], Amedeo Balbi[4], Nicoletta La Rocca[3], Laura Silva[5], Erica Bisesi[5], Michele Maris[5], Giuseppe Murante[5], Manuele Ettore Michel Gangi[6], Micol Bellucci[6]. [1]Department of Biology, University of Rome Tor Vergata [2]DLR-Department of Planetary Laboratories, Berlin, [3]Department of Biology, University of Padua, [4]Department of Physics, University of Rome Tor Vergata, [5]INAF – Astronomical Observatory of Trieste, Italy, [6]Italian Space Agency

The astonishing capability of life as we know it to adapt to extreme environments provides new insights into the question of whether life is unique in our planet or whether there are inhabited worlds in the Solar system or around other stars [1]. Extremophiles colonize a variety of inhospitable places, that provide a proxy for possible past or present habitability of Mars or the icy moons Enceladus and Europa [2]. Moreover, the existence on Earth of cyanobacteria capable of oxygenic photosynthesis under infrared light supports the possibility of exotic photosynthesis in exoplanets orbiting M-dwarf stars, the most common stars in our Galaxy, that are characterized by a strong infrared emission [3]. Exposure of extremophiles to non-Earth conditions by using space platforms or laboratory simulations is a powerful tool to expand the boundaries of habitability and investigate biosignature detectability. Among desert cyanobacteria, there a few capable of Far-red light photoacclimation (FaRLiP) that can utilize far-red light for oxygenic photosynthesis in environments with attenuated visible light and enriched far red light due to physical conditions or the presence of competing photosynthetic organisms [4]. Notably FaRLiP cyanobacteria provide a unique model system to gain insight into the habitability of astrobiological relevant targets. If life ever occurred on Mars, it may have retreated to near-surface, protected environments as surface habitability disappeared. Such a possibility is supported by the survival of biofilms of a desert cyanobacterium capable of FaRLiP exposed to Mars-like simulations [5]. Furthermore, the investigated FaRLiP desert strains showed a remarkable stability of macromolecules relevant as biosignatures after six years of air-dried storage [6] a feature relevant for future passive experiments beyond the low Earth orbit, as foreseen on the Moon surface [7]. Desert cyanobacteria capable of FaRLiP are a suitable experimental strain also for investigating the possibility of oxygenic photosynthesis on planets around M-dwarf stars with an emission spectrum peaking in the infrared (ref.). Since the ultraviolet radiation environment - particularly within the UVC band - is a decisive factor in determining the potential habitability of planetary surfaces, FaRLiP cyanobacteria have been exposed to UVC up to 78 kJ/m^2, a dose within the modelled range of surface fluences for major M-dwarf flares. Results suggested that this cyanobacterium could potentially endure in the worst-case scenario of limited atmospheric protection. i.e, immature ozone layer or ozone depletion by large flares. Furthermore, the possibility for photosynthesis driven by geothermal light at deep-sea hydrothermal vents hold promises for the habitability of icy moons [8].

References: [1] Martins Z. et al. (2019) *Space Sci. Rev.*, 209, 43–81. [2] Carré L, et al. (2022) *Astrobiology,* 22, 322–367. [3] Claudi R. (2021) *Life*, 11, 10. [4] Gan F. et al. (2015) *Life*, *5*, 4–24. [5] Di Stefano G. (2025) *Life* 15, 622. [6] Di Stefano G., et al. (2025) *Int. J. Astrobiol*., 24, e14. [7] Cockell C.S. (2024), *Discover Space*, 128, 5. [8] Perez N. et al. (2013) *Astrophys. Space Sci*., 346, 327–331

THE PREBIOTIC PRODUCTION OF OLIGONUCLEOTIDE SEQUENCES FROM 3',5' CYCLIC NUCLEOTIDE PRECURSORS: WHAT WE HAVE LEARNED FROM FIELD EXPERIMENTS

G. Costanzo[1,2], A. Piacentini[3,4] and C. Mazzoni[3,4], [1]IBPM-CNR Rome , [2]IAPS-INAF Rome, (contact: giovannamaria.costanzo@cnr.it), [3]Department of Biology and Biotechnology "Charles Darwin" Sapienza University, Rome, [4]IRSA-CNR Rome

Introduction: Studying terrestrial analogue environments helps us develop a better understanding of where and how life can exist and what evidence of it may be preserved. In collaboration with colleagues at the Institute for Space Astrophysics and Planetology (IAPS-INAF) in Rome [1], we have proposed Bagno dell'Acqua (formerly Specchio di Venere), an endorheic lake on Pantelleria Island in Sicily, Italy, as a new Mars-like environment in which to study prebiotic chemistry and as a source of microorganisms adapted to living in extreme environments.

Producing oligonucleotide sequences from nucleotide precursors in the absence of enzymes and template molecules is one of the most challenging issues in modern origin-of-life research. Studies of polymerization targeting 3′,5′ cyclic nucleotide monophosphates [2] place special emphasis on identifying conditions compatible with sustainable oligonucleotide production over longer time scales, in geochemical contexts relevant to early Earth and extraterrestrial environments. We present results showing the role of the Bagno dell'Acqua lake environment in the prebiotic synthesis of RNA oligonucleotides from 3′,5′ cyclic nucleotides.

Results: Alkaline lakes, also known as 'soda lakes', are particular and uncommon terrestrial environments. These lakes are characterised by a high pH value, unusual chemistry and the presence of microbial life, making them interesting places to study as Martian analogue sites. Bagno dell'Acqua is a soda lake with a surface area of approximately 0.2 km², characterised by a pH value of pH ≥9. The lake is fed continuously by thermal springs on its shores, as well as by meteoric and seawater. In the thermal spring area, the temperature ranges from 34°C to 54°C, and the pH value is approximately 6.2. Combined VNIR reflectance and Raman spectroscopy revealed that the main mineralogical species observed in Lake Bagno dell'Acqua are Mg-smectite and aragonite [1].

We conducted three *in situ* campaigns on Pantelleria Island over three consecutive years (2023, 2024 and 2025). During these campaigns, we incubated 3',5' cyclic guanosine, cytosine and adenosine monophosphates (hereafter abbreviated as cGMP, cCMP and cAMP respectively) at 50°C in the thermal spring located on the shore of the Bagno dell'Acqua lake (see Figure 1), under different experimental conditions and kinetics, to observe whether the chemical and physical composition of the lake water, along with the environmental conditions, allowed for the spontaneous formation of RNA oligomers.



Figure 1. Satellite image taken from https://earthexplorer.usgs.gov/ (access date: October 16, 2023) reporting the location of the thermal spring where the samples were incubated.

Most of our observations refer to cGMP [3], the nucleotide that is favoured for stacking interactions (i.e. non-covalent bonds that occur between the aromatic nitrogenous bases of adjacent nucleotides, causing them to stack spontaneously). These observations can be summarised as follows:

-RNA oligomers were obtained from cGMP monomers that were dried and suspended in lake water, with lengths of up to **16 units**;

-a comparison of the results of experiments carried out in Tris-HCl buffered water and lake water clearly demonstrates that **pH alone** is insufficient for efficient polymerization;

-the intervention of **dissolved salts** in water is imperative, particularly in the protection of newly formed polymers from their hydrolytic degradation;

-the remarkable **photostability** exhibited by nucleosides and nucleotides suggests the possibility of a selection process that favours these compounds based on their inherent ability to resist UV light and high-energy radiation;

-it is conceivable that a process of abiogenesis may have occurred in **sunlit geothermal pools**, with abiotically polymerised cGMP being a plausible component of this process (TiO_2 could act as a catalyst);

-water reconstituted in the laboratory also catalyses polymerization. However, the **kinetics are slower**, taking between 1 and 3 hours for lake water and 3–48 hours for reconstituted water (Figure 2).

-**Larger quantities** of polymers are produced in lake water, with an average length of six units for lake water at one hour, compared to just over five units for reconstituted water at 24 hours.

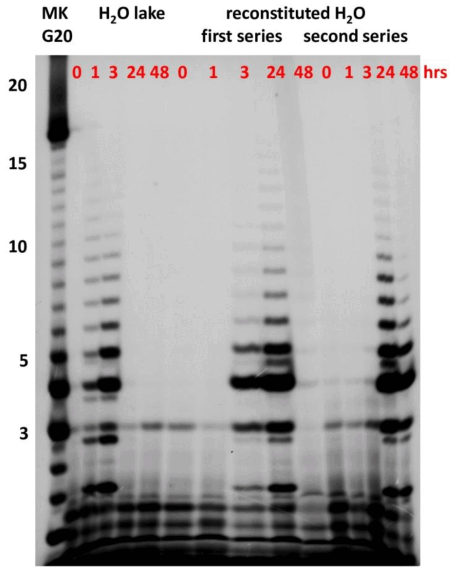


Figure 2. PAGE (PolyAcrylamide Gel Elecrophoresis) comparison of cGMP polymerization *in situ* in the Bagno dell'Acqua hot spring between lake water and reconstituted water. Lane 1: marker 5′ ^{32}P-ribo G20. Lanes 2-6: lake water. Lanes 7–11: first series of samples of reconstituted water. Lanes 12-16: second series of samples of reconstituted water. The experiment was conducted in duplicate to prove its reproducibility. Each sample was prepared by lyophilizing 150 µL of 1 mM 3′,5′ cGMP, suspended *in situ* in 150 µL of lake water or reconstituted water and subsequently incubated at 50◦C in the thermal spring illustrated in Figure 1 for the indicated time. Each sample was treated and labeled independently with [γ-^{32}P]ATP . For the shortest oligomers, two or three different hydrolysis products (respectively, 2′,3′ P-bridged, open form, and loss of the 3′ phosphate) are observed.

The analyses of cAMP and cCMP monomers are currently under investigation.

References:

[1] Bruschini E. et al. (2024) *PSS*, 245 (105893). [2] Šponer J.E. et al. (2021) *Life*, 11(8), 800, https://doi.org/10.3390/life11080800. [3] Ubertini V. et al. (2025) *Int. J. Mol. Sci.,* 26, 6952, https://doi.org/10.3390/ijms26146952.

Acknowledgements:
This work was supported by the Italian Space Agency (ASI) n. 2023-1-U.0 "Modeling Chemical Complexity: all' Origine di questa e di altre Vite per una visione aggiornata delle missioni spaziali (MIGLIORA)" and : N◦ 2023-3-HH.0 ″Attività scientifica di preparazione all'esplorazione marziana". The authors wish to thank the Pantelleria National Park Authority for the logistic support provided.

THE ROLE OF CONVECTION IN SUSTAINING PUTATIVE ECOSYSTEMS IN THE SUBSURFACE OCEANS OF ICY MOONS. S. Pagnoscin[1,2,3], J. von Hardenberg[4], J. R. Brucato[2], and A. Provenzale[3], [1]Department of Physics and Astronomy, University of Florence, Via G. Sansone 1, Sesto Fiorentino, Firenze (silvia.pagnoscin@unifi.it), [2]INAF - Astrophysical Observatory of Arcetri, Largo E. Fermi, 5, Firenze [3]Istituto di Geoscienze e Georisorse del CNR, Via Moruzzi 1, 56124 Pisa, Italy, [4]Department of Environment, Land, and Infrastructure Engineering, Politecnico di Torino, 10129 Torino, Italy.

Introduction: Among the ocean worlds of the Solar System, the icy moons of the gaseous giants Jupiter and Saturn (e.g., Europa, Ganymede and Enceladus) are of particular astrobiological interest. These satellites are entirely covered by ice but host global, salty oceans beneath their thick icy shells. Such oceans are generated and maintained by intense tidal stresses exerted by their parent planets, which provide enough energy not only to keep water in liquid form, but also to sustain water–rock interactions at the seafloor, especially in moons where the ocean is in direct contact with the rocky mantle (such as Europa and Enceladus). In this framework, these extraterrestrial oceans represent prime targets in the search for life beyond Earth, as they simultaneously offer the key ingredients for life as we know it: liquid water, the necessary chemical elements, and energy.

It is therefore natural to ask whether a putative ecosystem could emerge and persist in these exotic environments, and whether we might ever detect its signatures. In the first approximation, we focus on chemosynthetic lifeforms that rely on the chemical energy released when reductants and oxidants meet [1]. Reductants are primarily produced by water-rock interactions (hydrothermal activity) on the seafloor, while oxidants are expected to be generated at the icy surface and subsequently transported into the ocean through the ice shell. An ecosystem can then be sustained if reductants and oxidants are both present, can physically meet within the water column, and if the ocean is sufficiently well mixed.

In this context, ocean dynamics plays a major role. In particular, ocean convection, which can transport water from the seafloor to the ice–water interface through rising plumes [2], may promote the encounter between reactants and the homogenization of their concentrations throughout the ocean. This could ensure also organisms' stable distribution all over the water column including up close to the water-ice interface, thereby enhancing the probability of detecting life at or near the surface through ice dynamics and tectonic processes [3,4].

Here, we investigate the role of convection in sustaining a putative ecosystem in the subsurface oceans of icy moons through ocean and ecosystem modeling.

Methods: We model the ocean as a Newtonian fluid layer, set in a 3D box with thickness D and horizontal sides 2πD undergoing Rayleigh-Bénard convection. Periodic boundary conditions are used on the vertical boundaries at x=0, 2πD and y=0,2πD while boundary conditions on temperature and velocity on the horizontal boundaries are set with proper equations according to the case study. Gravity is aligned with the vertical direction, and it points opposite to the z axis. The model includes rotation that can be set at any direction in the y-z plane. The fluid density is a function of temperature and salinity; here we first use the Boussinesq approximation so that density becomes independent of pressure, and subsequently we consider a situation where the unperturbed state is compressible while density perturbations are kept incompressible. In first approximation we do consider the ocean as made of pure water, hence neglecting salinity effects. Once defined the theoretical model, simulations will use RBSolve [5,6], a 3D Navier-Stokes Fortran code in the Boussinesq approximation.

To describe the evolution of a putative ecosystem, we couple the convective flow with the transport and reaction of two scalar fields: (i) a reductant/nutrient field N (e.g. H_2) continuously supplied at the seafloor by hydrothermal activity, and (ii) a field P representing primary producers (chemosynthetic organisms that feed on the energy released by mixing reductants and oxidants). Assuming that sufficient oxidants are already present in the ocean, we focus on the dynamics of reductants and producers and describe their interaction through simple reaction terms that account for primary production, consumption of reductants, and biomass losses.

Preliminary findings and future work: Our preliminary results indicate that ocean dynamics, and convective motions in particular, plays a crucial role in the distribution of nutrients and in the maintenance of biological activity throughout the water column. Convection efficiently redistributes reductants supplied at the seafloor and can sustain non-negligible concentrations of producers not only in the deep ocean but also near the ice–water interface. The system evolves toward statistically steady states in which N and P remain finite and spatially extended, suggesting that convection can help sustain and vertically connect a putative ecosystem in icy-moon oceans.

Future work will explore more realistic scenarios focusing on the transport of both reductants and oxi-

dants and will investigate a more complex ecosystem network including, for example, a further complete food chain with predators and preys.

References: [1] Chyba C. F. and Phillips C. B. (2001) *PNAS, 90,* 801–804. *Possible ecosystems and the search for life on Europa.* [2] Pagnoscin S. (2025). *Convection in the subsurface ocean of icy moons and response of the upper ice layer,* Icarus, 116875. [3] Mitri G. and Showmann A. P. (2005) *Convective–conductive transitions and sensitivity of a convecting ice shell to perturbations in heat flux and tidal-heating rate: Implications for Europa,* Icarus, 177(2), 447–460. [4] Schmidt B.E. (2011) Nature 479(7374), 502-505. [5] Von Hardenberg J. (2008). *Large-scale patterns in Rayleigh–Bénard convection,* Physics Letters A, Vol. 372, Iss. 13. [6] Novi L. et al. (2019). *Rapidly rotating Rayleigh-Bénard convection with a tilted axis,* Physical Review Vol 99, Iss. 5.

XXI Congresso Nazionale di Scienze Planetarie

Sessione Dinamica dei corpi celesti naturali ed artificiali

POTENTIAL INTERACTION OF 99942 APOPHIS WITH THE HIGH EARTH ORBIT POPULATION DURING THE 2029 CLOSE APPROACH

G. Schettino [1] and A. Rossi[1]
[1]Istituto di Fisica Applicata "Nello Carrara" (IFAC) – Consiglio Nazionale delle Ricerche (CNR), via Madonna del Piano 10, 50019 Sesto Fiorentino (FI); g.schettino@ifac.cnr.it, a.rossi@ifac.cnr.it

Introduction: The asteroid 99942 Apophis will pass close to the Earth in 2029, reaching a minimum distance of about 32 000 km above the Earth surface on April 13th, 2029. Whilst, out of the equatorial plane of the Earth, the flyby will be closer than the geosynchronous (GEO) radius, at r_{geo} ~ 36000 km of altitude.

To exploit the unique opportunity of closely follow an asteroid of notable size (the mean diameter of Apophis is about 340 meters), ESA has planned a rendezvous mission, RAMSES (Rapid Apophis Mission for Space Safety), to be launched in 2028 [1]. RAMSES is planned reach the asteroid before its close approach to our planet and to conduct a survey of the possible changes of shape, surface, orbit, rotation and orientation due to the tidal interaction with the Earth. The obtained measurements will provide precious information about both the asteroid itself (composition, interior structure, etc.) and its response to external forces [2,3] to be used for scientific and planetary defense purposes.

The geometry of the Earth flyby is such that most of the geosynchronous spacecraft will be unaffected. However, together with the "purely" geosynchronous controlled spacecraft, there exists a large population of abandoned spacecraft and debris on inclined (Fig. 1) and elliptical orbits whose apogee extends beyond r_{geo}.

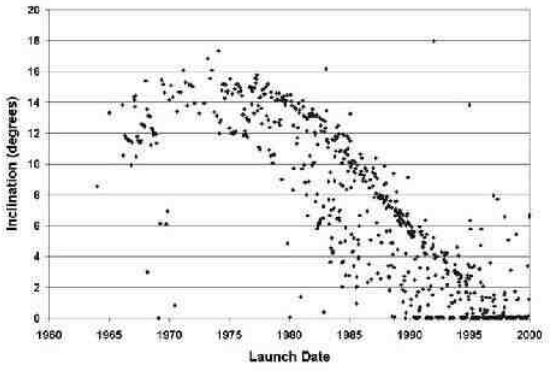


Figure 1: distribution of equatorial inclination objects in the GEO region as a function of their launch date. The wave like structure shows how the inclination of old abandoned objects tend to oscillate around the stable Laplace plane at 7.5 deg, reaching values as high as 15 deg (e.g. [4]).

In the present work, we perform a comprehensive statistical analysis of the spatial distribution of passive and active objects in the vicinity of Apophis trajectory, as expected on April 2029. The final aim is to build a worst-case scenario being representative of the most possible hazardous distribution of debris. Assessing the risk of collision that both Apophis and Ramses could experience is a fundamental task to be addressed and quantified before 2029.

Mathematical Methods: The statistically representative distribution of objects in April 2029 has been built according to the following steps. We started from the real distribution of debris obtained by the US Catalogue of the Two-Line Elements (TLE). From the catalogued list, as of September 2025, all the high Earth orbit objects, with apogee above 30000 km, were extracted (the gran total amounted to about 3250 objects). The considered list included GEO-orbiting objects, objects crossing the GEO ring and highly eccentric objects with apogee in the GEO region (GTO, Molniya, etc). To build a statistically-representative sample of objects which suitably describes the April 2029 distribution around the GEO orbit, we considered the main perturbative effect that may cause a change in the position of an orbiting object. Namely the lunisolar perturbation and the gravitational harmonics (mainly J2) causing a change in the orientation of the orbital plane, in particular for uncontrolled objects. Therefore, we sampled the nominal TLE-extracted values of equatorial inclination between 0 and 15°, right ascension of the ascending node (*RAAN*) and argument of perigee (ω) at steps of 10° from 0° to 360°. Moreover, the mean anomaly (from the original M_0) along the whole orbit was sampled similarly.

The obtained sampled statistical population is expected to properly mimic the real distribution of spacecraft and debris at the time of Apophis arrival, considering also the existence of non catalogued objects in the region. In fact, it is well known that the TLE catalogue is actually almost complete only for objects larger than about 50 cm – 1 m in the GEO region.

The TLEs provide mean elements, expressed in the so-called TEME (True Equator Mean Equinox) reference system. These elements are then transformed into Cartesian state vectors ($\boldsymbol{X}_s$, $\boldsymbol{V}_s$) in the J2000 reference. The J2000 position vectors of Apophis ($\mathbf{X}_A$) during the close approach are obtained from the Spacecraft, Planet, Instrument, C-matrix Events (SPICE) kernels maintained by NASA's Navigation and Ancillary Information Facility (NAIF). The distance between $\boldsymbol{X}_s$ and $\boldsymbol{X}_A$ in the J2000 reference is finally computed.

For each of the objects, we looked for the worst-quadruplet (i, M_0, $RAAN$, $\omega)_w$, that is, the combination providing the minimum possible distance of that object from Apophis during its close approach to the Earth.

Results: The ongoing analysis has shown that the current distribution of objects in the GEO region can have very close approaches with the incoming asteroid. Distances below 10 km were found for dozens of objects (the final list of close approaches will be shown at the conference).

The orbital behavior of the potentially dangerous debris has been analyzed in details. As an example, Fig. 2 shows the case of a space debris stemming form the fragmentation of the COSMOS 1481 spacecraft. The figure shows the orbits of the debris, in the worst possible scenario, compared with the Apophis trajectory in red (the GEO ring has been shown for clarity too). Potentially, an object of this kind could pass just few kilometers away from Apophis.

The uncertainty in the position of the orbiting objects, along with the existence of the unobserved population, makes the odds of a collision of Apophis against a man made object not null even if very unlikely. It is worth noting that a collision at close approach might endanger the scientific measurements planned on the surface of Apophis.

Moreover, potential risks could be posed also to the operations of RAMSES in the vicinity of the asteroid. This is supporting the need of a thorough analysis of spatial distribution of debris at that epoch with a quantitative evaluation of the overall collision risk.

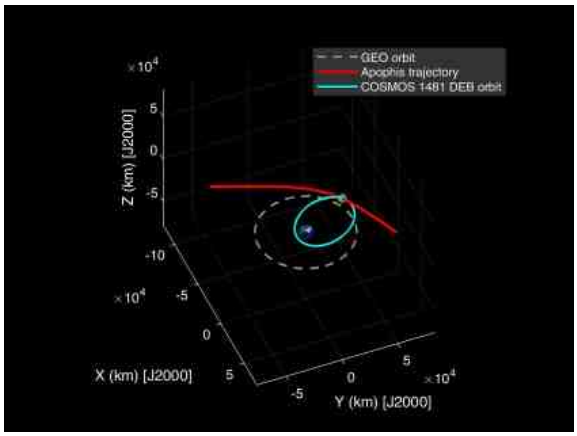


Figure 2: relative geometry of the Apophis trajectory (red line) and of the orbit of the COSMOS 1481 debris (cyan). The green circle shows the possible location of the debris at closest approach.

References:

[1] *https://www.esa.int/Space_Safety/Planetary_Defence/Ramses_ESA_s_mission_to_asteroid_Apophis* [2] Scheeres D.J. , L.A.M. Benner, S.J. Ostro, A. Rossi, F. Marzari, P. Washabaugh, *Icarus*, 178 (2005) 281–283 [3] Hirabayashi M., *Icarus*, 443 (2026) 116754 [4] Rosengren A.J., *Advances in Space Research* 53, 8, 1219-1228.

ESTIMATING THE STEADY-STATE NUMBER OF EARTH'S COORBITAL BODIES DERIVED FROM LUNAR EJECTA. E. M. Alessi[1] and R. Jedicke[2], [1]Istituto di Matematica Applicata e Tecnologie Informatiche "E. Magenes", Consiglio Nazionale delle Ricerche, Milan, Italy, elisamaria.alessi@cnr.it, [2]Institute for Astronomy, University of Hawaii, Honolulu, USA, jedicke@hawaii.edu

Introduction: When we talk of coorbital motion, we assume a three-body problem where two of the three bodies orbit the central one in approximately the same amount of time. In other words, the coorbital motion is a 1:1 mean motion resonance. Different asteroids and moons in the solar system exhibit this behavior with respect to a given planet and are of particular interest because they usually show a quite stable evolution. Given the recent hypothesis that the asteoroid Kamo'oalewa, in coorbital motion with the Earth, could have a lunar provenance [1], we deepen here this possibility, by estimating the steady-state number of Earth's coorbitals coming from lunar ejecta, originated by a high enough energetic impact.

Methods: We analyze the data obtained for 12000 particles by numerical simulation in [2], considering the time series of the orbital evolution when the given particle is not captured by the Earth. First, these time series are analyzed looking for possible coorbital intervals, defined as the intervals of time when the semi-major axis crosses 1 au at least 4 times consecutively. These potentially coorbital intervals are refined in a second step to look for the following coorbital regimes: quasi-satellite, horseshoe, tadpole, compound, assuming the notation used in [3]. To this end the time series of the resonant angle is analyzed (see Figure 1).

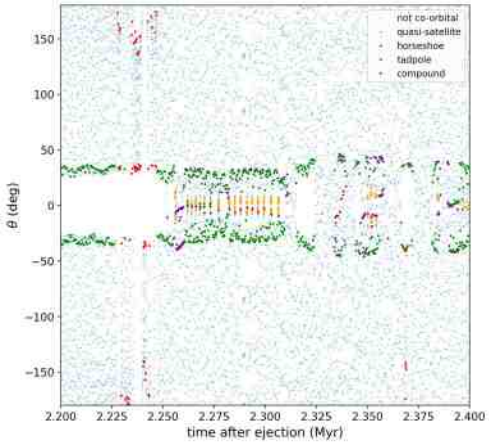


Figure 1 Example of analysis of the time series of the resonant angle to distinguish different coorbital regimes.

Given this set of coorbital states, then we applied the methodology used in [2], based on our understanding of the existing scaling laws, to estimate the corresponding steady-state number.

Moreover, the distribution in orbital elements of the coorbitals found is compared with the actual distribution of known Earth's coorbitals, and the capability of distinguishing between different coorbital regims allows us to estimate the frequency of transition from one regime to another (see Figure 2).

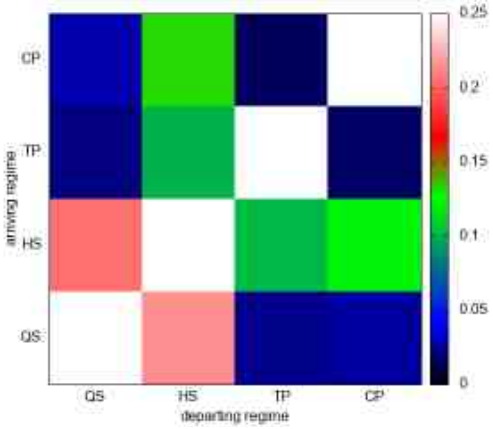


Figure 2 Frequency of transition between different coorbital regimes.

References:
[1] Sharkey B. N. L. et al. (2016) *Communications Earth & Environment, 2,* 231. [2] Jedicke R. et al. (2025) *Icarus, 438,* 116587. [3] Cortese F. et al. (2025) *Nonlinear Dynamics,* 113, 19541-19557.

Acknowledgments: The integrations were performed on the Università di Pavia EOS HPC cluster. We are grateful to Gabriele Merli and Tommaso del Viscio who helped in this. E.M. Alessi acknowledges support from Fondazione Cariplo and the short-term mobility programme of CNR.

XXI Congresso Nazionale di Scienze Planetarie

Sessione Divulgazione, Didattica e Comunicazione

A ROLE-PLAYING GAME FOR THE DISSEMINATION OF PLANETARY DEFENCE. M. Mochi[1], R. Paoli[1] and G. Tommei[1] . [1]Department of Mathematics, University of Pisa, Largo Bruno Pontecorvo, 5, Pisa (PI) 56127

Introduction: The effectiveness of game-based learning methods [1] in facilitating understanding of complex concepts, arousing the interest of students and encouraging memorization is widely recognized [2], especially in the field of STEM subjects [3]. In particular, role-playing games entail a deep involvement of the student in the presented scenario and allow to experience issues from a unique perspective. Given this quality of role-playing games, we propose their use as effective means for scientific dissemination of the concepts underlying Planetary Defence.

Methodology: In two instances in 2025 we carried out a Planetary Defence laboratory for high school students at the IIS Chini-Michelangelo in Camaiore, Italy. The laboratory is structured over four days, for a total duration of 10 hours. It consists of three phases:

Phase 1. A series of lectures aimed at describing the status of Planetary Defence and providing insights about the various steps that follow the discovery of an asteroid. Covered topics include (but are not limited to) generalities about minor bodies of the solar system, with a focus on Near-Earth Objects and the process that leads from the first observation to discovery of a new object. Orbit determination is introduced, showing how it leads to the computation of the impact corridor and probability of impact.

One lesson is dedicated to space missions and deflection methods that could prevent an asteroid from colliding with the Earth, exemplified by the DART and Hera missions.

Phase 2. The discovery of a potentially dangerous asteroid is simulated in the form of a role-playing session, that allows students to identify with the main actors of the Planetary Defence framework and put into practice the notions acquired in Phase 1.

The simulation is inspired by a course held by Federica Spoto at the “2019 Natural Space Risks Summer School” of the Paris Observatory, and is modelled upon the "2024 Interagency Tabletop Exercise", sponsored by the NASA Planetary Defence Coordination Office (PDCO) and the Federal Emergency Management Agency (FEMA).

The participants are divided into three groups: Astronomers, Orbit Calculators and Engineers. The groups are then confronted with the hypothetical scenario, set in 2023, of the discovery of an asteroid with a small probability of impacting the Earth in the following 15 years. The probability gradually grows with each new observation night, until it crosses the threshold that make it advisable to develop Planetary Defence missions. At this point, the students need to decide which actions to take in order to avoid the impact and protect the population.

Throughout the simulation, the participants are required to perform tasks according to their assigned role. For instance, Astronomers analyse images of the night sky to identify the asteroid and try to estimate its apparent magnitude by means of the easy-to-use software Aperture Photometry Tool (APT) [4]. Orbit Calculators are required to use the CNEOS Orbit Viewer (https://cneos.jpl.nasa.gov/orbits/custom/ttx24.html) to visualize the object's orbit, find the dates of close encounters with the Earth and, among these, identify the date of possible impact. Engineers are required to use the NEO Deflection App (https://cneos.jpl.nasa.gov/nda/), made available by CNEOS, to assess the feasibility of a deflection mission and to calculate the timing and costs. All groups collaborate to assess the potential damage caused by an impact and establish a definitive course of action.

Based on the choices made, a score is assigned (unique for all students) between 1 and 19, obtained subtracting one point from the maximum value for each choice that has led to the increase of the uncertainties involved (e.g. attempting the deflection without first estimating the mass of the asteroid). The moderator extracts a number between 1 and 20: if this number is less than or equal to the score obtained by the students, the mitigation plan is successful, and the impact is avoided. Otherwise, the impact happens, and students take measures to contain the damage.

Phase 3. A constructive discussion about the results of the simulation and a critical analysis of the choices made during Phase 2. The moderator retraces the various stages of the simulation, highlighting the consequences of the steps taken and proposing, when appropriate, ideas for alternative courses of action and clarifying any doubts of the students. At this stage, a strong emphasis is placed on the importance of international collaboration.

The students are then presented with a self-evaluation questionnaire, that is used to assess the impact of the simulation on their understanding of Planetary Defence.

Results: Results of the analysis of the administered questionnaire show a generally positive perception of the laboratory and of the simulation in particular. A majority of

students perceived an overall benefit in memorization and attention maintenance due to the simulation.
According to the students' self-evaluation, the theoretical lessons were more effective than the simulation in delivering contents for most of the presented themes. However, a significant fraction of the students affirmed that although most concepts were grasped during the theoretical lessons, comprehension of their importance and implications was reached only during the simulation. Thus, even if the simulation does not seem to represent a potential substitute for theoretical lessons in delivering knowledge, it deserves to be considered as a valid tool to support learning and to put concepts into a real-life context.

Improved version in 2026: The project participated in the SISP-AC selection for teaching and dissemination activities to be held in schools in 2025-2026 (Bando Didattica e Divulgazione 2025) and was granted financial support. This will allow some improvements to be implemented in the 2026 edition of the laboratory.

We plan to involve representatives of the media, political sciences and Civil Protection, to present their connection to Planetary Defence during the theoretical lessons and to engage with the students during the simulation. This will give the participants a broader view of the issues faced by the Planetary Defence community from various perspectives.

To improve the versatility and repeatability of the laboratory, we will restructure it in a format that can be performed in a single day, thus facilitating the scheduling of future sessions.

Finally, we also wish to extend the project to a wider audience, by organizing a session for the general public, to be held on the occasion of the 2026 Asteroid Day.

References: [1] Hanghøj, T. (2013). de Freitas, S., Ott, M., Popescu, M. M. & Stanescu, I. (eds.), IGI Global, 81-101. [2] Terracina A. et al. (2016) 2016 IEEE 16th ICALT, 148–152. [3] Randi M. and Carvalho H. (2013) *Brazilian Journal of Medical Education*, 37, 80. [4] Laher, R. et al. (2012) *Publications of the Astronomical Society of the Pacific*, https://doi.org/10.1086/666883.

ASTEROIDALERT ESCAPE ROOM: SISP–AC OUTREACH CALL 2024 A. Farina[1], M. Lazzarin[1], A. C Mura[1,2], A. Baggetta[1], J. Jonckheere[3], J. Bermudez[4], M. Montis[5], A. Visentin[1], F. La Forgia[1], F. Amadori[6,7], F. Cabras[1], L. Fiaccadori[1], I. Albanese8,[1,4], E. Martellato[2], P. Ochner[1,2], S. Ciroi[1] and **NEOPOPS TEAM**.
[1] Department of Physics and Astronomy, Padova University, Vicolo dell'Osservatorio 3, 35122 Italy,
[2] Istituto Nazionale di Astrofisica (INAF) - Osservatorio Astronomico di Padova, Vicolo dell'Osservatorio 5, 35122 Padova, Italy
[3] Gran Sasso Science Institute, Via Iacobucci 2, 67100, Italy
[4]INFN - Sezione di Padova, I- 35131, Padova, Italy
[5]Infn - laboratori nazionali di legnaro (oppure INFN-LNL), Viale dell'Università 2, 35020 Legnaro, Italy
[6]INAF - Osservatorio Astrofisico di Torino, via Osservatorio 20,10025 Pino Torinese, Italy
[7]Dipartimento di Fisica, Università degli Studi di Torino, via Pietro Giuria 1, I-10125, Torino, Italy
[8]Centro di Ateneo di Studi e Attività Spaziali "Giuseppe Colombo", Via Venezia 1, I-35131 Padova - Italy

Introduction: The AsteroidAlert project is a science outreach activity based on an Escape Room format and is designed for high-school students visiting the Asiago Astrophysical Observatory. The initiative introduces participants to the scientific relevance of studying Near-Earth Objects (NEOs), objects that may pose a threat to Earth and are therefore central to planetary-defense efforts and international monitoring programs. In recent years, NASA's DART mission [1], ESA's Hera mission [2] and the upcoming ESA Ramses mission have highlighted the growing interest in mitigation strategies and in the analysis of the physical properties of NEOs. AsteroidAlert takes inspiration from this scientific context and turns it into an outreach activity based on active learning and collaboration between the participants. The aim is to help students understand both the scientific motivations and the broader implications of studying these bodies. The activity also provides an opportunity to introduce them to the basic principles of the scientific method, group work and the decision-making processes typical of astronomical research. Through a narrative inspired by planetary defense, students collaborate to analyze information, use scientific tools, and make decisions based on data, experiencing an environment similar to that of a real research group.

Scientific Idea: The scientific idea behind AsteroidAlert focuses on planetary defense and on the role of NEOs as a potential threat to the Earth. The project aims to introduce students to the basic principles of small-body research and to explain why the scientific community invests in the monitoring and physical characterization of these objects. Within this framework, the activity touches on topics such as asteroid taxonomy, basic photometry, astronomical coordinates and the essential principles of telescope pointing. The activity provides a realistic setting: students take on complementary roles and work together to collect data needed to deflect an asteroid, simulating a decision-making process similar to that used by research groups involved in planetary defense. The scientific idea is presented in a concrete way, through a narrative that makes the threat believable and helps participants understand the social value of this field of study.

Description: AsteroidAlert is a science-based escape room divided into three phases and it lasts about 120 minutes. The activity combines a narrative setting, scientific clues and collaborative tasks to simulate the work of a research group studying a potentially hazardous asteroid. Students find themselves inside the dome of the Asiago Astrophysical Observatory in the year 2059, at a time when astronomers no longer observe with telescopes because of the fall of asteroid Apophis in 2029. In an old observatory with a broken telescope, students must try to repair it after receiving a call from ESA reporting a new threat: a potentially hazardous asteroid on its way towards Earth. Their task is to restore the instrument and collect new observations to be sent to ESA, in order to avoid a second impact thirty years after the first Apophis's. The first phase includes welcoming and introduction, during which students receive the scientific and narrative context of the activity. The activity was carried out inside the multimedia dome of the Asiago Observatory during the PCTO programme in July 2025. The second phase is operational, and students are divided into three complementary roles: (i) The astronomers analyze scientific material, reconstruct the physical properties of the NEO and interpret simplified data. (ii) The technicians work on restoring the telescope through simulated maintenance, dome orientation and system reactivation. (iii) The computer scientists focus on reactivating a fictional artificial intelligence used to calculate the ephemerides of the asteroid. The tasks are carried out by using different materials, including manuals, tablets, lockboxes and visual aids, all designed to promote teamwork. In the final phase, the groups combine the gathered information to reactivate the Galileo telescope, simulate the observation of the asteroid, and send the results to ESA.

Motivation: The choice of using an escape room comes from the need of involving students in an ac-

tive setting that highlights collaboration, time management, and problem solving, which are important in any planetary defense approach. Unlike a traditional lesson, this format allows participants to be active throughout the activity and supports learning based on interaction. The format develops both scientific and transversal skills. The use of roles and tasks distributes complementary responsibilities: astronomers, technicians, and computer scientists must work together to interpret clues, apply scientific ideas, and combine different pieces of information. This structure reflects the collaborative nature of research on NEOs and helps students understand why cooperation is essential in risk-mitigation activities. The narrative setting increases engagement and makes the asteroid threat believable. The limited time helps students to see the scientific process as dynamic and goal oriented.

Team and student feedback: The project was developed by a group of PhD students, master's and bachelor's astronomy students, researchers, university professors, computer scientists, and science communicators. The feedback collected through a final questionnaire shows a high level of appreciation. Students valued the immersive nature of the activity, the effectiveness of the different roles and the importance of cooperation between groups. Future plans include the introduction of a fourth coordinating role, an expansion of the computer-science tasks using Arduino boards, a better integration of the final phase, and the possibility to extend the project to more classes and schools.

Conclusions: AsteroidAlert demonstrated to be an effective format to introduce students to Solar System studies and planetary defense through a participatory and cooperative approach. The project shows how combining scientific content with interactive dynamics can support meaningful learning and help developing an interest in the study of Near-Earth Objects. AsteroidAlert was made possible thanks to the award from the Call for "Bando per attività divulgativa e didattica presso Scuole Secondarie di primo e secondo grado Anno 2024" of the "Società Italiana di Scienze Planetarie – Angioletta Coradini" (SISP-AC). Considering the topic of planetary defense and the study of NEOs, this outreach project is included in the European Near-Earth Object Physical Observations and Properties Simulation (NEOPOPS) project funded by ESA.

Acknowledgment: The project NEOPOPS is funded by a programme of the European Union implemented by ESA (agreement No. 4000147191/25/D/MRP).We gratefully acknowledge the *Società Italiana di Scienze Planetarie – Angioletta Coradini* for the award granted. We also thank the Asiago Astrophysical Observatory for providing access to its facilities and for their support and availability during the execution of the escape room activity.

References:

[1] Rivkin, A., et al. (2021). *The Double Asteroid Redirection Test (DART): Planetary defence investigations and requirements*. Planetary Science Journal, 2, 173.

[2] Michel, P. et al. (2022). *The ESA Hera Mission: Detailed Characterization of the DART Impact Outcome and of the Binary Asteroid (65803) Didymos.* Planetary SCience journal, 3, 160.547, 2022.

XXI Congresso Nazionale di Scienze Planetarie

Sessione Piccoli Corpi
Comete

EARLY CN OUTGASSING AND PRODUCTION RATES OF C/2024 E1 (WIERZCHOS) AT 4 AU. A. C. Mura[1,2] , F. La Forgia[1], M. Lazzarin[1], G. Cremonese[2] , P. Cambianica[2], A. Farina[1], G. Munaretto[2],
[1]Dipartimento di Fisica e Astronomia "Galileo Galilei", vicolo dell'Osservatorio 3, 35122, Padova, Italy, email: alessandra.mura@studenti.unipd.it [2]INAF, Astronomical observatory of Padova, vicolo dell'Osservatorio 5, 35122, Padova, Italy.

Introduction: Studying the activity and driving mechanisms of comets at large heliocentric distances has been an active research field for several years. According to early models of comets activity [1], the formation of a coma was mainly attributed to the sublimation of water ice. Consequently, beyond the snowline of the Solar System, located between 2.5 and 3.5 AU, cometary activity was not expected. However, observations soon began to dismount this model with several examples of comets found active well beyond 4 AU. A famous example of this being comet Hale Bopp [2].

To date, high distance cometary activity is not unprecedented, with many cases of activity beyond 3 AU also in short period comets [3] and several cases of comets active > 20 AU.

To account for the observed activity at greater distances, several mechanisms have been suggested. Among the most commonly proposed are the sublimation of supervolatiles such as CO and CO_2, the phase transition of amorphous water ice into its crystalline form, a process that releases previously trapped volatile gases [4], but also mechanisms such as polymerization of condensed-phase HCN [5].

Our understanding of high distance cometary activity is becoming increasingly relevant with the upcoming ESA Comet Interceptor mission [6]. Scheduled for launch in 2028, this mission aims to perform the first close encounter with an Oort Cloud comet, or possibly an interstellar object, whose target will only be selected after launch. A detailed characterization of the activity development of Dynamically New Comets (DNCs) is therefore essential for the mission's success [6].

Comet C/2024 E1 (Wierzchos) was discovered on March 3 by the Mt. Lemmon Survey [7] at approximately 8 AU, already displaying a 4" coma and sights of a tail. It was later observed with NIRSpec, the near-infrared spectrograph on the James Webb Space Telescope, by [8] at about 7 AU. As expected, no absorption feature of water ice were detected, while strong CO_2 emission was observed. Interestingly, no CO bands were identified, despite CO being more volatile than CO_2.

Given the optimal approaching geometry of its orbit with high altitudes in the northern hemisphere, we issued a spectroscopic follow-up campaign of this target at the Large Binocular Telescope (LBT) Arizona, USA, to monitor the evolution of its activity from large to small heliocentric distances before and after perihelium. The first part of our program covers from 6.3 to 3.3 AU inbound and was aimed to detect any sights of high distance activity in the visible spectrum of E1.

Here we present the first part of our observative program for comet E1, in its pre-perihelium phase, from 6 to 3 AU.

Observations and Data Reduction: The observations were performed at the LBT in binocular mode (equivalent area 11.4m) with Multi-object Double Spectrographs (MODS), which consist of two multi-objects spectrograph mounted on each Gregorian focus of the LBT. MODS provides a spectral range of 0.32-1.1 micron with a field of view of 6' x 6' and is equipped with medium resolution (R ~ 2000) gratings and a set of long-slit masks. The CCD provides a pixel scale of 0.120 arcsec/pixel. We required the 2.4" longslit mask. This first part of the program is composed of a total of four observative runs: September 2024 and April, May and July 2025.

All spectra were pre-reduced, wavelength- and flux-calibrated with the aid of the Spectroscopic Interactive Pipeline and Graphical Interface (SIPGI) [9]. The flux calibration was applied to the single bidimensional spectra that were later stacked and used to compute the total flux of the CN radical along the slit.

The final monodimensional spectrum is divided by a solar analog star and subtracted by the continuum dust spectrum to better highlight the gas emission. The dust continuum was extracted by selecting wavelength regions free of expected molecular emission, interpolating the continuum shape in these regions with a polynomial function, and then subtracting the resulting fit from the comet's spectrum.

Analysis: Among the four dates of observations, three show the CN radical B-X (0-0) violet band (~3882 Å), respectively at 4.1, 3.8 and 3.3 AU (Fig. 1). This particular band is one of the most common and extensively studied features in cometary spectra; however, it is rarely observed beyond the region where water-ice sublimation can account for cometary activity, that is, beyond 3.0–3.5 AU.

We fitted a gaussian function centered on CN emission peak to retrieve the total emitted flux. SIPGI provides the reduced spectra with the associated error, which we propagated along the stacking procedure and considered alongside the residuals of the gaussian fit.

The molecular production rate (Q, molec s-1) was computed using the Haser coma model [10]. The main parameters describing the emitting species are their scale lengths [11] and fluorescence efficiencies (g-factors, erg s-1) [12]. In this context, the CN radical is a daughter species, with HCN assumed to be its parent molecule [13].

Results: We obtain an increasing CN production rate among the April, May and July spectra, of (1.84 ± 1.50) 10^{23}, (3.30 ± 1.24)10^{23} and (41.11 ± 3.96) 10^{23} molecules s^{-1} respectively. The upper limits on production rates of C2 and C3 on July spectrum, are respectively 17.7 10^{23} and 5.54 10^{23}.
We obtain a ratio with CN of $\log(Q(C_2)/(Q(CN)) < -0.37$ and $\log(Q(C_3)/(Q(CN)) < -0.87$.
Following the criteria of [14], these results tentatively classifies this comet as carbon-chain depleted, as it holds the relation $\log(Q(C_2)/Q(CN)) < 0.02$ and $\log(Q(C_3)/Q(CN)) < -0.86$.

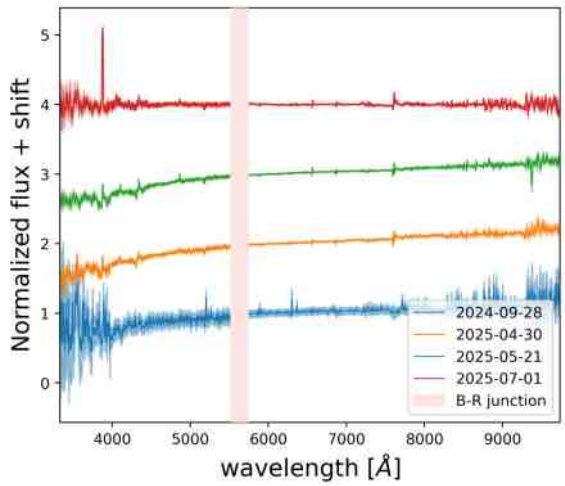


Fig 1: All the spectra of comet C/2024 E1 collected for the first part of the observative program with MODS@LBT. The red region indicates the junction between the blue and red channel.

References: [1] Whipple, F. L. 1950, ApJ, 111, 375
[2] Sekanina, Z. 1996, A&A, 314, 957
[3] Mazzotta Epifani, E., Palumbo, P., Capria, M. T., et al. 2007, Monthly Notices of the Royal Astronomical Society, 381, 713
[4] Prialnik, D. & Bar-Nun, A. 1992, A&A, 258, L9
[5] Rettig, T. W., Tegler, S. C., Pasto, D. J., & Mumma, M. J. 1992, The Astrophysical Journal, 398, 293
[6] Jones, G. H. & et. al. 2024, Space Science Reviews, 220, 9
[7] Green, D. W. E. 2024, Central Bureau Electronic Telegram 5364, CBET, 5364, central Bureau for Astronomical Telegrams
[8] Snodgrass, C., Holt, C. E., Kelley, M. S. P., et al. 2025, MNRAS, 541, L8
[9] Gargiulo, A., Fumana, M., Bisogni, S., et al. 2022, Monthly Notices of the Royal Astronomical Society, 514, 2902
[10] Haser, L. 1957, Bulletin de la Societe Royale des Sciences de Liege, 43, 740
[11] Langland-Shula, L. E. & Smith, G. H. 2011, Icarus, 213, 280
[12] Schleicher, D. G. 2010, The Astronomical Journal, 140, 973
[13] Fray, N., Bénilan, Y., Cottin, H., Gazeau, M.-C., & Crovisier, J. 2005, Planetary and Space Science, 53, 1243
[14] Cochran, A., Barker, E., & Gray, C. 2012, Icarus, 218, 144

COMET 3I/ATLAS THROUGH THE CASSIS STEREO CAMERA ONBOARD EXOMARS/TGO. G.Cremonese[1], N.Thomas[2], M.Almeida[2], A.Pommerol[2], J.Wray[3], P.Cambianica[1], G.Munaretto[1], M.Pajola[1], [1]Astronomical Observatory of Padova-INAF, Italy, gabriele.cremonese@inaf.it, [2]Dept. of Physics, University of Bern, [3]Georgia Inst. of Technology, USA.

Introduction: The discovery of 3I/ATLAS (C/2025 N1) [1] marks the arrival of only the third known interstellar object (ISO) entering our Solar System, after 1I/'Oumuamua in 2017 [2] and 2I/Borisov in 2019 [3,4]. Unlike its predecessors, 3I was identified early in its inbound trajectory, enabling the first pre-perihelion spectroscopic observations at a heliocentric distance of 4.47 au. These early data, obtained with the VLT/MUSE integral-field spectrograph [5], revealed a dusty, active cometary body with a compact coma but no gaseous emissions from C_2, CN, NH_2, or [OI]. The optical reflectance spectrum was red and featureless, with a normalized slope of ~18%/1000 Å—redder than most Solar System comets, and similar to irradiated Trans-Neptunian Objects, suggesting the coma originated from processed surface layers rather than fresh ices. CN was later detected, with production rates increasing from $Q(CN) \sim 10^{24}$ s^{-1} at ~3.5 au in mid-August [6,7] to $\sim 10^{25}$ s^{-1} at ~2.2 au in mid-September [8], while no emission was detected from C_2 or C_3. These constraints imply strong carbon-chain depletion, with $\log Q(C_2)/Q(CN) < -0.77$ [6], a characteristic shared with 2I/Borisov [9]. Simultaneous photometry revealed a gradual brightening and a growth in the dust production parameter, $Af\rho \approx 300$ cm, consistent with mild but sustained activity. The derived gas-to-dust ratio, $\log Q(CN)/Af\rho \approx 22.4$, lies at the lower end of values for Solar System comets [6]. Dynamic modeling suggests that 3I/ATLAS originated from the Milky Way's thick disk, implying ancient formation under low-metallicity, water-rich conditions [10]. Water has indeed been detected as both vapor [11] and icy grains [12,13], but the coma of 3I/ATLAS contains even more abundant CO [13]—similar to 2I/Borisov [15]—and CO_2 [13,14]. The observed evolution—from a red, dust-dominated body to the onset of outgassing and perhaps more rapid brightening once inside ~2 au [16]—reveals that interstellar comets may undergo similar compositional transitions as Oort Cloud comets, yet preserve distinct chemical fingerprints. The study of 3I/ATLAS thus provides a rare glimpse into the chemical diversity and evolutionary pathways of extrasolar minor bodies, bridging the gap between Solar System comets and material formed around other stars.

CaSSIS: The Colour and Surface Stereo Imaging System (CaSSIS) [17] is a multi-filter stereo camera on board the European Space Agency ExoMars Trace Gas Orbiter (TGO) satellite. CaSSIS is designed and operated to provide colour images of the Martian surface in four filters centred at (effective wavelength ± bandwidth) 499.9 ± 118.0 nm (BLU), 675.0 ± 229.4 nm (PAN), 836.2 ± 94.3 nm (RED), and 936.7 ± 113.7 nm (near-IR; NIR), and 3D terrain models from stereo observations [18]. Its four filters and their relatively high absolute radiometric accuracy of 2.8% [19] make it an useful asset to study even non-Martian surface targets, such as the two Martian Moons Phobos and Deimos [20] and, more recently, the 3I/ATLAS interstellar comet.

Preliminary results: CaSSIS obtained a set of images of the interstellar object, 3I/ATLAS, during its close approach to Mars on 3 October 2025. The comet was 0.2 au from Mars leading to an image scale of ~320 km/px. The comet was recorded in all four colours available in the CaSSIS system covering the 440-1000 nm wavelength range in broad bands. The comet showed measurable activity (Fig. 1). The data were also used to considerably improve the ephemeris because of the very different viewing direction with respect to the Earth-comet one. The data are noisy because the comet was more than 6 orders of magnitude fainter than the usual targets of CaSSIS. However, we expect to be able to provide Afrho, dust distributions, and some colour information following detailed analysis.



Figure 1. CaSSIS PAN image stack of 3I/ATLAS.

References: [1] Seligman, D. et al. (2025) Astrophys. J. Lett., 989, L36. [2] Meech, K. et al. (2017) Nature, 552, 378-381. [3] Jewitt, D. and Luu, J. (2019) Astrophys. J. Lett., 886, L29. [4] Guzik, P. et al. (2020) Nature Astron., 4, 53-57. [5] Opitom, C. et al. (2025) MNRAS, 544, L31-L36. [6] Salazar Manzano, L. et al. (2025) Astrophys. J. Lett., 993, L23. [7] Rahatgaonkar, R. et al. (2025) arXiv:2508.18382. [8] Hutsemékers, D. et al. (2025) arXiv:2509.26053. [9] Opitom, C. et al. (2019) Astron. Astrophys., 631, L8. [10] Hopkins, M. et al. (2025) Astrophys. J. Lett., 990, L30. [11] Xing, Z. et al. (2025) Astrophys. J. Lett., 991, L50. [12] Yang, B. et al. (2025) Astrophys. J. Lett., 992, L9. [13] Cordiner, M. et al. (2025) Astrophys. J. Lett., 991, L43. [14] Lisse, C. et al. (2025) Res. Notes AAS, 9, 242. [15] Cordiner, M. et al. (2020) Nature Astron., 4, 861-866. [16] Zhang, Q and Battams, K. (2025) arXiv:2510.25035. [17] Thomas, N. et al. (2017) Space Sci. Rev., 212, 1897-1944. [18] Re, C. et al. (2022) Planet. Space Sci., 219, 105515. [19] Thomas, N. et al. (2022) Planet. Space Sci., 211, 105394. [20] Munaretto, G. et al. (2025) Astron. Astrophys., 700, L1.

Acknowledgments: This work has been developed under the ASI-INAF agreement n.2024-40-HH.0

Statistical Analysis of Cometary Ices: Inheritance or Chemical Reset?

M. Lippi[1], L. Podio[1] and C. Codella[1], [1]INAF Osservatorio Astrofisico di Arcetri, Largo Enrico Fermi 5, 50125 Firenze, Italy.

Introduction: Comets accreted from the gas and dust in our protoplanetary disc approximately 4.6 billion years ago. Soon after formation, they were scattered and stored far enough away from the Sun, where they remained significantly frozen until this day, most likely maintaining the majority of their original mineralogical and chemical properties.

Comparing molecular abundances in comets to those in planet-forming disks surrounding young solar analogues (10^4 — 10^6 years old) can thus reveal significant insights in the physical, chemical, and evolutionary processes that shaped our and other planetary systems, including the degree of the chemical reprocessing in the disk (inherited vs reset scenarios [1,2,3]).

Recent cometary studies have revealed a wide chemical diversity among comets [1,4,5] which is consistent with the numerous processes that may have occurred in our protoplanetary disc, and with the dynamical models that predict the comet dispersion into their current reservoirs [e.g., 6]. This makes it quite complicated to classify these bodies from the chemical point of view, and to link the observed differences to each comet formation site.

Here, we will present a statistical methodology that we implemented to properly interpret molecular abundances measured in comets, and to compare the results to similar abundance ratios measured in star- and planet-forming regions [7].

Methodology: For each species detected in comets, we first searched for evidence of significant differences in composition depending on different dynamical classes that could be linked to the evolution of the comet material after storage. In fact, Jupiter Family comets may be more evolved than Oort Cloud ones, due to their proximity to the Sun.

Secondly, we investigated the reliability of the abundance ratios as probes of the cometary ice composition by looking at variations due to chemical or physical processes occurring in the coma during the observations, as differences in outgassing at different heliocentric distances and before and after perihelion. We further analysed potential biases introduced by instrumental and modelling effects by comparing abundances estimated from infrared spectroscopy to those retrieved from observations at (sub-)millimetre wavelengths [e.g., 8, 9], as well as with 67P/Churyumov-Gerasimenko (hereafter, 67P) data collected via mass spectroscopy during the ESA-Rosetta mission [10].

Finally, we compared molecular abundance ratios of iCOMS and other species in comets to those measured in protoplanetary disks, and more in general in planet-forming regions.

Results: An example is shown in Fig. 1. Here, the statistical analysis of the abundance ratios [CH_3OH/H_2CO] and [NH_3/CH_3OH] reveals a few trends correlated to the observing conditions. In particular it is possible to notice a dependency with the heliocentric distance, due to an excess of H_2CO mixing ratios with respect to water for comets observed within 1 au from the Sun. Moreover, strong discrepancies are observed between the averaged abundances retrieved through ground-based spectroscopy and those obtained for comet 67P with the mass spectrometer on board of the Rosetta spacecraft. While some of these differences can simply be explained by data variability, others are statistically significant, and may drastically change our understanding of the comet chemistry in the context of planet formation. In this respect, our study highlights the significance of large sample statistics to properly constrain the range of molecular abundances in comets prior to any comparison.

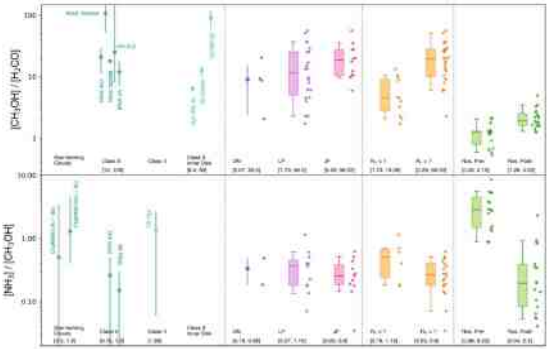


Fig 1: Results of the ProDisCo project highlighting the need of synergistic and statistical approaches to compare different objects (i.e., comets, and planet-forming regions), and different methodologies.

When compared with star-forming systems at different evolutionary stages, the [CH_3OH/H_2CO] and [NH_3/CH_3OH] abundance ratios in comets are compatible with those measured in Class 0 and in the inner disk of Class II objects, thus pointing to an inheritance scenario.

We will further show results obtained considering more complex species such as methyl cyanide, formamide, isocyanic acid, formic acid (see for example Fig. 2, Lippi et al in preparation), highlighting the caveats found when comparing comets and star-/planet forming regions and the need for increasing the statistics to reach firm conclusions.

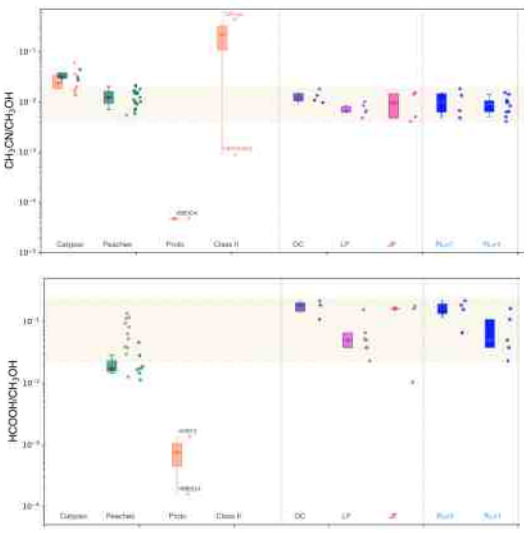


Fig 2: Statistical comparison of the abundance ratios [CH_3CN]/[CH_3OH] and [HCOOH]/[CH_3OH] in comets and star- and planet forming regions.

References:

[1] Mumma, M.J., Charnley, S.B., 2011, ARAA, 49, 471; **[2]** Ceccarelli, C. Et al., 2023, Protostars and Planets VII, ASPC; **[3]** Podio, L. et al., 2020, A&A 642, L7; **[4]** Lippi, M., et al., 2021, AJ, 162, 74; **[5]** Dello Russo, N., et al., 2016, Icarus, 278, 301; **[6]** Morbidelli, A. & H. Rickman, 2015, A&A, 583, A43; **[7]** Lippi et al., 2024, ApJ, 970, L5; **[8]** Biver N., et al., 2021, A&A 651, A25; **[9]** Biver N., et al., 2014, A&A 566, L5; **[10]** Läuter M., et al., 2020, MNRAS 498, 3995–4004.98, 3995–4004.

XXI Congresso Nazionale di Scienze Planetarie

Planetologia sperimentale e di laboratorio
Sessione "Traces of Life"

BACTERIA, SALTS AND BRINE MIXTURES : INFRARED SPECTRAL MAPPING OF A LABORATORY ANALOGUE FOR HABITABILITY ON ICY MOONS. S. Rubino[1], F. Furnari[1], S. Stefani[1], G. Piccioni[1], F. Tosi[1], G. Di Stefano[2], D. Billi[2], L. Tonietti[3], A. Rotundi[3]. [1]INAF-IAPS, Istituto di Astrofisica e Planetologia Spaziali, Rome – Italy, [2]Università di Roma - Tor Vergata, Dipartimento di Biologia, Rome – Italy, [3]Università degli studi di Napoli "Parthenope", Dipartimento di Scienze e Tecnologie, Naples – Italy.

Introduction: Europa, one of Jupiter's Icy Moons, harbors a liquid water ocean in contact with a geothermally active sub-surface allowing for chemical reactions [1-2-3], which are of particular exobiological interest. Liquid water oceans have also been detected/postulated for other icy moons, such as Ganymede and Enceladus, orbiting Jupiter and Saturn respectively, making them also of exobiological interest. The Europa Clipper mission (NASA) and the JUICE probe (ESA) [4, 5] will both be exploring the Galilean moons system, with particular focus on Europa and Ganymede respectively. Prior to the probes' arrival in the Jovian system, it is of great importance to assess the presence and detectability of the bio-signatures associated with possible life on icy moons with the instruments onboard. The laboratory work presented here is focused on determining such biosignatures on laboratory analogues of an "inhabited" icy moon surface, made of a mixture of brines and microbial organisms as our proxy for Life. This investigation may also support the identification of biosignature more generally in ice covered exoplanets.

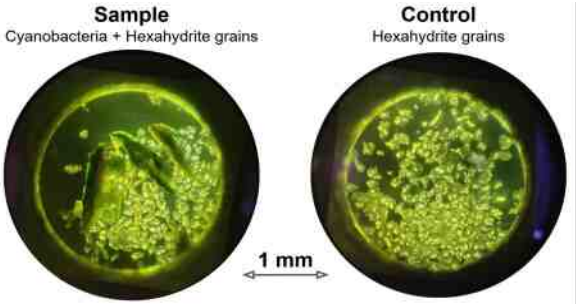


Figure 1 – Investigated laboratory "footprints" in Cu washers.

Materials and Methods: Our proxy for Life is represented by Desert Cyanobacteria (*Chroococcidiopsis* spp.), an extreme-tolerant bacteria exhibiting oxygenic photosynthetic behaviour [6]. The strain considered for this work is able to use infrared light for oxygenic photosynthesis, possibly allowing its survival through the use of the thermal glow of hydrothermal vents. In its extreme-tolerant form, the cyanobacterium enters a desiccated state, which allows it to resist low-Earth orbit conditions and Mars-like conditions. Other laboratory simulations have been carried out to test its different properties (e.g.: limits of photosynthetic performance, radioresistance) [7-8-9-10]. For this work, we created two laboratory "footprints" (cf. Figure 1) of an "inhabited" icy moon surface, "Sample" with a mixture of cyanobacteria and hexahydrite grains (MgSO4 , H2O) and "Control" with only hexahydrite grains. Hexahydrite is a salt expected to be found on the Jovian Icy Moons surfaces. The two "footprints" are assembled inside a Cu washer, sandwiched between two ZnS windows. The system is put inside a cryo-cell to be exposed to vacuum down to P ~ $1E^{-3}$ mbar and to cryogenic temperature T = 100 K, to emulate the surface of icy moons. While the environment of the cyanobacteria is being changed toward more extreme conditions, the spectral properties from visible to mid-IR (0.5 - 12 μm) of the "footprints" are being monitored using an infrared microscope via spectral mapping in transmission mode.

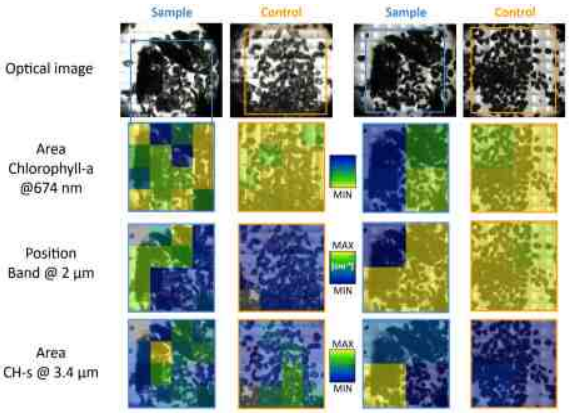


Figure 2 – Spectral indices tested to spatially differentiate bacteria from salts at ambient (P, T) and at vacuum/cryogenic conditions. The position of the band at 2 μm does not differentiate at vacuum/cryogenic conditions due to the peak-position shift of the band for hexahydrite.

Results and Discussion: In the visible spectral range, the spectral features of the cyanobacterium (associated with the Chl-a pigment, cf. Figure 2) and that of hexahydrite are well separated, enabling a direct spatial differentiation in the maps at both ambient conditions and cryogenic/vacuum conditions.

In the near-IR range, the spectral features of the cyanobacteria get lost in the features of the hydrated salt due to spectral overlap with the water-associated features. Spectral indices such as peak-position, which work for spatial differentiation at ambient (T, P) do not work at cryogenic/vacuum conditions due to changes in the position of the spectral features of hexahydrite (Figure 2).

In the mid-IR range, the aliphatic C-H stretching band at 3.4 μm is efficient for spatial differentiation at both ambient and cryogenic conditions (Figure 2), although it is not in itself a biosignature (abiotic molecules can also have C-H bonds).

Further laboratory work is required to fully understand the cyanobacteria/salts interactions at cryogenic/vacuum conditions. For instance, in this work samples were first put under vacuum and subsequently under cryogenic conditions, while a future work involving brines will focus on first achieving cryogenic conditions and then decreasing the cryocell pressure.

The biological samples which have been stressed here have been recovered to ascertain their survivability.

References: [1] Belton, M. J. S. et al. Science 274, 377–385 (1996). [2] Smith, B. A. et al. Science 206, 927–950 (1979). [3] Pappalardo, R. T. et al. J. Geophys. Res. 104, 24015–24055 (1999). [4] Phillips, C. B. & Pappalardo, R. T. Eos (Washington DC) 95, 165–167 (2014). [5] Grasset, O. et al. Planet. Space Sci. 78, 1–21 (2013). [6] Billi, D., Baqué, M., Verseux, C., Rothschild, L. & de Vera, J.-P., Adaption of Microbial Life to Environmental Extremes 133–146 (2017). [7] de Vera, J.-P. et al. Planet. Space Sci. 74, 103–110 (2012). [8] Baqué, M. et al. Orig. Life Evol. Biosph. 43, 377–389 (2013). [9] Di Stefano, G. et al. Life (Basel) 15, 622 (2025). [10] Billi, D. et al. Applied and Environmental Microbiology 66, 1489–1492 (2000).

Additional Information: This work is funded through the European Union and Regione Campania's FESR 2007/2013 O.O.2.1 initiative, and by the ASI-INAF agreement n.2023-6-HH.0 (Resp.: G. Piccioni).

THE IMPACT OF DIFFERENT CATIONS IN SULFATES ON THE PHOTOSTABILITY OF URACIL UNDER MARTIAN-LIKE UV IRRADIATION.

C. García-Florentino[1], A. Alberini[1,2], S. Biancalani[1,3,4,5], F. Renzi[1,2], M. Battistuzzi[1], G. Poggiali[1], J. R. Brucato[1], T. Fornaro[1], [1]INAF–Astrophysical Observatory of Arcetri, L.go E. Fermi 5, 50125 Florence, Italy, (cristina.garcia@inaf.it); [2]Department of physics and astronomy, University of Florence, Via Giovanni Sansone 1, 50019, Sesto Fiorentino (FI), Italy; [3]Department of Physics, University of Trento, Povo, Italy; [4]Italian Space Agency (ASI), Rome, Italy, [5]Department of Earth Sciences, University of Florence, Florence, Italy

Introduction: Searching for biosignatures, such as the identification of organic molecules, has become one of the main goals of the exploration programs on Mars[1]. Even if Mars was subjected to the same meteoritic infall as The Earth[2], the occurrence of organic molecules on Mars nowadays is scarce due to the harsh environmental conditions. Among the different degradation factors, UV radiation is specially harmful as it can promote the degradation of organic molecules in a few hours[3]. In this context, the preservation of organics on the Martian surface is only expected within the mineral matrices that can confer a protected environment[4]. Among different minerals on Mars, sulfates (mainly calcium and magnesium), which constitute ~40% by weight of the bedrock, are likely of evaporite origin and could have been formed by direct precipitation from water or during early burial[5], that may have supported the preservation of trapped organics over long geological timescales[6]. In addition, one of the Perseverance's instruments, the Scanning Habitable Environments with Raman and Luminescence for Organics and Chemicals (SHERLOC), a deep UV Raman and fluorescence spectrometer, found interesting Raman features that may be attributed to organics co-located with sulfate minerals[7-9].

In this context, this work aims to asses the effect of different sulfates on the preservation of the nucleobase uracil against Martian-like UV radiation. Uracil, already detected on interplanetary bodies[10], was selected as an organic molecule because it could have arrived on Mars by meteoritic impact. Among the sulfates, epsomite ($MgSO_4 \cdot 7H_2O$), anhydrite ($CaSO_4$), mirabilite ($Na_2SO_4 \cdot 10H_2O$) and iron sulfate (II) heptahydrate ($FeSO_4 \cdot 7H_2O$) were selected as the mineral phases in order to study the effect of the different cations composing the sulfates in the photoprotection of possible biomarkers, such as uracil.

Material and Methods:

Uracil previously solubilised in water was adsorbed at a 10 wt% concentration on each different sulfate. The solutions/suspensions were kept under rotation on a test-tube rotator for 24 h and afterwards dried and recrystallized in an oven at 30 °C.

The samples were characterized by Diffuse Reflectance InfraRed Fourier Transform Spectroscopy and Deep Ultraviolet Raman spectroscopy.

A Newport Oriel 300 W Xenon arc discharge lamp with a spectral range between 200 and 930 nm was used as UV source for the irradiation experiments. The samples were all irradiated for a total time of 4200 s (1h 10 min). Infrared spectra were recorded after different UV irradiation steps to monitor the degradation of the IR bands associated to uracil. The UV-induced degradation for all the observed uracil bands when adsorbed into the minerals was studied. From the degradation curves obtained from the integrated IR bands changing along the irradiation time, the experimental degradation rate, bexp (s^{-1}), degradation half-life times, $t_{1/2}$ (s) and the constant parameter degradation cross section (σ) were calculated and afterwards extrapolated to their Martian values assuming a Martian flux per area (φMars) of 1.4·1015 photons/s·cm^2 in the 190–325 nm spectral range[11].

Results and discussion:

On one hand, the IR characterization of the uracil adsorbed onto the different sulfates showed few shifts of the bands respect to the bands of pure uracil, indicating few mineral-molecule interactions. This may suggest a partial co-precipitation of pure uracil with the mineral or an addition of uracil into the mineral matrices as an inclusion. The most important shifts can be appreciated for the bands associated to both carboxylate groups when uracil is adsorbed onto iron sulfate (II) suggesting a possible interaction via these functional groups in this case.

On the other hand, the DUV-Raman mapping showed two different kind of adsorptions. The adsorption of uracil onto magnesium and iron sulfates resulted completely homogeneous and with no band changes respect to pure uracil. However, the adsorption of uracil onto calcium and sodium sulfates showed a partial co-precipitation of pure uracil in some points of the mapping, but some interactions on the points where uracil is together with the mineral. For both minerals, a shift in the raman bands related to the carboxylate group can be appreciated, indicating a possible interaction through this functional group also in these minerals. In addition, for the adsorption onto sodium sulfate, new bands appeared, not observed in the mineral blank. Finally, the DUV raman spectra showed that both calcium and sodium sulfates changed their hydration state during the adsorption process.

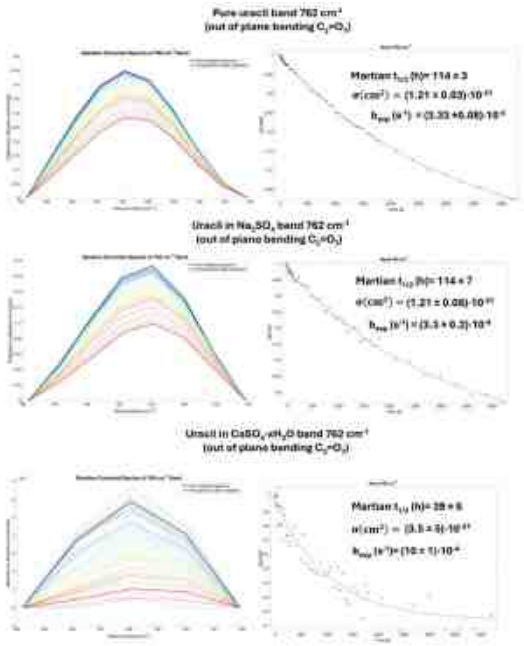


Figure 1. Baseline corrected fastest fundamental bands of uracil degraded at the different irradiation times (on the right). Degradation curves for some uracil fastest fundamental bands degraded, experimental degradation rates (b_{exp}) obtained from the degradation curve fits, cross sections (σ) and Martian half-life times ($t_{1/2}$) (on the left).

The UV-induced degradation for all the observed uracil bands when adsorbed into the minerals was studied. In Figure 1, some of the degradation curves and calculated Martian half-lifetimes for the fastest degraded band are shown. According to the mean-weighted value of the Martian half-life times calculated for all the appreciable bands of uracil in different sulfates, the photoprotection of each mineral can be ordered as follows: $CaSO_4 \cdot xH_2O$ <$FeSO_4 \cdot xH_2O$ < $MgSO_4 \cdot xH_2O$ < Na_2SO_4 < pure uracil. This result demonstrates that all the sulfates present a photocatalytic effect in the degradation of uracil in comparison to the stability of the pure uracil under UV radiation. The most photocatalytic sulfates are $CaSO_4 \cdot xH_2O$ and $FeSO_4 \cdot xH_2O$ with Martian half-life times of 30 and 48 hours and the least Na_2SO_4 and $MgSO_4 \cdot xH_2O$ with Martian half-life times of hundreds of hours in the range of the degradation observed for pure uracil.

Conclusions:

This work highlights the difficulties to assess a general photoprotective/photocatalytic behavior of the minerals to preserve organic molecules, which is affected by the specific molecule-mineral interactions or other types of adsorption (inclusions). This makes very difficult to give general rules for the best mineral targets as it not only depends on the mineral but also on the interactions with the specific organic molecule. Definitely, the different cations of the sulfates and their hydration states provoke a different interaction/inclusion that together with their different UV absorption properties lead to a predominant photocatalytic behaviour in comparison to the stability of pure uracil. Among the studied sulfates, $MgSO_4 \cdot xH_2O$ and Na_2SO_4 are the ones preserving uracil for the longest time. However, it is equally important to emphasise that uracil is in all the cases stable for longer than 12 hours of UV irradiation, which corresponds to the time of exposure to martian ambient conditions after the abrasions performed by Perseverance before SHERLOC can take a measurement.

Acknowledgements: ASI/INAF Agreement 2023-3-HH.

References:

[1] Fornaro, T. et al. (2020). *Front. Astron. Space Sci. 7*. [2] Zhu et al.(2022). *Science Advances, 8(46)*. [3] Fornaro et al. (2018). *Icarus, 313:38–60.*[4] Fornaro, T. et al. (2018). *Life 8, 56.* [5] Squyres et al. (2004), *Science 306, 1709–1714.* [6] Sephton et al.(2023), *Journal of the Geological Society 180, jgs2022-152.* [7] Sharma et al. (2023). *Nature 619, 724–732.* [8] Murphy et al. (2025) LPSC 2025. [9] Teresa et al.(2025) Nat Astron 1–14. [10] Oba et al. (2023). *Nat Commun 14, 1292.* [11] Patel et al. (2002). *Planetary and Space Science 50(9):915–927.*

INVESTIGATING THE STABILITY OF 9-METHYLANTHRACENE IN MAGNESIUM AND CALCIUM SULFATES UNDER UV IRRADIATION TO ASSIST DETECTION OF ORGANICS ON MARS.

F. Renzi[1,2], T. Fornaro[1], A. Alberini[1,2], S. Biancalani[1,3,4,5], G. Poggiali[1], C. García Florentino[1], M. Battistuzzi[1] and J. R. Brucato[1].

[1]INAF- Astrophysical Observatory of Arcetri, L.go E. Fermi 5, 50125 Firenze, Italy (francesco.renzi@inaf.it); [2]Department of physics and astronomy, University of Florence, Via Giovanni Sansone 1, 50019, Sesto Fiorentino (FI), Italy; [3]Department of Physics, University of Trento, Povo, Italy; [4]Italian Space Agency (ASI), Rome, Italy, [5]Department of Earth Sciences, University of Florence, Florence, Italy

Introduction: Mars remains a central focus in astrobiological exploration, with numerous missions searching for traces of ancient life. Although current Martian conditions are inhospitable, evidence indicates that the planet once hosted environments similar to early Earth, with hydrological activity, diverse geological features, and a dynamic atmosphere. A major target in the search for biosignatures on Mars is to identify minerals capable of preserving potential biological and organic evidence. However, the Martian surface is exposed to UV radiation and cosmic rays, which can degrade organic material [1]. Perseverance, the rover from NASA's Mars 2020 mission [2], is currently exploring the Martian surface to investigate its geological and chemical context and to search for potential evidence of past habitable environments. In recent observations some strong spectral features attributed to aromatic organic molecules associated with traces of aqueous alteration in minerals were observed, including the presence of sulfates and carbonates. Indeed the SHERLOC instrument onboard Perseverance has identified complex Raman features in the Quartier target on the floor of Jezero Crater, in the spectral ranges 1300-1500 and 1600-1700 cm^{-1}, which are relevant to organics, in association with sulfates [3,4].

Here we investigated the photostability of 9-methylanthracene (9MA), a ploycyclic aromatic hydrocarbon proposed as one of the candidates to be the source of Quartier organic signals [5], under martian like UV irradiation and when associated with magnesium and calcium sulfates, the primary minerals detected alongside organic matter.

Materials and methods: Analog samples of the Quartier target containing 9-methylanthracene were prepared to simulate potential natural interactions occurring either in an early Martian aqueous environment or during a subsequent dry stage. [5,6]. Sample analysis was carried out with a Bruker VERTEX 70v FTIR spectrometer equipped with a Praying Mantis™ located at INAF–Astrophysical Observatory of Arcetri using Diffuse Reflectance Infrared Fourier Transform (DRIFT) to probe molecule-mineral interactions. A Newport Xenon enhanced UV lamp was pointed onto the sample inside the spectrometer via an optical fiber. This setup enabled in situ UV irradiation experiments, allowing assessment of the photostability of the organic compound when associated with minerals under simulated Martian surface conditions. This experiment was carried out for three different samples: pure 9MA, 9MA at 10 wt.% concentration with anhydrite (anhydrous calcium sulfate) and 9MA 10 wt.% with epsomite (magnesium sulfate eptahydrate).

Results and discussion: Calcium sulfate showed a potential photocatalytic effect on 9-methylanthracene (9MA), reducing, by more than half in most cases, the half-lives of infrared bands associated with fundamental vibrational modes with respect to the experimental results obtained with pure organic compound. In contrast, the behaviour of magnesium sulfate is slightly photoprotective, extending the half-lives of all monitored bands beyond 11 sols (Martian days). This finding is particularly significant, as Perseverance observed stable organic signals in Quartier after 11 sols without any detectable degradation [5]. These results therefore support 9MA as a strong candidate contributing to the organic spectral features detected by the rover instrument.

Moreover, each irradiation experiment confirmed the formation of the 9MA dimer phase [7], as the principal infrared indicators of its presence were consistently observed in the spectra of all three irradiated samples.

References: [1] Fornaro, T., Steele, A., & Brucato, J. R. (2018) *Life*, *8*(4), 56. [2] Farley, Kenneth A., et al. (2020), 216(8), 142. [3] Scheller E. L. et al. (2022), Science, 378(6624), 1105-1110. [4] Sharma S. et al. (2023), Nature, 619(7971), 724-732. [5] Fornaro, Teresa, et al. (2025) *Nature Astronomy*, 1-14. [6] Fornaro, Teresa, et al. (2020) *Frontiers in Astronomy and Space Sciences* 7, 539289. [7] Mabied, Ahmed F., et al. (2012) *Structural Science* 68.4 , 424-430.

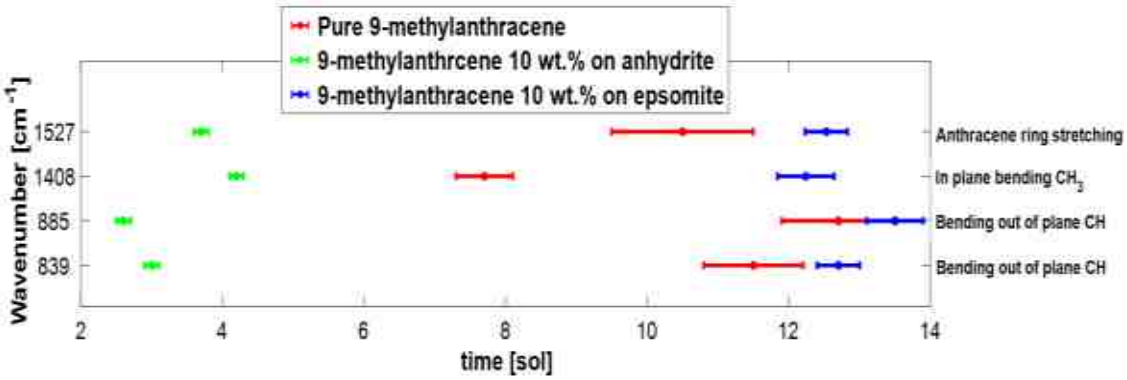


Figure 1 Comparison between half-lives of four fundamental infrared bands of 9-methylanthracene (9MA) in three different irradiated samples; pure 9MA (red points), 9MA with anhydrous calcium sulfate (green points) and 9MA with hydrated magnesium sulfate (blue points). Calcium sulfate reveals a potential photocatalytic effect on the organic molecule, while magnesium sulfate a slightly photoprotective effect. All half lives are expressed in martian days (sols) and are evaluated for specific Jezero crater conditions.

Acknowledgements: ASI/INAF Agreement 2023-3- HH.

DIELECTRIC CHARACTERIZATION OF PERCHLORATE SOLUTIONS AS ANALOGUES OF MARTIAN SUBGLACIAL LIQUID WATER. Gabriele Turchetti[1], Barbara Cosciotti[1], Sebastian Emanuel Lauro[1], Elisabetta Mattei[1], Elena Pettinelli[1] [1] Mathematics and Physics Dept., Roma Tre University
*Corresponding author: Gabriele.turchetti@uniroma3.it

Introduction: The study of the Martian environment is of considerable scientific interest for understanding the evolutionary history of the Red Planet and of the whole Solar System. The past presence of liquid water at the surface makes Mars an appealing target from an astrobiological perspective as well, since potential signatures of past life may still be preserved at the surface or within the subsurface. In 2018, the analysis of data acquired by the MARSIS radar [1] onboard the *Mars Express* mission revealed signals consistent with the presence of liquid water beneath the Martian south polar cap [2][3], in the region known as Ultimi Scopuli, at a depth of approximately 1.5 km. Given the significance of this discovery, substantial effort has since been devoted to exploring alternative interpretations, either related to specific materials in the crust or to instrumental effects, and to investigating the temperature and compositional conditions of the putative lake. A key question concerns how liquid water could exist at temperatures likely far below the standard freezing point. A plausible explanation involves the presence of perchlorate salts in solution. These salts, in particular Calcium perchlorate $Ca(ClO_4)_2$ and magnesium perchlorate $Mg(ClO_4)_2$, have been already detected through various missions on Martian surface [4][5] and are known to significantly depress the freezing point of water to values compatible with Martian subsurface polar temperatures. The aim of this work is therefore to investigate the dielectric properties of mixtures of ice and perchlorate salts in order to determine the thermophysical conditions under which such mixtures may produce radar echoes comparable to those observed by MARSIS. This study allows also to analyse the possibility of the presence of stable brines in other regions Martian subsurface. The eutectic diagram shown in Fig.1 [6] describes sthe general behaviour of water solutions defining three regions: solid, liquid, and mush. In this latter the solution is a mixture of solid purer ice and salty liquid water (brines). The parameters that determine this regions are the eutectic concentration *Ce* and the eutectic temperature *Te*: a water solution with eutectic concentration of the contaminant remains liquid until the eutectic temperature, therefore even below the freezing point of water. Above the eutectic temperature and below the freezing point of pure water, a solution with a lower concentration than the eutectic is in the mushy region. Below the eutectic temperature all the solution is **generally** completely frozen (not always!). Different salts have different eutectic parameters, then perchlorate solutions could be in a mushy state depending on the temperature and on the perchlorate.

Methods: In our laboratory we perform measurements of electromagnetic properties of perchlorate solutions in the temperature range 195 K-292 K in the radar frequency range (1 MHz - 100 MHz).
The measurement of the electromagnetic properties and, in particular, of dielectric permittivity allow us to analyse the state of the sample (solid, liquid, or mushy) and also the compatibility with MARSIS data. In our range of frequency and temperatures, the real part of the complex dielectric permittivity increases with temperature changing abruptly at the transition temperatures: *Te* and 273 K. In this way we are able to infer the state of the sample: the values of solid solutions of salt and ice is between 3 and 3.5 depending on the quantity of salt, higher values mean the presence of a liquid part in the sample (mushy solution), the value of 80 is indicative of liquid water. Echoes detected by MARSIS have the threshold at the value of 30.

Sample Preparation: Perchlorate solutions have been prepared by mixing double distilled water with granular perchlorates with a hot-plate stirrer. The solution has been poured into a measurement cell with a coaxial cage transmission line inside that allow the propagation of the signals in the sample to measure its electromagnetic properties. We placed the cell in an ultra-freezer at the temperature of 193K to freeze the sample. After the freezing processes has become stable it has been taken out and connected to a Vector Network Analyzer (VNA) that estimated the scattering parameters through the coaxial cage inside the cell. These parameters have been measured with increasing temperature from 195 K to 292 K. A platinum thermoresistance (pt100) monitored the temperature during all the process (the freezing part and the measuring part). We computed the electromagnetic properties from scattering parameters by applying the Nicholson-Ross-Weir algorithm [7][8]. Further details on the measurement procedure can be found in [9][10].

Results: We performed the measurements varying several parameters, including the residence time in the ultrafreezer, the size of the measurement cell, and the perchlorate concentration, in order to assess the influence of each of these factors on the electrical properties. An interesting result concerns magnesium perchlorate (eutectic temperature of 216 K [11]), which was found to remain in a mushy state at different concentrations even below its eutectic temperature (Fig.2), exhibiting permittivity values around 6-7 at 195 K. These permittivity values increase modestly with increasing salt concentration,

yet they do not reach the values detected by from MARSIS observations at the radar operating frequency (4 MHz). These non-freezing phenomena represent a metastable condition that appears to depend in some cases on the residence time in the ultrafreezer and on the dimensions of the measurement cell, although occasionally they occur in a seemingly random manner. Such behavior needs further investigation, particularly to understand how these metastable states might scale up to larger systems, such as those potentially characterizing Martian subglacial brines. On the other hand calcium perchlorate solutions (eutectic temperature of 198K [12]) has been found always in a mushy state at temperature slightly below its eutectic temperature showing values coherent with MARSIS data at lower temperature with respect to magnesium perchlorate solutions.

Conclusion: These results provides key information for the comprehension of the possible persistence of brines in Martian subsurface. Further measurements will allow the characterization of the metastability phenomenon and a complete understanding of the possible habitability of mushy solutions.

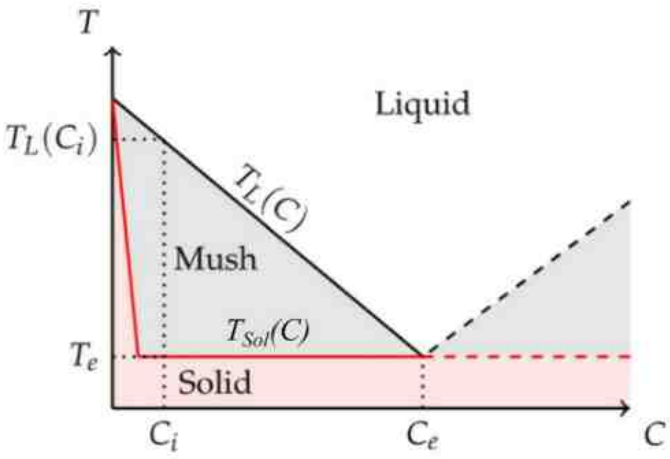


Figure 1: Eutectic diagram [6]. Te and Ce are the eutectic parameters. In the red region the solution is in a solid state, in the grey area it is in a mushy state.



Figure 2: A sample of magnesium perchlorate just taken out from the ultra-freezer in a mushy state at 195 K.

References:

[1] Picardi, Gand, et al. *ISBN 92-9092-556-6, 2004, p. 51-69* 1240 (2004): 51-69.
[2] Orosei, Roberto, et al. (2018) *Science* 361.6401 490-493.
[3] Lauro, Sebastian Emanuel, et al. (2021) *Nature Astronomy* 5.1: 63-70.
[4] Quinn, R., et al. (2013) Astrobiology, 13(6), 515-520.
[5] Bravenec, A. and Catling, D. (2023) Acs Earth and Space Chemistry, 7(7), 1433-1445. .
[6] Parkinson, James RG, et al. *JCP: X* 5 (2020): 100043.
[7] Nicolson, A. M., and G. F. Ross. *IEEE Transactions on instrumentation and measurement* 19.4 (1970): 377-382.
[8] Weir, William B. " *Proceedings of the IEEE* 62.1 (1974): 33-36.
[9] Cosciotti, Barbara, et al. *JGR: Planets* 128.3 (2023): e2022JE007513.
[10] Brin, Alessandro, et al. *Icarus* 374 (2022): 114800.
[11] Stillman D. E. and Grimm R. E. (2011) JGR. 116.
[12] Rivera-Valentín, Edgard G., et al. *Nature astronomy* 4.8 (2020): 756-761

ION IRRADIATION OF ICES ON ORGANIC REFRACTORIES IS A SOURCE OF CO_2 AND CO ON TNOs

M. Germanà[1,2], D. Fulvio[2], R. G. Urso[2], G. A. Baratta[2], C. Scirè[2] and M. E. Palumbo[2].
[1]Dipartimento di Fisica e Astronomia, Università degli Studi di Catania, via Santa Sofia 64, 95123 Catania (IT)
[2]INAF-Osservatorio Astrofisico di Catania, via Santa Sofia 78, 95123 Catania (IT)

Introduction: The presence of complex organic compounds and ices, such as solid CO_2 and CO, is reported in outer Solar System bodies, as also testified by recent James Webb Space Telescope (JWST) observations of Trans-Neptunian objects (TNOs) [1, 2]. Spectral features attributed to complex organics may include absorption from organic refractory materials [3]. Similarly, several icy moons of the giant planets exhibit frozen volatiles, including CO_2, CO and possibly organic compounds [4, 5]. The presence of CO_2 and CO, along with organic compounds, could be attributed to endogenous or exogenous mechanisms. In this regard, radiation processing may play a primary role. Various laboratory experiments have investigated the production of CO_2 and CO through energetic processing of ices and organic materials [6-11].

In this work, we use simulants of refractory organic matter possibly present at the surface of TNOs and comets to assess the formation of $^{13}CO_2$ and ^{13}CO at the interface between an O-bearing ice (either H_2O or O_2) and organic refractory material. Through this work, we seek to gain more insights on the role of ion irradiation of organic refractory materials coated with O-bearing ices in the production of CO_2 and CO, constraining recent observations of outer Solar System bodies.

Methods: Experiments are carried out at the Laboratory for Experimental Astrophysics (LASp) at INAF-OACT (Catania, Italy). An organic refractory residue (ORR) is formed after 200 keV H^+ irradiation of $^{13}CH_4$ ice (on Silicon substrate) deposited in an Ultra-high vacuum (UHV) chamber ($P \leq 10^{-9}$ mbar, T=18 K) and subsequently warmed-up to room temperature. The choice of ^{13}C isotope instead of the commonly used ^{12}C allows clear distinction of the process results from possible unavoidable contaminations.

Four distinct experiments are performed by depositing an H_2O or O_2 ice layer (T=18 K) onto the same ORR, and irradiating the sample (ice layer + ORR) with 200 keV H^+ (Table 1).

Table 1. List of the experiments performed in this study. The irradiation is performed at T=18 K with 200 keV H^+. The experiment names indicate the type of ice cap deposited on the same ORR surface: *W* for water ice and *O* for oxygen ice.

Experiment	Ice cap on the ORR	Fluence max (ion cm^{-2})	Dose max (eV/16u)
1. W1-ORR	H_2O	$+ 7.2 \times 10^{15}$	192
2. W2-ORR	H_2O	$+ 8.7 \times 10^{15}$	234
3. O-ORR	O_2	$+ 1.7 \times 10^{16}$	374
4. W3-ORR	H_2O	$+ 7.2 \times 10^{15}$	192

Infrared spectra are collected at different irradiation steps for each experiment. At the end of each experiment, the sample was gently warmed up to room temperature, leaving the processed ORR without the ice layer on top. CO_2 and CO formation is evaluated by calculating their resulting column densities.

Results: The production of $^{13}CO_2$ and ^{13}CO is observed in all four experiments, as evidenced by the appearance of their IR absorption bands at about 2275 and 2090 cm^{-1}, respectively. In W1,2,3-ORR experiments, $^{13}CO_2$ and ^{13}CO formation reaches a steady state above an irradiation dose of about 100 eV/16u. $^{13}CO_2$ and ^{13}CO column densities data as a function of the dose fit well with a single exponential law. The resulting $^{13}CO_2$ and ^{13}CO saturation values are higher in W1-ORR than in the subsequent W2-ORR experiment. This evidence suggests that continuous irradiation compacts the ORR, reducing its efficiency in supplying C atoms to react with O ions from the ice and form $^{13}CO_2$ and ^{13}CO. Whereas, in O-ORR experiment, $^{13}CO_2$ and ^{13}CO production do not reach saturation, despite the sample receiving an irradiation dose of about 400 eV/16u. In this case, the $^{13}CO_2$ and ^{13}CO column densities as a function of the dose follow a trend that fits well with a double-exponential law, suggesting the onset of a second formation mechanism beyond a certain threshold. This may be due to the higher abundance of O ions originating from the overlying ice, which can also diffuse into the ORR more efficiently compared to the OH radicals. In support of this explanation, IR spectra of the bare ORR, acquired after each experiment, reveal O-bearing molecules trapped within the ORR, with a maximum reached after the experiment where the O_2 ice is used on top of the ORR. These trapped O-bearing molecules were absent in the as formed ORR.

Finally, we will compare these results with CO_2 and CO data obtained by recent JWST observations of TNOs.

Conclusions: This study contributes to constraining the role of ion irradiation in forming CO_2 and CO at the interface of organic refractory materials covered with ices of astrophysical importance. Such processing may play a primary role in outer Solar System bodies, such as TNOs and other icy surfaces across the Solar System.

Acknowledgements: This work is supported by the Istituto Nazionale di Astrofisica (INAF) through the PhD scholarship provided for the XXXIX cycle

for the PhD in Physics. This work has been developed under the ASI-INAF agreement n. 2023-6-HH.0. MG thanks INAF for the support through the grant INAF Laboratori Spaziali 2023, Misure in riflettanza di campioni extraterrestri e analoghi di superfici planetarie, C63C24001150005.

References:

[1] Pinilla-Alonso N. et al. (2025) *Nat. Astron., 9,* 230. [2] De Prá M. N. et al. (2025) *Nat. Astron., 9*, 252. [3] Quirico E. et al. (2023) *Icarus, 394*, 115396. [4] Cartwrigth R. et al. (2015) *Icarus, 257*, 428. [5] Tosi F. et al. (2024) *Space Scie. rev., 220*, 59. [6] Ioppolo S. et al. (2009) *A&A, 493*, 1017. [7] Garozzo M. et al. (2011) *A&A, 528*, A118. [8] Mennella V. et a. (2004) *ApJ, 615*, 1073. [9] Mennella V. et al. (2006) *ApJ, 643*, 923. [10] Gomis O. and Strazzulla G. (2005) *Icarus, 177*, 570. [11] Fulvio D. et al. (2012) *ApJL, 752*, L33.

XXI Congresso Nazionale di Scienze Planetarie

Sessione Focus S1

Water in the Inner Solar System: Past Activity and Climatic Evolution

ESKER-LIKE RIDGES IN THE SOUTH POLAR ICE-CAP ON MARS: POSSIBLE EVIDENCE OF ICE MELTING. L. Guallini[1], G. Caprarelli[1-2], A. Grau Galofre[3], S. Nerozzi[4], R. Orosei[1], [1]Istituto di Radioastronomia – Istituto Nazionale di Astrofisica (IRA-INAF) (Via Piero Gobetti 101, 40129 Bologna, Italy, luca.guallini@inaf.it), [2]Centre for Astrophysics, University of Southern Queenland (Australia), [3]LPG-CNRS, Nantes Universite (France), [4]LPL, University of Arizona (USA)

Introduction: Permanent ice caps cover the Martian polar regions, forming the Amazonian [1][2] Polar Layered Deposits (PLD) units [3]. The PLD are composed of water ice with ~5-15% of dust [3][4], generally characterized by a plan-parallel stratigraphy [5][6] locally disturbed by unconformities. These manifest as erosional surfaces probably related to obliquity-driven warmer periods [7][8]. Unlike in the NPLD [9], in the Southern Polar Layered Deposits (SPLD), glacial-tectonic structures [10] (X1 for locations) and englacial folding [11] have also been found. The presence of deformation structures suggests movement of the ice sheet, likely arising from the viscous response to the weight distribution of the SPLD and its interaction with basal topography, as observed on Earth [e.g., 12]. However, presently the exact mechanisms involved to internal deformation are not determined. In the region of Ultimi Scopuli observational evidence suggests ice deformation occurs in response to basal bedrock reliefs [11], whereas in Promethei Lingula observations indicate possible soft-sediment processes related to basal melt [10]. The presence of unconformities and englacial structures points to a complex Late Amazonian geo-climatic history recorded by the polar deposits. This history is yet to be fully revealed, but it is likely that it would be relevant to understand also the origin of putative liquid brines discovered by the radar sounder MARSIS at the base of the SPLD in Ultimi Scopuli [13][14] (X2 for approximate location). Thus, investigations of the SPLD are continuing, in an effort to define as much of the geological record of the region to add to the reconstruction of climate events on Mars.

Here we report the preliminary results of our morphological investigation of selected areas at the margins of the SPLD, in and around Ultima Lingula, Australe Lingula and Promethei Lingula (Fig. 1), where elevation and imagery data show ridges resembling eskers, that is the remnants of subglacial meltwater drainage systems emplaced below glaciers and ice-sheets, carrying sediment which then becomes exposed upon ice retreat. Eskers have previously been described in the southern hemisphere of Mars: Argyre Planitia and Dorsa Argentea Formation (DAF; early Hesperian) show generally well-developed, braided and elongated ridges interpreted as eskers [15][16][17][18]. Also, the ridges under discussion are already listed in previous geologic maps of the South Pole [6], though without detailed consideration. Ours is the first study to analyze these structures in direct relation to the SPLD. This is all the more relevant because of the above mentioned unconformities and englacial deformation structures which, together with the possible detection of basal liquid brines in Ultimi Scopuli, contextually support the presence of eskers in areas of the south polar region by indicating a long history of climatic changes. On the other hand, eskers are possibly much older than the englacial folds and possible brines. All this calls for new investigations and insights aimed to revitalize the discussion around the dynamics and potential for subglacial melting of the Southern polar cap glacial body of Mars.

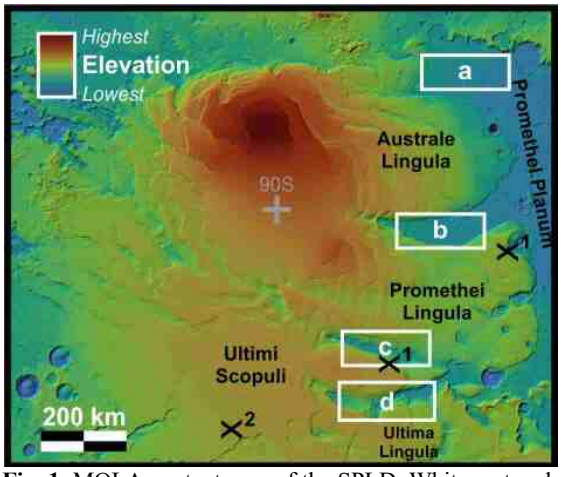


Fig. 1. MOLA context map of the SPLD. White rectangles mark the study areas where the ridges are located. These are shown in detail in Fig. 2.

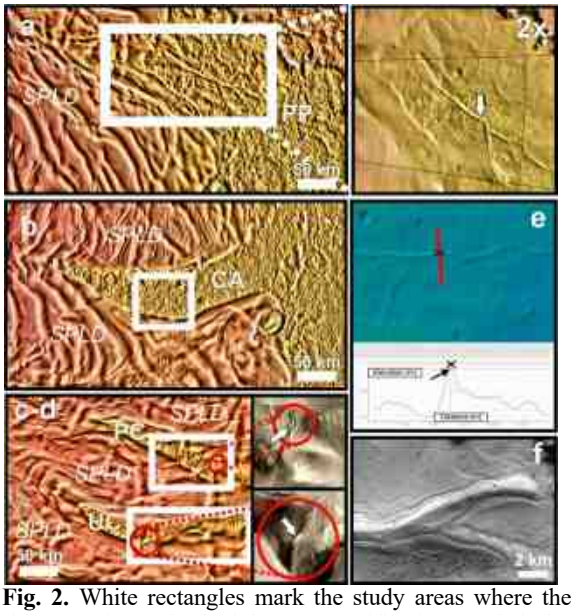


Fig. 2. White rectangles mark the study areas where the ridges are located. The inboxes magnifications (red circles and black squares) are to highlight example ridges (data from MOLA + THEMIS IR and HRSC). **(a-d)** MOLA+shaded reliefs of the ridges in PP (a), CA (b), PC

and UC (c-d). (**e**) Example cross-section profile of a ridge. The arrow points to a split crest, possibly evidence of residual ice on top of the ridge or of its pristine morphology. (**f**) Appearance of the ridges in Promethei Planum in CTX images, likely covered by residual ice.

Dataset: The region has been analyzed using high-resolution visible image (MRO CTX, 6.0 m/pixel; [19]) and THEMIS IR mosaics [20]. Topographic basemaps is from MGS MOLA (512 pixel/degree; 112 m/pixel; [21]); (Fig. 2). The images acquired during the Martian winter are typically cloudy, indicating the seasonal deposition of CO_2.

Results: The ridges (Fig. 2a-f) are particularly evident on the floor of Ultimum (UC) and Promethei Chasmata (PC) and Chasmata Australe (CA) (Figs. 2b-d) and are deposited on the bedrock exposed between distinct SPLD lingulae. Here the ridges cross the chasmata floors from side to side. In plan-view, these ridges, some tens of km long, appear linear or sinuous and/or branching into Y-shaped junctions. Other two cases (Fig. 2a) are observed in the basal margins of Australe Lingula, extending towards the Promethei Planum (PP) region. This is the best developed system: here the ridges are 100-1000s m wide, up to 10s of m high (Fig. 2e), with both symmetric and asymmetric profiles, more than 100 km long, and presenting multiple order branching. Ubiquitous ice on top of the ridges partially masks or alters the morphometry of the ridges (Fig. 2f). Nevertheless, in the first instance, the crests appear sharp/round or flat and in some cases possibly split in two (or more) parts by troughs (i.e., multi-crested; black arrow in Fig. 2e). Ridges are also locally eroded and cratered.

Discussion and Conclusions: All the observed characteristics seem to be consistent with the ridges being eskers on Earth. Thus, also based on contextual knowledge of the area, we interpret the ridges described as eroded remnants of possible eskers. The "esker hypothesis" is supported by the glacial context (emerging from the SPLD; inboxes in Fig. 2), and also by the morphology and morphometry of the ridges, that is consistent with terrestrial eskers (Fig. 3; e.g. [21], [22]) and with the ones observed in the Dorsa Argentea region on Mars. On Earth, eskers are formed by the sediment transported in subglacial channelized drainage systems, flowing towards the ice margin. When ice retreats, the channelized sediment retains its shape and hence it looks like a ridge. Thus, their long axis follows the direction of glacial ice flow at the time of emplacement and can give us an idea of the former glacial geometry; in addition, they require basal melt of the ice to form. We cannot determine whether they represent different generations of eskers, because as said all exposed ridges are modified by post-exhumation processes, either buried by ice mantling or resurfaced by meteoritic impact. However, these morphologies would indicate at least one period of ice sheet retreat, implying that the basal layers of the SPLD were much more extensive in the past. Thus, the orientation and lengths of the ridges provide a conservative estimate of the extent and geometry of the former SPLD ice cover, and the direction of movement of the flowing ice within the chasmata.

The identification of fluvio-glacial morphologies in the same region where englacial folding and possible subglacial liquid water have been found implies that the Martian south polar cap has been much more dynamic through time than previously thought and opens the door to basal thermal anomalies present through time in this region. In future studies we will examine higher resolution imagery of the areas, we will use the method of impact crater chronology to date ridge exposure, and we will search through the radar sounder (MARSIS and SHARAD) database to look for evidence of subsurface structures, in order to add information to the constantly evolving reconstruction of the climatic and geological events that shaped the south polar region of Mars.



Fig. 3. Example esker in Finland (LiDAR topography; data from National Land Survey of Finland).

References: [1] Herkenhoff K. and Murray B. (1990), doi: 10.1029/JB095iB09p14511; [2] Koutnik M. et al. (2002), doi: 10.1029/2001JE001805; [3] Byrne S. (2009), doi: 10.1146/annurev.earth.031208.100101; [4] Lauro et al. (2022), doi: 10.1038/s41467-022-33389-4; [5] Tanaka K.L. and Kolb E.J. (2001), doi: 10.1006/icar.2001.6675; [6] Kolb E.J. and Tanaka K.L. (2001), doi: 10.1006/icar.2001.6676; [7] Milkovich S.M. and Plaut J.J. (2008), doi: 10.1029/2007JE002987; [8] Guallini L. et al. (2018), doi: 10.1016/j.icarus.2017.08.030; [9] Smith et al., 2024, doi: 10.1016/j.icarus.2024.116125;[10] Guallini et al. (2012), doi: 10.1016/j.icarus.2012.06.023; [11] Guallini et al. (2025), Abs. 1874, 56th LPSC; [12] Bell et al. (2014), doi: 10.1038/NGEO2179; [13] Orosei et al. (2018), doi: 10.1126/science.aar72; [14] Lauro et al. (2021), doi: doi.org/10.1038/s41550-020-1200-6; [15] Head J.W. (2000), Abs. 1116, 31st LPSC; [16] Head J.W. (2000), Abs. 1117, 31st LPSC; [17] Banks M.E. et al. (2009), doi.org/10.1029/2008JE003244; [18] Tanaka K.L. et al. (2014), Map 3292 USGS; [19] Malin et al. (2007), doi: 10.1029/ 20 06JE0 02808; [20] Christensen et al. (2001), doi: 10.1029/2000JE001370 ; [21] Smith et al. (2001), doi: 10.1029/20 0 0JE0 01364; [22] Shreve R.L. (1985), doi:10.1130/0016-7606(1985)96<639:ECITOG>2.0.CO;2; [23] Huddart D. et al. (1999), doi.org/10.1111/j.1502-3885.1999.tb00219.x.

Acknowledgements: This research was supported by the Next Generation EU program, Mission 4, Component 1, through project "Combining mAchine Learning and optImization for Planetary remote Sensing missiOns" (CALIPSO), Unique Project Code C53D23010010001.

Evidence of recent warm-based glaciation and meltwater drainage from eskers at Deuteronilus Mensae, Mars

G. Munaretto[1], S. Bertoli[1], F. Tusberti[1], A. Tullo[1], F. Butcher[2], S. Byrne[3], A. Grau Galofre[4], G. Cremonese[1], M. Massironi[5], C. Re[1], C. Rossi[1] , M. Pajola[1], A. Lucchetti[1], N. Thomas[6]
[1] INAF, Osservatorio Astronomico di Padova
[2]School of Geography and Planning, University of Sheffield, Winter Street, Sheffield S10 2TN, UK
[3]University of Arizona, Tucson, USA
[4]Laboratoire de Planétologie et Géosciences, Nantes Université, Univ. Angers, Le Mans Université, CNRS UMR 6112, 44300, Nantes, France
[5] Department of Geosciences, University of Padova, IT
[6] Physikalisches Institut, University of Bern, CH

Introduction: Eskers are elongated sinuous ridges formed by sediment deposition within subglacial channels, created by meltwater draining beneath or within glaciers. On Earth, they are critical for reconstructing past glacial processes, including ice-sheet dynamics, meltwater drainage patterns, and former ice extent and flow direction [1,2]. On Mars, the identification of eskers provides a unique opportunity to investigate the planet's glacial history and past water availability [3]. Their presence on Mars is particularly intriguing because they indicate that specific thermal or climatic events enabling the production of meltwater occurred in the recent (< 1 Gyr ago) past [3,4,5,6]. Martian eskers have been predominantly identified in the planet's mid-latitudes, often associated with viscous flow features (VFFs), which are interpreted as debris-covered glaciers [6], and at the margins of the South Polar Cap [7]. Key mid-latitude regions include Phlegra Montes [3], Tempe Terra [e.g., 4,5,8] and NE Hellas [9]. These studies suggest that even during the predominantly cold and arid Amazonian epoch, locally elevated geothermal fluxes, suggested by the presence of tectonic and/or impact structures enabled subglacial melting. We identified three new candidate eskers associated with VFFs in the Deuteronilus Mensae region of Mars. By analzying their morphology, morphometry, topography, geologic context and cratering record, we aim to test whether they are indeed eskers and discuss their possible formation scenarios. The lack of association with clear tectonic and/or impact structures providing significant geothermal heat could indicate a potential for a climatic driver for the meltwater source

Data & Methods: We assess the morphology and topography of the three identified candidate eskers (named R1, R2 and R3 Fig. 1) by analyzing CaSSIS [10] and HiRISE [11] digital elevation models (DEMs) and monochrome and colour composite images at 4.65 m/px and 0.3 m/px, respectively. In particular, HiRISE DEMs and orthophotos at 1.0 m/px are used to digitize the esker crests in QGIS. From these, following [5,8], we digitize transects perpendicular to the esker crestline (Fig. 2A, B), sample the elevation profile along each of them and measure base width and height (Fig. 2C,D).

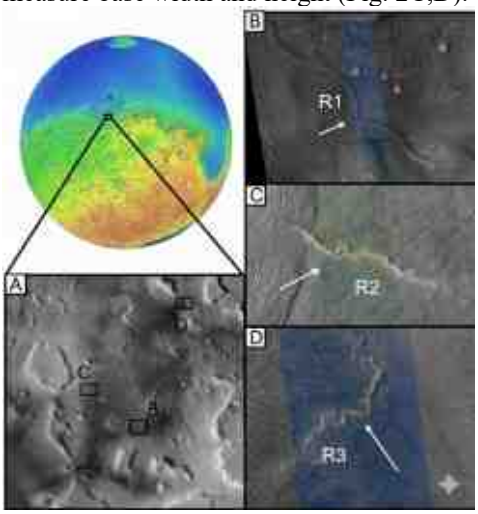


Fig. 1 Mars elevation map in orthographic projection indicating the location of Deuteronilus Mensae. A) CTX mosaic of the location with the three identified eskers, labeled as D1, D3 and D3 and depicted in panesl B, C and D, respectively

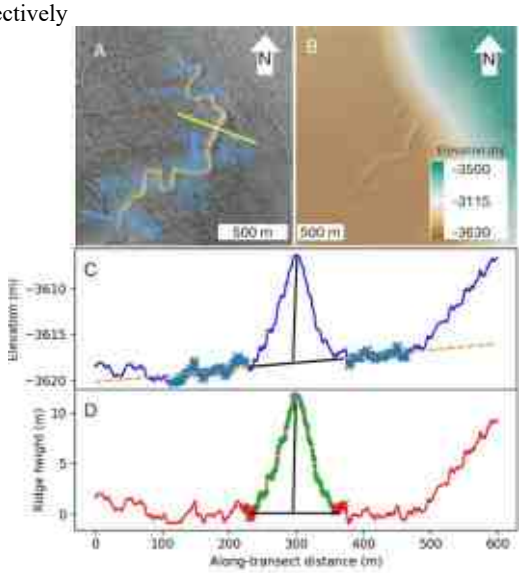


Fig. 2 (A) HiRISE orthophotos showing the digitized crestline (orange) and transects (light-blue) and hillshaded DTMs (B) for ridge R3. Elevation along the yellow transect in panel (C) and after subtraction of the basal topography (D). The black lines indicate the ridge peak height and the base width.

We also relied on the global CTX mosaic [12] to count all craters on the ridges, LDAs, and underlying plains (Fig. 3A), and fitted modelled crater retention ages using the CraterStats software (Fig. 3B-D).

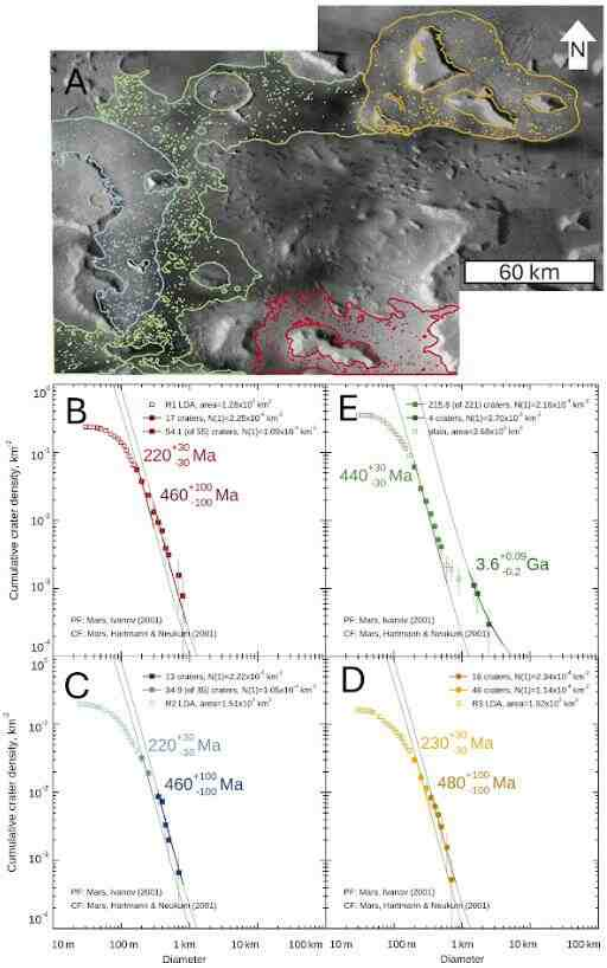


Figure 3 A) CTX global mosaic showing of the crater counting areas (coloured outlines) and the mapped impacts. Crater CSFDs of the R1-R3 ridges LDAs (B-D, respectively) and plains units (E).

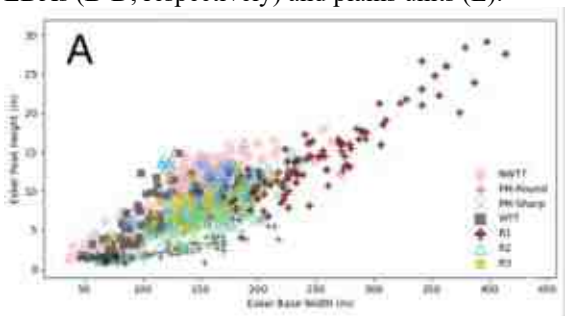


Figure 4 Base width vs Peak height comparison between R1-R3 ridges and other martian Eskers

Results & Future Developments: HiRISE and CaSSIS DEMs and images suggest the ridges emerge from within the center of the LDAs, parallel to the past ice flow inferred direction. This rules out an origin as recessional, lateral or median moraines. An inverted fluvial origin is also excluded due to the absence of fluvial features. Therefore, an esker origin seems more plausible given the geologic context of the study area. We compared width vs height for the R1-3 rdiges with other martian eskers. We find that R2 and R3 have similar 3D morphometries while R1 also has wider and taller portions following the same trend, thereby reinforcing an esker hypothesis. This provides novel insights suggesting that episodes of localized warm-based glaciation and meltwater production occurred through the geologic history of Deuteronilus Mensae. In particular, our modelled crater retention ages indicated this occurred approximately 200-400 Myrs ago, during the Amazonian.

Acknowledgments. The authors wish to thank the spacecraft and instrument engineering teams for the successful completion of the instrument. CaSSIS is a project of the University of Bern and funded through the Swiss Space Office via ESA's PRODEX programme. The instrument hardware development was also supported by the Italian Space Agency (ASI) (ASI-INAF agreement no.I/018/12/0), INAF/Astronomical Observatory of Padova, and the Space Research Center (CBK) in Warsaw. Support from SGF (Budapest), the University of Arizona (Lunar and Planetary Lab.) and NASA are also gratefully acknowledged. Operations support from the UK Space Agency under grant ST/R003025/1 is also acknowledged. This work has been developed under the ASI-INAF agreement n. 2024-40-HH.0. FB acknowledges a Leverhulme Trust Early Career Fellowship

References:[1] Shreve, R. L. (1985). *Geological Society of America Bulletin*, 96(5), 639–646. [2] Storrar,et al., (2014). *Quaternary Science Reviews*, 105, 1–25. [3]Butcher FEG et al.,*Annals of Glaciology*.2022;63(87-89):33-38. [4] Gallagher, C., & Balme, M. R. (2015). *Earth and Planetary Science Letters*, 431, 96–109. [5] Butcher, F. E. G. et al., (2017). *Journal of Geophysical Research: Planets*, 122(12), 2445–2468. [6] Woodley, S. Z., et al., (2022). *Icarus*, 386, 115147. [7]Butcher, FEG et al., Icarus 275, 65–84. doi: 10.1016/j.icarus.2016.03.028 [8] Butcher, F. E. et al., (2020). *Earth and Planetary Science Letters*, 542, 116325. [9] Grau Galofre et al., 2024 *Icarus*, *420*, p.116211 [10] Thomas, N., Cremonese, G., Ziethe, R., et al. (2017) Space Sci. Rev., 212, 1897–1944.[11] McEwen, A. S. et al., (2007) J. Geophys. Res. Planets, 112, E5. [12] Dickson, J. L., B. L. Ehlmann, L. Kerber, C. I. Fassett (2024). The Global Context Camera (CTX) Mosaic of Mars: A Product of Information-Preserving Image Data Processing. Earth and Space Science, 11 (7). DOI: 10.1029/2024EA003555.

ARE CARBONATES HIDING AMONG MARTIAN CLAYS? Jeremy Brossier, Francesca Altieri, Maria Cristina De Sanctis, and Andrea Raponi. Institute for Space Astrophysics and Planetology (IAPS), National Institute of Astrophysics (INAF), Via del Fosso del Cavaliere 100, 00133 Rome, Italy (jeremy.brossier@inaf.it).

Session Focus: (S1) Water in the Inner Solar System – Past Activity and Climatic Evolution
Presentation: Talk

Introduction – Carbonates identified on Mars may offer valuable insights into the planet's past atmosphere, climate and water history. These minerals contain the carbonate ion (CO_3^{2-}), typically bonded with metal cations such as Fe^{2+}, Mg^{2+} , or Ca^{2+} to form siderite ($FeCO_3$), magnesite ($MgCO_3$) or calcite ($CaCO_3$). Their formation generally requires liquid water and carbon dioxide, implying a warmer, wetter, and more CO_2-rich environment on early Mars. Carbonates can form through the alteration of basaltic rocks involving surface water, shallow groundwater or even deeper hydrothermal solutions (Fig. 1).

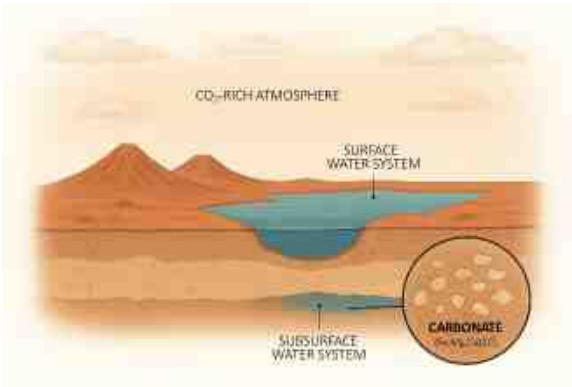


Figure 1 – Simplified illustration depicting the precipitation of carbonates under a CO_2-rich atmosphere on early Mars, driven by the chemical alteration of volcanic rocks occurring through surface and subsurface aqueous environments.

On Mars, carbonates were first identified from orbit in the Nili Fossae region [1], and subsequent in-situ measurements have confirmed their presence at multiple sites explored by rovers, including Gusev, Jezero and Gale craters [2–4]. Nevertheless, carbonate-rich deposits remain far less abundant than predicted for a planet that once had a dense CO_2 atmosphere. This scarcity suggests either that Mars' early atmosphere contained less CO_2 than previously thought, or that carbonates are mostly buried, altered, or otherwise hidden. Furthermore, the acidic conditions derived from widespread volcanism during the Hesperian period may have dissolved existing carbonates or prevented their formation.

In this study, we explore the possibility that carbonates might be hidden within clay-rich deposits identified on Mars [5], as already suggested in Oxia Planum [6,7]. We examine their near-infrared signatures in CRISM datasets (1–4 µm) to assess possible clay–carbonate assemblages and implications for past aqueous environments.

Data & Methodology – CRISM targeted cubes were first processed using the CAT ENVI toolkit to apply standard atmospheric and photometric corrections. Corrected cubes were then denoised using the "*column-by-column*" ratio method, which reduces noise and residual atmospheric effects, while enhancing diagnostic spectral features. After correction and denoising, we calculated the band depths at 1.9 and 2.3 µm to identify pixels with strong paired absorptions – signatures typical of ferromagnesian clays on Mars [5,7]. This approach allows us to recognize the clay-rich deposits potentially containing carbonates, and thereby select the regions of interest (ROIs) for each of the 506 cubes in this study. Mean spectra for these ROIs were subsequently extracted and analyzed. Many of these ROIs also exhibit a broad, recurrent absorption around 2.5 µm, suggesting possible carbonates. Beyond 3 µm, carbonates are expected to display two distinct absorptions near 3.4–3.5 and 3.9 µm. Determining the exact positions of these diagnostic absorptions is essential to characterize and assess the compositional nature of the carbonates on Mars.

Preliminary Results & Discussion – Applying this workflow to 506 CRISM cubes reveals consistent spectral signatures supporting the coexistence of carbonates and clays. When carbonates occur alongside other hydrated minerals (e.g., clays or sulfates), their near-infrared signatures are often obscured. In the presence of clays, the 2.3 µm absorption band is mainly influenced by the clay composition, particularly its Fe and Mg content [8]. In contrast, this band is substantially reduced or may even disappear when sulfates are present [9]. Conversely, the 2.5 µm absorption band remains largely unaffected by either clays or sulfates, and thus provides a reliable diagnostic indicator for detecting and characterizing carbonates within the 1–3 µm spectral range.

Previous studies [8] have shown that the 2.3 µm band is controlled by the clays, with its position varying from 2.29 to 2.32 µm, as expected from the ferromagnesian clays. More precisely an absorption at 2.29 µm indicates Fe-rich clays (nontronites), while an absorption at 2.32 µm corresponds to Mg-rich clays (saponites). Intermediate values may reflect the presence of vermiculites or ferrosaponites, as proposed for Oxia Planum [6,7]. Overall, the 2.3 µm band is centered near 2.302 ± 0.007 µm (Fig. 2A), characteristic of clays, and therefore cannot be used as a diagnostic feature for carbonates on Mars.

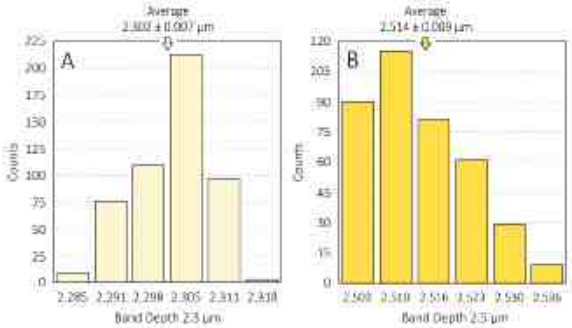


Figure 2 – Histograms showing the distribution of band positions for absorptions near 2.3 and 2.5 µm, both appearing in clay – carbonate deposits.

As for the 2.5 µm band, it remains an important feature for accurately characterizing the carbonates. It has been recognized in approximately 385 cubes, exhibiting variable intensities. The 2.5 µm band is often weak, which makes it difficult to identify directly through index maps [10]. However, exact band positions can be determined using continuum removal for each cube in which the 2.5 µm band is observed. Overall, values range from 2.50 to 2.54 µm, with an average value of 2.514 ± 0.009 µm (Fig. 2B). An absorption near 2.50 µm is indicative of Mg-rich carbonates (magnesites), while absorptions at longer wavelengths typically correspond to Fe- and Ca-rich carbonates (siderites, calcites) [1].

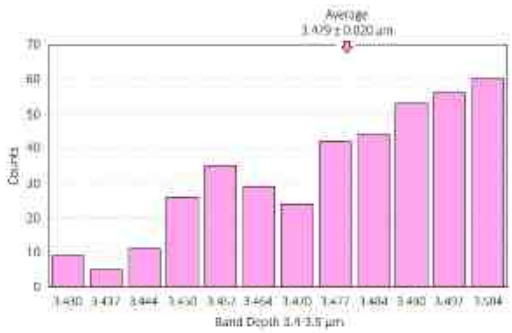


Figure 3 – Histogram showing the distribution of band positions for the absorption near 3.4–3.5 µm, consistent with mixed Fe–Mg carbonates .

To further support our analysis, we also examined spectral signatures beyond 3 µm. Carbonates typically exhibit deep absorptions near 3.4–3.5 µm and 3.9 µm. Differences in carbonate composition can be distinguished based on the band centers within the 3.4–3.5 µm range, spanning from magnesites at 3.42 µm to siderites and calcites near 3.45–3.50 µm [11]. This band is often weak or missing, likely due to a strong water absorption near 3 µm induced by the clays. Nevertheless we extracted possible band centers for absorptions occurring within the 3.4–3.5 µm range, yielding values between 3.43 and 3.50 µm. The average value, 3.479 ± 0.020 µm (Fig. 3), is consistent with values previously reported [11].

Taken together, these values suggest the presence of mixed Fe,Mg-rich carbonates. Siderites and magnesites are widely considered the most plausible carbonates for Mars, as they align with the planet's geochemical, thermal, and hydrological evolution – unlike calcites or dolomites. Martian basalts, being rich in Fe and Mg, readily supply Fe^{2+} and Mg^{2+} ions through weathering in CO_2-bearing waters, promoting the formation of Fe,Mg-rich carbonates. Consequently, Martian carbonates may represent a siderite–magnesite solid solution [12]. Siderites and magnesites form a continuous solid solution series in which Fe^{2+} and Mg^{2+} can freely substitute for one another, consistent with previous observations [1–4]. For instance, analyses by the Spirit rover within Gusev crater revealed Fe,Mg-rich carbonates with an approximate composition of $(Fe_{0.45}Mg_{0.55})CO_3$ [2].

Final Remarks – We analyzed over 500 CRISM cubes containing ferromagnesian clays to identify and characterize carbonates possibly present with them. Precise determination of the 2.3, 2.5 and 3.5 µm absorption band positions suggests that the carbonates on Mars most likely consist of Fe–Mg solid solutions spanning the siderite–magnesite compositional range. As a next step, spectral mixing modeling will be conducted to further evaluate the spectral behavior of clay–carbonate assemblages. This approach will also provide valuable guidance for laboratory analyses.

Carbonates are key indicators for reconstructing the atmosphere, climate and aqueous environments of early Mars. Moreover, their association with clays offers important clues for its potential habitability and the preservation of biosignatures. The observed co-precipitation of clays and carbonates across the studied outcrops further strengthens the exobiological relevance of these regions, where biosignatures may still be preserved.

Fundings – This work is supported by the Italian Space Agency (ASI), with the project ASI-INAF n.23-3-HH.0 entitled "*Attività scientifica di preparazione all'esplorazione marziana*".

References – [1] Ehlmann et al. (2008) *Science*. [2] Morris et al. (2010) *Science*. [3] Clavé et al. (2023) *JGR*. [4] Tutolo et al. (2025) *Science*. [5] Brossier et al. (under review) *JGR*. [6] Mandon et al. (2021) *Astrobiology*. [7] Brossier et al. (2022) *Icarus*. [8] Bishop et al. (2013) *JGR*. [9] Sheppard et al. (2025) *Frontiers Astron. Space Science*. [10] Viviano-Beck et al. (2014) *JGR*. [11] Bultel et al. (2019) *JGR*. [12] Beck et al. (2024) *Earth and Space Science*.

ALKALINE VS ACIDIC AQUEOUS WEATHERING ON MARS – A COMPARATIVE STUDY FROM EARTH ANALOGS. E. Bruschini[1], M. Ferrari[1], Cristina Mazzoni[2], M. Ingrassia[3], Stefano Fazi[4], Agnese Piacentini[2], Giovanna Costanzo[5], Giovanni B. Andreozzi[6], Paolo Ballirano[6], Tania Ruspandini[6], Stefania Stefani[1], A. M. Conte[3], L. Di Bella[6], C. Perinelli[6], F. L. Chiocci[6], S. De Angelis[1], J. Brossier[1], F. Altieri[1], Giuseppe Piccioni[1], M. C. De Sanctis[1]
[1]IAPS-INAF (contact: enrico.bruschini@inaf.it), [2]BBCD – Sapienza University of Rome, [3]IGAG-CNR Rome, [4]IRSA-CNR Rome, [5]IBPM-CNR Rome, [6]DST – Sapienza University of Rome,

Introduction: Among the inner Solar System planets, Mars, together with Earth, exhibits an exceptionally complex geological history [e.g. 1]. Multiple lines of evidence indicate that liquid water once played an important role in shaping its surface and possibly creating transiently habitable environments [2]. Yet, despite decades of remote sensing and in-situ investigations, the planet's hydrological and geological evolution remains only partly understood. Understanding these processes is fundamental to reconstructing Mars' past and assessing its potential for having supported life. Terrestrial environments that share mineralogical and geomorphological similarities with planetary bodies, known as planetary analogs, give us the possibility to test hypotheses and improve our interpretation of minerals–environment relationships. The focus of this work is the characterization of two planetary analog sites where we observe intensive water/rock interaction in two different geochemical settings thus providing insights into the diversity of water–rock interactions that may have occurred on ancient Mars. The two analog sites are the Lake Bagno dell'Acqua (hereafter LBA) in Pantelleria, Sicily (alkaline aqueous weathering) and the Solforata di Pomezia – Riserva Naturale di Decima Malafede (hereafter SP), Latium, Italy (acidic aqueous weathering) (see Figure 1).



Figure 1 – (top) Lake Bagno dell'Acqua in Pantelleria, Sicily, and (bottom) Solforata di Pomezia in Latium, Italy.

Methods: Several samples of rocks and sediments were collected in the two field sites. The rocks and sediments used for the mineralogical characterization were thermally treated at (343 K for 48 h) to remove excess water and then analyzed with a wide range of techniques including reflectance spectroscopy (visible to mid-infrared), Raman spectroscopy, powder X-ray diffraction and scanning electron microscopy. In addition, the physical-chemical water parameters (pH, T, O_2) were measured on site with portable probes. The microbial communities were identified and quantified after DNA extraction and sequencing. We used fluorescence microscopy to visualize the distribution of organic materials in the sediments and rocks.

Results: Our results highlight a complex interplay between physical and chemical parameters of the water bodies and the secondary minerals formed because of water-rock interaction. Both the investigated sites are characterized by the presence of relatively recent volcanics which experienced extensive interaction with water bodies. The mineralogical associations observed in LBA e SP are however vastly different. In the case of LBA the water of the lake has an overall alkaline nature with a pH = 9 (except for the thermal spring where the pH is slightly acidic). We report the diffuse presence of carbonates (mostly aragonite) and Mg-smectite resulting from the weathering of the volcanic minerals of the sediments [3]. A peculiar feature of LBA is the presence of microbialites: organosedimentary rocks formed by interaction between the microbic community and inorganic components present in the system. The mineralogy of the investigated samples of microbialites greatly differ from sample to sample but in the overall it resembles the mineralogical association of the sediments [3, 4, 5]. In the microbialite the carbonate phase is often found as a thin layer with a distinctive convoluted patterns typical of stromatolites. Since aragonite formation in these samples is induced by microbial activity [e.g. 4-5] the presence of carbonate and its textural features is a clear example of biofeature. Even though we do not observe such a clear convoluted pattern in the case of Mg-smectite, there are strong indications that biotic processes play a significant role in the formation of this phase [e.g. 4, 5, 6]. Indeed Mg-smectite is strictly related to aragonite in the microbialite system [4, 5].

It is likely that such a "biotic" Mg-smectite may represent at least a fraction of the Mg-smectite present in the sediments, the remaining, in turn, may derive from the weathering of volcanic minerals in the sediment (or by precipitation from the lake water). Another widespread mineral phase is hydrous silica which can be found either as a consequence of dissolution of diatom frustules or as direct precipitate from aqueous solutions.

In SP we observe the presence of small water bodies (ponds) characterized by very low pH values ($1 < pH < 3$). The secondary minerals formed by the acidic alteration of the volcanics from the Alban Hills Volcanic complex are dominated by S-bearing phases, namely: native sulfur, sulfates (jarosite, halotrichite, alunite, gypsum, bassanite) and minor amounts of Fe-sulfides. The coexistence of sulfur phases in a very small area is indicative of complex redox reactions which take place in this site. Halloysite is the only phyllosilicate found. Despite the low silica content of the volcanic emplaced in this area, hydrous silica is particularly abundant, and it results from the extreme weathering of the pyroclastic units outcropping in the area. Jarosite is the most abundant sulfate, and it is found both as sediment, likely precipitated by Fe^{3+}-rich aqueous solutions, or as vein cross-cutting the halloysite rich rocks. The presence of hematite rich/laterite-like soils is peculiar of the SP. Often goethite is found as thin layers covering the weathered pyroclastic rocks. Despite the extreme values of pH the sediments are characterized by a diverse microbial community. The microbial species are very different from ponds to ponds although their role in the formation of sediments needs to be addressed.

Conclusion: LBA and SP are characterized by vastly different secondary minerals formed as a result of the interaction between volcanic rocks and water with different physical and chemical features. The association of minerals found in LBA (carbonates + smectites) closely resemble those emplaced on Mars during the Noachian era (older than 3.7 Gyr) while the mineralogical association observed at SP (sulfates and Al-phyllosilicates) is similar those deposited during the Hesperian era (3.0–3.7 Gyr). Finally, the strong oxidation observed in SP is very similar to the general oxidation observed on Mars during the Amazonian era (3.0 Gyr to present). The results obtained here highlight the importance of using Earth analogues as benchmark to validate our understanding of the physical and chemical processes observed on Mars or other planets.

Fundings and Acknowledgments: This work is supported by the Italian Space Agency (ASI), with the project ASI-INAF n.23-3-HH.0 entitled “Attività Scientifica di Preparazione all’Esplorazione Marziana” as well as Minigrant INAF (Ricerca Fondamentale INAF). LBA and SP are protected natural areas under the management of Parco Nazionale Isola di Pantelleria (LBA) and Ente Regionale RomaNatura – Riserva Naturale di Decima Malafede (SP). We sincerely thank both organizations for authorizing sample collection for this project.

References:

[1] Carr, M. H., and Head III, J. W. (2010) *EPSL, 294(3-4),* 185–203. [2] Ehlmann et al. (2011) *Nature, 479,* 53-60. [3] Bruschini et al. (2024) *PSS*, 245 (105893). [4] Ingrassia et al. (2024) *Minerals*, 14(10), 1013, [5] Mazzoni et al. (2024) *Front. Microbiol.*, 15, 1391968, [6] Del Buey et al. (2023) Appl. Clay Sci. 238, 106932

XXI Congresso Nazionale di Scienze Planetarie

Sessione Focus S5

Planet formation and evolution in solar system analogues

A CHANGE OF PARADIGM IN PLANET FORMATION: OUTFLOW CAVITY WALLS AS HIDDEN FACTORIES FOR LARGE DUST GRAINS: Sabatini[1], Linda Podio[1], Claudio Codella[1], Eleonora Bianchi[1], Lisa Giani[1], Manuela Lippi[1], Marta De Simone[2], Cecilia Ceccarelli[3], Claire J. Chandler[4], Nami Sakai[5], and Satoshi Yamamoto[6]

[1]Istituto Nazionale di Astrofisica (INAF), Osservatorio Astrofisico di Arcetri, Italy (giovanni.sabatini@inaf.it); [2]European Southern Observatory, Karl-Schwarzschild-Strasse 2 D85748 Garching bei Munchen, Germany; [3]Univ. Grenoble Alpes, CNRS, IPAG, 38000 Grenoble, France; [4]National Radio Astronomy Observatory, PO Box O, Socorro, NM 87801, USA; [5]RIKEN Cluster for Pioneering Research, 2-1, Hirosawa, Wako-shi, Saitama 351-0198, Japan; [6]SOKENDAI (The Graduate University for Advanced Studies), Shonan Village, Hayama, Kanagawa 240-0193, Japan

Abstract: Planet formation models still face a crucial challenge: millimeter-sized dust grains in protoplanetary discs migrate rapidly inwards, hindering their growth into planetesimals - the building blocks of planets. However, recent high-resolution ALMA observations, taken as part of the FAUST Large Programme ("*Fifty AU STudy of the chemistry in the disk/envelope systems of Solar-like protostars*"; *Codella et al. 2021*), suggest an alternative scenario.

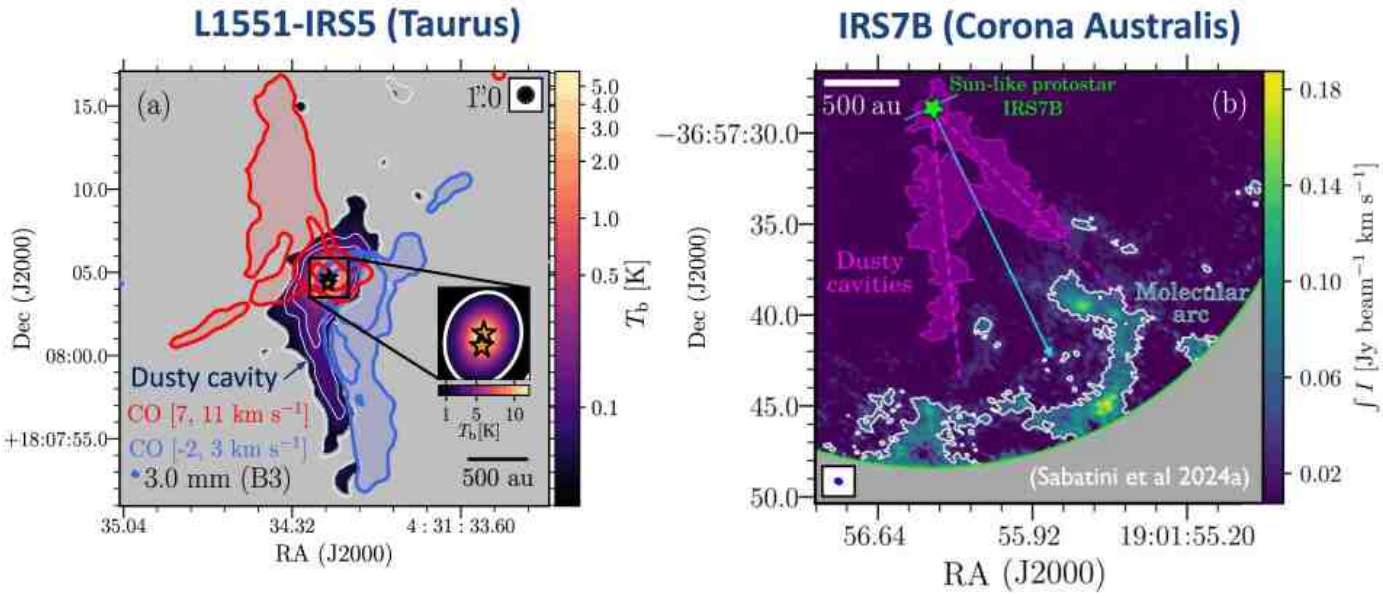
We have discovered dust-rich cavity walls associated with the protostellar objects IRS7B and L1551, located in the Corona Australis (CrA) and Taurus star-forming regions, respectively (see **Figure 1**; *Sabatini et al. 2024a, 2025*). The sub-mm spectral index (α_{mm}) of the dust Spectral Energy Distribution (SED) derived from the ALMA Band 3 (3 mm) and Band 6 (1.3 mm) observations indicates efficient grain growth in the cavity walls.

In this talk, I will present new results from other young protostellar systems observed in ALMA-FAUST. I will look at the implications of dust growth in outflow cavities and how this mechanism could overcome the radial drift barrier, potentially revolutionising our understanding of planet formation. I will also discuss the impact of these dusty structures on the chemical evolution of protoplanetary systems and, in this context, the advantages advantages of exploiting current and future astronomical facilities such as the South African MeerKAT radio telescope and the Square Kilometre Array Observatory (SKAO).

References:

[1] Codella, C., Ceccarelli, C., Chandler, C., et al. 2021, Frontiers in Astronomy and Space Sciences, 8, 227 [2] Sabatini, G., Podio, L., Codella, C., et al. 2024a, A&A, 684, L12 [3] Sabatini, G., Bianchi, E., Chandler, C. J., et al. 2025, A&A, 698, L16

Figure 1: (a) The L1551 IRS5 Class I binary system from Sabatini et al. (2025). Color map: Thermal dust continuum emission at 3 mm mapping the circumbinary disc and the dusty cavity walls structure. Transparent red and blue areas: The red- and blue-shifted CO (2-1) outflow emission. (Right) Sketch illustrating how. (b) The IRS7B Class 0/I binary system from Sabatini et al. (2024a). Color map: Molecular emission traced by the CH_3OH observed in FAUST. Transparent magenta areas show the observed dusty cavity walls.



EXOPLANET OBSERVATIONS AT OSSERVATORIO POLIFUNZIONALE DEL CHIANTI: ITS ROLE IN GLOBAL RESEARCH NETWORKS.

L. Betti[1,2], C. Calamai[1,2], R. Ciantini[1,2], R. Claudi[1,3], L. Fini[1,2], L. Fossi[1,2], A. Liberti[1,2], M. Michelagnoli[1,2], V. Noce[1,2], E. Pace[1,2], I. Parenti[1,2], V. Pettina[1,2], R. Stanga[1,2]
[1] Osservatorio Polifunzionale del Chianti
[2] Università degli Studi di Firenze
[3] INAF/OAA – Osservatorio Astrofisico di Arcetri
[4] INAF/OAPd – Osservatorio Astronomico di Padova

Introduction: During the last quarter of the century, many discoveries have been made in the field of exoplanets, thanks to the involvement of space and ground telescopes. Indeed, more than 6,000 exoplanets have been found, and many more are awaiting confirmation. The Osservatorio Polifunzionale del Chianti (OPC) – a multipurpose facility, that follows many fields, from astronomy and scientific outreach to geology – is keen on the exoplanetary research; as a matter of fact, it started the follow-up activity from its very beginning [1] and it is still engaged in several international collaborations, such as NASA TESS Follow-Up Observing Program (TFOP), ESA Ariel ExoClock project and INAF Global Architecture of Planetary Systems (GAPS) program.

Research activities: The main exoplanet-related activities at OPC are focused on:

- confirming transits through follow-up photometry and ruling out false positives (TFOP);
- updating and refining the ephemerides of known exoplanets (ExoClock);
- conducting simultaneous observations with the Telescopio Nazionale Galileo (TNG) to combine photometric and spectroscopic measurements (HARPS-N spectrometer) to monitor young stars' activity and characterize planetary systems.

The measurements are performed using an 80 cm Ritchey-Chrétien telescope (on loan from the INAF-Turin Observatory), with a focal ratio F/8 and 19.6 arcmin x 19.6 arcmin field of view, equipped with a Moravian G4-KAF09000 CCD and a set of Johnson-Cousins photometric filters (I, R, V, B, U).

Results: In the last year, several observations were carried out using differential photometry. These measurements enabled testing and validation of the procedures, producing stable and accurate light curves for multiple targets. This work summarizes the most relevant results obtained during the last activities and highlights the growing precision of the observational capabilities of the telescope setup at OPC. It presents a selection of the variety of exoplanet research activities discussed above, illustrated through representative targets, including TOI-2134c (TFOP), CoRoT-10b (ExoClock), and TOI-1420b (GAPS).

All these transit observations are scientifically significant for different reasons: although only a partial transit was observed, the measurement of TOI-2134c (Figure 1) is included as it forms part of a joint observation between a ground-based telescope network and Hubble Space Telescope (HST) in support of TESS mission; CoRoT-10b (Figure 2) is classified as an alert in the ExoClock catalogue, as the uncertainties in its most recent ingress and egress times exceed the tolerance required by the upcoming Ariel mission, making continued monitoring necessary; TOI-1420b (Figure 3) – studied jointly by the OPC and TNG teams to connect photometric and spectroscopic analyses – has also recently become the target of an ExoClock observing campaign.

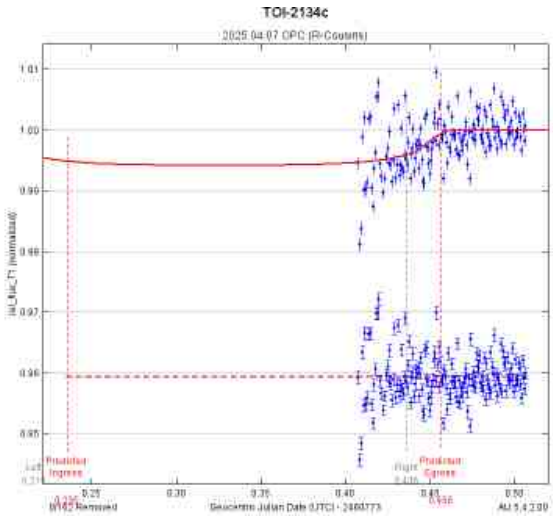


Figure 1. Egress phase of the TOI-2134c exoplanetary transit, as part of the TESS collaboration. The residues are shown in the lower part of the figure. The transit was observed simultaneously with the Hubble Space Telescope (HST), which was unable to measure either the ingress or the egress phases, making the OPC observation essential for its analysis.

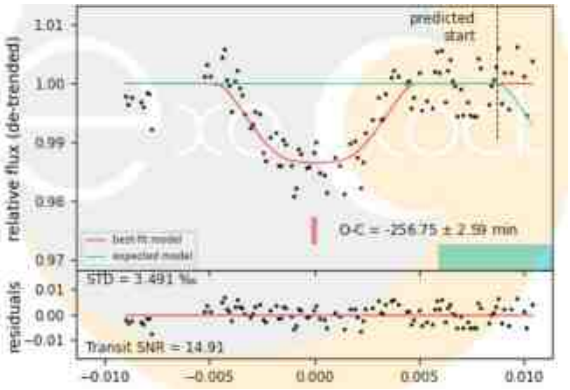


Figure 2. Light curve of the CoRoT-10b transit observed at OPC as part of the EcoClock collaboration. The O-C (the difference between the observed and expected transit mid-times) is reported above. The residues are shown in the lower part of the figure.

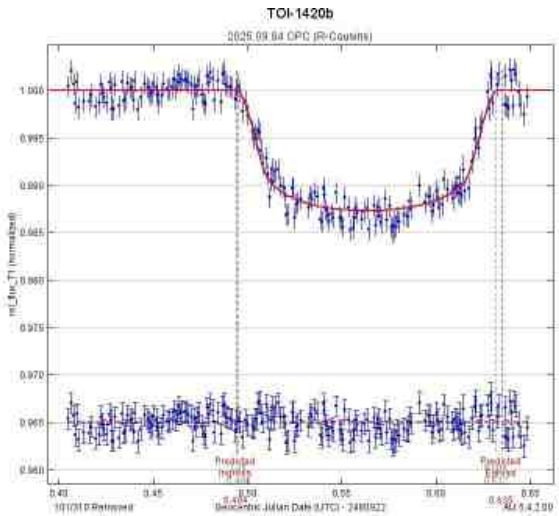


Figure 3. Light curve of the TOI-1420b transit observed at OPC as part of the GAPS collaboration. This transit was observed simultaneously with the TNG observatory. The residues are shown in the lower part of the figure.

Conclusions: For years, measurements carried out at OPC have contributed to updating the target catalogs of TFOP and ExoClock [2],[3] by providing high-quality photometric follow-up, while its participation in GAPS observational campaigns since 2017 further supports the detailed characterization of confirmed exoplanetary systems. These results are driven by a continuously growing team of young researchers from the University of Florence, working alongside experienced senior researchers. Together, they embody a dynamic, evolving reality that increasingly contributes to coordinated, community-driven exoplanet research.

References:

[1] Naponiello L., Betti L., Biagini A. et al. (2020), Experimental Astronomy, 50, 169-183
[2] Kokori A., Tsiaras A., Edwards B. et al. (2023), The Astronomical Journal, 265, 4
[3] Kokori A., Tsiaras A., Pantelidou G. et al. (2025) , arXiv – Accepted for publication

XXI Congresso Nazionale di Scienze Planetarie

Sessione Focus S5

From Orbital Data to Scalable Landing-Site Frameworks

The Space Science Data Center (SSDC) Science Computing Hub (SciComHub): a centralized platform for data access, processing, analysis, and software development. G. Nodjoumi[1,2] V. Camplone[1], E. Rognini[1], M. Giardino[3], M. Perri[1], A. Zinzi[3] - [1]INAF/Osservatorio Astronomico di Roma (INAF-OAR), Via Frascati 33, 00078, Monte Porzio Catone (RM), Italy, [2]School of Science, Constructor University Bremen gGmbH, Bremen, DE, [3]Agenzia Spaziale Italiana (ASI), Via del Politecnico snc, 00133, Rome, Italy,

Introduction: Planetary science workflows often require complex software stacks, ranging from specialized geospatial libraries to legacy codebases. The installation and configuration of these tools, such as the Integrated Software for Imagers and Spectrometers (ISIS) and the NASA Ames Stereo Pipeline (ASP), pose significant barriers to entry for researchers and students [1][2]. Furthermore, ensuring the reproducibility of scientific results is increasingly challenging when software environments vary across local machines. To address these challenges, the Europlanet Geologic MApping of Planetary surfaces (GMAP) initiative has developed a cloud-based processing environment [3]. This work presents the deployment of the GMAP JupyterHub at the Space Science Data Center (SSDC) of the Italian Space Agency (ASI). By leveraging High-Performance Computing (HPC) infrastructure, this platform provides a reproducible, containerized environment for planetary data processing, as well as galactic and stellar data analysis.

Deployment and Scalability (Kubernetes & Podman): The platform utilizes robust, container-based architecture designed for high scalability and security.

Containerization: We employ Docker and Podman technologies to pack software environments. Podman is specifically utilized for its rootless container execution capabilities, which enhances the security posture within the shared HPC environment by preventing containers from running with elevated privileges.

Orchestration: To manage these containers efficiently at scale, the SSDC deployment currently runs via Kubernetes. This orchestration layer ensures the system's stability, even during concurrent usage by multiple researchers, by dynamically allocating resources based on user demand. *Future SLURM Integration:* While the current interactive sessions are managed by Kubernetes, future development will bridge this cluster with the facility's SLURM scheduler. This will enable users to make a seamless submission of memory-intensive batch jobs from their notebooks to the HPC nodes, optimizing the workflow for long-running processes.

Services Integration: The platform is designed to function as a hub that interconnects with other established SSDC services.

Planetary Science: The environment integrates with MATISSE (Multi-purpose Advanced Tool for the Instruments of the Solar System Exploration) [5,6]. Users can process raw data within JupyterHub using tools like ISIS/ASP and seamlessly visualize or further analyze the spectral products via MATISSE interfaces. The integration with MATISSE extends the platform's capabilities to include an automated pipeline for landing site analysis. This workflow synthesizes engineering constraints, such as surface roughness, slope, and solar illumination derived from Digital Elevation Models (DEMs), with scientific requirements based on geological and mineralogical data. With user-defined parameters and spatial weighting, the system produces suitability maps to enhance landing safety and scientific results, thus connecting engineering and science teams.

Galactic and Stellar Science: Expanding beyond planetary surfaces, the platform supports astrophysical workflows by integrating with SEDBuilder (Spectral Energy Distribution Builder). This allows researchers to combine the computational power of the JupyterHub with the spectral analysis capabilities of SEDBuilder for galactic and stellar research.

Authentication and Access: Currently, access to the platform is managed via a "usage by request" model to ensure optimal resource allocation during the initial rollout. However, the architecture is designed to support federated authentication standards. Future updates will integrate eduGAIN support, allowing seamless login for researchers from academic institutions worldwide using their institutional credentials.

Customized Processing Environments: A core feature of this deployment is the use of custom Docker images. These images allow users to switch instantly between different software stacks without installation conflicts. *Planetary Science:* We provide pre-configured images containing essential tools for planetary geology and cartography, including USGS ISIS, NASA ASP, GDAL, and GRASS GIS. These images facilitate the creation of Digital Terrain Models (DTMs) and map-projected mosaics directly within the browser. *Galactic and Stellar Science:* Expanding beyond planetary surfaces, new custom images have been deployed at SSDC to support galactic and stellar data processing. These environments include specific libraries for astronomical data reduction and analysis, broadening the platform's utility to the wider

astrophysics community. *Legacy Code Support:* Recognizing that significant scientific value resides in legacy software, the platform supports code development and execution in Fortran, C, and C++. A dedicated jupyter-fortran image allows researchers to compile and run legacy scientific codes within a modern notebook interface, bridging the gap between historical algorithms and modern data science workflows.

GPU Capabilities and Future Work: The integration of *Machine Learning (ML)* and *Deep Learning (DL)* into planetary science is growing rapidly. To support this, the SSDC deployment is being upgraded to grant users access to GPU capabilities. Future Docker images will come pre-loaded with ML frameworks such as TensorFlow and PyTorch, optimized for the underlying HPC hardware. This will enable users to perform resource-intensive tasks, such as training neural networks for automated crater counting or surface feature classification, directly on the platform. The Europlanet GMAP JupyterHub at ASI SSDC represents a significant step toward a unified, reproducible, and collaborative environment for space science. By centralizing resources and standardizing software environments, we enable researchers to focus on scientific discovery rather than software management.

Virtual Observatory (VO) Integration: Future developments will also focus on bridging the gap between data processing and dissemination. We plan to implement tools that simplify the adoption of IVOA protocols, utilizing a pre-configured environment to guide users through the often-complex process of metadata creation. This feature will allow researchers to effortlessly publish products derived from locally hosted SSDC datasets into the Virtual Observatory, ensuring compliance with international standards while reducing technical barriers.

References: [1] Sucharski T. et al. (2020) USGS-Astrogeology/ISIS3, ISIS 4.2.0 public release. [2] Beyer R. A. et al. (2018) Earth and Space Science, 5(9), 537–548. [3] Brandt C. H. et al. (2024) Europlanet-Gmap/Docker-JupyterHub, Zenodo. [4] Nodjoumi G. et al. (2025) Earth and Space Science, 12, e2025EA004251, https://doi.org/10.1029/2025EA004251. [5] A. Zinzi, M.T. Capria, E. Palomba, P. Giommi, L.A. Antonelli, (2016) Astronomy and Computing, Volume 15, 2016,Pages 16-28, ISSN 2213-1337. [6] V. Camplone, A. Zinzi, M. Massironi, A.P. Rossi, F. Zucca, (2024) Astronomy and Computing, Volume 48, 2024, 100852, ISSN 2213-1337.

Funding: Supported by ASI-INAF agreement n. 2025-33-HH.0.

MATISSE: INTEGRATING PLANETARY DATA FOR ADVANCED AND TARGETED ANALYSIS

V.Camplone [1] G. Nodjoumi [1,2], A. Zinzi [3], E. Rognini [1]

[1] INAF/Osservatorio Astronomico di Roma (INAF-OAR), Via Frascati 33, 00078, Monte Porzio Catone (RM)
[2] School of Science, Constructor University Bremen gGmbH, Bremen, DE
[3] Agenzia Spaziale Italiana (ASI) Via del Politecnico snc, 00133, Rome

Introduction

The selection of landing sites for future space missions requires the accurate integration of heterogeneous data originating from different instruments, orbiters, and missions. MATISSE (Multi-purpose Advanced Tool for Instruments for the Solar System Exploration) [1], [2] is a web-based tool developed to facilitate the access, visualization, and comparison of multi-instrument and multi-mission datasets related to various bodies of the Solar System. Thanks to its flexible architecture, MATISSE enables essential analyses for identifying safe and scientifically valuable areas. This tool has become essential for geologists studying the composition and geological history of planets, offering a unique platform for terrain-based geological analyses. The new version, MATISSE 2.0 (https://tools.ssdc.asi.it/Matisse/), introduces significant updates and improvements, including the integration of geological maps of Mercury, Ceres, and the Moon, as well as newly available datasets for users. MATISSE is currently the only tool capable of performing data searches based specifically on geological surface features. This capability makes it particularly valuable for those working on planetary mapping or needing to interpret data within a well-defined geological context. By integrating information from multiple missions and instruments, MATISSE simplifies dataset analysis and interpretation while expanding scientific research opportunities and supporting new advancements in planetary exploration.

MATISSE Updates and New Features:

MATISSE currently integrates data from numerous space missions, including Dawn, Mars Express, MRO, MESSENGER, CLEM, LRO, LICIACube, and Venus Express. This broad availability of datasets enables the comparison of observations acquired with different instruments, geometries, and resolutions. The tool also provides the capability to analyze surface thermal models for Ceres and Mercury [3], expanding its potential for studying the physical and environmental properties of planetary surfaces. In recent years, an advanced functionality has been introduced that allows users to search data based on a selected geological unit: once the unit is chosen, users can run a dedicated query that returns only the data relevant to that specific geological unit. This process optimizes dataset usage and allows analyses to be tailored to the geological characteristics of interest. Data retrieved through MATISSE are accurately georeferenced and projected, enabling precise identification of their location within the selected units. The mapped and projected data are then carefully integrated and aligned with existing geographic information, ensuring comprehensive, accurate, and context-rich analysis.

In recent months, MATISSE has undergone further expansion through the integration of lunar datasets and the complete USGS global geological map. The addition of these datasets significantly enhances the tool's analytical potential, allowing users to apply geological unit based searches, already available for Mercury [4] and Ceres [5] to the lunar surface as well [6].

This functionality is especially relevant to landing site selection, as it enables the rapid identification of the geological units most suitable from a scientific perspective, focusing on areas capable of maximizing scientific return. In this way, MATISSE supports a more targeted and efficient preliminary assessment, optimizing the overall decision-making process.

Another major update concerns the ability to perform targeted searches based on a crater of interest: users can select a specific crater and instantly access all available datasets for that area, including morphological, spectral, and thermal products. This feature is particularly useful for detailed studies of impact structures, for characterizing their internal morphologies and associated geological units, and for identifying candidate sample sites for future robotic or human missions. For Mars, a dedicated catalog of terraced craters has also been implemented, classifying them as single, multiple, or questionable according to the scheme proposed by Ali Bramson [7]. This update allows users to precisely locate specific crater types and analyze their morphological characteristics in greater detail, supporting studies on crater evolution, impact mechanics, and subsurface stratigraphy. Together with geological unit searching capabilities, these new additions make MATISSE an exceptionally

powerful tool for integrated analysis of impact structures across multiple planetary bodies, further strengthening its role in landing site selection, where understanding the morphological and geological context is crucial.

Conclusions:

The recent developments of MATISSE confirm the central role of the tool in planetary research, establishing it as an advanced platform for the integration, analysis, and visualization of heterogeneous data from numerous space missions. The expansion of its functionalities—from the integration of geological units to the addition of new crater catalogs, as well as the inclusion of lunar datasets and global geological maps—has made MATISSE even more versatile and capable of meeting the continuously growing needs of the scientific community.Thanks to these innovations, users can conduct more accurate, targeted, and geologically contextualized analyses, significantly enhancing their ability to interpret the evolutionary history of planetary surfaces and to support complex decision-making processes, such as the selection of future landing sites. MATISSE is therefore not only a technological tool but a fully-fledged working environment for planetary exploration, able to adapt and grow alongside the new challenges and opportunities offered by current and future space missions.The tool continues to evolve and expand its capabilities: in the coming months, new datasets and additional functionalities will be added, aiming to provide the scientific community with an increasingly complete and cutting-edge tool for the comparative study of planetary bodies.

References: [1] Zinzi, A., Capria, M.T., Palomba, E., Giommi, P., Antonelli, L.A., 2016. MATISSE: a novel tool to access, visualize and analyse data from planetary exploration missions. Astron. Comput. 15, 16–28. https://doi.org/10.1016/j.ascom.2016.02.006.
[2] V. Camplone, A. Zinzi, M. Massironi, A.P. Rossi, F. Zucca, (2024) Astronomy and Computing, Volume 48, 2024, 100852, ISSN 2213-1337, https://doi.org/10.1016/j.ascom.2024.100852.
[3] Rognini, E., Capria, M. T., Tosi, F., De Sanctis, M. C., Ciarniello, M., Longobardo, A. N. D. R. E. A., ... & Russell, C. T. (2020). High thermal inertia zones on Ceres from Dawn data. Journal of Geophysical Research: Planets, 125(3), e2018JE005733.
[4] Wright, J., Rothery, D.A., Balme, M.R., Conway, S.J., 2019. Geology of the Hokusai quadrangle, H05), Mercury. J Maps 15 (2), 509–520.https://doi.org/10.1080/17445647.2019.1625821.
[5] Nass, A., 2023. Geologic map of ceres [Dawn Mission] - Global dataset based on the 15 individual quadrangle maps [Data set]. In Icarus, Versione 01, Vol. 316, 1–204. doi: 10.5281/zenodo.7989802.
[6] Fortezzo, S. C., Spudis, P. D., & Harrel, S. L. (2007). Release of the digital unified global geologic map of the moon at 1: 5,000,000. Proc.(a)(b) Zhanchuan Cai (Senior Member, IEEE) received the Ph. D. degree in computer software and theory from Sun Yat-sen University, Guangzhou, China, in.
[7] Bramson, A. M., Byrne, S., Putzig, N. E., Sutton, S., Plaut, J. J., Brothers, T. C., & Holt, J. W. (2015). Widespread excess ice in arcadia planitia, Mars. Geophysical Research Letters, 42(16), 6566-6574.

XXI Congresso Nazionale di Scienze Planetarie

Sessione Focus S5

The meteorites and impactites collections in Italy

THE METEORITE AND IMPACTITE COLLECTION OF THE ITALIAN MUSEUM OF PLANETARY SCIENCES: SCIENTIFIC AND CULTURAL SIGNIFICANCE. D.Faggi[1] and M.Morelli[1],
[1] Museo Italiano di Scienze Planetarie – Fondazione ParSeC, Via Galcianese 20/H, Prato, Italy.
e-mail: faggi@fondazioneparsec.it

Introduction: A meteorite collection holds a significance that exstends far beyond the material value of its specimens. From a scientific perspective, meteorites provide irreplaceable information on the origin and evolution of the Solar System, the chemical and physical processes that shaped planetary bodies, and the presence of compounds such as water and organic molecules. At the same time, they represent a natural and cultural heritage: extraterrestrial rocks that are tangible witnesses of both cosmic and Human history, capable of enriching museums and communities while promoting scientific outreach.

The Italian Museum of Planetary Sciences (MISP), founden in 2005, is the only Italian institution **entirely dedicated to planetary science**. It hosts the most extensive meteorite collection in Italy, together with a notable collection of impactites and a mineralogical collection. The Museum is a **type specimen** (holotypes) **official repository** recognized by the Nomenclature Committee of the Meteoritical Society [1].

The meteorite collection: The MISP meteorite collection comprises **553 distinct meteorites**, totaling **1618 specimens**, including **274 thin sections** and **250 epoxy mounts**. The collection has been built through acquisitions from meteorite hunters and dealers, as well as field expeditions in Mauritania (Adrar and Erg Chech), Libya (Hammadah al Hamra, al-Kufra), Egypt (Lybian Desert, Great Sand Sea), Algeria (Acfer), Chile (Atacama), and Morocco (Hamada du Draa) [2] [3] [4]. As official repository, MISP currently houses **312 type specimens**, with **32 additional new meteorites** under classification. Among the holotypes, the collection includes significant specimens such as the **Matera** and **Cavezzo** meteorites, both recovered in collaboration with the **PRISMA- INAF** network [5].

The collection includes several specimens with distintive aesthetic characteristics that are currently on display in the museum halls: a slice of the Estherville mesosiderite, big slices of the Imilac and Seymchan pallasites, a ~700 g fragment of the Martian shergottite Dar al Gani 670, and a 272 kg fragment of the metallic Nantan meteorite.

From a scientific and classificatory perspective, the collection is representative of most known meteorite groups, including both **chondrites** and **achondrites**. Recent acquisitions have focused on expanding the systematic coverage, particularly through the inclusion of **ungrouped achondrites.** Noteworthy examples include **Erg Chech 002** and **Ksar Ghilane 022**.



Figure 1 – Estherville, mesosisderite (MSP 2267/1)

The Museum also preserves **25 distinct lunar meteorites** from different lithologies, making it the **largest lunar collection in any Italian museum**.

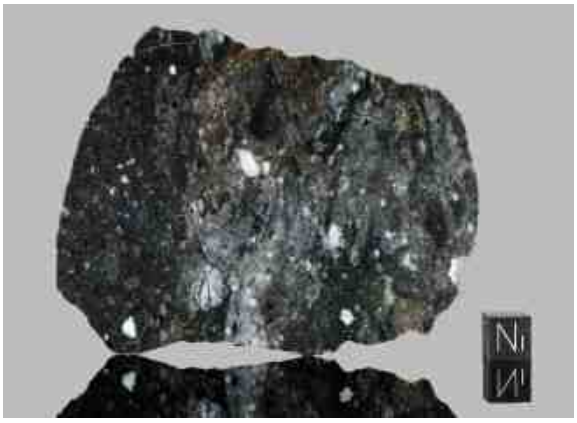


Figure 2 - Timétrine 001, Lunar Melt breccia (MSP 9073/1), ©2025 Chinellato Matteo

The complete catalog has been published in *Meteoritics & Planetary Science* [1] and it is accessible trough the Museum's official website.

A large portion of the collection has been catalogued following the **Italian National Standard for Planetological Heritage (BN-PL)** [6] and the resulting datasets are fully available in Open Access on the **General Catalog of Cultural Heritage**.

Specimens that are not on display in the museum halls are preserved in humidity- controlled cabinets to prevent alteration.

The impactite collection: the collection includes **268 specimens**, comprising **tektites**, **impact glasses**, **suevites**, **melt rocks**, **impact melt breccias**, **impact breccias** and **shatter cones**. Among them thare are samples from both confirmed (35 sites) and unconfirmed terrestrial impact structures

Conclusions: Together, the meteorite and impactite collections make MISP a unique reference center for preservation, study, and dissemination of planetary materials in Italy, fostering both scientific research and cultural awareness.

References:[1] Morelli M. et al. (2023) *Meteoritics & Planet. Sci., 58, 945-954,* doi:10.1111/maps.13974. [2] Cigolini et al. (2012) *Meteoritics & Planet. Sci.* 47, 1772-1788. [3] Orti L. et al. (2008) *Meteoritics & Planet. Sci.,* 43, 1629-1639. [4] Pratesi et al. (2005) *Meteoritics & Planet. Sci.,* 40, 1653 – 1672 [5] Gardiol et al. (2021) 15th Europlanet Science Congress 2021 EPSC2021-208. [6] Franza A. et al. (2022) *Cataloguing and Classification Quarterly,* 60 (3-4), 266-296, https://doi.org/10.1080/01639374.2022.2063466.

THE VATICAN METEORITE COLLECTION AT THE VATICAN OBSERVATORY. R. J. Macke, SJ[1], [1]Vatican Observatory, V-00120 Vatican City-State, email:rmacke@specola.va

Introduction: The Vatican collection of meteorites boasts 1225 specimens of 542 distinct meteorites, including representatives of all the main meteorite types. The collection originated through the personal collection of Adrian-Charles Marquis de Mauroy (1848-1927), and has grown slowly but steadily over the past nearly 120 years. The collection has been a valuable resource for research. In addition to the measurement of physical properties (primarily density and porosity) by members of the Vatican Observatory, researchers outside the Vatican Observatory have conducted numerous diverse studies on specimens from the collection.

We continue to grow the collection and seek to improve our methods of curation. Recently we are developing a computer database of full-color 3d models of the collection to better document and visualize the collection. When completed, it will be incorporated into a publically-accessible database to improve the visibility and utility of the collection.

History: Adrien-Charles Marquis de Mauroy, once president of the French Mineralogical Society, had what was in his day one of the largest private meteorite collections in the world[1]. In 1907, he donated 104 specimens to the Vatican Observatory, followed by 50 more in 1912. In 1935 (after his death), his widow consort donated the remainder of the collection, making about 1000 specimens total. The collection continues to grow, largely through donations from generous benefactors.

With the development of the astrophysical laboratory at the Vatican Observatory after 1935, meteorites became a valuable source of material for research. Initially, the laboratory did spectroscopy of a few select meteorites [2,3]. In the 1990s, research shifted toward physical properties, with an emphasis on non-contaminating and non-destructive techniques. The combination of the "glass bead method" and ideal-gas pycnometry for density and porosity made possible the rapid survey of entire collections with portable tabletop instruments [4,5].

Curation of the collection was spotty until G. Consolmagno became curator in 1993. He organized the collection, established and updated a database to house a detailed catalog, and promoted the collection to outside researchers seeking meteoritic material for their studies. After R. Macke became curator in 2014, the control and documentation of meteorite loans was improved with loan agreement forms to be signed by the recipient and by a representative of the institution.

Contents of the Collection: The Vatican Meteorite collection currently contains 1225 specimens (i.e. unique catalog numbers; some catalog entries contain multiple fragments or collected powders that are not individually counted) of 542 distinct meteorites. Because the collection originated from a 19th-century collection, many of the stones are from observed falls. Some have historic significance, such as Ensisheim (fell 1492) and L'Aigle (fell 1803). More recent falls include Torino (1988), Chelyabinsk (2013), Serra Pelada (2017), Aguas Zarcas (2019), and Tarda (2020). Despite the abundance of falls, they constitute only half of the collection. The finds (many of which also originated from the Marquis' collection) are dominated by irons, mesosiderites, and pallasites.

Half the stones are chondrites (Table 1). Irons constitute about ¼ of the stones. Achondrites are fewer in number but more valuable for research. Our Chassigny thins sections in particular have been popular for SEM studies of martian meteorites. There are also a few items noteworthy in themselves. For example, our specimen of the martian meteorite Nakhla has been handled by two Popes. The collection is also entrusted with one of the Apollo lunar specimens gifted to the Vatican by the United States.

The majority of the specimens are between 1 and 100 g, suitable for most physical properties measurements. The largest 15-20 specimens (mostly irons) are too big for most studies and are currently suitable only for display. The collection also contains 74 thin sections.

Table 1: Summary of the contents of the Vatican Meteorite Collection

Category	No. Stones	No. Mets	Total Mass (kg)
Chondrite	654	305	51.2
Ord. Chond.	581	273	49.8
Carb. Chond.	60	27	1.1
Enst. Chond.	8	4	0.12
Rumurutiite	5	1	0.20
Achondrite	83	40	1.2
HED	36	16	0.55
Lunar	11	7	0.055
Martian	21	9	0.25
Ureilite	3	2	0.25
Angrite	1	1	0.0007
Aubrite	8	4	0.061
Prim. Achond.	3	1	0.021
Iron	385	169	117.1
Stony-Iron	103	29	9.7
Mesosiderite	38	9	3.7
Pallasite	65	20	6.0

Research on the Collection: The Vatican meteorite laboratory is currently equipped for measurement of physical properties. Grain density is measured by ideal-gas pycnometry utilizing compressed nitrogen gas. The lab contains two pycnometers: one (Quantachrome Ultrapycnometer 1000) for smaller specimens and another custom-built design [6] for slabs and larger pieces up to 10 cm wide. For bulk densities, the glass beads were replaced in 2015 by a laser scanner (NextEngine model 2020i) and, in 2025, by a structured light scanner (Einscan Scanner3D SP V2). Magnetic susceptibility is measured by a ZH-Instruments SM-30 handheld magnetic susceptibility meter. Until recently, there was also an apparatus for measuring heat capacity by liquid nitrogen immersion, but this has been superceded by a better instrument in the lab of collaborator C. Opeil at Boston College [cf 7].

In addition to studies at the Vatican Observatory itself, the collection is available for researchers worldwide. Preference is given for nondestructive studies, but destructive studies on small samples may also be allowed on a per-case basis. The collection typically loans a few specimens per year, but there is neither a quota nor a set limit to the number of loans that may be transacted.

Ongoing Curation Activities: The Digital 3D Database: The meteorite catalog database has developed over the years, beginning with the Marquis' original typewritten catalog. Curator Consolmagno converted the catalog to a FilemakerPro digital database, which curator Macke later ported to Ninox. The database not only contains details about each specimen, but also a record of the provenance and research history. Photographs are included of original labels and other provenance, as well as photos of the specimens themselves. However, flat photos often present a misleading impression of the actual shape of the meteorite.

This past year the laboratory acquired a structured light scanner to preserve each specimen in a digital 3d computer model. The scanner creates a 3d mesh of the shape of the object and overlays photographic textures to reproduce the meteorite in full color (Fig. 1). SLS scans are much faster than laser scans, taking only a few minutes per specimen. This makes it possible to survey the entire catalog in a reasonable timeframe. The manufacturer recommends objects be at least 30 mm per side with no dark surfaces, but so far we have found the scanner capable of handling much smaller meteorites and it captures even the dark fusion crusts of ordinary chondrites. Issues yet to be addressed include acute wedges (the two sides don't easily align if the angle is too sharp to scan both sides simultaneously) and specular surfaces.

With this new database of 3d models, the meteorite catalog itself will also be updated. The current catalog is not accessible online; the new one will include tiered access (levels include: curator, internal use, and external users) to limit externs from accessing sensitive or unnecessary information. The 3d scans will be included in this new system and will be accessible to external users. We have yet to commit to any particular database software for this project, and are seeking input from the curation community for recommendations.

Concluding Note for Researchers: The Vatican Meteorite Collection represents a valuable resource for meteorite research. Through ongoing curation efforts, the collection will increase in usefulness and accessibility in the years to come. Any meteoriticist looking to receive a loan of material for their research should contact the curator directly at rmacke@specola.va.



Figure 1: The meteorite Agen (VO Catalog number 0003) on the SLS scanner, along with three views of the resulting computer model of the meteorite.

References: [1] Maffeo S. (2001) *La Specola Vaticana: Nove Papi, Una Missione.* [2] Gatterer A. and Junkes J. (1940) *Comm. Pont. Academ. Sci.* 4, 191-223. [3] Salpeter E. W. (1952) *Ricerche Spettroscopiche: Pub. del Lab. Astrophys. della Specola Vaticana 1938-1978*, v.2. [4] Consolmagno G. J., and Britt D. T. (1998) *Meteoritics & Planet. Sci.* 33, 1231-1241. [5] Consolmagno G. J., et al. (2006) *Meteoritics & Planet. Sci.* 41,331-342. [6] Macke R. J. et al. (2013) *LPSC XLIV*, Abstract #1398. [7] Macke R. J. et al. (2019) *Meteoritics & Planet. Sci.* 54, 2729-2743.

POTENTIAL OF IMAGING SPECTROSCOPY AND SEM-EDS TO MAP THE SURFACE MINERALOGICAL COMPOSITION OF NWA 4966 and NWA 6726 CARBONACEOUS CHONDRITES.

S. Pascucci[1] (simone.pascucci@cnr.it), A. Lettino[1], A. Palombo[1], E. La Francesca[2], G. Filacchione[2], A. Galiano[2], S. De Angelis[2], M. Casalini[3] and G. Pratesi[3]. [1]Institute of Methodologies for Environmental Analysis (IMAA)- Italian National Research Council (CNR), C. da S. Loja, 85050 Tito Scalo, Italy, [2]Institute for Space Astrophysics and Planetology, IAPS-INAF, Via Fosso del Cavaliere, 100, 00133, Rome, Italy. [3]Università degli Studi di Firenze – Dipartimento di Scienze della Terra, Florence, Italy.

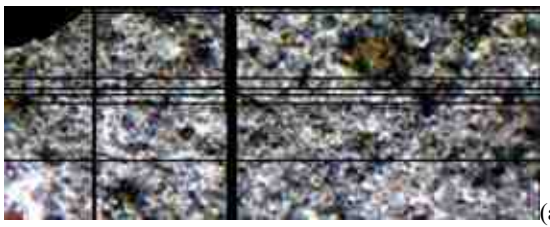
Introduction: Spectroscopy studies of Carbonaceous Chondrites (CCs) under controlled laboratory conditions provide crucial insight into their surface composition and the evolutionary processes of their parent bodies (asteroids) [1, 2]. Comparing the reflectance spectra of asteroids with those of meteorites, typically through Visible-Infrared (VIS-IR) imaging spectroscopy, is a powerful approach for inferring asteroidal surface composition [3]. To this end, we performed VIS-IR spectroscopy using SPIM hyperspectral cameras (0.4-5.1 μm) and Scanning Electron Microscopy with Energy Dispersive X-ray Spectroscopy (SEM-EDS) on thin sections of NWA 4966 (CK4) and NWA 6726 (CO3.2). These laboratory analyses were conducted to retrieve and map surface composition at high spectral and spatial resolutions. Using the high-resolution SEM-EDS techniques, we analyzed and mapped the main elemental compositions of the CC matrices, chondrules, and Calcium-Aluminum-rich Inclusions (CAIs). Results highlight the challenges associated with using VIS-IR spectroscopy and SEM-EDS techniques at the micrometer scale and recommend their combined application. This work investigates the potential utility of combining VIS-IR and SEM-EDS analytical techniques for the spectral characterization of CC meteorites and the assessment of their terrestrial weathering..

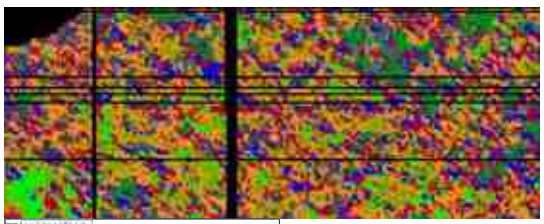
Laboratory Setup and Samples Description: The two CC meteorite slabs have been investigated using the SPectral IMager (SPIM) instrument in use at the INAF-IAPS laboratory [4,5]. The facility consists of an imaging spectrometer operating in the 0.35-5.10 μm-range [4,5], and contains the laboratory spare of VIR spectrometer onboard the Dawn mission and successfully applied in spectral analysis and data validation for supporting the ExoMars mission [4]. By moving the sample-holder (XY optical axes direction) of the stage it is possible to acquire at each step an image of the slit of 9 mm × 38 μm, thus obtaining a spectrum (of 696 bands) for each pixel along the slit [3,4]. Moreover, to retrieve the slabs elemental composition, SEM lab measurements have been used. The SEM uses a field emission source (FESEM, Zeiss Supra 40) and is equipped with an energy-dispersive X-ray spectrometer (EDX, Oxford INCA Energy 350 and X-ACT Silicon Drift Detector LN2-free). Secondary electrons were used to construct images enlarged up to x200,000 and resolved up to 5 nm. The SEM-EDS allowed us to perform semi-quantitative analyses with virtual standards present within the INCA software, preloaded for microanalysis.

The two samples analyzed are slabs of about 3.0x2.0 cm, and the investigated area is 9.7x3.8 mm^2. According to the Meteoritical Bulletin, the NWA 4966 original sample is constituted mainly of olivine ($Fa_{34.45\pm0.5}$), pyroxene ($Fs_{28.6\pm0.3}$ $Wo_{3.1\pm0.6}$, n=2), with a matrix of about 75 % in volume, with included big chondrules (about 15% in volume) with diameter up to 0.7 mm, and minor type-C CAIs presence and low presence of metals. While the NWA 6726 is composed of a matrix of about 30-40% in volume (mainly composed of olivine (Fa) and pyroxenes (Opx and Cpx) with also taenite, troilite and rare kamacite) with dispersed small chondrules (about 40-50% in volume) of less than 0.15 mm in diameter, and rich in small CAIs (about 13% in volume).

Data and Methods: To derive the reflectance images from the two SPIM raw images, the procedure proposed by [5] has been applied using an iterative procedure developed in the IDL code. Then, an absorption band parameterization procedure has been set up in ENVI/IDL environment for automatically analyzing the absorption features of the spectra of each pixel of the acquired SPIM images. Moreover, a classification procedure by first reducing dimensions, finding the Independent Components (IC) and whitening the data with ICA (ENVI) and then applying the K-means clustering, we are able to find out sensitive groupings and patterns that might be lost in the high-dimensional space so to extract as much information as possible from the SPIM reflectance imagery. After that, to the obtained classes it was assigned a label and color based on the SEM-EDS results. The SEM-EDS images acquired on the two CC slabs, have been used (a) to manually identify peaks of the elements and export the spectra of interest on chosen targets (e.g., CAIs, chondrules, matrix, FeS inclusions) and (b) to retrieve from the EDX images a map on a pixel-by-pixel basis of the main elements so to derive the distribution of the main phases by assigning to them different colors.

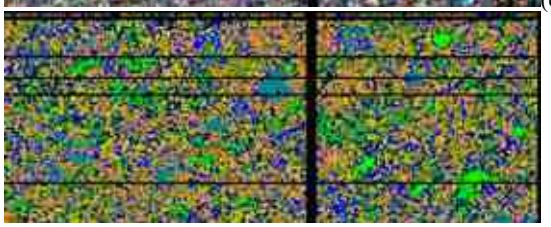
Results and Discussion: Figure 1b shows the final map and relative legend obtained for the NWA 6726 slab in which: (a) four classes describe well the fragmented chondrules (chon), about 3 times the abundance of the CAIs, almost type A, with a higher Mg content in the rims; (b) three classes describe the matrix variability made almost of pyroxenes (Fa) mixed with other minor phases and (c) inclusions of small CAIs and (d) Fe/Ni metal partially altered/hydrated to phyllosilicates. Figure 1d shows the NWA 4966 map. Its analysis reveals that the matrix is made of a variegate mixture of pyroxenes (with both low and high-Ca content), Cr-rich spinel, high Ca- pyroxene mixed with Kamacite and FeS and other minor elements (Al, P, K) and plagioclase. In chondrules we find Fayalite with high-Ca content and Cr, plagioclase, Ferrosilite and spinels. Diffused small CAIs with a high content of Ca are mainly found in association with phyllosilicates (and anorthites and spinels) and in some spots also Ca-Al-rich glass. Highly oxidized metal inclusions are present.


(a)




(b)


(c)




(d)

Fig.1. (b) and (d) K-means classification derived from the ICs extracted from the SPIM reflectance images of the (a) NWA 6726 (R:1.00 µm; G:0.75 µm; B:0.56 µm) and (c) NWA 4966 slabs (R:3.00 µm; G:2.00 µm; B:1.00 µm), respectively.

Furthermore, the maps of the Band Depth and Band Area measured under the Continuum Removed absorption band at ~1 µm clearly show and confirm the distribution of iron silicates, while that at ~4 µm provides strong evidence of the distribution of carbonates (probably of terrestrial origin).

Imaging spectroscopy has the advantage of being sensitive to both crystalline and amorphous materials and it can be used from up close (returned-space samples) to far away, but spectrum of a meteorite can be strongly influenced by contaminating factors.

The mineralogy determined by VIS-IR features corresponds quite well to the mineralogy observed with greater resolution and higher accuracy on X-ray maps of the five CC samples. While minor phases in the inclusions like chromite or anorthite observed by SEM-EDX in the CC samples could not be clearly identified from the VIS-IR SPIM spectra. SEM-EDS provides µm-scale resolved information on the mineralogy and chemical composition of anhydrous phases, but slices need to be coated to be analyzed with a good resolution and signal by reducing scattering effects and noise in the EDX X-ray data.

Conclusions and Future Work:

The potential of VIS-IR imaging reflectance and the SEM-EDS X-ray spectroscopy alongside high-res imaging technique to retrieve and map the surface composition at high spectral/spatial resolutions of two available CC meteorites thin slabs (NWA 4966-CK4 and NWA 6726-CO3.2) has been assessed. Future work will include: (a) the use of other meteorite slabs to verify the effectiveness and replicability of the proposed procedure; (b) the application of other analytical techniques (e.g., Mössbauer spectroscopy, TEM, XRD) for chondrules and CAIs type identification and to try to understand their formation/alterations mechanisms [6].

References: [1] Amano K. et al. (2023), *Science Advances*, 9(49), 1-19. [2] Galiano A. et al. (2025), Meteoritics & Planetary Science, 60(3), 570-595. [3] Tang Y.J. et al. (2025), *The Astronomical Journal*, 169(4), 201. [4] Coradini A. et al. (2011), Vol. 6, *EPSC-DPS2011-1043*. [5] De Angelis S. et al. (2015), *Rev.Sci.Instr*. 86, 093101. [6] Cloutis E. et al. (2012) *Icarus*, 252, 39-82.

SCALEA, A NEW ITALIAN METEORITE: DESCRIPTION AND CHARACTERIZATION

V. Moggi Cecchi[1], G. Pratesi[2,3], T. Cuppone[2], X. Shehaj[2,4,5] 1. [1]Museo "La Specola" – Sistema Museale di Ateneo, Università di Firenze; email: vanni.moggicecchi@unifi.it 2. [2]Dipartimento di Scienze della Terra, Università degli Studi di Firenze, Firenze, Italy. [3]INAF-Istituto di Astrofisica e Planetologia Spaziali, Roma, Italy. [4]Agenzia Spaziale Italiana, Roma, Italy. [5]Dipartimento di Fisica, Università degli Studi di Trento, Trento, Italy.

Introduction: The Italian landscape has unfavorable environmental conditions that do not allow long-term conservation of meteorites on the fall site. For this reason the recovery of fall meteorites is an extremely rare event. Due to the presence of numerous urbanized, cultivated, wooded or mountain areas, systematic recovery campaigns for meteorite falls on the Italian territory have never been organized in recent times, except in cases of the falls of the Cavezzo and Matera meteorites, that were monitored through the all-sky cameras of the Prisma network: in both cases a relatively easy discovery of centimeter-sized fragments that allowed scientists to perform a complete characterization was allowed by a precise determination of the fall area [1,2,3].

The Scalea meteorite: The recent recovery of the Scalea meteorite represents a very interesting case. Mr. Maurizio Sassone, owner of a beach resort in the town of Scalea, Cosenza, on September 11th, 2024 at 12.34 CET personally witnessed the fall of a stone a few meters away from him, exactly in the strip of land between the shoreline and the furnishings of his resort. While walking on the limestone shore he heard a loud whistle and a dull thud. Immediately after he saw a couple of meters aside a small crater, 30 cm-wide and 10 cm-deep, and a dark brown stone about 6x4x4 cm wide, with a small grey chip on top, in the center of the crater (Figure 1). Without removing the object he made a detailed photographic report and collected the object and a small quantity of white sand from the surrounding area. After contacting one of the authors, he brought the stone to the Meteocert Laboratory of the Sistema Museale di Ateneo-Dipartimento di Scienze della Terra of the University of Florence where the investigations regarding its nature and its complete characterization were conducted.



Figure 1: the fall site with the Scalea meteorite

General features:

A first detailed stereoscopic microscope observation confirmed the suspected meteoritic origin of the stone: some distinguishing features, like an almost complete dark brown fusion crust with several small cracks on the external surface, a rounded and oriented shape and several parallel streaks on one side, which appears ablated and partially remelted, support this hypothesis [4]. The meteorite is a whole rounded stone weighing 189g, completely covered by a dark-brown fusion crust with a small chip displaying a pale grey, fine grained texture consisting of green and white small crystals, with few metal spots (Figure 2) pointing to a possible classification of the meteorite as ordinary chondrite [5]. On one side the meteorite shows an almost plane surface with a thinner crust, elongated parallel streaks and remnants of a small barred olivine chondrule.



Figure 2: photography of the main mass of Scalea

No other chondrules have been detected on the surface but several cracks are visible at the stereoscopic microscope scale. Traces of a white, fine grained powder have been observed on small cavities of the surface, probably due to the impact with the seashore. Once collected and analyzed by means of Micro-Raman spectrometry, the powder resulted to be formed by calcite, a composition fully compatible with the limestone fine-pebble beach where the stone fell and has been recovered, thus confirming the provenance of the meteorite from this site. After the extraction of a 1 g fragment the meteorite was completely characterized for classification and then cut into two pieces weighing 167 and 19 grams, respectively. The meteorite was submitted for approval to the NomCom of the Meteoritical Society and approved on October, 20th 2025 as L5 ordinary

chondrite (fall), with the name Scalea [6]. The type specimen, weighing 20.1 g, one chip and one thin section are on deposit at Museo di Storia Naturale dell'Università di Firenze (Inventory# MSN-Fi 3751-I); Maurizio Sassone owns the main mass, now weighing 167 g;

Instruments and methods:

Optical microscopy was performed at the microscopy laboratory of the Sistema Museale di Ateneo, Università di Firenze, Italy, using an Axioscope 5 polarizing optical microscope equipped with Axiocam-HR camera. SEM-BSE images have been performed at the Centro di Servizi di Microscopia Elettronica e Microanalisi (MEMA) of the University of Firenze with a Zeiss EVO-40. Electron microprobe analyzer–wavelength dispersive spectrometry (EMPA-WDS) analyses have been performed at the Firenze laboratories of the IGG – CNR (National Council of Research) with a JEOL-JXA 8230 microprobe.

Textural features:

The thin section displays a brecciated texture with two different lithologies: the predominant one is consisting of a medium-grained aggregate of olivine and pyroxene crystals, with minor plagioclase, all ranging in size 100 to 300 µm. Scattered PP, POP and BO chondrules and chondrule fragments are visible (Figure 3).

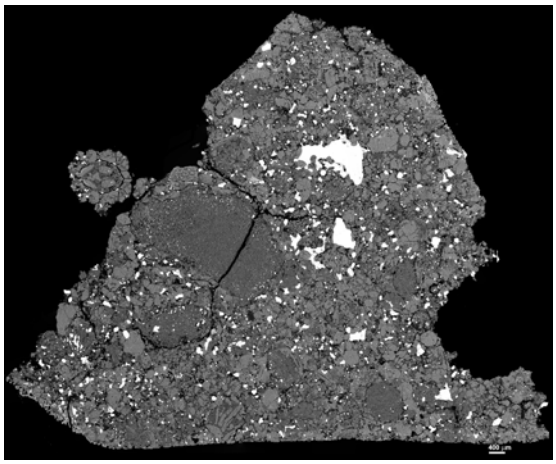


Figure 3: SEM-BSE photomosaic of the thin section of the meteorite displaying the chondritic texture

The other one consists of few fine-grained chondrules and aggregates, mainly consisting of small low-Ca pyroxene and olivine grains, with minor high-Ca pyroxene and plagioclase, all with a mean grain size ranging 30-40 um (Figure 4). Opaque phases are represented by Si-free Fe,Ni alloys (kamacite, taenite and rare tetrataenite) and Cr- and Ni-free troilite in both lithologies, ranging in size 100-1000 µm in the coarse-grained and 10-80 µm in the fine-grained one. Chromite and apatite are present as accessory minerals, ranging in size 80-150 µm; sharp extinction of olivine indicates shock stage 1; both at the optical microscope and at the SEM scale no weathering is detected, since Fe,Ni alloys and troilite are unaltered, confirming null permanence on the ground.

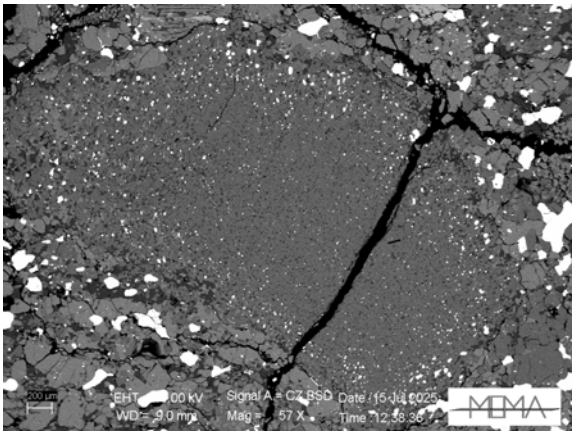


Figure 4: SEM-BSE image of the fine-grained lithology area; grey areas are silicatres; white spots are opaques

Minerochemical features:

For classification purposes, the general minerochemical features of the matrix and of selected phases were analyzed by EMPA on both the typical chondritic medium-grained texture and the fine grained one. Silicates are mainly consisting of olivine ($Fa_{24.9\pm0.3}Fo_{75.1\pm0.3}$; Fe/Mn = 53.31±0.3, N = 54); and Low-ca pyroxene ($Fs_{19.5\pm0.1}En_{79.0\pm0.1}Wo_{1.5\pm0.1}$; Fe/Mn = 30.22±0.2, N = 40) without remarkable differences between chondrules and matrix; rare diopside ($Fs_{8.0\pm0.1}En_{47.6\pm0.2}Wo_{43.1\pm0.2}$; N = 8), and an Ab-rich plagioclase ($An_{10.2}Or_{5.3}$, N = 17); Chromite: Cr_2O_3 = 55.3, FeO = 30.2, Al_2O_3 = 5.0, TiO_2 = 3.1, MgO = 3.0, V_2O_3 = 0.6, MnO = 0.4, ZnO = 0.3, all in Ox Wt.%; Apatite: CaO =52.3, P_2O_5 = 42.4, Na_2O = 0.5, FeO = 0.6, Cl = 5.5, F = 0.8, all in Ox Wt.%;

Discussion and conclusions

According to textural and compositional data the meteorite has been classified as a brecciated L5 ordinary chondrite, with medium degree of shock and medium degree of weathering [5,6].

This publication has been funded by EU - Next Generation EU Mission 4, Component 2 - CUP B53C22002150006 - Project IR0000032 – ITINERIS - Italian Integrated Environmental Research Infrastructures System

References:

[1] Pratesi G. et al. (2025). *Meteoritics & Planet. Sci, in press*. [2] Barghini D. et al. (2024). EPSC2024-449, https://doi.org/10.5194/epsc2024-449. [3] Pratesi G. et al. (2021) *Meteoritics & Planet. Sci., 56,* 1125-1150. [4] Moggi Cecchi et al. (2025) *SGI-SIMP Congress*, abs.258 https://doi.org/10.1111/maps.13695. [5] Grady M. et al. (2014), Atlas of Meteorites, 1st ed., CUP, Cambridge, 384 pp. https://doi.org/10.1017/9781139016308. [6] Gattacceca, J. et al. (2025) MAPS, in press;

XXI Congresso Nazionale di Scienze Planetarie

Sessione Meteore, Meteoriti e Polvere interplanetaria

Uncontaminated Cosmic Dust from the Upper Stratosphere: DUSTER Collections and Multi-Analytical Characterization of micron and sub-micron particles

Luca Tonietti[1,2], Vincenzo Della Corte[2], Alessandra Rotundi[1,2], Zelia Dionnet[3], Luigi Folco[4], Onofrio M. Maragò[5], John R. Brucato[6], Stefania Stefani[7], Stefano Rubino[7], Giuseppe Piccioni[7], Fabio Cozzolino[2], Ivano Bertini[1,2], Laura Inno[1,2]. 1. Department of Science and Technology, Parthenope University of Naples, Naples, Italy. 2. INAF-OAC, Osservatorio Astronomico di Capodimonte, Naples, Italy. 3. CNRS, Institut d'Astrophysique Spatiale, Université Paris-Saclay, Orsay, France. 4. Dipartimento di Scienze della Terra, Università di Pisa, Pisa, Italy. 5. CNR-IPCF, Istituto per i Processi Chimico-Fisici, Messina, Italy. 6.INAF-Astrophysical Observatory of Arcetri, Florence, Italy. 7. INAF-IAPS, Istituto di Astrofisica e Planetologia Spaziali, Rome, Italy.

The stratospheric region between 30 and 40 km is one of the most suitable and accessible environments to collect pristine interplanetary and interstellar dust particles (IDPs), where terrestrial contaminators such as volcanic, aeolian, or anthropogenic aerosol is negligible [1-3].

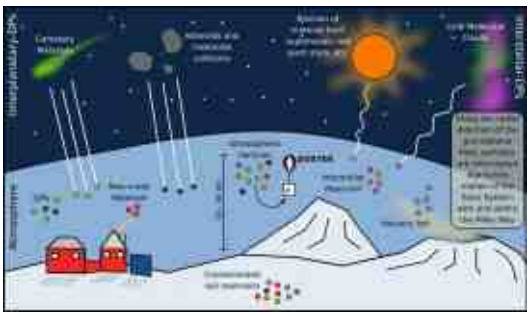


Figure 1. Schematic overview of the DUSTER collection concept: Interplanetary Dust Particles (IDPs) from comets, asteroids, and meteoroid collisions, as well as interstellar dust from supernovae and dense molecular clouds, enter Earth's atmosphere. Most man-made and terrestrial materials, e.g. volcanic, remain confined to the troposphere or lower stratosphere. The high-altitude stratospheric window, 30 - 40 km, is a unique reservoir for extraterrestrial matter, allowing DUSTER to collect stratospheric particles in a near-contamination-free environment, enabling the recovery of pristine IDPs and possible interstellar dust, intercepted due to the solar system's motion within the Milky Way.

The DUSTER (Dust in the Upper Stratosphere Tracking Experiment and Retrieval) project is a balloon-borne sampling instrument specifically developed to collect IDPs with minimal contamination and structural integrity, at collection speed of 7 m/s and flow rates > 1 m3/h. DUSTER includes an adhesive-free collection substrate (Collector), fitted with 13 Transmission Electron Microscope (TEM) grids, directly exposed to the stratospheric airflow. The collection strategy is designed to ensure low-impact speed capture, avoiding particle fragmentations or alterations. The Collector and the Blank, i.e. an identical but unexposed collector, are imaged pre- and post-flight to identify possible pre-existing non-stratospheric particles to be excluded from the sample collection, if observed on the Collector, and to be considered as contaminants, if observed on the Blank. The conceived stringent contamination control protocol positions DUSTER as the only system capable of returning ultra-clean cosmic dust for high-resolution up-to-date laboratory investigations. Four DUSTER stratospheric balloon campaigns have successfully collected IDPs: Svalbard, Norway (2008) and Kiruna, Sweden (2011, 2019, 2021) [4]. We focus here on particles coming from the most recent campaigns (Kiruna, 2019 and 2021). These collections yielded hundreds of particles ranging in size from 0.1 to 50 µm, with a predominance in the 1 µm range. The preliminary SEM-based morpho-classification reveals a compositional and structural diversity including compact mineral fragments, porous aggregates, and spherules. Energy-dispersive X-ray (EDX) analyses have confirmed the presence of mineral phases including silicates and carbonates, indicating both primitive and processed origins [4, 5].

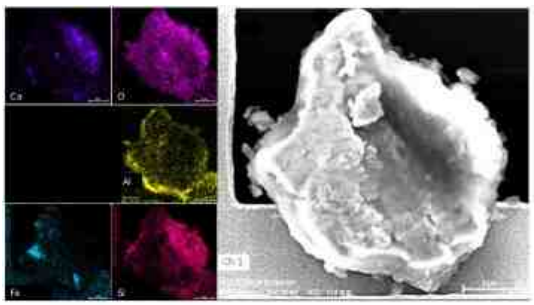


Figure 2. SEM and EDX elemental maps of a stratospheric particle collected by DUSTER. The right image shows a secondary electron micrograph of the collected particle, highlighting its irregular morphology and fragile structure. Elemental maps obtained via Energy-Dispersive X-ray Spectroscopy (EDX) reveal the distribution of key elements: calcium (Ca), oxygen (O), aluminum (Al), silicon (Si), and iron (Fe).

The PRIN 2022 research project "Cosmic Dust II: Cosmochemistry and Space Tweezers Technologies for Solar System Science and Exploration", funded by the Italian Ministry of University and Research (MIUR), builds on this unique IDPs collection in order to investigate the cosmochemical and mineralogical characteristics of extraterrestrial particles with sizes ranging from about 0.5 µm to 50 µm, a dimension gap yet to be filled. Within this frame-

work, a selected subset of DUSTER IDPs i.e., a total of 11 > 10 μm and 10 < 5 μm, is now undergoing a comprehensive multi-analytical technique campaign. These particles have been selected from the Kiruna 2019, 2021 DUSTER collections based on their dimension, morphology, mineralogy, and surface preservation. On particles larger than 10 μm in size an initial high-resolution SEM imaging, followed by non-destructive spectroscopic techniques, including micro-Infrared (μIR), micro-Raman, and nano-Raman spectroscopy allow to map mineral phases and organic functional groups. In particular, Raman analyses allow us to identify silicates, sulfides, and carbonaceous matter, μIR spectra provides key data on sample mineralogy including carbonates, hydrated phases. IDPs smaller than 5 μm in size are observed with high-resolution transmission electron microscopy (HR-TEM) and 3D electron diffraction tomography (EDT), offering structural and chemical characterization at nanometer scale of nanoparticles assemblages and amorphous versus crystalline domains. Few selected particles will undergo destructive analytical techniques, including nano-scale Secondary Ion Mass Spectrometry (nanoSIMS) for measurement of isotopic compositions at sub-micron scale. This last analysis is critical for tracing potential presolar grains and to understand the source-region signatures within the solar system, but also very challenging when applied to DUSTER collections.

Through this multi-analytical techniques cascade, ranging from μIR to nanoSIMS, we aim to build an integrated dataset for each particle, allowing us to characterize its composition, formation history, and potential astrobiological significance. These results are expected to have implications not only for understanding the composition of the near-Earth dust complex and identifying its parent bodies, but also for the broader goals of astrobiology, planetary geology, and Solar System exploration.

References: [1] Flynn, 1997. Collecting interstellar dust grains. Nature, 387, 248. [2] Brownlee 1985. Cosmic dust: collection and research. Annu. Rev. Earth Planet. Sci. 13(1),147-173. [3] Della Corte & Rotundi, 2021. Collection of samples. In Sample Return Missions: The Last Frontier of Solar System Exploration, ed. A.Longobardo. Elsevier, 269-293. [4] Della Corte et al., 2012. In Situ Collection of Refractory Dust in the Upper Stratosphere: The DUSTER Facility. Space Science Reviews, 169, 159-180. [5] Rietmeijer et al., 2016. Laboratory analyses of meteoric debris in the upper stratosphere from settling bolide dust clouds. Icarus, 266, 217-234.

Acknowledgements: We acknowledge the PRIN2022/MUR (Ministero dell'Università e della Ricerca) "Cosmic Dust II: Cosmochemistry and Space Tweezers Technologies for Solar System Science and Exploration" project, ID# 2022S5A2N7, CUP n. I53D23000740006.

SPECTROSCOPIC AND GEOCHEMICAL CHARACTERIZATION OF LUNAR BRECCIA NWA 11421: INSIGHTS INTO THE LUNAR CRUST–MANTLE COMPOSITION AND IMPLICATION FOR MOON EXPLORATION.

A. Alberini[1,2], F. Renzi[1,2], G. Poggiali[1], F. Alberquilla[3], S. Biancalani[4,5,6,1], C. García-Florentino[1], A. Roussel[1], M. Battistuzzi[1], J. Aramendia[3], J. M. Madariaga[3], T. Fornaro[1] and J. R. Brucato[1]

[1]INAF- Astrophysical Observatory of Arcetri, L.go E. Fermi 5, 50125 Firenze, Italy (andrew.alberini@inaf.it); [2]Department of Physics and Astronomy, University of Florence, Via Giovanni Sansone 1, 50019 Sesto Fiorentino, Florence; [3]Department of Analytical Chemistry, Faculty of Science and Technology, University of the Basque Country (UPV/EHU), Barrio Sarriena s/n, 48940 Leioa, Spain; [4]Department of Physics, University of Trento, Via Sommarive 14, 38123 Povo, Trento, Italy; [5]Italian Space Angency (ASI), viale del Politecnico snc, 00133, Rome, Italy; [6]Department of Earth Sciences, University of Florence, via G. La Pira 4, 50121, Florence, Italy;

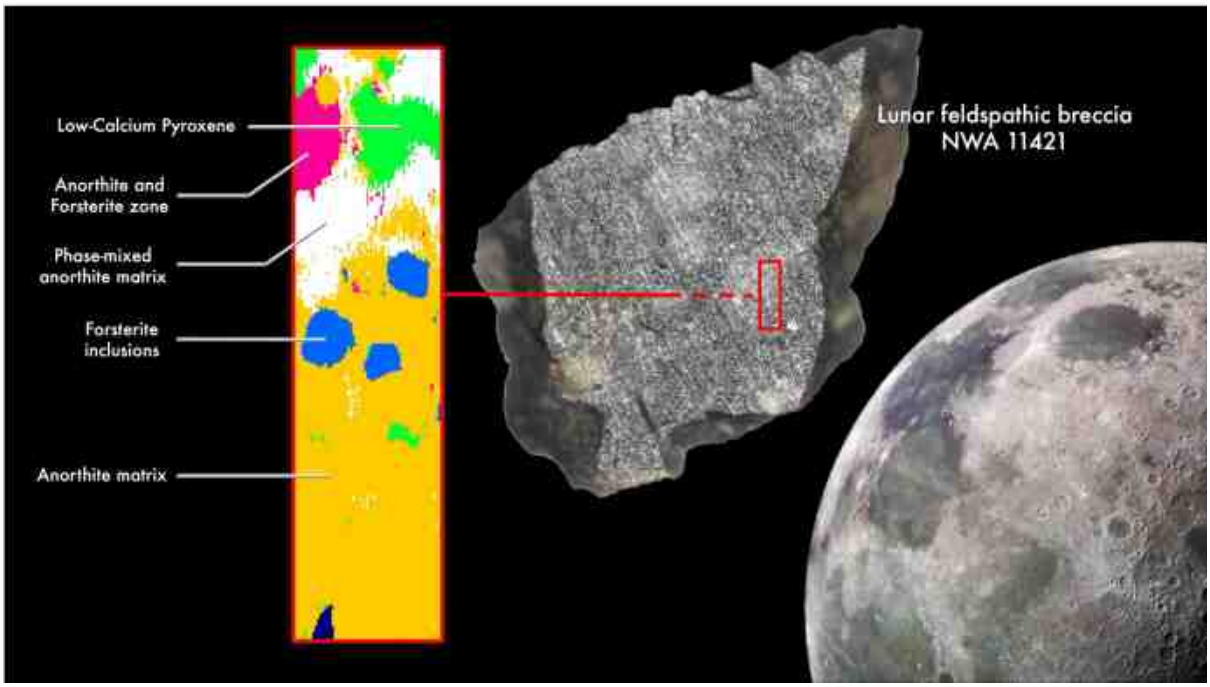


Figure 1 - Microscopic image of NWA 11421 with a magnified view of one of the areas analyzed (red rectangle) using HYPERION 1000 μ-FTIR microscope. Cluster analysis of this region revealed the presence of an anorthositic matrix containing inclusions of forsteritic olivine and low-calcium pyroxene.

Introduction: Lunar meteorites are a valuable source of information for understanding the Moon's geology because they originate from different areas across the lunar surface. In contrast, the samples from the Apollo/Luna missions are restricted to precise locations on the visible side and do not necessarily represent the overall composition of the lunar surface [1][2]. Therefore, the meteorites provide a more global perspective on lunar mineralogical diversity and offer key insights into its overall composition and evolution [1][2][3][4].

NWA 11421 is a lunar meteorite discovered in Morocco in 2017 (total mass ~ 912 g), classified as a feldspathic breccia [5]. Petrographically, it consists of angular to subrounded whitish clasts up to 1 cm in size set into a greyish vitreous groundmass. Dominant mineral phases reported in the Meteoritical Bulletin include low-Ca pyroxene, high-Ca pyroxene, olivine and calcic plagioclase. Minor phases include chromite, ilmenite, fayalite, pyrrhotite, FeNi metal and barite [5]. Of particular significance is the discovery, within NWA 11421, of a dunite clast measuring approximately 1 cm, interpreted as the first fragment of lunar mantle material identified to date [6]. Indeed, the discovered dunite clast exhibits a homogeneous mineral composition, suggesting internal chemical equilibrium and derivation from a deep-seated, mantle-derived source, offering a unique window into the lunar interior beyond the crustal materials typically sampled [6].

This study aims to refine the characterization and broaden the statistical dataset of these samples, en-

hancing our understanding of feldspathic lunar meteorites and assessing the possible presence of dunitic clasts indicative of a mantle-derived origin.

Material and Methods: A comprehensive suite of non-destructive analytical techniques were used. At the INAF–Astrophysical Observatory of Arcetri, bulk Visible and Near/Mid-Infrared reflectance spectroscopy was performed using Diffuse Reflectance Infrared Fourier Transform (DRIFT) collected by a Bruker VERTEX 70v FTIR interferometer, equipped with a Harrick Praying Mantis™ accessory. This configuration provided overall spectral information representative of the entire sample. For microscale assessments, the same VERTEX 70v system was interfaced with a HYPERION 1000 μ-FTIR microscope equipped with a 64×64 pixel Focal-Plane Array (FPA) detector (~ 2 μm spatial resolution) performing cluster analyses. Complementary chemical mapping was carried out at the IBeA research group of the University of the Basque Country (EHU), using μ-EDXRF, which provided high-resolution elemental distribution maps (particularly useful for identifying compositional zoning and supporting spectral interpretations), and Raman imaging employed as a supportive technique to confirm mineral textures and phase associations, reinforcing the identifications derived from FTIR and X-ray fluorescence analyses.

Results and Discussion: NWA 11421 matrix results are indicative of calcic plagioclase (e.g., Figure 1) due to the strong characteristic Reststrahlen bands in the range 10.4 – 11.2 μm (960 – 890 cm^{-1}), predominantly anorthite with some diagnostic features compatible with bytownite. Inclusions and zones enriched of ferromagnesian low-calcium pyroxenes were detected. Specifically, pigeonite is the dominant pyroxene phase, as inferred by the characteristic 9.1 μm (1100 cm^{-1}) infrared peak, with minor contributions from the Mg-rich enstatite and Fe-rich ferrosilite. Forsteritic olivine was also observed in close association with calcic plagioclase along the breccia matrix (Figure 1). All these findings support and confirm the mineralogical composition previously reported in the Meteoritical Bulletin [5].

A key objective of the ongoing analysis is the identification and spectroscopic confirmation of possible dunite fragments within the breccia. Preliminary spectral and compositional data suggest the presence of localized forsteritic olivine-rich region with consistent dunite infrared spectroscopic features. If confirmed, this would provide further support to earlier petrological studies identifying a dunite clast in NWA 11421 [6], reinforcing a possible origin from the Moon's upper mantle.

Finally, this study serves as a test to assess the effectiveness and applicability of these non-destructive techniques for future in situ analyses during human and robotic lunar exploration. The ability to analyze extraterrestrial materials without altering or consuming the sample is of paramount importance – particularly when dealing with rare specimens such as lunar meteorites or limited material returned from the Moon.

References:

[1] Korotev R. L. (2005) *Chem. Erde*, 65, 297–346.
[2] Joy K. H. and Arai T. (2013) *Astron. Geophys.*, 54, 4.28–4.32.
[3] Joy K. H. et al. (2016) *Earth Moon Planets*, 118, 133–158.
[4] Warren P. H. (2005) *Meteorit. Planet. Sci.*, 40, 477–506.
[5] The Meteoritical Bulletin, No. 106. https://www.lpi.usra.edu/meteor/docs/mb106.pdf
[6] Treiman A. H. and Semprich J. (2023) *Am. Mineral.*, 108, 2182–2192.

Acknowledgements: ASI/INAF Agreement 2023-3-HH.

EVIDENCE FOR A NEW CR-LIKE CARBONACEOUS (CX) GROUPLET

Cuppone T.[1*], Carli C.[2], Casalini M.[1], Greenwood C.R.[3], Pratesi G.[1,2] 1 Dipartimento di Scienze della Terra, Università degli Studi di Firenze, Firenze, Italy 2 Istituto di Astrofisica e Planetologia Spaziali – INAF, Roma, Italy 3 School of Physical Sciences, The Open University, Milton Keynes, MK7 6AA, UK

Introduction: Thanks to the results in a companion study of geochemical composition and $\Delta^{17}O$-$\varepsilon^{54}Cr$ isotopic systematics, the brachinite NWA 13489 has been recently suggested to be an ungrouped primitive achondrite with carbonaceous affinity [1]. Its petro-mineralogic-geochemical similarities with other ungrouped achondrites, namely NWA 10503 and NWA 10859, prompted us to investigate other meteorites which could be related to, like the C3-ungrouped NWA 11961 and another brachinite, NWA 12573, which displays anomalous petrographic and mineralogic features (higher olivine FeO/MnO compared to other brachinites), making all of them possible candidates of a new carbonaceous chondrite group named "CX" [2]. Here, we present results on the mineral chemistry of these meteorites, that strongly suggests a common origin for NWA 10503-10859-11961-13489, reinforcing the hypothesis of a new CR-like carbonaceous grouplet existence. On the other hand, NWA 12573 is not a brachinite, being instead a possible new Tafassites member [3].

Samples and methods: The specimens used for this work consist of a 5.53 g endcut for NWA 10503, two small fragments 1.1 and 0.9 g (kindly donated by Ben Hoefnagels) and a polished thin section for NWA 10859 (loaned by University of Washington, Washington, USA), a 3.9 g full slice for NWA 11961 (from the Institute for Space Astrophysics and Planetology of the National Institute of Astrophysics, IAPS/INAF, Italy) and a 0.65 g slice for NWA 12573 (kindly donated by Dr. Li Shijie of Institute of Geochemistry Chinese Academy of Sciences, Guizhou, China). Samples have been object of petro-mineralogic analyses (optical and scanning electron microscopy, SEM) and microanalyses (electron microprobe, EMPA). A small aliquot (200 mg) for each sample was analyzed for bulk geochemistry (Inductively Coupled Plasma - Mass Spectrometry, ICP-MS), oxygen isotopes (Isotope-Ratio Mass Spectrometry - IR-MS) and chromium isotopes (and Thermal Ionization Mass Spectrometry - TIMS).

Results: NWA 11961 shows a disequilibrated chondritic texture (chondrules mean size 1110±680 μm, N=77) with a chondrule/matrix ratios of ~0.4 and CAI ~0.14 vol vol%, similar to CR chondrites [4]. NWA 10503, NWA 10859 and NWA 12573 show petrographic (i.e., recrystallized granoblastic textures) and mineralogic features nearly identical to those of NWA 13489. In detail, 10503-10859-13489 show mean $Fa_{31.7\pm0.3}/Fa_{30.8\pm0.2}/Fa_{31.1\pm0.6}$ (FeO/MnO = 82.9±4.0/83.5±3.4/82.9±3.8, respectively, Fig. 1), while NWA 12573 has slightly higher Fa content (mean $Fa_{35.0\pm0.5}$, FeO/MnO = 87.2±3.9). In 10503-10859-13489 the only pyroxene is clinopyroxene, while in NWA 12573 orthopyroxene is the main pyroxene (Cr_2O_3-Al_2O_3-MnO compositions different from brachinites) with subordinate clinopyroxene.

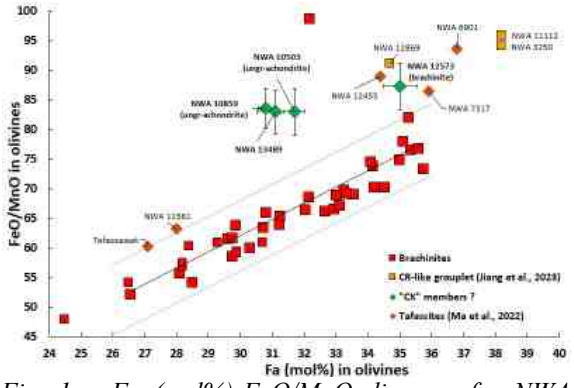


Fig. 1 – Fa (mol%)-FeO/MnO diagram for NWA 10503, NWA 10859 and NWA 12573 olivines, compared with NWA 13489, brachinites and Tafassites from literature (diagram from [1] after modifications).

Plagioclases describe a trend line with 10503-10859-12573-13489 in An(mol)-K(a.p.f.u) space, parallel to and well defined from the brachinite one [1], although NWA 12573 has a closer affinity to Tafassites.

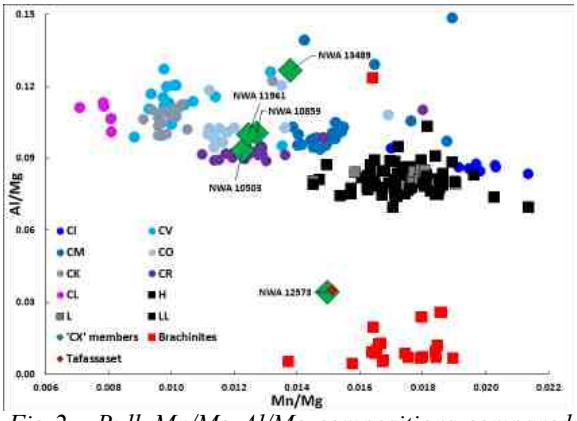


Fig 2 – Bulk Mn/Mg-Al/Mg compositions compared with NWA 13489, CC-OC groups, brachinites and Tafassites from literature (diagram from [1] after modifications).

Similarly, 10503-10859-11961 bulk major element compositions are similar to that of NWA 13489 and compatible with a CR-like source, while NWA

12573 is intermediate to carbonaceous groups and brachinites (Fig. 2). Apparently, 10503-10859-11961-13489 follow the well known CC volatility trend, with volatile contents as low as CL level (CI>CM>CO≥CV≥CK>CR>CL [5]). However Ga content is higher than expected following the CC depletion trend and Zn in NWA 11961 is at the same concentration compared to the other (and most) metamorphosed members (10503-10859-13489). The trace element composition of NWA 10503-10859-11961 presents a slightly suprachondritic REE pattern and evident positive Zr_{CI} and Hf_{CI} anomaly (i.e., 2.2-2.7xCI) and negative Nb_{CI} anomaly (i.e., Zr/Nb_{CI} 4.9-5.1xCI).

Discussions: The high Zr_{CI} contents (for NWA 10503-13489, NWA 10859-11961 not available yet) exclude any relationship with known carbonaceous meteorite groups [5]. Since the refractory and immobile nature of Zr-Hf-Nb (not affected by thermal metamorphism or terrestrial weathering), the anomalies could be related to ultra-refractory material contribute to the material which 'CX' PB accreted from (and up-to-now never described in other CCs). If NWA 10859-11961 Zr_{CI} - Zr/Nb_{CI} values will confirm the NWA 10503-13489 anomalies, it will be possible to use Zr and Nb as geochemical marker for the 'CX' grouplet and future new members identification.

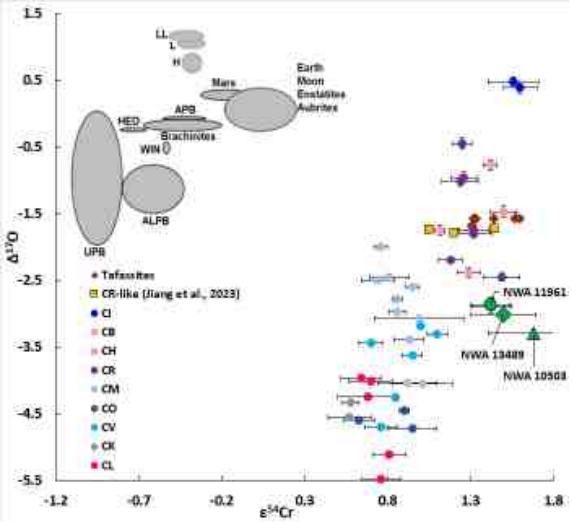


Fig 3 – The $\varepsilon^{54}Cr$-$\Delta^{17}O$ compositions of NWA 10503-11961-13489 compared to other meteorite groups (diagram from [6] after modifications).

Finally, even chromium isotopic composition for NWA 10503-11961 agrees with that of NWA 13489 (NWA 10859-12573 under analyses), confirm the CR-like nature of the grouplet (Fig. 3).

Results: Analyses on 4 previously unrelated meteorites, two ungrouped achondrites (NWA 10503-10859), one C6/7-ungr formerly a brachinite (NWA 13489) and one C3-ungr (NWA 11961) show common mineralogical, geochemical and isotopic features, allowing to propose the membership to a new CR-like grouplet, referred to in literature as 'CX'. Mineral-chemistry, geochemical and O-Cr isotopic data allow to distinguish 'CX' from other CC groups, whose members probably belonged to a layered parental body, with a chondritic crust (NWA 11961) covering a highly metamorphosed inner portion (NWA 10503-10859-13489). Another brachinite (NWA 12573) has been misclassified, revealing a CR-like composition possible related to Tafassites.

Future analysess: LA-ICP-MS (Laser Ablation Inductively Coupled Plasma - Mass Spectrometry) will be performed on two samples (the C3-ungr NWA 11961 and NWA 10859) for in-situ trace elements compositions, in order to understand which mineral phase contributes to the positive zirconium anomaly, to better constraint the source material which 'CX' accreted from. Moreover, we will characterize the VNIR reflectance properties to discuss the variation with respect to the other charbonaceaous chondrite groups.

References: [1] Cuppone et al. (2025) *Meteoritics & Planet. Sci. 60,* 1861-1876. [2] Irving A. J. et al. (2019) *LPSC L*, Abstract #2542. [3] Ma et al. (2022), *Geochem. Pers. Lett. 23*, 33-37. [4] Kallemeyn et al. (1994), *Geochim. et Cosmo. Acta 58*, 2873-2888. [5] Braukmuller et al. (2018) *Geochim. et Cosmo. Acta 239*, 17-48. [6] Zhu et al. (2021) *Geochim. et Cosmo. Acta 301*, 158-186.

Aknowledgements: This study was carried out within the Space It Up project funded by the Italian Space Agency, ASI, and the Ministry of University and Research, MUR, under contract n. 2024-5-E.0 - CUP n. I53D24000060005.

A NEW MICROMETEORITE FROM MOUNT GARIGLIONE UNVEILS NEW INSIGHTS ABOUT THE ORIGIN OF EXTRATERRESTRIAL (Al,Cu)-ALLOYS.

Agrosì G.[1], Mele D.[1], Johan Villeneuve[2], Catelani T.[3] & Bindi L.[3]
[1]Dipartimento di Scienze della Terra e Geoambientali, Università di Bari, [2]Centre de Recherches Pétrographiques et Géochimiques – CNRS, Nancy, [3]Dipartimento di Scienze della Terra, Università di Firenze.

Introduction: In recent years, the discovery of meteorites and micrometeorites containing unusual Al- and Cu-alloys dispersed in a chondritic matrix has aroused great interest in the scientific community, which is questioning the origin of this strange combination and the possible parent bodies. The exceptionality of these findings is due to the contrasting geochemical behavior of their components. Actually, copper is a moderately volatile chalcophile element, while aluminium is a highly refractory lithophile element. Up to now, only few cases of (Al,Cu)-bearing meteorites are known. They show a broadly chondritic composition and the (Al,Cu)-alloys show different stochiometric ratios, from pure Al to pure Cu, with the prevalence of khatyrkite ($CuAl_2$), cupalite and stolperite (CuAl). The first discovery of this unusual assemblage occurred in the Khatyrka meteorite [1].

Khatyrka is very famous for the first and, up to now, unique discovering of natural quasicrystals [2], [3], [4], [5]. Some years later a second finding of (Al,Cu)-metallic alloys arose in a cosmic microspherule discovered in the Nubian Desert of Sudan [6], [7]. Recently, a scoriaceous microspherule (FB-A1) was found on top of Mt. Gariglione (Catanzaro, Italy) [8], another un-melted coarse-grained micrometeorite was discovered in Congo (NG-1) [9] and, at last, two new scoriaceous microspherules with chondritic affinity (NMM/L1 and NMM/L2) were found among the micrometeorites collected from urban rooftops in Norway, belonging to Project Stardust collection [10].

The increasing discoveries of new (Al,Cu)-bearing micrometeorites suggest that these exotic alloys may be more widespread than previously thought and open the question about the origin and nature of source of this unusual metallic alloy.

In this work, we report the discovery of a second micrometeorite, named FB-A2, containing (Al,Cu)-alloys at Mt. Gariglione in southern Italy. This new micrometeorite, although having a chondritic nature, appears significantly different from FB-A1 and adds new insights about the origin of this rare material.

Methods: Non-destructive analyses by SEM and a μ-CT were carried out at the University of Bari (Italy). Then, the sample was embedded in epoxy resin and polished for further SEM and EPMA analyses performed at the University of Florence (Italy). Finally, oxygen isotope measurements were obtained by SIMS at CRPG-CNRS (Nancy, France).

Results: A first optical examination of FB-A2 reveals a different shape than FB-A1 [8]. Actually, FB-A1 is a scoriaceous, elongated, subspherical micrometeorite, whereas FB-A2 exhibits an irregular shape. Both the samples show remarkable portions with an unusual metallic luster. If FB-A1 showed metallic droplets extruded on the surface, FB-A2 shows one corner made of a material with "silvery" metallic luster (Fig. 1).

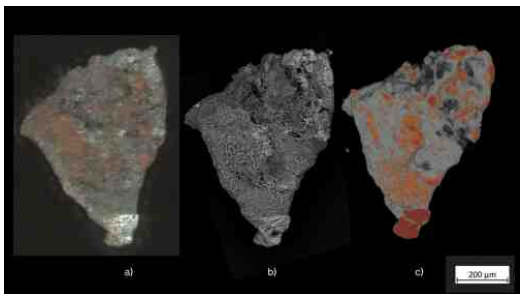


Figure 1. FB-A2 a) optical image of micrometeorite. Note the corner with silvery luster; b) SEM-BSE image; c) μ-CT 3D reconstruction. Note the red and orange particles corresponding to metallic alloys.

Preliminary SEM-EDS analyses, carried out on the unpolished sample, confirm a composition similar to FB-A1, consisting of Fe-Ni metals with variable composition, Fe-Ni sulfides and oxides of the spinel group disseminated into a silicate matrix. EDS analyses were focused mainly on the metal at the corner of the sample. In Figure 2 the BSE image (Fig. 2a) and the corresponding chemical maps (Fig. 2b) reveal that the portion with metallic luster corresponds to (Al,Cu)-alloys with variable composition.

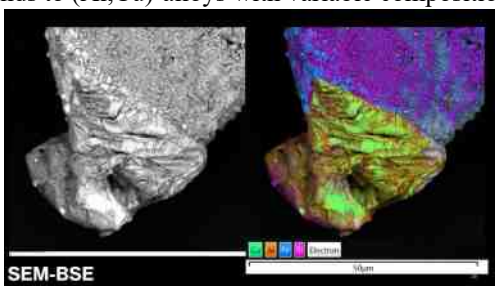


Figure 2. FB-A2 a) SEM-BSE image of the corner with silvery luster; b) SEM-EDS multilayers image.

The bulk distribution of phases and voids obtained by μ-CT indicates a higher porosity of the corner with (Al,Cu)-alloys. The porosity value is very similar to that calculated for FB-A1, suggest-

ing a relationships between the degassing processes and the impact between the silicatic matrix and the (Al,Cu)-bearing parent body.

The metal at the corner exhibits worm-like intergrowths of nearly pure Al immersed in a matrix made of khatyrkite ($CuAl_2$). The contact between the silicatic matrix and the metallic corner is characterized by the presence of micrometric sub-spherical (Fe-Ni)-alloys with variable composition. The inner part of these droplets exhibits voids, suggesting melting and degassing processes of precursor grains, likely sulfides.

Chemical analyses on the polished surface reveal that the matrix consists of a silicate glass with olivine composition (Fo_{43}), relict olivine crystals (Fo_{89}), clinoenstatite and Ca-rich pyroxenes ($En_{67}Wo_{33}$).

Moreover, the fayalitic matrix fills and replaces all discontinuities related to partial melting resorption. Small crystals of phosphates, oxides and sulphides, finely aggregated, were also found on the boundary portions of the sample.

To verify the origin of FB-A2, secondary ion mass spectrometry $^{18}O/^{16}O$ and $^{17}O/^{16}O$ measurements were taken on the relict olivine and pyroxene crystals. The data indicate an isotopic composition unlike that of any terrestrial minerals. As for all the (Al,Cu)-bearing micrometeorites previously found, the oxygen isotope composition of FB-A2 lies along the line corresponding to anhydrous minerals of carbonaceous chondrites (the CCAM).

Conclusions

Comparisons between the data acquired on FB-A2 and FB-A1 reveal that both micrometeorites show evidence of impact between two different parent bodies: a carbonaceous chondrite and a (Al,Cu)-bearing material, confirming what observed on the previously studied micrometeorites. The observed differences between FB-A2 and FB-A1 can be merely explained by different melting degrees. Furthermore, the presence of the exotic (Al,Cu)-alloys, which have so far only been found in carbonaceous chondrites and not in other types of extraterrestrial materials, suggests that the collision involving these chondritic parent bodies and the bodies containing these alloys primarily took place in the region of the Solar System associated with the CCAM.

References:

[1] MacPherson G.J., et al., (2013) *Meteoritics & Planetary Science*, 48(8), 1499-514.
[2] Bindi L., et al., (2009) *Science* 324, 1306–1309.
[3] Bindi L., et al., (2011) *Am. Mineral.* 96, 928–931
[4] Bindi L., et al., (2015) *Am. Mineral.*100, 2340–2343
[5] Bindi L., et al., (2016) *Sci. Rep.* 6, 38117
[6] Suttle M.D., et al. (2019) *Sci. Rep.*, 9, 2426.
[7] Ma C. et al., (2023), *Met. Planet. Sci.*, 58, 1642-1653.
[8] Agrosì G. et al., (2025) *Comm. Earth Environ*. 6, 271.
[9] Genge M., et al., (2025) *Earth Plan. Sci. Lett.*, 656, 119276
[10] Bindi L., et al., (2025) *Met. Plan. Sci.*, 60, 1609-1620.

Additional Information: If you have any questions or need additional information regarding the preparation of your abstract, send an e-mail message to **segreteria@scienzeplanetarie.it.**

REVEALING IMPACT SIGNATURES IN UREILITE DIAMONDS AND GRAPHITE THROUGH NANOSCALE ANALYSIS. A. Barbaro[1*], F. Nestola[1,2], S. A. Singerling[3], J. Nava[1], F. E. Brenker[3].[1]Department of Geosciences, University of Padova, Italy (*anna.barbaro@unipd.it), [2] Museum of Nature and Humankind, University of Padova, Italy, [3]Schwiete Cosmochemistry Laboratory, Department of Geoscience, Goethe University, Frankfurt, Germany

Introduction: Ureilites are achondritic meteorites mainly composed of olivine and pigeonite, with minor carbon phases such as graphite and diamond, as well as Fe-Ni alloys. They are believed to have originated from a common parent body known as the Ureilitic Parent Body (UPB) [1], which was later disrupted by catastrophic impacts. Based on mineralogical and petrological analyses, the UPB is estimated to have reached a diameter of 180–200 km prior to fragmentation. Ureilites display a wide range of shock stages (from US1 to US7 [2]), making them excellent samples for investigating the effects of shock metamorphism on extraterrestrial crystalline carbon phases.

Research aim: The formation of diamonds in ureilites remains a subject of ongoing debate. Current evidence suggests a shock-induced origin [3, 4]. This study investigates the relationship between shock stage and carbon nanostructure development, testing the hypothesis that diamond formation in ureilites results from high-pressure dynamic shock events.

Samples and Methods: Five ureilitic meteorites collected from Frontier Mountain, Antarctica (FRO 95028 [S2], FRO 01089 [S3], FRO 97013 [S3/S4], FRO 01088 [S5], FRO 01012 [S6]) were analyzed. Carbon aggregates were manually extracted from shock-affected regions. Focused ion beam (FIB) lamellae were produced at the Department of Geosciences, University of Padova, using a TESCAN-SOLARIS SEM/FIB system. Nanoscale structural features were examined via transmission electron microscopy (TEM) using a Talos F200-X G2 S/TEM operating at 200 kV at the Schwiete Cosmochemistry Laboratory, Goethe University, Frankfurt.

Results and Discussion: TEM imaging revealed distinct shock-related nanostructures in diamond, including stacking faults, diaphite lamellae, and nano-twinning [5]. Progressive deformation features were correlated with increasing shock stages, consistent with the transformation of graphite into diamond under transient high pressures and temperatures. These nanoscale observations are in agreement with previous micro-X Ray Diffraction and micro-Raman spectroscopy results [4], collectively providing strong support for a shock-derived origin of ureilitic diamonds and transformation of graphite. The observed defect sequences align with impact-driven metamorphic processes, clarifying the role of impacts in carbon phase evolution within ureilites.

Conclusions: The systematic relationship between shock intensity and diamond nanostructure strongly supports impact-related processes as the primary mechanism for diamond formation in ureilites. These results contribute to resolving the long-standing debate on the genesis of carbon phases in ureilitic meteorites [5].

Acknoledgments: This work is supported by BARB_PNRR_RICERCA25_01 YR PNRR project to A. Barbaro (ID: SOE_20240000020), the Alexander Von Humboldt Foundation, the Dr. Rolf M. Schwiete Stiftung and, the German Research Foundation (DFG grants n. INST 161/1021-1 and BR 2015/39-1). The “Museo Nazionale dell’Antartide, Siena, Italy”, made the samples available.

References:

[1] Goodrich C. A. (1992) Meteorit. Planet. Sci., 27, 327–352. [2] Stöffler D. et al. (2018) Meteorit. Planet. Sci., 53, 5–49. [3] Nestola F. et al. (2020) Proc. Natl. Acad. Sci. USA, 117, 4549–4554. [4] Barbaro A. et al. (2023) Earth Planet. Sci. Lett., 625, 118201. [5] Barbaro A. et al. (2025) Carbon, 224, 120583.

COATED IMPACT MELT BOMBS FROM THE WABAR CRATERS (SAUDI ARABIA) . L. Folco[1,2], and M. Masotta[1,2], [1]Dipartimento di Scienze della Terra, Università di Pisa, [2]CISUP, Università di Pisa (luigi.folco@unipi.it; matteo.masotta@unipi.it).

Introduction: We studied the structural, petrographic and geochemical characterists of impact melt bombs from the Wabar crater field, Saudi Arabia (**Figure 1**). The study provides insights into the poorly known physical interaction between impactor and target impact melts during the formation of impact craters in rocky planetary surfaces.



Figure 1. *Coated impact melt bombs from Wabar. The specimen at the TLHC is broken and reveals the thickness of the dark glass coating and the pumiceous texture of the white glass core. The specimen at the BLHC is oriented with a rounded front face (right) and a rough grossly filamentous rear surface.*

The Wabar crater field: The Wabar crater field is located in the Rub Al-Khali sand desert (Empty Quarter) of the southern Arabaian peninsula at 21°30.2′N, 50°28.4′E [1], and it is known to the scientific community since 1933 [2]. It consists of three simple (bowl-shape) craters with diameters of 64 m (named "crater A"), 116 m (named "rater B") and 11 m. They are mostly eroded and partly buried in sand dunes. The craters were formed by the impact of a trail of pieces of an iron meteorite (IIIAB group; [3]) onto a sand dune sheet. The main masses recovered weigh 2040 and 210 kg. Patches of ejecta, consisting of scattered angular fragments of whitish shocked-lithified target material (sand), and impact melt lapilli and bombs up to few tens of cm across, are occasinaly exposed in between sand dunes around the craters [1]. Oxidized centimetric fragments of the iron meteorite impactor are intermixed with the ejecta deposit. Based on thermoluminescence dating methods, the impact occurred 290 ± 38 years before present [4].

Samples and methods: We studied four impact melt bombs from the Wabar craters (**Figure 1**) collected in situ by Romano Serra (Osservatorio Astronomico del Cielo e della Terra, San Giovanni in Persiceto, Bologna, Italia) in February 2025 and donated to us for research. The four specimens were first investigated using a ZEISS Stemi 2000 steremicroscope equipped with an Axicam 105 camera to obtain information about overall lithology, structure and morphology. One specimen was then sectioned for petrographic investigation under a ZEISS Crossbeam 550 microanalytical field-emission scanning electron microscope, and for bulk geochemical analysis using a laser ablation inductively coupled plasma mass-spectrometry system consisiting of an Elemental Scientific NWR-193 (Ar-F) excimer laser equipped with a TwoVol2 two-volume cell coupled with a PerkinElmer NexION 2000 ICP-MS. All instrumentation was made available through Centro per la Integrazione della Strumentazione della Università di Pisa (CISUP).

Results and discussion: The four impact melt bombs studied here are up to 15 cm across. They consist of a mm-thick coat of dark glass enveloping a core dominated by pumiceous white glass (**Figure 1**). The dark glass coating often shows oriented structures with a smoothish convex front side and a rough and grossly filiamentous rear side.

The dark glass is a siliceous vesicular glass rich in Fe (~8 wt%), Ni (~4000 μg/g) and other siderophile trace elements. The white glass consists of a frothy silica-rich (~93 wt%) core with embedded and partly resorbed shocked lithic clasts of target material. The white glass is interpreted as the result of impact melting of the target material, the dark glass of the mixing between impactor plus target melts under oxidizing conditions at the impactor-target contact stage [1, 5].

We interpret the dual impact melt assemblage of the Wabar impact melt bombs in the context of the the contact and excavation stages in the formation of simple craters during hypervelocity impacts. During the contact stage, the dark glass forms at the impactor-target interface, the taget material just below also melts to form the white glass. During the subsequent excavation stage, there is a great deal of mass

movement of melted materials initially down into the expanding transient cavity and then laterally up and over the transient cavity walls and crater rim. It is during the end of the contact stage and the beginning of the excavation stage that the dark melt impregnates and entrains masses of the more viscous shock-fractured white glass. Upon the subsequent excavation flow, the melt bombs form through fragmentation along the dark glass network, since the dark glass is much less viscous than the almost pure silica white glass. During subsequent ballistic ejection, the dark glass coating is still hot and plastic, and oriented structures are formed due to aerodynamic drag. In summary, the coated impact melt bombs from Wabar tell us the story not just of the type of impact melts produced at the impactor-target interface, but also of their displacement and their physical interaction during the contact and excavation stages in a simple crater-forming event.

Similar, but smaller (mm-sized) dark glass coatings of white glass masses, namely lapilli, have been reported from the Wabar crater field [6] and Kamil Crater, Egypt [7], but their origin was not discussed. Nevertheless, such reports, coupled with the present study, document that this dual melt assemblage in impact melts bombs and lapilli is actually a common feature in the inventory of impact products of simple craters. We propose to term this new kind of ejecta with the term “coated impact melt bombs or lapilli” according to size, highlighting their significance in understanding the processes and products of impact cratering on solid bodies of the solar system.

Acknowledgments: Romano Serra (Osservatorio Astronomico del Cielo e della Terra, San Giovanni in Persiceto, Bologna, Italia) is kindly acknowledged for providing the samples from Wabar studied in this work. Funding: ASI-MUR SpaceitUP! ID# 2024-5-E.0 – CUP n. I53D24000060005.

References: [1] Gnoss et al. (2013) *Meteorit. Planet. Sci., 48*, 2000–2014. [2] Phylby et al. (1993) *Geographical J.,* 81, 1–21. [3] Buchwald V. F. (1975) Handbook of iron meteorites. Berkeley: University of California Press. 1418 p. [4] Prescot et al. (2004) *J. Geophys. Res., 109,* 1–8. [5] Hamann et al. (2018) *Meteorit. Planet. Sci., 53,* 1594-1632. [6] Newsom and Boslough (2008) *LPSC XXXIX*, abstract no. 1460. [7] Folco et al. (2015) *Meteorit. Planet. Sci.* 50, 382–400.

XXI Congresso Nazionale di Scienze Planetarie

Sessione Piccoli Corpi
Asteroidi

DYNAMICS AND ORIGIN OF THE NEA PAIR 2021 PH27 AND 2025 GN1. A. Carbognani[1], M. Fenucci[2, 3], T. Santana-Ros[4], M. Micheli[2] [1]INAF - Osservatorio di Astrofisica e Scienza dello Spazio, Via Gobetti 93/3, 40129 Bologna, Italy [2]ESA ESRIN / PDO / NEO Coordination Centre, Largo Galileo Galilei, 1, 00044 Frascati (RM), Italy [3]Deimos Italia, Via Giuseppe Verdi, 6, 28060 San Pietro Mosezzo (NO), Italy [4]Departamento de Física, Ingeniería de Sistemas y Teoría de la Señal, Universidad de Alicante, e Institut de Ciències del Cosmos (ICCUB), Universitat de Barcelona (IEEC-UB), Spagna.

Introduction: In a previous paper, we explored the possibility that the near-Earth asteroid (NEA) 2021 PH27 is also an active asteroid like (3200) Phaethon, the progenitor of the Geminid meteor shower [1]. However, the minimum orbit intersection distance (MOID) of 2021 PH27 with respect to Earth is large, about 0.22 au, while in the case of Phaethon, it is only 0.0188 au. Instead, Venus' MOID is low with a value of about 0.0146 au, and 2021 PH27 could be the Phaethon of Venus. Unfortunately, the bright fireballs in Venus' atmosphere are very difficult to observe, and this hypothesis is not confirmed.

The recent discovery of the NEA 2025 GN1 in a heliocentric orbit close to that of 2021 PH27 reopened the question [2]. These two asteroids have a similar orbit, so it is possible that there could be other smaller meteoroids on the same orbit. Hence, there is a need to understand the dynamical origin of this pair of asteroids.

Asteroid pairs consist of two asteroids with very similar orbital elements which are not gravitationally bound together: they are found between the main-belt, Hungaria, and NEAs populations. The possible formation mechanisms of asteroid pairs are (1) catastrophic collision, (2) rotational fission due to the Yarkovsky-O'Keefe-Radzievski-Paddack (YORP) effect or (3) dissociation of binary systems. Based on observational data, pairs of asteroids are likely former binary systems in which the two components were separated by the YORP effect [3].

Physical characteristic of 2021 PH27 and 2025 GN1: The osculating orbital elements of 2021 PH27 and 2025 GN1 are very similar and they also share not only the orbit but have the same colour indices, and the two NEAs are classified as X-type asteroids [2]. Assuming the absolute magnitude given by the MPC with H_V = 17.67 for 2021 PH27 and H_V = 20.06 for 2025 GN1, we get a diameter of 1.2 ± 0.2 km and 0.4 ± 0.2 km. About the rotation period of 2021 PH27, the data suggests a period of about 3.49 h.

Past dynamical evolution: The past dynamical evolution of the pair 2021 PH27 and 2025 GN1 was investigated by backwards numerical simulations. Numerical integrations were performed with the mercury software package, by using a symplectic hybrid integrator able to solve close approaches with planets. The dynamical model included the gravitational attraction of the Sun and of all the planets from Mercury to Neptune. Due to the low perihelion distance of about 0.13 au, which the two asteroids currently achieve, the effects from general relativity are also modeled.

For each asteroid, we propagated 1000 orbital clones, which were sampled from the covariance matrix of the orbit by assuming a Gaussian statistics. The orbital elements do not undergo large changes until −11 kyr and −12 kyr for 2025 GN1 and 2021 PH27, respectively. At the two mentioned epochs, the uncertainties in the orbital elements grow large due to the effect of close encounters with Venus.

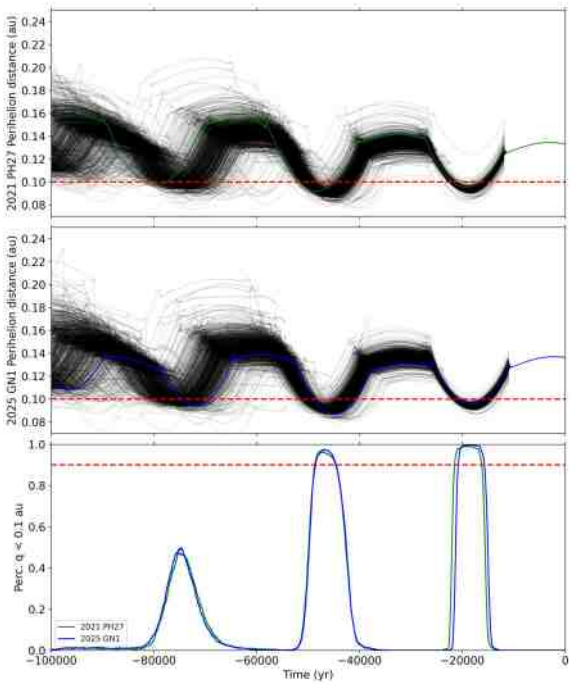


Fig. 1 - The perihelion distance of 2021 PH27 (top) and of 2025 GN1 (middle). The bottom panel is the probability that the perihelion distance is smaller than 0.1 au.

Many close encounters between clone pairs are found before −10 kyr at a relative velocity of about 1 km/s; however, they are all at distances larger than 150 000 km. After 10 kyr of backwards evolution, close encounters still appear even at smaller distances; however, they are randomized as a result of close encounters with Venus. Despite the complex history of Venus' close approaches, there are two clear instances at which q < 0.1 au with a probability larger than 90%, with some instances reaching peaks > 99%. The first one happened between about −17 and

−21 kyr, while the second one happened between −45 and −48 kyr.

Discussions: As we have seen in the previous sections, 2021 PH27 and 2025 GN1 have very similar Keplerian elements for at least 40-100 kyr in the past and are of identical spectral type, and these support a common origin. There are at least four possible disaggregation mechanisms that could affect an asteroid with a low perihelion and subject to close passes with the planet Venus:

1.Venus flybys below the Roche limit, resulting in tidal fragmentation.

2. Tidal fragmentation driven by the Sun due to low perihelion value.

3. Fragmentation following the increase in surface temperature due to the low perihelion.

4. The YORP effect, which increases the asteroid's rotation frequency up to the spin barrier value, forms a binary system which subsequently separates into two components.

The mareal fragmentation due to low flyby with Venus and the Sun can be excluded, because the minimum distance is not below 0.001 au and 0.08 au respectively and this exclude the points 1 and 2.

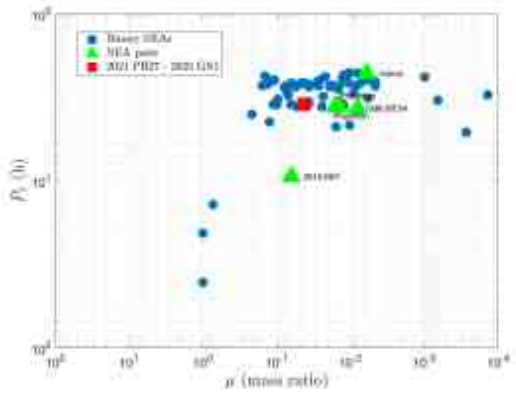


Fig. 2 - Plot of the primary rotation periods as a function of the mass ratio for the best-known 69 NEA binary system.

About point 3, the mechanism that can destroy an asteroid with a perihelion too close to the Sun, but above the Roche limit, is not clear yet, but it appears to be related to the temperature its surface can reach, and there can be several mechanisms at work simultaneously [4]. It could be a consequence of thermal fracturing of the surface: fragments are swept away by radiation pressure, and the asteroid looses mass during a prolonged low perihelium interval. Or it could depend on the anisotropic emission of thermal photons, i.e. the YORP effect, or the anisotropic emission of gas molecules that sublimate and increase the rotation frequency until they break up, mimicking the YORP effect. Alternatively, asteroids can contain volatile materials that, during sublimation, exert sufficient force to fragment the body. Given that 2021 PH27 and 2025 GN1 had perihelion between 0.1 and 0.08 au, which occurred at −17/−21 kyr and −45/−48 kyr, it is possible that the parent asteroid was broken apart because it was located within a region dangerous for the integrity of asteroids.

The last hypothesis is that the pair 2021 PH27-2025 GN1 originated from the rotational disintegration of a former binary asteroid by the YORP effect. The red square representing the pair (see Fig. 2) overlaps well with the general trend of the binary NEAs and the other NEA pairs; this supports the hypothesis that 2021 PH27 was originally a binary system and that the pair was born by rotational dissociation. The doubling of the actual rotation period is possible in about 150 ± 50 kyr, so it is reasonable to think that the YORP effect was actually able to increase the rotation frequency enough to fragment the parent asteroid during the parent's dynamical lifetime.

Conclusions: We investigated the origin of the NEA pair 2021 PH27-2025 GN1. Its dynamical evolution in the past has been reconstructed up to −100 kyr, finding a similar trend for the orbital elements. In the last 100 kyr, there have been seven flybys with Venus, but at minimum distances so as not to have tidal disruption. Even the perihelion values are not low enough to enter in the Roche limit of the Sun. Instead, both asteroids have undergone a similar orbital evolution, and the perihelion has dropped in the range 0.1-0.08 au, which occurred at −17/−21 kyr and −45/−48 kyr. This leads to enhanced thermal fragmentation, gas and thermal photon emission from the surface (YORP effect). The rotation period of the primary and the mass ratio it is indistinguishable from known binary systems among NEAs. This fact suggests an origin from rotational disintegration due to the YORP effect or gas emission of a rubble pile during low perihelion phases. This disintegration formed an unstable binary system with a low mass secondary that, separating, formed the pair of asteroids that we see today. Due to close encounters with Venus that make their orbits chaotic, it has not been possible to establish an age of separation.

The low perihelion value makes it plausible that meteoroids could be emitted from the surface, as happens at (3200) Phaethon, so the existence of a meteoroid stream associated with the pair is very likely. If it exists, this meteoroid stream causes, due to the small value of the MOID, a meteor shower in the atmosphere of Venus.

References: [1] Carbognani, A. et al. (2022) *MNRAS* 511, L40–L44. [2] Sheppard, S.S et al. (2025) *ApJ* 987, L18. [3] Pravec P. et al. (2010) *Nature* 466, 1085–1088. [4] Granvik, M. et al. (2016) *Nature,* 530, 303–306.

NEOPOPS – THE NEO PHYSICAL OBSERVATIONS AND PROPERTIES SIMULATION

E. Dotto[1], E. Mazzotta Epifani[1], S. Bagnulo[2], M.A. Barucci[3], M. Birlan[4,5], J. Bourdelle de Micas[1], J.-L. Cano[6], M. Devogèle[7], A. Farina[8], P. Fatka[9], F. Ferri[8], M. Fulchignoni[3], S. Ieva[1], F. La Forgia[8], M. Lazzarin[8], A. Mura[8], D. Perna[1], P. Pravec[9], and M. Siciliano[10]
[1]INAF – Osservatorio Astronomico di Roma, via Frascati 33, Monte Porzio Catone (Roma), Italy, jules.bourdelledemicas@inaf.it, [2]Armagh Observatory & Planetarium, College Hill, BT61 9DB, Armagh, Northern Ireland, UK, [3]LIRA, Observatoire de Paris, 5 place Jules Janssen, 92195, Meudon, France, [4]Astronomical Institute of the Romanian Academy, 5 - Cutitul de Argint, Bucharest, Roumaine, [5]LTE, Paris Observatory, 77 av Denfert-Rochereau, 75014 Paris Cedex, France, [6]Planetary Defense Office, ESA ESOC, Robert-Bosh-Strasse 5, 64293 Darmstadt, Germany, [7]ESA NEO Coordination Centre, European Space Agency, Largo Galileo Galilei 1, Frascati, 00044, Roma, Italy, [8]University of Padova, Department of Physics and Astronomy "Galileo Galilei", Vicolo dell'Osservatorio 3, 35122, Padova, Italy, [9]Astronomical Institute of the Academy of Sciences of the Czech Republic, Fričova 298, Ondřejov, CZ-25165, Czech Republic, [10]Resolvo S.r.l, Via di Novoli 91/S 50127, Firenze, Italy

Introduction: NEOPOPS - The NEO Physical Observations and Properties Simulation, is an international project funded by the Horizon Europe Programme of the European Union. Its purpose is to contribute significantly to the physical characterization of the Near-Earth Objects (NEOs) through increasing the networking of the Member States' assets in terms of observations and modelling.

Fostering NEO physical characterization is a major goal of the EC entrusted tasks to ESA on Planetary Defence, building on previous EC initiatives devoted to planetary defence such as the NEOShield, NEOShield-2 and NEOROCKS projects.

The project: Past surveys devoted to NEO discovery and physical characterization have provided the necessary ground to investigate major issues related to NEO impact monitoring and mitigation.

This joint effort has led to discussion on and identification of scientific, technological and operational breakthroughs that need to be achieved urgently. In particular, extensively coordinated scientific research and innovative technical developments are necessary to improve our knowledge of the physical nature of small NEOs and to significantly reduce the risk of unannounced impacts.

The main objective of NEOPOPS is to tackle this scenario providing a radically new approach, aiming:

- to organise follow-up astronomical observations of NEOs efficiently, in order to obtain high-quality data to derive their physical properties, giving priority to timely addressing potentially hazardous objects;
- to dramatically improve statistical analysis, modelling and computer simulations aimed at understanding the physical nature of NEOs, with a focus on small-sized objects, which are of paramount importance for designing effective mitigation measures both in space and on the ground;
- to foster European and international cooperation on NEO physical characterization, providing scenarios and roadmaps with the potential to scale-up at a global level the experience gained during the project;
- to cooperate with ESA to significantly improve public understanding and perception of the asteroid hazard, counteracting the spreading of fake news and unjustified alarms.

The team: The NEOPOPS team is composed by 6 partners of 4 countries (Tab. 1) addressing different observational techniques in order to consolidate and further enhance the NEO physical characterization from the ground and contribute to the execution of rapid response exercises for characterising newly discovered objects, thus facing the challenge posed by the so-called "imminent impactors".

Tab. 1: The NEOPOPS team and responsibilities.

Participant	WP – Leadership	Country
Istituto Nazionale di Astrofisica Prime	WP1 – Project Office WP4 – Spectroscopy WP6 – Rapid Response	Italy
Resolvo Srl	WP1 – Project Office	Italy
Armagh Observatory and Planetarium	WP5 – Polarimetry	UK
University of Padova	WP4 – Small telescopes exploitation	Italy
LIRA-Observatoire de Paris	WP3 – Photometry	France
Astronomical Institute of the Czech Academy of Sciences	WP2 – Lightcurves	Czech Rep.

Acknowledgments: The NEOPOPS observations contract is funded by the Horizon Europe Programme of the European Union and implemented by ESA (agreement No.4000147191/25/D/MRP).

NEOVST: A MINI 4-SDSS-COLORS SURVEY OF NEWLY-DISCOVERED NEAR-EARTH OBJECTS THROUGH THE VLT SURVEY TELESCOPE. P. H. Hasselmann[1], D. Perna[1], E. Dotto[1], J. D. P. Deshapriya[1] , S. Ieva[1], L. Galluccio[1,2], J. Bourdelle de Micas[1], E. Mazzota Epifani[1], V. Petropoulou[3]. [1]INAF-Osservatorio Astronomico di Roma, Rome, Italy. [2]Université Côte d'Azur, Observatoire de la Côte d'Azur, CNRS, Laboratoire Lagrange, France. [3]Agenzia Spaziale Italiana, Rome, Italy.

Introduction: Near-Earth Objects (NEOs) provide a window into the smallest population of asteroids and comets that originated from more distant regions of the Solar System. Most of this objects are product of collisional processes at various stages of the Solar System's evolution, making them important for probing compositions that may have contributed to the delivery of water and organics to Earth and the inner planets.

As NEO discoveries increase—currently at about 3,000 objects per year—the majority are not followed up with physical characterization. These properties provide insights into their internal structure and material strength in the event of atmospheric entry [1,2], as well as their potential as targets for future mining, exploration, and planetary defense missions [3]. Therefore, anticipating an increase in new discoveries with the start of LSST operations, we initiated a year-long, monthly photometric observation campaign of NEOs discovered in the past two years (2022–2023) and visible with the 2.61-m VLT Survey Telescope (VST) at Cerro Paranal, Chile. The main instrument on the VST is OmegaCAM, a multi-filter, 32-CCD camera with a Field of View (FoV) of 1 square degree [4]. This capability enables the tracking of very fast-moving NEOs and also brings important collateral science: due to its wide FoV, many other small bodies can be observed simultaneously. These secondary targets are also identified and analyzed to enhance their characterization and astrometric determinations.

Observations: The observations were carried out from February to September 2023, two nights scheduled every month around full moon. The targets were observed cycling through SDSS *r'i'z'g'r'* filters in exposure times of 10 to 30s depending on the observational conditions. Every target was observed for 1 hour. In total, we acquired 5519 image cubes covering 72 NEAs, and likely 5 to 10 times thiat number of background SSO depending on the pointing region. The magnitude limit is estimated to r'=21.5 for SNR=3 and exposure time of 20s. The cubes are radiometrically calibrated in the Astro-Wise environment through the VST pipeline available by ARES cluster at INAF-Osservatorio di Capodimonte [5]. The final products are single Mosaics of the 32 CCD in absolute Jansky flux and positions in celestial coordinates. We are also provided with a list of sources measured with SExtractor for every Mosaic [6]. See Fig. 1 for an example of final product, and the main target and secondary targets within the FOV.

Methodology: The analysis is mainly carried through procedures developed in Python3 language and the use of Scikit-image, Astropy, Photutils, and Astroquery libraries, organized in four steps:

1. Querying SSOs and Fixed Sources in the Field. We catalog all fixed and moving sources over mag=23 to help identifying the main and secondary targets, and obtaining the photometry of field stars for flux quality check. We also perform a quality check on the field's celestial coordinate alignment and correct any residual miss-offsets. The moving object ephemeris is obtained from OBSPM/IMCEE API service (https://ssp.imcce.fr/webservices/miriade/howto/vision/) and the fixed sources from several catalogs bundled under the Astropy/VO service.

2. Moving Objects Locus Detection. We crop all loci of 0.04°x0.04° from the field that might show potential SSOs. The cropping is centered in the expected target position, but often offset by few millidegrees. Additionally, targets often fall in the gaps between CCDs (0.02° wide), which may reduce the number of detections or photometric quality.

3. Target Tracking, Cube alignment, stacking. After each locus for a given target are cropped, we align them according to Sky-Fixed and SSO-fixed coordinates. After removing fixed sources, we applied Hough Transform [7] to detect linear tracks corresponding to SSO apparent motion. The cube is then centered onto the target, and then a stacked cube product is subsequently generated.

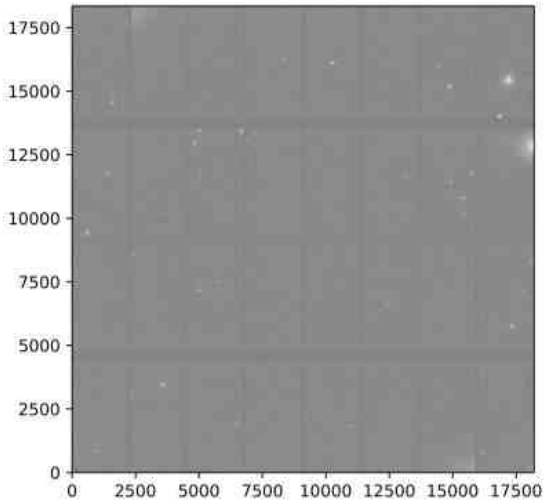
4. Aperture, Lorenz and PSF Photometry. We perform the photometry for the target and field stars using aperture photometry, Lorenz fitting, and 2D PSF analysis. We also check for signs of fast rotation throughout the image sequences. We then compare the field star photometry with SDSS and VST/Atlas sources to cross-check the flux quality [8,9].

Preliminary Results and Future Steps: To this date, data analysis has been completed for the first 3 observing months and for all 107 primary targets and secondary objects under exposure time ≥ 20s (Apparent magnitude distribution in Fig. 2). All data has been flux calibrated.

The asteroids colors cluster in the usual bimodality between feature ("S-like") and featureless ("C-like"), i.e., the presence or not of 1-micron silicate band (***i'-z'***). In Fig. 3, we plotted all primary and secondary targets with at least two available colors,

in which NEAs are highlighted in red. We observe a significant diversity in the spectrophotometry of NEAs even within a small sample. Qualitativaly, we estimate spectra ranging from usual S/C types to A/L, Q and B/F types.

Finally, we inform that in 2024 the NEOVST was approved for a new volley of monthly observations through VST from February to September 2025. We focused on scattered monthly observations of newly discovered NEAs, with exposure times of 30s (*r*'), 40s (*i'*,*g*') 50s (*z*'), and two 1-hour sequences per target. We aim to improve the signal of background stars for better astrometric positioning, and better sampling of phase and rotational curves. Observations have been concluded in September, and the data calibration down to April 2025 has been already carried out.



(a)



(b)

Figure 1: (a) A full mosaic of 32 CCDs for the acquisition of 2023-02-04 UT 05:15:09 for the main target the NEA 2022 YM5. Obtained for SDSS r' filter and radiometrically calibrated. (b) The main target (magenta) and secondary targets (yellow) in the FOV.

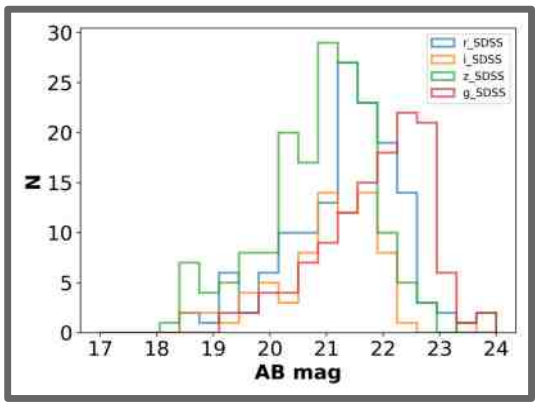


Figure 2: SDSS apparent magnitude distribution of all targets.

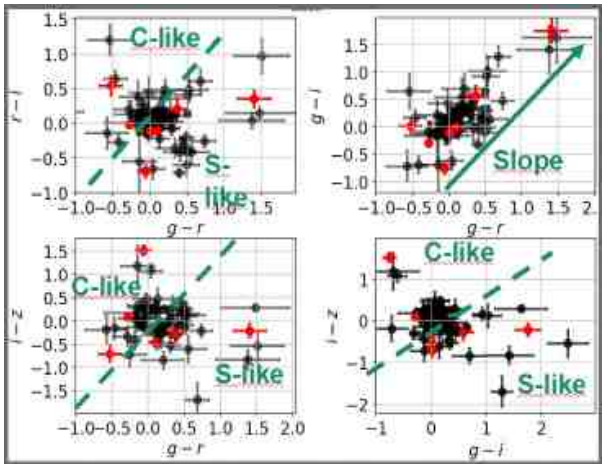


Figure 3: SDSS color mosaic of the asteroids observed in the February+March+April 2023 run (7 NEAs + 15 MBAs). The data is overlay by the approx. loci of "S-like" and "C-like" asteroids. Many objects lack the SDSS z' magnitude due to the weaker band efficiency.

References: [1] Perna,D., Barucci,M.A., & Fulchignoni,M. 2013, A&ARv, 21, 65. [2] Perna,D., Dotto,E., Ieva,S., et al. 2016, AJ, 151, 11. [3] Sanchez,J.-P., & McInnes,C.R. 2013, ed. V.Badescu, 439 [4] K. Konrad,R. Bender,E. Cappellaro, et al. 2004, GIA 5492, 484–494. [5] McFarland,J.P., Verdoes-Kleijn,G., Sikkema,G. *et al.* 2013, *ExpAstron* 35, 45–78. [6] *Bertin,E. & Arnouts,S. 1996,* A&A Supp 317, 393. [7] P.V.C. Hough. 1959, Proc.Int.Conf. High Energy Accelerators and Instrumentation. [8] Gunn,J. E.; Siegmund, W. A.; Mannery,E. J., et al. 2006, ApJ 131 (4): 2332–2359. [9] T. Shanks,N. Metcalfe,B. Chehade, *et al.* 2015. *MNRAS* 451 (4), 21: 4238–4252.

DUST DYNAMICS AND PLASMA SIMULATIONS IN SUPPORT OF PLANETARY DEFENSE MISSIONS SUCH AS HERA AND RAMSES. S. L. Ivanovski[1,2], L. Calderone[1], L. Biasiotti[1]
[1]INAF-Osservatorio Astronomico di Trieste, [2]Universita di Trieste (stavro.ivanovski@inaf.it)

Introduction: Developing a suite of models that can address different physical scenarios in the encounter of asteroids is a timely question for planetary defense science. The role of plasma events in dust dynamics in the close vicinity of the asteroid has not been tackled methodologically. After the successful launch of the ESA/HERA mission [1] on October 7, 2024, it is timely to recall what we have learned from the NASA Double Asteroid Redirection Test (DART) impact [2] and the ASI/Light Italian Cubesat for Imaging of Asteroids (LICIACube) [3] mission. Among the scientific objectives of the HERA mission is to determine the physical properties of Dimorphos, including its internal structure, and to constrain binary formation scenarios. Here we present how dust dynamics simulations can help constrain the physical properties of the dust in the asteroid and/or in the binary system, together with a plasma model which can accelerate particles and change their dynamics in the encounter with the asteroid. Such a scenario could be of interest to study the environment of an asteroid that can be subject to strong plasma events, as in the planned ESA/JAXA RAMSES mission to Apophis in 2029.

The models: We couple two models - the 3D+t model – LIMARDE [4] and the MHD model that analyzes shock dynamics and space weather event observations MIM [5]. Dust dynamical simulations are constrained with laboratory observations [6], impact simulations, and near-field observations such as the LICIACube [7] images, and simulate the long-lived ejecta. The model computes single particle trajectories, dust rotational frequencies and velocity, as well as particle orientation at any time and distance. We compute the dust velocity distribution based on the physical properties (size, mass, and shape) derived from the LICIACube observations. The results are useful to check the role of particle fragmentation and to constrain the physical properties based on the dynamical properties of the ejected dust in the near- and mid-environment.

The MIM model studies the MHD instabilities in space weather events and the velocity changes in the plasma flow that can contribute to changes in the dynamics of particles in the vicinity of the asteroid.

Results: The first group of results regards the dust dynamics modeling that will be coupled with the plasma model. We carried out a numerical analysis to determine how many and which non-spherical particles remain gravitationally bound to the Didymos system, how much mass escapes, and the corresponding percentages relative to the total (see Figure 1).

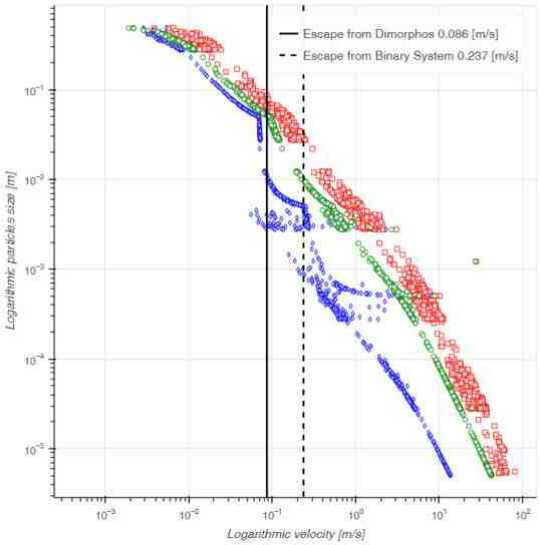


Figure 1. Logarithmic-scale plot showing the relationship between particle velocity and size. This graph refers specifically to the 120th second of the simulation in the presence of a vapor plume, without fragmentation, and includes data for 1000 oblate particles (red squares), 1000 prolate particles (blue diamonds), and 1000 spherical particles (green circles).

References:

[1] Michel, P. et al. (2022) *PSJ, 160*. [2] Rivkin, A.S. et al. (2021) *PSJ, 2*. [3] Dotto, E. et al. (2021) *PSS, 199*. [4] Fahnestock et al. (2022) *PSJ*. [5] Biasiotti, L. et al. (2024) *Frontiers, 11*. [6] Ormo, J. et al. (2022) E&PSL, *594*. [7] Dotto, E. et al. (2024) *Nature, 627*.

RAMSES MISSION UPDATE: PREPARING FOR APOPHIS' 2029 CLOSE APPROACH TO EARTH

M. Lazzarin (1), P. Michel (2), M. Kuppers (3), S. Green (4), P. Tortora (5), S. Ulamec (6), J.B. Vincent (7), P. Abell (8), S. Sugita (9), P. Martino (10)

(1) Padova University, Vicolo dell'Osservatorio 3, 35122 Padova, Italy, monica.lazzarin@unipd.it, (2) Universite Cote d'Azur, Observatoire de la Cote d'Azur, CNRS, Lagrange Laboratory, CS34229, 06403 Nice Cedex 4, France, michelp@oca.eu, (3) ESAC/ESA, Camino bajo del Castillo S/N, Urbanizacion Villafranca del Castillo, 28692 Villanueva de la Canada, Madrid, Spain, Michael.Kueppers@esa.int, (4) The Open University, Milton Keynes MK7 6AA, UK,(5) University of Bologna, Department of Industrial Engineering, Via Montaspro 97, I-47121, Forli (FC), Italy, (6) German Aerospace Center (DLR), RB-MUSC, Linder Hohe 1, 51147 Cologne, Germany, (7) DLR Institute of Planetary Research, Berlin, Germany, (8) NASA Johnson Space Center, 2101 NASA Parkway, Mail Code XI, Houston, TX 77058-3696, USA, (9) University of Tokyo, 7-3-1 Hongo, Bunkyo-ku, Tokyo 113-0033, Japan, (10) ESTEC/ESA, Keplerlaan 1, 2201 AZ, Noordwijk, The Netherlands, Paolo.Martino@esa.int.

Introduction: The ESA RAMSES (Rapid Apophis Mission for SpacE Safety) mission is dedicated to the close monitoring and characterization of the potentially hazardous asteroid (99942) Apophis in the months surrounding its exceptionally close passage by Earth on 13 April 2029. During this encounter, Apophis will pass at approximately 30,000 km from the Earth's surface, well inside the geostationary orbit region, making it a unique natural experiment to observe how a near-Earth asteroid responds to planetary tidal forces.
RAMSES, part of ESA's Space Safety Programme, builds upon the operational and technological heritage of the Hera mission [1]. The mission concept includes a main spacecraft and two CubeSats and is scheduled for launch in spring 2028 on a direct trajectory to reach Apophis roughly two months before closest approach. Mission development is progressing, with final confirmation expected following the ESA Council at Ministerial Level (CMIN25) in late November 2025.

Scientific Objectives: RAMSES addresses key open questions regarding the mechanical, dynamical, and structural response of small bodies subjected to strong tidal perturbations.
The principal scientific goals include the determination of Apophis' orbital evolution, spin state, shape, and geophysical properties before, during, and after the Earth encounter. High-resolution global imaging will be acquired to map the asteroid's morphology with ≤10 cm/pixel resolution, enabling the identification of local terrain disturbances, landslides, boulder rearrangement, and other surface expressions of tidal stress.

Radio Science experiments will provide precise measurements of rotation state, orientation, gravity field, and potential body deformations, while also contributing to mass determination. A major objective is to assess whether Apophis undergoes internal reorganization due to tidal forces. Internal structure and material heterogeneities will be investigated by a low-frequency radar aboard an Orbiter CubeSat, while the Lander CubeSat, equipped with a seismometer, gravimeter, and magnetometer, will attempt surface deployment prior to the encounter to record in-situ seismic signals generated during the tidal passage.

RAMSES will also conduct a detailed thermal investigation using TIRI, a thermal infrared camera provided by JAXA and derived from Hera heritage. Thermal inertia mapping will improve the assessment of the Yarkovsky effect and help quantify potential alterations of surface thermal properties after the encounter. Additional VNIR instruments, including the CHANCES multispectral camera and the HAMLET hyperspectral imager, will supply compositional maps and spectral diagnostics to detect any resurfacing, exposure of fresh material, or space-weathering variations.

Dust activity and particle lofting—possibly triggered by tidal forces or interactions with Earth's magnetosphere—will be monitored by VISTA and a plasma spectrometer, which will search for transient dust clouds, particle acceleration, and surface refreshing events.

Mission Architecture and Payload: RAMSES inherits its overall platform design from ESA's Hera spacecraft but is adapted for a fast direct transfer to Apophis and continuous operations during the Earth encounter. The main spacecraft will serve as a communication hub using an inter-satellite link system, enabling data relay between the CubeSats and Earth while simultaneously contributing to gravity-field mapping.
The payload suite comprises:

- **Asteroid Framing Cameras** for global mapping and surface change detection;
- **Radio Science** for mass, heterogeneity, and tidal deformation analysis;
- **TIRI** (JAXA) for thermal characterization;
- **CHANCES** VNIR spectral camera and **HAMLET** VNIR hyperspectral imager for mineralogical mapping;
- **Plasma Spectrometer** for monitoring dust–magnetosphere interactions;

- **6U-XL Orbiter CubeSat** carrying a low-frequency radar for internal structure probing;
- **6U-XL Lander CubeSat** equipped with seismometer, gravimeter, and magnetometer for the first attempt at seismic monitoring on an asteroid during a tidal event.

Both CubeSats will be released prior to the Earth encounter and will operate autonomously, providing distributed measurements that complement the main spacecraft's observations.

RAMSES represents the lead of a coordinated international campaign that includes JAXA's DESTINY+ flyby and NASA's OSIRIS-APEX mission[2], creating a synergistic multi-mission timeline covering pre-encounter, encounter, and post-encounter phases. The launcher will be provided by JAXA.

Conclusion: RAMSES will be the first mission to directly measure the real-time response of an asteroid to strong terrestrial tidal forces. The combined dataset will yield unprecedented information on Apophis' internal structure, regolith properties, mechanical strength, and rotational dynamics. These measurements will be essential for planetary defense modelling by validating theories on tidal deformation, resurfacing processes, and structural stability during close planetary encounters.

Furthermore, the 2029 passage of Apophis will be visible to more than two billion people worldwide, providing a rare public engagement opportunity aligned with the United Nations designation of 2029 as the International Year of Asteroid Awareness and Planetary Defense. RAMSES will supply live observations that will enhance scientific, planetary defense and societal impact.

Acknowledgments: The authors acknowledge support from ESA, ASI, CNES, DLR, JAXA, NASA.

References: [1] Michel P. et al. (2022) *Planet. Sp. Sci*. 3, 160-180. [2] D. DellaGiustina et al. (2023) *Planet. Sp. Sci.*, 4, 198-219

XXI Congresso Nazionale di Scienze Planetarie

Sessione Astrobiologia e Astrochimica
Mars

ORGANICS DETECTION ON MARS BY THE MARS 2020 PERSEVERANCE ROVER. T. Fornaro[1], G. Poggiali[1], J. R. Brucato[1], S. Sharma[2,3], R. S. Jakubek[4], R. Bhartia[5], A. Steele[3], A. E. Murphy[6], M. M. Tice[7], M. D. Schulte[8], K. P. Hand[2], M. D. Fries[9], W. J. Abbey[2], A. Alberini[1,10], D. Alvarado-Jiménez[11,12], K. C. Benison[13], E. L. Berger[9], S. Biancalani[1,14,15,16], A. J. Brown[17], A. P. Broz[18,19], W. P. Buckley[4], D. K. Buckner[20,21], A. S. Burton[22], S. V. Bykov[23], E. L. Cardarelli[24], E. A. Cloutis[25], S. A. Connell[19], C. Garcia-Florentino[1], F. Gómez[26], N. C. Haney[4,27,28], C. Lee[4,27,28], V. Lino[11], P. Manini[29], F. M. McCubbin[9], M. E. Minitti[30], R. V. Morris[9], Y. Phua[31], N. Randazzo[32], J. Razzell Hollis[33], F. Renzi[1,34], S. Siljeström[35], J. I. Simon[9], A. Srivastava[3], N. Tasinato[11], K. Uckert[2], R. C. Wiens[19] and A. J. Williams[36], [1]INAF–Astrophysical Observatory of Arcetri, Florence, Italy, teresa.fornaro@inaf.it, [2]Jet Propulsion Laboratory, California Institute of Technology, Pasadena, CA, USA, [3]Carnegie Science Earth & Planets Laboratory, Washington, DC, USA, [4]Amentum JETS II, NASA Johnson Space Center, Houston, TX, USA, [5]Photon Systems Incorporated, Covina, CA, USA, [6]Planetary Science Institute, Tucson, AZ, USA, [7]Department of Geology and Geophysics, Texas A&M University, College Station, TX, USA, [8]Mars Exploration Program, NASA Headquarters, Washington, DC, USA, [9]Astromaterials Research and Exploration Science Division, NASA Johnson Space Center, Houston, TX, USA, [10]Department of Physics and Astronomy, University of Florence, Florence, Italy, [11]Scuola Normale Superiore di Pisa, Pisa, Italy, [12]IUSS, Scuola Universitaria Superiore Pavia, Pavia, Italy, [13]Department of Geology and Geography, West Virginia University, Morgantown, WV, USA, [14]Department of Physics, University of Trento, Povo, Italy, [15]Italian Space Agency (ASI), Rome, Italy, [16]Department of Earth Sciences, University of Florence, Florence, Italy, [17]Plancus Research, Severna Park, MD, USA, [18]Department of Earth Sciences, University of Oregon, Eugene, OR, USA, [19]Department of Earth, Atmospheric, and Planetary Sciences, Purdue University, West Lafayette, IN, USA, [20]NASA Goddard Space Flight Center, Greenbelt, MD, USA, [21]Oak Ridge Associated Universities, Oak Ridge, TN, USA. 22Planetary Science Division, NASA Headquarters, Washington, DC, USA, [23]Department of Chemistry, University of Pittsburgh, Pittsburgh, PA, USA, [24]Department of Earth, Planetary and Space Sciences, University of California, Los Angeles, CA, USA, [25]Centre for Terrestrial and Planetary Exploration, University of Winnipeg, Winnipeg, Manitoba, Canada, [26]Centro de Astrobiología (CAB), CSIC-INTA, Torrejón de Ardoz, Spain, [27]Texas State University, Houston, TX, USA, [28]NASA Johnson Space Center, Houston, TX, USA, [29]Department of Chemical Sciences, University of Naples Federico II, Naples, Italy, [30]Framework, Silver Spring, MD, USA, [31]Division of Geological and Planetary Sciences, California Institute of Technology, Pasadena, CA, USA, [32]Department of Earth and Atmospheric Sciences, University of Alberta, Edmonton, Alberta, Canada, [33]Natural History Museum, London, UK, [34]University of Pisa, Pisa, Italy, [35]RISE Research Institutes of Sweden, Stockholm, Sweden, [36]Department of Geological Sciences, University of Florida, Gainesville, FL, USA.

Introduction: The detection of organics on Mars is key to assessing whether the planet was ever habitable and inhabited. Although organic molecules have been previously detected on Mars, their nature, origin, and preservation mechanisms remain highly debated. The suite of instruments onboard the NASA Mars 2020 Perseverance rover has been designed to map at a microscopic level the distribution of elements, minerals, and possible organic molecules, from which to derive information about their potential biotic vs abiotic origin.

In this contribution, we review the recent discoveries of organic materials and associated mineralogical features across different environments explored by the Perseverance rover in Jezero crater, providing a comprehensive discussion on their diverse origins and astrobiological relevance [1][2][3].

The Scanning Habitable Environments with Raman and Luminescence for Organics and Chemicals (SHERLOC) instrument, a deep UV (DUV) Raman and fluorescence spectrometer, has been key in characterizing these organics. SHERLOC detected complex Raman features consistent with polycyclic aromatic hydrocarbons (PAHs) (such as methylanthracenes and dihydroxynaphthalenes) spatially associated with sulfate minerals [2]. These detections occurred across various terrains: on the Jezero crater floor (in the altered igneous rock target Quartier), and on the Jezero fan top (in the fluvial sandstone target Pilot Mountain).

The association with sulfates suggests a crucial role for salt-mediated preservation, shielding the organic matter from harsh surface oxidizing conditions and UV radiation. Laboratory UV irradiation experiments on PAHs embedded in hydrated magnesium sulfate confirmed the mineral's photoprotective properties: compounds such as 2,6-dihydroxynaphthalene and benzo[a]pyrene in hydrated magnesium sulfate remain detectable by SHERLOC even after exposure for several sols to martian ambient UV once revealed by Perseverance's abrasion tool [4].

Proposed formation scenarios for the PAHs found in these rocks include endogenous igneous processes (PAHs formed from magmatic gases and preserved in situ by sulfates) or ex situ igneous formation followed by fluid transport of the PAHs and their subsequent co-precipitation with sulfates in the

pores of igneous rocks (Fig. 1). Although no direct evidence of biogenicity was found, the possibility that they are resistant alteration products from the chemical weathering of ancient biotic compounds cannot be completely ruled out. Also, assessing whether these PAHs are related to the organic carbon of potential biotic origin found in the Bright Angel formation in the Jezero margin unit [3] requires further investigations.

Distinguishing definitively between biotic, prebiotic, and abiotic scenarios is beyond the capabilities of in situ instrumentation. Therefore, the core samples collected by Perseverance from these rocks, are of crucial astrobiological importance. The return of these samples to Earth as part of the potential future Mars Sample Return Campaign is the ultimate goal for high-sensitivity and high-resolution characterization. In the meantime, continued laboratory research and the analysis of mission data remain essential to refine our understanding of the Martian organic cycle.



Fig. 1. Sketch of potential mechanisms for the presence of PAHs in sulfates in Quartier and Pilot Mountain. Scenario 1A describes an in situ igneous process for PAH formation from magmatic gases trapped in pores of igneous rocks of Jezero crater, followed by preservation by sulfates precipitated as consequence of aqueous alteration, which might be consistent with Quartier observations. Scenario 1B describes an ex situ igneous formation of PAHs, occurred outside Jezero crater, followed by fluid transportation of PAHs towards Jezero crater, where PAHs might have been co-precipitated with sulfates or trapped and preserved within sulfate cement crystals. This scenario might be consistent with both Quartier and Pilot Mountain observations, and the selective accumulation of PAHs in these rocks instead of macromolecular carbon (MMC) due to its lower mobility in fluid phases. Scenario 2 describes a potential hydrothermal formation of PAHs and transportation by hydrothermal groundwaters that might have been related to regional hydrothermalism associated with Syrtis Major volcanism. Scenario 3 describes a potential exogeneous delivery of PAHs or production during shock impact processes. Scenario 4 describes a potential biotic origin of the PAHs as chemical weathering products of ancient biotic compounds. The locations of the Quartier and Pilot Mountain targets in Jezero crater are shown on an image taken by the High Resolution Stereo Camera on ESA's Mars Express orbiter (Credits: ESA/DLR/FU-Berlin/NASA/JPL-Caltech). Green arrows indicate in situ formation mechanisms, while blue arrows indicate ex situ formation mechanisms.

References:

[1] Sharma S. et al. (2023) *Nature*, *619*, 724–732. [2] Fornaro T. et al. (2025) *Nature Astronomy,* https://doi.org/10.1038/s41550-025-02638-z. [3] Hurowitz, J. A. et al. (2025) *Nature*, *645*(8080), 332–340. [4] Alberini A. et al. (in press) *Nature Scientific Reports*.

Acknowledgements:

This research was supported by the Italian Space Agency (ASI) through the ASI/INAF agreement no. 2025-12-HH.0, and by European Union—Next Generation EU through the PRIN MUR 2022 “Experimental and computational analog studies to support identification of organics on Mars by the NASA Mars 2020 Perseverance rover”.

PROJECT ANOXYMARS: STUDYING THE DETECTABILITY OF ANOXYGENIC MICROORGANISMS AHEAD OF THE EXOMARS MISSION. M. Battistuzzi[1,2], A. Alberini[1,2], S. Biancalani[1,3,4,5], F. Renzi[1,2], G. Poggiali[1], C.G. Florentino[1], A. Roussel[1], T. Fornaro[1] & J.R. Brucato[1]

[1]INAF- Astrophysical Observatory of Arcetri, L.go E. Fermi 5, 50125 Firenze, Italy (mariano.battistuzzi@inaf.it); [2] Department of Physics and Astronomy, University of Florence, Via Giovanni Sansone 1, 50019 Sesto Fiorentino, Florence; [3]Department of Physics, University of Trento, Via Sommarive 14, 38123 Povo; [4]Italian Space Agency (ASI), viale del Politecnico snc, 00133, Rome, Italy; [5]Department of Earth Sciences, University of Florence, via G. La Pira 4, 50121, Florence, Italy;

ESA-NASA ExoMars mission [1], targeting a 2028 launch, will land at Oxia Planum. This site comprises a portion of a fluvial-deltaic sedimentary system formed during the late Noachian/Early Hesperian and is rich in clay minerals, known for their capacity to preserve biosignatures. Evidence suggests the area was once submerged, forming a delta fan with hydrated silica-bearing deposits. Critically, early Amazonian volcanic deposits subsequently covered and protected these older sediments, potentially shielding preserved biosignatures from surface radiation. Erosion in the last couple billion years has been gradually exposing these ancient sedimentary rocks to the Martian superficial radiative environment [2]. This makes Oxia Planum an ideal location to search for well-preserved organic compounds, putative microorganisms, or their degradation products.

The AnoxyMars project will directly support the ExoMars mission by investigating the detectability of diverse anoxygenic microorganisms (both photosynthetic and non-photosynthetic) through the instrumentation onboard of the Rosalind Franklin rover. Microorganisms will be systematically exposed to ionizing and UV radiation simulating the Martian surface and subsurface conditions that the rover will be able to probe. Our selected microorganisms represent metabolisms that existed during Earth's Archean eon, prior to oxygenic photosynthesis, and similarly could represent analogous early Martian life forms. These taxa are sourced from anoxic marine, lacustrine, palustrine, and freshwater habitats, aligning with the paleoenvironments proposed for Oxia Planum.

This presentation will provide an overview of the project AnoxyMars, highlighting its direct relevance to the ExoMars mission. We will detail the experimental methodology and the types of data we expect to obtain. Our findings will directly inform the Rosalind Franklin rover science team on which biosignatures could be more likely expected at various probing depths. This information will significantly enhance the mission's ability to detect traces of extinct (or potentially extant) life on Mars.

References: [1] Vago, J.L. et al. (2018) *From Habitability to Life on Mars* 309–347, ISBN 9780128099353. [2] Quantin-Nataf, C. et al. (2021) AsBio 21, 345–366.

Microbial Community Divergence and pH-Driven Biomineralization in Two Terrestrial Analogs to Mars

A. Piacentini[1,2], S. Fazi[1,2], G. Costanzo[3], E. Bruschini[4], M. Ferrari[4], C. Mazzoni[1,2]
[1]BBCD – Sapienza University of Rome (contact: agnese.piacentini@uniroma1.it), [2]IRSA-CNR Rome, [3]IBPM-CNR Rome, [4]IAPS-INAF, Rome.

Introduction: Extreme environments on Earth represent powerful natural laboratories for exploring microbe–mineral interactions relevant to Mars. Alkaline systems rich in carbonate and acidic Fe-sulfate–dominated sites mirror key geochemical regimes encountered on the Martian surface. Understanding how microbial communities respond to these contrasting conditions provides insight into the potential formation, alteration, and preservation of biosignatures.

In this study, we compare two chemically divergent terrestrial analogs: the alkaline Lake Bagno dell'Acqua, in Pantelleria, Italy [1] and an acidic site in Solforata di Pomezia, Latium, Italy. These environments span a wide pH spectrum and host distinct mineralogical substrates, allowing for an assessment of how microbial metabolisms, including carbonate-forming pathways [2], Fe-oxidation [3], and enzyme-mediated biomineralization, drive mineral transformations under Mars-relevant conditions.



Figure 1. (Top) Solforata di Pomezia in Latium (Italy). (Bottom) Lake Bagno dell'Acqua in Pantelleria in Sicily (Italy).

Material and methods: Water temperature, pH, and electrical conductivity were analyzed on field. Sediment samples were collected from both sites to characterize Microbial communities through 16S rRNA gene sequencing. Genomic data were screened for metabolic pathways associated with biomineralization, including those related to carbonic anhydrase and urease.

Results: Sediments collected from the alkaline Lake Bagno dell'Acqua reveal microbial communities that are strongly enriched in taxa typically associated with carbonate-forming microhabitats. This pattern suggests not only the presence of microorganisms capable of surviving under high-pH conditions, but also a pronounced community-driven potential for microbially induced carbonate precipitation (MICP). The taxonomic composition indicates that these communities rely on metabolic strategies well-suited for alkaline environments, such as the activity of alkalinity-tolerant heterotrophs and microorganisms able to reshape local chemical microgradients. Such microgradients—particularly those involving pH, carbonate saturation, and organic matter turnover—play an essential role in controlling mineral nucleation and subsequent crystal growth.

Further support for this interpretation comes from laboratory-cultured isolates obtained from the same sediments. Genomic analyses of these isolates show that they encode key enzymes directly implicated in biomineralization processes, including carbonic anhydrase and urease. These enzymes are known to accelerate carbonate precipitation by locally increasing carbonate alkalinity or inducing pH shifts, thereby reinforcing the notion that the Bagno dell'Acqua system hosts an active and metabolically versatile carbonate-precipitating microbial consortium.

In contrast, sediments from the Pomezia solforata exhibit microbial communities with a drastically different ecological and functional character. Here, the dominant taxa belong to acidophilic Proteobacteria specializing in biogeochemical transformations of iron and sulfur. The heavy representation of Fe-oxidizing lineages is striking and aligns with the abundant jarosite—a potassium iron sulfate mineral—found throughout the sediments. Jarosite formation is favored in low-pH, oxidizing, metal-rich environments, and the co-occurrence of these acidophiles with jarosite strongly suggests that biologically mediated iron oxidation contributes to the ongoing development of Fe-sulfate mineral phases at this site. The ecological pressures imposed by the solforata's acidic and geochemically reactive conditions thus select for microbes with specialized metabolic adap-

tations distinct from those thriving in the alkaline lake system.

A multivariate comparison of community composition using Bray–Curtis principal coordinates analysis (PCoA) underscores the profound differences between the two sites. The ordination displays a pronounced separation, reflecting how extreme pH regimes—highly alkaline at Bagno dell'Acqua and strongly acidic at Pomezia—act as powerful selective forces. These environmental constraints drive the assembly of fundamentally different microbial ecosystems, each capable of mediating distinct biogeochemical processes and shaping characteristic patterns of mineral formation.

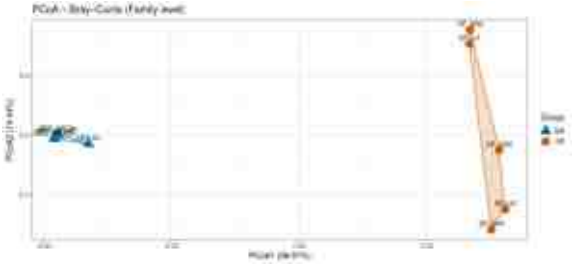


Figure 2. PCoA based on microbial family level for both environments. BA: Bagno dell'Acqua Lake, SP: Solforata of Pomezia.

Conclusion: Taken together, the contrasting microbial signatures and their associated mineralogical imprints highlight two divergent biomineralization pathways operating under opposite physicochemical conditions. These findings have broader implications for the interpretation of potential biosignatures on Mars, where sediments may exhibit comparable chemical heterogeneity.

Understanding how microbial processes respond to and exploit extreme pH environments on Earth provides a valuable framework for identifying biologically influenced mineral phases and deciphering the ecological strategies of hypothetical extraterrestrial life in similarly variable settings.

References:

[1] Bruschini et al. (2024) *PSS*, 245 (105893).
[2] Mazzoni et al. (2024) *Front. Microbiol.*, 15, 1391968
[3] Daoud & Karamanev (2006) Min. Eng., 19, 960–967

Acknowledgment

We acknowledge the Starting Grant for Research Projects 2024 – Type 1 (Sapienza University of Rome, protocol AR124190789DD09A). We also acknowledge the support of the MINI GRANTS 2023 RSN-3 INAF – Bando di Astrofisica Fondamentale 2023. This work was also supported by the 2024 Mobility Grant for Young Researchers and PhD Students, awarded by the Società Italiana di Scienze Planetarie.

Bagno dell'Acqua and the Solforata di Pomezia are protected natural areas managed, respectively, by the *Parco Nazionale Isola di Pantelleria* and *RomaNatura – Riserva Naturale di Decima Malafede*. We sincerely thank both authorities for authorizing sample collection and for their collaboration in support of this project.

ASSESSING THE VIABILITY OF ANTARCTIC CRYPTOENDOLITHIC COMMUNITIES EXPOSED TO MARS-LIKE CONDITIONS

Del Franco C.[1] (carmen.delfranco@unitus.it), Belmonte Lopes R.[1], Pezzilli S.[2], Pedone M.[2], Baqué M.[3], Lorek A.[3], Garland S. [3], Selbmann L.[1].

[1]*Department of Ecological and Biological Sciences, University of Tuscia, Viterbo, Italy.*
[2]*ASI- Italian Space Agency, Rome, Italy*
[3]*German Aerospace Center (DLR), Institute of Space Research, Planetary Laboratories Department, Berlin, Germany.*

Introduction: Mars is still one of the main astrobiological targets [1] to evaluate the possibility of life on Earth-like planets [2], whose discovery has encouraged to deepen knowledge of their potential habitability [3]. With the modern approach, the so-called 'Planetary Field Analogues' (PFAs) are involved in investigating this possibility by studying terrestrial life forms that can live in areas where environmental conditions are so extreme to be compared with extraterrestrial ones [4]. Among the PFAs are the 'Martian analogues on Earth' [3], including the ice-free areas of continental Antarctica, as the McMurdo Dry Valleys [5]. These regions were considered as incompatible with life but, in the last 30 years, life was found there, albeit limited to special microorganisms that can survive adopting cryptoendolithism as survival strategy, finding refuge in the interstices of the porous rocks [6]. For this, Antarctic cryptoendolithic communities can be considered astrobiological models to investigate the possibility of past or present life on Mars or Mars-like planets. In this context, the CRYPTOMARS project aims at evaluating the survival of these communities once exposed to Mars-like conditions, to outline the characteristics of a putative microbial community capable of living on Mars [7].



Figure 1: Map of the sampling sites in the McMurdo Dry Valleys, Southern Victoria Land, Antarctica.

Materials and methods: Colonised rock samples from Battleship Promontory and Linnaeus Terrace (Southern Victoria Land, Antarctica) were selected, fragmented in 2 cm diameter discs, reactivated by hydration and incubation at 15 °C for 96 h, and shipped to the Planetary Analogue Simulation Laboratory-PASLAB [8] of the German Aerospace Center (DLR) in Berlin. Samples were exposed to Mars-simulated environments for 21 days (the equivalent of one month on Mars), into the Mars Simulation Chamber (MSC) [9]. After treatment, samples were powdered and viability was evaluated with a polyphasic approach, including seeding on solid medium for the detection of cultivable species [10], the Propidium MonoAzide (PMA) coupled to qPCR assay as a molecular evaluation of cells with intact membranes [11], and Fluorescein Diacetate [12] and ATP [13] assays to detect the presence of metabolic activity.

Results and discussion: Growth on solid medium showed presence of viable and cultivable species after three months, clearly indicating their capacity to replicate after the treatment.
Concerning the molecular test, the results of the Propidium MonoAzide assay showed no differences in order of magnitude between PMA-treated and PMA-untreated samples, indicating the presence of a comparable amount of cells with undamaged membranes in the samples.
The fluoresceine diacetate and the ATP assays confirmed the presence of active metabolism in treated samples, with no statistically significant differences with respect to the untreated ones.
The results of the experiments clearly indicate that, based on the assays hitherto applied, no differences in terms of survival and metabolic activity were detectable between treated and untreated samples. This information provides a clear picture of the antarctic cryptoendolithic communities' resistance breadth to the martian-simulated environment, and will be supplemented by a multi-omic characterisation of them including metagenomics, metabolomics, and lipidomics.

References:

[1] Hansen, A. A., Merrison, J., Nørnberg, P., Lomstein, B. A., & Finster, K. (2005). Activity and stability of a complex bacterial soil community under simulated Martian conditions. International Journal of Astrobiology, 4(2), 135-144.
[2] Carré, L., Zaccai, G., Delfosse, X., Girard, E., & Franzetti, B. (2022). Relevance of earth-bound extremophiles in the search for extraterrestrial life. Astrobiology, 22(3), 322-367.
[3] Cockell, C. S., Bush, T., Bryce, C., Direito, S., Fox-Powell, M., Harrison, J. P., ... & Zorzano, M. P. (2016). Habitability: a review. Astrobiology, 16(1), 89-117.
[4] Cassaro, A., Pacelli, C., Aureli, L., Catanzaro, I., Leo, P., & Onofri, S. (2021). Antarctica as a reservoir of planetary analogue environments. Extremophiles, 25(5), 437-458.
[5] Forte, E., Dalle Fratte, M., Azzaro, M., & Guglielmin, M. (2016). Pressurized brines in continental Antarctica as a possible analogue of Mars. Scientific reports, 6(1), 33158.
[6] Friedmann, E. I. (1986). The Antarctic cold desert and the search for traces of life on Mars. Advances in Space Research, 6(12), 265-268.
[7] Selbmann, L., Del Franco, C., Stoppiello, G. A., Ripa, C., Lopes, R. B., Donati, C., ... & Pezzilli, S. (2025). The CRYPTOMARS project: a multi-omic approach for studying Antarctic cryptoendolithic communities as

Martian-analog life-forms. International Journal of Astrobiology, 24, e17.
[8] Lorek, A., Garland, S. P., Baqué, M., & Helbert, J. (2024, September). The Planetary Analog Simulation Laboratory (PASLAB). In 55th Lunar and Planetary Science Conference, The Woodlands, Texas (Vol. 270).
[9] Lorenz, C., Bianchi, E., Poggiali, G., Alemanno, G., Benesperi, R., Brucato, J. R., ... & Baqué, M. (2023). Survivability of the lichen Xanthoria parietina in simulated Martian environmental conditions. Scientific Reports, 13(1), 4893.
[10] Onofri, S., Barreca, D., Selbmann, L., Isola, D., Rabbow, E., Horneck, G., ... & Zucconi, L. (2008). Resistance of Antarctic black fungi and cryptoendolithic communities to simulated space and Martian conditions. Studies in Mycology, 61(1), 99-109.
[11] Canini, F., Adams, B. J., D'Acqui, L. P., D'Alò, F., & Zucconi, L. (2024). Antarctic rock and soil microbiomes: Shared taxa, selective pressures, and extracellular DNA effects. Geoderma, 446, 116918.
[12] Green, V. S., Stott, D. E., & Diack, M. (2006). Assay for fluorescein diacetate hydrolytic activity: optimization for soil samples. Soil Biology and Biochemistry, 38(4), 693-701.
[13] Dragone, N. B., Diaz, M. A., Hogg, I. D., Lyons, W. B., Jackson, W. A., Wall, D. H., ... & Fierer, N. (2021). Exploring the boundaries of microbial habitability in soil. Journal of Geophysical Research: Biogeosciences, 126(6), e2020JG006052.

MICROBIALLY INFLUENCED EVAPORITIC TEXTURES AND MICROBIOTA OF THE MAKGADIKGADI PAN (BOTSWANA): ANALOGUES FOR MARTIAN BIOSIGNATURE FORMATION.

Tarozzi A.1,*, Franchi F.2,3,4, Cavalazzi B.1,5
[1]Department of Biological, Geological and Environmental Sciences, University of Bologna, Bologna, Italy. [2]Dipartimento di Scienze della Terra e Geoambientali, Università degli Studi di Bari - Aldo Moro, Bari, Italy. [3]Botswana International University of Science and Technology, Palapye, Botswana.
[4]School of Geosciences, University of the Witwatersrand, Johannesburg, South Africa.
[5]Department of Geology, University of Johannesburg, Johannesburg, South Africa.

*Corresponding author email: alice.tarozzi2@studio.unibo.it

Evaporitic playa systems provide valuable terrestrial analogues for investigating the formation and preservation of biosignature under environmental conditions similar to those proposed for early Mars. The Makgadikgadi Pan in Botswana—among the largest evaporitic basins on Earth—combine hypersaline, alkaline, and seasonally dynamic conditions, making it an ideal natural laboratory for studying microbe–mineral interactions of astrobiology relevance [1].

This study focuses on the surface salt crusts of Ntwetwe Pan, part of the Makgadikgadi Pan in Botswana, with the aim of characterizing their mineralogy, microtextures, and microbial structures, and evaluating their astrobiological relevance [2]. Samples were collected along a ~280-meter transect across salinity and moisture gradients. X-ray diffraction revealed halite as the dominant mineral, accompanied by widespread calcite and quartz, and by thenardite and trona in zones of elevated salinity. SEM-EDS analyses identified complex microfabrics—mineralized filaments, EPS-like matrices, and fine-grained coatings— indicative of microbial mediation in mineral precipitation and entrapment. A clear spatial pattern trend emerged: crusts from the margins were enriched in carbonates and exhibited well-preserved filament mineralization, while central samples, dominated by halite and trona, displayed poorer EPS preservation and weaker biosignature encapsulation. These findings underscore the role of environmental gradients in shaping the preservation potential of biosignatures. Along the transect, several features resembling potential biosignatures—such as spheroidal aggregates, acicular crystals, and vermicular cavities—were documented. Although some of them initially suggested a biogenic origin, their regular morphologies, lack of associated carbon, and mineralogical composition pointed instead to an abiotic origin likely due to rapid crystallization and dissolution–reprecipitation cycles under intense evaporative conditions.

The Makgadikgadi Pan represents a valuable natural laboratory for refining biosignature detection strategies in Martian evaporitic environments such as Jezero Crater and Meridiani Planum [3]. While rapid mineral precipitation in these systems may enhance microbial preservation, it can also generate abiotic features that closely resemble biogenic structures. This study reinforces the importance of a multidisciplinary approach—combining morphology, geochemistry, and mineralogy—in distinguishing true biosignatures, and provides critical insights for shaping the scientific goals of future astrobiology missions.

This study is a contribution to the Space It Up project funded by the Italian Space Agency, ASI, and the Ministry of University and Research, MUR, under contract n. 2024-5-E.0 - CUP n. I53D24000060005.

References:

[1] Franchi, F. et al. (2025). Microbial abundance across a salinity and mineralogical transect in the Ntwetwe Pan of Botswana: A terrestrial analogue for playa deposits on Mars. Planetary and Space Science, 255, 106028.

[2] Tarozzi, A., et al., (IN PREP.). Microbial fossilization across salinity gradients in the salt crusts of Ntwetwe Pan (Botswana).

[3] Schmidt, G. et al. (2023). Structural influences on groundwater circulation in the Makgadikgadi salt pans of Botswana? Implications for martian playa environments. Frontiers in Astronomy and Space Sciences, 10, 1108386.

FUNCTIONAL ECOLOGY OF BACTERIA IN ANTARCTIC CRYPTOENDOLITHIC COMMUNITIES FROM DRY AND COLD CONDITIONS ANALOGOUS TO MARS ENVIRONMENTS. R. Belmonte-Lopes[1] (ricardo.lopes@unitus.it), C. Del Franco[1], C. Donati[2], S. Pezzilli, M. Pedone, and L. Selbmann[1], [1]Department of Ecological and Biological Sciences, University of Tuscia, Viterbo, Italy, [2]Edmund Mach Foundation, San Michele all'Adige, Italy, [3]ASI – Italian Space Agency, Rome, Italy.

Introduction: While our ability to search for life in other planets is currently limited by distance and technical challenges, one of the most promising approach is the study of life in "Planetary Field Analogues", which represent extreme environmental conditions found on Earth that could be similar to the ones found in other planets [1]. Mars is one of the closest to Earth astrobiological targets [2], and among the "Martian analogues in Earth" are the ice-free areas of continental Antarctica [3,4]. These cold and dry areas were at first considered lifeless until the decade of 1980, when occurred the discovery of the cryptoendolithic communities that inhabit porous spaces inside rocks [3]. These communities thrive in conditions faithfully reproducing the Martian conditions hypothesized during the late Noachian period on Mars, and can provide insights into the possibility of life at present Mars conditions due to analogous changes from warmer and wetter to cold and dry environments. Under these premises, the CRYPTO-MARS project aims to utilize multi-omic approaches to outline biodiversity as well as metabolic and genomic bases allowing these communites to face and adapt such conditions to figure out the characteristics of a putative microbial assemblage able to colonize present or past Mars environments [5]. Here we present the preliminary results of the characterization of the functional ecology of the bacterial metagenome assembled genomes (MAGs) from these communities.

Methods: A total of 87 samples of endolithically colonized sandstone were collected through 2004 and 2018 in nine different sampling sites in southern Victoria Land, Antarctica, in altitudes ranging from 834-3,100 m a.s.l. The communities' metagenome were sequenced for WGS in a Illumina sequencer, with the metagenomes being assembled and the MAGs binned using the DOI-JGI Metagenome Annotation Pipeline [6]. The obtained medium and high quality MAGs were dereplicated with dRep [7], classified with GBDB-Tk [8], and analyzed regarding functional diversity using microTrait [9], with a trait variability threshold of 0.01 and a guild size cutoff of 3 MAGs.

Results: A total of 1,269 medium or high quality MAGs of bacteria's were recovered from the samples, resulting in a total of 316 MAGs after the dereplication step. The predominant mechanism of stress resistance identified in the MAGS were the production of reactive oxygen species (ROS) scavenging enzymes (98% of the MAGs) against oxidative stress, production of ATP-dependend proteases against pH changes (100%), production of compatible solutes (94%) and biosynthesis and exportation of extra cellular polysaccharides (89%) to resist desiccation and osmotic stress, and mRNA stabilization (96%) to resist low temperatures. The predominant forms of substrate uptake were transport of metal ions (100% of the MAGs), inorganic ions (100%), organophosphorous compounds (99%), and free amino acids (99%), while the main forms of substrate degradation were the degradation of proteins (100% of the MAGs), breakdown of cellulose (100%), xylan and heteroxylan (100%), chitin (98%), and mixed linkage glucans (98%). Additionally, the main forms of substrate assimilation were ammonia assimilation to glutamate (99% of the MAGs) and glutamine (97%), and assimilation of C1 compounds through methanotrophy with the formaldehyde-serine pathway (92%). The predominant forms of resource use were aerobic respiration through the oxidative (88% of the MAGs) and non-oxidative (73%) pentose phosphate pathway, and the fermentation of pyruvate to short-chain fatty acids (62%). Although carotenoids as neurospore and lycopene were identified in about 70% of the MAGs and other accessory pigments were also present, and chlorophyll a was present in 15% of the MAGs, complete oxygenic photosystems I and II were identified in only 1.9% of the MAGs. The anoxygenic photosystem II was identified in about 9% of the MAGs, associated with bacteriochlorophyll g. Hydrogenotrophy from H_2/CO_2 and hydrogenotrophic methanogenesis were identified in 10% of the MAGs, being a more prevent form of chemolithoautotrophy than the ones related to sulfur and nitrogen. The mean minimal doubling time calculated for the MAGs is of 10.1 hours (ranging from 0.5-33 hours), and the mean optimal growth temperature of 32.5 ºC (ranging from 21-42 ºC).

The calculated number of functional guilds to explain 70% of the traits variance is of 56, of which 40 included 3 or more MAGs, with the largest ones including 15 MAGs. The two biggest guilds (each including 15 MAGs) differed, among other traits, in their capacity to uptake biopolimers, transport of lipids and peptides, capacity of breaking different kinds of sugars, and utilization of methane through the H4F pathway. The presence of the anoxygenic photosystem II was predominant in two guilds (in-

cluding 11 and 8 MAGs), with both guilds presenting chlorophyll a and bacteriochlorophyll g. Hydrogenotrophy from H_2/CO_2 and hydrogenotrophic methanogenesis were predominant in two guilds (including 10 and 8 MAGs), with one utilizing the H4MPT pathway and being the only guild not able to break chitin, while the other used more widespread forms of conversion of formaldehyde in methane as the serine or the oxidative pathways.

Discussion: The present results indicates a considerable bacterial diversity in the cryptoendolithic communities of the sandstones of the cold and dry areas of Antarctica, as well as in the types of strategies concerning their functional ecology. Some stress resistance traits were widespread in the obtained MAGs, suggesting convergent strategies to cope with the extreme environmental conditions based on RNA stabilization, production of extracellular polysaccharides, and ROS enzymes. Almost all recovered MAGs presented proteins related to chitin breakdown, which indicates that the bacterial communities present in the samples are structured in a symbiotic relationship with lichenic associations formed by the fungi and green algae present in these communities, as fungi are the only microorganism in these communities that produce chitin. A relatively large number of MAGs showed the capacity to use formaldehyde through the methanotrophic serine pathway, with methanogenesis being associated with a smaller set of MAGs capable of hydrogenotrophy from atmospheric H_2/CO_2 forming two different functional guilds. Although more MAGs were identified as being capable of anoxygenic photosynthesis than oxygenic photosynthesis, the wider distribution of accessory phototrophic pigments as neurospore and lycopene suggests that is possible that the traits related to oxygenic photosynthesis are more widespread than found in our results. The MAGs of the organism capable of anoxygenic photosynthesis were grouped in two different functional guilds, but both presented bacteriochlorophyll g and chlorophyll a, suggesting the capacity of shifting between oxygenic and anoxygenic photosynthesis.

Interestingly, the optimum growth temperature estimated from the MAGs suggest much higher temperatures than the ones that occurs in Antarctica. Although psychrophyles are poorly fit by the regression methods used due to the small number of available genomes and different mechanisms of thermoadaptation [10], previous studies showed that the photosynthetic temperature optimal of Antarctic lichens is much lower than the optimal for algae and fungi that forms the lichen, and that these communities adapt to a wide range of thermal conditions shifting the ratios of producer-to-consumer organisms [11,12]. Thus, as the bacteria of the present study are component of lichen dominated microbial communities, it is possible that they benefit from the thermal adaptation generated by these, allowing them to survive to temperatures much lower than their optimal growth temperatures.

In conclusion, the wide number of functional ecologies found from in the bacterial community from an apparently lifeless dry and cold environment demonstrates a large set of possible ways in which life can adapt to Mars-like conditions, highlighting the possible interactions between the organisms in these communities can tremendously increase their ability of survival.

References:

[1] Cassaro, A. et al. (2021). *Extremophiles*, 25, 437–458. [2] Cockwell C. S. et al. (2016) *Astrobiology*, 16, 89–117. [3] Friedmann E. I. (1986) *Adv. Space Res.*, 16, 265–268. [4] Forte E. et al. (2016), *Sci. Rep.*, 6, 33158. [5] Selbmann L. et al. (2025) *Astrobiology*, 24, e17. [6] Huntemann M. et al. (2016) *Stand. Genomic Sci.*, 11,17. [7] Olm M. R. et al. (2017) *ISME J,* 11, 2864–2868. [8] Chaumeil P. A. et al. (2022) *Bioinformatics*, btac672. [9] Karaoz U. and Brodie E. L. (2022) *Front. Bioinfor.*, 2, 918853. [10] Sauer D. B. and Wang D-N. (2019) *Bioinformatics*, 35, 3224–3231. [11] Friedmann E. I. and Sun H. J. (2005) *Microb. Ecol.*, 49, 523–527. [12] Sun H. J. and Friedmann E. I. (2005) *Microb. Ecol.*, 49, 528–535.

XXI Congresso Nazionale di Scienze Planetarie

Sessione Planetologia sperimentale e di laboratorio

PRELIMINARY TESTS TO COMBINE X-RAY MICROTOMOGRAPHY AND DIELECTRIC MEASUREMENTS TO ASSESS THE RADAR PROPERTIES OF PURE ICE, F. Cimbolli Spagnesi, Università degli Studi Roma Tre, flavia.cimbollispagnesi@gmail.com.

Introduction: Two large space missions, ESA's JUICE and NASA's EUROPA Clipper, are on their way to reach the icy satellites of Jupiter in the early 2030s. One of the main goals of the missions is to find liquid water below/inside the icy crusts and to assess the habitability conditions of these ocean worlds. On board these missions radar sounders will play a fundamental role in detecting the position, depth, and composition of water. ESA's JUICE, for example, is equipped with the 9 MHz ground-penetrating radar RIME (Radar for Icy Moon Exploration), designed to examine ice down to a depth of 9 km. Specifically, RIME uses radio waves to create an electromagnetic image of the subsurface, resulting from the interaction between the waves and the materials present at depth. The physical and chemical properties of these materials can be represented by two parameters: complex dielectric permittivity and complex magnetic permeability. These parameters also define the electromagnetic behavior of these materials: deriving their values from the inversion of radar data allows us to characterize the materials that make up the internal structure of the satellites. However, presently our understanding of the composition and thermal state of such icy crusts are poorly constrained - as we will explore in detail in the next chapter. This ambiguity makes the detection of liquid water using radio waves very difficult. Therefore, it is of paramount importance to perform systematic measurements of the dielectric properties of a large set of icy materials having different salt composition and temperature, to define the range of penetration of the radar signals in different scenarios and to assess the detectability limit of the water. To reach this goal, as a first step, it is important to determine the dielectric properties of pure water ice in the frequency range typical of planetary radar sounders (1-100MHz). This is precisely the aim of the Work Package 1 of the SWIM (Surfing radio Waves to detect liquId water in the solar systeM) project, led by Professor Elena Pettinelli's team at the Planetary Ice Physics Laboratory of the Department of Mathematics and Physics at Roma Tre University, in which my work is taking place. These measurements are very challenging, but at the same time they represents a fundamental step for the other WPs of the project, and will also provide fundamental datas for ice physics research. To overcome the difficulties and significantly improve the reliability of the measurements (especially at very low temperatures), methods will first be developed to create ice with highly reproducible physical characteristics, with sample quality (i.e., structural defects) monitored using CT microtomography. Multi-instrument measurements will then be performed - simultaneously and under the same environmental conditions - to assess the dielectric behavior of pure water ice in the 1-100MHz frequency band. The scope of this work was to optimize the laboratory procedure to assess such properties, combining X-ray computed microtomography images with low/high frequency dielectric measurements. In the beginning the experimental work was focused on defining a procedure to produce polycrystalline Ih ice samples, minimizing the presence of defects like air bubbles and cracks, which are known to affect the results of the dielectric measurements. To reach this goal different samples were prepared using different sample holders and cooling rate, and then analysed qualitatively and quantitatively using microtomography. Once the best procedure to minimize ice defects was assessed, samples of pure ice were produced in a climatic chamber in two different measuring cells, the microtomography and a dielectric cells, to test the possibility to perform structural analysis and dielectric measurements on the same type of ice. Dielectric measurements were tested using both a capacitive cell connected to an LCR-meter instrument and a coaxial line connected to a VNA. The results of this work confirm that this procedure can be successfully applied to control the integrity of the sample and to assess, at the same time, the dielectric properties of the ice. However, to better explain the results obtained from this experimental work and to clarify the importance of carrying out such investigations, it is necessary to first introduce some fundamental concepts of pure ice physics - both from a dielectric and structural point of view.

References: [1] Bjerrum N., Structure and properties of ice, K. dankse Videnks. Selks. Mat.-fis. Medd. 27 (1), 3-56, 1951. [2] Bjerrum N., Structure and properties of ice, Science, N.Y. 115, 385-90, 1952. [3] Carte A. E., Air Bubbles in Ice, Proc. Phys. Soc. 77 757, 1961. [4] Eigen M., De Maeyer L., Self-dissociation and protonic charge transport in water and ice, Proc. Roy. Soc. Lond. A 247, 505-33, 1958. [5] Eigen M., De Maeyer L., Spatz H.C., Über das kinetische Verhalten von Proto- nen and Deuteronen in Eiskristallen, Berichte der Bunsengsellschaft 68, 19-29, 1964. [6] Grosso G., Pastori Pallavicini G., Solid State Physics, Second Edition, Aca- demic Press, 2014. [7] Fletcher N.H., The Chemical Physics of Ice, Cambridge University Press, 1970. [8] Levi L., Milman O., Suraski E., Electrical conductivity and dissociation constants in ice doped with HF and NH_3 in different ratios, Trans. Faraday Soc. 59, 2064-75, 1963. [9] Pettinelli E., Cosciotti B., Di Paolo F., Lauro S.E., Mattei

E., Orosei R., Vannaroni G., Dielectric properties of Jovian satellite ice analogs for subsurface radar exploration: A review, Reviews of Geophysics, 2015.
[10] Sihvola A., Electromagnetic Mixing Formulas and Applications, Iet Electromagnetic Waves Series 47, The Institution of Engeneering and Technology, 1999.

Laboratory investigation of ice analogs including O_2, to constrain the surface composition of Solar System icy moons A. Migliorini[1] , Z. Kanuchova[2], S. Ioppolo[3], L.E. Borchert[3], G. Strazzulla[4], F. Tosi[1], G. Piccioni[1]
[1]Institute for Space Astrophysics and Planetology, INAF, Italy; [2]AstronomicalInstitude of SAS, T. Lomnica, Slovakia; [3]Aarhus University, Denmark; [4]Catania Observatory, INAF, Italy.

Introduction: Molecular oxygen has been observed on the surface of the icy Galilean moons, from ground and space [1, 2, 3, 4]. Two absorption bands at 577.5 nm and 627 nm were identified. Based on laboratory experiments, the observed features have been reckognized as the result of a double transition between adjacent molecules [i.e. 5, 6]. This requires a high quantity of O_2 that has to be constantly replenished on these surfaces. However, a debate is still open about the origin and maintenance of this molecule on the surface of the Galilean moons, because the surface temperature is higher than the sublimation temperature for O_2 that would not allow keeping the molecule on the surface in the solid phase.

In order to help answering this question, we performed laboratory experiments on pure O_2 ice and mixtures with ices analogs of the Solar System moons, including H_2O, CO_2, N_2, CH_4, NH_3 and CH_3OH, to investigate the properties of these surfaces after irradiation and annealing.

Laboratory experiments: Experiments were performed using the ultra-high vacuum apparatus mounted on the AU-UV beam line at ASTRID2 synchrotron facility, covering overall the 200-700 nm spectral band [7]. To prepare the samples, oxygen was first introduced into the vacuum chamber to form an O_2 ice layer, and then the second species was deposited on top of it at 8 K. This approach was used to create stratified ice layers and to study the role of each layer in the icy moons of the Solar System. Icy samples were subsequently irradiated with 1keV electrons and V-UV absorption spectra were acquired at selected irradiation steps and at temperatures during subsequent heating, up to the complete sublimation of the ice. Using this method, a possible diffusion of O_2 molecules through the unaltered or top-irradiated ice was studied.

Results: Thanks to four laboratory campaigns in 2019, 2021, 2023, and 2024 we have obtained spectra of pure O_2 ice layers and its mixtures with H_2O, N_2, CO_2, N_2, CH_4, NH_3 and CH_3OH, so far, in the vis range for different mixtures, exploring the temperature range 8-80K, when possible [4, 8].

In the pure O_2 spectra, the two O_2 bands at 577.3 and 627.5 nm are visible, while for temperatures higher than 35 K the bands disappear because of O_2 desorption. We reported slight changes in the band shape and position with temperature, in agreement with [5], as well as differences in the relative intensities of the two bands.

In the mixtures, we observed that the spectral profile, shape, relative intensities, and peak position of the two O_2 bands vary as a function of the mixing ratios, ice composition, and temperature. A blue shift of the band centers on the order of 2 nm is observed with increasing temperature in all the considered mixtures, when O_2 is the dominant species. Spectra of the O_2:CH_4 mixture (1:1) and (10:1) are shown in Figures 1 and 2, respectively, as an example. As it can be seen, the position of the two bands, indicated by the vertical lines in Figure 1, does not change with increasing temperature for the mixture O_2:CH_4 (1:1), while the peaks are blue shifted in the case of (10:1) proportion of the two species (see vertical lines in Figure 2).

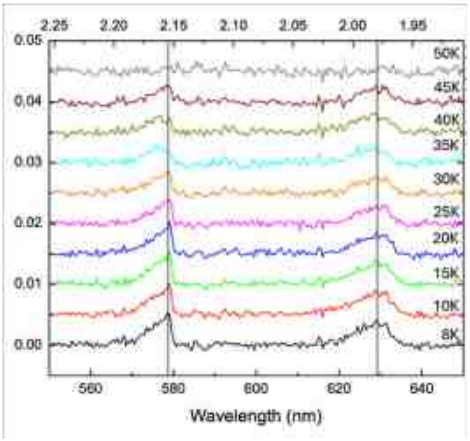


Fig. 1. Spectra of the mixture O_2:CH_4 (1:1) at temperatures in the range 8-50K. The O_2 (1,0) and (0,0) absorption features at 577.5 and 627 nm are observed up to 45K, with similar relative intensities.

Furthermore, in the case of mixtures including NH_3 and CH_3OH, the (1,0) band shape changes from the α- to β-phase with increasing temperature, still compatible with the icy form.

In the present work, we also show comparison with the spectrum of Ganymede, obtained with ground-based facilities, confirming that the observed O_2 bands are likely a combination of the different ice forms, following [5], supporting the idea that O_2 might be trapped in a cold subsurface layer within the Ganymede's icy surface [9].

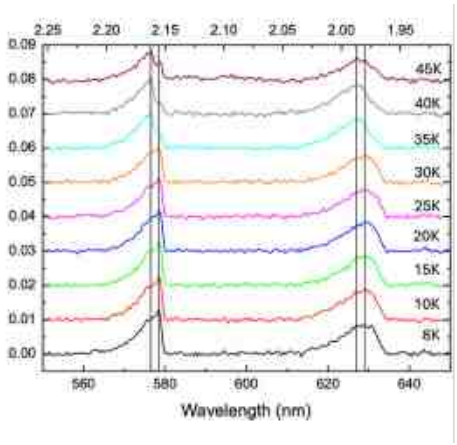


Fig. 2. Spectra of the mixture O_2:CH_4 (10:1) at temperatures in the range 8-45K. Vertical lines indicate the position of the band centers. The position of band centers is shifted by about 2 nm towards the shorther wavelengths with increasing temperatures.

The presented laboratory investigation contributes to build-up a background for the future interpretation of data acquired with the MAJIS instrument [10] on board the ESA JUICE mission.

Acknowledgement: The research presented in this work was supported by ASI-INAF agreement nr. 2023-6-HH.0.

References:

[1] Spencer et al. (1995), *J. Geophys. Res. Planets* 100 (E9), https://doi.org/10.1029/95JE01503;
[2] Spencer and Calvin (2002) *ApJ* 124, https://doi.org/10.1086/344307;
[3] Trumbo et al. (2021) *Planet. Sci. J.* 2, https://doi.org/10.3847/PSJ/ac0cee;
[4] Migliorini et al. (2022) *Icarus* 383, https://doi.org/10.1016/j.icarus.2022.115074;
[5] Landau et al. (1962) *Spectrochim. Acta* 18, https://doi.org/10.1016/0371-1951(62)80047-2;
[6] Mason et al. (2006) *Faraday Discuss.* 133, https:doi.org/10.1039/B518088K;
[7] Kanuchova et al. (2025) *Astron. Astrophys.* 517, https://doi.org/10.1051/0004-6361/201014061;
[8] Migliorini et al. in prep.
[9] Vidal et al. (1997) *Science* 276, https://doi.org/10.1126/science.276.5320.1839;
[9] Piccioni et al. (2019), In: *2019 IEEE 5th International Workshop on metrology for AeroSpace,* https:doi.org/10.1109/MetroAeroSpace.2019.8869566.

Mafic Mineralogy in the VNIR, support of synthetic or peculiar composition to the mineralogical analysis of remote sensed surfaces. C. Carli[1], F. Carraro[1], G. Giuli[2], V. De Santis[2], M. Rondinelli[2], A. Migliorini[1], S. Fonte[1] [1]IAPS-INAF (Via del Fosso del Cavaliere 100, 00133, Rome; cristian.carli@inaf.it), [2]School of Science and Technology, Geology div., University of Camerino (Via Gentile III da Varano 7, 62032 Camerino).

Introduction: Surface of differentiated planets, as well as several asteroid types (S-Type, A-Type, V-Type, etc) are mineralogicaly characterized in the visible to the near-infrared (VNIR) mainly by the evidence of absorption features which could be attributed to mafic minerals, i.e. olivine and pyroxene. Those mineral phases are mainly characterized in VNIR spectral range by absorption features attributed to Fe^{2+} in octahedral site, M1 and M2. Those absorptions are recognized on different planetary surfaces (e.g. [1], [2]) or asteroids (e.g. [3]) and terrestrial analogues or meteorites spectra are used to constrain the retrieved mineral composition. Nevertheless, terrestrial analogues material (e.g. rocks, minerals, systematic mineral mixtures) are affected by differences in mineral chemistry, and in particular by Fe^{2+}/Fe^{3+}, which is not constrained by the main pyroxene absorption (in general called Band I and Band II since they occurred closer to 1 μm and 2 mm). In addition, synthetic mafic mineral and extraterrestrial material, produced at controlled fO_2, where Fe^{3+} is negligible, shows the presence of interesting weak spin forbidden absorptions (e.g. [4], [5], [6]) Moreover, bodies closer to the Sun, i.e. Mercury and Near Earth Asteroids, could be formed at reduced condition where mafic minerals are almost iron-free, revealing potential other absorption features as suggested by [7].

Mafic phases are often cogenetic and their relative abundances permit to define different rock types. In literature different approaches of data analysis and relationships between spectral indicators have been used to describe the variability with respect of mineral chemistry and relative abundances between different mafic phases (e.g. [8], [9]). Nevertheless, those relationships are defined with respect to peculiar pyroxene or olivine compositions.

Here, we preliminary report a work on synthetic and peculiar mafic mineral compositions. We compare our results with previous published mafic mineral spectra of similar composition to remark differences from terrestrial and synthetic analogues by using all the different present absorptions as well as the different spectral indicators in a more systematic way.

Methods, Sample and Analytical approach: Reflectance spectra of new samples are acquired at Spectroscopy LABoratory at IAPS-INAF, where a Fieldspec Pro is coupled with a goniometer. The data cover the spectral range 0.35–2.50 μm with a spectral resolution of 3 nm in the VIS and 10 nm in the NIR, at fixed illumination and emergency angles of 30° and 0°, respectively. The source was a QTH lamp and the spot illuminated had a diameter of about 6 mm. The standard reference calibration was performed with a Spectralon optical standard 99%. Spectra are an average of 200 acquisitions.

Samples are synthetic orthopyroxenes from [10], synthetic olivine [11], Chromium diopsides from Bellecombe (Aosta) and from Chamachhu (Pakistan) and Aegirine from Malawi [12]. They were ground and sieved at grain size smaller than 100 μm, for each sample we acquired three spectra which are than averaged.

The spectra after the acquisition have been correct with respect to the continuum, which was subtracted following the approach used by [13]. We calculated than Band Center, Band Depth, Band Width and Band Area using the Hyperlab web app (https://hyperlab.iaps.inaf.it/) [14].

Preliminary Results: In figure 1a we can see the systematic variation of synthetic orthopyroxene after continuum removal, whereas figure 1b highlights the reflectance spectra of spin forbidden absorptions. Here the characterized synthetic pyroxenes have a well defined occupancy data obtained by Rietveld structure refinement [10], which was not present in past reflectance work about synthetic orthopyroxene [4], suborting the attribution not only of Band I and Band II, but also of the weaker spin forbidden bands. The main spectral parameters will be calculated for all of them comparing with previous published synthetic and natural pyroxene.

Figure 2 instead shows the comparison of two olivine, one at Mg,Fe with Fo50, whereas the other is a Ca,Fe peculiar olivine found also in angrite meteorites. The spectra show the main absorption, but the Ca,Fe olivine have a less symmetric and a band minimum shifted at lower wavelengths. They also shows both the spin forbidden in a different position with respect to orthopyroxene and some differences are visible also between the two synthetic olivines.

Future Comparison: We will discuss the variation of the spectral indicators of the different absorptions from the measured spectra, taking into account also literature data of mafic minerls, synthetic or natural, similar to those present in this work, and analysed with the same approach and tool. We will arise of parameters, such as Band center of Band I and II varies, as well as, Band Areas and Band Area Ratio change for the different phases. Moreover we

will introduce relationship from spin forbidden to Band I and II. This discussion should support a revision of the used spectral indicators and the relative interpretation for pyroxene-olivine bearing rocks and relative surface of parental bodies.

References:

[1] Carli C. et al. (2025) RemoteSensing, 17 (22), 378x; https://doi.org/10.3390/rs1722378x [2] Poulet F. et al. (2007) J.G.R. E08S02. https://doi.org/10.1029/2006JE002840. [3] Ammanito E. et al. (2012), M.&P.S. 48, 2185–2198. https://doi.org/10.1111/maps.12192. [4] Klima R. et al. (2007) M.&P.S. 42 (2), 235–253. https://doi.org/10.1111/j.1945-5100.2007.tb00230.x [5] Carli C. et al. (2018) M.&P.S. 53, 2228-2242, https://doi.org/10.1111/maps.13056. [6] Migliorini A. et al. (2021) MNRAS 2021, https://doi.org/10.1093/mnras/stab332. [7] Lucchetti A. et al. (2018) JGR, 123, 2365–2379. https://doi.org/10.1029/2018JE005722. [8] Cloutis E. et al. (1986) J.G.R. 96, 22809–22826. https://doi.org/10.1029/91JE02512. [9] Cloutis E. et al. (1991) J.G.R. 91 (B11), 11,641–11,653. https://doi.org/10.1029/JB091iB11p11641. [10] Giuli G. et al. (2002) E.J.M. 14, 429–436. Doi: 10.1127/0935-1221/2002/0014-0429. [11] Wu et al. (2004) Phys. Rev. B 69, 104106, https://doi.org/10.1103/PhysRevB.69.104106. [12] Amathauer G and Rossman G. R. (1984) Phys. Chem. Miner, 11, 37–51, https://doi.org/10.1007/BF00309374. [13] Clark R. and Roush T. (1984). J.G:R. 89, 6329–6340, https://doi.org/10.1029/JB089iB07p06329. [14] Carraro F. et al. (2025) EGU25-8332 https://doi.org/10.5194/egusphere-egu25-8332.

Acknowledgments: C.C., F.C., S.F. were supported by INAF 2023 under the 'Call for Funding of Fundamental Research 2023', in the Data Analysis Grant category. G.G. V.DS., M.R. were supported in this study by the Space It Up project funded by the Italian Space Agency, ASI, and the Ministry of University and Research, MUR, under contract n. 2024-5-E.0 - CUP n. I53D24000060005. C.C. and A.M. were supported by ASI agreement n. 2022-8-HH.0 for ESA's Hera mission.

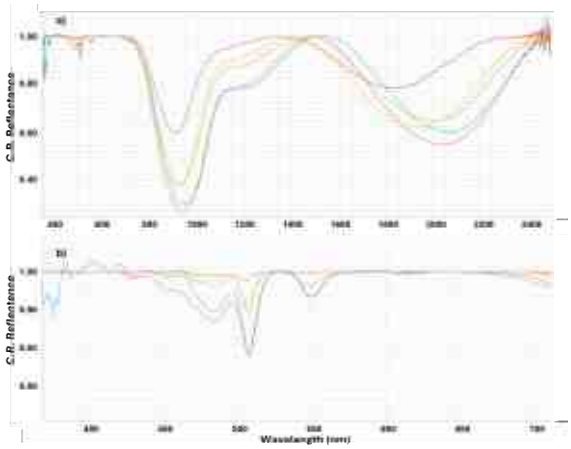


Figure 1 – Continuum removed reflectance spectra from this work of different synthetic pyroxene from [10]. a) full measured spectral range with two main absorptions; b) inset of spectral range from 400-700 nm to highlight the variation of spin forbidden absorption. En90: red; En60: yellow; En40: green; En20: orange; En0: cyan.

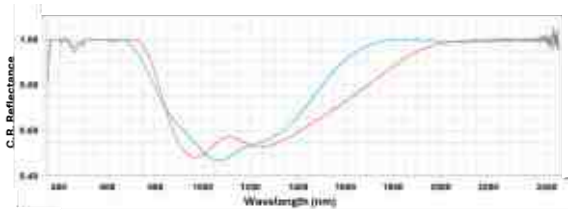


Figure 2 – Continuum removed reflectance spectra of olivine synthetic composition. Cyan is a Fo50 with a typical olivine spectrum ($MgFe[SiO_4]$) , whereas orange is a kirshsteinite ($(CaFe[SiO_4])$) found also in angrite meteorite. Kirshsteinite show a wide absorption like Fo50 but less symmetric with a minimum at lower wavelength. Spin forbidden are present in both cases but different from those of pyroxene (e.g. [5]).

MARTIAN SIMULANTS FOR GUSEV AND GALE CRATERS IGNEOUS PRODUCTS: RHEOLOGICAL, MINERALOGICAL AND SPECTRAL CHARACTERIZATION.

Alessandro Pisello[1], Maximiliano Fastelli[1], Bernard Schmitt[2], Pierre Beck[2], Olivier Poch[2], Francesco P. Vetere[3], Paola Comodi[1] and Diego Perugini[1].

[1]Department of Physics and Geology, University of Perugia, I-06100 Perugia, Italy
[2]Univ. Grenoble Alpes, CNRS, IPAG, 38000 Grenoble, France
[3]Dipartimento di Scienze Fisiche, della Terra e dell'Ambiente (DSFTA), University of Siena, Via Laterina, 8, 53100 Siena, Italy

Introduction:

The most common type of rock present on the surface of terrestrial planets in the Solar System are volcanic-magmatic rocks, which are constituted by lava flows and fragmented pyroclasts whose texture presents both glassy and crystalline silicate phases.

Planet Mars is, besides the Earth, the most diverse terrestrial planet in the Solar System, presenting magmatic rocks with compositions ranging from ultramafic/basaltic to alkaline/trachy-andesitic [1].

Understanding the influence that chemical composition and different phases (both crystalline and amorphous) have on the spectral response of volcanic rocks is pivotal to deduce remotely sensed spectra that are commonly used to interpret the geology of terrestrial planets. Thus, we synthesized Martian simulants with two putative Martian compositions, on which we performed cooling experiments together with a rheological, mineralogical and spectral characterization in order to provide a reference to interpret the geological processes that have occurred on Mars.

Methods:

Samples were created by mixing powdered oxides to mimic the composition (Table 1) of volcanic rocks/powders from Gusev and Gale craters, as they were hypothesized from data belonging to different missions [1].

Table 1: Composition of the starting materials accounted

	Gusev	*Gale*
SiO2	47.33	52.04
TiO2	0.57	0.66
Al2O3	11.19	15.83
FeO	19.12	10.89
MnO	0.42	0.18
MgO	10.29	4.44
CaO	8.17	6.76
Na2O	2.76	7.06
K2O	0.14	2.14

The powders were molten at 1450°C to form a silicate melt, which were then quickly cooled to produce glasses.

Then, for each of the produced glasses three cooling experiments were conducted in a Gero HTRV 70-250/18, equipped with Anton Paar rheometer [see 2 for reference]. Powdered glass was brought to superliquidus temperature and, after having reached the equilibrium, it was cooled down at a 100°C/h rate to crystallize. Crystallization was monitored through the measurement of viscosity during cooling, so that three phases were individuated and sampled: (1) the point at which crystals start nucleating, (2) the point at which crystal were grown and (3) a final point of advanced crystallization where viscosity was not measurable anymore due to extreme rigidity of the samples (see arrows in Fig. 1).

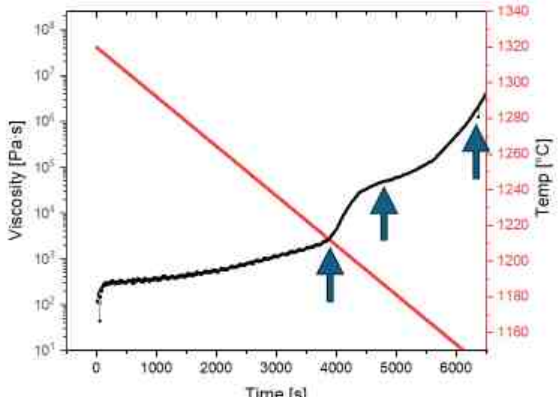


Figure 1: Example of Viscosity path during cooling for Gale simulant. Arrows indicate stages at which experiments were stopped.

The synthesized samples were analyzed using X-ray powder diffraction (XRPD), and quantitative phase analysis (QPA) was performed using the Rietveld [3] profile fitting method with internal standards to determine amorphous content [4].

Spectral analyses:

Reflectance spectra were collected at the Cold Surface Spectroscopy (CSS) facility (https://cold-spectro.sshade.eu) located at the Institut de Planétologie et d'Astrophysique (IPAG), Grenoble, France. The instrument used was the SHINE Spectro-Gonio Radiometer. The instrument is equipped with a cryogenic simulation chamber, CarboN-IR, to control the temperature of the samples. Spectra were collected in the 1-4.2 μm spectral range at different low temperatures between 105 and 290 K. The sample is cooled to a given temperature and then held for about 5–10 min under few millibars of dinitrogen to wait for thermal equilibrium and then during the measurement time, about 65–80 min depending on

some acquisition parameters. We kept each sample for 70–90 min at a given temperature before starting our measurements.

First results and future perspectives:

The three products synthesised from Gusev's chemical composition show evidence of magnetite, clinopyroxene, and orthopyroxene as the main crystalline phases with an amorphous content ranging from 100 to 70% by weight. The products synthesised from Gale's chemical composition are characterised by clinopyroxene and magnetite as the main mineralogical species with a glass content between 100 and 60% by weight.

Preliminary spectral investigations suggest us that for samples with identical bulk chemical composition but different mineralogical assemblage, the spectral response within Visible and Near InfraRed (VNIR) and mid-infrared (MIR) is deeply different. VNIR spectra are influenced by the nucleation of iron-related phases, whereas MIR spectra are dependent on Si-bearing phases.

The mechanism influencing the shape of spectra results in fact, from a complex interaction of the spectral response of different mineral/amorphous phases. In this way, the shape is easily misinterpreted as the features of the different phases, which are often no longer recognizable. An in-depth analysis has helped us understand which characteristics can be taken into consideration when interpreting this type of igneous material, but a more comprehensive study of the different compositions is needed for a complete evaluation of this approach.

Spectral characterization at low temperature is currently ungoing and will shed light on the influence of temperature on the detection of silicate phases.

References:

[1] McSween Jr, H. Y. (2015). Petrology on mars. American Mineralogist, 100(11-12), 2380-2395. [2] Vetere, F., Petrelli, M., Perugini, D., Haselbach, S., Morgavi, D., Pisello, A., ... & Holtz, F. (2021). Rheological evolution of eruptible Basaltic-Andesite Magmas under dynamic conditions: The importance of plagioclase growth rates. *Journal of Volcanology and Geothermal Research*, *420*, 107411. [3] Rietveld H. M. (1969) *Appl. Cryst* 2.2: 65-71 [4] De la Torre A. G. (2001) *Appl. Cryst.*, 34(2), 196-202.

Additional Information:

This work was carried on thanks to ASI-UniPG agreement 2019-2-HH.0 and in the framework of Trans-National Access research project selected and funded by Europlanet-2024 RI (European Union’s Horizon 2020 RI under grant agreement No. 871149). We also acknowledge the support from MUR in the framework of SUPER-C, ‘Dipartimento di Eccellenza 2023-2027’.

CHARACTERIZATION OF AN EXOMARS MISSION REFERENCE GYPSUM SAMPLE USING PAYLOAD-ANALOG TECHNIQUES. S. Biancalani[1,2,3,4]; T. Fornaro[4], C. García-Florentino[4], G. Poggiali[4], L. Coloma[5], F. Alberquilla[5], A. Alberini[4], J. Aramendia[5], J. M. Madariaga[5], G. Pratesi[3], M. Bellucci[2], F. Renzi[4], M. Battistuzzi[4], and J. R. Brucato[4], [1]Department of Physics, University of Trento, Via Sommarive 14, 38123 Povo, Trento, Italy, sole.biancalani@unitn.it; [2]Italian Space Angency (ASI), viale del Politecnico snc, 00133, Rome, Italy; [3]Department of Earth Sciences, University of Florence, via G. La Pira 4, 50121, Florence, Italy; [4]INAF–Astrophysical Observatory of Arcetri, L.go E. Fermi 5, 50125 Florence, Italy; [5]Department of Analytical Chemistry, Faculty of Science and Technology, University of the Basque Country (UPV/EHU), Barrio Sarriena s/n, 48940 Leioa, Spain.

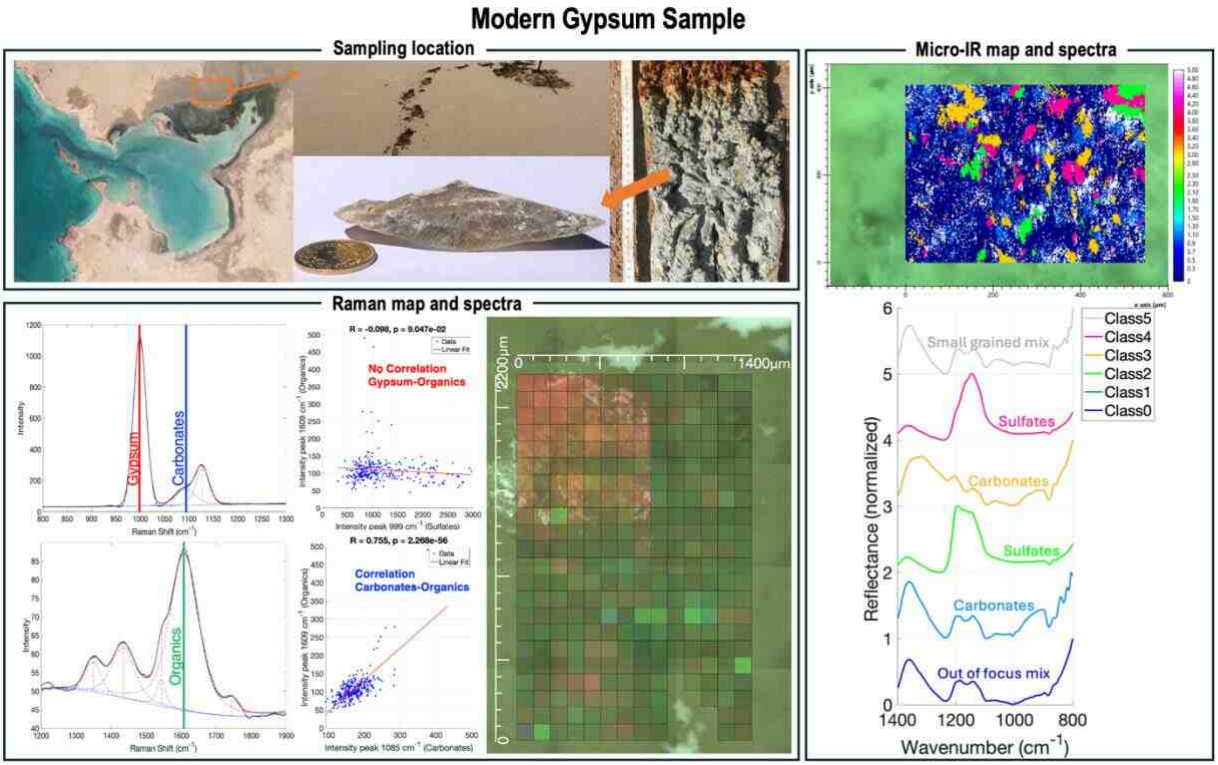


Figure 1 Sampling location of the gypsum crystals (courtesy of T. Bontognali), Raman map and spectra with organic-mineral correlation evaluation, and Micro-IR map and reststrahlen region spectra of the clustered minerals.

Introduction: Mars is one of the main focus of astrobiological research because of its complex history and potential for harboring signs of life. Studying Martian geology offers unique insights into the planet's past environments, which might have been favorable for life due to its past Earth-like conditions[1,2].

The oldest rocks on Mars are still accessible due to the absence of plate tectonics, and thus may provide evidence of past life[3]. This hypothesis drives current and future exploration missions, like the ExoMars program and NASA's Mars 2020, which aim to detect and understand biosignatures that may be preserved in subsurface Martian rocks[4,5]. The dataset assembled by these and other space missions make the study of terrestrial analogs for Martian soil of critical importance.

Laboratory studies of analogs provide data to interpret Martian surface and subsurface samples as well as a controlled environment for studying the potential preservation of biosignatures in Martian rocks and regolith. In this framework we present new result on the multi-technique characterization of analog material included in the ExoMars mission reference sample dataset.

Material and Methods: The samples were collected by Tomaso Bontognali for the ExoMars Mission Reference Sample Campaign in the Dohat Faishakh sabkha (Qatar) and consist of gypsum crystals formed in a modern evaporitic environment. The samples were crushed with a "MOMA-like" Jaw Crusher (slit 0.3 mm) at MPS, and then shipped to the laboratories in sterile vials.

The characterization of the samples was conducted using payload-analog instruments for ExoMars' Rosalind Franklin and Mars2020's Perseverance rovers, and other advanced techniques

that could be relevant for the NASA-ESA Mars Sample Return mission.

The characterization performed at the INAF-Astrophysical Observatory of Arcetri included: (1) infrared spectrometry with Bruker VERTEX 70v Fourier Transform InfraRed spectrometer (range 8000-400 cm^{-1}, resolution of 4 cm^{-1}); (2) infrared mapping with a Bruker Hyperion 3000 microscope, equipped with a Focal Plane Array (FPA) detector (spatial resolution of 2 μm, range 5000-800 cm^{-1}, resolution of 6 cm^{-1}); (3) 248.6 nm deep UV (DUV) fluorescence with a DUV Raman PL 200 instrument by Photon Systems (spatial resolution 100 μm, 248.6 nm excitation laser, range 250-620 nm, resolution of 1.2 nm); (4) DUV Raman (same instrument, range 300-3500 cm^{-1}, resolution of 10 cm^{-1}).

Further characterization of the samples was done at the IBeA research group of the University of the Basque Country (EHU), by performing: (1) 532 nm and 785 nm Raman analyses with a Renishaw inVia micro-spectrometer interfaced with a Leica DMLM microscope and a Peltier-cooled CCD detector (spatial resolution ~1 μm, depending on the chosen laser wavelength and objective, range 100-4000 cm^{-1}, spectral resolution of 1 cm^{-1}); (2) elemental composition distribution mapping from sodium to americium ($_{11}$Na-$_{95}$Am), using a Bruker Tornado M4 Energy Dispersive X-ray Fluorescence spectrometer (Bruker Nano GmbH, Berlin, Germany) equipped with an XFlash® silicon drift detector with an energy resolution of 145 eV at Mn Kα and 25 μm of spatial resolution.

Results and discussion: Mineral characterization showed mainly gypsum with carbonates (dolomite and aragonite) and with minor presence of quartz and smectites. Micro-IR mapping allowed the detection of 20-40μm sulfate and carbonate grains. Organics were detected using DUV and green Raman spectrometry, with positive spatial correlation with carbonates, while no correlation was found between organics and sulfates. DUV Fluorescence main signal was assigned to organics. In the IR analyses, the organic detection was not possible because the C-H stretching bands were covered by stronger carbonate bands. The spatial co-location of the IR, DUV Raman and DUV fluorescence maps confirmed the correlation between organics and carbonates in this sample.

This pattern, consistent with previous studies[6], may represent an actual biosignature, further supported by microfossil evidence and features suggesting past microbial activity detected by the preliminary analyses of the sample.

The comparative detection performances of the techniques employed and the possible impact on the rovers' analyses and choice of the targets will be discussed.

Acknowledgements: This work was supported by ASI/INAF 2023-3-HH.0 agreement. This abstract and related research have been conducted during and with the support of the Italian national inter-university PhD programme in Space Science and Technology. The funding of the PAMMAT project "*Alteration processes in Mars and Moon Meteorites, and Terrestrial Analogues at different environments: Mars2020, Rosalind Franklin and Returned Samples from Mars and Moon*" (Grant No. PID2022-142750OB-I00, Spanish Agency for Research/ Spanish Ministry of Science and Innovation/ European Regional Development Fund, DOI: MCIN/AEI/10.13039/501100011033/FEDER,UE) is acknowledged.

References: [1] Ardvison R. E. et al. (2014), Science, 343, 6169. [2] Grotzinger J. P. et al. (2014), Science, 343, 6169. [3] Williford K. H. et al. (2018), Elsevier, 275-308. [4] Farley K. A. et al. (2020), Space Science Reviews, 216(8), 142. [5] Vago J. L. et al. (2017), Astrobiology, 17(6-7), 471-510. [6] Brauchli M. et al. (2016), Carbonates and Evaporites, 31(3), 339-345.

Ma_MISS SPECTROSCOPIC MEASUREMENTS ON THE EXOMARS/RFM MISSION REFERENCE SAMPLES

[1]M. Ferrari, E. [1]Bruschini, [1]S. De Angelis, [1]M. C. De Sanctis, [1]F. Altieri, [2]E. Ammannito
[1]INAF-IAPS, Via del Fosso del Cavaliere, 100, 00133, Rome, Italy (marco.ferrari@inaf.it); [2]ASI, Via del Politecnico snc, 00133, Rome, Italy.

Introduction: Identifying and characterizing ancient habitable environments on Mars is a primary challenge in planetary exploration. Within this framework, the ESA/NASA ExoMars/Rosalind Franklin Mission (RFM) is designed to search for biosignatures in ancient, well-preserved martian sedimentary settings. The Rosalind Franklin rover combines a drill capable of reaching 2 m depth with an integrated suite of scientific instruments, enabling the analysis of both the geologic context and subsurface samples that are comparatively shielded from surface degraders such as ultraviolet radiation and oxidants (Vago et al., 2017). Validating instrument responses and performance on terrestrial analog samples is therefore essential to set realistic detection thresholds and operational strategies. In particular, Ma_MISS (Mars Multispectral Imager for Subsurface Studies), integrated into the drill string, acquires 0.5–2.3 μm reflectance spectra directly from borehole walls during drilling, providing in situ access to composition, hydration state, grain size, and stratigraphic discontinuities (De Sanctis et al., 2017).

Here we report on a coordinated Mission Reference Samples (MRS) measurement campaign led by the Rover Science Operations Working Group (RSOWG) Micro group, in which a sample suite was selected to bracket the mineralogical and textural variability expected at Oxia Planum, the landing site of the mission (Mandon et al., 2021; Fawdon et al., 2024). Crucially, each sample was prepared as shared aliquots to be measured across the entire rover payload, enabling cross-payload sample characterization and end-to-end operations rehearsals that connect laboratory protocols to the in situ observations planned for Oxia Planum.

Sample Selection: Within the ExoMars/Rosalind Franklin Mission (RFM) Sample Measurements Campaign, 16 representative Mission Reference Samples (MRS) were selected from 31 proposals. Selection followed a dedicated international workshop of the Rover Science Operations Working Group (RSOWG Micro group), where members of the ExoMars science community presented candidate samples with details on mineralogical composition, formation environment, physical properties, and prior laboratory characterizations. Each sample received an ExoMars Biosignature Score (EBS; Vago et al., 2017), a qualitative index of its potential to preserve or exhibit biosignatures detectable by the rover payload. The primary criterion was relevance to the compositional and sedimentological characteristics of the geological units identified at Oxia Planum, ensuring each specimen could serve as a terrestrial analog for preparatory on-ground measurements.

Among the selected materials, three were provided as controlled pairs to enable direct comparisons: EM08/EM08P (reference vs organic-bearing), OPSA_blank/OPSA_org (without vs with organics), and Modern gypsum/ Modern gypsum washed (as collected vs specific treatment). The full list of the 16 MRS used in this Ma_MISS measurement campaign is reported in Table 1.

PROPOSER	SAMPLE
A. Azua-Bustos	Atacama Red Stone
J. Bridges	Watchet Bay, gypsum-veined playa/floodplain
B. Bultel	Granby, vermiculite-bearing hydrothermal basaltic tuff
M. Ferrari	Cap-1, subsurface hydrothermal/pedogenic clay
E. Javaux	Proterozoic mudstone with MISS
	1KN34, Proterozoic mudstone with microfossils
A. Krzęsińska	Otago, vermiculite preserving organic matter; altered Fe-chlorite schist
D. Loizeau	Iceland, recent lava with morphological biosignatures
L. Whyte	University Valley, Antarctic permafrost
	Lost Hammer Spring sediments, sub-zero hypersaline methane seep; subsurface life analogue
T. Bontognali	Modern gypsum with prokaryotic biomarkers
	Modern gypsum, washed version
T. Fornaro	OPSA-org Oxia Planum laboratory analogue doped with organics
	OPSA-blank, reference version of OPSA-org
F. Westall; S. Adeli	EM08P, artificial Martian volcanic sediments with salts and organics
	EM08, reference version of EM08P

Table 1. List of the 16 selected Mission Reference Samples, with the proposer name.

Experimental setup: VIS–NIR spectra were acquired primarily with the DAVIS_MOT (Drill for Analogues and Visible Infrared Spectrometer_Ma_MISS Optical Tool; De Angelis et al., 2022), a laboratory replica of the Ma_MISS instrument that reproduces the flight optical performance. This system provides a focal distance of 0.6 mm, an illumination spot of ~1 mm diameter, and an effective spatial resolution of 120 μm. The operating spectral range is 0.4–2.2 μm, which is slightly different than the flight instrument due to the coupling with two Avantes commercial spectrometers.

For this study, DAVIS_MOT was used in static mode to perform single-point acquisitions on unbored sample surfaces. For each specimen, 10 spatially distributed spots were measured to capture sub-millimetric heterogeneity and to assess signal stability/reproducibility. To provide a spectroscopic comparison baseline, we also measured the samples with an ASD FieldSpec 4 (0.35–2.5 μm). For each sample, 10 repeat acquisitions were averaged to improve SNR, and a Spectralon 99% reference calibration was applied.

Results: VIS–NIR measurements acquired with DAVIS_MOT and FieldSpec 4 on the Mission Reference Samples consistently point to matrices dominated by Fe/Mg-bearing phyllosilicates, with subordinate contributions from hydrated salts, sulfates, and Fe-bearing phases. The spectra systematically express the main clay- and water-related absorptions expected for such assemblages, together with iron-related features in the visible and near-infrared range.

Comparisons between organic-doped materials and their inorganic counterparts demonstrate that the Ma_MISS instrument is sensitive to very weak organic contributions embedded in fine-grained matrices, down to sub-wt% levels. In the paired samples, the presence of organics is expressed as subtle additional structure in the near-infrared region classically associated with C–H overtones and combination modes, superimposed on the common clay–H_2O spectral pattern shared with the corresponding blank materials. These differences are reproducibly observed with both DAVIS and FieldSpec 4, indicating that they are linked to the introduced organics rather than to variations in the mineral framework.

Measurements on paired samples with identical mineralogy but different water content further show that the Ma_MISS configuration is capable of resolving small variations in hydration state, even when the bulk mineral assemblage remains unchanged. Overall, the dataset confirms that Ma_MISS VIS–NIR spectroscopy can jointly constrain first-order mineralogy and hydration while retaining sensitivity to weak organic signatures in ExoMars/RFM-relevant analogs.

Conclusions: VIS–NIR measurements on the Mission Reference Samples consistently reveal a first-order mineralogy dominated by Fe/Mg phyllosilicates, with additional hydrated salts, sulfates, and Fe-bearing phases.

Differences between DAVIS_MOT and FieldSpec 4 are largely confined to very shallow features and primarily reflect spatial scale: DAVIS_MOT resolves sub-millimetric heterogeneity, whereas FieldSpec 4 provides millimetric averages that stabilize the signal.

The DAVIS_MOT results confirm that Ma_MISS will be able to resolve the expected mineralogy at Oxia Planum and provide subtle spectral indications of organics in the shallow subsurface. Coordinated use of CLUPI (textures/coatings), WISDOM (stratigraphy), MicrOmega and RLS (mineralogy), and MOMA (organics) data on these samples will be essential to validate and refine these detections and to prioritise measurements once on Mars.

References: De Angelis et al. (2022), Review of Scientific Instruments, 93, 123704. De Sanctis et al. (2017), Astrobiology, 17(6–7), 612–620. Fawdon et al. (2024), Journal of Maps, 20(1), 2302361. Ferrari et al. (2023), Astrobiology, 23(6), 691–704. Mandon et al. (2021), Astrobiology, 21(4), 464–480.Vago et al. (2017), Astrobiology, 17(6–7), 471–510.

Acknowledgements: This activity is funded in the framework of the Accordo ASI-INAF n. n. 2023-3-HH.0.

IDENTIFYING EARTH ROCK ANALOGS OF OXIA PLANUM IN PREPARATION FOR THE ROSALIND FRANKLIN MISSION. M. Rasmussen[1], A. Frigeri[1], F. Altieri[1], J. Brossier[1], J. Trisic Ponce[1], L. Rossi[1] and M. C. De Sanctis[1]. Istituto di Astrofisica e Planetologia Spaziali, Istituto Nazionale di Astrofisica, INAF-IAPS, Rome, Italy (monica.rasmussen@inaf.it).

Introduction: The ExoMars Rosalind Franklin Mission (RFM) is scheduled to launch by the European Space Agency in 2028 with an expected touchdown at Oxia Planum, Mars in 2030. In its search for evidence of past and present life [1], the Rosalind Franklin rover has been equipped with a drill capable of reaching 2.0 m in the Martian subsurface, which will allow micron-scale spectrometry imaging of the borehole wall using the Mars Multispectral Imager for Subsurface Studies (Ma_MISS) instrument [2]. Ma_MISS will provide novel subsurface data of *in situ* mineralogy and, potentially, biosignatures. The Close-Up Imager (CLUPI) instrument will also provide high resolution imagery of drill site, the drilling cuttings and the first centimeters of the hole [2].

Drill testing: In preparation for RFM, the rover and its equipment have been created in duplicate for terrestrial testing. Drill tests have been conducted on a first batch of analog materials (gypsum, tuff, geyserite) selected primarily for their engineering properties [3], and spectroscopy investigation with the Ma_MISS Laboratory Model (DAVIS) is in progress on these samples [4]. However, the rover will be drilling natural Martian rocks which are inevitably more variable than idealized materials. Further complexity arises when we consider that the landing site is highly eroded, and clay target materials can form *in-situ* or be deposited under various geologic scenarios. Therefore, drilling formations that are analogous to the expected deposits at the landing site will aid in: 1) ensuring drilling operations are successful, 2) allowing informed interpretation of drilling telemetry to better characterize Martian rocks, and 3) providing an appropriate test of Ma_MISS and CLUPI data collection and interpretation capabilities on complex, natural rocks representing reasonable drill site scenarios.

Analog sample selection: We are creating an analog rock sample catalog housed at INAF-IAPS in Rome, where the Ma_MISS Laboratory Model is located. Rock samples are selected and characterized for their relevance to Mars missions. Appropriate samples are selected for the next stage of drilling and data collection, based on common interpretations of the Oxia Planum landing site formation: fluvial-deltaic deposition, lacustrine deposition, subaerial soil formation (pedogenesis), subsurface alteration, and surface or subsurface hydrothermal alteration (e.g., [5]).

Analog sample rocks are first identified based on their depositional environment. For example, we have sampled boulders from the Rio Tinto region , Spain (Fig. 1, [6]), which were deposited in a fluvial environment which is highly acidic. This one sample contains multiple complex features which we are likely to encounter in fluvial-deltaic deposits on Mars: varying grain sizes of hard, quartz-rich sedimentary rock, layered formations, larger pebble inclusions, and highly acidic weathering environments. Other samples will include, e.g., naturally developed volcanic soils, rocks with both hot and cold geothermal alteration, lake deposits containing biological material, and sedimented aeolian rocks.

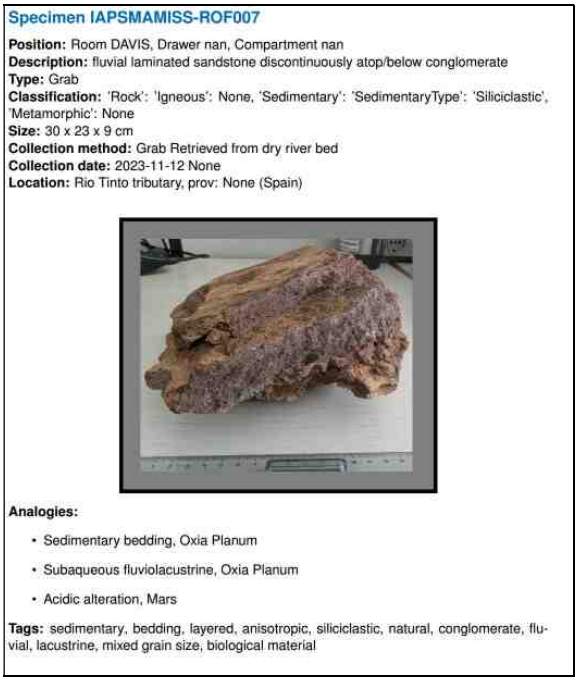


Figure 1: Analog sample catalog page in progress. This boulder was collected from a tributary of the Rio Tinto, Spain. Quantitative data about sample specifications and collection are included, and interpreted analogous environments are listed below. Analog tags are searchable within the database allowing researchers without geologic expertise to identify rocks appropriate for their analytical goals.

Analog scenarios for drill testing: We propose future drill testing configurations that will address realistic geologic scenarios we may encounter at Oxia Planum and represent increasing geological and geotechnical complexity. For example, Pedogenesis is variable depending on source material and climate,

so *in situ* weathering can result in highly variable materials. As an initial test, we will use two relatively uniform deposits to simulate an unweathered basaltic rock with a weathered volcanic ash overlying the deposit (Fig. 2). This scenario is simplified by cutting the rocks horizontally and creating an artificial horizontal boundary between them, allowing a controlled test on drill performance across the soil-rock interface. The upper lithology sample will be particularly useful for understanding the degree to which drill telemetry can be used to interpret lithology, and the capabilities of CLUPI for viewing.



Figure 2: Left, natural basalt weathering profile (photograph by Lisa Worrall). Right, simulation basalt weathering scenario with weathered rock on top (lighter) and unweathered basalt below (darker).

Next, we intend to drill a laminated rock representing deposits in, e.g., high energy fluvial settings and/or aggradational bars. For this scenario the Rio Tinto sample will be used (Fig. 1) due to its gradation from silt sized grains on one side up to pebble-sized clasts. The highly acidic environment of Rio Tinto also provides an interesting biological sample for Ma_MISS analysis.

The third analog drilling scenario represents multiple depositional scenarios: lacustrine deposition, fluvial-lacustrine deposition, or overbank/flood deposits. The analog rock for drilling is siltstone we have collected from the eastern Italian Alps which contains visible laminae, wavy surface features, and approximately 1 mm thickness veins. The veins add an extra level of analysis representing hydrothermal alteration.

Analog Catalog: Analog samples are collected and cataloged in a format similar to the Mineral Identified through CRISM Analysis (MICA) Library [7], allowing the Ma_MISS team to being to incorporate more geologic criteria into test sample selection. Each catalog entry (work in progress shown in Figure 1) contains the collection criteria for the sample, but also interpretations of appropriate analogous environments. These interpretations are discussed and annotated by team geologists and are tied, where appropriate, to particular geologic units or locations within the landing site. Each sample is also tagged with various index parameters, noting that one sample can represent many scenarios and is tagged appropriately. The database is meant to provide consistent data to various teams within the ExoMars mission and beyond.

In conclusion, the sample catalog contains diverse rocks providing the mission team appropriate test cases which are relevant to specific, realistic geologic scenarios at Oxia Planum, Mars.

Acknowledgements: This work is supported by ASI-INAF contract n.2023-3-HH.0 Esplorazione di Marte.

References: [1] Vago J. L. et al. (2017) *Astrobiology, 17*, 471-510. [2] De Sanctis M.C. et al. (2022) *Planet. Sci. J. 3,* 142. [3] Rossi L. et al. (2024) IAC, Paper ID 85365. [4] De Angelis S. et al. (2014) *Planet. and Space Sci.*, 101, 89-107. [5] Brossier J. et al. (2022) *Icarus, 386*, 115114. [6] Frigeri A. et al. (2024) Planetary Analog Workshop, Abstract 2024LPICo3043.8015F. [7] Viviano C. E. et al. (2014) *JGR: Planets*, *119*(6), 1403-1431.

XXI Congresso Nazionale di Scienze Planetarie

Sessione Focus S6

Advanced image processing and Artificial Intelligence/Machine Learning for planetary exploration

UNSUPERVISED MACHINE LEARNING OF FTIR SPECTRA FROM TWO HAYABUSA2 RYUGU PARTICLES REVEALS STRATIFIED REGOLITH EVOLUTION

M. Angrisani[1], M. D'Amore[2], X. Shehaj[3], E. Palomba[1], M. Romani[4], M. Cestelli Guidi[4], T. Catelani[3], A. Longobardo[1], F. Dirri[1] , G. Pratesi[3]

[1]INAF-Istituto di Astrofisica e Planetologia Spaziali (INAF-IAPS) Roma, Italy, (marianna.angrisani@inaf.it); [2] German Aerospace Center Institute of Planetary Research: Deutsches Zentrum fur Luft- und Raumfahrt DLR Institut fur Planetenforschung; [3]Dipartimento di Scienze della Terra, Università degli Studi di Firenze, Firenze, Italy; [4]INFN-Laboratori Nazionali di Frascati;

Introduction: Machine learning (ML) has become a powerful tool in planetary science for handling large, complex, and nonlinear datasets. In spectroscopy, ML methods enable the detection of subtle compositional and textural variations that are often overlooked by conventional approaches such as median or band ratio analyses. Applications could span from orbital hyperspectral remote sensing to laboratory analyses of extraterrestrial materials and returned samples, providing an efficient method to uncover compositional heterogeneity, alteration trends and surface processes.

In this study, we apply unsupervised ML to micro-Fourier Transform Infrared (FT-IR) data acquired from two particles (A0226 and C0242) returned from the C-type asteroid (162173) Ryugu by the Hayabusa2 mission. These particles, collected from different stratigraphic depths (from Touchdown 1 and Touchdown 2) [1], provide a unique window into the asteroid's regolith evolution and the effects of space weathering.

Methods: The Ryugu particles (A0226-1, A0226-2, C0242) were examined via micro-FTIR spectroscopy using custom holders in N_2 to avoid contamination [2]. High-resolution FTIR mapping (2.5–16 µm) targeted OH (~2.7 µm), CH (3.3–3.4 µm), and carbonates (3.4–3.9 µm), with additional Reststrahlen/Christensen signatures.

We analyzed different FT-IR spectral parameters using the Uniform Manifold Approximation and Projection (UMAP) algorithm for nonlinear dimensionality reduction and the Hierarchical Density-Based Spatial Clustering of Applications with Noise (HDBSCAN) algorithm for cluster identification. The resulting 2D UMAP embedding (Fig.1) was then clustered with HDBSCAN (Fig.2), enabling the identification of spectral populations without predefined assumptions on cluster number or geometry. The clusters were spatially correlated with micro-imaging data of the two Ryugu particles.

Results: The global analysis of the reflectance spectra of Ryugu particles reveal a consistent ~2.7 µm OH absorption indicative of hydrated silicates, with the subsurface particle C0242 showing deeper bands and higher organic/carbonate content than the surface-derived A0226 samples, indicating better preservation of primitive material, while A0226 exhibits a ~150 nm Reststrahlen shift consistent with space-weathering–induced silicate modification [3].

Using the combination of UMAP and HDBSCAN, five distinct spectral clusters (labeled from 0 to 4) were identified, corresponding to variations in hydration, carbonate abundance, and organic content.

These unsupervised machine learning applied to FT-IR parameters provides an objective framework to assess compositional heterogeneity and space-weathering effects at the microscale:

- *Clusters 3 and 4* represent Ryugu's mineralogical baseline, dominated by Mg-rich phyllosilicates with minor Fe, carbonates, and organics. Cluster 4 shows slightly higher reflectance, possibly linked to microscale roughness variations [4, 5, 6].
- *Cluster 1* exhibits reduced M–OH and carbonate band depths and blueshifted Christiansen and Reststrahlen features, consistent with dehydration or carbonate loss from localized heating or solar-wind exposure [7,8].
- *Cluster 2,* found only in A0226 particles, shows the lowest hydration, organic, and carbonate signals and a redshifted, broadened RF. These indicate advanced space weathering from micrometeoroid bombardment and fine-grained regolith formation, absent in the more pristine C0242 sample.
- *Cluster 0***,** rare in A0226 but covering ~11 % of C0242, is characterized by strong 2.7–2.8 µm hydration bands, clear carbonate/organic features, and a flat scattering continuum. These signatures suggest fine grain size and enhanced volume scattering associated with the pyramidal surface of C0242.

Collectively, the clustering and spectral trends indicate: (1) carbonates and hydrated phyllosilicates in Clusters 3–4 record early aqueous alteration; (2) Clusters 1–2 represent post-alteration modification from thermal and SpWe processes;
(3) the absence of Cluster 2 in C0242 reflects reduced surface exposure; (4) differences between Clusters 1 and 2 (coarser vs. finer phyllosilicates) support a stratified, dynamically mixed regolith.

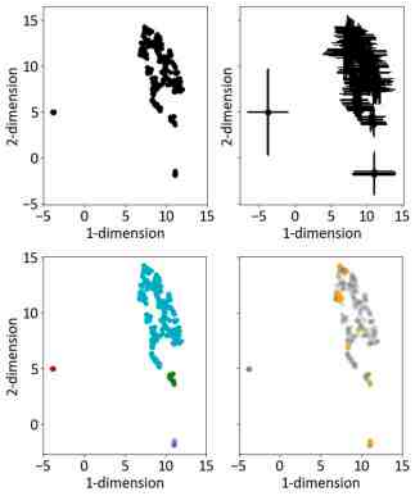


Figure 1: *Upper left: Mean UMAP projection after 100 iterations. Upper right: Mean UMAP projection with corresponding error bars. Bottom left: HDBSCAN clustering results showing clusters labeled 0 to 3. Bottom right: Outliers assigned to cluster 4 are highlighted in colour.*



Figure 2: *Projection of clusters onto the surface of the particle A0226-1, A0226-2 and C0242, with each cluster represented by a distinct colour (0-red, 1-green, 2-blue, 3-black, 4-orange). This visualization illustrates the spatial distribution of clusters across the particle surface, highlighting region-specific variations in spectral properties.*

Furthermore, following [9], we modeled the time-dependent attenuation of the 2.72 µm OH band as $D(t)=D_0\ e^{(-t/\tau)}$, adopting $\tau \approx 5.9$ Myr from experimental scaling ($D/D_0 = 0.43$ after 5 Myr). Using Cluster 3 as the fresh spectral reference ($D_0 = 0.221 \pm 0.004$), the derived OH band depths yield exposure ages of ~10^6 yr for the subsurface particle C0242 and ~1.5×10^6 yr for the surface particle A0226, implying an age difference of ~5×10^5 yr. These results align with resurfacing timescales inferred from crater and irradiation models, indicating that A0226 represents a more weathered surface layer, whereas C0242 retains characteristics of a less-altered, recently buried regolith domain.

Conclusion: Overall ML-based spectral analyses confirm that Ryugu's mineralogy is consistent with CI-type chondritic material but exhibits local heterogeneity driven by space weathering and surface textural effects. Subsurface material (C0242) is more pristine, while A0226 exhibits signs of long-term space weathering.

The UMAP–HDBSCAN framework successfully discriminates against subtle spectral features and provides a transferable methodology for analyzing complex planetary materials in future sample-return and in situ missions.

References: [1] Tsuda, Y., et al. 2020, Acta Astronautica, Volume 171, p. 42-54., 10.1016/j.actaastro.2020.02.035; [2] Shehaj X. et al., 2025, Earth, Planets and Space, Volume 77, Issue 1, id.108, 10.1186/s40623-025-02245-2; [3] Brunetto R. et al., 2018, Planetary and Space Science, Volume 158, p. 38-45, 10.1016/j.pss.2018.05.008; [4] Cloutis et al. 2011, Icarus, Volume 212, Issue 1, p. 180-209, 10.1016/j.icarus.2010.12.009 ; [5] Rosi, F., Cartechini, L., Sali, D., & Miliani, C. (2019). Physical Sciences Reviews, 4(11), 20180006. ; [6] Invernizzi et al., 2022 Microchemical Journal, 172, 106874;
[7] Noguchi T. et al., 2023, Nature Astronomy, Volume 7, p. 170-181, 10.1038/s41550-022-01841-6; [8] Bates, H. C. (2021) Journal of Geophysical Research: Planets, 126, e2021JE006827. 649 https://doi.org/10.1029/2021JE006827 ; [9] Matsuoka et al 2023, Communications Earth & Environment, Volume 4, Issue 1, article id.335, 10.1038/s43247-023-00991-3

Acknowledgments: The Ryugu samples used in this paper were distributed through the 2AO Announcement of Opportunity for Hayabusa2 samples (AO2). These samples were referred to the Ryugu Sample Database at https://www.darts.isas.jaxa.jp/curation/hayabusa2/

Mercury's surface classification through Graph Attention Networks (GATs)

L. Spina[1], N.A. Vergara Sassarini[1], C. Re[1], R. La Grassa[1], A. Tullo[1], G. Cremonese[1]

[1] *INAF, Astronomical Observatory of Padova, Vicolo dell'Osservatorio 5, 35122 Padova, Italy;*

Abstract

In this work, we address the challenge of mapping Mercury's surface by leveraging the power of advanced and recent statistical techniques known as Graph Attention Networks (GATs). We frame the problem by representing the surface data as a graph, where each pixel in the image corresponds to a node connected to its nearby pixels, creating a network that naturally incorporates spatial relationships. Each node is characterized by multimodal feature vectors derived from combining different types of data: topographic measurements from Digital Terrain Models (DTMs) and spectral information from MESSENGER's 8-color global maps. This allows the model to learn patterns that consider both the physical shape and color composition of the surface.

Introduction

The mapping of planetary surfaces represents a fundamental activity in planetary science, offering invaluable insights into the formation history, surface processes, and compositional variations of celestial bodies [1,2]. Accurate and detailed maps are also essential for identifying potential landing sites and planning future exploration missions. These products are mostly constructed from visible image datasets, providing topographic and albedo information that is typically used to delineate geomorphological units. However, generating such maps requires specialized expertise and remains a time-intensive task prone to operator bias and subjective interpretation. Moreover, many existing maps rely on a geomorphology-led approach, often overlooking compositional and physical properties, with spectral information treated as secondary.

A first step toward reducing this subjectivity was made by Vergara Sassarini et al. (2025), who produced explorative geological maps of Mercury using unsupervised learning through a Gaussian Mixture Model approach. Building on that foundation, the present work adopts a more advanced, graph-based technique, Graph Attention Networks (GATs), which further minimizes operator involvement by fully automating the extraction of morpho-spectral patterns. This development is timely for unraveling the complexities of Mercury's surface and for preparing the community for the forthcoming BepiColombo dataset [3,4].

Methods

The core of our approach is an autoencoder built on GATs, which compresses the high-dimensional input features into a simpler, lower-dimensional latent space and then reconstructs the original data. A key feature of the network is its attention mechanism, which adaptively adjusts the importance (weights) of the connections between neighboring pixels based on their similarity. This means the model learns to focus more on relevant neighbors, integrating spatial proximity and contextual information when encoding each pixel's features.

This attention-guided autoencoding leads to two main benefits. First, the output maps are noticeably clearer and less noisy compared to traditional methods that analyze pixels independently, because their spatial correlations are explicitly modeled. Second, the latent space representation has reduced dimensionality and filtered noise, making it ideal for clustering algorithms to identify distinct geological units or "species" on Mercury's surface.

Results

We adapted this methodology from previous applications in astrophysics [5] and successfully applied it to the planetary surface mapping problem. Validation on a well-studied quadrangle of Mercury, the H-05 Hokusai, also the test area used in the unsupervised classifications [6], demonstrates that our method produces geologically meaningful and spatially coherent classification maps (Fig.1). Unlike previous clustering methods guided by geological hypotheses or pre-selected reference regions, the proposed GAT architecture solely depends on statistical correlations in the datasets, ensuring a fully objective and reproducible mapping procedure. These results highlight the effectiveness of using graphs and attention-based neural networks to combine multimodal data and spatial relationships. This new method might be used in the planning of the acquisitions of SIMBIO-SYS [3], on board the BepiColombo mission, and in the data analysis.

Acknowledgement: This work has been developed under the ASI-INAF agreement n. 2024-40-HH.0

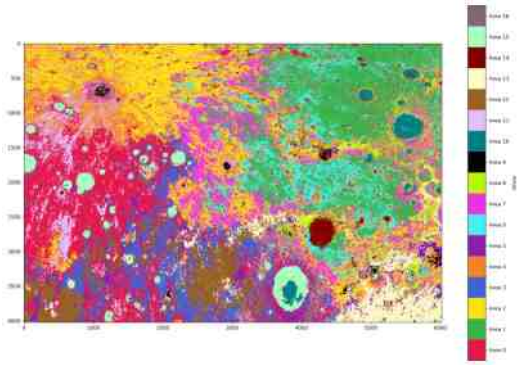


Figure 1. Output of the GAT after classification. The model identifies 16 classes, plus one additional class assigned to noise (Cluster 16). The resulting map highlights prominent morphological features, including craters larger than ~17 km in diameter, clearly outlining their rims, portions of their ejecta blankets, and smooth floor materials. It also captures more subtle surface features such as crater rays and the occurrence of pyroclastic deposits (e.g., Nathair Facula).

References

[1] Luna et al. (2024). Journal of Geophysical Research: Planets, 129(10), e2024JE008442;
[2] Galluzzi (2019).Planetary cartography and GIS, 207-218;
[3] Cremonese et al. (2020). Space Science Reviews, 216(75), 75;
[4] Benkhoff et al. (2021). Space Science Reviews, 217(8), 90;
[5] Spina et al. (2025), A&A, 702, A267;
[6] Vergara Sassarini et al. (2025). EGUsphere, EGU25-19408

TERRACED CRATERS ON MARS: ANALYSIS IN ARCADIA PLANITIA AND DETECTION IN ADDITIONAL REGIONS VIA DEEP LEARNING

M. Faletti [1,2], G. Cremonese [2], E. Martellato [2], V.T. Bickel [3], A. Tullo [2], S. Bertoli [2], G. Munaretto [2], F. Marzari [4], A. Zinzi [5], C. Re [2]

[1] Centro di Ateneo di Studi e Attivita Spaziali "Giuseppe Colombo", Via Venezia 15, 35131, Padova, Italy, maddalena.faletti@inaf.it, [2] INAF-OAPd, Vic. Osservatorio 5, 35122, Padova, Italy, [3] Center for Space and Habitability, Universität Bern, [4] Dipartimento di Fisica, Università di Padova, [5] Agenzia Spaziale Italiana

Introduction: Water ice plays a fundamental role in the geological history of Mars, making the planet a primary target for supporting human activities and the search for past life. Ice distribution is a key constraint for the interpretation of the paleo-Martian climate, while the amount of sub-surface ice (in terms of pore filling towards excess ice) provides essential information about depositional processes [1,2]. In this context, impact craters become a valuable tool for investigating deeper surface layers. Their morphology reflects the mechanical properties of the target material and can reveal variations in density, strength, ice concentration, porosity, and composition, and thus they can provide hints for the presence of water ice.

Craters formed in ice-rich substrates seem to exhibit lower depth-to-diameter ratios (d/D) than those formed in dry regolith. This difference is attributed to the different resistance between ice and rock, as well as post impact processes such as viscous relaxation and slumping [3]. This effect is particularly evident in simple craters, which are more sensitive to the local properties of the substrate [4].

To conduct this study, we focused on simple craters exhibiting a terraced morphology in selected regions of Mars.

The state-of-the-art database of Martian terraced crater have been published by [2]. In this abstract, we leverage on the large amounts of newer high-resolution images and novel automatic crater detection methods based on off-the-shelf convolutional neural networks (CNNs) to expand the sample of known Martian terraced craters. The resulting improved dataset will be pivotal to extract and analyze morphometric measurements such as d/D, terrace dip angles and better understand the underlying stratigraphy responsible for the terraced morphologies.

Data: The catalog proposed by [2] was used as the reference database for the analysis. The database includes 187 craters, located in Arcadia Planitia and with diameters ranging from 125 m to 2 km. Among these, 62 have a single well-defined terrace, 35 show two distinct terraces, while the remaining 90 were classified as uncertain due to the presence of poorly distinguishable or difficult to interpret terraced morphologies.

To investigate these craters in detail, High Resolution Imaging Science Experiment (HiRISE) [5] and the Colour and Stereo Surface Imaging System (CaSSIS) [6] stereo pairs were used to generate Digital terrain models (DTMs). In addition, Context camera (CTX) [7] images were employed to extend the identification of craters with similar morphology to other regions of the Martian surface.

Methods: *Morphological Analysis*: A morphological analysis and a d/D ratio study are conducted on a selected sample of terraced craters taken from the catalog [2], comparing them with a sample of bowl-shaped craters identified across the Martian surface. The analysis is carried out using the open-source QGIS software integrated with custom Python scripts.

Deep Learning Algorithm: To strengthen the analysis, we are currently developing a deep learning-driven approach to identify craters with characteristics similar to those already studied, starting with areas adjacent to Arcadia Planitia.

The methodology employs a CNN trained via supervised learning. The success of the method predominantly depends on the quality of the training data. Rectangular bounding boxes are manually created in CTX images to identify terraced craters. The training data also includes negative examples (e.g., bowl-shaped craters) to reduce false positives. Common data augmentation techniques (rotation, flipping, scaling) are applied to increase data variability and diversity, preventing overfitting.

During inference, the CNN outputs a bounding box and a confidence score for each feature it detects. Non-Maximum-Suppression is applied to remove duplicates, and an optimal confidence threshold is selected to balance precision and recall. The confidence score indicates how certain the detector is about a detection with 1 being the highest and 0 the lowest. Image coordinates also allow the georeferencing of detection and the estimation of the physical size of the object.

Model performance is evaluated using standard metrics. Recall measures the proportion of terraced craters correctly detected in the test-set, ranging from 0 (none detected) to 1 (all detected). Precision describes how many detections are actually correct, and average precision (AP) shows the stability of

precision-recall relationships across different confidence levels in one single number. [8]

Results: *Morphological Analysis*: Focusing on the d/D ratio, terraced craters systematically show lower values than bowl-shaped ones, supporting the hypothesis that the presence of ice in the substrate could reduce the strength of the target material during the impact. All analyzed craters are smaller than 2 km in diameter and should therefore be strength-dominated, meaning that their morphology is controlled mainly by the strength of the material rather than by gravity. Furthermore, the presence, number, and arrangement of terraces, shows a significant variability, potentially related to the stratified subsurface. The shape and decentralized pattern can provide information about the impacts themselves, such as their angle and direction.

Deep Learning Algorithm: In the first test, the CNN effectively distinguishes terraced craters from bowl-shaped ones in the test-set, showing high precision, and producing no false positives at confidences beyond 0.8. Overall, the model also achieves high recall, with a good balance between recall and precision at intermediate confidence levels.

Using this confidence threshold of 0.8, the first test identifies two groups of terraced craters (*Figure 1*) in a region adjacent to Arcadia Planitia. Specifically, in the yellow group at 152°E (named 0.8_152E), 350 candidates are identified, while in the fuchsia group at 167°E (0.8_167E), 171 candidates are found.

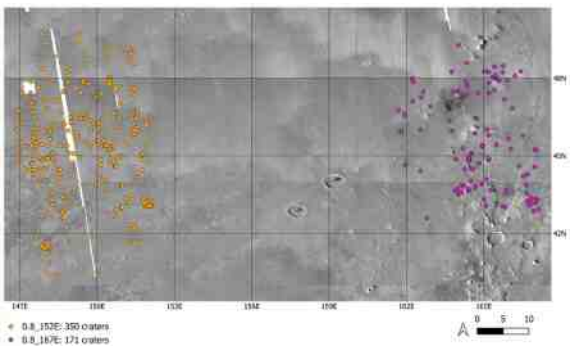


Figure 1: *Distribution of terraced craters identified in the first test.*

Following expert validation, approximately 70% of the 0.8_152E candidates and 77% of the 0.8_167E candidates are confirmed as terraced.

At the moment, our updated catalog includes 529 craters, of which 401 are confidently identified as terraced and 128 are classified as questionable.

The numbers of terraced and questionable craters for each group are reported in *Table 1*.

Conclusions and Future work: The results obtained from this initial test are highly promising and provide a strong basis for further development of the project. The next phase will involve extending the identification and analysis to much more extended areas of Mars, with a focus on the mid-latitudes. The specific regions will be selected based on the results of a preliminary global survey of the Martian surface.

Table 1: *Summary of* Terraced *and* Questionable *craters reported in Bramson et al [2] and in the two regional catalogs (e.g., 0.8_167E, 0.8_152E). The* Updated catalog *row shows the total number of craters identified in this work.*

Catalog	*Terraced*	*Questionable*	*Total*
Bramson et al. [2]	97	90	187
0.8_152E	243	20	263
0.8_167E	61	18	79
Updated catalog	401	128	529

Acknowledgments: This work has been developed under the ASI-INAF agreement n.2024-40-HH.0

References: [1] Bramson, A. M., Byrne, S., Putzig, N. E., Sutton, S., Plaut, J. J., Brothers, T. C., & Holt, J. W. (2015) *Geophysical Research Letters*, *42*(16), 6566-6574. [2] Bramson, A. M., Byrne, S., & Bapst, J. (2017) *Journal of Geophysical Research: Planets*, *122*(11), 2250-2266. [3] Douglass, B. S., & Bell, J. F. (2025 *LPI Contributions*, *3090*, 2677. [4] Robbins, S. J., & Hynek, B. M. (2012) *Journal of Geophysical Research: Planets*, *117*(E6). [5] McEwen, A. S., Eliason, E. M., Bergstrom, J. W., Bridges, N. T., Hansen, C. J., Delamere, W. A., ... & Weitz, C. M. (2007) *Journal of Geophysical Research: Planets*, *112*(E5). [6] Thomas, N., Cremonese, G., Ziethe, R., Gerber, M., Brändli, M., Bruno, G., ... & Wray, J. J. (2017) *Space science reviews*, *212*(3), 1897-1944. [7] Malin, M. C., Bell III, J. F., Cantor, B. A., Caplinger, M. A., Calvin, W. M., Clancy, R. T., ... & Wolff, M. J. (2007) *Journal of Geophysical Research: Planets*, *112*(E5). [8] Bickel, V. T., Conway, S. J., Tesson, P. A., Manconi, A., Loew, S., & Mall, U. (2020) *IEEE Journal of Selected Topics in Applied Earth Observations and Remote Sensing*, *13*, 2831-2841.

THREE-DIMENSIONAL IMAGING OF SUBSURFACE STRUCTURES WITHIN MARTIAN SOUTH POLAR LAYERED DEPOSITS USING MARSIS RADAR DATA. A. Margheri[1] , R. Orosei[2], I. Catapano[3] and S.E. Lauro[4]. [1]University of Trento, alessio.margheri@unitn.it, [2]INAF/IRA - Bologna, [3]Institute for Electromagnetic Sensing of the Environment IREA-CNR, [4]Department of Mathematics and Physics - Roma Tre University.

Introduction: The Mars Advanced Radar for Subsurface and Ionospheric Sounding (MARSIS) is a space-borne sounding radar on board of ESA's Mars Express spacecraft, which reached Mars in 2003. Its primary objective is to map the distribution of water and ice in Mars' crust, with secondary goals including subsurface geologic probing, surface characterization, and ionospheric sounding [1]. The instrument uses synthetic aperture techniques to enhance subsurface echoes over surface clutter. Sounding below Mars' surface is challenging due to the need for a low-carrier frequency and the influence of the ionosphere, which varies with solar activity and time of day. To address these challenges, MARSIS incorporates an ionospheric sounder to aid in frequency selection while studying the ionosphere itself.

The analysis of radar profiles collected between May 2012 and December 2015 showed evidence of liquid water trapped below the ice of the South Polar Layered Deposits (SPLD) [2]. Strong bright subsurface reflections were found within a 20km wide zone, surrounded by much less reflective areas, and were interpreted as caused by the presence of liquid water.

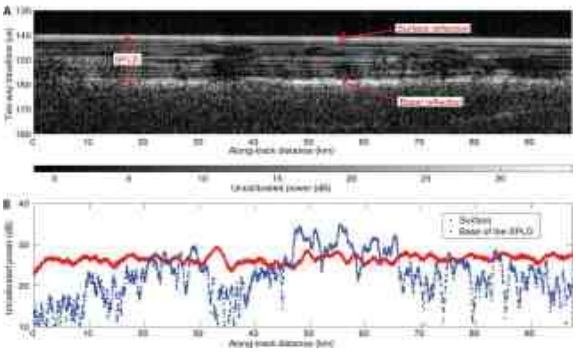


Fig. 1: MARSIS radargram of orbit 10737 showing strong basal echoes beneath the SPLD that have been interpreted as due to the presence of liquid water (from [2]).

Method: The objective of this work is to perform 3D mapping of subsurface structures in the putative lake region to assess the topology and spatial extent of bright radar reflectors. First, we selected only orbits directly crossing the reflector location, reducing the initial dataset of 65 radargrams acquired within a 200 km radius around the reflector to 3 orbital passes. This extremely limited dataset poses intrinsic constraints on reconstruction quality.

Among the various 3D reconstruction algorithms available in the literature, we adopted a microwave tomography (MWT) approach [3]. This algorithm obtains a focused image of the scene under test in the vertical imaging domain by solving an inverse scattering problem formulated in the frequency domain. The MWT approach is particularly well-suited for MARSIS data processing due to several key characteristics:

1. **Inhomogeneous Medium Modeling** The algorithm accounts for electromagnetic wave propagation through stratified, inhomogeneous media. This is critical for MARSIS, which must handle signal propagation through the Martian ionosphere before reaching the surface [4].

2. **Flexible Geometry Handling** MWT can process data from arbitrary measurement configurations, accommodating MARSIS's unique orbital geometry and varying observation angles without requiring ground-coupled assumptions.

3. **Linear Inverse Scattering with Regularization** Based on the Born Approximation and solved via regularization techniques (e.g., TSVD), the algorithm provides robust reconstruction in the presence of noise and parametric uncertainties - common issues in planetary radar data affected by ionospheric disturbances and instrument limitations.

4. **Interface Modeling** The ray-based propagation model explicitly accounts for interfaces (ionosphere-surface, surface-subsurface), enabling more accurate depth estimation and dielectric contrast retrieval compared to standard time-domain processing.

These characteristics make MWT a natural choice for processing MARSIS data, where traditional ground-based GPR processing methods fail to adequately address the orbital standoff configuration and ionospheric effects.

Results: Preliminary results obtained from our implementation of the algorithm show the presence of a very bright reflector in the intersection zone

between the various orbits. However, periodic lateral artifacts are also present in the reconstruction, whose origin we investigated systematically. First, we tested the algorithm on synthetic data, obtaining optimal reconstruction of the scene with no artifacts. This clearly demonstrates that the presence of artifacts in the real data reconstruction is attributable to residual phase differences between the considered radargrams.

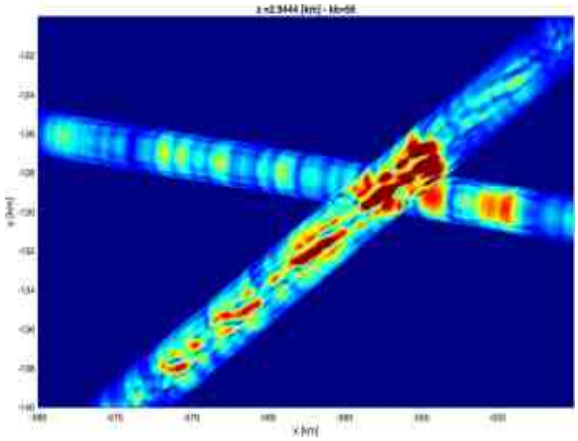


Fig. 2: Basal echo brightness for orbits 10737, 12840 and 15110.

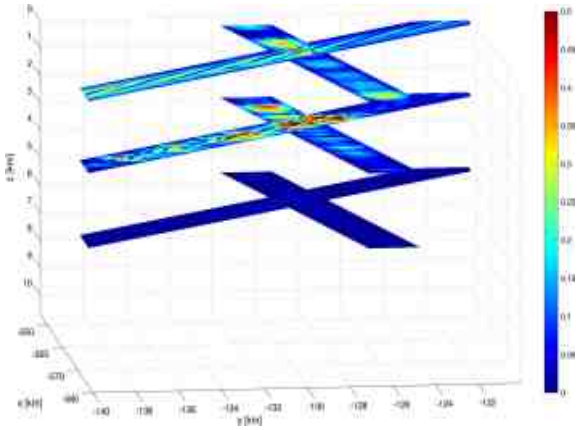


Fig. 3: Volume slices of the intersection of orbits 10737, 12840 and 15110.

We therefore re-analyzed the processing chain applied to the raw data acquired by MARSIS to identify possible error sources. We discovered that the data contain a remnant phase induced by on-board signal processing that manifests as rapid lateral phase oscillations. This results from on-board signal demodulation—specifically, mixing the antenna-received data with a local oscillator signal followed by appropriate low-pass filtering to obtain spectrally down-converted data restricted to the real baseband—prior to sampling. Additionally, the residual delay is consistent with the estimated uncertainty in the spacecraft's radial velocity and with phase differences due to ionospheric effects, the latter being extremely difficult to parameterize due to its high temporal and spatial variability.

Future work: We are currently working on reducing noise and phase variations across the different radargrams to produce coherent 3D reconstructions of the putative lake region. Successful completion of this task will enable us to produce 3D reconstructions of other zones within the SPLD, where radargrams show the presence of very bright subsurface reflectors whose nature has not yet been analyzed in detail.

References: [1] Picardi G. et al. (2004) ESA SP, 1240, 51–69. [2] Orosei R. et al. (2018) *Science*, 361, 490–493. [3] Catapano I. et al. (2021) *IEEE Geosci. Remote Sens. Mag.,* 9, 2–24. [4] Cartacci M. et al. (2025) *Icarus*, 434, 116545.

XXI Congresso Nazionale di Scienze Planetarie

Sessione Focus S3

Atmospheric Observation and Spectral Modeling in Planetary Science

Advanced σ Radiative Transfer Model: Enhancing Atmospheric Remote Sensing for Earth and Planetary Exploration.

G. Masiello[1], T. Maestri[2], G. Liuzzi[1], M. Martinazzo[2], L. Cassini[1], E. Fabbri[2], R. Inglese[1], G. Proietti Pelliccia[2], C. Serio[1]

[1]Dipartimento di Ingegneria, Università della Basilicata, viale dell'ateneo Lucano, 10, 85100 Potenza, Italy (guido.masiello@unibas.it)

[2]Dipartimento di Fisica e Astronomia, "Augusto Righi" – Università di Bologna, viale Berti-Pichat, 6/2, Bologna, 40127, Italy.

The σ radiative transfer model represents a significant advancement of the σ-IASI model [1], developed under the auspices of the Italian Space Agency (ASI) to support hyperspectral infrared remote sensing missions, including the ESA Earth Explorer FORUM (Far-infrared Outgoing RAdiation Mission) [2]. This model is engineered for the rapid and accurate simulation of spectrally resolved radiance and its analytical Jacobians across a broad spectral range (5-3000 cm^{-1} or 3-100 micron), accommodating diverse sky conditions and observation geometries. The model, based on the gases optical depth parametrization, implements two key advancements: Efficient Cloud and Aerosol Treatment and an innovative treatment of atmospheric layer inhomogeneity.

The model implements Tang's adjustment method extended to represent cloud and aerosol scattering at different observational angles. This significantly accelerates calculations for high-resolution simulations, maintaining accuracy.

The model incorporates an innovative treatment of atmospheric layer inhomogeneity and the "linear-in-T" correction, which complements the established "linear-in-tau" approach. These features are crucial for precisely addressing complex atmospheric phenomena, especially in regions with dense clouds and temperature gradients, effectively minimizing simulation biases.

The model that is a general-purpose model also provides enhanced Scalability and Flexibility. This allows the model to adapt seamlessly to various instrument resolutions and applications, making it a highly flexible tool for a wide range of remote sensing studies involving atmospheric composition, clouds, and climate.

The robust capability of σ to handle the full complexity of atmospheric physics, particularly in the far-infrared and under challenging cloud/aerosol conditions, has direct implications for planetary science. The model's framework, successfully utilized in the advanced Optimal Estimation tool for the IASI/MetOp interferometer [3], is adaptable to other planetary atmospheres. Notably, previous iterations of this model have been successfully applied to measurements acquired on Mars [4], demonstrating its potential for characterizing atmospheric structure, temperature profiles, and aerosol/cloud properties on other worlds. The new enhancements further solidify σ as a state-of-the-art tool for analyzing hyperspectral infrared data in both Earth and planetary remote sensing applications.

References:

[1] Masiello G. et al. (2024) *JQSRT*, 312, 108814.
[2] Palchetti L. et al., (2020) *BAMS, 101:E2030–46*.
[3] Serio C. et al. (2024) *JQSRT*, *329,* 109211.
[4] Liuzzi et al. (2015) *Appl. Opt., 54/9, 2334-2346*

NEW LABORATORY MEASUREMENTS OF THE CO_2-H_2 COLLISION-INDUCED ABSORPTION IN THE [4000, 4750] CM^{-1} SPECTRAL RANGE FROM 240 K TO 500 K

F. Vitali[1,2], S. Stefani[1], G. Piccioni[1], H. Tran[3], M. Snels[4], D. Grassi[1], C. Boulet[5], D. Biondi[1] and A. Boccaccini[1]
[1]IAPS-INAF, Via del fosso del cavaliere 100, 00133 Rome, Italy, [2]Università degli studi di Roma "Tor Vergata", Via Cracovia 50, 00133, Rome, Italy, [3]Laboratoire de Météorologie Dynamique/IPSL, CNRS, École Polytechnique, Institut Polytechnique de Paris, Sorbonne Université, École Normale Supérieure, PSL Research University, Palaiseau F-91120, France, [4]ISAC-CNR Via del fosso del cavaliere 100, 00133, Rome, Italy, [5]Institut des Sciences Moleculaires d'Orsay (ISMO), CNRS, Universite Paris-Sud, Universite Paris-Saclay, F-91405 Orsay, France
francesca.vitali@inaf.it

Introduction: Accurate knowledge of the collision-induced absorption (CIA) of a CO_2-H_2 mixture is important not only to have a better comprehension of the early-Martian atmosphere, as well as CO_2-rich planetary atmospheres, but also for the present and future investigation of exoplanetary ones.
As far as we know, very few experimental data are present in the literature for the CO_2-H_2 CIA band in the [4000, 4750] cm^{-1} spectral range, all at room temperature.
Here we present new experimental measurements in this spectral range for six temperatures from 241 K to 498 K.
Our results have been compared with the existing laboratory data and the available theoretical calculations.

Experimental setup: The experimental setup used for the presented activity is called PASSxS and can be visualized in Fig.1.
It consists of an atmospheric simulation chamber made of two stainless steel concentric vessels. The inner one contains the gas or mixture of gases under investigation, while the external can be evacuated to ensure thermal insulation of the sample chamber from the external environment. The chamber can sustain pressures up to 70 bar, it can be heated up to 550 K, and cooled down to 100 K. Moreover, the inner vessel contains a Multi-Pass cell, characterized by an optical path of 3.27 m, coupled with a high-resolution FT-IR spectrometer. The maximum resolution achievable is 0.002 cm^{-1}. For a more detailed description of the experimental setup refer to [1].



Figure 1: A picture of the experimental setup

Experimental measurements: By using a CO_2+H_2 gaseous mixture for a total pressure of 12 bar, with 17% of volume mixing ratio (VMR) of CO_2, we measured the CO_2-H_2 CIA in the [4000, 4750] cm^{-1} spectral range for six temperatures, from 241 K to 498 K, at a resolution of 1 cm^{-1}. While some measurements at room temperature have been recently performed by Fakhardji W. et al. [2] and D. Mondelain et al. [3], presently there is a lack of experimental data for other temperatures.
Fig. 2 shows the measured CO_2-H_2 CIA absorption coefficients for all six temperatures explored.

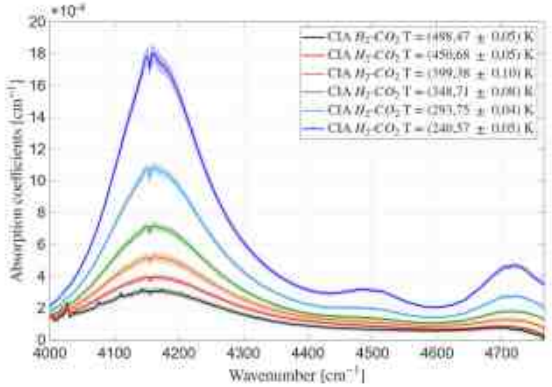


Figure 2: CO_2-H_2 CIA absorption coefficients for a total pressure of 12 bar with 17% of VMR of CO_2 at different temperatures

Experimental procedure: In the considered spectral range, the total CIA absorption coefficients, K_{mix}, for a CO_2+H_2 mixture are composed of two different contributions, as shown in the equation below.

$$K_{mix} = k_{H2\text{-}H2}\,\rho_{H2}\,\rho_{H2} + k_{CO2\text{-}H2}\,\rho_{H2}\,\rho_{CO2}$$

The first term represents the CIA absorption due to the H_2-H_2 collisions, given by the product between the H_2-H_2 binary absorption coefficients ($k_{H2\text{-}H2}$) and the H_2 density squared. The second term represents the CIA opacity due to the CO_2-H_2 collisions coming from the product between the CO_2-H_2 binary absorption coefficients ($k_{CO2\text{-}H2}$), CO_2 density, and H_2 density.

To retrieve the CO_2-H_2 CIA absorption coefficients from the measurements, we employed the following procedure.
For every temperature, we first inserted 10 bar of pure H_2 gas and measured the H_2-H_2 CIA. Then, we added 2 bar of CO_2 and recorded the spectral radiance of the total gaseous mixture at the same temperature as for the pure H_2 case. Finally, we evacuated the chamber and measured the spectral radiance of the background.
The CO_2-H_2 absorption coefficients have been obtained by subtracting the H_2-H_2 CIA from the total CO_2+H_2 CIA absorption coefficients, and can be visualized in Fig.2. Then, the CO_2-H_2 binary absorption coefficients have been obtained by dividing the CO_2-H_2 absorption coefficients by the product of the H_2 and CO_2 densities.
It is worth mentioning that the allowed absorption of CO_2 around 4750 cm^{-1} has been removed using the theoretical calculation made by Ha Tran. This procedure allowed us to retrieve part of the absorption of the third peak of the CIA band.

Results and discussion: At room temperature, our experimental data have been compared with two previous sets of measurements from [2] and [3], and semi-classical calculations based on the approach described in [4]. This comparison is shown in Fig. 3.
It can be noted that there is an excellent agreement with the data recorded by Mondelain et al., while the measurements from Fakhardji et al. present a smaller absorption throughout their considered spectral range.
The theoretical models compared to our data at room temperature have been calculated with two different potentials, one from [5] (dashed black line in Fig. 3) and the more recent one from [6] (dotted black line in Fig. 3).
In both cases, the band shape has been calculated by using the isotropic part of the potential, while the integrated band intensity has been calculated using the total potential (both the isotropic and anisotropic parts).
It can be observed that, using the potential from [5], the main peak of the band is well represented at this temperature, while the model shows a poor agreement with the experimental measurements in the rest of the spectral range. Moreover, using the potential from [6], a difference between the model and the measurement is noted throughout the entire band.

Future perspectives: It is worth noting that these data represent the first laboratory measurements of the CO_2+H_2 CIA at temperatures different from the room temperature case in the [4000, 4750] cm^{-1} spectral range. Moreover, few theoretical works reproducing the CIA absorption of the considered band are available.
As a consequence, having laboratory measurements is crucial not only to understand the temperature dependence of the CO_2-H_2 CIA considered band, but also to support the theoretical modeling.
Following the method used in the recent work of Tran et al. [7], we plan to build some empirical

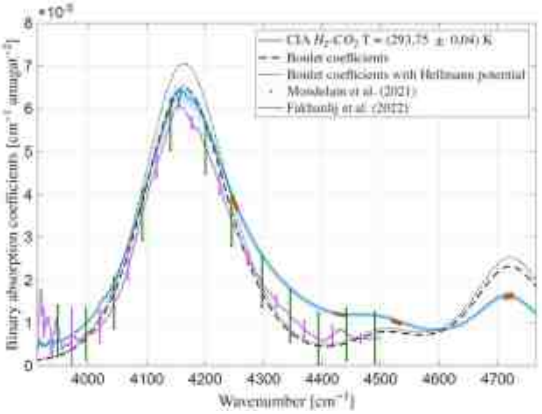


Figure 3: Experimental CO_2-H_2 binary absorption coefficients at room temperature (light blue solid line) compared with existing experimental data and theoretical calculations

models starting from the CO_2-H_2 CIA measurements. Finally, we will perform some high-resolution measurements of a CO_2-H_2 mixture to obtain a reliable H_2-broadening coefficient for CO_2 lines, which is so far not available at different temperatures.

References:

[1] Snels M. et al. (2021), AMT 14, 7187–7197, doi: https://doi.org/10.5194/amt-14-7187-2021
[2] Fakhardji W. et al., Journal of Quantitative Spectroscopy and Radiative Transfer, Volume 283, 2022, doi: https://doi.org/10.1016/j.jqsrt.2022.108161
[3] D. Mondelain et al., Journal of Quantitative Spectroscopy and Radiative Transfer, Volume 260, 2021, doi: https://doi.org/10.1016/j.jqsrt.2020.107454
[4] Turbet M. et al. (2020), Icarus, Vol. 346, doi: https://doi.org/10.1016/j.icarus.2020.113762
[5] Li H et al., J Chem Phys, 2012, doi: 10.1063/1.3428619
[6] Hellmann R. et al. (2025), International Journal of Thermophysics, Vol. 46, No. 67, doi: https://doi.org/10.1007/s10765-025-03524-6
[7] Tran H. et al., Icarus, Vol. 422, 2024, doi: https://doi.org/10.1016/j.icarus.2024.116265

Acknowledgements: This work has been developed under the ASI-INAF agreement n. 2023-6-HH.0.

The upgrade of the experimental setup has been partially funded by the EMM (Earth Moon Mars) project of PNRR (WP 1500-13).

INFRARED SPECTRAL DIAGNOSTICS OF JUPITER'S MOON-INDUCED AURORAL FOOTPRINTS

Chiara Castagnoli[1,2] (chiara.castagnoli@inaf.it), Alessandro Moirano[3,1], Alessandro Mura[1], Bianca Maria Dinelli[2], Alessandra Migliorini[1], Francesca Altieri[1], Raffaella Noschese[1], Roberto Sordini[1], Federico Tosi[1], Alberto Adriani[1], Davide Grassi[1], Giuseppe Piccioni[1] and Christina Plainaki[4,5]

[1] Institute for Space Astrophysics and Planetology, National Institute for Astrophysics (INAF-IAPS), Rome, Italy, [2] Institute of Atmospheric Sciences and Climate, National Research Council (CNR-ISAC), Bologna, Italy, [3] Laboratory for Planetary and Atmospheric Physics, STAR Institute, University of Liège, Liège, Belgium, [4]Agenzia Spaziale Italiana (ASI), Rome, Italy, [5] Max Planck Institute for Solar System Research (MPS), Göttingen, Germany

Introduction: Jupiter's auroral footprints are distinctive emissions originating from the electromagnetic coupling between the planet's ionosphere and its four Galilean moons [1]. As they orbit through Jupiter's rapidly corotating plasma, these satellites act as obstacles that generate Alfvén wave disturbances propagating along the magnetic field lines. These waves accelerate electrons toward Jupiter's ionosphere, where they produce emissions observed radio to X-ray frequencies. Since the discovery of these moon-induced auroras**,** called "footprints", significant efforts have been made to unravel the mechanisms driving them, as they provide unique insights into the Jovian magnetosphere and satellite–planet interactions.

Problem: The Juno mission, by providing unprecedented access to Jupiter's polar regions, has been decisive in advancing our understanding of the morphology of these emission structures and the electrodynamic processes driving them, revealing exceptional detail across both the ultraviolet [3-4] and infrared ranges [5–9]. While these observations have greatly expanded our knowledge of Jupiter's auroras, most investigations of Jupiter's auroral footprints have focused primarily on imaging, leaving their spectral dimension largely unexplored. To address this gap and advance the characterization of these auroras, this study examines their infrared H_3^+ emission spectra to constrain its column density and temperature.

Method: We combined L-band images (integrated radiance in the 3.3-3.6 μm range) and spectra slits (covering 2-5 μm) acquired by the JIRAM (Jovian InfraRed Auroral Mapper) [10] aboard Juno from month year to month year to generate composite maps of the auroral footprints (e.g., *Figure 1*). The L -band images provided the spatial context necessary to identify spectra sampling the footprints of Io, Europa, and Ganymede, which were the primary targets of this work. Following the methodology adopted in previous JIRAM analyses of Jupiter's auroral spectra [11], these mean spectra were analyzed to derive the temperature and column density of H_3^+ across different footprint regions, including the Main Alfvén Wing (MAW), the Transhemispheric Electron Beam (TEB), and the Reflected Alfvén Wing (RAW). MAW spots are due to Alfvén waves coming straight from the moon. The RAWs are caused by multiple reflections of the Alfvén waves on the density gradient at the boundary of the plasma sheet. Finally, the TEB spot is produced by the acceleration of electrons away from Jupiter in the main Alfvén wings and precipitating in the opposite Jovian hemisphere.
The derived H_3^+ parameters were then compared among these regions to evaluate variations in ionospheric energy deposition and emission altitude.

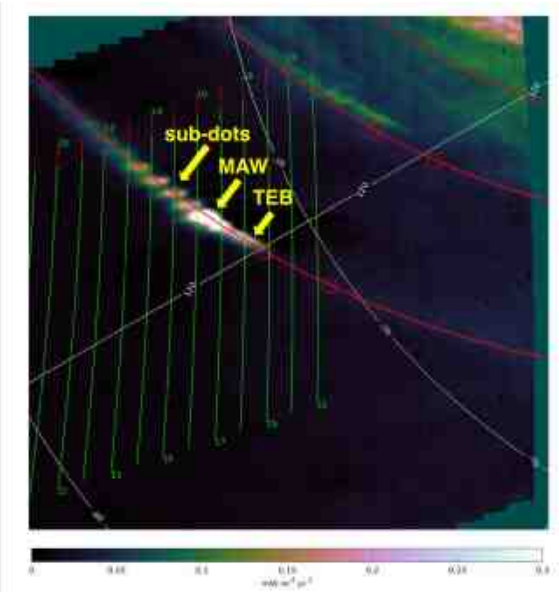


***Figure 1**. Example of a map obtained combining the L-band imager data acquired during orbit 14 (7 July 2018), registered in a single scanning session (from 07:01:44 to 07:11:46 UT) with the spectral slits measured simultaneously. Each slit is numbered and consists of both green and red dots. Red dots indicate the pixels typically ignored due to instrumental issues. Red lines show the trajectories of the footprints: moving from the equator toward the pole one can find Io, Europa, and Ganymede. Red squares mark the position of the footprints in the first and last images of the sequence as predicted by the model developed by [12].*

Results: The MAW (*Figures 2a* and *3a*) and RAW spots of the Io and Ganymede footprints exhibited H_3^+ temperatures and column densities comparable to those along Jupiter's main auroral oval [13,14], suggesting similar ionospheric conditions and emission altitudes. In contrast, the TEB of the Io footprint (*Figure 2b*) appeared to originate from hotter, higher-altitude layers than its MAW, consistent with energy deposition in the upper ionosphere, whereas the TEB of the Ganymede footprint (*Figure 3b*) was associated with colder, denser, lower-altitude regions, indicating particle precipitation penetrating deeper into the atmosphere. Such a contrast could also reflect the presence of a thermal inversion at the location of Io's footprint. In this scenario, the MAW emission peak would lie above the core hot region of the thermal inversion layer, while the TEB, associated with deeper energy deposition by more energetic particles, would sample warmer altitudes within the inversion. However, dedicated modeling efforts and additional observations will be required to verify this hypothesis. Due to limited data coverage, a similar characterization could not be performed for the Europa footprint. **[nota che ho cambiato dove inizia il paragrafo sotto]**

~~Neverthless, t~~These results provide important diagnostics of the physical and thermal conditions in Jupiter's upper atmosphere at the locations of the satellite footprints, offering new insight into the vertical structure and underlying nature of the moon-induced auroras on Jupiter.

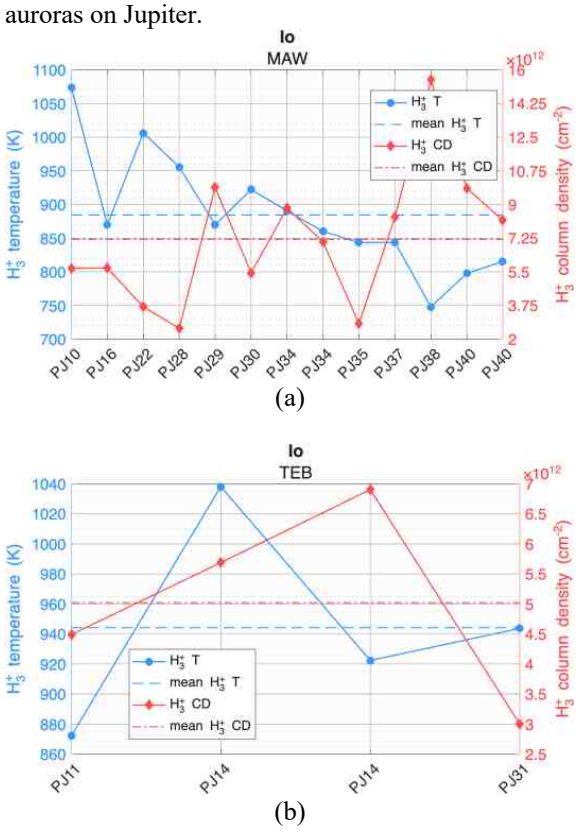


Figure 2. Retrieved values of H_3^+ temperature (blue) and column density (red) from the inversion of the mean JIRAM spectra of the MAW (a) and TEB (b) of the Io footprint.

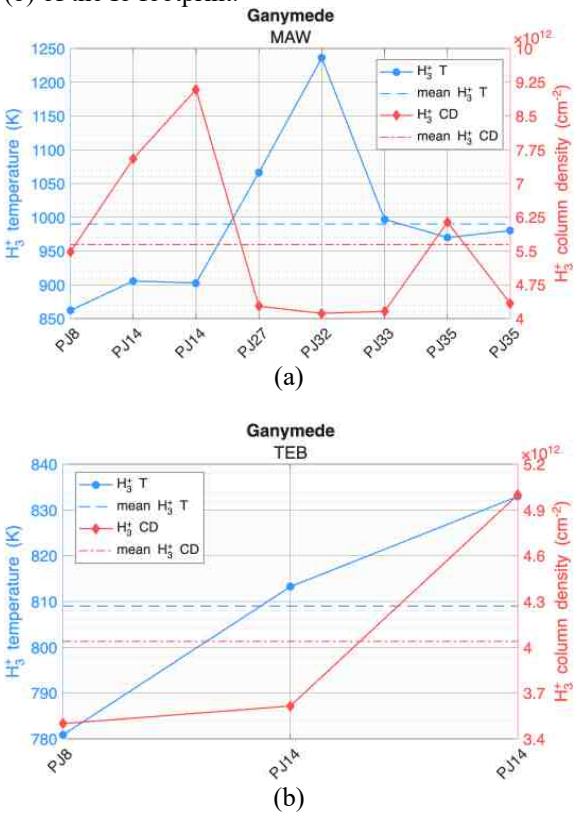


Figure 3. Retrieved values of H_3^+ temperature (blue) and column density (red) from the inversion of the mean JIRAM spectra of the MAW (a) and TEB (b) of the Ganymede footprint.

References: [1] Kivelson at al. (2004). In F. Bagenal, T. E. Dowling, & W. B. McKinnon (Eds.), *Jupiter. The Planet, Satellites and Magnetosphere* (pp. 513–536). [2] Clarke et al. (2004). In F. Bagenal, T. E. Dowling, & W. B. McKinnon (Eds.), *Jupiter. The Planet, Satellites and Magnetosphere* (Vol. 11, pp. 639–670). [3] Bonfond et al. (2017). *JGR: Space Physics*, 122 , 7985-7996. [4] Hue et al. (2023). *JGR: Space Physics*, 2023. [5] Mura et al. (2017). *GRL*, 44, 5308-5316. [6] Mura et al. (2018). *Science*, 361. [7] Moirano et al. (2021). *JGR: Space Physics*, 126. [8] Moirano et al. (2023). *JGR: Space Physics*, 128. [9] Mura et al. (2025). *PSJ*, 6 (2), 49. [10] Adriani et al. (2017). *Space Sci. Rev.,* 213 [11] Castagnoli et al. (2025). *PSJ* , 6 (4), 93. [12] Connerney et al. (2022). *JGR*: Planets, 127. [13] Adriani et al. (2017). *GRL*, 44. [14] Dinelli et al. (2017). GRL, 44.

Acknowledgements: The authors thank the Italian Space Agency (ASI) for supporting the JIRAM project (this work has been funded with ASI contract 2016-353 23-H.0).

JUICE-MAJIS EARTH GRAVITY ASSIST DATA OVERVIEW AND COMPARISON WITH PRISMA.

G. Piccioni[1], F. Oliva[1,*], E. D'Aversa[1], A. Migliorini[1], F. Poulet[2], Y. Langevin[2], A. Zinzi[3], M. Giardino[3], E., Lopinto[3], G. Sindoni[3], C. Plainaki[3].
[1]*Istituto di Astrofisica e Planetologia Spaziali* (IAPS/INAF), Rome, Italy;
[2]*Institut d'Astrophysique Spatiale, CNRS/Université Paris-Saclay, 91405 Orsay Cedex, France*;
[3]*Agenzia Spaziale Italiana.*

***Correspondence: fabrizio.oliva@inaf.it**

JUpiter ICy moons Explorer (JUICE) spacecraft performed a first-ever Lunar-Earth gravity assist maneuver on August 20, 2024. The *Moon and Jupiter Imaging Spectrometer* (MAJIS) was switched on and, at Earth, registered multispectral images over the Western Pacific Ocean at tropical latitudes. Other Earth-observing instruments were coordinated to observe in conjunction with MAJIS, with the purpose of validating its spectral observations with independent measurements as close as possible in both space and time. In this analysis, we focus on the comparison with PRISMA imaging spectrometer data (400 – 2500 nm), not coincident with the MAJIS ones, but providing a useful benchmark for testing its instrumental response over ocean and clouds (see Figure 1).

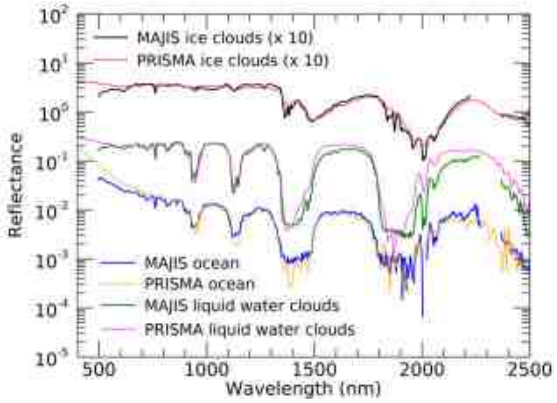


Figure 1: comparison between MAJIS and PRISMA reflectances over similar ocean and clouds scenes.

We explore the two datasets' information content to investigate Earth's atmospheric composition, temperatures, and high altitude waves and emissions. MAJIS spectral range (500 - 5540 nm) allows the identification of major and minor atmospheric gases, like O_2, H_2O, CO_2, O_3, CH_4, N_2O. Exploiting wavelengths in the visual range, we derive spectral indexes suitable for identifying different types of surfaces, like ocean, sand and vegetation, and test them on PRISMA data. Land features in MAJIS are instead observed in nighttime and twilight conditions and therefore we characterize them through considerations on their spectral contrast (both in the solar and thermal parts of the spectrum) with respect to ocean and clouds.

We analyze clouds' altitudes and verify that ice crystals are widespread in the data, allowing for an investigation of their properties (e.g. crystallinity, density, sizes) through different spectral features' analysis. Finally, high altitude emissions from CO_2 and O_3 are detected and exploited as a tracer for atmospheric gravity wave packets. These are likely induced by thunderstorms, whose presence is also witnessed by lightning activity detected by MAJIS itself (D'Aversa et al., this congress).

The present analysis demonstrates MAJIS capabilities in investigating a planetary environment and provides information on several atmospheric phenomena that are of interest for the future science foreseen at Jupiter. Moreover, it highlights the potential in investigating the properties of H_2O ice, which is one of the main scientific objectives of the JUICE mission at the Jovian icy satellites.

Acknowledgements

The Italian participation to JUICE mission is funded by the Italian Space Agency (ASI). In particular, this work has been developed under the ASI-INAF agreement n. 2023-6-HH.0. PRISMA products are generated by IAPS-INAF under a license from ASI Original PRISMA Product - © Italian Space Agency (ASI) – 2024. ASI retains copyright on the ORIGINAL Product "PRISMA Product - © Italian Space Agency (ASI) 2024. All rights reserved".

XXI Congresso Nazionale di Scienze Planetarie

Sessione Pianeti e Satelliti
Outer Solar System

PHOTOMETRICALLY CORRECTED MAPS OF SATURN MID-SIZED ICY MOONS FROM CASSINI-VIMS OBSERVATIONS. M. Galinier[1], M. Ciarniello[1], G. Filacchione[1], A. Raponi[1], V. Galluzzi[1], E. D'Aversa[1] and B. Gorga[1]. [1]INAF-IAPS, Institute for Space Astrophysics and Planetology, Rome, Italy (marjorie.galinier@inaf.it).

Introduction: The Visual and Infrared Mapping Spectrometer (VIMS) onboard Cassini collected thousands of hyperspectral data cubes of the surface of the five inner mid-sized moons of Saturn (Mimas, Enceladus, Tethys, Dione and Rhea) between 2004 and 2017 [1]. These moons are characterized by an icy surface affected by endogenous activity and exogenous processes, such as cratering events, weathering from the interaction with solar wind particles, interplanetary dust, and energetic particles trapped in Saturn's magnetosphere; UV irradiation, and accumulation of E-ring particles [2]. The agents darkening the surfaces of Saturn's icy moons are possibly the same over the whole Saturn system, yet there is no consensus to date on what these darkening agents are [3].

We exploited the VIMS dataset of spatially resolved spectra, covering independently the VIMS-V (from 0.35 to 1.05 microns) and VIMS-IR channel (from 0.85 to 5.1 microns) wavelength range, to study all five inner moons of Saturn. In this work, we relied on previous works [1,4] to further improve the production of photometrically corrected maps of the moons. Our final goal is to apply a radiative transfer modeling to these maps, to explore different potential compositions of the darkening agents and to deduce the mechanisms leading to the darkening of the moons.

Methods: Exploiting the VIMS dataset, we produced photometrically corrected maps of the moons at full VIMS spectral resolution for the first time. To do so, we used a photometric correction method based on the Akimov theory [1,5].

For each moon, we considered only radiance factor spectra I/F acquired with incidence angle $i \leq 70°$, emission angle $e \leq 70°$, phase angle $10 \leq g \leq 120°$, a Cassini-satellite distance $D \leq 100{,}000$ km, to avoid grazing illumination geometries and large shadowing effects, and we filtered out the pixels with an irregular photometric response. We also filtered out the spectra saturated in any VIS or IR wavelength band respectively, to take into account only pixels having an even linear response. For each moon and at each wavelength, we then derived the equigonal albedo from the considered spectra, and we plotted it with respect to phase angle [1]. We averaged the phase curve data into bins of 5 degrees in phase angle, and performed a quadratic fit to the binned phase curve data. This procedure allowed us to retrieve the photometric parameters associated to each VIMS wavelength band, for each moon. An example of phase curve fit is given in Fig.1, for Dione at 1294.82 nm.

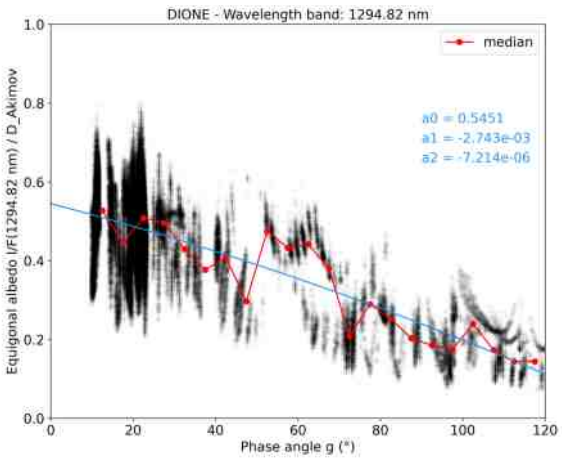


Fig.1: Dione phase curve fit at λ= 1294.82 nm. Black crosses are the observed data, red dots are the average values computed across bins of 5° in phase angle, blue curve is the best quadratic fit with parameters a_0, a_1 (in deg^{-1}), a_2 (in deg^{-2}).

Next, we collected the spectra of each moon in each VIMS wavelength band considering a phase angle of $10 \leq g \leq 90°$, to avoid potentially spurious spectra acquired at extreme phase angles [1]. We filtered out the pixels saturated at each wavelength band independently, for the VIS and IR range, to keep as much data as possible for the production of the spectral maps. We then used the calculated photometric parameters to scale the observed spectra to standard illumination conditions (i=30°, e=0°, g=30°) for each wavelength band, modeling the reflectance I/F of each pixel as the product of a phase function and a disk function, the last modeled according to the Akimov theory [1,5]. We finally developed additional filtering steps, to remove potentially spurious data (e.g partially-filled pixels like the ones along the moons' limb or terminator, saturated spectra). The final amount of spectra considered for each moon and each wavelength range is given in Table.1.

Using the dataset of spectra scaled to standard illumination conditions, we then produced photometrically corrected maps of the moons. The maps were made by reporting on a cylindrical projection each pixel (and their corresponding spectrum) of a moon's

surface, according to the pixel's average latitude and longitude. The median spectrum of each tile of the map was then calculated at each wavelength, sampled at 0.5° in both longitude and latitude (i.e., 2 pixels per degree ppd) [1]. Finally, we bridged the VIS and IR spectra in order to study the full VISIR spectra of the moons [6].

Table.1: Final number of pixels for each moon.

Range	Mimas	Enceladus	Tethys	Dione	Rhea
VIS	7568	60438	58754	100329	92584
IR	3711	44972	31895	78031	54756

Results: The produced maps of photometrically-corrected I/F at 1294.82 nm for each moon are displayed in Fig.2. Mimas' map is of the least good quality because of the scarcity of the observations of this moon, but an albedo contrast between its leading and trailing hemisphere is still noticeable. Enceladus' surface is rather uniform and bright, with slightly distinguishable tiger stripes at low latitudes. Tethys' map shows a darker trailing hemisphere, and a thermal anomaly region lens [7] on the leading equatorial region. Finally, Dione and Rhea show the highest albedo contrast between their leading and trailing hemispheres, and bright wispy terrains are clearly distinguishable across the trailing side of Dione. The highest I/F on Dione is measured on the fresh Creusa crater (76°W;52°N).

Even if some photometric residuals and seams remain in these maps, the maps' quality is generally improved compared to previous studies [1], and a map has been generated for each VIMS wavelength for the first time. These maps will be further analyzed, and the variability of the spectral properties over the surface of each moon will be studied.

The next step of this work is to derive compositional maps of each moon by using the Hapke radiative transfer modeling [4]. We will apply such modeling to Dione as a first test, and we will fit each spectrum of its surface at full VIMS resolution, considering a set of chosen parameters and varying their abundance and grains sizes.

Acknowledgements: This work is supported by the INAF data analysis grant "Mid-sized Saturnian icy Satellites Investigation by Spectral modeling" (MISSIS) and by the project "Preliminary study of payloads for missions to Saturn's moon Enceladus" ASI - INAF agreement n. 2024-19-HH.0.

References: [1] Filacchione, G., Ciarniello, M., D'Aversa, E., et al. 2022, Icarus, 375, 114803. [2] Hendrix, A. R., Buratti, B. J., Cruikshank, D. P., et al. 2018, in Enceladus and the Icy Moons of Saturn, ed. P. M. Schenk, R. N. Clark, C. J. A. Howett, A. J. Verbiscer, & J. H. Waite, 307 [3] Clark, R. N., Curchin, J. M., Jaumann, R., et al. 2008, Icarus, 193, 372. [4] Ciarniello, M., Capaccioni, F., Filacchione, G., et al. 2011, Icarus, 214, 541. [5] Shkuratov, Y., Kaydash, V., Korokhin, V., et al. 2011, Planet. Space Sci., 59, 1326. [6] Christou, A. A., Borisov, G., Dell'Oro, A., Cellino, A., & Devogèle, M. 2021, Icarus, 354, 113994. [7] Howett, C. J. A., Spencer, J. R., Hurford, T., Verbiscer, A., & Segura, M. 2012, Icarus, 221, 1084.

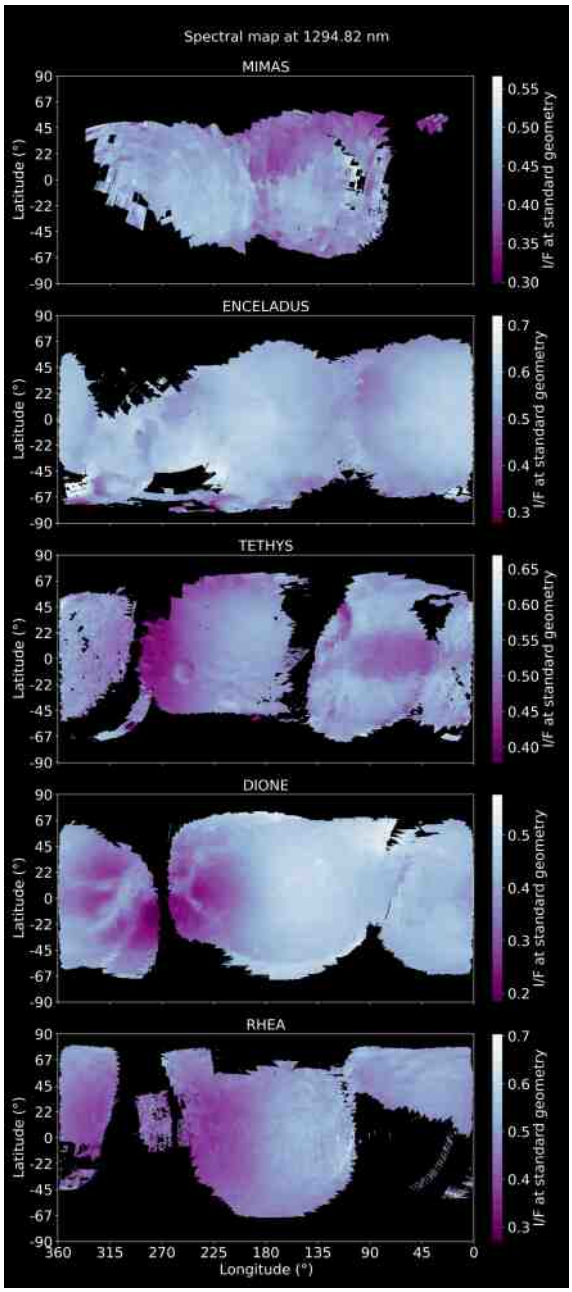


Fig.2: Spectral map of photometrically-corrected I/F at 1294.82 nm of the five mid-sized moons of Saturn. Each map has a resolution of 2 ppd and is shown in equirectangular projection centered at 180° with a West-positive notation.

ESA'S L4 MISSION: A NEW VOYAGE TO THE OCEAN WORLD ENCELADUS

A. Lucchetti[1], Zita Martins, Emma Bunce, Olivier Grasset, Rachael Hamp, Alice Le Gall, Frank Postberg, Olga Prieto-Ballesteros, Lorenz Roth, Paolo Tortora, Audrey Vorburger (**L4 Expert Committee**),
Vania Da Deppo, Caroline Freissinet, Axel Hagermann, Maximillian Hamm, Quang Hung Hoang, Carly Howett, Florian Kehl, Pawel Knapkiewicz, Niels Ligterink, Andoni G. Moral Inza, Antti Näsilä, Robert Prevedel, Stephan Ulamec, Vassilia Spathis (**L4 Payload Working Group**),
Jörn Helbert, Tara-Maria Bründl, Martin Haag, Martin Lindner, Björn Ordoubadian, Sven Wittig (**ESA-ESTEC**)
[1]*National Institute of Astrophisics – Astronomical Observatory of Padova (INAF-OAPD), Padova, Italy,*

Introduction

As part of its Voyage 2050 Science Programme , the European Space Agency (ESA) is preparing its fourth Large-class (L4) mission that aligns with the Voyage 2050 recommendation to pursue the science theme "Moons of the Giant Planets".

Following the recommendation, ESA convened an L4 Expert Committee (EC) to define the mission's scientific scope and target.

While initial internal feasibility studies conducted by ESA's Concurrent Design Facility (CDF) explored options ranging from a Saturn orbiter to landing on moons like Europa, Titan, or Ganymede, the EC prioritized Saturn's moon Enceladus [1]. Enceladus was identified as the most compelling target due to its significant astrobiological interest as an ocean world and the fact that no other space mission has committed to visiting this moon.

The Scientific Case for an Enceladus Mission

The continued exploration of icy moons suggests that subsurface oceans are common, but they are typically hidden under thick ice shells, forcing their habitability to be assessed indirectly. This paradigm shifted with the Cassini mission in July 2005, which definitively detected water vapor plumes and jets of ice particles erupting from Enceladus during its flyby [2].

This activity is concentrated at the moon's south pole, in a region of linear fractures referred to as "tiger stripes". These "tiger stripes" are geologically active and significantly warmer than their surroundings. This cryovolcanism ejects a mixture of vapor and icy grains, composed of water, salts, and organics, directly into space. It is now generally accepted that Enceladus possesses the three necessary conditions for a habitable environment: the presence of liquid water, a source of energy, and a specific set of chemical elements. Crucially, this activity means Enceladus provides a unique opportunity to measure its ocean water "in-situ" and directly search for biosignatures. Cassini demonstrated this capability by measuring the plume composition as it passed through [3], despite its instruments not being designed for such measurements. The L4 mission will be designed and optimized specifically for this search.

Mission Concept: Orbiter and Lander

Set to arrive in the Saturnian system in the early 2050s, the L4 mission will have a payload complement focused on exploring habitability, prebiotic chemistry, and the search for biomarkers.

The mission concept represents a significant step forward in exploration: it will not only place an orbiter around Enceladus but will also deploy a lander on the moon's south pole area [4]. No space agency has previously landed on Enceladus, offering substantial potential for new scientific discoveries. The EC has recommended that the lander be deployed near the active "tiger stripe" region, while the orbiter will be equipped with plume sampling capabilities.

Landing presents a unique challenge and opportunity: the surface is coated with fine, icy particles originating from the plumes, effectively "snow" precipitating from the subsurface ocean. This material may continuously fall onto the landing site and the lander. This presents a remarkable opportunity, as it could deliver material rich in salts, organics, and even biosignatures directly into the lander's scientific instruments. As of today, no payloads have been selected, but the L4 Expert Committee Report outlined a preliminary set of payloads that could satisfy the science objectives.

The mission is characterized by significant design drivers, including mass, power, and data, making new technologies with fewer resource requirements highly desirable. Miniaturisation of payload designs is strongly encouraged. To meet the power demands in the outer solar system, the orbiter will use large solar arrays, which will also enable a high-power solar electric propulsion system. The lander is designed for a minimum operational lifetime of two weeks on the surface, powered entirely by batteries.

Current Status and Path Forward

ESA is currently leading the effort, with continued support from the EC, to further consolidate the science requirements. Since March 2025, a new Payload Working Group (PWG) has been established to assist ESA. This group will help define a "Strawman payload" by analyzing payload concepts, performance trade-offs, technical maturity,

and technology gaps [5]. A critical challenge is the reliable detection of biosignatures. This requires dedicated study of processes to prevent spacecraft-induced or forward contamination, as well as false positives. Adherence to planetary protection regulations is a key design consideration. To meet the target mission adoption date of 2034 (TBC), it is essential to identify critical technology gaps and advance the development of prototypes to the recommended Technology Readiness Level. This mission will advance European expertise in several key fields, including in-orbit assembly, landing technologies, operating in extreme environments, and novel scientific instrumentation.

References: [1] Martins, Z., et al.: Expert Committee for the Large mission covering the science theme “Moons of the Giant Planets”, 2024.[2] Porco, C. C., et al.: Cassini observes the active South Pole of Enceladus, Science, Vol. 311, pp.1393-1401, 2006.[3] Postberg, F., et al.: Macromolecular organic compounds from the depths of Enceladus, Nature,Vol. 558, pp. 564-568, 2018. [4] Helbert, J., et al.: The Mission to Enceladus – The ESA L4 mission, EPSC-DPS2025-1307, 2025. [5] Bründl, T.-M. The Tentative Payload Complement for the L4 Flagship Mission to Enceladus EPSC-DPS2025-1389, 2025.

SYNCHRONIZED ERUPTIONS ON IO A. Mura[1], F. Tosi[1], F. Zambon[1], G. Piccioni[1], R. Sordini[1], M. Paris[1], A. Cicchetti[1], R. Noschese[1], G. Sindoni[2], C. Plainaki[2], [1]INAF, [2]ASI

Abstract: On December 27, 2024, Juno's JIRAM (Jovian InfraRed Auroral Mapper) instrument observed an unprecedented volcanic event on Io's southern hemisphere, covering a vast region of ~ 65,000 km², near 73°S, 140°E. Within the imaged region, only one hot spot was previously known (Pfd454). This feature was earlier estimated to cover an area of 300 km² with a total power output of 34 GW. JIRAM results show that the region produces a power output of 140 - 260 TW, over 1,000 times higher than earlier estimates and likely exceeding the brightest eruption ever recorded on Io, that of Surt in 2001 (~80 TW). Three adjacent hot spots also exhibited dramatic power increases: P139, PV18, and an unnamed feature south of the main one that surged to ~1 TW, placing all of them among the top 10 most powerful hot spots observed on Io. A temperature analysis of the features supports a simultaneous onset of these brightenings and suggests a single eruptive event propagating beneath the surface across hundreds of kilometers, the first time this has been observed on Io. This in turn would imply a connection among the hotspots' magma reservoirs, while other nearby hotspots that have been known to be active in the recent past, such as Kurdalagon Patera, appear unaffected. The simultaneity supports models of massive, interconnected magma reservoirs. The topology of these regional magma systems may resemble that of an large-scale sponge, in which the massive reservoirs are the pores, interconnected through a largely solid outer shell.

Discussion: We have observed a large volcanic outburst on Io, with the most intense power output ever recorded. Several other large eruptions that occurred simultaneously nearby have revealed, for the first time, the structure and vast extent of the connections between different paterae on Io: a system of apparently interconnected magma reservoirs situated hundreds of kilometers from each other. The details of this system, and how triggering occurred, are still unclear; for instance, are individual shallow reservoirs connected by discrete dykes to a larger chamber at depth, or are they a large-scale manifestation of partially-molten material (a "sponge"; de Kleer et al. 2019b)? An extensive subsurface magma system on Io would help to explain the observations of globally distributed lava lakes (Mura et al., 2025a), where the lake surfaces are thought to move vertically. If there were regional connections between paterae, they might all respond together and similarly to forcing from a large magma source.

An eruption of this magnitude is likely to leave a long-lived signature. Previous large eruptions at Io have left varied features such as a large area thought to be pyroclastic deposits (Pillan patera eruption in 1997, see McEwen et al. 1998), large red sulfur rings, or small, maybe fissure-fed lava flows (Tvashtar in 1999, see Lopes et al., 2004). Surface changes resulting from the eruption, and the temporal evolution of the event, can be further studied with upcoming data from Juno.

Our observations support the emerging picture of extensive regional magma systems on Io rather than volcanism being sourced from a globally magma ocean (cf. Park et al. 2025). The topology of these regional magma systems may in some ways resemble that of an enormous sponge. In this model, discrete, large subsurface reservoirs are the pores, interconnected through a largely solid outer shell. Future observations by Juno may clarify the late 2024 eruptive event's nature, which could have left pyroclastic deposits or lava flows akin to previous large eruptions, offering insights into Io's volcanic and tectonic regimes. Earth-based observations of this region may also be possible, although the observational geometry is extremely limited owing to the region's high latitude. Remaining questions about changes from this eruption and the interconnectedness of magma in Io's interior may not be answerable in detail without future exploration.

Acknowledgments

We thank Agenzia Spaziale Italiana (ASI) for the support of the JIRAM contribution to the Juno mission. This work is funded by the ASI–INAF Addendum n. 2016-23-H.3-2023 to grant 2016-23-H.0.

References

de Kleer, et al.2019a. GRL, 46(12), pp.6327-6332.
Lopes, R.M.C. et al., 2004, Icarus, 169(1), pp. 140–174.
McEwen AS, et al.1998. Science, 281(5373):87-90.
Mura, A., et al., 2025a. JGR Planets, 130.
Park, et al., 2025. Nature.

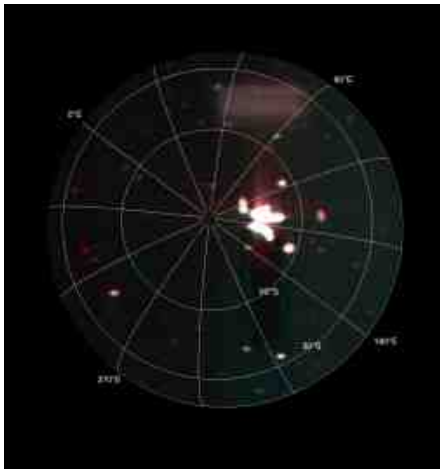


Figure 1. Raw data from JIRAM, taken on Dec. 27, 2024, from a distance of ~100,000 km (unprocessed data). The spacecraft was looking at the south pole of Io; the extreme event feature is clearly visible to the right of the pole

XXI Congresso Nazionale di Scienze Planetarie

Sessione Pianeti e Satelliti
Moon and Mercury

GLOBAL THERMOPHYSICAL CHARACTERIZATION OF MERCURY'S DIURNAL TEMPERATURE CYCLE: THERMAL AMPLITUDES, GRADIENTS, AND STRESS INDICES IN SUPPORT OF BEPICOLOMBO SIMBIO-SYS

P. Cambianica[1], G. Cremonese[1], E. Simioni[1], A. Tullo[1], S. Bertoli[1], C. Re[1], M. Massironi[2,3], E. Martellato[1]

[1]INAF- Astronomical Observatory of Padova, vicolo dell'Osservatorio 5, Padova, Italy, pamela.cambianica@inaf.it

[2]University of Padova, Via Gradenigo, Padova, 35122, Italy

[3]Centro di Ateneo di Studi ed Attivita' Spaziali "G. Colombo", University of Padova, Padova, 35122, Italy

Introduction

Mercury undergoes the most extreme diurnal temperature cycle in the Solar System, with surface temperatures fluctuating from below 100 K during the long nights to more than 700 K at local noon. These dramatic variations, resulting from Mercury's 3:2 spin–orbit resonance and its highly eccentric orbit, generate the largest diurnal thermal gradients of any planetary body. The resulting thermal stresses influence rock breakdown, regolith evolution, and volatile stability, and play a key role in shaping the planet's surface over geological time.

Understanding these thermal processes is also crucial for interpreting spectral and imaging data, as the surface temperature directly affects the radiative properties, spectral slopes, and inferred composition of surface materials. The characterization of Mercury's thermal environment is therefore essential for both planetary surface science and the optimization of orbital observations.

The forthcoming ESA–JAXA BepiColombo mission, expected to enter orbit around Mercury in late 2026, offers a unique opportunity to investigate these processes in unprecedented detail. The Mercury Planetary Orbiter (MPO) will carry the Spectrometer and IMagers for MPO Bepicolombo Integrated Observatory SYstem (SIMBIO-SYS) suite [1], composed of three complementary instruments:

- the STereo Camera (STC), designed to map global topography and morphology at 58 m/px [2];
- the High-Resolution Imaging Channel (HRIC), targeting selected regions at ≈5 m/px [3];
- the Visible and Infrared Hyperspectral Imager (VIHI), providing global spectral data at ≈120 m/px [4] .

Interpreting SIMBIO-SYS observations requires an accurate and physically consistent model of surface and subsurface temperature variations. These datasets will not only provide geological and compositional context but also demand quantitative correction for thermal effects. In this framework, our goal is to develop a global thermophysical model of Mercury capable of predicting temperature fields, thermal amplitudes, and stress-related quantities across the entire planet.

While previous studies have mainly addressed local or regional scales [e.g., 5, 6], only one global model [7] derived from MESSENGER data has provided full-surface temperature maps. Our approach extends such a model by deriving diagnostic maps of diurnal amplitude (ΔT), longitudinal thermal gradients, and a thermal stress index (S_{therm}), parameters that are directly relevant for surface fatigue processes and instrument target planning.

Methods

The model solves the 1D time-dependent heat conduction equation for each surface element of Mercury's globe:

$$\rho(z)\,C(T)\,\frac{\partial T(z,t)}{\partial t} = \frac{\partial}{\partial z}\left[\,k(z,T)\,\frac{\partial T(z,t)}{\partial z}\,\right],$$

where T is temperature, t time, z depth, and ρ, C, and k are the bulk density, specific heat capacity, and thermal conductivity of the regolith, respectively. All thermophysical parameters vary with both depth and temperature [6].

At the surface, a radiative energy balance governs the boundary condition:

$$(1-A)\,S(t)\,\cos\theta(t) = \epsilon\sigma T_0^4(t) - k(z,t)\,\left.\frac{\partial T(z,t)}{\partial z}\right|_{z=0},$$

where A is the bolometric Bond albedo, S(t) is the solar flux at Mercury, cos(θ) the cosine of the solar incidence angle (zero when the Sun is below the horizon), ε the surface emissivity, and σ the Stefan–Boltzmann constant. Each grid element is treated as an independent vertical column extending to 2 m depth, resolved by 40–60 layers with a time step of 6 hours, ensuring numerical stability of the diffusion equation. The model is forced by the MESSENGER global DTM (665 m, equirectangular projection), and simulations are run over multiple Mercury solar days (176 Earth days each) until thermal equilibrium is achieved.

This 1D scheme offers a compromise between physical fidelity and computational efficiency, allowing us to simulate the entire surface of Mercury with depth-dependent thermal properties while retaining diurnal and seasonal variability.

Results

The global ΔT distribution (see Fig. 1) exhibits a clear two-lobed structure with maxima (520–550 K) at 0° and 180° longitude, corresponding to the subsolar longitudes of Mercury's 3:2 resonance, and minima (~400 K) at ±90°. The diurnal amplitude decreases smoothly toward the poles (<200 K), consistent with reduced insolation. The longitudinal thermal gradient peaks between -60° and -90°, with values up to 150 K deg^{-1}. These regions correspond to strong transitions between hot and cold longitudes and often coincide with crater walls and scarps, suggesting locally enhanced thermo-mechanical stress.

The thermal stress index S_{term} varies from 0.08 to 0.14 K h^{-1}, with highest values at the equator and subsolar longitudes, where rapid diurnal cycling favors thermal fatigue. High-latitude and dawn–dusk regions show lower values (<0.10 K h^{-1}), indicating thermally stable conditions.

A comparison with DTM slopes shows a weak correlation (r = –0.06), suggesting that global thermal variability is governed primarily by illumination geometry rather than surface morphology. Local effects such as shadowing become significant only at small scales, inside craters or steep terrains.

Conclusions and implications for BepiColombo

This study provides a planet-wide quantification of Mercury's diurnal thermal amplitudes, gradients, and stress indices. The results establish a global thermophysical framework that directly supports the BepiColombo/SIMBIO-SYS mission, offering predictions of temperature conditions for different illumination regimes.

These thermal maps will:

- Contextualize HRIC, STC, and VIHI data within accurate temperature environments;
- Support the identification of regions with strong diurnal stress or thermally stable conditions;
- Enable multi-instrument synergy for comprehensive surface characterization;
- Contribute to understanding of thermoclastism, rock fatigue and regolith formation.

By linking Mercury's spin–orbit dynamics, illumination geometry, and surface thermophysical properties, this work strengthens the scientific foundation for BepiColombo, providing a benchmark for both global analyses and detailed site investigations.

References

[1] Cremonese, G. et al. (2020) *Space Sci. Rev.*, 216, 75. [2] Cremonese, G. et al. (2009) *PS.*, 305-322. [3] Zusi et al., 2019, Applied optics, 58(15), 4059-4069. [4] Capaccioni et al., (2010), IEEE Transactions on Geoscience and Remote Sensing, 48(11), 3932-3940. [5] Vasavada, A. R. et al. (1999) *Icarus*, 141, 179–193. [6] Cambianica, P. et al. (2024) *Planet. Space Sci.*, 253, 105983. [7] Bauch, K. E. et al. (2021) *Icarus*,354,114083.

Acknowledgments:

This work was supported by the Istituto Nazionale di Astrofisica (INAF), decreto 3/25

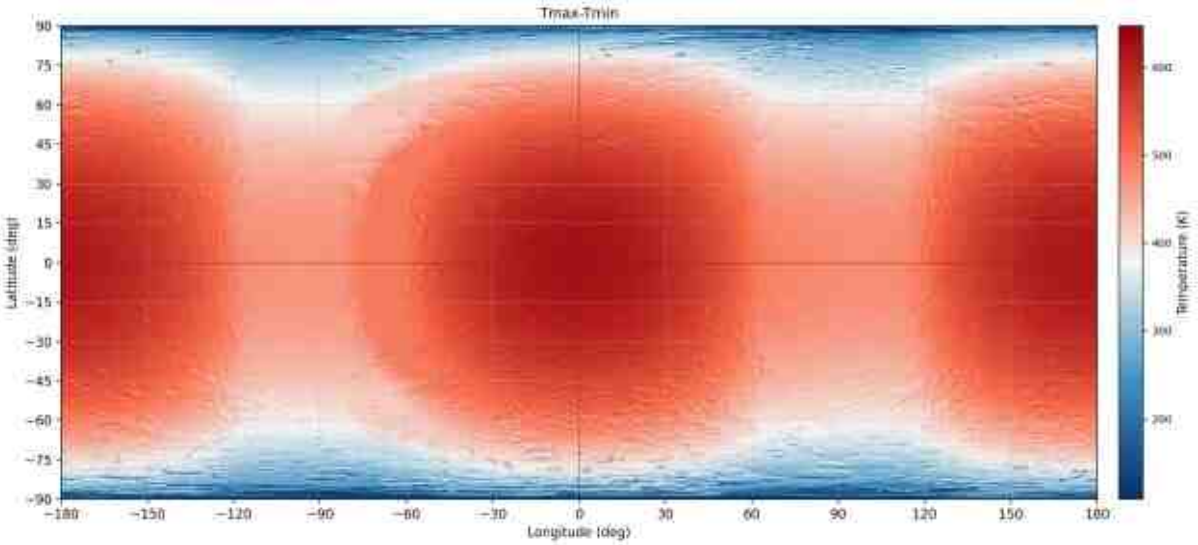


Fig.1 Global map of the diurnal temperature amplitude on Mercury.

HIGH-RESOLUTION OBSERVATIONS OF THE EARTH-MOON SYSTEM WITH THE JANUS INSTRUMENT DURING THE JUICE LEGA FLYBY

P. Palumbo[1], A. Lucchetti[2], R. Hueso[3], A. Antuñano[3], N. Baby[4], T. Kenkmann[5], M. Massironi[6], M. Pajola[2], J.L. Rizos[7], K.Stephan[4], F. Tosi[1], L. Agostini[1], C. Tubiana[1], L. Penasa[2], A. Aboudan[8], M. Aye[9], E.Kersten[4], K.D. Matz[4], R. Politi[1], F. Trauthan[4], A. Zinzi[9], L. M. Lara[7], M.R. Patel[10], G. Portyankina[4] & the JANUS team
[1]INAF-IAPS, Italy; [2]INAF-OAPD, Italy; [3]UPV/EHU, Bilbao, Spain; [4]DLR, Berlin, Germany; [5]Friburg University; [6]Geosciences Dept., Padova University, Italy; [7]CSIC-IAA Astrophysics Institute of Andalucia, Granada, Spain; [8]CISAS G. Colombo, Padova University, Italy; [9]Freie University, Berlin, Germany; [9]Italian Space Agency (ASI), Rome, Italy; [10]School of Physical Sciences, Open University, Milton Keynes, UK

Introduction The ESA JUICE (JUpiter ICy moons Explorer) mission, launched in April 2023, successfully performed the Lunar-Earth Gravity Assist (LEGA) maneuver on August 19-20, 2024. This maneuver provided a unique opportunity to operate the JANUS (Jovis, Amorum ac Natorum Undique Scrutator) imaging system under operational conditions similar to those expected in the Jovian system. JANUS is a modified Ritchey-Chrétien telescope (103.6 mm aperture, 467 mm focal length, 1.3x1.7deg^2 FoV with 1504x2000 pixel and 15 microrad/pixel IFoV) equipped with 13 filters covering the 340-1080 nm range. During LEGA, JANUS acquired high-resolution images of both the Moon and Earth, supporting performance verification and validation of data processing tools. Data processing allowed for the first time the implementation of the calibration pipeline based on ground measurement and comparison with data obtained by other instruments and missions. This work presents the first results on the lunar morphological and spectrophotometric analyses and terrestrial atmospheric observations, highlighting how these data prepare for future scientific investigations at Jupiter.

Moon Observations: During the Moon flyby, JANUS observed the dayside covering latitudes between 17°S-16°N and longitudes 107°E-7°. Acquisitions included multi-filter sequences (4 to 13 filters) with varying solar incidence angles 90° to 29°, achieving spatial resolutions between 20 and 60 m/px. The analysis focused on a crater and on a mare – highlands transition area.

Langrenus Crater is located at the eastern boundary of Mare Fecunditatis, this complex crater (~132 km diameter) was imaged at ~20 m/pixel ground sampling using four filters (Blue, Red, NIR1, NIR2; see Fig1). The images reveal fine morphological details, such as well-preserved terraces and a central peak. The high spatial resolution of the JANUS data enabled a detailed geomorphological mapping of the Langrenus crater geological units along with a comparison with lower resolution LRO WAC dataset. In addition, a crater size-frequency distribution (CSFD) analysis was performed on the extensive crater floor coupled with a structural mapping of the area. Spectrophotometric analysis through different clustering techniques revealed regions consistent with pyroxene-bearing material, suggesting significant compositional diversity.

Highlands between Fecunditatis and Tranquillitatis maria: the transition zone between the mare and adjacent highlands showed a variety of geological features, including wrinkle ridges and volcanic domes. These "hill-shaped" domes are distinct from classical mare domes, maybe directly associated with pre-existing impact craters, which they have visibly deformed or intruded. Color composites allowed distinguishing fresh materials from mature soils.

Earth Observations: JANUS observed Earth for over 30 minutes at a closest distance of 8,408 km, acquiring sequences from the night-side to the day-side over the Pacific Ocean. These observations served as analogs for future investigations of Jupiter's atmosphere. The observations included very different features as for examples below.

Airglow and city lights: night-side images captured Earth's airglow at limb and anthropogenic lights (from Madagascar to sout-east Asia), providing an analog for studying Jovian aurorae and lightning.

Cloud analysis: dawn and morning images over the Philippines and the Pacific Ocean showed tropical convective systems. Elongated cloud shadows allow for altitude measurement. The use of the 940 nm filter, sensitive to water vapor absorption, allowed isolating high-altitude clouds, a technique crucial for determining relative cloud altitudes on Jupiter by using the methan absorption filters. Cloud motion on the short time difference allowed by Earth fly-by was used to test the potential for winds retrieval from image correlation algorithms (Fig. 2).

Earth-Moon Portrait: Days after LEGA, from a distance of 5.6 million km, JANUS acquired a full portrait of the Earth-Moon system in all filters, including narrow-band filters like H-alpha and Sodium.

Discussion and Conclusion: The LEGA flyby demonstrated that the JANUS system is fully operational and capable of acquiring high-resolution multi-filter imagery. Lunar analyses confirmed the ability to distinguish geological units based on color and morphological variations, showing strong consistency with previous missions but with improved spatial resolution. Earth observations validated strategies for studying atmospheric dynamics, including image correlation for wind retrieval and image stacking to

improve signal-to-noise ratio. However, comprehensive analyses are currently ongoing. Detailed geological mapping of the Langrenus crater and spectral investigations of the mare-highland interface are being finalized to better identify mineralogical concentrations. Similarly, wind retrieval potentials and spectral trends of terrestrial features are under further examination. The updated results of these ongoing investigations will be presented. In conclusion, JANUS is ready for future scientific operations in the Jupiter system, where these techniques will be applied to unravel the surface history of icy moons and the dynamics of the gas giant's atmosphere.

Acknowledgements: *JANUS has been funded by the respective Space Agencies: ASI (lead funding agency), DLR, Spanish Research Ministry and the UK Space Agency. Main hardware-provider Companies and Institutes are Leonardo SpA (Prime Industry), DLR-Berlin, CSIC-IAA and Sener. PI and Italian team members acknowledge ASI support in the frame of ASI-INAF agreement n. 2023-6-HH.0. Part of this work was carried out at the Jet Propulsion Laboratory, California Institute of Technology, under contract with NASA*

References: *[1] Palumbo P. et al. (2025) SSR, 221. [2] Grasset O. et al. (2013) PSS, 78, 1-21. [3] Lucchetti A. et al. (2025) EPSC Abstracts, Vol. 18, EPSC-DPS2025-311. [4] Hueso R. et al. (2025) EPSC Abstracts, Vol. 18, EPSC-DPS2025-553.*

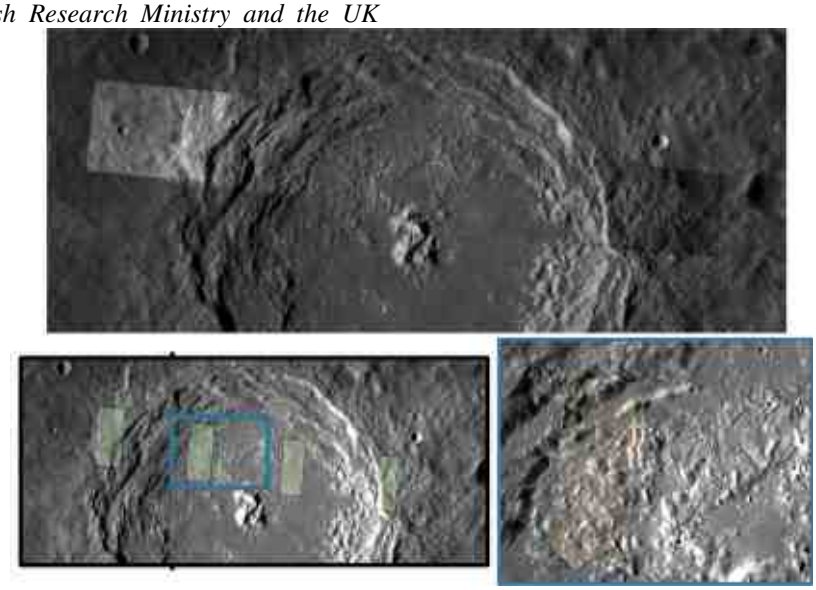


Figure 1*: JANUS images of the Langrenus crater overlaid on the LROC basemap with 100 m resolution. Bottom Left: The green box highlights areas imaged using four different filters. Bottom Right: A close-up of the crater floor, showing the RGB composite product.*



Figure 2*: Multi-filter images reveal the strong water absorption bandit 940nm. A false color violet – 940 – 910 image shows a green-dark ocean, yellow deep clouds and elevated whiteclouds. Cloud tops are 10 km above the surface from their shadows. Wind vectors in the anvil cloud are near 30 m/s from images separated by 8.5 s at a distance of 7,635 km and resolution of 126 m/pixel.*

OH/H_2O FORMATION AND STABILITY IN THE LUNAR MID-LATITUDES: INSIGHTS FROM THE MAIRAN CRATER REGION

F. Colaiuta[1,2], F. Tosi[2], F. Zambon[2], G. Pratesi[3,2]. [1]Dipartimento di Fisica, Sapienza Università di Roma, Rome, Italy. [2]Istituto Nazionale di Astrofisica – Istituto di Astrofisica e Planetologia Spaziali (INAF-IAPS), Via del Fosso del Cavaliere, Rome, Italy. [3]Dipartimento di Scienze della Terra, Università degli Studi di Firenze, Florence, Italy.

Introduction: Hydration on the Moon, in the form of OH/H_2O, has been recognized as a global scale phenomenon [1,2]. However, its behavior at local scales and across the lunar diurnal cycle remains poorly constrained. Addressing these dynamics is crucial for understanding volatile sources, stability, and potential In-Situ Resource Utilization (ISRU). The Mairan crater region (~41.6°N, 44.5°E; Figure 1a) represents a particularly suitable case study, owing to reported hydrogen anomalies. Furthermore, it presents also the rare availability of spatially and temporally overlapping imaging spectroscopy datasets, acquired by the Chandrayaan-1/Moon Mineralogy Mapper (M^3) in both global-mode and target-mode observations [3,4].

Methods and context: We selected high-quality M^3 datasets acquired during OP1B (global-mode, ~08:15 LST) and OP2A (target-mode, ~15:40 LST) mission phases, ensuring the best radiometric stability [4] and enabling diurnal comparisons (Figure 1b).

Data were photometrically corrected following the M^3 team pipeline [4], smoothed with a Savitzky-Golay filter, and thermally calibrated using three independent algorithms: (i) Clark et al. (2011) empirical method [5], (ii) Li & Milliken (2016) spectral channel-ratio semi-empirical approach [6], and (iii) Wohlfarth et al. (2023) roughness-informed model [7].

To link hydration with surface properties, we analyzed several spectral indices and further applied a Fully Constrained Least Squares (FCLS) unmixing in the 0.7–2.3 μm spectral range. OH/H_2O abundance was quantified via the *Effective Single-Particle Absorption Thickness* (ESPAT), which is linearly correlated with OH/H_2O abundance [8]. This index is derived from single scattering albedo retrievals based on Hapke's radiative transfer model [9]. A cluster-based analysis was also performed on target-mode data, to mitigate SNR limitations [10] and isolate terrain units.

Results from spectral indices and unmixing: Cluster analysis of M^3 target-mode data reveals seven distinct units (Figure 2) and highlights clear links between spectral features and hydration behavior. In the early morning, the ~3.0 μm absorption is broad and shifted toward ~2.85 μm, consistent with hydration being hosted in multiple regolith phases under cooler conditions. However, the spectral resolution and temperature-dependent band behavior limit firm interpretation of this shift. By mid-afternoon, the feature sharpens into a well-defined band centered at ~2.75 μm, which is diagnostic of structurally bound OH in defect-rich silicates and indicates retention of solar wind–implanted protons in specific hosts [11].

A key compositional control emerges from the 2 μm region: terrains showing a weaker and broader 2 μm absorption band correspond to higher OH/H_2O abundances (Figure 3). This spectral behavior is characteristic of agglutinate-rich soils, where the amorphous glassy component tends to dilute and broaden pyroxene absorptions. Accordingly, FCLS unmixing confirms a positive correlation between OH/H_2O and agglutinate content, reinforcing their role as favorable long-term reservoirs. Finally, no significant correlation is found with the OMAT parameter [12], implying that hydration persistence is not dictated by overall optical maturity but rather by microstructural properties of specific regolith phases.

Diurnal variability and comparison with lunar samples: The comparison between early morning and mid-afternoon observations reveals a strong diurnal variability in hydration in our region of interest. In the morning (~08:15 LST, global-mode), OH/H_2O abundances are relatively high and broadly distributed across different regolith phases, ranging from ~140 to 450 ppm. These estimates depend on the assumed grain size [8], which in this case is constrained to the 0–75 μm range based on FCLS analysis. Under these cooler conditions, hydration appears widespread and not strongly selective.

By mid-afternoon (~15:40 LST, target-mode), OH/H_2O abundances decrease drastically to ~30–100 ppm, resulting in a 60–80% reduction. These values are particularly significant because they are consistent with hydration levels measured in agglutinates from Apollo and Chang'e 5 samples [13, 14] reinforcing the interpretation that space-weathered glasses act as the main hosts of structurally bound OH/H_2O under warmer conditions. At this stage, hydration becomes more localized and persists mainly within agglutinate-rich terrains, where defect-rich glassy matrices provide stable sites for proton retention against thermal desorption.

Spectral unmixing in the 2.5–3.0 μm range further supports this interpretation, with crushed silica and irradiated Apollo samples (LS78421 and LS73131) [15] emerging as the best analogues for the ~2.75 μm band, while endogenous contributions, such as OH-apatite, remain negligible within statistical uncertainties.

Conclusions: Our results reveal a dual hydration regime: in the early-morning, OH/H_2O is widespread but transient, while in the mid-afternoon only a

smaller, stable fraction remains, preferentially hosted in agglutinate glasses. The strong correlation between ~2.75µm band depth and agglutinate abundance shows that regolith microstructure, rather than bulk composition or optical maturity, controls hydration stability. The observed diurnal decrease (60–80%) underscores the dynamic nature of lunar hydration and confirms its primarily exogenous origin. This framework refines our understanding of volatile behavior at mid-latitudes local scale and highlights agglutinates as key reservoirs for stable OH/H_2O.

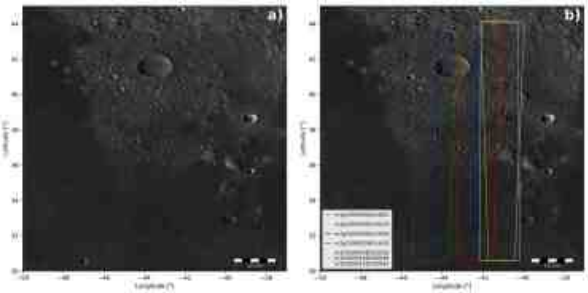


Figure 1. Mairan crater region from the LROC/NAC **(a)** and the M^3 datasets used for this work **(b)**.

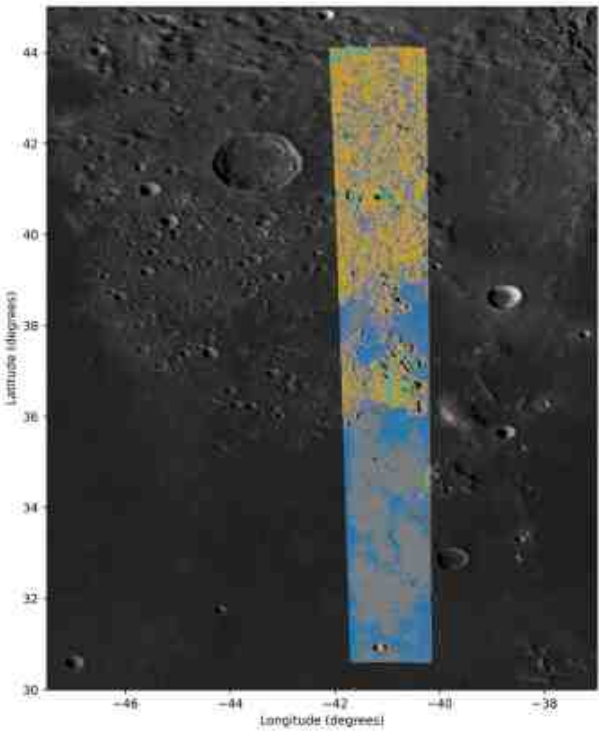


Figure 2. Clusters derived from the K-Means algorithm. Within the overlapping area for global and target-mode data (Figure 1b), seven units are identified: Oceanus Procellarum (OP1 and OP2) and Mairan Peninsula (MP1, MP2, MP3, MP4 and MP5) clusters.

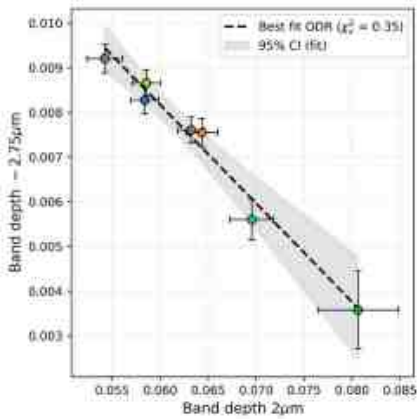


Figure 3. The depth of the ~2.75µm band is examined in relation to the ~2.0µm band depth for the Li&Milliken [6] thermal removal method. Color scheme is the same of Figure 2. The two indices show a correlated trend, as indicated by the best-fit regression (black dotted line). The same trend is observed for Clark and Wohlfarth thermal removal methods [5,7].

Acknowledgments: The authors acknowledge support from the Space It Up project, funded by the Italian Space Agency and the Italian Ministry of University and Research to promote collaboration and innovation in the space sector on nine lines of research, from observation and protection of the Earth to extra-terrestrial exploration, from artificial satellites to remote sensing. Contract n. 2024-5-E.0 – CUP n. I53D24000060005.

References:

[1] Pieters (a), C.M. et al. (2009) *Science, 326(5952), 568-572.*
[2] Clark, R.N. (2009) Science, 326(5952), 562-564.
[3] Pieters (b), C.M. et al. (2009) *Current Science, 96(4), 500-505.*
[4] Green, R.O. et al. (2011) *Journal of Geophysical Research, Planets, 116(E10).*
[5] Clark, R.N. et al. (2011) *Journal of Geophysical Research, Planets, 116(E6).*
[6] Li, S. & Milliken, R.E. (2016) *Journal of Geophysical Research, Planets, 121(10).*
[7] Wohlfarth, K. et al. (2023) *Astronomy & Astrophysics, 674(A69).*
[8] Li, S. & Milliken, R.E. (2017) *Science Advances, 3(9).*
[9] Hapke, B. (1984) *Icarus, 59(1), 41-59.*
[10] Clark, R.N. et al. (2024) *The Planetary Science Journal, 5(9).*
[11] McLain, J.L. et al. (2021) *Journal of Geophysical Research: Planets, 126, e2021JE006845.*
[12] Lucey, P.G. et al. (2000) *Journal of Geophysical Research, Planets, 105(E8).*
[13] Liu, Y. et al. (2012) *Nature Geoscience, 5, 779–782.*
[14] Zhou, C. et al. (2024) *Science Advances, 10(19), eadl2413.*
[15] Yeo, L.H. et al. (2025) *Journal of Geophysical Research, Planets, 130(E3).*

THE MoonSWA PROJECT: INTEGRATED SPECTRAL AND LABORATORY ANALYSIS OF LUNAR SPACE WEATHERING. Francesca Zambon[1], Stefano Rubino[1], Rosario Brunetto[2], Federico Tosi[1], and Cristian Carli[1]. [1]INAF - IAPS, Roma, Italy [2]Université Paris-Saclay, CNRS, Institut d'Astrophysique Spatiale, Orsay, France. E-Mail: francesca.zambon@inaf.it

Introduction: Airless planetary bodies such as the Moon are continuously exposed to the harsh space environment, including solar wind irradiation, cosmic ray flux, micrometeorite impacts, and diurnal thermal cycling. These processes, collectively referred to as space weathering [1], induce progressive and irreversible alterations in the optical, chemical, and physical properties of surface materials. On the Moon, the effects of space weathering were first identified through the analysis of Apollo and Luna mission samples and are mainly manifested as (1) a decrease in albedo (surface darkening), (2) a reddening of the spectral slope, and (3) a weakening of absorption bands near 1 μm and 2 μm associated with mafic minerals such as pyroxene and olivine [2, 3].

The formation of nanophase metallic iron ($npFe^0$) particles within agglutinates and along grain rims is recognized as the main driver of these spectral modifications [4]. The gradual fading of bright rays around young craters into mature regolith exemplifies the cumulative visual effect of space weathering on the Moon's surface. Additionally, due to the Moon's synchronous rotation and its periodic exposure to the Earth's magnetotail, the spatial distribution of weathering intensity is expected to be non-uniform, with asymmetric solar wind implantation patterns [5].

In this framework, the Moon Space Weathering Analysis (MoonSWA) project — selected within the INAF 2023 Fundamental Research Call — aims to investigate the spectral effects of space weathering in the visible and near-infrared ranges by combining remote sensing analysis, laboratory irradiation experiments, and integrated data interpretation. The outcomes of MoonSWA will also contribute to the scientific context of the ESA/ASI LUMIO mission, dedicated to monitoring meteoroid impacts on the lunar farside through optical observations of transient luminous flashes.

Dataset and Methods: The MoonSWA project follows a multi-pronged methodological approach:

Spectral Analysis of Lunar Regions – Selected lunar areas, including basaltic maria and highland crater interiors, are analyzed using publicly available multispectral and hyperspectral datasets. Primary sources include M^3 (Moon Mineralogy Mapper), Clementine, and LRO/Diviner data products. The spectral characterization focuses on the 1 μm and 2 μm absorption bands of pyroxenes and olivine, assessing band depth, position, and continuum slope as indicators of mineral composition and weathering degree.

Laboratory Irradiation Experiments – Irradiation campaigns are conducted at the INGMAR–SIDONIE ion bombardment platform (IAS/IJCLab, Orsay, France). Lunar meteorites have been exposed to He^+ ions at 20 keV, to simulate solar wind ion fluxes to reproduce and assess their spectral effects. Reflectance spectra are measured before and after irradiation, covering the spectral range between 0.4-16 μm.

Integrated Analysis – The project integrates remote sensing observations with laboratory results through comparative spectral modeling. This synergy aims to quantify the relationship between $npFe^0$ abundance, spectral slope variation, and albedo reduction, enabling the calibration of space weathering indices applicable to lunar datasets.

Results: The first irradiation campaign has been successfully completed, targeting three lunar meteorite samples: NWA-13859, NWA-14188, NWA-8786 [6]. Preliminary reflectance spectra confirm the expected darkening and reddening trends after exposure to ion fluxes, consistent with theoretical models of $npFe^0$ formation. The observed spectral evolution provides quantitative constraints on the optical maturity parameter (OMAT) and supports the calibration of weathering timescales under known irradiation conditions.

In parallel, the selection of regions of interest (ROIs) on the lunar surface is ongoing. Preliminary analysis focuses on contrasting environments, including young craters and mature mare regions, to map the variability of space weathering signatures at local and regional scales. Data comparison with laboratory-irradiated analogs will allow for improved interpretation of the maturity state and compositional heterogeneity of lunar terrains.

Future Work: Upcoming activities will focus on the integration of laboratory and remote sensing datasets to establish a unified model of spectral alteration across the visible and near-infrared range.

Furthermore, the project aims to extend the experimental irradiation campaign to include H^+ ions bombardment, reproducing more realistic space weathering conditions. The final objective is to deliver a quantitative framework linking physical processes to observable spectral parameters, enhancing the scientific return of future missions such as LUMIO.

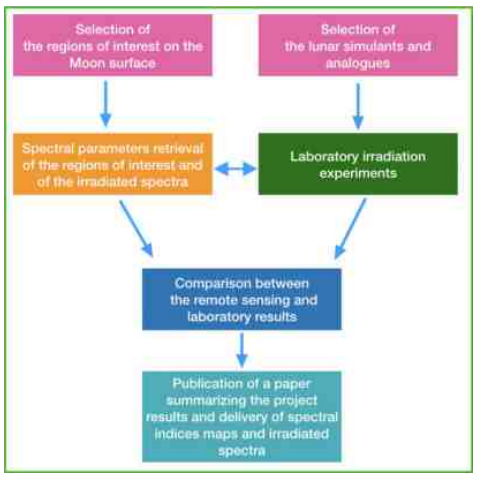


Figure 1: Schematic workflow of MoonSWA activities.

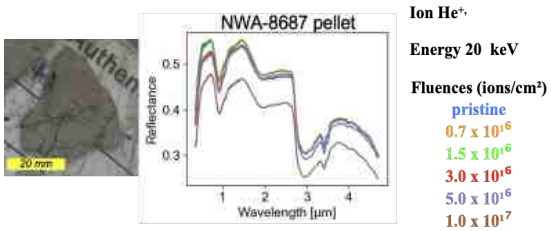


Figure 2: Example of spectra before and after irradiation on the lunar meteorite sample NWA-8687.

References: [1] Pieters, C.M., & Noble, S.K. (2016). JGR, DOI: 10.1002/2016JE005128. [2] Burns, R.G. (1993). Mineralogical Applications of Crystal Field Theory. Cambridge Univ. Press. [3] Pieters, C.M. et al. (1993). JGR, DOI: 10.1029/93JE02467. [4] Noble, S. et al. (2005). MAPS, DOI: 10.1111/j.1945-5100.2005.tb00390.x. [5] Kallio, E. et al. (2019). PSS, DOI: 10.1016/j.pss.2018.07.013. [6] Rubino, et al. (2025). EPSC-DPS Conference Abstracts.

Acknowledgements: This project is funded by "Bando Ricerca Fondamentale INAF 2023" - MoonSWA mini-grant (PI: F. Zambon). Lunar meteorite samples are provided by the "MELODY" project selected in 2020 in the framework of the PRIN INAF 2019 (RIC) call (PI: F. Tosi). We acknowledge financial support from the LUMIO project funded by the Agenzia Spaziale Italiana (ASI-PoliMi agreement n. 2024-6-HH.0). The authors thank P. Benoit-Lamaitrie, J. Bourçois and C. Bachelet for access to SIDONIE and O. Mivumbi and K. Guernon for technical support with INGMAR.

XXI Congresso Nazionale di Scienze Planetarie

Sessione Focus S4
Volatile and refractory material emissions in planetary environments: a modeling perspective

WHEN SHAPE MEETS TEMPERATURE: MORPHOLOGICAL AND THERMOPHYSICAL INTERACTIONS IN MERCURY'S PERMANENTLY SHADOWED CRATERS

Bertoli S.[1], Cambianica P.[1], Munaretto G.[1], Cremonese G.[1], Massironi M.[2], Martellato E.[1], Lucchetti A.[1], Pajola M.[1], Simioni E.[1], Tullo A.[1], Re C.[1]

[1] INAF – Osservatorio Astronomico di Padova, Italy (silvia.bertoli@inaf.it); [2] Università degli Studi di Padova, Dipartimento di Geoscienze, Italy

Introduction: The polar regions of Mercury host Permanent Shadowed Regions (PSRs), i.e. areas that remain in constant shadow due to the planet's low obliquity [1]. These conditions allow surface temperatures to drop to extremely low values [2], potentially enabling the accumulation and long-term stability of water ice. The presence of radar-bright deposits in PSRs, first observed from Earth-based radar data [3,4], was interpreted as water ice, an hypothesis later supported by comparisons with icy deposits in other planetary bodies (e.g., Mars) [5], hydrogen abundance measurements taken by the NASA MESSENGER mission [6], and thermal models [7]. Morphological studies of PSR-hosting craters [8] revealed features potentially linked to ice-related processes, which itself could be triggered by the specific thermal environment of PSRs. On airless bodies like Mercury, local topography significantly influences solar illumination and, consequently, the thermal behavior of surface volatiles. In this study, we investigate the thermal environment of selected PSR-bearing craters using shape-based thermophysical modelling [9], with the goals of: (1) characterizing their thermal conditions, (2) predicting the evolution of their surface features, and (3) assessing whether temperature regimes could influence the formation of specific landforms or viceversa.

Methodology: We applied a multi-disciplinary approach, combining geomorphological and morphometric characterization of the craters with thermophysical modeling. The six craters selected for this work (Angelou, Desprez, Fuller, Jimenez, Laxness and Ensor) are located above 80°N, and present different amount of radar bright material, morphologies and ages [8,10]. In addition, high-resolution digital terrain models (DTMs) are available for them [11], data which is pivotal for a detailed thermophysical model.

To investigate the thermal environment, we performed a detailed thermophysical analysis using a shape-based 3D thermophysical model [9]. This model calculates the surface and subsurface temperature of each facet in a 3D mesh over 176 Earth days, (1 Hermean solar day and two years), incorporating direct insolation, multiple scattering of visible and infrared light, thermal emission, and terrain shadowing. The Sun is simulated as a disk, accounting for its large angular size in Mercury's sky and divided into 100 sectors. This approach enables accurate modelling of both full shadows and penumbral regions, which are critical in high-relief terrains like crater interiors.

Results: From a morphological perspective, we identified several features that may be linked to the thermal environment of PSRs. Fuller crater exhibits numerous fractures on its floor. Classified as "landforms of uncertain origin" [8], these features may be related to subsurface ice acting as permafrost. On Earth, permafrost forms when the ground remains below freezing for at least two consecutive years [12]. Previous studies [6, 13] suggest that crater floors hosting PSRs may contain a lag deposit composed of dark, carbon-rich material interpreted as the residue of sublimated ice. Such a deposit could behave like the active layer in terrestrial permafrost, potentially deforming and cracking due to thermal gradients induced by adjacent sunlit terrains. Alternatively, the fractures could be associated with the cooling of impact melt or volcanic infill, both processes commonly observed on Mercury [14]. Fuller crater also hosts a Rough Unit near its central peak. This unit appears darker and rougher than both the smooth crater floor and the landslide material, and may represent the result of interactions between ice and the overlying lag deposits.

In contrast, Ensor and Laxness craters contain bright material along their shadowed walls. These deposits correspond to ejecta from small impacts that may have excavated and emplaced subsurface ice [8, 15]. It is therefore important to assess whether these regions are associated with high thermal gradients.

From the thermophysical model, we obtained the maximum, minimum temperatures and their gradient for each of these craters. The results are presented in Fig. 1, which shows also the inner morphology of selected craters.

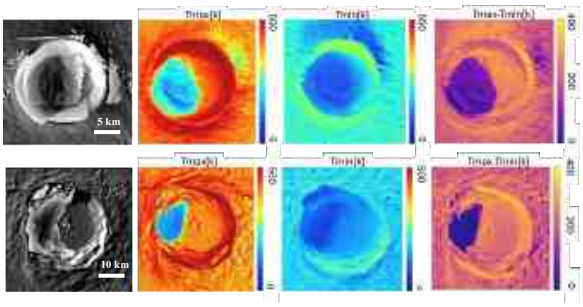


Fig. 1 – The image shows an example of the results for two craters (Angelou and Desprez).

Discussions: Starting from how the thermal environment could modify or create shape, we evaluated the ΔT, which in PSRs seems ranging between 50 K and 150 K. Even moderate warming can induce slow ice deformation, micro-fracturing, and local redistribution of lag deposits. Bright deposits in Laxness crater [15], which are suggested to be ice deposits directly exposed to surface due to small impacts, experience a ΔT of about 140 K (Fig. 2). This could induce slow sublimation, confirming that these deposits are younger than the ice covered by the lag deposits.

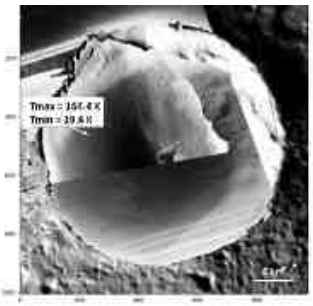


Fig. 2 - Laxness crater with the indication of MAX and MIN temperature of the small bright ejecta.

Within Fuller crater, the PSRs experience a ΔT ranging between 30 K and 50 K, in particular in the regions highlighted by [8]. At this gradients, thermal expansion and microcracking of the ice are possible, suggesting a sort of "periglacial" behaviour of the lag deposits, with the formation of fractures (Fig. 3).

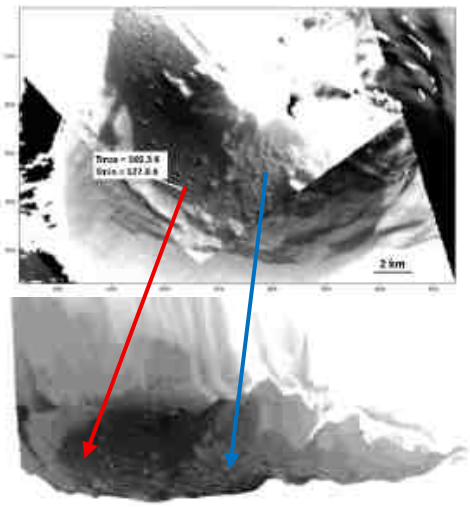


Fig. 3 - Inner view of Fuller crater. The Tmax and T min are referred to the fractures located on the floor (the red arrow in the 3D model). The blue arrow indicates the Rough unit.

On the other hand, we can evaluate how the crater shape could influence the temperature.
We highlighted that some PSRs exhibit uniformly low ΔT values, while others display strong spatial variability, with localized zones experiencing significantly higher thermal amplitudes. Thus, we compared the median ΔT values derived for each PSR with the corresponding depth-to-diameter ratio (d/D), used as a morphometric indicator of crater shape. The analysis revealed a positive correlation between the mean ΔT and d/D (Fig. 4). A higher d/D indicates a more confined geometry, with steeper walls and a reduced sky-view factor, which enhances mutual radiative coupling and self-heating within the crater.

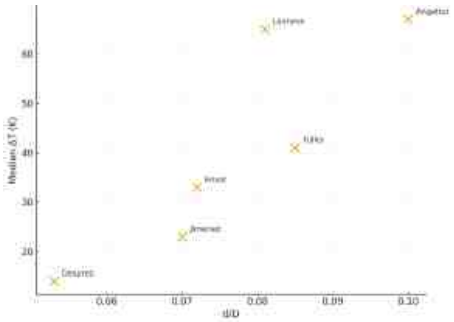


Fig. 4 – The table shows the correlations between the median ΔT of the PSRs of the selected craters and the d/D ratio

Conclusions: Our results show that the morphology and the thermal environments are strictly connected on Mercury's PSRs. The positive correlation between d/D and the ΔT indicates that more confined craters experience larger thermal contrasts. Bright internal ejecta in craters such as Laxness show very high ΔT (~140 K), consistent with exposed ice undergoing slow sublimation, while PSRs in Fuller display moderate ΔT (~30–50 K), potentially promoting the thermal cracking of lag deposits.

Future analysis will include the quantitative modelling of sublimation rates, by using T_{min} maps to assess how these thermally distinct environments translate into actual volatile loss or preservation.

Aknowledgements: This work has been developed under the ASI-INAF agreement n. 2024-40-HH.0

References: [1] Margot J.-L. et al. (2012), JGR:Planets, 117. [2] Susorney H. C. M. et al. (2021), The Planet. Sci. J., 2. [3] Harmon and Slade (1992), Science, 258, 640–643 [4] Harmon et al. (2011), Icarus, 211, 37-50. [5] Butler et al. (1993), JGR, 98, 15003 – 15023. [6] Wilson et al. (2019), JGR:Planets, 124, 721 – 733. [7] Paige et al. (2013), Science, 339, 300 – 303. [8] Bertoli et al. (2024), Journal of Maps [9] Cambianica P. et al (2024), PSS, 253 [10] Bertoli et al. (2025), PSS., 264 [11] Hamill et al. (2020), Planet. Sci. J. [12] Dobinski, W. (2011), Earth-Science Rev., 108, 158 – 169. [13] Syal M. B. et al. (2015), Nature Geoscience, 8 [14] Xiao Z. et al. (2014b), JGR:Planets, 119, 1496 – 1515. [15] Deutsch A. N. et al. (2019), EPSL, 250, 26 – 33

SOLAR ACTIVITY EFFECTS ON LUNAR SURFACE AND IMPACT. L. Calderone[1], L. Biasiotti[1] and S. Ivanovski[1,2] [1] Astronomical Observatory of Trieste INAF, Via G.B. Tiepolo 11I-34143 Trieste, Italy
[2] University of Trieste, Trieste, Italy
(lorenzo.calderone@inaf.it)

Introduction: Space weather events, such as solar flares and coronal mass ejections (CMEs), can significantly influence the lunar environment and potentially modulate the flux and dynamics of meteoroid impacts. This study investigates the interaction between extreme solar activity and micrometeoroid streams, focusing on erosion processes and dust redistribution on the Moon's surface. Observations and theoretical modeling suggest that while moderate interplanetary CMEs may not drastically alter surface morphology, high-energy events can act as "sandblasters," removing volatile materials and reshaping the regolith.

This research is conducted within the framework of the LUMIO (Lunar Meteoroid Impact Observer) mission [1], a 12U CubeSat equipped with the LUMIO-Cam- a dual-spectrum optical instrument designed for continuous monitoring in the visible and near-infrared. Operating from a quasi-halo orbit around the Earth-Moon L2 point, LUMIO aims to detect and characterize impact flashes on the lunar far side, providing valuable data on meteoroid flux and impact frequency.

Methods and results: To complement observational data, we perform numerical simulations using the LIMARDE code [figure 1]. Particles are initialized with a spatial distribution of a few tens of meters [2], velocities ranging from tens to a few thousand meters per second [3], and radii varying from millimeters to micrometers [4]. These simulations aim to probe dust behavior under microgravity conditions following kinetic impacts, while simultaneously accounting for space weather effects that can modulate the system's energy, including both the kinetic contribution and the potential charging of particles.

We explore whether simultaneous occurrences of CMEs and meteoroid impacts can amplify ejecta dynamics and alter dust behavior, with implications for lunar surface evolution and future exploration. By investigating CME effects on dust dynamics before and after impacts, this study contributes to a deeper understanding of solar-lunar interactions in planetary science.

This research has been carried out in the framework of the LUMIO project, supported by the Italian Space Agency and the National Institute of Astrophysics.

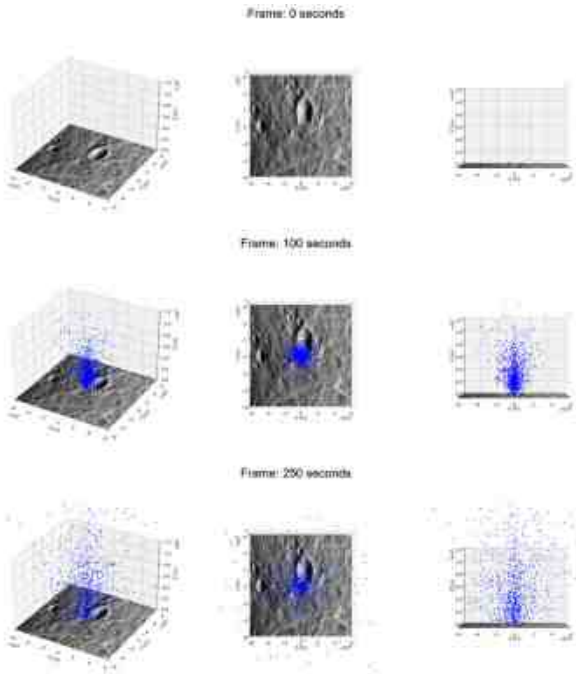


Figure 1: Simulation of a plume of one thousand particles using the LIMARDE code at three different time points (0 seconds, 100 seconds, and 250 seconds), viewed from three different angles.

Reference:

[1] Cipriano A. M., Dei Tos D. A. and Topputo F. (2018) Front. Astron. Space Sci., 5, 29, https://doi.org/10.3389/fspas.2018.00029;
[2] Ivanov B. A., Neukum G., Bottke W. F. and Hartmann W. K. (2002) Asteroids III, 89–101, https://ui.adsabs.harvard.edu/abs/2002aste.book...89I ;
[3] Yang C., Li Z. and Zhang X. (2022) A&A, 658, A80,https://doi.org/10.1051/0004-6361/202140810s;
[4] Szalay J. R., Pokorný P., Sternovsky Z., Kupihar Z., Poppe A. R. and Horányi M. (2019) JGR Planets, 124,143–154, https://doi.org/10.1029/2018JE005756;

IMPACT-INDUCED SULFUR MELTING ON MARS: A POTENTIAL SOURCE OF NATIVE SULFUR DETECTED BY THE NASA'S CURIOSITY ROVER

L. Maggioni[1,2], W. Rapin[3], O. Forni[3] , D. Baratoux[3] , M. Formisano[1], M. C. De Sanctis[1], G. Magni[1], F. Altieri[1]

[1]INAF-IAPS, Rome, Italy. Email: luca.maggioni@inaf.it,[2]University of Rome Tor Vergata, Rome, Italy, [3]IRAP, Toulouse, France

Introduction: During its exploration of Gale Crater, NASA's Curiosity Rover discovered several bright, decimeter-sized clasts composed of nearly pure native sulfur within the Gediz Vallis channel [1]. These fragments, totaling an estimated $10^7 - 10^8$ kg of material [2], represent the first detection of elemental sulfur on Mars. On Earth, native sulfur forms in volcanic, hydrothermal, or evaporitic settings, and rarely as solidified lava flows [3].

To explain Curiosity's observations, recent studies [4, 5] have proposed low-temperature geochemical mechanisms. In contrast, we explore the hypothesis that the deposits result from the solidification of molten sulfur produced by the melting of sulfur-rich substrate during a meteoritic impact. Geological mapping reveals an eroded and breached crater (~390 m in diameter, ~80 m deep) upstream of Gediz Vallis, within the light-toned yardangs unit (Fig. 1), consistent with a meteoritic origin. We suggest that local enrichment in native sulfur could have melted during such an impact, with the molten material flowing a few kilometers downslope before solidifying into the deposits observed by Curiosity. Small lunar impact craters on basalts (< 1 km) produce well-documented melt pools [6], supporting the plausibility of this mechanism.

To test this hypothesis, we performed numerical simulations using the iSALE shock-physics code (2D, Version Dellen) [7, 8, 9] to estimate the amount of molten sulfur produced under plausible impact conditions.

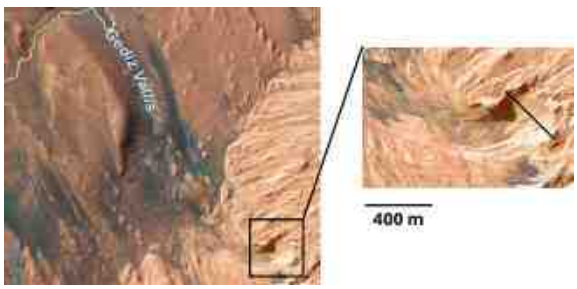


Figure 1*: HiRISE map of the study area. Left: Gediz Vallis with the Curiosity rover traverse (white line). Right: zoomed view of the partially collapsed crater and the adjacent valley interpreted as the pathway of molten sulfur flow.*

Model: The two-dimensional version of iSALE models vertical impacts in an axially symmetric cylindrical geometry. Although this setup excludes oblique impacts, previous studies [10] show that impact velocity is the dominant factor controlling melt production.

We performed iSALE simulations of a dunite projectile impacting a basaltic target at velocities of 7 km/s and 10 km/s, consistent with typical impact speeds on Mars [11]. Projectile radii were set to 12 m and 10 m, respectively, to reproduce the observed crater diameter. Dunite approximates Main Belt asteroids, as most small bodies are ordinary chondrites. Each cell in the iSALE Eulerian grid contains a massless Lagrangian tracer that follows the motion of the original material and records its thermodynamic history. Due to the absence of a high-pressure equation of state (ANEOS) for sulfur [12], direct modeling of a solid sulfur substrate was not possible. We therefore assume sulfur is a minor component of the target, with crater formation and shock propagation dominated by basalt, and consider shock-induced heating as the primary melting mechanism [13]. The amount of melted sulfur was then estimated using available thermodynamic data. In particular, using the limited Los Alamos shock data [14] for sulfur together with M-ANEOS [15], a tool for generating ANEOS tables, we reconstructed the sulfur Hugoniot curve (Fig.2).

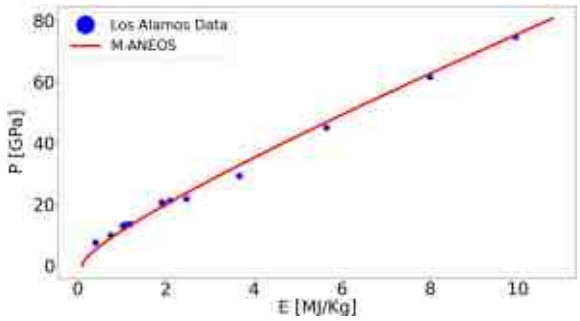


Figure 2: *Comparison between the Hugoniot curve generated by M-ANEOS (red line) and experimental shock data from Los Alamos (blue dots) for rhombic sulfur. The plot shows the relationship between specific internal energy (E) and Pressure (P).*

At this point, from the iSALE tracers, we extracted peak shock pressures and mapped them onto this Hugoniot to obtain corresponding shock energies, which we compared with the pressure-dependent energy required for melting: $E_m \approx c_p[T_m(P_{peak}) - T_0] + L_f$. Where $c_p = 710$ J/(Kg K) and $L_f = 5.4 \times 10^4\ J/kg$ are the specific heat at constant pressure and the latent

heat of fusion of sulfur at 1 bar, respectively. The initial surface temperature is $T_0 = 220$ K, and $T_m(P_{peak})$ is the pressure-dependent melting temperature derived from experimental data up to 65 GPa [16, 17, 18] (see Fig.3). Accounting for possible PdV losses (10-30%) [19], we identified tracers exceeding the sulfur melting threshold and estimated their post-shock release temperatures using a Mie–Grüneisen isentropic approximation with constant Gruneisen parameter $\Gamma = 1.13$, computed at 1 bar. Comparing these release temperatures with the 1 bar melting temperature of sulfur (388 K) allowed us to determine regions where molten sulfur could persist.
Finally, we quantified the melt distribution by identifying tracers rising more than one projectile radius above the surface as ejected [20], allowing us to estimate the volumes of molten material retained within and expelled from the crater.

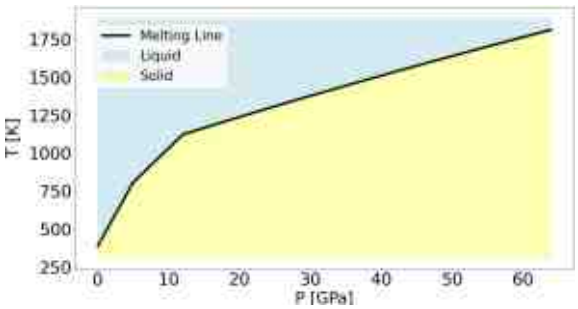


Figure 3: *Reconstruction of the sulfur melting curve from 1 bar to 65 GPa.*

Results: The total volume of material melted by shock-wave propagation for the two impact velocities is shown in Fig.4, which illustrates how melt production varies with the spatial resolution of the iSALE grid, expressed in cells per projectile radius (cppr). Previous studies suggest that 40 cppr provides a good balance between computational cost and accuracy for reproducing shock-induced melting [13]. During crater excavation, the molten material evolves dynamically, but the melted volume retained within the crater stabilizes after 4 s, with roughly 20–25% of the total melt remaining. This fraction is largely independent of grid resolution. Based on the total melted volumes obtained at 40 cppr, the corresponding melt pool volumes range from 11960 m^3 to 27250 m^3.
Finally, given that our model assumes impact dynamics dominated by basalt with sulfur as a minor constituent, we adopt a sulfur fraction of 20%. Under this assumption, the sulfur mass retained in the crater pool ranges between 5×10^6 kg to 1.1×10^7 kg (using a sulfur density of 2050 kg/m^3). Localized sulfur enrichment in the subsurface could raise this estimate considerably, yielding values compatible with the sulfur mass detected by Curiosity. The observed crater morphology shows signs of partial collapse, suggesting an oblique impact. Given the structure's relatively young age, its morphology likely preserves the original form. We propose that rim collapse may have enabled molten material to flow from the crater floor into the adjacent channel, which terminates near the location where Curiosity detected sulfur-rich deposits.

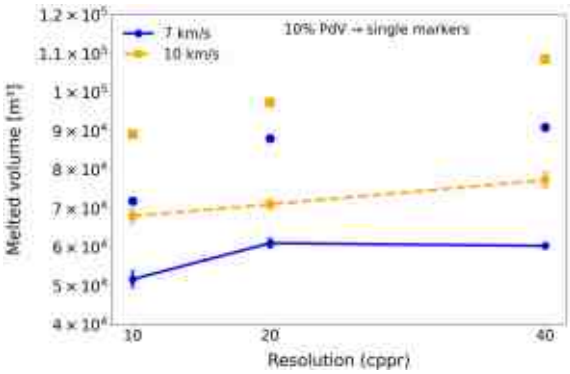


Figure 4: *Dependence of melted volume on numerical resolution. Vertical bars show the range of melt volumes for 20–30% of energy lost to PdV work. Filled single markers indicate the case of 10% PdV loss.*

Conclusions: The results of this work suggest that asteroid impacts may represent a plausible mechanism for melting native sulfur on Mars. Further modeling is required to refine this scenario, starting with simulations at additional impact velocities to capture Mars' asymmetric velocity distribution [11]. In the longer term, the development of a dedicated sulfur equation of state will be essential to also simulate sulfur-rich substrates. Overall, these results provide key input to ongoing geological investigation of the sulfur deposits found by Curiosity. The arrival of the rover at the Yardangs region will provide a unique opportunity to test this impact-melting hypothesis and place new constraints on the observed crater morphology.

References: [1] Vasavada A.R. et al. (2025), LPSC, [2] Dietrich D.E. et al. (2025), LPSC, [3] Yamamoto M. et al. (2017), [4] Berger J.A. et al. (2025), LPSC, [5] King P.L. et al. (2025), LPSC, [6] Plescia J. B. et al. (2012), [7] Amsden A. A. et al., (1980), [8] Collins G. S. et al., (2004), [9] Wünnemann K. et al., (2006), [10] Pierazzo E. et al., (2000), [11] Ivanov B. A. et al. (2001), [12] Thompson, S. L et al. (1972), [13] Pierazzo E. et al. (1997), [14] Bakanova A. A. (1975), [15] Thompson, S. L et al. (2019), [16] Arveson S. M. et al. (2019), [17] Brazhkin V. V. et al. (1991), [18] Deaton B. C. et al. (1965), [19] O'Keefe J. D. et al. (1997), [20] Liu T. et al., (2022).

Acknowledgments: This work is supported by the ASI-INAF grant "Attività scientifica di preparazione all'esplorazione marziana 2023-3-HH.0".

AN EXOGENIC CONTRIBUTION TO LUNAR WATER ICE: A COMETARY POST-IMPACT PLUME THROUGH SMOOTHED PARTICLE HYDRODYNAMICS. G. Magni[1], M. Teodori[1], M. Formisano[1], L. Maggioni[1,2], M. C. De Sanctis[1], P. O. Hayne[3,4] [1]INAF-IAPS, Via del Fosso del Cavaliere, 100, Roma 00133, Italy, email: gianfrancomagni@gmail.com, [2]Department of Physics, University of Rome Tor Vergata, Via della Ricerca Scientifica, 1, Roma 00133, Italy, [3]Department of Astrophysical and Planetary Sciences, University of Colorado Boulder, 80309 Boulder, CO, USA, [4]Laboratory for Atmospheric and Space Physics, University of Colorado Boulder, 80303 Boulder, CO, USA.

Introduction: The release of volatiles from planetary objects provides insights on the processes that shape the formation and evolution of the target, as well as its physical conditions and the internal structure. In addition, volatile emissions are often associated with water-rich reservoirs, which are relevant from an astrobiological standpoint.

On the Moon, an increasing evidence of water ice in Permanent Shadowed Regions [1-3] (PSRs) as well as a day-night variability involving the surface and the exosphere, is asking for a description of the delivery scenario, that is, whether the origin of such water is endogenous or exogenous [4]. Here, we present preliminary results concerning the evolution of a plume as resulting from the impact of a small cometary-like object over the Moon's surface, an event that can contribute to the exogenic inputs to lunar water ice, in particular in PSRs.

Methods: Volatile emissions involve several complex phenomena that require numerical models to characterize the dynamical and thermal behavior. In this work, we adopt a Lagrangian method called Smoothed Particle Hydrodynamics (SPH) [5-7], to simulate the evolution of a post-impact plume on the surface of the Moon. Such a particle-based mesh free approach uses volume elements and a statistical description to solve hydrodynamic equations, providing the spatial and temporal evolution of physical properties like velocity, density, and thermal energy.

Our model was satisfactorily used for the plumes of Enceladus [8-10], and considers a multi-component plume, made of water vapor and icy grains, thanks to a treatment for phase transitions. The viscous interaction between the two components shapes the dynamics of the material. Furthermore, the solar radiation alters the thermal distribution according to the optical properties of each component. We also account for thermal conduction with the Moon's surface, which can lead to surface deposition of vapor. Such physical processes can affect the outcomes since they alter the thermal and dynamical behavior of the volatile material.

Results: Our simulation results characterize the dynamical and thermal behavior of the volatile material, altered by the aforementioned processes.

Initial conditions. We adopt scaling relationships [11-12] to relate crater, ejecta, target and impactor properties. We assume that the impact produces a crater of 20 km, due to an impactor with a velocity ~ 15 km/s [13]. The target density is 1100 kg/m^3 [14], and the impactor density is 500 kg/m^3 (average density of comets) We assume the ejecta thermal energy fraction [15] and composition (only water vapor), adiabatically scaling from impactor size to the produced crater size. Thus, our vapor begins with a density of ~ 0.3 kg/m^3 and T ~ 1500 K.

Boundary conditions. In our simulations, boundaries are the surface of the Moon and a PSR of 5 km in radius, which can collect material. This additional crater is located nearby the impacting region, which is at the south pole. For the thermal interaction with the Moon's surface we consider a rough estimate of the surface temperature from the DIVINER data [16]. For the crater, we assume a linear temperature profile with a crater floor at 50 K and crater rim at 100 K. We also check for phase transition within the crater.

Results. We simulate 5 hours of evolution of the ejecta plume, using 2.5 x 10^5 SPH pseudo-particles, assuming a size for icy grains of 1.0 μm.

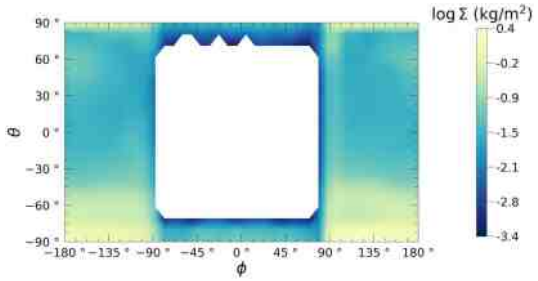


Figure 1: Distribution of the deposited ice surface density Σ after t=5 h.

After 1.5 h of evolution, the water vapor has covered all the Moon, producing a transient exosphere, with an over-density of vapor in the illuminated regions. On the contrary, shadowed regions and poles yield an efficient surface deposition of ice, as shown in Figure 1. A slightly larger amount of ice is present close to the impact (south pole, θ=-90°).

As shown in Figure 2, the plume is dominated by vapor, which interacts with shadowed regions and soon populates the deposited ice component (~20%). Ice is present in the plume only initially, it is subdominant with respect to vapor and its fraction shows a decreasing trend. Plume ice interacting with the surface can accumulate, contributing to the deposited ice component.

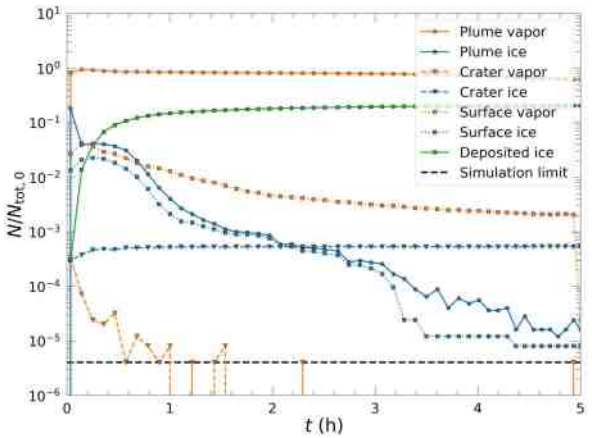


Figure 2: Evolution of numerical fractions for vapor and ice according to their dynamical phase.

After ~ 1 h, a fraction of the plume overcomes the Hill limit, producing a significant loss of material at the end, that is ~18% of the initial amount.

The most interesting result concerns the PSR. Here, vapor enters only initially and ice dominates, reaching a stable value (Figure 3).

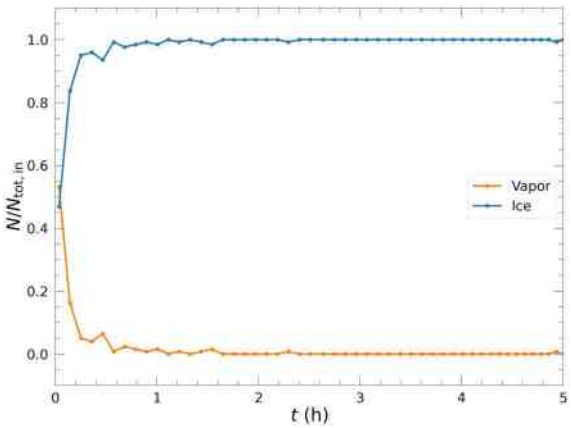


Figure 3: Temporal evolution of the fraction of vapor and ice within the PSR.

Ice within the PSR reaches a fraction of ~0.05% of the total initial material. Dynamical accumulation criteria allow the ice to move as flying one, leading to accumulation in the crater floor, giving a temporal increase of the average ice density within the PSR.

Conclusions: Our SPH model can follow the behavior of the post-impact ejecta of a cometary-like object. In particular, ice deposits within PSRs can be stable against sublimation for a very long time, according to thermal properties (cold traps) [17]. We plan to explore free parameters, such as the location and distance of the impact area and the PSR. In particular, we can take advantage of Eulerian methods [18-19] to better characterize the thermal behavior of the PSR, providing a better description of volatile interaction with the surface on local scales. In addition, we can take advantage of the results of numerical simulations for impacts to consider more robust initial conditions. In addition, our model can include the presence of dust and its interaction with the other components [20-21], mainly gaseous ones, particularly important in several planetary objects phenomena. However, this aspect is still missing for the scientific target addressed in this work as refining of the considered physical processes is needed.

Our model provides a numerical tool applicable to different targets interested by volatile emissions, such as the possible release of vapor-ice-dust mixtures, triggered by drilling activities [22-23], planned for ExoMars and Prospect missions, or cometary activity [20], as well as support mission to the Moon such as the Emirates Lunar Mission.

References:

[1] Li et al. 2018, PNAS, 115, 8907.
[2] Sanin et al. 2017, Icarus, 283, 20.
[3] Ohtake et al. 2024, ApJ, 963, 124.
[4] Thiemens et al. 2024, PNAS, 121, 52.
[5] Gingold & Monaghan 1977, MNRAS, 181, 375.
[6] Lucy 1977, AJ, 82, 1013.
[7] Monaghan 2005, Rep. Prog. Phys. 68, 1703.
[8] Teodori et al. 2026, Icarus, 443, 116765
[9] Teodori et al. 2025, EPSC-DPS2025-308.
[10] Teodori et al. 2024, EPSC2024-55.
[11] Housen et al. 1983, J. Geophys. Res. 88, 2485.
[12] Housen & Holsapple 2011, Icarus, 211, 856.
[13] Ivanov et al. 2001, SSR, 96, 87.
[14] Hayne et al. 2017, J. Geophys. Res. Planets 122, 2371.
[15] Melosh 1989, Impact cratering: a geologic process.
[16] Hurley et al. 2015, Icarus, 155, 159.
[17] Schorghofer et al. 2024, Planet. Sci. J. 5, 99.
[18] Formisano et al. 2018, J. Geophys. Res. 123, 2445.
[19] Formisano et al. 2024, PSS, 251, 105969.
[20] G. Rinaldi et al. 2025, EPSC-DPS2025-1556.
[21] Maggioni et al. 2025, PSS, under review.
[22] Maggioni et al. 2025, EPSC-DPS2025-613.
[23] Maggioni et al. 2025, MNRAS, 543, 3310.

Additional Information: This work was supported by ISSI within the project “Thermophysical Characterization of Ice-Rich Areas on the Surface of Specific Planetary Bodies: Conditions for the Formation of a Transient Exosphere”, INAF Theory Grant “Thermophysical modeling of Permanently Shadowed Regions (PSRs) on Moon and Mercury” and INAF MiniGrant “PLUMES-Planetary fractures Lagrangian simUlations for Multi-component EmissionS”.

XXI Congresso Nazionale di Scienze Planetarie

Sessione Sviluppo di Strumentazione

DEVELOPMENT OF QUARTZ CRYSTAL MICROBALANCES FOR ENCELADUS APPLICATIONS

A. Longobardo[1], V. Della Corte[2], E. Palomba[1], F. Dirri[1], E. Nardi[1], C. Gisellu[1], M. Angrisani[1], F. Cozzolino[2], G. Sindoni[3], [1]INAF-IAPS, via Fosso del Cavaliere 100, 00133, Rome, Italy, [2]INAF-OAC, salita Moiariello, Naples Italy, [3]ASI (Italian Space Agency), via del Politecnico, 00133, Rome, Italy

Introduction: The study of Enceladus is crucial for understanding the potential for life beyond Earth. Its subsurface ocean, active plumes, and organic-rich composition make it a prime target for astrobiology. In this context, NASA's New Frontiers 5 mission could provide groundbreaking insights by directly sampling plume material. Investigation of Enceladus may help to answer fundamental questions about habitability in our solar system.

Basic principles: We present a feasibility study of quartz crystal microbalances (QCM) for an Enceladus application. Microbalances would represent a subsystem of a Dust Next Generation Sensor under study, based on the heritage of Rosetta's GIADA [1], that would also include an Optical Stage and an Impact Sensor and Counter [2].

QCMs are dust and ice sensors that measure cumulative mass flux, by monitoring frequency variation of quartz crystals. Moreover, the occurrence of resistors built on crystals, acting as heater and temperature sensor, respectively, would allow Thermo-Gravimetric Analysis (TGA), a technique used on several fields, including planetary sciences [3, 4], to monitor thermodynamical processes as sublimation, desorption and frosting.

Goals and activity: In an Enceladus mission, QCMs would:

- Measure the dust and water ice flux, e.g., from plumes;
- Measure the organic content in dust and ice particles by means of TGA;
- Assess contamination issues, by cooling crystals and allowing deposition of contaminants.

Currently, we are selecting the best QCM configuration, basing on current heritage, such as VISTA/Hera [2] and high-temperature microbalance [3]. The configuration will be mainly based on temperature range needed to perform TGA in the Enceladus environment, Moreover, the effect of radiation dose on crystal performances is under study.

Once identified scientific and technical requirements, a breadboarding and test phase will take place.

References:

[1] Colangeli, L. et al. (2007), Space Science Review, 128, 1-4, 803-821

[2] Della Corte, V. et al. (2025), EPSC, this session

[3] Palomba, E. et al. (2025), EPSC, session MITM18

[4] Longobardo, A. et al. (2024), Italian Congress of Planetary Science

Acknowledgements: This work has been funded by the ASI-INAF agreement N. 2024-19-HH.0

HISCAL, the new Hyperspectral Imaging Spectrometers CALibration Facility in INAF-IAPS

S. Stefani[1], G. Filacchione[1], M. Ciarniello[1] , D. Biondi[1] , A. Boccaccini[1] , G Piccioni[1], M. C. De Sanctis[1], F. Capaccioni[1], E. La Francesca[1] , C. Cencia[1] , S. De Angelis[1] and M. Ferrari[1]

[1]IAPS-INAF, via del Fosso del Cavaliere 100, 00133 Rome Italy
Stefania.Stefani@inaf.it

Introduction: In the last 30 years the planetary science group in INAF-IAPS has played a primary role in the field of spaceborne VIS-IR spectrometers. A total of 8 spectrometers have been launched and successfully operated on as many missions by IAPS PI-led teams: Cassini-VIMS, MarsExpress-Omega, Rosetta-VIRTIS, VenusExpress-VIRTIS, Dawn-VIR-MS, Juno-JIRAM, BepiColombo-SIMBIOSYS-VIHI, and Juice-MAJIS. All these experiments have been tested and calibrated before launch at the industrial contractor's premises or at institutes abroad. Thanks to the experiences acquired during the calibration campaigns of those payloads, it has been possible to design and realize in INAF-IAPS the Hyperspectral Imaging Spectrometers CALibration Facility (HISCAL) with the aim to provide optical setups and reference standards necessary to calibrate spaceborne imaging spectrometers starting with the next experiment to be delivered, MIST-A, the Mid-Wave Infrared (MWIR) Imaging Spectrometer for Target-Asteroids [1] that will be launched aboard the MBR Explorer spacecraft as part of the Emirates Mission to the Asteroid Belt (EMA) in 2028.

The HISCAL facility is designed for the calibration of the spectral, spatial, geometric and radiometric performances of VIS-IR imaging spectrometers and to perform functional and performances tests under controlled conditions thanks to the modular design and level of automation of the setup.
In this contribution we are reporting about the HISCAT configuration and experimental activities.

Experimental Setup: HISCAL is designed as a modular optical system hosting a target/source group at the focus of a collimator (Off-axis parabola, F=1020 mm, D=200 mm) mounted on a hexapod to finely control the position of the collimated beam with resect to the optical pupil of the payload under test (Fig. 1). A custom optical bench hosts the hexapod and the auxiliary equipment. Different groups of targets (pinholes, slits, MTF patterns) and sources (QTH and pencil lamps, IR emitters, blackbody, and monochromator) can be used as sources depending on the purpose of the measurement and spectral range. These elements are interchangeable on the focus of the off-axis parabola thanks to a common mechanical interface placed on a three-axis micrometric mount necessary to adjust its position. The focusing position is checked by means of an autocollimator device. With the aim to reduce the mechanical loads on the optical bench, the monochromator and its VISIR source are mounted on a dedicated shelf of the optical bench structure. The monochromator's exit slit is feeding the test slit/pinhole placed on the collimator's focal plane holder through a bundle of IR optical fibers (15 fibers, core diameter 300 µm, cladding diameter 360 µm, NA=0.3, length 1.5 m, in linear arrangement on both terminals).
The collimator's optical bench is mounted on a hexapod (HEX), which enables six-axis (3 translations: ±50 mm in X, Y, ±25 mm in Z; 3 rotations: ±15° in θx, θy, ±30 in θz) movements with a repeatability ≤ ±0.6 in X, Y, Z and ≤9 µrad in θx, θy, θz and maximum velocity < 1 mm/s. A flat Folding Mirror (FM) placed at the collimator's exit allows further fine adjustments of the optical beam in azimuth and elevation thanks to two micrometric rotation stages. The HEX and FM positions, as well as the source parameters (e.g. the BB temperature, lamps and emitters currents, monochromator settings) are controlled and pre-settable through a dedicated Optical Control System (OCS) PC. A fiber-fed IR spectroradiometer is used on the collimator's pupil to check the calibration beam.

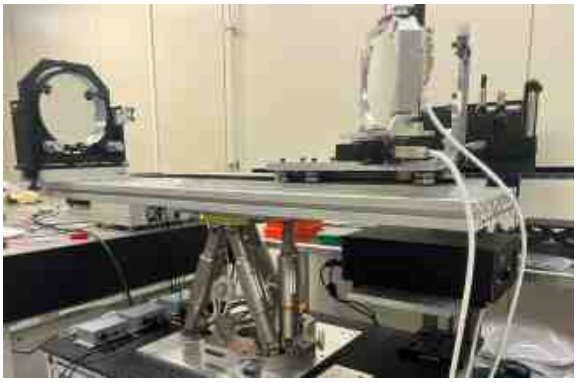


Figure 1: Photo of the HISCAT collimator and FM mounted on the HEX during optical checks.

The HISCAT optical bench is housed within one of the IAPS clean rooms (ISO7) and aligned with respect to the optical entrance window of a ThermoVacuum Chamber (TVC). For the specific thermal needs of the MIST-A experiment (operative

temperature of the optical head <135K, IR detector <85 K) a new liquid-nitrogen cooled TVC is currently under procurement (Fig. 2). The TVC opening door, including its 260 mm diameter CaF_2 optical window, will be accessible from the clean room to allow the interface with the HISCAL bench. The TVC outer cylinder has a diameter of 1350 mm, an internal cold shroud of diameter 1150 mm and a removable plate measuring approximately 900×1200mm. The shroud and the plate can be cooled and heated, separately, in the range between 93-403 K with a stability of ± 1 K/ 3h and a rate between 0.5-2 K/min. Apart hosting the MIST-A optical head and electronics unit, inside the TVC is placed an IAPS-made customized extended black body source whose temperature is settable and stabilized within the range 130-370 K. The 100×100 mm emitting flat surface of the blackbody is mounted on a motorized translation stage which allows to place it on the optical pupil (aperture stop) of MIST-A during the measurements dedicated to characterize its radiometric response, flat field and linearity.



Figure 2: Design of the Thermo-Vacuum Chamber under procurement for the MIST-A calibration campaign.

Future perspectives: The MIST-A technical and scientific teams are currently testing the HISCAT optical setup and subsystems, checking its opto-mechanical performances and functionalities with different configurations with the aim to prepare it for the next calibration campaign of the MIST-A instrument scheduled during summer 2026 in IAPS. This will be the first time an imaging spectrometer for planetary exploration will be calibrated and tested in INAF-IAPS under the instrument's team responsibility. The HISCAF facility and expertise will remain available in IAPS for the calibration of similar instruments in the future.

References: [1] Filacchione et al., 2024, COSPAR, b1.1-0037.

Acknowledgments: INAF/IAPS, Rome, is the MIST-A PI institute and it is responsible for instrument's calibration, science activities and operations. Leonardo S.p.A. from Campi Bisenzio (Florence) is the MIST-A industrial contractor in charge of the instrument's design, assembly, qualification and testing. The primary funding source for the program is the Italian Space Agency (ASI) through science contract 2023-21-HH.1.2025, and industrial contract 2025-33-I.0. MIST-A science team acknowledges financial support from INAF and administrative/technical support from IAPS personnel. The HEX procurement has been supported by INAF throught the Bando per il potenziamento dei Laboratori Spaziali (2023) and ASI through the MIST-A science contract. We recognize financial support from Regione Lazio (Bando Progetto NanoMicroFab@STESY) and INAF for the procurement of the TVC.

ASI-SSDC: TOWARDS A NEW ROLE SUPPORTING INNOVATION AND SPACE MISSIONS. A. Zinzi[1], G. Nodjoumi[2], V. Camplone[1], E. Rognini[2], M. Giardino[1], A. Bonchi[1], M. Pietrosanto[1], A. Terracina[1], S. Puccetti[1], A. Giunta[1], D. Perna[2], M. Stangalini[1], [1]Agenzia Spaziale Italiana, Via del Politecnico snc, 00133, Roma, Italy, [2]INAF-OAR, angelo.zinzi@asi.it

Introduction: The Space Science Data Center (SSDC) is an ASI research infrastructure with long-lasting experience in supporting the utilization and fusion of data acquired by space missions, by means of international standards, such as those of the Virtual Observatory (VO) [1] and FAIR principles [2] and the development of scientific webtools.

After a multi-decadal experience in this field, ASI recently decided to expand its activities, aiming at maintaining SSDC in its role of focal point inside the interested communities.

The very first application of this new SSDC course of action is part of the new agreement among ASI and INAF for the technical activities of the center, comprising innovative activities, Ground Segment (GS) support and data dissemination.

Innovative activities: Scientific research nowadays cannot be fully implemented without the use of edge technologies, such as artificial intelligence (AI) or diffuse infrastructure.

In order to satisfy this requirement, the new agreement started in November has a series of work packages designed to orient the development of the center towards these new fields.

In particular, AI algorithms will be developed to support fundamental scientific applications, such as analysis and detection of transient phenomena in astronomical images, even comprising asteroids, and the study of radiation environments in support of missions in orbit.

Another important activity added regards the exploitation of AI in support of Ground Segment architectures of innovative design, with smart user interfaces even able to simplify the decisions.

These innovations are thought to converge in a distributed scripting platform making use of containerization, the SSDC SciComHub, based on the work by [3], making it possible to easily access the whole infrastructure, from datasets to tools, passing from Ground Segment pipelines, in a single web-based software environment.

Ground Segment support: Albeit SSDC has a long-lasting experience in the participation to Ground Segments of space missions, with a series of commitments including the development of scientific pipelines devoted to the data analysis and reduction (e.g., [4]), or the design of navigable big-data archives using innovative technologies (e.g., [5]), in this new course, the idea is to exploit the expertise present in the center in an horizontal way and not only for some dedicated missions.

It is indeed now planned to work in cooperation with all the space mission teams of interest. This approach will likely foster the bear of such expertise outside SSDC, so that new space missions will easily include aspects of Ground Segment analysis starting from the proposal phase, thus simplifying the work to be done afterwards.

Data dissemination: These new activities are not thought to overcome the ones became "classical" for the center during its multi-decadal existence.

On the contrary, it is desirable that the activities devoted to archive management and scientific tools development will be boosted by the innovative ones: once the data, together with the processing pipelines and dedicated AI algorithms able to add scientific value to them, are fully integrated in the SSDC infrastructure, it would be straightforward to transfer this expertise inside dedicated archives, tools or distributable software packages.

SSDC for planetary sciences: In this new view of SSDC, planetary sciences can be seen as fully integrated, since, thanks to its interdisciplinary nature, it has been always developed using an horizontal approach.

The main planetary sciences tool, MATISSE [6] [7], by means of a modular design, is already able to propose to the user different kinds of data.

We are already working to include a series of interesting activities related to the Ground Segment support, such as integrating processing pipelines for a series of instruments already flying and operating, or the models pertaining to giant planet atmospheres or thermophysics of rocky bodies.

In the very next future these activities will gain a boost, thanks to the new approach officially followed by SSDC, and therefore we are expecting that new missions will exploit the SSDC infrastructure, helping to standardize the way planetary science datasets are processed and maintained.

References: [1] Djorgovski S.G. and Williams R. (2005) https://doi.org/10.48550/arXiv.astro-ph/0504006. [2] Wilkinson M.D. et al. (2016) *Sci Data* **3**, 160018. https://doi.org/10.1038/sdata.2016.18. [3] Nodjoumi G. et al. (2025) *ESS*, 12, 5, https://doi.org/10.1029/2025EA004251. [4] Zinzi A. et al. (2022) *Planet. Sci. J.*, 3, 15,

https://doi.org/10.3847/PSJ/ac6509. [5] Montalto M. et al. (2021) *A&A*, 653, A98, https://doi.org/10.1051/0004-6361/202140717 [6] Zinzi A. et al. (2016) *A&C*, 15, https://doi.org/10.1016/j.ascom.2016.02.006 [7] Camplone V. et al. (2024) *A&C*, 48, https://doi.org/10.1016/j.ascom.2024.100852

Acknowledgements: This work has been done with the support of the ASI-INAF agreement 2025-33-HH.0

XXI Congresso Nazionale di Scienze Planetarie

Sessione Focus S8

Beyond the visible: Uncovering interior composition and processes through tectonic and geodynamic lenses

STRUCTURAL ANALYSIS OF ARIEL'S SURFACE. S. Tonoian[1,2], A. Lucchetti[2], M. Massironi[1], C.B. L. Penasa[2], Beddingfield[3], D. Hodgetts[4], R. Pozzobon[1], M. Pajola[2], C. Rossi[2]. [1] Dipartimento di Geoscienze, Università degli studi di Padova, Via G. Gradenigo 6, 35131, Padova (susanna.tonoian@phd.unipd.it), [2] INAF-OAPD Osservatorio Astronomico di Padova, Vicolo dell'Osservatorio, 5, 35122 Padova, Italy, [3] Johns Hopkins University Applied Physics Laboratory, Laurel, MD 20723, USA, [4] VRGeoscience Limited.

Introduction: Discovered by amateur astronomer William Lassell in 1851, Ariel remained little more than a point of light for over a century and its proximity to Uranus made it difficult to be observed it from Earth. Then, Voyager 2 flyby in 1986 revealed a dynamic and geologically complex surface of the Uranian satellite. Ariel's surface exhibits diverse terrains, including smooth regions that indicate resurfacing and relatively recent geological activity [1]. Compositional studies have confirmed the presence of CO and CO_2 ices within these areas [2], possibly sourced from the interior. In addition, the possible detection of NH_3-bearing species [3] further supports the evidence of cryovolcanic activity. Ariel may also host a subsurface liquid layer [4], raising questions about its internal dynamics and potential habitability. In this work, we investigate how global processes have influenced Ariel's icy crust. In particular, we mapped surface' fractures to quantitively measure dips and orientations to better constrain Ariel's stress regimes and deformation mechanisms.

Data and Methods: In this study, two types of Digital Elevation Models (DEMs) were used: one global DEM [5] and two local DEMs [6] (Figure 1).

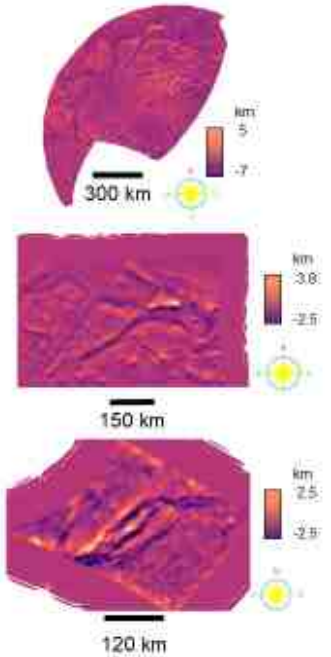


Figure 1. From top to bottom: Global DEM in South Pole projection, and local DEMs centered on Pixie and Kachina Chasmata. All DEMs are derived from Voyager 2 ISS data.

All datasets were derived from Voyager 2 Imaging Science Subsystem (ISS) data and processed using the USGS Integrated Software for Imagers and Spectrometers (ISIS). The models have comparable spatial resolutions of approximately 1 km/pixel and 995–1300 m/pixel for the global and local DEM, respectively. The local DEMs, projected stereographically and centered on the targeted chasmata Pixie and Kachina, cover different surface areas.

The global DEM displays repetitive noise and zone-dependent artefacts, whereas the local DEMs exhibit smoothed appearance that suppresses fine-scale topographic details, most noticeably affecting crater rim morphology. However, the noise in the global DEM follows a systematic and recognizable pattern, thus, it can be visually identified and excluded during manual measurements. As a result, the global DEM was used as the primary dataset for structural interpretation, while the local DEMs served mainly for cross-validation.

Following previous mapping approaches, the South Pole projection was chosen to enhance the visibility of structural features, which appear distorted near the poles in an equidistant cylindrical projection. Geological mapping was performed in QGIS by manually digitizing structural lineaments as polyline shapefiles at a working scale of 1:1,000,000, using the image mosaic as a base layer. A rose diagram showing the global orientation of all mapped structures was produced using the Line Direction Histogram plugin [7] to evaluate Ariel's dominant deformation patterns.

Orientation and dip data for the main structural features were extracted from the DEMs through manual three-point measurements using the Dip and Azimuth tool in VRGS [8]. The resulting data were then plotted on stereonets within the software for visualization and analysis of fault orientations.

Results: The geological mapping (Figure 2) included a higher number of small structural features toward Ariel's south polar region with respect to what was previously identified [9] that are significant for understanding the moon's tectonism. Four main categories of structures were recognized: fault scarps, fractures, ridges, and medial grooves, following the classification schemes from [5], [9], [10].



Figure 2. Structure map of Ariel displayed at a scale of 1:15,000,000 in Equidistant Cylindrical projection with mosaic from the Voyager 2 images and Rose diagram on the right side.

Since the mapping was performed in a South Pole projection, the orientations are expressed relative to the projection's reference frame rather than absolute geographic north, due to projection-specific coordinate distortions. The dominant structural orientations range between 70–90° and 250–270° (ENE–WSW), while the least represented features trend 335–25° and 155–205° (S–N).

Manual measurements confirm these trends: stereonet plots show fault poles clustered in the northeast and southwest quadrants. Among the mapped chasmata, Kewpie, Brownie, and Korrigan exhibit low dip angles (<20°) and only slight asymmetry, whereas Sylph, Pixie, and Kra display more moderate dips and clear asymmetry in cross-section.

Discussion: Rose diagram reveals anisotropy with preferred orientation, which strengthens the hypothesis that the extension direction is controlled by tidal stresses [11]. Measured dips of 10–24° are significantly lower than the ~60° typical for normal faults with a friction coefficient of 0.6 by Byerlee's law [12]. These shallow dips and asymmetric geometries imply reduced friction, likely reflecting deformation above a ductile, ammonia-rich layer that weakens the icy lithosphere. The detection of ammonia and CO on Ariel's surface [13] supports this interpretation, indicating recent endogenic activity and potential persistence of subsurface liquids. Stress modeling [14] further suggests that tidal forces from past orbital resonances generated stresses >1 MPa, sufficient to fracture the ice shell and drive resurfacing.

Conclusion: This study demonstrates that Ariel's surface deformation is dominated by extensional tectonism aligned along an ENE–WSW trend, shaped by anisotropic stresses and low-friction fault behavior with-in a volatile-rich ice shell. These findings are consistent with large-scale tidal and thermal influences inferred for Uranus's moons [11]. Future missions should prioritize high-resolution topographic imaging and spectroscopic analysis to validate these results and confirm the potential existence of a sub-surface ocean beneath Ariel's fractured, geologically active surface.

Acknowledgements: This activity has been developed under the ASI/UniBo-CIRI agreement n. 2024-5-HH.0.

References: [1] Kirchoff M. R., Dones L., Singer K., & Schenk P. (2022) Planet. Sci. J., 3(2), 42. [2] Cartwright R. J., Emery J. P., Grundy W. M., Cruikshank D. P., Beddingfield C. B., & Pinilla-Alonso N. (2020) Icarus, 338, 113513. [3] Cartwright R. J. et al. (2021) Planet. Sci. J., 2(3), 140. [4] Castillo-Rogez J. C. et al. (2023) J. Geophys. Res. Planets, 128(1), e2022JE007432. [5] Schenk P. M. & Moore J. M. (2020) Phil. Trans. R. Soc. A, 379, 20200102. [6] Beddingfield C. B., Cartwright R. J., Leonard E., Nordheim T., & Scipioni F. (2022) Planet. Sci. J., 3(5), 112. [7] Tveite H. (2025) Line Direction Histogram Plugin, QGIS, updated 20 Oct 2025. [8] VRGeoscience Ltd. (2003) VRGS Software, available at: www.vrgeoscience.com. [9] Beddingfield C. B., Cartwright R. J., Jozwiak L. M., Nordheim T. A., & Patterson G. W. (2025) Planet. Sci. J., 6(2), 45. [10] Croft S. K. & Soderblom L. A. (1991) Uranus, pp. 561–628. Univ. of Arizona Press, Tucson. [11] Strom C. et al. (2026) Icarus, 444, 116822. [12] Watters T. R. & Schultz R. A. (2010) Planetary Tectonics. Cambridge Univ. Press. [13] Cartwright R. J. et al. (2024) Astrophys. J. Lett., 970(2), L29. [14] Strom C., Nordheim T. A., Patthoff D. A., & Fieber-Beyer S. K. (2026) Icarus, 444, 116822.

POSSIBLE LOCAL SUBDUCTION AND SPREADING PROCESSES IN VINMARA PLANITIA, VENUS: GEOLOGICAL AND GEOPHYSICAL CONSTRAINTS

Davide Sulcanese [1,2] (davide.sulcanese@unich.it), Giuseppe Mitri [1,2], Camilla Cioria [1,2], Edoardo Santero Mormile[1,2,3], Mafalda Ianiri[1,2], Suzanne E. Smrekar[4], Scott Hensley[4], [1]Dipartimento di Ingegneria e Geologia, Università d'Annunzio, Pescara, Italy; [2]International Research School of Planetary Sciences, Università d'Annunzio, Pescara, Italy; [3]University of Trento, Trento, Italy; [4]Jet Propulsion Laboratory, California Institute of Technology, 4800 Oak Grove Dr., Pasadena, CA 91109, United States of America

The lack of a global system of mobile plates on Venus implies that heat loss and lithospheric stress must be accommodated through alternative tectonic regimes [1-5]. Local fragmentation of the Venusian lithosphere into mobile crustal blocks (*campi*) has recently been proposed on the basis of Magellan data [7], suggesting that plate-like behavior may occur regionally without global plate tectonics. Here we investigate one such candidate domain within Vinmara Planitia, focusing on a single *campus* that hosts two contrasting tectonic systems: the ridge belt Ahsonnutli Dorsa and the groove belt Surupa Dorsa.

We combined Magellan SAR imagery and altimetry [6] with gravity, emissivity and meter-scale roughness datasets to characterize the morphology, topography and subsurface structure of this region. Ahsonnutli Dorsa consists of an arcuate, ~300 km long ridge belt with systematic east-verging shortening structures. The associated topography shows a deep trench-like depression flanked by an outer rise, and a chain of small volcanic edifices landward of the belt. Cartesian flexure modelling of six topographic profiles revealed trench curvatures and elastic thicknesses comparable to those of terrestrial subduction systems, supporting an interpretation as a cohesive compressional wedge above a shallow décollement.

In contrast, Surupa Dorsa is a ~1000 km long groove belt dominated by extensional faulting and a broad, axial topographic high (~750 m) that parallels the main fault trend. The fault pattern, elevation structure and distribution of volcanic edifices resemble those of fast-spreading mid-ocean ridges on Earth. Bouguer gravity anomalies showed locally reduced values where the groove belt widens, consistent with lower effective lithospheric density beneath the axis, while an increase in microwave emissivity toward the groove center may indicate relatively young or less altered surface materials.

Reconstructed kilometer-scale offsets of tessera fragments along WSW–ENE faults south of Ahsonnutli Dorsa are consistent with rotation of a rigid block about a single Euler pole, implying near-orthogonal spreading at Surupa Dorsa and oblique convergence at Ahsonnutli Dorsa. Taking together, these observations support a working hypothesis in which localized subduction- and spreading-like processes operate within a single Venusian lowland block, in line with plutonic-squishy lid scenarios [5]. If confirmed by future missions such as VERITAS and EnVision [8, 9], this type of localized plate-like behavior would provide a valuable analogue for early Earth and for tectonics on rocky exoplanets lacking fully developed global plate tectonics.

Acknowledgements
D.S. and G.M. acknowledge support from the Italian Space Agency (Grant No. 2022-15-HH.0).

References
[1]Solomatov, V. S. & Moresi, L. N. Stagnant lid convection on Venus. J. Geophys. Res. Planets 101, 4737-4753 (1996). [2] Lenardic, A. The diversity of tectonic modes and thoughts about transitions between them. Philos. Trans. R. Soc. A 376, 20170416 (2018). [3] Solomatov, V. S. & Moresi, L. N. Three regimes of mantle convection with non-Newtonian viscosity and stagnant lid convection on the terrestrial planets. Geophys. Res. Lett. 24, 1907-1910 (1997). [4] Moresi, L. & Solomatov, V. Mantle convection with a brittle lithosphere: Thoughts on the global tectonic styles of the Earth and Venus. Geophys. J. Int. 133, 669-682 (1998). [5]Lourenço, D. L., Rozel, A. B., Ballmer, M. D. & Tackley, P. J. Plutonic-squishy lid: A new global tectonic regime generated by intrusive magmatism on Earth-like planets. Geochem. Geophys. Geosyst. 21, e2019GC008756 (2020). [6] Ford, J. P. Guide to Magellan Image Interpretation (NASA, 1993). [7] Byrne, P. K. et al. A globally fragmented and mobile lithosphere on Venus. Proc. Natl Acad. Sci. USA 118, e2025919118 (2021). [8]Smrekar, S. et al. VERITAS (Venus emissivity, radio science, InSAR, topography, and spectroscopy): A discovery mission. IEEE Aerosp. Conf. 1-20 (2022). [9] EnVision Definition Study Report (2023) ESASCI-DIR-RP-003.

CORONAL REPAVING OF VENUS'S SURFACE. N. J. Montiel[1] and B. De Toffoli[1], [1] Department of Geosciences, University of Padova, Padova, Italy (nicholasjohn.montiel@unipd.it)

Introduction: Venus, despite lacking Earth-like plate tectonics [1], shows evidence of ongoing geological activity at volcanoes, rift zones, and coronae [2,3]. The cratering record is ambiguous and allows for differing interpretations of the planet's resurfacing history [4,5]. Recently published, global datasets for coronae [6] and volcanoes [7] on Venus reveal a regional anti-correlation between volcanic edifices and coronae. When this information is combined with detailed geological mapping and radar imagery [8], it allows for the characterization of coronal repaving of Venus's surface.

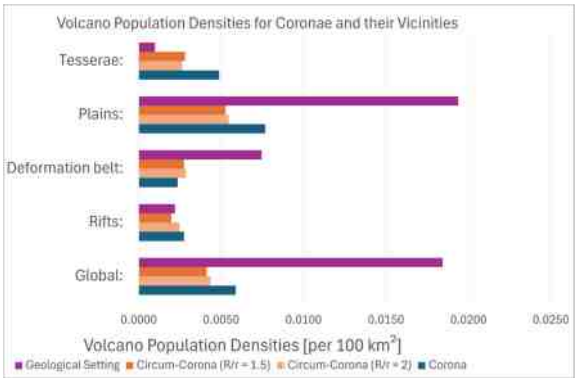


Figure 1: Bar chart showing the average population density of volcanoes for corona interiors (blue), the circum-coronal regions (R/r = 1.5 and R/r = 2, dark and light orange), and the geological unit (purple) that the coronae are found in as well as the same for the entire planet, per 100 km^2.

Methods: We calculate the population densities of volcanoes for different geological settings, within coronae, and in the vicinity of coronae to determine how the setting of a corona affects the associated volcano population. From there, we pick sixty-eight named coronae that are well-mapped by the USGS Astrogeology division [e.g. 9]. Using cross-cutting relationships between volcanoes and mapped units, we can determine whether pre-coronal, syn-coronal, and post-coronal volcanic edifices are present in and around an individual corona. From this, we build a histogram of the ages of volcano populations relative to coronae, constraining the geological evolution of the area. In addition, we supplement this with mapping volcanic edifices in relation to young or well-preserved flows emanating from coronae to better understand their relationship.

Results: Based on the population distributions of volcanoes and coronae on Venus, we conclude that there is an anticorrelation between coronae and volcanic edifices on a regional scale (Fig. 1). Furthermore, aside from at tesserae and rift zones, this relative reduction in volcano population density around coronae is universal. Since rift zones are thought to be some of the youngest features on the surface [10] and tesserae the oldest [11], these may represent scenarios in which evidence of volcanism is destroyed by ongoing activity and in which volcanism is rare, respectively. This suggests that the population density of volcanism around coronae is controlled by the potential repaving or resurfacing of these regions.

When the tectonostratigraphic relationships between coronae and volcanic edifices is examined (Fig. 2) we find that, while volcanic edifice formation peaks during corona formation for coronal interiors, in the regions around coronae most volcanic edifices formed after the corona had developed. This implies that any pre-existing volcanoes were either buried or destroyed by activity related to corona formation.

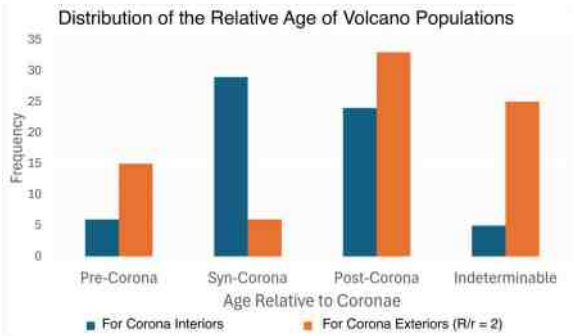


Figure 2: Histogram showing the distribution of the age categories present in each corona interior (blue) and exterior region up to 1 corona radius away (orange), based on mapped tectonostratigraphic relationships. The interior age distribution peaks for syn-coronal and post-coronal volcanoes, consistent with the erasure of pre-coronal volcanic edifices and the replacement of them with volcanoes that are part of corona formation and evolution. The exterior age distribution shows few pre-coronal and fewer syn-coronal volcanoes, consistent with the erasure of pre-coronal volcanic edifices without replacement until after the corona has finished forming (hence the peak for post-coronal volcanoes).

This interpretation is supported by the observation of volcanic fields preserved in the process of being erased at Aruru, Fakahotu, Qakma, and Maslenitsa Coronae. At Fakahotu Corona in particular, a dense volcanic field abruptly terminates at the edges of a well-defined lava flow emanating from Fakahotu itself (Fig. 3). Aruru Corona shows a similar phenomenon, while Qakma and Maslenitsa Coronae exhibit possible tectonic disruption of pre-existing volcanic edifices.

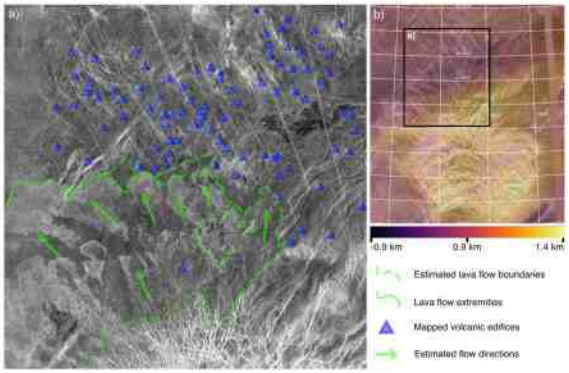


Figure 3: a) Radar image showing a lava flow emerging to the north-east of Fakahotu Corona into a pre-existing cluster of volcanoes, seemingly preserved in the process of destroying the cluster. Blue triangles mark volcanic edifices identified in either the global volcano database or in the USGS geological map quadrangle V-3. The flow is mapped as Lobate plains material (pl). [12]. b) Topographic map of Fakahotu Corona overlain over radar images, showing the context in which the above flow is observed.

Conclusion: The anti-correlation between coronae and volcanoes, the dominance of post-coronal volcano populations around coronae relative to pre-coronal populations, and the observation of process that can erase evidence of pre-existing volcanic edifices all suggest that lava flows and tectonic activity emanating from coronae repave or resurface the surrounding region up to at least two coronal radii from the corona center (~100s of kilometers). This process and scale is consistent with a patchwork resurfacing of the planet [5, 13] and suggests that geological activity on Venus is modulated by corona-forming mechanisms.

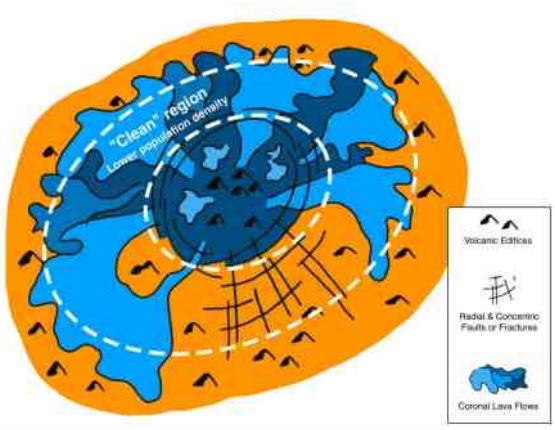


Figure 4: Schematic showing the processes that may be at play to create a "clean" region around coronae. Lava flows from vents inside the corona and from the annulus (shades of blue) flow outward to bury or erode pre-existing volcanic cones. To a lesser extent, faults emanating from the corona may also degrade those same volcanic cones. This creates a region (outlined with white dashed lines) where the population density of small volcanic edifices is reduced relative to the geological background (orange).

Acknowledgements: This research was supported by the European Union NextGenerationEU programme and the 2023 STARS Grants@Unipd programme "HECATE".

Additional Information: A more comprehensive version of this work is available as a pre-print at the ESS Open Archive: DOI: 10.22541/essoar.176031230.02438825/v1. [14]

References: [1] Lourenço D. L. (2023). Estranged planetary twins. *Nature Geosci.*, *16*(1), 2–3. [2] Smrekar, S. E. et al. (2023). Earth-like lithospheric thickness and heat flow on Venus consistent with active rifting. *Nature Geosci.*, *16*(1), 13–18. [3] Smrekar S. E. et al. (2023). Earth-like lithospheric thickness and heat flow on Venus consistent with active rifting. *Nature Geosci.*, *16*(1), 13–18. [4] Strom R. G. et al. (1994). The global resurfacing of Venus. *JGR: Planets*, *99*(E5), 10899–10926. [5] Herrick R. R. et al. (2023). Resurfacing History and Volcanic Activity of Venus. *Space Sci. Rev.*, *219*(4), 29. [6] Gülcher A. J. P. (2025). Coronae on Venus: An Updated Global Database and Insights Into Morphology, Spatial Distribution, Geological Setting, and Lithospheric Properties. *JGR: Planets*, *130*(5), e2024JE008749. [7] Hahn R. M. & Byrne P. K. (2023). A Morphological and Spatial Analysis of Volcanoes on Venus. *JGR: Planets*, *128*(4), e2023JE007753. [8] Ford P. (1997). *Venus Magellan Global Topography 4641m* (Version 2) [Dataset]. Planetary Data System. [9] Stofan E.R. et al. (2012), Geologic map of the Hecate Chasma quadrangle (V–28), Venus: USGS Scientific Investigations Map 3163, pamphlet 12 p., 1 sheet, 1:5,000,000 scale. [10] Price M. & Suppe J. (1994). Mean age of rifting and volcanism on Venus deduced from impact crater densities. *Nature*, *372*(6508), 756–759. [11] Ivanov M. A. & Head J. W. (2015). The history of tectonism on Venus: A stratigraphic analysis. *Planetary & Space Sci.*, *113–114*, 10–32. [12] Ivanov M. A. and Head J. W. III. (2008). Geologic map of the Meskhent Tessera quadrangle (V-3), Venus: USGS Scientific Investigations Map 3018. [13] O'Rourke J. G. et al. (2014). Venus: Interpreting the spatial distribution of volcanically modified craters. *Geophys. Res. Letters*, *41*(23), 8252–8260. [14] Montiel N. J., De Toffoli B. (2025) Coronal Resurfacing on Venus. *ESS Open Archive.*

CARBON CHAIN DIVERSITY IN L1544 AND IRAS 16293-2422: AN ASTROCHEMICAL PATHFINDER STUDY FOR THE SKAO Lisa Giani[1], Eleonora Bianchi[1], Anthony Remijan[2], Claudio Codella[1,3], Giovanni Sabatini[1], Linda Podio[1], Cecilia Ceccarelli[3], Marta De Simone[4], Nadia Balucani[5], Paola Caselli[6], Eric Herbst[7,8], Francois Lique[9], Silvia Spezzano[6], Charlotte Vastel[10] and Brett McGuire[11,12], [1]INAF, Osservatorio Astrofisico di Arcetri, Largo E. Fermi 5, I-50125, Firenze, Italy (lisa.giani@inaf.it), [2]National Radio Astronomy Observatory, Charlottesville, VA 22903, USA, [3]Univ. Grenoble Alpes, CNRS, IPAG, 38000 Grenoble, France, [4]European Southern Observatory, Karl-Schwarzschild Str. 2, 85748 Garching bei Munchen, Germany, [5]Dipartimento di Chimica, Biologia e Biotecnologie, Via Elce di Sotto 8, 06123 Perugia, Italy, [6]Max-Planck-Institut fur extraterrestrische Physik (MPE), [7]Department of Chemistry, University of Virginia, Charlottesville, VA 22904, USA, [8]Department of Astronomy, University of Virginia, Charlottesville, VA 22904, USA, [9]Université du Rennes, CNRS, IPR (Institut de Physique de Rennes) UMR 6251, F-35000 Rennes, France, [10]IRAP, Université de Toulouse, CNRS, UPS, CNES, 31400 Toulouse, France, [11]Department of Chemistry, Massachusetts Institute of Technology, Cambridge, MA 02139, USA, [12]National Radio Astronomy Observatory, Charlottesville, VA 22903, USA.

Introduction: A surprisingly rich chemistry has been observed in the earliest stages of Sun-like star formation, highlighted by the gas-phase detection of complex molecules relevant to prebiotic chemistry, such as interstellar complex organic molecules (iCOMs; mainly C-bearing species containing at least six atoms) [1]. Recent radio observations have also revealed an active chemistry involving complex carbon-bearing species, including cyclic hydrocarbons such as benzonitrile (c-C_6H_5CN) and cyanocoronene ($C_{24}H_{11}CN$) [2,3]. This peculiar carbon chain chemistry is still mostly unexplored due to limitations in current radio facilities, and the origin of these species and whether they undergo further growth, possibly contributing to the molecular inventory of planetary systems, remain open questions.

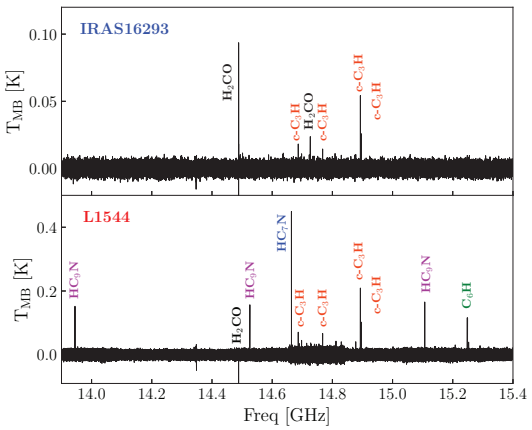


Figure 1: Full continuum-subtracted spectra (in main-beam temperature, T_{MB}) of the IRAS 16293-2422 envelope (Upper panel) and the L1544 prestellar core (Lower panel) observed in Ku Band (13.9-15.41 GHz).

Observations: We present recent observations performed using the 100-m Green Bank Telescope (GBT, US) of the prestellar core L1544, and the protostellar system IRAS 16293-2422 (Fig. 1). In L1544, we detected several complex carbon-bearing species, including C_2S, C_3S, C_3N, c-C_3H, polyynes ($C_{2n}H$) and cyanopolyynes ($HC_{2n+1}N$) [4]. In IRAS 16293-2422, we detected c-C_3H and, for the first time, HC_7N. Thanks to the high spectral resolution, we refine the rest frequencies of several c-C_3H and C_6H transitions. We perform radiative transfer analysis, highlighting a chemical difference between the two sources: IRAS 16293-2422 shows column densities 10 to 100 times lower than L1544.

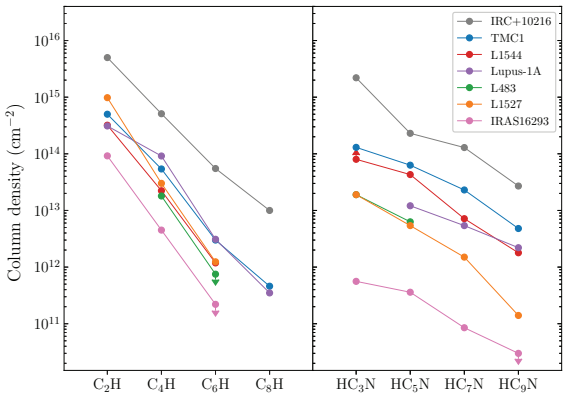


Figure 2: Comparison between column densities of polyynyl radicals $C_{2n}H$ (Left panel) and cyanopolyynes $HC_{2n+1}N$ (Right panel) measured in different star-forming regions [5,6].

The column densities of $C_{2n}H$ and $HC_{2n+1}N$ measured in L1544 and IRAS 16293-2422 exponentially decay with increasing molecular size. Interestingly, the same exponential decay is observed in other prestellar cores, dark clouds, and protostellar sources (Fig. 2). This supports a chemical connection between the $C_{2n}H$ and $HC_{2n+1}N$ families, and suggests inheritance along the star formation process and that the same gas-phase chemistry is at work at all stages and in different star-forming regions.

Astrochemical modeling: We perform astrochemical modeling, employing an up-to-date chemical network with revised reaction rates for the formation of HC_5N [7]. Models reproduce the decreasing trends of cyanopolyyne and polyynyl radical abundances, but underestimate the abundances of cyanopolyynes longer than HC_5N, suggesting that the chemical network still requires the integration of key reactions that regulate the formation of long cyanopolyynes. We propose that additional ion–molecule reactions are crucial for the formation of these species.

Future impact of SKA observations on carbon chain chemistry: This work paves the way for future astrochemical studies with next-generation radio interferometers such as the Square Kilometre Array Observatory (SKAO) [8]. Thanks to the high angular resolution and sensitivity, the new SKA facilities will allow the exploration of carbon-chain chemistry down to spatial scales of ~100 au within planet-forming regions, resolving structures such as accretion streamers, protostellar envelopes, outflows and disks that remain unresolved in single-dish observations (e.g. with the GBT). Specifically, SKA will reach a 3σ sensitivity of ~0.6 K/beam with a ~1.3" beam (corresponding to 100-200 au for nearby star-forming regions) in 100 hours of integration time, and down to ~0.2 K/beam in 1000 hours (Fig. 3).

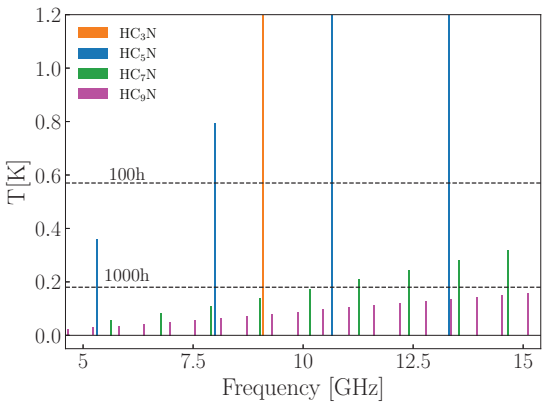


Figure 3: Predicted line intensities of HC_3N and cyanopolyynes which are still undetected in disks (HC_5N, HC_7N, HC_9N). We assume that the column densities of cyanopolyynes scale accordingly to what observed in the prestellar core L1544 (Fig. 2). The horizontal dashed lines indicate the 3σ sensitivity obtained with SKA-Mid AA4 at a spectral resolution of 0.34 km s^{-1}, and for a beam of 1.39”×1.33” in 100 and 1000 hour integration times.

Under these conditions, multiple transitions of cyanopolyynes up to $HC_{11}N$, along with their precursors C_4H and C_6H, will be detectable in several sources. When combined with updated chemical reaction networks, these observations will provide crucial constraints on the formation pathways of carbon chains and cyanopolyynes, shedding light on their potential prebiotic role and on the inheritance of organic material from the pre- and protostellar phases to the bodies of newly formed planetary systems, such as asteroids and comets.

References:

[1] Ceccarelli C. et al. (2023) *A&A, 652*, L9. [2] Cernicharo J. et al. (2023) *A&A, 674*, L4. [3] Wenzel G. et al. (2025a) *Nature Astronomy, 9,* 262. [4] Bianchi E. et al. (2023) *ApJ, 944*, 208. [5] Oyama T. et al. (2020) *ApJ, 890*, 39. [6] Giani L. Et al. (2025b) *MNRAS,* staf1941. [7] Giani L. et al. (2025a) *MNRAS, 537,* 3861. [8] https://www.skao.int/en.

The Oxygenic Photosynthetic Habitability of M-stars acquaplanets.

M. Maris[1,a,b], N. La Rocca[2], M. Battistuzzi[3,2], L. Silva[1,a,b], E. Bisesi[1,a,c], G. Murante[1,a,b], J. Von Hardenberg[4], J. A. Caballero[5] , A. Balbi[6] and D. Billi[7], [1]INAF – Trieste Astronomical Observatory (Via G.B. Tiepolo 11. 34135, Trieste, Italy), [2]Biology Department Padua University, Padua, Italy, [3]INAF / Arcetri Astronomical Observatory, Florence, Italy, [4]DIATI, Politecnico di Torino, Torino, Italy, [5]Centro de Astrobiología, CSIC-INTA, Madrid, Spain, [6]Physics Department, Rome University "Tor Vergata", Rome, Italy, [7]Biology Department, Rome University "Tor Vergata", Rome, Italy, [a]IFPU – Institute for the Fundamental Physics of the Universe, Trieste, Italy, [b]Fondazione ICSC, Casalecchio di Reno (BO), Italy, [c]CNR - Institute of Geosciences and Georesources, Pisa, Italy.

Introduction:

JWST has recently observed Earth mass exoplanets such as GJ 486b [1], GJ 3929b [2], and K2-18b [3]. At the same time, the construction of the Extremely Large Telescope (ELT) [4] is progressing, while space missions like Life Interferometer For Exoplanets (LIFE) [5] and Habitable Worlds Observatory (HWO) [6] are under preparation. Together, these efforts pave the way for the search for gaseous biosignatures in the spectra of habitable exoplanets. The strength of such biosignatures depends on the productivity of a potential biosphere, which in turn is shaped by planetary conditions, chiefly temperature and surface irradiance.

Here we present a study within the Italian Space Agency's ASTERIA collaboration [7] , aimed at assessing the potential for oxygenic photosynthesis on habitable aquaplanets around M dwarfs—i.e., their Oxygenic Photosynthetic Habitability. These planets are expected to be spin-synchronous, with a permanently illuminated hemisphere and a thick clouds coverage [8].

In order to provide the ASTERIA collaboration with a tool to analyze the results of the experiments in progress, we implemented a Python package called PHOXTROT aimed at estimating the photosynthetic oxygen productivity over the surface of an aquaplanet orbiting an M-dwarf. The code extends the method outlined by [9] to include the temperature dependence, under the assumption that cyanobacteria are free-floating on the illuminated ocean surface. In the current version, the biological model at the root of PHOXTROT is based on cyanobacteria such as *Mycrocistis aeruginosa* and *M. weisembergii* [10,11].

We applied PHOXTROT to climate maps produced by the 3D GCM PLASIM code [12] to obtain the distribution of the oxygenic photosynthesis efficiency across the illuminated surface of a set of exoplanet models. To have a broad set of climate models, we take the planet parameters from a sample of representative potentially habitable M-dwarf exoplanets [13] taken from the Habitable World Catalog of the Arecibo Observatory [14].

A typical output for an aquaplanet with parameters similar to that of TOI700d is presented in Fig.1 where the radial profile of oxygen productivity (expressed as micromoles of oxygen produced for unit mass of Chlorophyll *a* and unit time) is plotted against the angular distance from the substellar point. The blue curve represents the pure response to the irradiance at surface. Green represents the case in which the model photosynthetic organism responds to temperature like a mesophile (organisms whose optimum of growth is in the range 15-45 °C), while the red curve is for the case of a thermophile-like organism (whose optimum of growth is in the range 45-80 °C).

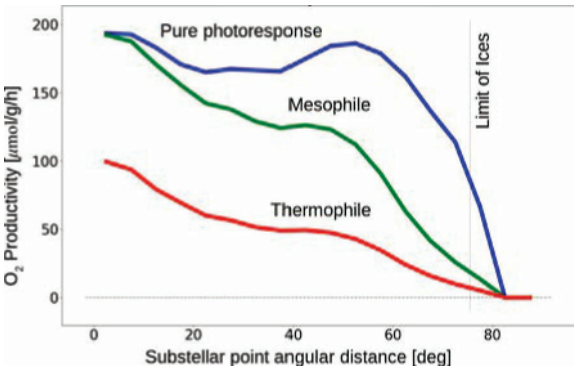


Fig.1 Oxygen productivity (μmoles of O_2/g of Chl *a*/h), as a function of the angular distance from the substellar point.

The results of this analysis extended to the whole sample of exoplanet models suggest that the key limiting factor for oxygenic photosynthesis is the ocean temperature. In contrast, surface irradiance does not appear so limiting, as underexposed regions are frozen and thus not productive, while the thick cloud coverage, typically predicted for this kind of aquaplanets [8,13], provides protection against excessive exposure in the subsolar region.

Next steps will include the extension of this analysis to include a wider range of model organisms, their potential vertical distribution below the ocean surface, as well as the effect of the UV irradiance from the parent star.

References:

[1] Moran et al. 2023 ApJL **948** L11. [2] Xue et al. 2025, https://arxiv.org/abs/2508.12516. [3] Madhusudhan et al 2025 ApJL **983** L40. [4] Bowens et al. 2021 A&A **653** A8. [5] Quanz et al. 2022 A&A **664** A21. [6] HWO

https://science.nasa.gov/astrophysics/programs/habitable-worlds-observatory/. [7] D. Billi 2025 in this conference. [8] Lobo and Shields, ApJ, 2024, **972**, 71. [9] Hall et al. 2023, ApJL, **948**, L23, [10] Yang et al. 2020 Environ Sci Eu., 32:24, [11] Battistuzzi et al. 2023, Frontiers in Plant Science, 2023, **14**-2023, [12] Fraedrich et al., 2012, The European Physical Journal Plus, **5**, 53, [13] Bisesi et al. 2025 submitted. [14] http:// phl.upr.edu/hwc.

LABORATORY EXPERIMENTS ON THE ORIGIN AND EVOLUTION OF EXTRATERRESTRIAL OZONE FROM ION IRRADIATED ICES AND ICY MIXTURES

D. Fulvio, R. G. Urso, C. Scirè, G. A. Baratta, G. Strazzulla and M. E. Palumbo
INAF-Osservatorio Astrofisico di Catania, via Santa Sofia 78, 95123 Catania (Italy)

Introduction: When considering the possible biosignatures to look for in extraterrestrial worlds, Ozone (O_3) results to be one of the most promising species [1-3]. Ozone is a byproduct of molecular oxygen (O_2) – a fundamental species for the sustenance of life – and belongs to the limited group of small species of biological interest potentially detectable from the mid-infrared (MIR) to the ultraviolet (UV). In fact, its detection, in some cases, could be easier than the one of O_2, therefore representing an indirect proof of atmospheric O_2 in those cases where this is not directly observable. Recent works show that O_3 could be soon detected in exoplanetary atmospheres by the James Webb Space Telescope (JWST) [4-6] as well as in planetary atmospheres and surfaces in the solar system by the JUpiter ICy moons Explorer (JUICE) [7-8] and Europa Clipper [9-10] space missions (in addition to the already mentioned JWST). Nevertheless, we noticed a lack of insight when considering the possible radiolytic production of O_3 within ices of different oxygen-bearing species which may be found on icy extraterrestrial surfaces (and consequently also released to enrich their atmospheres).

Methods: We therefore performed a comparative laboratory study on the production of O_3 from several ion irradiated ices and icy mixtures: CO, CO:N_2, CO:SO_2, CO_2, H_2O:CO_2, N_2O, NO_2:N_2O_4, and pure O_2. Unless otherwise specified, the experiments were performed at the Laboratory for Experimental Astrophysics (LASp) in Catania (Italy) and the samples, at 16 K, were processed with 200 keV protons and analyzed by FTIR spectroscopy.

Results: One of the main goals of this study is to contribute to the understanding of how much O_3 could be produced by energetic charged particles irradiating different oxygen-bearing ices and compare these results to the case of O_2 ice. Indeed, it is well known that ion bombardment may be very effective in inducing chemical, physical and structural changes on the icy surfaces of the satellites of giant planets, trans-Neptunian objects and extraterrestrial worlds outside the solar system, due to the ubiquitous presence in space of energetic charged particles (i.e., solar/stellar wind, cosmic rays, and magnetospheric ions) interacting with these icy surfaces [11-16]. We will show various alternative and complementary abiotic sources of O_3 that are not related to the presence of O_2 and whose origin is connected to the interaction between ices and energetic charged particles and, in particular, we will show that depending on the starting ices/mixtures the amount of abiotic O_3 produced by ion irradiation can account for up to 1/3 of the O_3 amount related to the presence of O_2 [17]. It is therefore necessary to take into account these (and similar) processes to have a clear picture on the origin of O_3, once detected.

Conclusions: We believe that these results may have a great impact in the field of astrobiology, planetary sciences, and exoplanets characterization, especially in view of the future exploration of the icy worlds of the solar system and the current and future exploration of exoplanets by the ongoing and upcoming space missions [17].

Acknowledgements: D.F. acknowledges financial support by the INAF-Ricerca Fondamentale 2022 program, “Laboratory experiments on Complex Organic Molecules (COMs) of interest for Astrobiology” (Minigrants RSN3). The Italian participation to JUICE mission is founded by the Italian Space Agency (ASI). In particular, this work has been developed under the ASI-INAF agreement n. 2023-6-HH.0

References: [1] Domagal-Goldman S. D. et al. (2014) *ApJ., 792*, 90. [2] Meadows V. et al. (2018) *Astrobiology, 18*, 6, 630-662. [3] Catling D. C. et al. (2018) *Astrobiology, 18*, 6, 709-738. [4] Triaud A. H. M. et al. (2024) *Nature Astronomy, 8*, 17-29. [5] Kempton E. M. -R. and Knutson H. A. (2024) *Reviews in Mineralogy and Geochemistry, 90*, 411-464. [6] Schwietermman E. W. and Leung M. (2024) *Reviews in Mineralogy and Geochemistry, 90*, 465-514. [7] Poulet F. et al. (2024) *Space Science Reviews, 220*, 27. [8] Tosi F. et al. (2024) *Space Science Reviews, 220*, 59. [9] Becker T. M. et al. (2024) *Space Science Reviews, 220*, 49. [10] Blaney D. et al. (2024) *Space Science Reviews, 220*, 80. [11] Fulvio D. et al. (2019) *MNRAS, 483*, 381-391. [12] Gerakines P. et al. (2001) *J. Geophys. Res. Planets, 106*, 33381. [13] Herbst E. (2014) *Phys. Chem. Chem. Phys., 16*, 3344. [14] Rothard H. et al. (2017) *J. Phys. B. At. Mol. Opt. Phys., 50*, 062001. [15] Ada Bibang P. C. J. et al. (2019) *Low Temp Phys., 45*, 590-597. [16] Urso R.G. et al. (2020) *ApJ Letters, 894*, L3. [17] Fulvio D. et al. (2025) *ACS Earth Space Chem., 9,* 1479-1487.

INVESTIGATION INTO THE ORIGINS AND DETECTION OF BIOMOLECULE HOMOCHIRALITY IN EARLY EARTH/MARS ENVIRONMENT. R. Mitri[1,2], G. Mitri[3,1], T. Pietrangelo[2], P. Tortora[4], T. Alajarin-Rouchouse[4,7], D. Calabria[4], S. Fulle[2], M. Locatelli[5], M. Mirasoli[4], M. Pedone[6], S. Piccirillo[6], [1]International Research School of Planetary Sciences, Università d'Annunzio (rukiah.mitri@unich.it), [2]Department of Neuroscience, Imaging and Clinical Sciences, Università d'Annunzio, [3]Dipartimento di Ingegneria e Geologia, Università d'Annunzio, [4]CIRI Aerospace, Università di Bologna, [5]Dipartimento di Scienze, Università d'Annunzio, [6]Agenzia Spaziale Italiana, [7]ELISA Aerospace.

Introduction: A chiral molecule is characterized by an asymmetric spatial arrangement of its atoms which gives rise to enantiomers with distinct chemical and biological properties. Electron transport through chiral molecules is a function of its spin orientation, the direction which it travels and the molecular handedness. This effect is known as Chirality Induced Spin Selectivity (CISS) and arises in part due to the coupling between the electron's spin with its linear momentum, which creates an effective local magnetic field, as it travels through the asymmetric charge density of the chiral molecule [1]. CISS research has shown that the asymmetric charge distribution of chiral molecules during electron transport causes a transient net spin polarization that manifest as a symmetric spin pair at opposite ends of chiral molecule which differs in spin orientation depending on the handedness of the molecule [2,3]. Thus, the behavior of the chiral molecule is similar to a ferromagnet (FM), in that both preferentially transmit electrons of one spin type and also have directionality. In fact, chiral molecules have been shown to have measurable magnetic properties by Hall Effect sensors [4].

The interaction between transient polarized spins in the chiral molecule and the polarized spins in the ferromagnetic surface is enantiospecific and depends on the spin alignment between the molecule and the magnetic surface [5]. The spin-exchange interactions between chiral molecules and magnetized FM have been used for enantioselective adsorption and crystallization of biomolecules [6,7]. Thus, external magnetic fields can tune the spin polarization direction, enabling enantioselective adsorption, crystallization, and catalysis. Alternatively, due to this spin exchange interaction, the chiral molecule can also induce and enhance magnetization in the surface layers of ferromagnetic surfaces [8,9].

While CISS experimental results have been demonstrated with biomolecules such as amino acids, peptides and DNA, simple sugars have not yet received much attention. Monosaccharides can be challenging for analysis due to their highly polar nature, multiple chiral centers and branching points. Monosaccharides have great importance prebiotically as the functional components of nucleotides, as energy sources and enablers of chemical reactivity due to their multiple hydroxy functional groups.

Enantioselective Adsorption: The enantioselective adsorptive properties inherent in CISS as a function of external magnetic field tuning could have been important in the origin of homochirality in prebiotic molecules. For example, Ozturk and Sasselov (2022) [10] proposed that ferromagnetic surfaces could act as a symmetry breaking agent for cyano-sulfidic prebiotic molecules such as glyceraldehyde in a lake with a magnetite lakebed. Glyceraldehyde is typically unstable in solution and tends to undergo keto–enol tautomerization to its non-chiral isomer dihydroxyacetone; additionally, this process can also lead to racemization. However, when glyceraldehyde is adsorbed onto or enclosed in a fatty-acid vesicle or micelle, prebiotic precursors of phospholipids, these processes are less likely to occur as free water necessary for isomerization and racemization is less available and glyceraldehyde hydroxyls may hydrogen bond with fatty acid headgroups instead of water. Additionally, micelles/vesicles can provide a neutral and slightly acidic pH environment that supports the hydrated glyceraldehyde form that is more stable.

In early Earth, lipid membranes could have not only protected fragile biomolecules but also may have driven homochirality of life to some degree. Recently Zhang et al. (2025) demonstrated that cyclic sugars can induce extended chiral water structures at an achiral lipid membrane's interface [11]. These supra-structures could act as spin-selective environments, amplifying CISS effects. Recent experimental work has provided evidence that archaeal and hybrid archaeal-bacterial membranes are enantioselective for some prebiotic biomolecules like D-ribose and D-deoxyribose sugars [12]. Sugars, as a function of their concentration, are significant factor for liposome morphology, membrane packing, pore formation and osmotic balance.

Fatty acid micelles and vesicles in early Earth are believed to have formed spontaneously in free water but they can also form on mineral surfaces. In fact, some minerals can even promote the adhesion and formation of lipid layers on their surface [13]. While fatty acid lipids react less than modern phospholipids to magnetic fields, if they encapsulate magnetite or greigite, they can respond to magnetic fields. Investigation of fatty acid micelles and vesicles on mineral surfaces with magnetite/gregeite components and prebiotic biomolecules such as glyceraldehyde and lactaldehyde with and without magnetic fields of varying strength and direction provide further insight

into the CISS effect and the possible origin of homochirality on early Earth/Mars.

Enantioselective Chromatography: Typically, monosaccharides, such as glyceraldehyde and glucose require different chromatographic strategies because of their polarity, stability, and structural complexity. CISS effect has the potential to make a universal chromatographic strategy for simple sugars and their derivatives by taking advantage of spin exchange interactions between ferromagnetic surfaces and chiral molecules. Recent research has shown that helicene SAMs act as spin filters where the handedness of the helicene determines whether spin-up or spin-down electrons are preferentially transmitted [14]. Proposed is a stationary phase of a magnetized ferromagnetic surface coated by a short layer of helicenes, heteroaromatic rings, which are inherently chiral due to their helical shape with the helicene layer functionalized with a boronic acid end group. Boronic acids are commonly used with sugars since they can reversibly interact with the hydroxy groups of sugars. The boronic acid group can serve to bring sugars into the vicinity of the magnetized surface for spin exchange interactions. The mobile phase is slightly basic with pH of 8-9 since boronic acid complexes with hydroxy (diol) groups are optimized. The ferromagnetic surface is externally magnetized with varying strength and direction.

Recently microfluidic chromatography is becoming increasingly popular given that it can miniaturize the chromatography apparatus on single chip. Microfluidic chromatography enables low sample consumption, rapid analysis and portability [15]. Further microfluidic chips can host multiple parallel channels with different workflows. Nanoparticle-based stationary phases integrated into microfluidic chromatographic chips can achieve high resolution separations taking advantage of the nanoparticle high surface area and tunable surface chemistry [16]. A microfluidic chip with an embedded solenoid to apply an uniform magnetic field strength and direction for a single channel chromatographic channel with a magnetic nanoparticle stationary phase coated with a SAM of helicenes functionalized with boronic acid end groups with a slightly basic mobile phase is used to investigate how the CISS effect could potentially serve as a method of universal detection of simple sugars and their derivatives.

The CASPR project is conducting an experimental and theoretical analyses regarding the effectiveness of CISS in inducing homochirality for prebiotic molecules in an early Earth/Mars scenario as well as investigating portable detection methods of chiral molecules with a focus on monosaccharides.

References: [1] Bloom, Brian P., et al. "Chiral induced spin selectivity." *Chemical Reviews* 124.4 (2024): 1950-1991.2. [2] Kumar, Anup, et al. "Chirality-induced spin polarization places symmetry constraints on biomolecular interactions." *Proceedings of the National Academy of Sciences* 114.10 (2017): 2474-2478. [3] Ghosh, Supriya, et al. "Effect of chiral molecules on the electron's spin wavefunction at interfaces." *The journal of physical chemistry letters* 11.4 (2020): 1550-1557. [4] Fontanesi, Claudio, et al. "Spin-dependent processes measured without a permanent magnet." *Advanced Materials* 30.41 (2018): 1707390. [5] Safari, Mohammad Reza, et al. "Enantioselective adsorption on magnetic surfaces." *Advanced Materials* 36.14 (2024): 2308666. [6] Banerjee-Ghosh, Koyel, et al. "Separation of enantiomers by their enantiospecific interaction with achiral magnetic substrates." *Science* 360.6395 (2018): 1331-1334. [7] Ozturk, S. Furkan, et al. "Origin of biological homochirality by crystallization of an RNA precursor on a magnetic surface." *Science advances* 9.23 (2023): eadg8274. [8] Ben Dor, Oren, et al. "Magnetization switching in ferromagnets by adsorbed chiral molecules without current or external magnetic field." *Nature communications* 8.1 (2017): 14567. [9] Ozturk, S. Furkan, et al. "Chirality-induced avalanche magnetization of magnetite by an RNA precursor." *Nature Communications* 14.1 (2023): 6351. [10] Ozturk, S. Furkan, and Dimitar D. Sasselov. "On the origins of life's homochirality: Inducing enantiomeric excess with spin-polarized electrons." *Proceedings of the National Academy of Sciences* 119.28 (2022): e2204765119. [11] Zhang, Li, et al. "Interfacial Self-Assembly of Sugars at Nanoscale Membranes Leads to Micron-Scale, Spectroscopically Ice-Like Chiral Suprastructures of Water." *Journal of the American Chemical Society* 147.37 (2025): 33413-33423. [12] Goode, Olivia, et al. "Permeability selection of biologically relevant membranes matches the stereochemistry of life on Earth." *PLoS Biology* 23.5 (2025): e3003155. [13] Hanczyc, Martin M., Sheref S. Mansy, and Jack W. Szostak. "Mineral surface directed membrane assembly." *Origins of Life and Evolution of Biospheres* 37.1 (2007): 67-82. [14] Ernst, Karl-Heinz. "Stereochemical recognition of helicenes on metal surfaces." *Accounts of chemical research* 49.6 (2016): 1182-1190. [15] Bao, Bo, et al. "Recent advances in microfluidics-based chromatography—A mini review." *Separations* 8.1 (2020): 3. [16] Nesterenko, Ekaterina P., et al. "Nano-particle modified stationary phases for high-performance liquid chromatography." *Analyst* 138.15 (2013): 4229-4254.

Acknowledgements: We acknowledge support from the Italian Space Agency (2023-11-U.0).

THE FANTASTIC FOUR: Tc, Re, Th, AND U IN GEOBIOLOGICAL PROCESSES. Gloria Giacchino[1], Luca Tonietti[2,3], Alessandra Rotundi[2,3], Sergio Calabrese[1,4]. 1) Dipartimento di Scienze della Terra e del Mare, University of Palermo, Palermo, Italy 2) Department of Science and Technology, Parthenope University of Naples, Naples, Italy. 3) INAF-OACN Osservatorio Astronomico di Capodimonte, Naples, Italy. 4) Istituto Nazionale di Geofisica e Vulcanologia, sez. Palermo, Italy.

Microorganisms play a fundamental role in shaping the chemical evolution of planetary surfaces and subsurfaces, yet their interactions with radioactive and redox-sensitive elements remain one of the least explored frontiers in geomicrobiology and astrobiology [1]. In particular, thorium (Th), uranium (U), technetium (Tc), and rhenium (Re) form an unusual group of elements i.e., the fantastic four, whose geochemical behavior, environmental stability, and biological interactions offer an opportunity to investigate both the limits of life on Earth and beyond [2]. Studying how microorganisms mobilize, transform, or tolerate these elements can therefore deepen our understanding of mineral weathering processes, metal resistance strategies, and the biochemical adaptations that allow life to persist in extreme environments.

This project develops an integrated conceptual framework to examine the microbial mobilization and transformation pathways of Th, U, Tc, and Re from mineral substrates. The research combines mineralogical characterization, geochemical speciation, and a systematic review of microbial mechanisms capable of influencing the environmental fate of these elements. By comparing elements with different redox behaviors, ranging from the well-known U(VI)/U(IV) cycle to the highly soluble pertechnetate form of Tc(VII), the project aims to elucidate how microbial metabolisms might either exploit these redox transitions or simply respond to them through detoxification or immobilization pathways.

Even though experimental data are still being generated, preliminary synthesis already reveals several key insights with implications for both Earth and planetary environments. First, microbial communities inhabiting radionuclide-rich environments may possess unique metal-handling strategies that reflect adaptations to chronic radiation stress, oxidative pressure, and scarcity of bioavailable energy sources. Second, the chemical similarity between ReO_4^- and TcO_4^- provides a valuable platform to explore microbially mediated transformations of redox-sensitive elements that have limited natural mineral expression on Earth, thereby offering a window into microbial flexibility when confronted with substrates not encountered during evolutionary history [3]. Third, Th, typically considered biologically inert in redox terms, may still undergo biologically mediated mobilization through indirect weathering processes, raising important questions about the extent to which microbes can influence nominally non-redox-active elements in extreme environments [4].

Many extraterrestrial settings of interest, including the Martian regolith, icy-moon subsurfaces, and environments affected by cosmic-ray-induced radiolysis, contain mineral phases or chemical conditions compatible with the presence, mobilization, or fixation of these elements [5]. Understanding how microorganisms interact with redox-active metals on Earth can therefore create new models of habitability, metabolic energetics, and biosignature formation in environments beyond our planet. In addition, the study of microbial survival and metabolic function in the presence of radiotoxic or chemically challenging species can help define the physiological limits of life, supporting future life-detection missions that must consider both biologically mediated and abiotic redox transformations.

The conceptual model presented in this project will guide the next phases of laboratory experimentation, geochemical modeling, and comparative analyses. This work aims to bridge geomicrobiology, mineralogy, and planetary science by providing a coherent framework for interpreting how life interacts with complex geochemical landscapes, both on Earth and potentially across the Solar System.

References:

[1] Merino et al. 2019. Front. Microbiol. 10:780.
[2] Lopez-Fernandez et al. 2020. Microb Biotechnol. 810-828.
[3] Werner et al. 2023. Resources Policy 103441.
[4] Tonietti et al. 2025 Front. Microb. (submitted).
[5] Atri et al. 2025. Int. Journal of Astrobio. 24:e9.

ORBIT DETERMINATION STUDY OF ARTIFICIAL SATELLITES USING OBSERVATIONAL DATA FROM THE SCHMIDT AND COPERNICO TELESCOPES AT THE MOUNT EKAR OBSERVING STATION.

L. Cortese[1,2], P. Borin[1], C. Arcidiacono[1], S. Zaggia[1], M. Simioni[1], R. Sordo[1], M. Gullieuszik[1], M. Dima[1]
[1]INAF – Astronomical Observatory of Padova, [2]Università degli Studi di Padova (luca.cortese@inaf.it)

Introduction: The growing number of satellites placed in orbit around the Earth has made the continuous and precise improvement of their orbit determination (OD) increasingly necessary. The commercial use of space is enormously increasing the number of Resident Space Objects (RSOs) and, consequently, the risk of collisions which leads to the creation of space debris.

Within the ASI–INAF agreement *"Space debris and long-term sustainability of space activities"*, the project of the Space Debris Team at INAF-OAPD aims to observe objects in GEO and MEO orbits with the 1.82m Copernico and the 67/92 Schmidt telescopes at the Asiago Mount Ekar Observing Station (INAF-OAPD). We perform imaging, spectroscopy, polarimetric and spectro-polarimetric observations of a selected sample of objects in the specified orbital regimes, providing a method to determine physical properties and orbital behavior of the target objects.

Observation strategy: The Schmidt telescope, operating in fully robotic mode, provides wide-field (~1 degree) multiband imaging of RSOs across orbital regimes from LEO to GEO. Observations are scheduled dynamically to optimize the visibility of selected targets and to monitor their photometric evolution. The Copernico telescope, equipped with the AFOSC instrument, is employed in parallel for higher-resolution imaging and spectroscopy of specific objects, enabling combined orbital and physical characterization. Both telescopes operate in steady pointing mode, as they cannot track fast-moving LEO or MEO targets. Two complementary observing strategies are adopted: (1) sidereal tracking, in which the telescopes remain fixed on the stellar background while the RSO crosses the field of view, allowing precise astrometric referencing of the object's track relative to background stars, and (2) steady pointing of GEO-like targets, suitable for long spectroscopy integrations on slowly moving objects. Observation planning is performed semi-automatically, using space-track.org queries. The two-line element (TLE) sets retrieved are then propagated to obtain Azimuth and Altitude of the pointing. The coordinated use of the two facilities provides added value thanks to complementary datasets for orbit determination, photometric and spectroscopic classification, and supports the ASI observational campaigns contributing to the Inter-Agency Space Debris Coordination Committee (IADC) and Fly-Eye network developments.

Orbits Dynamical Modeling: To propagate the orbital state of the target object, we will employ the Simplified General Perturbations-4 (SGP4) analytical propagator that allows us to propagate multiple trajectories from available TLEs. SGP4 propagator has some limitations in terms of precision and accuracy ([1], [2]). These propagation algorithms consider the main perturbation forces acting on a satellite: four zonal Earth gravity field harmonics, atmospheric drag, and solar radiation pressure. Using optical observations of Earth-orbiting objects, state information is expressed in terms of observational angles as a function of time, losing the precise knowledge of the range and range-rate. To determine the orbit of the observed objects, multiple observations must be combined ([3]). The purpose of this work is to propagate the orbits of the target objects and provide accurate trajectory evolution. Because observational data are used, we must take into account the main effects related to the observer's position, like atmospheric refraction, the aberration due to the composition of the observer's velocity with the speed of light, the light time correction due to the motion of the observed object, and the gravitational light deflection due to the Sun. We present here some preliminary results.

References: [1] Vallado, D.A. (2001) Springer Science and Business Media. [2] Kelso, T. (2007) *AIAA Spaceflight Mechanics Conference*. [3] Fujimoto, K. and Scheeres, D.J. (2013) Advances in Space Research 52

Acknowledgments: This work was carried out under the *"Space debris and long-term sustainability of space activities"* project, within the framework of the ACCORDO ATTUATIVO n. 2023-50-HH.0 between the Italian Space Agency (ASI) and the National Institute for Astrophysics (INAF).

ASTROMETRY OF NEAR-EARTH ASTEROIDS AND RESIDENT SPACE OBJECTS WITH THE TANDEM SYSTEM. S. Palmiotto[1], M. Barbetta[2], A. Carbognani[2], A. Buzzoni[2] *[1]Alma Mater Studiorum - University of Bologna, Department of Industrial Engineering, Via B. Carnaccini 12, Forlì, 47122, Italy [2]INAF-OAS, Osservatorio di Astrofisica e Scienza dello Spazio, Via P. Gobetti 93/3 Bologna, 40129, Italy*

Introduction: In the context of Space Surveillance and Tracking (SST) and Planetary Defense (PD), tracking near-Earth asteroids (NEAs) through optical observations plays a significant role. However, the astrometric observations of these bodies are challenging, as they pass close to Earth: due to their fast apparent motion, to get a good orbit solution, a temporal precision of the order of a few milliseconds and the ability to measure the position of streaks are required.

These observational difficulties are similar to those encountered in the astrometry of resident space objects (RSOs) in the Earth orbital environment. Given the growing population of active and inactive artificial satellites across the various geocentric orbital regimes, the activities of SST are becoming increasingly important for any efficient Space Traffic Management and Policy (STMP) aimed at quantifying and - when possible - mitigating the risk of collision between RSOs.

In the Loiano Astronomical Station (INAF-OAS), we developed our image processing pipeline, BOPAS (Bologna Observatory Pipeline for Astrometry of Satellites), for astrometry of satellite streaks, and tested it with observations of NEAs and RSOs using the TNDEM array, obtaining astrometric errors in the order of 1 arcsec.

The software is freely available on GitHub, where anyone can download and adapt it as needed.

The TANDEM system: The observations analyzed in this work were acquired with TANDEM (**T**elescope **A**rray e**N**abling **DE**bris **M**onitoring) [1], a wide-field telescope array conceived to complement the 1.52 m "G.D. Cassini" telescope, whose narrow FOV limits its efficiency for sky surveys and tracking of fast-moving targets. TANDEM consists of four 35 cm F/3 Newtonian telescopes mounted on the Cassini counterweight arm, with which it shares the RA, forming an equivalent collecting area comparable to a 70 cm F/1.5 instrument. DEC pointing can instead be decoupled from Cassini, allowing TANDEM to move the four telescopes along the declination axis in the range from -30° to +90°. Each telescope can be independently steered within a 10° radius around the common pointing direction. Each optical tube is equipped with a Moravian C4-16000 CMOS camera (1.75 arcsec/pixel), delivering a 2°×2° field of view corrected by a Wynne system. The cameras feature an electronic rolling shutter and they are equipped with BVRcIc filters.

The system supports multiple observing strategies: the four telescopes may converge on a single 2°×2° field or be arranged to cover up to 16 square degrees of sky. Concerning observations of RSOs, a custom MATLAB software - *TLE2Ephemeris*- was developed to compute the optimal arrangement of the four FOVs starting from the TLE of the target.

Image timestamps are assigned by the TANDEM's clock, connected to a local GPS Network Time Protocol server ensuring millisecond accuracy.



Fig. 1 - TANDEM array and the "Cassini" telescope (Loiano Astronomical Station, INAF-OAS).

After each observing session, raw images are automatically transferred via FTP protocol to a workstation, where a batch program runs our pipeline BOPAS to process them overnight, generating astrometric reports ready for analysis.

The astrometry pipeline: BOPAS is a MATLAB-based software designed to automatically process sidereal-tracking images containing satellite streaks. It integrates local Astrometry.net version for astrometric calibration using Gaia DR2 catalogue [2].

After calibration, images undergo a convolution with Gaussian filtering to smooth the noise and adaptive thresholding to detect streaks, which are identified as connected components exceeding user-defined area and aspect ratio thresholds.

The model of a convolved Gaussian Point Spread Function (PSF) is then fitted with each detected streak through a Levenberg–Marquardt least-squares optimization, allowing accurate centroid

determination even for faint or distorted streaks [3].

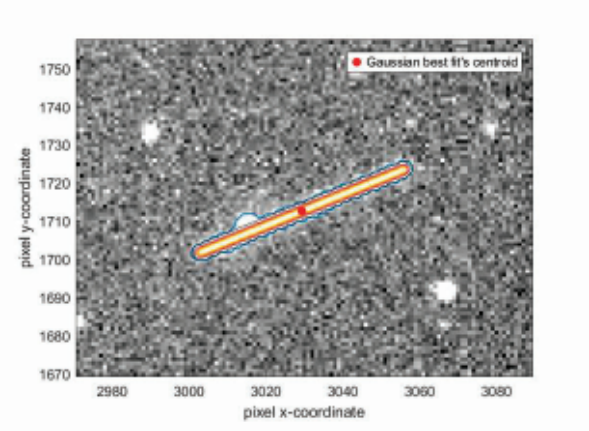


Fig. 2 - detected streak of the NEA 2025 FA22 and best fit with the convolved Gaussian PSF.

The Astropy python package is then called to project the centroid's pixel coordinates into topocentric right ascension (RA) and declination (DEC) coordinates at J2000.0. The pipeline then corrects the centroid's time tag for the cameras' electronic rolling shutter, filters out spurious detections by slope or ephemeris comparison, and produces standardized astrometric reports in CCSDS-TDM and MPC-ADES formats. The latter format includes uncertainties of the plate solve, SNR, and apparent magnitudes.

Test campaigns: Observing campaigns with the TANDEM telescope array between June 2024 and September 2025 demonstrated the reliability of BOPAS.

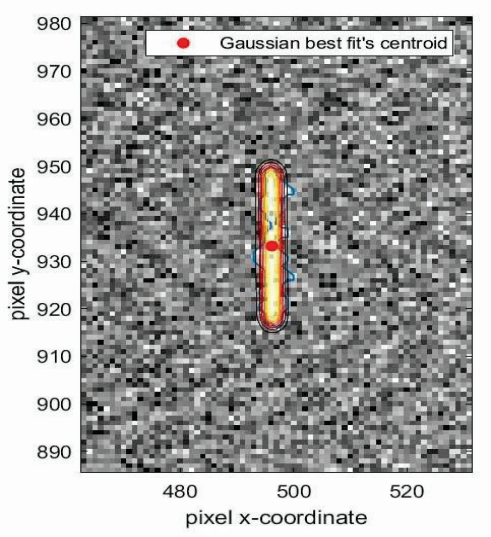


Fig. 3 - detected streak of the NEA 2022 EB5 and best fit with convolved Gaussian PSF.

To begin with, BOPAS was tested by processing images of the fast (NEA) 2022 EB5 taken by the staff of Osservatorio Astronomico della Montagna Pistoiese in March 2022. The astrometric uncertainty yielded by our pipeline is in the order of 1 arcsec, and the RMSE between astrometry by BOPAS and by Minor Planet Center (MPC) database is less than 1 arcsec.

Afterwards, a test campaign was conducted with TANDEM on the NEA 2025 FA22. Our telescope system managed to image the target's streak in all of the images and BOPAS successfully calibrated all of them, and measured all the detected streaks. However, the astrometric calibration's uncertainty is in the range 2-3 arcsec, probably due to the exposure time of 60 s needed to get a streak long enough to be detected, causing the CMOS sensor to saturate in case of bright objects.

Then, TANDEM and BOPAS were tested with observations of RSOs. Comparisons of astrometric positions of GNSS spacecraft from BOPAS with the respective precise ephemerides from ILRS data yielded RMSE < 1″ and timing biases below 20 ms. Orbit determination of the same spacecraft using the Java astrodynamics library Orekit resulted in a similar RMSE between observed positions and the ones associated with the determined trajectory. As for RSOs in low Earth orbit (LEO), orbit determination using Orekit yielded again RMSE < 1″.

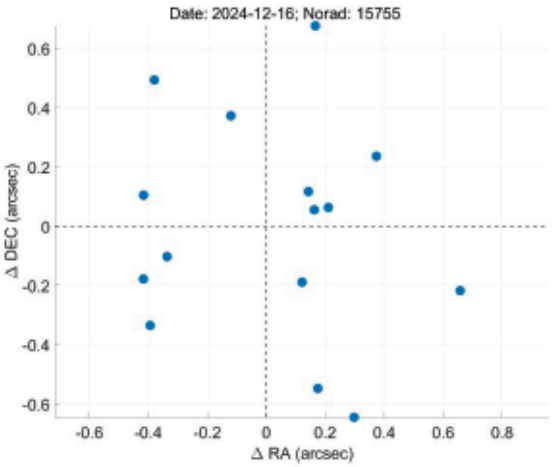


Fig. 4 - residual plot of the best fit orbit of NORAD 15755 in LEO.

References:

[1] Buzzoni, A., Carbognani, A., Di Luca, R., Diolaiti, E., Gualandi, R., Semola, A., ... & Schreiber, L. (2024). *The Astronomical Journal*, *169*(1), 53.

[2] Lang, D., Hogg, D. W., Mierle, K., Blanton, M., & Roweis, S. (2010). *The astronomical journal*, *139*(5), 1782.

[3] Vereš, P., Jedicke, R., Denneau, L., Wainscoat, R., Holman, M. J., & Lin, H. W. (2012). *Publications of the Astronomical Society of the Pacific*, *124*(921), 1197.

SECULAR EFFECTS IN SMALL BODIES IMPACT FREQUENCIES. A. Dell'Oro[1], [1]INAF-Osservatorio Astrofisico di Arcetri (Largo Enrico Fermi, 5 Firenze (Italy), E-mail: aldo.delloro@inaf.it).

Several models of the evolution of small bodies populations in which collisional processes play a significative role, as well as the interpretation of some important observational evidences, rely on our knowledge of some quantitative parameters related to the intensity of impactors fluxes. Evolution of the size distribution, expected number of asteroid families, chronology based on the surface cratering, collisional spin reset frequencies, production of dust, etc…, are only few examples of problems where impact frequencies and relative velocity distribution are key parameters. This applies to Main Belt Asteroids, Edgeworth-Kuiper belt objects or bodies forming debris disks around other stars in different phases of evolution.

The parameters of impact (frequency, relative velocity, impact geometry, and so on) are all fundamental quantities underpinning many models of global evolution of small bodies populations, depending on the dynamical behavior of the system under investigation. For those reasons, statistics of the parameters of impact requires a case-by-case careful model calibration.

The classical approach in Solar System studies is to try to compute the impact probabilities starting from the orbital elements of the bodies under investigation. Some analytic or semi-analytic theories to solve the problem have been developed, including the most general one developed so far [1]. In any case all those methods require as input a distribution of orbits, from which the probabilities of collision are derived. Regardless the validity of the particular method, the choice of orbital distribution is a critical point. In the case of debris disks around other stars, the forced solution is to start from simplified hypotheses about the distribution of the semimajor axes, and then to take into account the secular evolution of the other orbital elements produced by one or more perturbing planets (hidden or observed as well). In the case of our Solar System, we have at disposal detailed and abundant data about the orbits of different small body populations, that on the other hand require a careful removal of the biases produced by different observational selection effects A crude use of the available data entails implicit assumptions about the orbital distributions that can be wrong (especially with respect to the distribution of physical dimensions).

Another problem concerns the type of orbits to be used. For many asteroids populations we have at disposal both osculating and proper elements. While the former are valid for a limited interval of time, the proper elements are "quasi-constant" of motion describing some long-term essential dynamical features of the asteroids [2], fundamental for the identification of the asteroid families. But, the use of proper semimajor axes, proper eccentricities and proper inclinations alone do not enlighten all the features of the asteroid motion, affecting the computation of the statistical parameters of impact. The implications of using the osculating elements, as a representative snapshot of the dynamical status of the system, rather than proper elements as "mean" values of the previous one, have not been sufficiently investigated yet.

On the other hand the rigorous treatment of the secular orbital evolution in computing the impact statistics is not trivial. The most classical approach consists in approximating the orbital evolution assuming semimajor axes, eccentricities and inclination fixed, while node longitudes and arguments of perihelion are assumed uniformly distributed ([3], [4]). A first attempt to overcome these limitations showed the importance to take into account the non-uniform orientation of the orbits ([5]), but that model was not yet able to take into account the correlation between eccentricity and longitude of perihelion, or between inclination and longitude of the nodes caused by the secular perturbations. More recently a new mathematical approach has been developed in order to address this problem ([1]).

In the present contribution we aims to discuss some theoretical issues and advancement related to the problems mentioned above. We focus on the impact of the observational bias on the computation of the velocities and probability of collision among asteroids, and more in details we show how the statics of collision changes using osculating or proper elements in the framework of the classical mathematical approaches, rather than using more general methods able to take into account the subtle effects of the secular perturbations.

References:

[1] Dell'Oro A. (2017) *MNRAS*, *467*, 4817.
[2] Milani A., Knežević Z. (1990) *Cel. Mec. Dyn. Astr.*, *49*, 347
[3] Wetherill G.W. (1967) *JGR*, *72*, 2429
[4] Bottke W.F. et al. (1994) *Icar.*, *107*, 255.
[5] Dell'Oro A. and Paolicchi P. (1998) *Icar.*, *136*, 328.

Toward the First Meteor Detections on Mars: Predicting Brightness and Altitude Using the Erosion–Fragmentation Model. Maximilian Vovk[1] (mvovk@uwo.ca), Peter G. Brown[1] (pbrown@uwo.ca), Denis Vida[1] (dvida@uwo.ca). [1]Department of Physics and Astronomy, Western University, London, Ontario, Canada

Introduction: No confirmed meteors have yet been observed on Mars. Such detections would provide an independent sampling of the interplanetary meteoroid environment at 1.5 AU, constraining flux and particle properties away from Earth. Most prior Martian studies estimated influx using single-body ablation, predicting roughly half the Earth-visible rates at the same magnitude and favoring occurrence altitudes of ~50–90 km [1], with peak light typically near 75–85 km [2]. However, high-resolution measurements on Earth show that almost 90% of faint meteors tend to fragment, so single-body models cannot capture the dominant physics of light production and deceleration [3]. Moreover, it is well recognized that neglecting fragmentation biases parameter inference, typically inflating the inferred ablation coefficient σ and underestimating meteoroid bulk density ρ [4]. We therefore adopt the erosion–fragmentation model, following fragmentation-driven light-curve physics [5], to predict where (altitude) and how bright Martian meteors should appear.

Methods: We analyzed 155 faint meteors (mm-scale meteoroids) observed on Earth using: (i) EMCCD cameras (14.7°×14.7°, 32 fps, ~1.72 arcmin px^{-1}, limiting magnitude ≈ +10.5) [6]; and (ii) telescopic mirror-tracking system (1.5°×1.5°, 80 fps) that resolves fragmentation directly [7]. Physical parameters in the erosion–fragmentation model [5] (e.g. bulk density, ablation rate, erosion onset and rate, and fragment size release) were inferred with uncertainty bounds using Dynamic Nested Sampling [8]. The model was fit on observed meteor light curve and deceleration.

To project these meteoroids to Mars, we computed admissible encounter speeds consistent with heliocentric dynamics and Martian bounds (from escape to hyperbolic). Atmospheric densities were taken from the Mars Climate Database (MCD) [9]. Each event was re-simulated for Martian conditions using the model parameters inferred at Earth; for comparison, we propagated the same initial properties through a single-body ablation model.

Results: Brightness contrasts: Relative to our erosion–fragmentation model, the simple single-body ablation underpredicts brightness and shifts peak altitudes; discrepancies increase for weaker porous bodies and higher encounter speeds.

Peak-brightness altitudes: We map expected luminous-peak heights versus entry speed of mm size meteoroids, revealing speed-dependent, narrow altitude bands favored by fragmentation-driven light production in the Martian atmosphere.

Detection windows: By folding camera-like sensitivity thresholds into the predicted magnitude distributions, we identify observing altitudes that maximize detectability for future Mars orbiters, aerial platforms, or surface assets. These regimes directly inform required frame rate and limiting-magnitude requirements.

Conclusions: Our erosion–fragmentation predictions provide concrete observing constraints, altitude bands and meteor brightness expectations, to guide instrument design and pointing strategies for the first meteor detections on Mars. Such observations would tighten constraints on meteoroid flux and size, strength distributions at 1.5 AU, testing assumptions in current meteoroid-environment models and improving satellite risk assessments across the inner Solar System.

References: [1] Adolfsson, L. G., Gustafson, B. Å. S., Murray, C. D. (1996) *Icarus*, 119, 144–152. [2] Molina-Cuberos, J. G., López-Moreno, J. J., Arnold, F. (2008) *Space Sci. Rev.*, 137, 175–191. [3] Subasinghe, D., Campbell-Brown, M. D., Stokan, E. (2016) *MNRAS*, 457, 1289–1298. [4] Popova, O., Borovička, J., Campbell-Brown, M. (2019) "Modelling the entry of meteoroids," in *Meteoroids: Sources of Meteors on Earth and Beyond*, 25.9. [5] Borovička, J., Spurný, P., Koten, P. (2007) *A&A*, 473, 661–672. [6] Gural, P., Mills, T., Mazur, M., Brown, P. (2022) *Exp. Astron.*, 53, 1085–1126. [7] Vida, D., Brown, P. G., Campbell-Brown, M., Weryk, R. J., Stober, G., McCormack, J. P. (2021) *Icarus*, 354, 114097. [8] Speagle, J. S. (2020) *MNRAS*, 493, 3132–3158. [9] Millour, E., Forget, F., Lewis, S. R. (2014) *Mars Climate Database v5.1 User Manual*, ESTEC Contract 11369.

IRON OXIDATION STATE AND COORDINATION ENVIRONMENT IN BRAZILIAN TEKTITES

G. Giuli[1*], V. Desantis[1], A. P. Crosta[2], G. Gonçalves[3], L.Ferriere[4], *[1]School of Science and Technology-Geology Div., University of Camerino, Italy* *gabriele.giuli@unicam.it; *[2]Istituto de Geociencias, Universidade CAmpinas, Campinas, Brasil; [3]Instituto de Química, Universidade de São Paulo (USP), São Paulo, Brasil;[4]Natural History Museum, Abu Dhabi, EAU*

Introduction: Recently, ca. 500 samples of tektites from the Minas Gerais state and from Bahia state (Brazil) have been reported. The glass is mostly homogeneous, occasionally showing lechatelierite inclusions. In terms of chemical composition, it falls in the dacite and rhyolite fields of the total alkali versus silica diagram, with similar SiO2 and slightly higher Na2O+K2O content in comparison with other known tektites.

Instruments and methods

The samples used for XANES measurements have been prepared as polished thin sections or polished slides. XANES data have been collected at the Carnaúba beamline of the SIRIUS ring of the Brazilian Synchrotron Light Laboratory (Campinas, Brazil) using a Si (111) monochromator. The small X-ray beam size allowed it to probe several spots for each sample. Accurate analysis of the pre-edge peak energy and integrated intensity allowed to determine $Fe^{3+}/(Fe^{2+}+Fe^{3+})$ ratios on all samples with an estimated error of ±0.05 [2].

Experimental results

XANES data collected on 5 different samples display a good signal to noise ratio, allowing to extract information on the Fe oxidation state from the pre-edge region. The energy and integrated intensity of the pre-edge peak indicate that Fe is mostly divalent in these samples, with $Fe^{3+}/ (Fe^{2+} + Fe^{3+})$ ratios between 0.0 and 0.1. The pre-edge peak intensity is indicative of a coordination number of divalent Fe intermediate between 4 and 5.

Conclusion: We did not find significant differences in the shape and energy of Fe XANES spectra collected for different samples, nor between spectra collected within the same samples, testifying the homogeneity of the Fe redox in the analysed tektite samples. Both Fe oxidation state and coordination environment are similar to those of most tektites studied so far [3,4,5] and to Trinity glass [6].

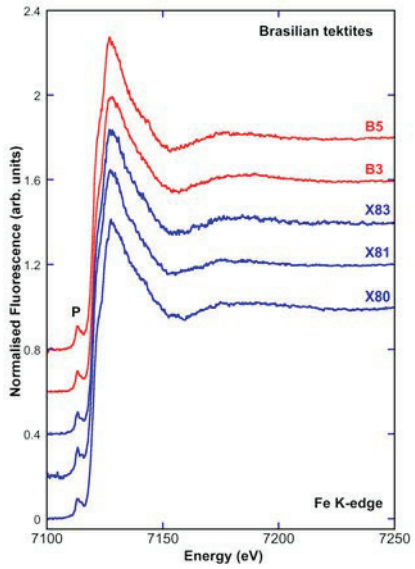


Figure 1 XANES spectra of the tektites studied

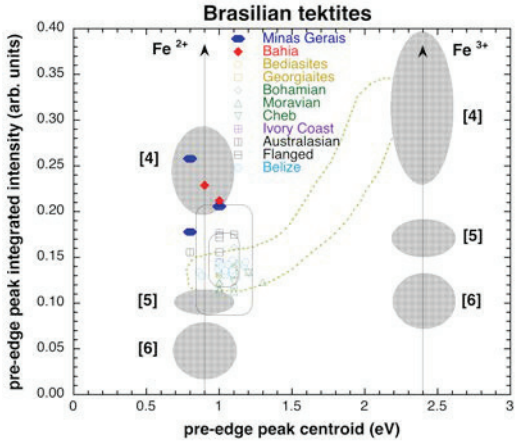


Figure 2 pre-edge peak centroid vs integrated intensity

References: [1] Koeberl C. et al. 2007. *MAPS* 42:709-729. [2] Giuli, G. et al. (2011) Amer.Miner., 96(4), 631-636. [3] Giuli, G. et al. (2002) Geoch. et Cosm. Acta, 66(24), 4347-4353. [4] Giuli, G. et al. (2010) Geological Society of America Special Paper, 465, 645-651. [5] Koeberl et al. *Geoch.a et Cosmoch. Acta*, 325. 252-257. [6] Giuli, G. et al. (2010) Geological Society of America Special Paper, 465, 653-660.

Keywords: tektites, XANES

EVIDENCE FOR MIXED-REDOX DUST AGGREGATION IN AN EL3 ENSTATITE CHONDRITE EET90992. P.Manzari[1], [1]Agenzia Spaziale Italiana (paola.manzari@asi.it)

Introduction: Enstatite chondrites (ECs) are among the most reduced materials in the Solar System and provide fundamental constraints on redox conditions, thermal regimes, and dust reservoirs in the innermost protoplanetary disk [1]. EL3 chondrites, in particular, preserve the least processed mineralogical assemblages of the EL group, including FeO-poor enstatite, metal–sulfide intergrowths, and volatile-sensitive phases thought to record early nebular condensation and accretion [2]. However, differentt studies, [3,4,5] have shown that ECs often retain strong internal heterogeneities, both in redox state and thermal history, challenging the traditional view of ECs as simple nebular condensates.

In this context, the EL3 chondrite EET 90299 offers an opportunity to test the coexistence and relative importance of nebular mixed-redox dust aggregation and parent-body impact modification. Although its silicate compositions are consistent with an EL3 affinity, preliminary observations reveal both EH-like opaque phases and oxidized silicate microdomains.

Materials and metehods: A polished thin section of EET 90299 was examined using backscattered electron (BSE) imaging and qualitative petrography. Quantitative compositions were obtained by SEM-EDS on silicates, metal, sulfides, feldspathic phases, and silica grains at the Department of Earth Sciences, in Bari. Enstatite compositions were recalculated to Wo–En–Fs molar components, and olivine compositions to Fo–Fa. Elemental bulk concentrations were derived from wide beam EDS in different areas of the section.

Results: Silicate compositions are consistent with an EL3 affinity. Enstatite shows En95–97Fs2–3Wo0.4–0.8, and the only olivine grain measured is Fo97Fa2.7. Bulk Fe/Si derived from micro-bulk estimates is ≈ 0.48, characteristic of EL type.

As for the composition of the opaque phases, kamacite grains contain 6–7 wt% Ni with negligible Si. Schreibersite is abundant, occurring as both discrete grains and exsolution lamellae, indicating crystallization under extremely reduced, P-rich conditions (≤ IW–6). Sulfides include Cr-rich troilite (up to 3.7 wt% Cr) and Mg–Mn-Fe monosulfides consistent with niningerite-alabandite intermediate compositions, a tracer of EH-like microenvironments.

In contrast, in the matrix oxidized silicate microdomains were found: in particular, a euhedral albite (Ab > 90) with inverse Na–Ca–Na zoning, (2) silica grains outside chondrules, and as crystals in the metal phases and (3) K-feldspar composition in some chondrule mesostasis.

Discussion: The coexistence of highly reduced opaque assemblages (Ni-rich metal + schreibersite + Mg,Mn-bearing monosulfides) with oxidized silicate components (albite, silica, K-feldspar) let think about a possible origin of EET90299 by accretion from dust from multiple redox reservoirs.

It has to be also noted that according to recent reinterpretation by Ardle et al., (2025) the mineral chemistry of Cr-sulfides and kamacite EET90299 could also be ascribed to shock impact.

Nevertheless, the albite's euhedral morphology, in the matrix let think about a xenocrystal formed in a moderately oxidizing nebular region with a subsequent incorporation into a reduced EL3 matrix. At the same time, Mn-rich monosulfide and schreibersite require extremely low fO_2 and fS_2, typical of EH-like conditions.

EET 90299 preserves a micro-scale redox mosaic, providing direct evidence for fine-scale heterogeneity in the inner early Solar System.

References:

[1] Piani et al. (2016) Earth and Planetary Science Letters, 445, 31–43.
[2] Lin & El Goresy (2002) *MAPS* 37, 577–599.
[3] McArdle et al. (2025). *MAPS*, 60. DOI: 10.1111/maps.70065.
[4] Goss et al. (2023) *MAPS* 58, 433–443.
[5] Weisberg et al. (2023) 2023. *Meteoritical Society 86th Meeting*, Abstract 6217.

MICROMETEOROIDS FLUX AND IMPACTS VAPORIZATION AT THE MOON.

P. Borin[1], E. Martellato[1], [1]INAF – Astronomical Observatory of Padova (patrizia.borin@inaf.it)

Introduction: The Earth–Moon system is constantly bombarded by meteoroids of different sizes. Fragments of asteroids and comets constantly encounter the Earth and Moon in their orbits and impact on them as meteoroids. The ejecta curtain produced during the crater excavation contributes to the extended and tenuous exosphere that has been observed to contain sodium and potassium. Different mechanisms and source processes have been proposed as possible sources of the sodium and potassium ([1], [2]), including sputtering by the solar wind, photon-stimulated desorption ([3], [4], [5]), thermal desorption ([6]), and micrometeoritic impacts ([7], [8], [9], [10], [11]). LUMIO (Lunar Meteoroid Impacts Observer) is a European Space Agency (ESA) mission that aims to characterise the lunar and near-Earth meteoroid environment by imaging impact flashes on the farside of the Moon. In this context, the present work has the final goal of estimating the Sodium production rate on the Moon caused by impacts of micrometeoroids that originate from the Main Belt asteroids and Jupiter family Comets. To estimate the total contribution of mass to the exosphere by the micrometeoroid impacts, it is necessary to take into account the impactor flux on the Moon, the surface composition, and the interaction with the exosphere. We used the dynamical model of the micrometeoroid flux at the heliocentric distance of the Moon developed by one of the authors([12]), which is furtherly extended in this work by considering mutual collisions, which were not initially included in it.

Dynamical Model: The developed dynamical evolution model of dust particles numerically integrates a (N+1)+M bodies problem (Sun+N planets+M bodies with negligible mass) with the high-precision integrator RA15. Radiation and solar wind pressure and Poynting-Robertson drag ([14]). We included mutual meteoroid collisions ([15]). Mutual collisions between dust grains effectively shape the characteristics of the entire meteoroid cloud. Obviously, collisions are more significant for meteoroids with longer dynamical lifetimes, thus mostly affecting larger meteoroids. This is because their dynamical evolution is much slower under the influence of Poynting-Robertson drag, which is inversely proportional to the particle's size. It is also important to consider different populations, like asteroids and comets. To calibrate our results, we use the flux curves obtained by Cremonese et al. (2012), who revised the dust particle flux impacting Earth by simulating the impact craters measured on the Long Duration Exposure Facility satellite with the shock physics code iSALE [13].

Results and Future Work: In this work, we present here preliminary results on the flux estimate in a limited range of particle dimensions, having implemented mutual collisions in the dynamical model. We would like to study the released elements in the exosphere of the Moon, taking into account different chemical compositions of the impactors and the lunar surface, then comparing these results with observations and investigating whether there are some asymmetries in the emission distribution depending on the impact sites. Comparing the new model results for the Earth-Moon system with the LUMIO data to identify whether the impacts might be related to possible meteor showers.

References: [1] Hunten and Sprague (1997), Adv. Space Res., 19. [2] Killen and Ip (1999), Rev. Geophys., 37. [3] Madey et al. (1998), J. Geophys. Res., 103. [4] Mendillo et al. (1999), Icarus, 137. [5] Yakshinskiy and Madey (2004), Icarus, 168. [6] Yakshinskiy and Madey (2000), Icarus, 168. [7] Cintala (1992), J. Geophys. Res., 97. [8] Mendillo and Baumgardner (1995), Nature, 377. [9] Cremonese and Verani (1997), Adv. Space Res., 19. [10] Verani et al. (1998), Planet Space Sci., 46. [11] Smith et al. (1999), Geophys. Res. Lett., 26. [12] Borin et al. (2009), A&A, 503. [13] Cremonese et al. (2012), ApJ 749. [14] Marzari and Vanzani (1994), A&A, 283. [15] Pokorny et al. (2018), ApJ 894.

Acknowledgments: This work has been funded by the Italian Space Agency through the agreement n. F43C23000340001 entitled "Supporto scientifico alla missione LUMIO".

3D porosity of lunar meteorite Tisserlitine 006

Macente A.[1], Pratesi G.[1], Shehaj X.1,2,3, Cuppone T.[1]

[1]Università degli Studi di Firenze [2]Università degli Studi di Trento, [3]Agenzia Spaziale Italiana

Introduction: Understanding the 3D porosity distribution in lunar meteorites could provide important information about Moon geological history and, eventually, possible signature of past fluid-rock interactions. This is particularly important for future development and use of *In-Situ Resources (ISRU)* for the next space missions [1–3]. Multiple processes must be taken into account to understand the origin of porosity in lunar meteorites. For example, when lunar regolith get lithified through impact shock, the final rock porosity provides an indirect indication of the shock experienced by the lunar regolith, thus becoming an important property to measure [4]. Additionally, porosity in meteorites can also form through other processes not directly linked to the original processes in the lunar soil. For example, *cracks* can be present that were originated during earth atmospheric entry (e.g. disaggregation) and they can also form during terrestrial alteration, often being filled by secondary minerals. *Vesicles* are also present in lunar meteorites. They usually derive from volatile degassing, indicating that the gas phase was present when the lunar lavas were molten [5] or originated from melting owing to the impact process. They can be present in agglutinates, aggregation of small lunar soil particles bonded together by flow-banded glass [5]. Thus, understanding the type, origin and spatial distribution of porosity in lunar meteorites is crucial to determine their formation, past events and shock history. Apollo lunar samples have been studied in great details, but there are not many studies investigating porosity in lunar meteorites, and only few using non-destructive imaging methods such as X-ray Computed micro-Tomography (XCT) [6–8]. Here, we investigated a few fragments of Tisserlitine 006, using a combination of imaging methods. Tisserlitine 006 is a lunar feldspatic fragmental breccia, found in Mali in 2023. These fragments were taken from the inside of the meteorite, where little terrestrial weathering should be present.

Methods: A few fragments of Tisserlitine 006 were first imaged through X-ray Computed Tomography to quantify the porosity, in terms of volume, pore size and connectivity, and to investigate its 3D spatial distribution. The type of porosity present in these fragments contains both vesicles and microcracks, entirely or partially filled. Porosity was also investigated in terms of shape and orientation. High density phases, most likely troilite and Fe-Ni alloys, were also found and analysed in 3D, to determine the shock history of the meteorite. Voxel sizes range from ~8 µm to 14.2 µm. The samples were subsequently prepared for SEM-EDX and EMPA analyses, to investigate in more details the porosity and mineral compositions. The choice of the plane for sectioning was informed by the XCT analyses, which therefore allowed a careful investigation of where to cut for SEM-EMPA analyses.

Results: Preliminary results have shown that the fragments vary a lot in terms of porosity type and distribution. 5 fragments of various sizes and shapes were analysed.

3D analyses. Fragment #1 is characterized by a great number of vesicles, some of which visible to the naked eye (Fig. 1). In this fragment porosity primarily consisted of vesicles, ranging from 27 to 456 µm equivalent spherical diameter, with 40% of the vesicles having less than 60 µm diameter, and accounting for 0.55 vol.% of the total sample. Most pores have sphericity values greater than 0.5, and aspect ratio close to 1, indicating that they are sub-spherical. We have not found any correlation between size and shapes, meaning that all vesicles, no matter the size, seem to be sub-spherical.

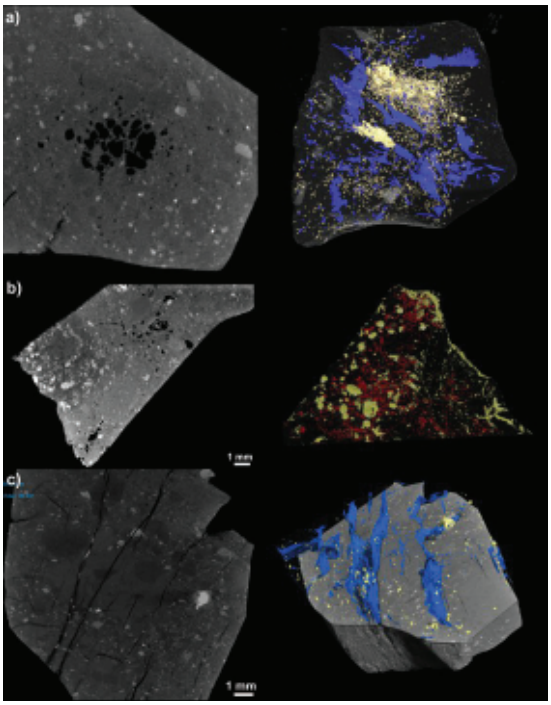


Figure 1. XCT vertical section and 3D rendering of a) porosity in Fragment #4, cracks in blue, spherical

pores in yellow; b) pores (inner pores in red, surface pores in yellow) of Fragment #1; c) cracks (blue) and high density phases (yellow) of Fragment #2.

Fragment #4 differs from Fragment #1 as it contains both vesicles and microcracks (Fig. 1a) Porosity in this sample accounts for 0.64% of the total sample volume, ~80% of which is characterized by spherical or sub-spherical pores (vesicles) and ~20% micro-cracks. The microcracks are notably characterized by high aspect ratios (> 2.2)). The majority of "round" pores (> 70%) have an equivalent spherical diameter < 100 µm.

Fragment #2 is completely different and characterised by the presence of mostly cracks (Fig. 1 c). There are two types of cracks: very large and planar fractures, most likely formed during terrestrial alteration, as they are filled in some areas with minerals and often rimmed by a lower density mineral compared to the matrix [9]; and *microcracks* which instead appears on the inside of large clasts, suggesting their origin from shock. The thickness of the large cracks reaches up to 200 µm.

SEM-EDX analyses. SEM – EDX investigation has revealed poikilitic texture of quenched olivine-pyroxene microcrystals indicating rapid cooling, the presence of Fe-Ni rich alloys, presence of small barite and carbonate-rich (mostly calcite) veins indicative of terrestrial alteration (Fig. 2). They also revealed the presence of schlieren, and that most vesicles are not "perfectly" spherical but rather show a strain component (Fig. 2).

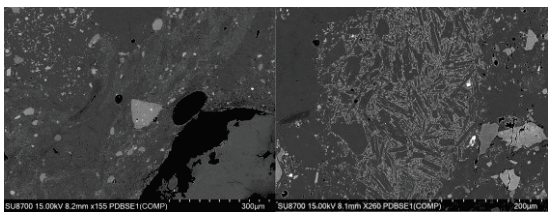


Figure 2. SEM images showing classical schlieren flow textures (left) and poikilitic olivine-pyroxene microstructures (right).

Conclusions: Shape and orientation XCT analyses in combination with EMPA-EDX chemical compositions helped understand better origin and formation history of Tisserlitine 006, thus providing important details about the shock history and terrestrial weathering of this meteorite.

References:

[1] S. Creech, J. Guidi, D. Elburn, IEEE Aerosp. Conf. Proc. 2022-March (2022).
[2] I. Crawford, Astron. Geophys. 58 (2017) 6.18-6.21.
[3] K. Hadler, D.J.P. Martin, J. Carpenter, J.J. Cilliers, A. Morse, S. Starr, J.N. Rasera, K. Seweryn, P. Reiss, A. Meurisse, Planet. Space Sci. 182 (2020) 104811.
[4] P.H. Warren, J. Geophys. Res. Planets 106 (2001) 10101–10111.
[5] G.H. HEIKEN, V. DAVID T., B.M. FRENCH, Lunar Source Book a User's Guide to the Moon, Cambridge University Press, n.d.
[6] A.J. Gawronska, C.L. Mcleod, E.H. Blumenfeld, R.D. Hanna, R.A. Zeigler, Icarus 388 (2022) 115216.
[7] T. Huang, E. Ganju, H. Torbatisarraf, M.S. Thompson, N. Chawla, 1472 (2024) 1455–1472.
[8] J. Goguen, A. Sharits, A. Chiaramonti, T. Lafarge, E. Garboczi, Icarus 420 (2024) 116166.
[9] M.R. Lee, P.A. Bland, Geochim. Cosmochim. Acta 68 (2004) 893–916.

Additional Information: "This study was carried out within the Space It Up project funded by the Italian Space Agency, ASI, and the Ministry of University and Research, MUR, under contract n. 2024-5-E.0 - CUP n. I53D24000060005."

A NEW ITALIAN METEORITE FROM MONTE BONDONE (TRENTO): DESCRIPTION AND PRELIMINARY DATA.

M.Morelli[1], V. De Santis[2], D. Faggi[1], and Gabriele Giuli[2], [1] Museo Italiano di Scienze Planetarie - Fondazione ParSec, Prato, Italy, e -mail: morelli@fondazioneparsec.it, [2]University of Camerino, School of Science and Technology, Geology div. Via Gentile III da Varano, 62032 Camerino (MC) Italy

Introduction: A meteorite recovery in Italy is a rare event. However, in addition to the recent falls in Cavezzo and Matera [1, 2] recovered thanks to the PRISMA – INAF network [3], some meteorites have been found during excursions in the mountains (Lago Valscura and Monte Costone meteorites).

In October 2021, Mr. Efrem Rigotti, while hunting for mushrooms on Monte Bondone (Trento), lost his car keys. Since he couldn't find them among the leaves on the ground, he asked a friend to help him with a metal detector. After some time of searching, when the metal detector beeped, they found not the keys, but a peculiar rock, distinct from the other dolomitic rocks cropping out in the area. Intrigued by its unusual characteristics, Mr. Rigotti brought the specimen home and attempted to cut it in his garage. Due to its unexpected hardness, he was unable to do so, and the rock remained forgotten until September 2024, when he contacted the Italian Museum of Planetary Sciences for a scientific evaluation.

Specimen: The specimen measures approximately 5x8 cm and appears to be a fragment of a larger mass that has not yet been recovered. The specimen appears compact, non-porous, and unaltered, with sharp, well-defined edges and no signs of rounding. It is dark to light grey in color and only a very tiny patch of fusion crust is present. A number of chondrules are clearly discernible on the specimen's surface. A chip of the sample (named ER-01) was embedded in resin, polished, and coated with graphite in order to perform FE-SEM analyses.

Instruments and methods: FE-SEM data (EDS analyses and BSE images) were collected by means of a Sigma300 Zeiss and a LEO1525 Zeiss operating at 15 kV and with a working distance of 8.0 mm. ZAF correction has been used to derive elemental abundances.

Experimental results

Textural characterization

A chondritic texture with defined chondrules (barred olivine, porphyritic olivine and radial pyroxene) can be observed. The matrix has a good recrystallization with no glass. Major phases are olivine, orthopyroxene and albitic plagioclase. Accessory phases are chromite and apatite-(CaCl). Opaque phases are abundant and consist mostly of kamacite and troilite. Melt pockets with metal and sulphide spherules and sulphide veins were recognized.

We assigned a weathering grade W0 as we did not notice any visible oxidation of metal or sulphides. The presence of shock melt pockets suggest a high shock degree. Further work is ongoing by means of Raman spectroscopy and EBSD in order to correctly determine the shock stage.

Minerochemical features

Follow the average chemical compositions of the mineral analysed together with their standard deviations: **olivine** Fa22.2±1.9, Fe/Mn=43.7±2.6 (n=12); **orthopyroxene** Fs17.7±1.03, En80.7±1.6, Wo1.5±1.2, Fe/Mn=24±6.7 (n=15); **plagioclase** An13.9±1.9, Ab84.6±2, Or1.48±0.13 (n=2); **chromite** Cr#=0.88 Mg#=0.21

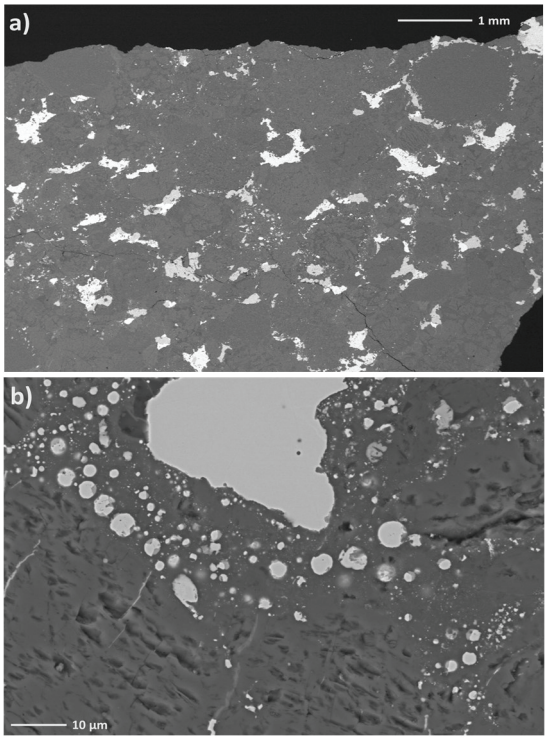


Figure 1: a) BSE-SEM image of ER-01 sample; b) detail of a melt pocket.

Conclusion: Textural and compositional data of olivines and pyroxenes suggest a classification as L5. The meteorite has been submitted for classification to the Nomenclature Committee of the Meteoritical Society.

References: [1] Gardiol et al. (2021) *Monthly Notices of the Royal Astronomical Society,* **501**(1),1215-1237 doi: 10.1093/mnras/staa3646 [2] Pratesi et al., 2025, Meteoritics & Planetary Science. 60, 2125-2148 https://doi.org/10.1111/maps.70025 [3] Colas et al., (2020) Astronomy & Astrophysics, **A53**, 1-23. Doi: 10.1051/0004-6361/202038649

FIRST FIND OF Ni_2S IN THE FUSION CRUST OF THE CAVEZZO L5 CHONDRITE.

M. Rondinelli [1], D. Gardiol [2], G. Pratesi [3], T. Catelani[3], A. Di Michele [4], G. Giuli [1],
[1] Università di Camerino, sez. Geologia, Via Gentile III da Varano 7, 62032 Camerino (MC), I marianglo.rondinelli@studenti.unicam.it; [2] OATO, Via dell'osservatorio 20, 10025 Pino Torinese (TO), I; [3] Università di Firenze, MEMA, Via G. Capponi 3R, 50121 Firenze, I; [4] Dipartimento di Fisica e Geologia, Università di Perugia, Via Pascoli, 06123 Perugia, I

Introduction: On January 1st at 18:26:53 UT, eight stations of the PRISMA network detected a brilliant fireball, named IT20200101, in the skies of northern Italy[1]. Thanks to the involvement of local people by an effective media campaign, two fragments were recovered, weighing 3.12 g (specimen 1) and 52.19 g (specimen 2), three days after the bolide was observed. In this contribution we describe the mineralogical composition focusing on the first find of Ni_2S.

Methodologies: The thin sections were borrowed from the Museum of University of Firenze; also few fragments of the crust from speciment 2 were embedded in resin, polished, and examined by FE-SEM and EBSD.

Results: Both optical observations and microchemical analyses of the meteorite interior were consistent with published classification as a L5 ordinary chondrite [2]. The fusion crust display a complex texture of sckeletal and acicular olivine, often with a rim richer in Fe than the core. The small size of most olivine crystal prevented to obtain an accurate composition for most of them. Magnetite dendrites are commonly associated to the olivines. Minor minerals found in the crust include euhedral crhomites, ilmenites, plagioclases in aggregates with chromites (Pl-chr assemblages). Rare pyroxenes in the fusion crust have been found rimming one of the Ni sulphide grains found.

Differences between specimens 1 and 2 fusion crusts: The fusion crust of specimen 1 is particularly thin and consists mostly micro- and nano-crystals of Olivines $(Mg,Fe,Ni)_2SiO_4$; minor Chromite $(Fe,Mg)(Cr,Al,Ti,V)_2O_4$ is also present. The interstices are disseminated by dendrites of Magnetite nanocrystals.

Conversely to the specimen 1, in all the fragments of crust analyzed and in the thin section of specimen 2, the fusion crust is generally thicker and display vascularity; the stratification of "melted crust", "outer substrate" and "inner substrate" described in Genge and Grady (1999) can be easily appreciated. [3]

Ni_2S: We have found four grains of a nickel sulfide whose composition is close to Ni_2S.

Several of these grains display submicroscopic inclusions of metallic Ni.

One of these Ni_2S sulfide grains is surrounded by a corona of microscopic pyroxene crystals with composition close to $En_{70}Fe_{28}Wo_2$.

Ni_2S has never been reported before neither in terrestrial nor in chondritic material.

Thus, in order to confirm the composition and in order to determine the structure of this phase, we are planning to cut a slice of one of these grains by FIB and to study this phase by Transmission Electron Microscopy to determine if we are actually observing the presence of a new phase or merely a mixture.

Preliminary examination by EBSD, allows to ascertain that the Ni_2S grains are not amorphous, and that the diffraction effects can be indexed and are compatible with a cubic unit cell with a 5.2 Å size

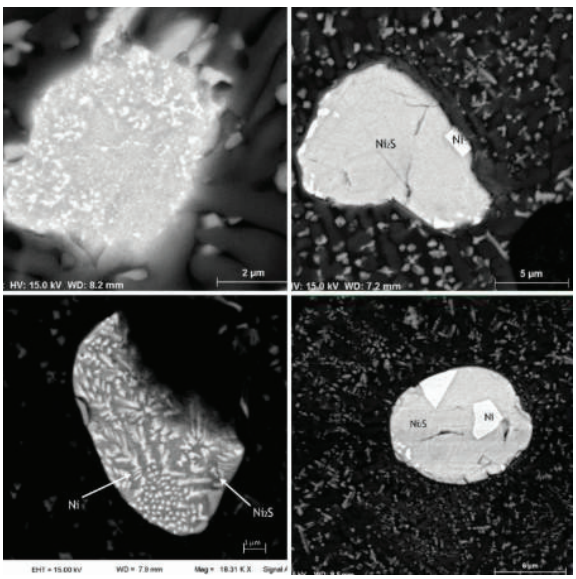


Fig.1. Representative grains of the Ni_2S sulphide found (light grey) containing metallic Ni inclusions (white). Above: the bright dendrites surrounding the Ni_2S grains are magnetite dendrites.

Below: another representative grains of the Ni_2S sulphide found (light grey) containing metallic Ni inclusions (white).

The bright dendrites surrounding the Ni_2S grains are magnetite dendrites; the dark crystals are pyroxenes.

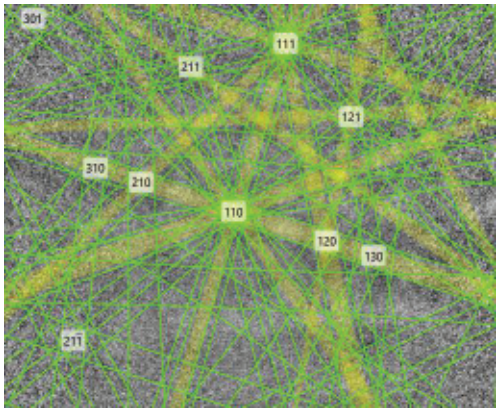


Fig.2. Electron BackScattered Diffraction pattern obtained on three of the four Ni_2S sulphide graind found. The diffraction effects can be indexed and are compatible with a cubic unit cell (a_0=5.2 Å)

References: [1] Gardiol D. et al., Cavezzo, The first Italian meteorite recovered by the PRISMA fireball net-work. Orbit, trajectory and strewn-field., (2020), Monthly Notices of the Royal Astro-nomicalSocie-ty, 501(1), 1215-1227.

[2] Pratesi G., Moggi Cecchi V., Greenwood C. R., Franchi I.A., Hammond S.J., Di Martino M., Barghini D., Taricco C., Carbognani A., Gardiol D., Cavezzo- The double face of a meteorite: Miner-alogy, petrography., (2021), Meteoritics; Planetary Science, 56(6), 1-26

[3] Genge M. J., Grady M. M., The fusion crusts of stony meteorites: Implications for the athmospher-ic reprocessing of extraterrestrial materials., (1999), Meteoritics & Planetary Science, 34(3), 341-356.

Acknowledgements: This work was carried out within the Space It Up! project funded by the Italian Space Agency (ASI) and the Italian Ministry of Uni-versity and Research (MUR) under contract No. 2024-5-E.0, CUP No. I53D24000060005.

COSMIC DUST FLUX DURING THE QUATERNARY: SIZE DISTRIBUTION OF SCORIACEOUS AND UNMELTED MICROMETEORITES FROM THE TRANSANTARCTIC MOUNTAINS COLLECTION. S. Ottaviani[1,2], L. Folco[1,3], M. D. Suttle[1,4], R. Repič[5], L. Mancini[5], T. Battiston[5], S. Iannini Lelarge[1,6] and M. Masotta[1,3], [1]Dipartimento di Scienze della Terra, Università di Pisa, [2]Dipartimento di Fisica e Geologia, Università degli Studi di Perugia (samuele.ottaviani@dottorandi.unipg.it), [3]CISUP, Università di Pisa, [4]School of Physical Sciences, The Open University, Milton Keynes, UK, [5]ZAG, Ljubljana, Slovenia, [6]CNR-IGG, Pisa.

Introduction: Micrometeorites (MMs) dominate the flux of extraterrestrial material that fall to Earth [1]. They are classified according to the degree of melting experienced during atmospheric entry heating into three groups: melted micrometeorites or cosmic spherules, unmelted micrometeorites and partially melted or scoriaceous micrometeorites [2]. About 10% of cosmic dust particles collected at the Earth's surface are unmelted or scoriaceous, thus preserving, at least in part, primary features of their parent bodies [3]. A significant number of unique large unmelted and scoriaceous MMs were recovered from 1-2 Myrs old sediments traps in the Transantarctic Mountains (TAM) [4,5]. Based on the petrographic characterization of 229 MMs, we report an unprecedented and statistically significant study of the size distribution of unmelted and scoriaceous MMs in the 200-2800 μm size range. This study complements previous assessment of micrometeorites size distribution which were based on totally melted TAM cosmic spherules [5] for a more accurate definition of the micrometeorites flux reaching Earth during the Quaternary.

Methods: Micrometeorites were identified based on their morphological and petrographic features using a stereomicroscope. To determine mass and size, the particles were weighed using a microbalance and imaged under a Field Emission Gun - Scanning Electron Microscope at CISUP (Pisa, IT). Backscattered electron (BSE) images provided textural criteria for the identification of unmelted and scoriaceous MMs (e.g., the presence of magnetite rims and dehydration cracks, scoriaceous structures, angular to subrounded morphologies, characteristic weathering products). Subsequently, the MMs were scanned using high-resolution X-ray computed microtomography at the ZAG institute (Ljubljana, SI), for a non-destructive, 3D textural classification into fine- or coarse-grained unmelted and scoriaceous MMs. To confirm our textural classification, 20 particles, representing a range of textures were sectioned and examined using BSE.

Results and discussion: The size distribution of the TAM unmelted and scoriaceous MMs is bimodal, with two main peaks at ~325 and 465 μm. A similar bimodal distribution was observed in TAM cosmic spherules, yet shift towards lower sizes with peaks at ~145 and 250 μm [5]. The discrepancy in the bimodal distribution of unmelted and scoriaceous MMs versus melted cosmic spherules in the TAM collection reflect the size-mass reduction produced by atmospheric entry heating leading to evaporative loss on a single population of extraterrestrial dust. We have identified an average mass loss of ~85%.

The analysis of the size distribution of the fine- and coarse-grained MMs reveals robust bimodality. The two distinct peaks in the scoriaceous plus unmelted MMs collection are centred at ~310 μm and 535 μm for fine- and coarse-grained MMs, respectively. This suggests that the bimodal distribution in the MM flux could potentially indicate at least two distinct populations of source bodies for the near-Earth interplanetary dust complex, namely dry, coarse-grained and evolved bodies (inner main belt asteroids), and hydrous, fine-grained and primitive bodies (outer main belt asteroids and comets), as strongly supported by previous studies [6,7].

Based on current MM mass flux estimates from TAM cosmic spherules [5] and the 85% mass loos due to ablative flight of the micrometeoroid flux, we calculate a time-averaged pre-atmospheric mass flux of cosmic dust over the Quaternary period of ~10 kt/yr. This is compatible to current estimates of 40 ± 20 kt/yr [1] and of ~15 kt/yr [8], suggesting that the flux has remained relatively constant over the recent geologic past.

Acknowledgments: PRIN2022 Cosmic Dust II, ID# 2022S5A2N7. ASI-MUR SpaceitUP! ID# 2024-5-E.0 – CUP n. I53D24000060005

References: [1] Love S. G. and Brownlee D. E. (1993) *Science, 262*, 550-553. [2] Genge M. J. et al. (2008) *Meteoritics & Planet. Sci., 43*, 497-515. [3] Van Maldeghem F. et al. (2023) *Geochim. Cosmochim. Acta., 354*, 88-108. [4] Rochette P. et al. (2008) *P. Nat. Acad. Sci. U.S.A., 105.47*, 18206-18211. [5] Suttle M. D. and Folco L. (2020) *JGR: Planets, 125(2),* e2019JE006241. [6] Suavet C. et al. (2010) *Earth Planet. Sci. Lett., 293*.3-4, 313-320. [7] Cordier C. and Folco L. (2014) *Geochim. Cosmochim. Acta.*, *146*, 18-26. [8] Rojas J. et al. (2021) *Earth Planet. Sci. Lett., 560*, 116794.

A PETROLOGICAL APPROACH TO THE STUDY OF CHONDRITES S. Borghetti[1], M. Di Martino[2], S. Ferrando[1,3], D. Faggi[4] , S. Ghignone[1], M. Morelli[4], R. Serra[5] and G. Vaggelli[3], [1]University of Torino, Department of Earth Sciences, Via Valperga Caluso 35, 10125, Torino, [2]Inaf – Turin Astronomical Observatory, [3]CNR, Institute of Gescience and Georesources, Via Valperga Caluso 35, 10125, Torino, [4] Italian Museum of Planetary Scienze - Fondazione ParSec, Prato, [5]Museo del Cielo e della Terra, San Giovanni in Persiceto (BO)

Introduction: This work is part of a master's thesis devoted to producing an analytical protocol for the petrographic and minerochemical study of chondrites and the creation of a "Laboratory for the petrological study of extraterrestrial material", which would make use of the acquired micro-analytical skills and the instrumentation available to arrive i) at their full classification, and ii) at the knowledge of the processes involved in meteorites genesis and evolution.

To reach this goal, a collaboration was established with the Italian Museum of Planetary Sciences, where an internship was conducted to study a collection of previously classified meteorite thin sections, typically used for educational purposes. Subsequently, we have studied five ordinary chondrites, two of which are already classified. The samples are provided by the museum "Cielo e Terra" in San Giovanni in Persiceto (Bologna, Italy) or by a private collection.

The methodological approach consists of: 1) measurements and macro-photographs of the samples; 2) petrographic observations under optical transmitted and reflected microscopy for microstructural and mineralogical identification; 3) SEM-EDS microanalyses on the mineral phases; 4) X-Ray compositional maps by SEM-EDS; 5) micro-Raman analyses.

Studied Meteorites: Five meteorites are available for this study: two meteorites are already classified as H and L ordinary chondrites (OC). The preliminary observations of the unclassified ones indicate that, from a chemical point of view, two samples can be classified as H OC and one as L OC. From a petrographic point of view, the two classified chondrites are type 5 and 6; the unclassified ones belong to types 4, 5 and 6. In general, the most common observed chondrules are: porphyritic olivines, barred olivines, porphyritic olivines and pyroxenes, granular olivine-pyroxene, radial pyroxenes, and more complex chondrules.

SEM-EDS data: SEM-EDS maps of the whole thin sections and on selected relevant microstructural sites, at higher magnification, will be performed in order to visualize the sample microstructures, to calculate the modal distribution of mineral phases with respect to metals, and finally to establish a method to compare different ordinary chondrites.

Moreover, EDS microanalyses on the mineral phases will be collected to compare their chemical composition with those from ordinary chondrites from the literature.

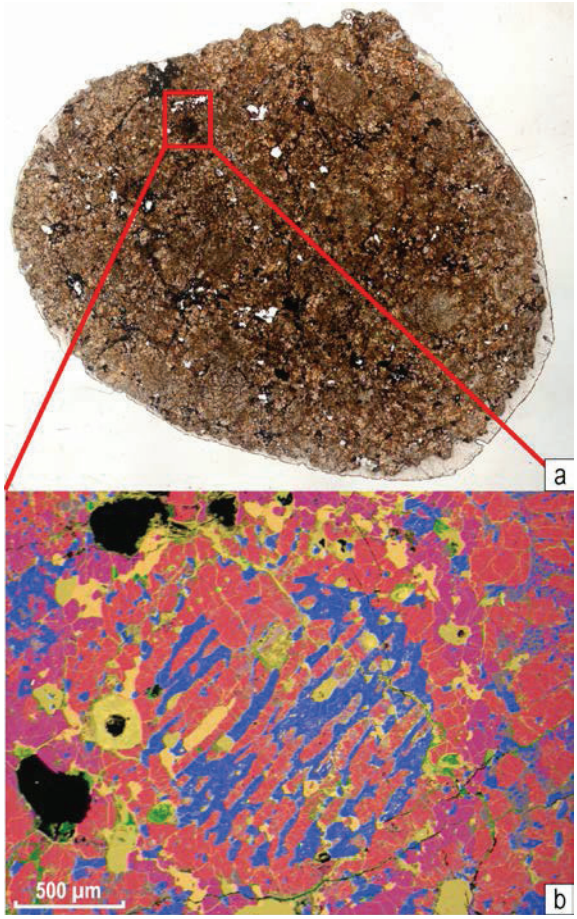


Figure 1: a) Scanning photomicrograph (plane polarized light) of a meteorite sample. b) EDS X-ray composite compositional map of a condrule, showing its microstructure and its constituting mineral phases, each represented by a distinct color.

Micro-Raman data: High resolution, micro-Raman analyses will be performed i) on polished thin sections to characterize small solid and fluid/melt inclusions present in the main mineral phases, ii) on the sample *tal quale* to characterize its alteration surface, and iii) on the dust extracted from the cracks to provide inferences on post meteor impact processes.

SYNTHESIS OF A NEW LUNAR REGOLITH BASED ON THE MICROCHEMICAL AND MINERALOGICAL CHARACTERIZATION OF LUNAR METEORITES. V. De Santis[1], M. Rondinelli[1], G. Pratesi[2], A. Franza[3,4], G. Giuli[1], [1]Università di Camerino, sez. Geologia, Via Gentile III da Varano 7, 62032 Camerino (MC), I, valeria.desantis@unicam.it, [2]Università di Firenze, MEMA, Via G. Capponi 3R, 50121 Firenze, I, [3]INAF-IAPS, Via Fosso del Cavaliere 100, 00133 Roma, I, [4]Università di Firenze, Dipartimento di Scienze della Terra, Via G. La Pira 4, 50121 Firenze, I.

Introduction: Lunar soil simulants have been produced since 1971, as the upcoming space missions needed astronauts to be trained in conducting scientific field works on the Moon's surface [1]. However, the first lunar soil simulants were not satisfactory in terms of chemistry and mineralogy, as they were focused on having the proper engineering properties [2].

Due to the scarcity and limited accessibility of real lunar soils and rocks samples, and as the interest in lunar colonization with In-Situ Resource Utilization (ISRU) is growing, the production of lunar soil simulants has increased over the years [2].

The objective of our work is to develop a new tunable lunar regolith simulant providing a reliable analog in terms of both mineralogy and bulk chemical composition that could be used for experiments on element extraction and for sintering experiments aimed at the production of building materials. In order to do this, we plan to synthesize some mineral components, e.g. anorthite, glass, and to find natural terrestrial analogs with suitable composition for other mineral components, e.g. olivine, pyroxene, and add them in adequate amounts.

Anorthositic rocks are major constituents of the highland regions of the Moon [3], so we aim at reproducing the composition of a regolith whose major component is anorthositic.

As lunar meteorites give access to unsampled areas of the Moon's surface [4], we analyzed microchemically and mineralogically feldspathic lunar breccias and use their mineralogical composition and mineral chemistry as a reference.

Samples and Methods: We performed microchemical and mineralogical characterization of some lunar feldspathic breccias, specifically of samples of the meteorites NWA 7948 [5], Bechar 007 [6], Gadamis 004 [7], NWA 15629 [8], and NWA 6687 [9], all feldspathic lunar breccias with low weathering grade [5-9], with the exception of [8] which is classified as mingled and [7] which is a ferroan anorthosite. The samples were analysed through FE-SEM at the University of Camerino and the University of Perugia and through FE-EMPA at the University of Firenze. Amorphous phases were identified through Raman spectroscopy at the University of Camerino. We also performed an X-ray Absorption Spectroscopy (XAS) investigation at Fe K-edge of plagioclase and glass on lunar meteorites in order to have a more precise information regarding the crystallographic structure of the mineral and the oxygen fugacity conditions needed for future synthesis. XAS analyses were performed at the European Synchrotron Radiation Facility (ESRF) in Grenoble.

Microcrystalline powders of minerals are synthetized using a muffle furnace in air at the University of Camerino.

Characterization of the synthetic powders was performed through X-ray Diffraction (XRD) at the University of Camerino.

Results: We started with the synthesis in air of anorthitic plagioclase with composition $An_{94.6}Ab_{5.1}Or_{0.3}$. XRD analysis of the synthesis products confirmed the purity and the structure, which is compatible with that of a disordered sodic anorthite (Fig. 1). Fe K-edge XAS analysis of impact glasses found in two meteorites, and of plagioclases allowed to ascertain the dominance of divalent Fe in both phases. These data are important in planning the oxygen fugacity conditions for the synthesis of Fe-bearing glasses and plagioclases.

We are now synthetizing glass in air focusing on the composition which resembles that of impact glass, vescicular glass of the agglutinates, and volcanic spherules found on lunar rocks and lunar meteorites. We plan to synthesize glass and possibly Fe-bearing anorthite also close to the IW buffer. We already found natural terrestrial olivines of suitable chemical composition from Praia do Norte, Portugal, ($Fa_{22.4-25.5}$) and Lanzarote, Spain, ($Fa_{\sim 33}$) and are currently searching for pyroxenes.

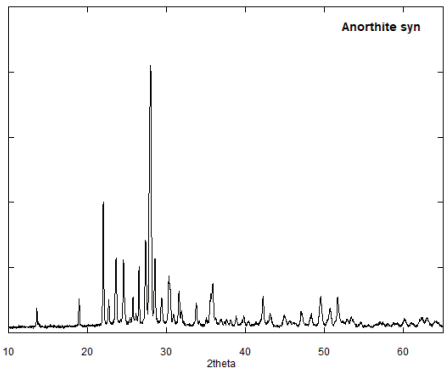


Fig.1. XRD diffrattogram of the synthetic anorthite powder.

References: [1] Slabic A. et al. (2024) *NASA Technical Reports Server (NTRS)*. [2] Taylor L. A., et al. (2016) *Planetary and Space Science, 126*, 1–7.

[3] Jaumann R. et al. (2012) *Planetary and Space Science, 74,* 15-41. [4] Korotev R. L. (2005) *Chemie der Erde, 65*, 297-346. [5] Zeng X. et al. (2018) *Meteoritics & Planet. Sci., 53*, 1030-1050. [6] Gattacceca J. et al. (2019) *Meteoritics & Planet. Sci.,* 54, 469-471. [7] Gattacceca J. et al. (2023) *Meteoritics & Planet. Sci.,* 58, 901-904. [8] Gattacceca J. et al. (2025) *Meteoritics & Planet. Sci.,* 60, 1587-1591. [9] Gattacceca J. et al. (2014) *Meteoritics & Planet. Sci.,* 49, E1-E101.

Acknowledgements: This work was carried out within the Space It Up! project funded by the Italian Space Agency (ASI) and the Italian Ministry of University and Research (MUR) under contract No. 2024-5-E.0, CUP No. I53D24000060005. We would like to thank Marco Minicucci for assistance at the SEM and Raman at UNICAM, Alessandro Di Michele for assistance at the SEM at UNIPG, Marine Cotte and Giovanni Lepore for help at ESRF, and Alessia Tombesi for assistance at the XRD.

PHYSICAL PROPERTIES OF L AND L/LL ORDINARY CHONDRITES AS DIDYMOS-DIMORPHOS ANALOGUE

Rossi E.[3], Cuppone T.[1*], Sebastiani M.[3], Pratesi G.[1,2] - 1 Dipartimento di Scienze della Terra, Università degli Studi di Firenze, Firenze, Italy 2 Istituto di Astrofisica e Planetologia Spaziali (INAF), Roma, Italy 3 Università degli Studi Roma Tre, Department of Civil, Computer Science and Aeronautical Technologies Engineering

Introduction: The HERA mission, supposed to rendevouz in late 2026 December with the binary asteroid 65803 Didymos, has the main goal to study the DART spacecraft impact site on Dimorphos (the Didymos satellite), occurred in September 2022, as planetary defense mission test within the Space Safety and Security Program of the European space Agency [1]. One of the DART main goal was to measure the momentum transfer efficiency resulting after DART's impact. HERA will investigate the interior structure of the bodies and characterize their surfaces comprehensively by using its instrument suite. Particular attention will be given to the crater produced by the DART impact, which is expected to have exposed pristine, primordial material from which Dimorphos is composed. This material is of special interest because it is largely unaffected by space weathering, thereby preserving the original mineralogical and compositional properties present since the formation of the binary system. In this study, we study some ordinary chondrites (OCs), belonging to L and LL groups, chosen because supposed to be the best Didymos-Dimorphos surface analogue, based on the correspondence of asteroid reflectance spectral fingerprint [2]. The determination of petrographic and mineralogical properties and their relation with some mechanical properties, like porosity, density and Young modulus will be integrated with spectroscopic data and would enormously increase our knowledge about Didymos-Dimorphos nature, especially in the perspective of future automatic robotic missions with both sample-returning goals and planetary defense technique.

Samples and methods: The specimens used for this work consist of a 2.73 g slice for Loro (L6), a 30 gr slice for Saratov (L4), both acquired from private meteorite dealers, and some Albareto (L/LL4) fragments, on loan from the GEMMA-UniMORE museum. Samples have been object of petro-mineralogic analyses (optical and scanning electron microscopy, SEM) and microanalyses (electron microprobe, EMPA). Bulk density and porosity has been measured after weighting, 3D scansion with Artec Micron structured light 3D scanner and X-ray microtomography technique (μCT) through a Bruker X-ray MicroCT SKYscan 1172. Some mechanical properties have been determinated by means of HSNM (High-speed nanoindentation mapping) technic with a Nanoindenter iNano within an ambient controlled home-made GloveBox. These last measures have been supported by EBSD mapping for local crystallographic orientation.

Preliminar results: Loro, Saratov and Albareto show petrographic and mineralogical characteristics congruent with those reported in literature, i.e., Fa/Fs 23.1±0.5/20.0±0.5 mol%, 22.6±0.7/16.8±3.9 mol% and 25.7±0.4/22.5±3.1 mol%, respectively.

Density values for Loro and Saratov are in the 3.10-3.33 gr/cm^3 range, in line with literature data for L and LL ordinary chondrites [3]. Porosity value for Saratov is 10.8% (from BSE images), while Loro has very low porosity, less than 1.5%, congruent with its high petrologic type. These values will be refined by forthcoming XCT analyses. Up to now, no porosity has been calculated for Albareto fragments, because the small size and possibly not representative for these analyses.

HSNM mapping: high-resolution mechanical property map (850x650 μm wide), with 100.000 indents, has been obtained on a single test area on Loro meteorite. Such mapping enables direct imaging of hardness (H) and reduced Young modulus variations (E_r) (Fig. 1) throughout the area. Aimed by EBSD mapping, an automatic Machine Learning (ML) clustering procedure allows the identification of 5 mechanical phase.

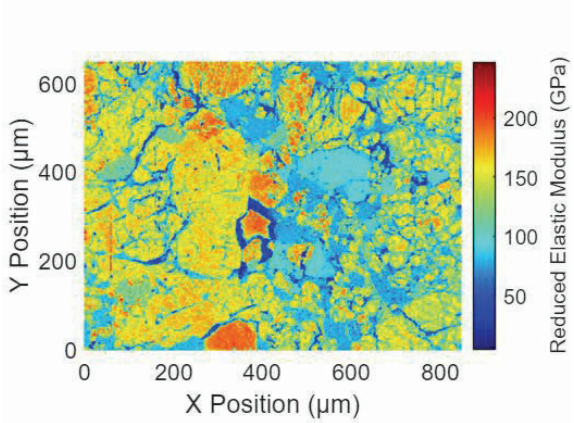


Fig 1 – Reduced Young modulus image map obtained with HSNM technic on Loro (L6) meteorite.

For each mechanical phase, it has been calculated the mean H and E_r values (Fig. 2). Mean H values (in GPa) are in good agreement with those calculated by [5] on Chelyabinsk L/LL5. Hovewer, our E_r values are systematically higher than those in Chelyabinsk, excepting for olivine. Moreover, the automat-

ic procedure has some limitations, since some mineral phases present in the mineral and EBSD maps are not recognized by (i.e., phosphate and chromite) and olivine from pyroxene are not always univocally resolved (Fig. 2).

Cluster Color	R. Elastic Modulus (GPa)	Mean Hardness (GPa)
Lega FeNi	181 ± 21	3.0 ± 1
Plagioclasio	79 ± 11	8.3 ± 1.2
Piros/Oliv	164 ± 12	13 ± 1
Troilite	104 ± 15	5.6 ± 1.3
Olivina	134 ± 13	11 ± 1.3

Fig 2 – H and E_r values (in GPa) for the mineral phases recognized by ML clustering procedure applied on HSNM maps.

Future analyses: Porosity value analysis will be implemented through a micro and nano porosity measures with Micro-nano X-Ray CT Easytom, at level of 250 nanometers (0.25μ). Further, we will also extend HSNM mapping to Saratov and Albareto samples with the aim to highlight possible E_r and H value variation as function of mineral composition and metamorphic maturation.

References: [1] Michel et al. (2018), *Adv. Space Res. 62*, 2261. [2] Ieva et al. (2022), *Planet. Sci. J. 3*, 183. [3] Wilkinson et al. (2003), *Meteoritics & Planet. Sci. 38,* 1533-1546. [4] Rossi et al. (2023), *Current Opinion in Solid State & Materials Science 27*, 101107. [5] Moyano-cambero et al. (2017), *ApJ 835*, 157.

Aknowledgements: This study was carried out within the project "Scientific Activities for HERA Mission" (ASI—Italian Space Agency)—UNIBO (University of Bologna) agreement n. 2022-8-HH.0.

UNVEILING THE COMPOSITION OF EET 87746 ANTARCTIC METEORITE BY A NON-DESTRUCTIVE APPROACH. Fanelli G.[1]*, Mele D.[1], Mangone A.[2], Agrosì G.[1], [1]Dipartimento di Scienze della Terra e Geoambientali (Università degli Studi di Bari "Aldo Moro"). *Corresponding author: g.fanelli33@phd.uniba.it, [2]Dipartimento di Chimica (Università degli Studi di Bari "Aldo Moro").

Introduction: The preservation of scientifically invaluable extraterrestrial specimens is pivotal. Therefore, non-destructive analytical methodologies have rapidly become fundamental tools, as they guarantee the structural and chemical integrity of the samples for extended use and validation across the scientific community. With this objective, a fragment of EET 87746, an Antarctic meteorite found in 1987 during the expeditions of the ANSMET (ANtarctic Search for METeorites) program at Elephant Moraine (Antarctica) is in progress. On the outer part, EET87746 is very altered and there are several deep fractures. 60% of the surface is characterized by a black fusion crust [1]. It is classified as an enstatite chondrite EH4 type (fig. 1)

The aim of this study is to create a 3D reconstruction of extraterrestrial materials by multi-analytical and non-destructive or minimally destructive approach to investigate the mineralogical composition of the meteorite, with particular focus on rare phases, mineral distribution and associations, textures and microstructures, to gain further insights into its origin and evolutionary history.

Methods: The mineralogical and chemical composition of EET 87746 was investigated using Scanning Electron Microscopy (SEM) and µ-Raman spectroscopy. These techniques were associated with the micro-computed tomography (µ-CT), a useful methodology to investigate porosity and to obtain volumetric data without sample destruction [2], [3].

Results: Preliminary results show that EET 87746 consists of chondrules – ranging in size from 0.5 to 1.5 mm – with enstatitic composition, immersed in a plagioclase mesostasis. They occur predominantly with spherical morphology, although fragments are also common. We have recognized olivine and also nickel-iron alloys (kamacite, easily recognizable in BSE images due to its bright white appearance), sulfides (troilite, daubréelite, niningerite and oldhamite) and phosphides (schreibersite).

Furthermore, this meteorite shows signs of surface alteration due to prolonged exposure to atmospheric agents. Indeed, it is important to highlight the presence of oxidised phases (jarosite and limonite) that are the sign of a heavily weathering, according to Bryan Mason [4], and Carol Schwartz [2]. Despite this, the internal features of EET 87746 are well preserved and CAIs are also present. In particular, by SEM analysis we detected augite, spinel and perovskite.

Additional information had been obtained from µ-Raman. Although this analysis is still in progress, we were able to acquire the typical perovskite spectrum. This confirms the presence of this mineralogical phase, which constitutes the CAIs.

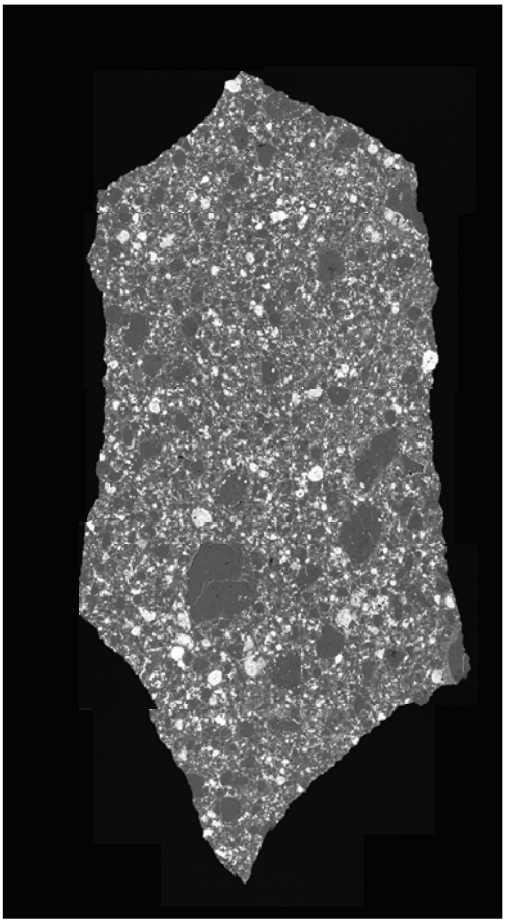


Figure 1 – SEM_BSE image of the polished surface

The data extrapolated from the µ-CT (fig. 2) – still in progress – will be correlated to the chemical-mineralogical composition. This will provide new compositional, porosity and mineralogical information without destroying the sample.

Discussion: Although the outer portion of the meteorite shows clear signs of alteration due to prolonged exposure to atmospheric agents , and despite the presence of oxidized phases such as jarosite and limonite , preliminary data confirm that the internal features of EET 87746 are well preserved.

The preliminary mineralogical investigation, conducted using Scanning Electron Microscopy, revealed the typical chondritic texture, with chondrules of enstatitic composition immersed in a plagi-

oclase mesostasis. A rich suite of characteristic minerals was identified, including olivine , Fe-Ni alloys (kamacite), sulfides (troilite, daubrelite, niningerite, and oldhamite), and phosphides (schreibersite).

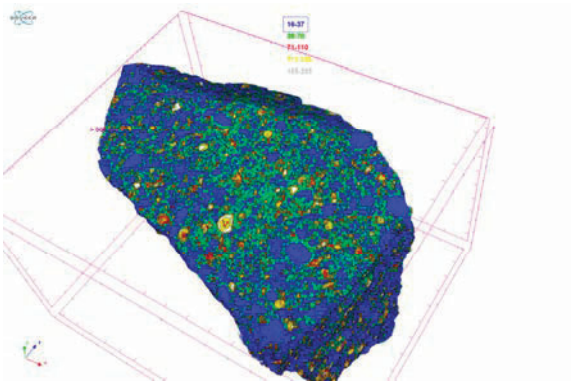


Figure 2 – 3D reconstruction of EET 87746 by µ-CT. The contrasting color scale represent mineralogical phases with different attenuation coefficient

A significant finding is the detection of CAIs. The presence of high-temperature minerals such as augite, spinel, and perovskite, the latter confirmed by µ-Raman spectroscopy, provides crucial data for understanding condensation processes and the physicochemical conditions in the earliest stages of solar system formation.

Conclusions: The applied multi-analytical and non-destructive methodology allowed us the characterization of the EET 87746 meteorite (EH4).

Preliminary results confirmed the typical composition of the extraterrestrial object, identifying various phases (including sulfides and phosphides) and documenting the alteration state, which contrasts with the excellent preservation of the internal structures.

In particular, the identification and preliminary characterization of the CAIs, composed of augite, spinel, and perovskite, constitute fundamental data for understanding its origins and the history of its parent body.

The integration of chemical-mineralogical data (SEM and µ-Raman spectroscopy) with the volumetric and porosity data obtained from the µ-CT, which is still in progress, is the next critical step of the study. The 3D reconstruction will allow the correlation of the spatial distribution of phases, microstructures, and porosity with the composition, offering a comprehensive and non-destructive view of the evolutionary history of the EET 87746 meteorite.

Acknowledgments: Thanks to NASA for the loan agreement with the Department of Earth and Environmental Sciences of Bari.

References: [1] Schwartz, C. (1989) – EET 87746. Meteoritical Bulletin, n. 71, The Meteoritical Society. [2] Manzari, P., Mele, D., Tempesta, G. & Agrosì, G. (2023) – New insights on the porosity and grain features of Al Haggounia 001, an impact-melt meteorite, 1-10. [3] Agrosì, G., Manzari, P., Mele, D., Tempesta, G., Rizzo, F., Catelani, T., Cheng, G., Yao, N., Villenueve, J. & Bindi, L. (2025) – Unique (Al, Cu)-alloys discovered in a micrometeorite from Southern Italy. Communications earth & environment, 1-10. [4] Mason, B. (1989) – EET 87746. Meteoritical Bulletin, n. 71, The Meteoritical Society.

THE METEORITES AND IMPACTITES COLLECTIONS AT THE DEPARTMENT OF PHYSICS AND GEOLOGY OF PERUGIA UNIVERSITY (ITALY).

P. Comodi[1], A. Zucchini[1], C. Pauselli[1], M. Morelli [2], D. Faggi [2], F. Frondini[1], L. Ricci[1], M. Fastelli[1] and A. Baldanza[1].
[1]Dipartimento di Fisica e Geologia, Università degli Studi di Perugia, Italy
[2] Museo Italiano di Scienze Planetarie, Fondazione Parsec, Prato, Italy

Introducton:

Celestial objects that fall to Earth have fascinated humans for thousands of years. Meteorites are scientifically invaluable as, alongside samples returned from missions, they are the only physical materials on Earth that reveal how the Solar System formed and evolved, e.g. [1], also carrying significant social and cultural meaning, e.g. [2]. Today, meteorites are preserved in both private collections and museums. Museums, however, play an especially important role as they make these rare objects accessible to the public, promote intellectual and cultural enrichment and provide researchers with valuable material for scientific study, thereby advancing our understanding of the Solar System. According to the Meteoritical Bulletin Database, 42 meteorites have been recovered in Italy. Many studies describe their preservation in Italian geomineralogical museum collections, even if most of these catalogues are not accessible online or through local or national repositories, leaving many specimens effectively hidden from view. Cataloguing is a key step in museum research, as proper documentation allows specimens to be used effectively for scholarly purposes. Making catalogues available online further ensures that these specimens become accessible to anyone wishing to study them.

The goals of this contribution are: (1) to introduce the Meteorite, Tectite and Impactite collection of the University of Perugia to the international community of planetary scientists and astronomers; (2) to show the collection and its potential use for historical research, public education and outreach; (3) to create new networks to deep on the scientific knowledge of some of the hosted samples

Collection history and description:

The Italian Center for Meteoritic Studies (CISM) was officially established in 1969 at the Institute of Mineralogy within the Faculty of Mathematical, Physical, and Natural Sciences at the University of Perugia. The aim of CISM was to enhance research on Italian meteorites and promote the dissemination of scientific knowledge in this field.

As early as 1964, Professor Bartolomeo Baldanza, assisted by his colleague Professor Giovanni Cocco, had begun collecting information on meteorite falls in Italy and had examined many specimens belonging to national and international museum collections. Five meteorite specimens (Siena, Messina, Canyon Diablo, Hembury, and Otasawian) laid the foundation of the collection in 1964, to which another 23 specimens were subsequently added, both as deposits and through exchanges with Italian and foreign scientific institutions, providing valuable support for the establishment of CISM.

A fundamental milestone in the research on meteorites that have fallen on national soil is certainly marked by the publication of "Italian Meteorites" in 1965 [3].

Starting in 1970, the collection of meteorite fragments on a global scale began through extensive postal correspondence (at that time, the Internet or Amazon did not exist) with the American Meteorite Laboratory (AML), the main supplier of meteorites, tektites, impactites, spherules, and shatter cones. There are also traces of correspondence with the National Aeronautics and Space Administration (NASA). Each request to the supplier (primarily AML) was recorded by adding the order date, the price, and the weight of the meteorite fragment, and finally, the arrival date.

The original catalog [4] was not revised until 2014, when the Department of Physics and Geology at the University of Perugia (Italy) initiated an update.

At present, the collection comprises 49 meteorite specimens well classified in [5]: 29 chondrites, 11 achondrites, 6 primitive achondrites, and 3 iron meteorites that cannot be assigned to a specific classification due to limited available information.

Among the 29 chondrites, 26 are ordinary belonging 11 samples of the H type, 13 to the L-type chondrites, and the rest are LL and L/LL types. The 3 chondrites out of the 29 samples are world-famous carbonaceous chondrites: two samples of Allende and one of Vigarano [6,7].

After starting to revisit the collection catalog in 2014, we realized that there was a very rare piece of pallasite, the Mineo pallasite, which was a matter of research during the last years [5,8,9]. The Mineo pallasite was acquired by the Department of Earth Sciences of the University of Perugia (Italy) in 1965 and it was firstly described by Baldanza (1965) [3] and Nagata (1979) [10]. Nowadays, the sample hosted by the University of Perugia (Italy) is the only known sample available in public collections [8].

Furthermore, the collection includes numerous tektites, impactites, and metallic spherules, as well as shatter-cone fragments. The tektites belong to four main varieties: moldavites (2 pcs), australites (11 pcs), fillipinites (2 pcs) and indochinites (18 pcs); and comprise portions representing different parts of

individual fragments and a range of morphologies (e.g., eroded cores, flanged buttons). In addition, several samples in the collection remain unclassified. The collection presents 2 shatter cones samples from the La Malbaie crater in Quebec (Canada), and metallic spherules sorted into four different sizes caming from Berringer crater in Arizona (USA). Although these materials have already been partially classified, they have never been the subject of detailed or modern analyses. The investigation of impact products through petrographic, mineralogical, elemental/chemical and texture composition might be a matter of future studies, to infer valuable information on the possible impact site, the possible target rocks involved in the impact event, and the broader dynamics of impact-related phenomena.

Discussions and future perspective:

The meteorite and impactite collection was among the first of its kind in Italy and reflects the original ideas and approaches of the period in which it was created. Today, it has an old-fashioned appearance, yet this style remains important to preserve as a testament to the significant classification work carried out at the time. In this framework, the colletion could be described through its historical contextualization and through the description of each sample according to the terminology and nomenclature currently used and all samples could be catalogued in the Catalogo Generale dei Beni Culturali of the ICCD (Istituto Centrale per la Catalogazione e la Documentazione). The present project aims to introduce an improvement initiative focused on exhibition innovation, new thematic installations, and a modernised visual design. The project also seeks to enhance digitalization and accessibility through the development of an open-access digital catalogue, the integration of augmented reality (AR), and bilingual (IT/EN) digital fact sheets accessible via QR codes, thereby valorising the existing heritage and making it more readily available to external research institutions and scholars.

We believe that this collection deserves a thorough re-evaluation, which could lead to the rediscovery of lesser-known specimens, such as the Mineo pallasite. A reorganisation that preserves the historical traces of the specimens, while providing a more modern framework and interpretative approach, could significantly increase their scientific value.

The purpose of this contribution is to raise awareness among the expert community of the existence and importance of the collection, promoting opportunities for collaboration in support of future work on the collection, both in terms of scientific research and public dissemination.

References:

[1] Russell S. S et al. (Eds. 2018) *Cambridge University Press.* 467. [2] Hamacher D. W. and Goldsmith J.(2013) *JAHH* 16:295–311. [3] Baldanza B. (1965) *Mineral. Mag.* 35, 214–232.
[4] Baldanza B. et al. (1969) Tipografia Porziuncola: Santa Maria degli Angeli, Italy. [5] Ricci L. et al. (2022) *Universe*, *8*(3), 156. [6] Grossman L. (1980) *Ann. Rev. Earth Planet. Sci.*, 8, pp. 559–608. [7] Trevisani E. (2011) *Rendiconti Lincei*. 2011, 22, 315–326. [8] Zucchini A. et al. (2018) *MAPS*, 53(2), 268-283. [9] Mugnaioli E. et al. (2022) *Mineral Mag. 86*(2), 272-281. [10] Nagata N. (1979) *Phys. Earth Planet. Inter.* 20, 324–341.

INTERPRETING IO'S THERMAL EMISSION: CONSTRAINTS FROM JUNO/JIRAM M-BAND OBSERVATIONS. F. Tosi[1] , A. Mura[1] and F. Zambon[1], [1]Istituto Nazionale di Astrofisica – Istituto di Astrofisica e Planetologia Spaziali (INAF-IAPS), Roma, Italy, federico.tosi@inaf.it.

Introduction: Characterizing Io's energy budget is essential for discriminating among tidal heating models and assessing whether volcanic output is consistent with shallow asthenospheric dissipation, deep-mantle heating, or more complex scenarios such as partial or global magma oceans [1,2]. The recent availability of near-infrared radiance maps from the Jovian Infrared Auroral Mapper (JIRAM) aboard NASA's Juno spacecraft [3] has motivated renewed analysis of Io's latitude-dependent volcanic thermal emission. Nevertheless, interpreting M-band (4.8 μm) radiance as a direct proxy for total thermal power requires a careful understanding of instrumental limitations and thermal degeneracies. Here we summarize recent results [4] critically re-evaluating JIRAM M-band imagery, highlighting key limitations that affect radiance retrieval and interpretations of Io's volcanic distribution.

Detector saturation and radiance underestimation: JIRAM's M-band imager exhibits nonlinear detector response above ~12,000 DN, with saturation occurring near 16,000 DN [5]. Many of Io's brightest volcanic hot spots routinely exceed these thresholds, leading to systematic underestimation of radiance in regions that dominate the global heat budget. Cross-comparison with co-located JIRAM spectrometer observations—whose responsivity remains linear across a broader dynamic range—demonstrates a clear departure from linearity for high-intensity detections [4] (**Fig. 1**). Because saturation preferentially affects the most powerful hot spots, any dataset excluding these pixels or lacking explicit correction procedures will underestimate total radiance and introduce biases into spatial analyses. Previous JIRAM-based studies [e.g., 6] acknowledged saturation challenges but applied different filtering thresholds and exclusion criteria, complicating direct cross-study comparison.

Limitations of M-band radiance as a proxy for total thermal emission: Relying solely on M-band radiance to estimate total volcanic thermal power introduces a strong temperature-dependent degeneracy. The ratio between bolometric radiance and 4.8-μm spectral radiance varies by more than an order of magnitude across plausible surface temperatures (200–1600 K), especially towards the low-temperatures cut-on. Without independent temperature constraints, narrow-band radiance cannot be reliably converted into total power output. This limitation becomes critical when analyzing features with substantial low-temperature components—patera crusts, lava lakes, and partially resolved thermal fields.

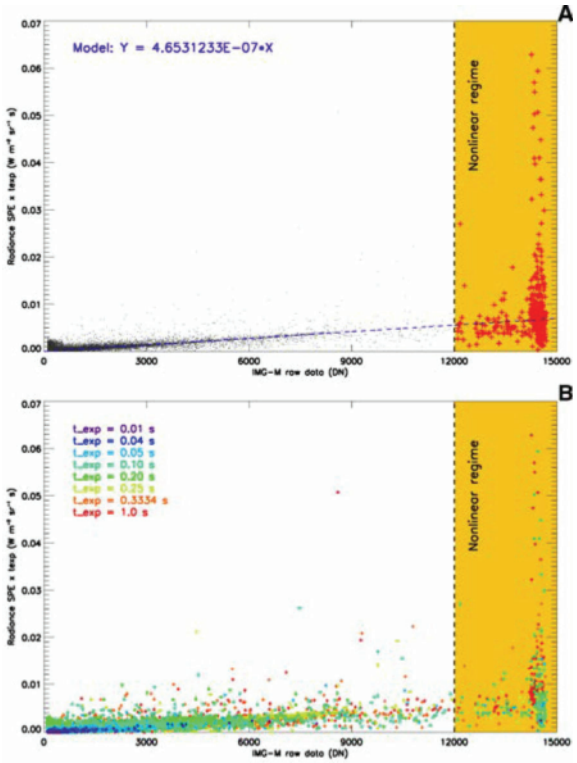


Figure 1: (A) Scatter plot of JIRAM M-band radiance vs. imager DN values from Juno orbits 5–43. The dashed blue line is the expected linear fit. Low-DN points (≤100, potential background noise) are excluded; high-DN points (>12,000) are highlighted in red. (B) Same data colored by exposure time.

New high-resolution JIRAM observations from the extended Juno mission reveal that many paterae host ring-like lava lakes with hot rims and cooler, spatially extensive interior crusts [7, 8]. Because the cooler crust emits little radiance in the M-band, this systematically underestimates total thermal output by factors as large as several hundred. Case studies (e.g., Chors Patera, Catha Patera, Pfu1063, **Fig. 2**) demonstrate scaling factors between M-band radiance and bolometric emission ranging from ~400 to ~800 (**Fig. 3**), vastly exceeding the empirically derived factors (~15–20) previously used in regional or global heat-flow estimates.

Temporal variability further complicates the interpretation. Observations document episodic transitions between ring-dominated and crust-dominated configurations, confirming that these systems are not in thermal equilibrium. Therefore, single-epoch observations cannot reliably represent long-term volcanic energy release or interior heating rates.

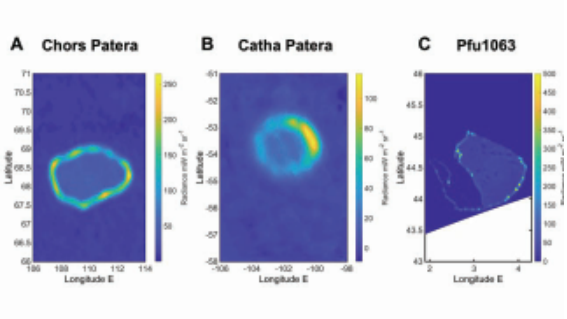


Figure 2: Thermal emission in the M-band (4.8 µm) and analysis of three lava lakes on Io: (A) Chors Patera, (B) Catha Patera, and (C) Pfu1063. For each lake, the vast majority of the total thermal emission originates from the low-temperature crust, which is severely underestimated by standard M-band measurements.

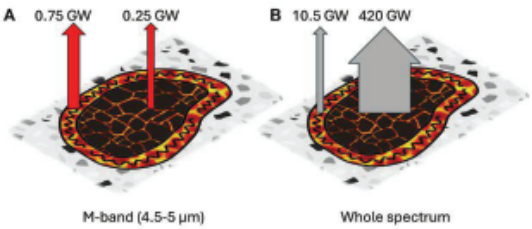


Figure 3: Power output from both the crust and the ring of Chors patera. The (A) panel shows contributions within the M-band, while the (B) panel shows the total power across all wavelengths.

Reassessing the statistical basis for latitudinal trends: Recent work report enhanced 4.8 µm radiance at low latitudes and an asymmetry between Io's northern and southern polar regions [6]. These conclusions depend heavily on the use of a 60° latitude threshold, a choice partly motivated by theoretical tidal-heating predictions. However, when treated purely as an empirical mapping parameter, this threshold produces results that lack statistical robustness.

A systematic re-analysis of binned and unbinned radiance densities reveals no significant correlation between absolute latitude and spectral radiance density across a wide range of bin widths (1°–30°). More than 50% of the observed radiance originates from only ~6% of volcanic sources, meaning that global patterns are dominated by a handful of extremely bright hot spots. When the latitude boundary is shifted to 50° or 40°, previously claimed north–south asymmetries reverse or diminish. This demonstrates that latitudinal trends are highly sensitive to threshold selection and are not supported by the dataset alone. Consequently, M-band imaging cannot be used to discriminate among asthenospheric, deep-mantle, or magma-ocean heating models without independent temperature constraints and broader spectral coverage.

Implications for Io's interior structure and future missions: Independent geophysical constraints from gravity, librations, and astrometry, including recent analyses of Juno data, argue against a deep global magma ocean inside Io, as such a layer would produce signatures incompatible with the observed rotational parameters, gravity field, moment of inertia, and expected geophysical response [9]. These findings further emphasize the risk of interpreting narrow-band infrared observations without incorporating multi-instrument and multi-wavelength datasets.

A robust characterization of Io's heat flow requires simultaneous use of:

1. full spectral radiance from 2–5 µm,
2. long-wavelength (>5 µm) thermal observations,
3. gravity, astrometry, and topography.

Future Io-dedicated missions should include instruments capable of flexible exposure control, broad wavelength coverage, and dynamic range suitable for resolving both high-temperature vents and low-temperature crusts. Combined with spatially continuous methods (kernel density estimation, geostatistical interpolation), such measurements will enable physically self-consistent reconstructions of Io's volcanic energy distribution.

Conclusion: Our reassessment shows that Juno/JIRAM M-band data, although highly valuable for mapping Io's volcanic activity, suffer from detector saturation, radiometric degeneracies, and statistical instability that limit their use as a standalone proxy for total heat flow. Temperature retrieval from full spectral datasets, transparent saturation treatment, and multi-wavelength approaches are essential to produce physically meaningful power estimates. Future missions to Io should prioritize extended spectral coverage beyond 5 µm, high dynamic range detectors, and coordinated gravity and imaging measurements to enable fully consistent modeling of Io's volcanic and interior processes.

Funding: This work is funded by the Italian Space Agency (ASI), ASI–INAF Addendum no. 2016-23-H.3-2023 to grant 2016-23-H.0.

References:

[1] Segatz M. et al. (1988) *Icarus, 75*, 187–206. [2] Tyler G. et al. (2015) *Astrophys. J., 810*, 17. [3] Adriani A. et al. (2017) *Space Sci. Rev., 213*, 393–446. [4] Tosi F. et al. (2025) *Front. Astron. Space Sci. 12*, 1668185. [5] Mura A. et al. (2020) *Icarus, 350*, 113898. [6] Davies A. G. et al. (2024) *Nat. Astron., 8*, 94–100. [7] Mura A. et al. (2024) *Commun. Earth & Environ., 5*(1), 340. [8] Mura A. et al. (2025) *J. Geophys. Res. Planets, 130*(2), 2024JE008723. [9] Park R. et al. (2025) *Nature, 638*(8049), 69–73.

ANALYSIS OF IO'S TIDAL RESPONSE AS A FUNCTION OF THE PROPERTIES OF THE PARTIALLY MOLTEN LAYER

M. Paris[1,2], A. Mura[1], F. Zambon[1], A. Genova[3], F. Tosi[1], G. Piccioni[1], A. Consorzi[4], G. Mitri[4], R. Sordini[1], R. Noschese[1], A. Cicchetti[1], S. Bolton[5], G. Sindoni[6], C. Plainaki[6] and the JIRAM team
[1]INAF, IAPS, Roma, Italy (matteo.paris@inaf.it), [2]Dipartimento di Fisica, Sapienza Università di Roma, Roma, Italy (matteo.paris@uniroma1.it), [3]Dipartimento di Meccanica e Ingegneria Aerospaziale, Sapienza Università di Roma, Roma, Italy, [4]Dipartimento di Ingegneria e Geologia, Università d'Annunzio, Pescara, Italy, [5]Southwest Research Institute, San Antonio, TX, USA, [6]Agenzia Spaziale Italiana, Roma , Italy.

Introduction: Jupiter's moon Io, the most volcanically active body in the Solar System [1, 2], exhibits intense internal heating believed to be driven by tidal friction. While tidal dissipation is widely accepted as the primary mechanism powering this volcanic activity, the spatial distribution and depth of heating generation remain unresolved [3]. The tidal response of Io is described by the Love number k_2 [4], whose real part quantifies the in-phase deformation induced by Jupiter's gravitational potential, while the imaginary part represents the out-of-phase anelastic response associated with internal energy dissipation [5].

Methods: Io's tidal response is analyzed by computing the degree-2 Love number k_2 as a function of the radial position at which mantle melting begins ($R_{\phi o}$) and the latent heat of fusion (L) of the constituent materials. The Love number is derived by solving the spheroidal oscillation equations for an initial three-layer structure (fluid core, viscoelastic mantle, and viscoelastic crust), using an adapted version of the California Planetary Geophysics Code (*CPGC*) [6] to iteratively link tidal dissipation to the mantle rheology.
Tidal dissipation is computed from radial and tangential displacement and stress fields [7], and the corresponding melt fraction is obtained following the approach of Bierson & Nimmo [8]. The viscosity, shear modulus, and Andrade rheology parameter β are iteratively updated based on the local melt fraction $\phi(r)$. The mantle is discretized into 67 layers, and the computation is iterated until k_2 converges, exploring a range of $R_{\phi o}$ and L values.
The fluid core is modeled with a density of $5150\ kg/m^3$ and a radius of $950\ km$. The mantle, $820\ km$ thick with a density of $\sim 3250\ kg/m^3$, consistent with plausible composition, follows Andrade rheology ($\alpha = 0.3$, initial β_0 between $10^{-13}\ Pa^{-1}s^{-0.3}$ and $10^{-12}\ Pa^{-1}s^{-0.3}$). The overlying $50\ km$-thick crust, sharing the mantle's density, is modeled with Maxwell rheology. Initial viscosities and shear moduli are set to $10^{21}\ Pa \cdot s$ and $40\ GPa$ for the mantle, and $10^{25}\ Pa \cdot s$ and $40\ GPa$ for the crust. The rheological parameters are selected in agreement with Park et al. [5], while the initial values of β_0 are chosen to remain consistent with the literature [5, 8].
In this work, two scenarios are considered: one with constant β, representing tidal heating concentrated in the deep mantle, and another with depth-dependent β, allowing dissipation to localize in the upper mantle. The resulting k_2 are compared with the observed estimates [5] and independently verified using the *ALMA3* code [9] to ensure consistency with the result obtained from *CPG*C.

Results: The results are presented in Figures 1-2-3. Figure 1 shows the behavior of k_2 as a function of the melting radius ($R_{\phi o}$) and latent heat of fusion (L), assuming a constant β ($\beta_0 = 10^{-12}\ Pa^{-1}s^{-0.3}$) throughout the mantle. Several combinations reproduce the real part of k_2 ($\Re(k_2) = 0.125 \pm 0.047$, [5]), while the modulus of the imaginary part slightly exceeds the estimated value ($|\Im(k_2)| = 0.0109 \pm 0.0054$) but remains within one standard deviation. Figure 2 illustrates the results for a depth-dependent β. The real part of k_2 remains consistent with observation over a broad range of $R_{\phi o}$ and L, whereas the modulus of the imaginary part lies marginally outside the $1-\sigma$ confidence interval but within $2-\sigma$. Figure 3 compares the variation of $\Re(k_2)$ and $|\Im(k_2)|$ with L (color-coded) and with the initial value of β_0 (grouped), for two representative melting radii: $R_{\phi o} = 1604\ km$ for the depth-dependent case and, $R_{\phi o} = 1340\ km$ for the constant case, for which reproduces the observed real component when $\beta_0 = 10^{-12}\ Pa^{-1}s^{-0.3}$.

Summary: The proposed methodology enables a detailed investigation of the possible configuration of Io's mantle by evaluating the influence of shear modulus, viscosity, volumetric tidal heating rate, and melt fraction $\phi(r)$ on the Love number k_2 and its phase lag. Several internal models featuring a partially molten mantle with $\phi(r)$ below the rheologically critical melt fraction [10, 11] yield to $\Re(k_2)$ values consistent with estimates from NASA's Juno mission. The inferred melt fraction remains below the threshold identified by Miyazaki & Stevenson [11], above which the partially molten layer would transition to a fully molten magma layer. Assuming an initial β_0 of the $10^{-12}\ Pa^{-1}s^{-0.3}$, the corresponding $|\Im(k_2)|$ fall within the $2-\sigma$ uncertainty of observational constraints. These results highlight the importance of performing sensitivity analyses of k_2 with respect to the initial parameter β_0 to refine constraints on Io's interior using Juno data [5], as illustrated in Figure 3.

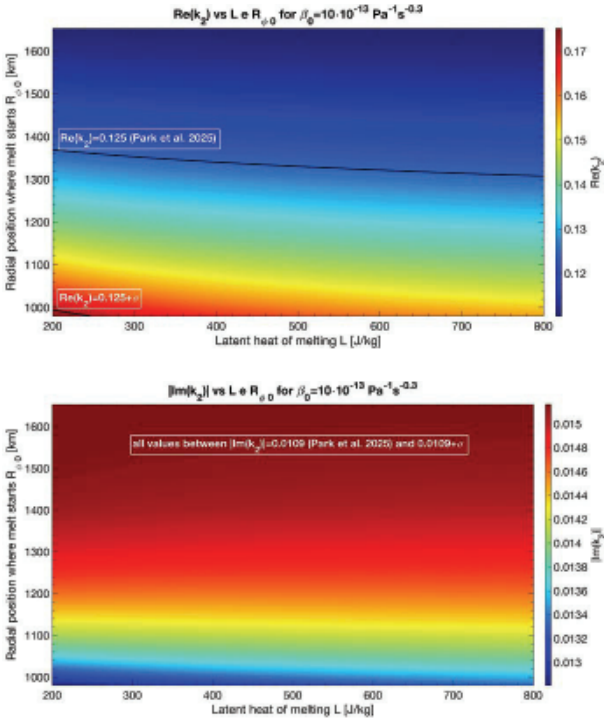


Figure 1: Love number k_2 as a function of the melting radius ($R_{\phi o}$) and the latent heat of fusion (L), assuming constant β. In the first panel, the estimated value of $\Re(k_2)$ from [5] (0.125 ± 0.047) is shown as a reference curve. The second panel omits the reference for $|\Im(k_2)|$, as all computed values exceed 0.0109 but remain within 1σ, i.e. below 0.0163.

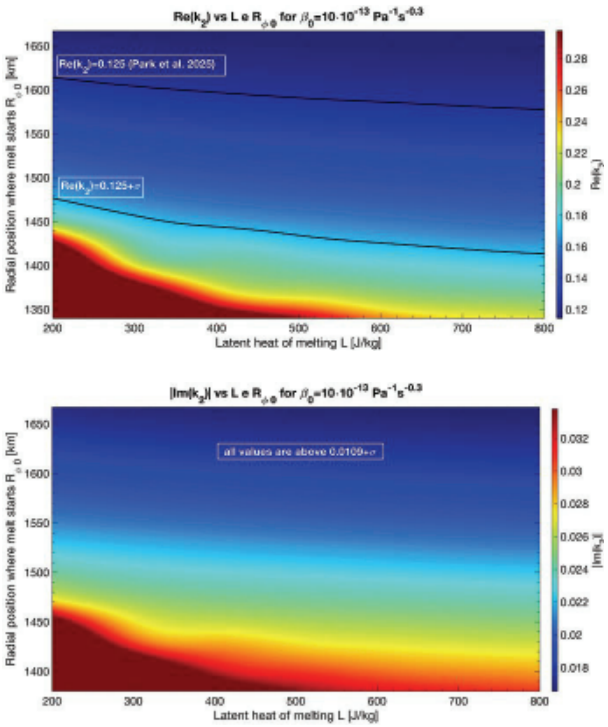


Figure 2: Same as Figure 1 but assuming a variable β. In the first panel, the estimated value of $\Re(k_2)$ from [5] (0.125 ± 0.047) is shown as a reference. In the second panel, no reference is shown for $|\Im(k_2)|$, as all values exceed 1σ, i.e. 0.0163.

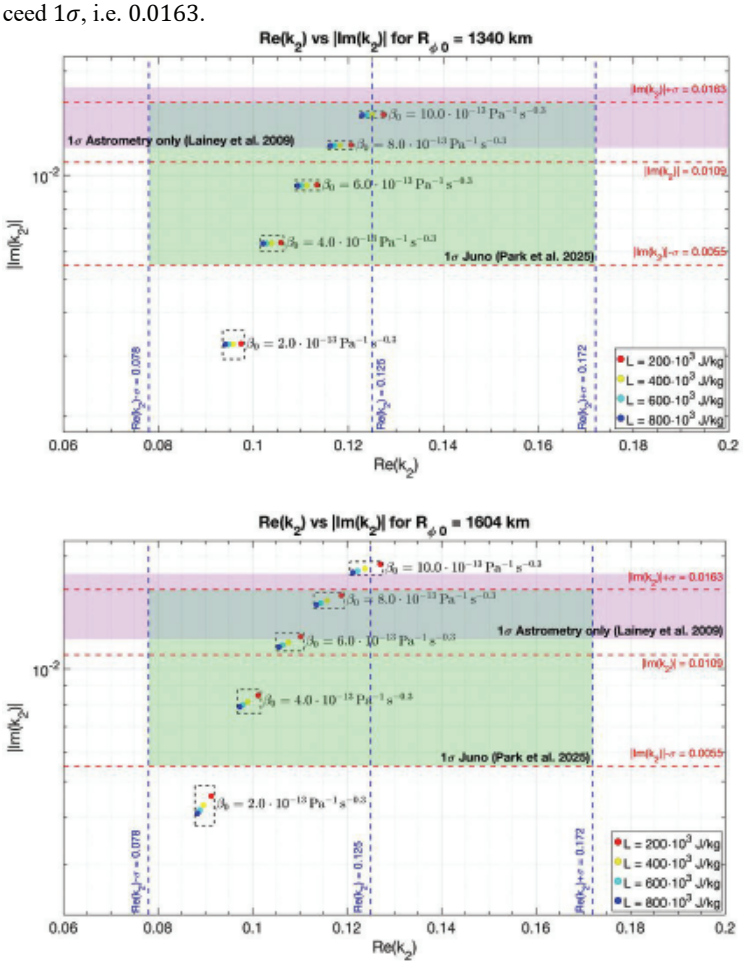


Figure 3: Variation of $\Re(k_2)$ and $|\Im(k_2)|$ as a function of L (colors) and initial β_0 (groupings), for two $R_{\phi o}$ values ($1604\ km$ for the depth-dependent case and $1340\ km$ for the constant case) for which agreement with the real part is achieved when initial $\beta_0 = 10^{-12}\ Pa^{-1}s^{-0.3}$.

Acknowledgements: We thank Agenzia Spaziale Italiana (ASI) for the support of the JIRAM contribution to the Juno mission; this work is supported by the ASI–INAF Addendum n. 2016-23-H.3-2023 to grant 2016-23 H.0.

References: **[1]** Lopes, R. M. C., and Spencer, J. R. (2007), *Springer*. **[2]** Lopes, R. M. C., De Kleer, K., and Keane, J. T. (2023), Springer International Publishing. **[3]** Keane, J., et al. (2021) Bull. Am. Astron. Soc., 53:178. **[4]** Efroimsky, M., and Lainey, V. (2007) JGR: Planets, 112(E12). **[5]** Park, R. S., et al. (2025) Nature, 638(8049):69–73. **[6]** Ermakov, A., and Akiba, R. (2024) California Planetary Geophysics Code, GitHub repository. **[7]** Beuthe, M. (2013) Icarus, 223(1):308–329. **[8]** Bierson, C. J., and Nimmo, F. (2016) JGR: Planets, 121(11):2211–2224. **[9]** Melini, D., Saliby, C., and Spada, G. (2022) Geophys. J. Int., 231(3):1502–1517. **[10]** Breuer, D., Hamilton, C. W., and Khurana, K. (2022) Elements, 18(6):385–390, **[11]** Y. Miyazaki and David J. Stevenson 2022 *Planet. Sci. J.* 3 256.

CASSINI STATES AND LIBRATIONS OF THE GALILEAN SATELLITES: A NUMERICAL APPROACH IN EULER ANGLES

G. Macrì[1] and S. Casotto[1], [1]Università di Padova (giulio.macri@phd.unipd.it).

Introduction: The problem of determining the correct initial conditions for the numerical integration of the rotational motion of a celestial body is a fundamental one. Indeed, even a slightly off initial guess can excite free rotational modes (i.e., free precession and free libration) with amplitudes much larger than the forced amplitudes. Tidal dissipation effects over long timescale have most likely damped all free modes, although small amplitudes at the free frequencies are still possible due to recent excitation mechanisms. Often, in the literature the problem of the initial conditions for the librations is avoided entirely by using linearized models, which allow to separate the solution to the differential equations as the superposition of a free libration term, that depend on the initial conditions, and a forced libration term that is independent of the initial conditions, allowing to determine an approximate solution in closed form. A similar linearized approach can be used to model obliquity. We employ the full triaxial rotational equations for the Euler angles that define the orientation of the Galilean satellites' principal axes in an inertial frame. To solve the problem of the initial conditions we propose an approach that makes use of the differential state transition matrix to determine initial conditions that lead to zero amplitudes of the free modes. We determine a set of three libration parameters for each of the four Galilean satellites assuming a rigid body model. These results are useful as an accurate reference rotation model for a solid satellite, and can serve as a basis for comparison with the libration and obliquity estimates that will be obtained from the Juice and Europa Clipper data in the 2030s, which will study in detail Ganymede and Europa, respectively.

Cassini states: The empirical laws that elegantly describe the Moon's rotation, commonly known as Cassini's laws, first appeared in a treatise by Giovanni Domenico Cassini in 1693 [1]. They can be summarized as follows [1–3]: 1. The period of the Moon's rotation about its polar axis equals its mean sidereal orbital period around Earth. 2. The descending node of the lunar equator on the ecliptic precesses at the same rate as the ascending node of the lunar orbit on the ecliptic. 3. The inclination of the lunar equator with respect to the ecliptic remains constant.

As shown in Fig. 2, Cassini states I and II differ based on whether ω and n are on the same side of p, or on opposite sides, respectively (see e.g., [4, 5]). All the Galilean satellites, contrary to Earth's Moon are expected to occupy a Cassini state I.

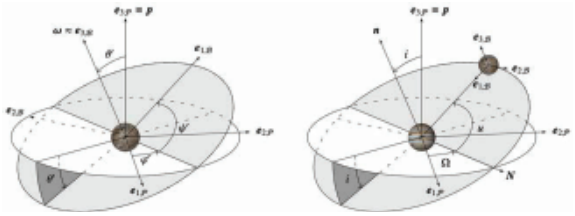
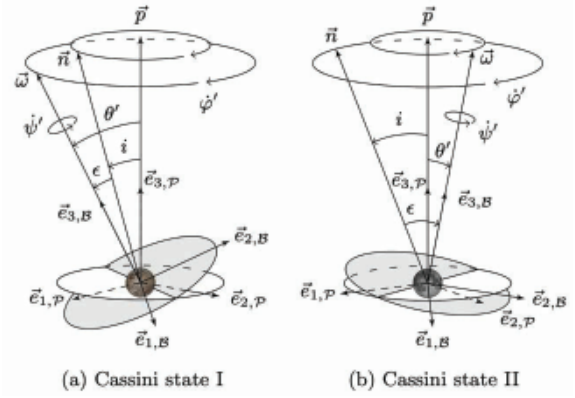


Fig. 1: Schematic representation of the relations between the Euler angles, Laplace frame P, principal axis frame B (left). Representation of the relationship between the orbit, and the orientation of these reference frames (right).

We define the perturbations to the Euler angles relative to the exact Cassini laws as three parameters τ, σ and ρ, such that (see, e.g., [6-7])

$$\theta' = \iota + \rho,\ \varphi' = \bar{\Omega} + \sigma,\ \psi' = \bar{u} + \pi - \sigma + \tau, \qquad (1)$$

where, ι is the mean inclination of the satellite's equator with respect to the Laplace plane normal (p). Then, the corresponding librational parameter (ρ) is the departure of θ′ from ι. We denoted by $\bar{u}$ the mean argument of latitude of the satellite u. We denoted by $\bar{\Omega}$ the mean longitude of the ascending node of the satellite's orbit.



(a) Cassini state I (b) Cassini state II

Fig.1: Schematic representation of the relative configuration of the Laplace plane normal $\vec{p}$, orbit normal $\vec{n}$, and spin axis $\vec{\omega}$ in Cassini states I and II. The obliquity ϵ is the angle between $\vec{n}$and $\vec{\omega}$. The circles represent the precession paths. The inclination i is the angle between $\vec{n}$ and $\vec{p}$. The angles are exaggerated for visualization purposes.

Free modes: Even without Jupiter exerting a time-variable torque, the satellites would oscillate regardless at discrete frequencies with amplitudes dependent on the initial conditions [6]. There are three free modes which correspond to the eigenfrequencies of the linearized equation [7]. These are a free longitudinal libration mode, a free wobble, and a free precession (e.g., [8]). The amplitudes of the

three modes depend on the initial conditions and are expected to be small due to dissipative effects, although they may have been excited in the recent past due to impacts, or other effects not modelled here. We aim to determine the initial conditions corresponding to the forced equilibrium, that is, the state in which the amplitudes of the free modes are minimized. Indeed, unless a recent excitation mechanism is present, it is reasonable to assume that these free modes have been damped by dissipative effects acting over long timescales. In order to determine the initial conditions that result in no free librations and precession we employ a differential correction technique based on the dynamical state transition matrix [9]. To this aim, the free frequencies components need to be identified. First an initial guess for the amplitudes and frequencies is obtained by performing a fast Fourier transform (FFT), to identify the peaks in the frequency spectrum corresponding to the free modes of the linearized equations. Then these frequencies and the corresponding amplitudes are used as an initial guess for a nonlinear least-squares fitting [10, 11]. Then the residuals are computed, and the same method is applied to the residuals. Lastly the frequencies are joined together.

Results and conclusions: We determined the initial conditions needed to numerically integrate the triaxial rotational equations. Three parameters, corresponding to the latitude and longitudinal librations, that is the deviation from the Cassini state I (Fig. 2a), are determined and a frequency analysis (not shown here) is performed. For Ganymede, we find a value of ι of about 0.226°. The obliquity ϵ of Ganymede varies between 0.0005° and 0.06658°, while the orbital inclination i ranges from 0.13053° to 0.24332°. The orbital recession period corresponds to 137.411 years and the rotation period is 7.155 days. The free precession of the spin axis has a period of 19.964 years. The period of free longitudinal libration is 186.508 days. The faster free nutation mode occurs with a period of 3.576 days. Future work should focus on extending the current framework to incorporate different plausible interior structure models to properly evaluate the effects of coupling mechanisms between the solid and liquid layers. Nevertheless, the results presented here provide an accurate rigid-body reference model that can be used to interpret future high-precision measurements from missions like Juice and Europa Clipper.

References: [1] Cassini J.-D. (1693) De l'Origine et du progrès de l'astronomie et de son usage dans la géographie et dans la navigation (Paris). [2] Colombo G. (1966) AJ, 71, 891. [3] Eckhardt D. H. (1981) Moon and Planets, 25, 3. [4] Ward W. R. and Hamilton D. P. (2004) AJ, 128, 2501. [5] Winn J. N. and Holman M. J. (2005) ApJ, 628, L159. [6] Eckhardt D. H. (1965) AJ, 70, 466. [7] Rambaux N. and Williams J. G. (2011) Celest. Mech. Dyn. Astron., 109, 85. [8] Varadi F., Musotto S., Moore W., and Schubert G. (2005) Icarus, 176, 235. [9] Casotto S. (2022) Lecture Notes on Celestial Mechanics, University of Padua. [10] Byrd R. H., Gilbert J. C., and Nocedal J. (2000) Math. Program., 89, 149. [11] Waltz R. A., Morales J. L., Nocedal J., and Orban D. (2006) Math. Program., 107, 391. [12] Bills, B. G. & Scott, B. R. 2022, Planet. Space Sci., 219, 105474

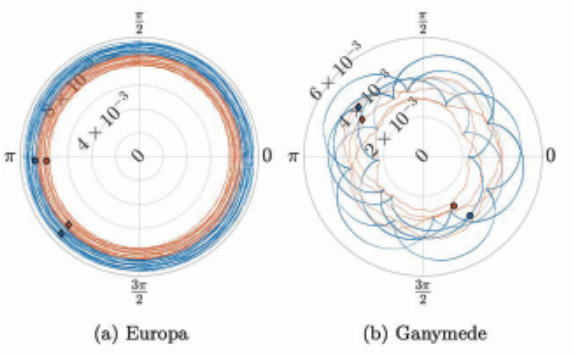


Fig.2: Projection of the spin axis $\vec{\omega}$ (blue) and orbit normal $\vec{n}$ (red) of Europa and Ganymede on their respective Laplace planes defined by $\vec{p}$. Units are in radians. Circle markers indicate the initial time at January10th 1600, while a diamond marker denotes the final time January 9th 2200. The precession is retrograde relative to the orbital revolution and rotation.

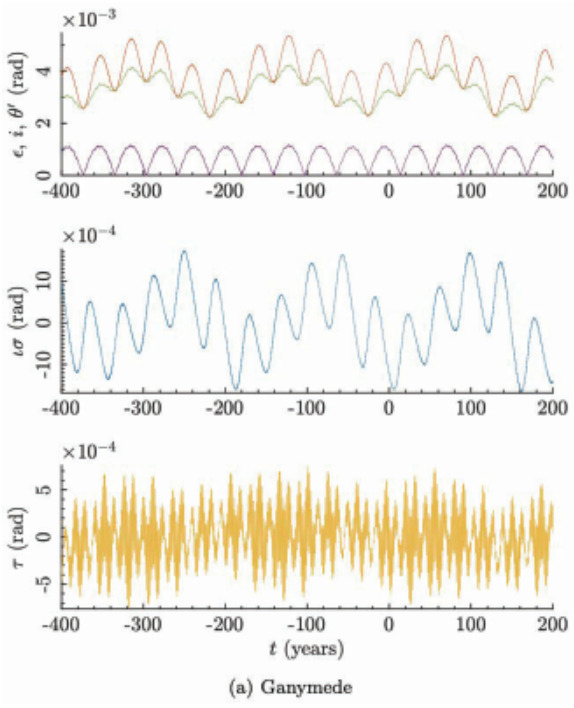


Fig. 3: Evolution of the obliquity (ϵ), orbital inclination (i) relative to the Laplace plane, and libration parameters ισ, τ, and θ′ = ι+ ρ, of Ganymede. Compare with [12].

INVESTIGATING THE COMPOSITION OF JUPITER'S ENERGETIC ION ENVIRONMENT. C. Plainaki[1,2], E. Roussos[1], N. Krupp[1], D. Grassi[3], P. Kollmann[4], A. Mura[3], and C. Grimani[5]. [1]Max Planck Institute for Solar System Research, Goettingen, Germany (plainaki@mps.mpg.de), [2]Agenzia Spaziale Italiana (ASI), Rome, Italy, [3]Institute of Space Astrophysics and Planetology, National Institute of Astrophysics (IAPS-INAF), Rome, Italy, [4]Johns Hopkins University Applied Physics Laboratory, Laurel, MD, USA, [5]Università di Urbino Carlo Bo, Via S. Chiara, 27, 61029 Urbino (PU) Italy.

Introduction and motivation: Jupiter's radiation belts represent one of the most extreme particle environments in the solar system hosting intense fluxes of energetic electrons, protons, and heavy ion populations with energies extending well above 5 MeV/nucleon - a critical energy range, not accessible by NASA Juno or other missions like ESA JUICE. To constrain the sources, acceleration, and loss processes of charged particles across a wide mass and energy range, it is of crucial importance to understand the heavy ion composition. In addition, high-energy heavy ions could also play a role in surface alteration (Hofmann et al. 2025) and exosphere generation processes at Jupiter's icy moons (Plainaki et al. 2015) through implantation (Strazzulla et al. 2003), sputtering and radiolysis (Galli et al. 2018). They also pose risks to spacecraft via single event upsets making their detailed mapping important for mission planning and radiation shielding design (Plainaki et al. 2022).

The first and so far only comprehensive investigation of Jupiter's energetic heavy ion composition above 5 MeV/nucleon was performed by NASA's Galileo mission (1995–2003), using the Heavy Ion Counter (HIC) that consisted of two particle telescopes, LET-B and LET-E, designed to measure ions with $Z \geq 6$ in the ~5–50 MeV/nucleon range. So far, HIC studies primarily focused on the dominant energetic ion species—carbon (C), oxygen (O), and sulfur (S). However, HIC was capable of resolving additional elements (e.g., nitrogen, neon, sodium and magnesium) and trace species at least up to iron (Z=26).

In this work, we analyze the full HIC dataset from the Galileo mission to characterize Jupiter's energetic ion composition, with an extra focus on the lesser-studied species. Our goal is to resolve variations that may reflect different source regions or mechanisms, essentially assessing whether these species are of external or internal origin.

The Heavy Ion Counter (HIC) on board Galileo: HIC consisted of two particle telescopes, LET-B and LET-E (Garrard et al. 1992; see Figure 1). LET-B was designed to measure ions with $Z \geq 6$ in the ~5–25 MeV/nucleon range using a stack of four solid-state detectors within a 25° conical aperture. LET-E had a similar configuration, but with five detectors and a broader angular acceptance (25°–45°), optimized for ions between 15-50 MeV/nucleon. LET-E also included a channel for instrument-penetrating >50 MeV/nucleon ions, with a broader 75° effective aperture.

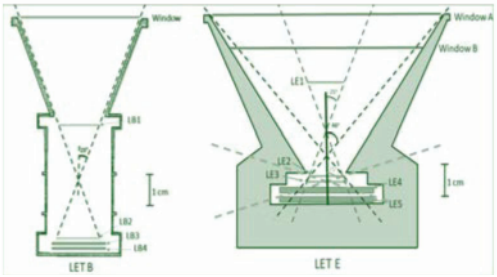


Figure 1: HIC telescopes and channels used in the current analysis. Adapted from Roussos et al. (2022).

HIC was originally added to the Galileo spacecraft to monitor the environment for energetic heavy ions with the potential to cause single event upsets in the spacecraft electronics (planetary space weather).

Data analysis and particle identification tecnhique: Analyzing the registered Pulse Height Analyzed (PHA) events, the relative contributions of the different ion species and energies can be distinguished. In this work, we use the well-established particle-identification dE/dx vs. total energy technique to determine the nuclear charge (Z) of the detected heavy ions (Garrett et al. 2011; Mewaldt et al. 2008).

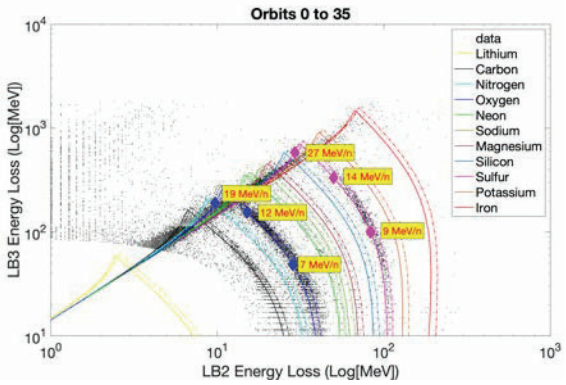


Figure 2: Coincident energy losses on LB2 and LB3 Solid State Detectors (SSDs) of the HIC LET-B telescope and simulated curves.

Preliminary results and discussion: The results of our Z-estimation technique are briefly presented in Figure 3, where they are classified with M-shell.

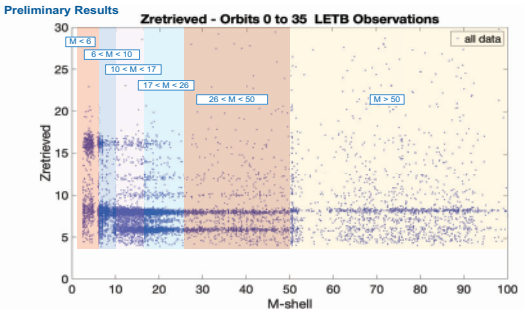


Figure 3: Retrieved atomic number, Z, for the LETB PHA events at different M-shells.

To quantify the abundance of each species we model the retrieved Z values (see Figure 3) considering the sum of a series of Gaussian functions, each one centred at Z=Zc (see Figure 4). For different M-regions: we resolve a non-linear inverse problem of Gaussian function superposition through a Bayesian inversion technique (Plainaki et al. 2025). Our fits confirm the existence of the well-known most abundant species of the Jovian magnetosphere (oxygen, sulfur, carbon), also at the high energy range, and indicate clearly some minor species like N, Ne, Mg, Al, Na. In Figure 4 we present our results for two different regions of the magnetosphere, i.e. inwards Io's orbit (upper panel) and between Europa and Ganymede (lower panel).

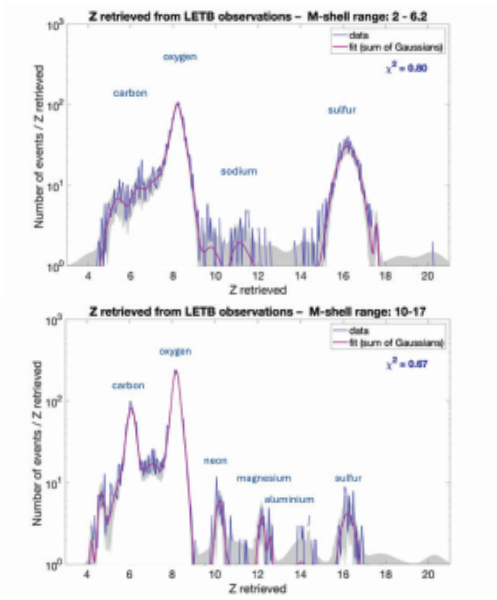


Figure 4: Distribution of PHA events with Z in the region inwards of Io's M-shell (upper panel) and between Europa and Ganymede (lower panel). In addition to the dominant ion populations, some minor species like magnesium, aluminium and neon are clearly distinguished.

Inside Ganymede's orbit, the S/O abundances are much higher than the SEP S/O abundance (~0.03; Reames, 2014). We find that at HIC energies, sulfur is likely not of solar origin and its acceleration is more efficient than oxygen's (see Figure 5). Our results are in general in good agreement with those by previous studies although the latter are often based on more limited datasets (e.g.: Cohen et al. 2001).

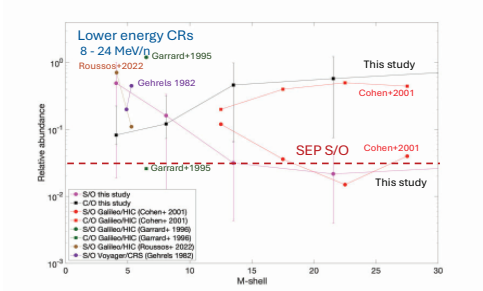


Figure 5: Estimated relative abundances at different M-shells based on the PHA event data in the LETB energy channel.

Concluding remarks: In this work, we identify the major energetic ion species of Jupiter's magnetosphere as well as some minor ones and we studied the variability of their abundances with M-shell, for the first time based on the entire Galileo HIC dataset. In the HIC energy range, oxygen is overall more abundant than sulfur. Inwards the M-shell of Io, S/O~0.5 and ~0.06 in the 8-24 MeV/n and 37-71 MeV/n energy ranges, respectively. These ratios increase at least until Ganymede's M-shell. Our ongoing investigations provide new feedback for modelers working on simulations of mass-dependent processes guiding the Jovian energetic ion distributions. They are particularly complementary for missions to the Jovian system like ESA's JUICE, which lacks an instrument equivalent to HIC. This ongoing study may help refine expectations of the energetic heavy ion environment that drives surface modification processes on Jupiter's Galilean moons.

References:

Cohen, C. M. S. (2001) *JGR 106, 29871–29881*
Galli, A. (2018) *Icarus 312, 1*
Garrard, T. L. (1992) *Space Sci. Rev. 60, 305*
Garrard, T.L. et al. (1996) *Science 274, 393–394*
Garrett, H.B. et al. (2012) *The Jovian Equatorial Heavy Ion Radiation Environment (JPL Publication, 2012)*
Gehrels, N. et al. (1981) *JGR* 86, 8906
Hofmann, F. et al. (2025) *Earth Planets Space 77, 70*
Mewaldt, R.A. et al. (2008) *Space Sci Rev 136, 285–362*
Plainaki et al. (2015) *Icarus, 245, 306-319*
Plainaki et al. (2022) *ApJ 940 186*
Plainaki, C. et al. (2025) *EPSC Abstracts 18, EPSC-DPS2025-1079*
Reames, D.V. (2014) *Solar Phys 289:977–993*
Roussos et al. (2022) *Sci. Adv. 8, eabm4234*
Strazzulla G. (2003) *Icarus 164:163–169*

IMPROVED TREATMENT OF STRAY LIGHT IN THE JIRAM-JUNO SPECTROMETER: APPLICATION TO JUPITER AURORAL OBSERVATIONS D. Grassi[1,2], A. Mura[1], C. Castagnoli[1], F. Biagiotti[1], R. Noschese[1], R. Sordini[1], and C. Plainaki[2,3], [1]IAPS-INAF, Rome, Italy (davide.grassi@inaf.it), [2]MPS, Göttingen, Germany, [3]ASI, Rome, Italy.

Introduction: The occurrence of stray light is a common problem in complex optical systems, such as space-borne spectro-imagers. Despite extensive efforts in the design and manufacturing of instruments, rays following unexpected paths may ultimately reach the detector, introducing systematic signal biases with adverse impacts on scientific analysis. The issue is particularly relevant for atmospheric sciences, where inferences on observed phenomena are usually drawn from *quantitative* results ultimately derived from spectral retrievals.

The serendipitous occurrence of signal biases in the spectral data of the Jovian Infrared Auroral Mapper (JIRAM) onboard the Juno mission orbiting Jupiter was first reported in [1]. The issue was further discussed in [2], where instrumental stray light was more specifically identified as the cause. A first tentative correction of the effect was presented in [3] in their analysis of H_3^+ emissions.

Here we present recent progress in the investigation of this issue, based on the analysis of a large subset of JIRAM data.

JIRAM dataset: JIRAM simultaneously acquires spectra over 256 contiguous square pixels arranged along a line (a "slit"), each pixel having an instantaneous field of view (IFOV) of 240 μrad. The spectra are sampled in the 5010–1990 nm range, with a spectral sampling step of about 9 nm. Characterizing spurious components in the spectra is extremely challenging when using data acquired over actual science targets (e.g., Jupiter or its moons), since the expected values of genuine scientific signals are, in principle, not known a priori. Consequently, in our analysis we focus on spectra acquired over the sky, where a zero signal is expected after the removal of dark calibration frames accounting for thermal contributions from the instrument.

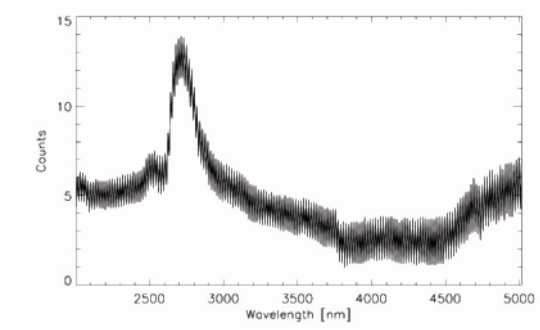


Fig. 1. Average JIRAM spectrum of the deep sky, with Jupiter covering part of the slit.

Data analysis: The average spectrum from pixels covering the sky, in slits that also include Jupiter (though on different pixels), is shown in Fig. 1. Under ideal conditions, only random fluctuations around the zero level should be observed. Two conclusions can be drawn from the signal actually observed: 1. The overall shape of the spectrum closely resembles that of an actual Jupiter spectrum (with a peak at 2370 nm and a signal increase for $\lambda > 4500$ nm), demonstrating that the spurious component includes a spectrally dispersed contribution. 2. The spectrally dispersed component alone cannot account for the spurious signals observed at 2300 nm, where Jupiter's spectra are expected to be very close to zero. This suggests that a non-dispersed component is also present.

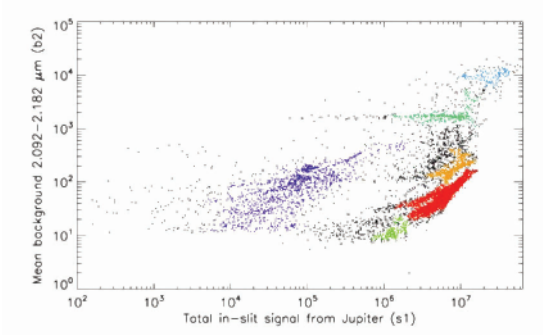


Fig. 2. Spurious signal measured on the sky as a function of the total in-field source signal (counts). Different colors represent distinct populations, as identified by the automatic clustering algorithm HDBSCAN.

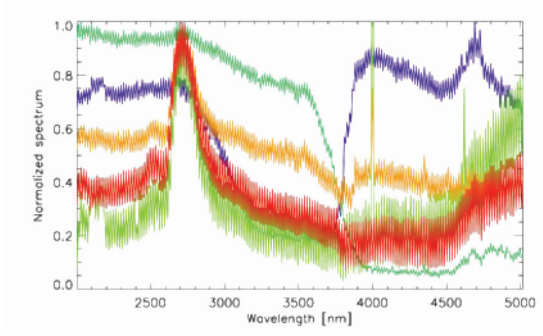


Fig. 3 Average spectra of the different populations shown in Fig. 2, normalized to their respective peak values.

If the stray light were primarily attributable to the presence of a strong source within the field of view (i.e., Jupiter), we would expect a spurious signal level proportional to the total in-field signal. However, an analysis of the entire JIRAM dataset revealed a much more complex picture, with different populations whose characteristics are driven, among other factors, by the source position within the slit. Notably, the purple population arises in cases where Jupiter is located on the left side of the slit rather than on the right. The high-background blue population is instead dominated by the effects of impinging energetic particles rather than by stray light.

The different populations shown in Fig. 2 are also characterized by distinctive spectral shapes (Fig. 3). Although our dataset does not allow us to distinguish between the dispersed and non-dispersed components of the stray light, we can nonetheless observe a combined spurious signal that varies gradually with wavelength for $\lambda < 3700$ nm.

Tentative correction of stray light for H_3^+ analysis: The previous observation prompted us to attempt an empirical removal of stray light from JIRAM spectra covering the Jupiter disk, using a polynomial fit in the spectral region of H_3^+ emissions, where a signal very close to zero is expected

outside the narrow auroral lines. The procedure also includes an iterative removal of outliers to improve robustness. Preliminary results are shown in Fig. 4.

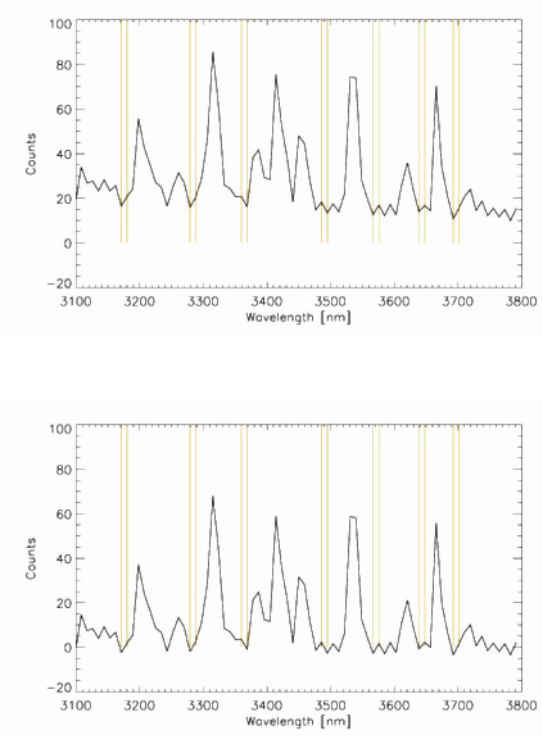


Fig. 4. Average spectrum of Jupiter's north pole, covering the spectral region of H_3^+ emissions.Upper panel: Original data. Lower panel: After correction. Vertical yellow lines indicate the spectral positions used for stray light removal.

Future steps: Average spectra of stray light, shown in Figs. 1 and 3, display a distinct pattern of point-to-point variations, indicating a different behavior of odd and even spectral sampling points. The amplitude of this effect does not show any obvious relation to the amplitude of the spurious component itself, but appears to remain approximately constant with wavelength for a given spectrum. A further correction for this effect can be envisaged based on: 1. Assessment of the effect's amplitude in the 2300 nm region, where the genuine signal is expected to be minimal, and 2. Removal of a pattern of the estimated amplitude in the H_3^+ emissions region.
Once fully implemented, these corrections could improve the reliability of H_3^+ abundances and temperatures inferred from JIRAM data.

References: [1] Grassi, D., et al., *MNRAS*, 503 (2021) [2] Tosi, F. et al. *Nature Astronomy*, 8 (2024) *Meteoritics & Planet. Sci., 32,* A74. [3] Castagnoli, C., et al., *PSJ*, 6 (2025)

Acknowledgments: This work is supported by the Italian Space Agency (ASI) under agreement 2016-23-H.0

MODELING THERMAL CONVECTION WITHIN EUROPA'S ICY LAYER: CONSTRAINTS ON SHELL THICKNESS

M.Formisano[1,*], M. Teodori[1,2], P. Hayne[3,4], M. Ciarniello[1], G. Magni[1]
[1]INAF-IAPS, Via del Fosso del Cavaliere 100, Rome (Italy) [2]Department of Mathematics and Physics, University of Campania "Luigi Vanvitelli", Viale Lincoln 5, Caserta (Italy) [3] Department of Astrophysical and Planetary Sciences, University of Colorado Boulder, Boulder, CO, USA [4]Laboratory for Atmospheric and Space Physics, University of Colorado Boulder, Boulder, CO, USA *(michelangelo.formisano@inaf.it)

Introduction: Jupiter's moon Europa is a critical target for planetary science primarily due to the strong possibility of a subsurface ocean and its implications for habitability. This likely ocean makes Europa a main focus for dedicated missions, including Europa Clipper and JUICE. Europa Clipper, for example, aims to confirm the ocean's existence and fully characterize its properties, such as depth, salinity, and thickness. Europa internal structure is well-constrained by its moment of inertia (MoI) factor, C/MR^2, determined to be 0.346 ± 0.005 [1]. Since this value is significantly less than the 0.4 expected for a uniform sphere, it confirms that Europa is differentiated. The commonly accepted internal structure features an iron-rich core, a silicate mantle, and an outer hydrosphere. Heat within the rocky interior is generated through radiogenic decay and the dissipation of tidal energy (e.g. [2]). The outer hydrosphere consists of a global subsurface ocean covered by a thick icy shell. This shell is widely believed to be composed of two primary layers: an inner, warm, ductile asthenosphere that may be undergoing solid-state convection (e.g.[3]), which is the predicted main heat source for the ice shell [4]; and an outermost cold, brittle, and elastic icy lithosphere. The occurrence of surface geology, such as chaotic terrains, pits, and domes [3], as well as a putative subduction-like convergent boundary [5], has been suggested as possible evidence of internal dynamics driven by solid-state convection within a thick ice shell (15–45 km, e.g.[6]). Conversely, some models propose a relatively thin (3–5 km thick) and conductive ice shell to explain surface features [7].

The precise thickness of Europa's ice shell remains a significant open question, with estimates varying widely based on the methodology used. Theoretical studies support the hypothesis that solid-state convection occurs within Europa's outer ice shell. These models typically incorporate two main physical mechanisms: the inclusion of tidal heating as the primary energy source (e.g.[6,8]) and the visco-elastic-plastic rheology of the ice itself [9]. Recently [11] demonstrate that the ice grain size is not a free parameter, but can be reliably estimated, showing also that the occurrence of solid-state convection within Europa's ice shell is directly linked to the magnitude of the tidal strain experienced by the moon.

The aim of this work is to constrain the onset of thermal convection by considering the ice shell thickness, the temperature gradient across the shell, and tidal heating as free parameters. We also investigate the influence of the adopted geometry (different width-to-length ratios) and boundary conditions (no-slip versus slip at the base). In particular, implementing a slip condition—unlike most previous studies—provides a more realistic representation of the interaction between the convective ice shell and the underlying ocean.

Numerical method: We used a 2-D Finite Element Method (FEM) model [12], implemented in the COMSOL Multiphysics software, to solve the Navier-Stokes equations coupled with the heating equation. The system of governing equations solved is as follows:

$$\rho\left[\frac{\partial \vec{u}}{\partial t} + \vec{u}\cdot\vec{\nabla}u\right] = \vec{\nabla}\cdot\left(-p\vec{I} + \vec{W}\right) + \rho\vec{g} + Q$$

$$\rho\left(\vec{\nabla}\cdot\vec{u}\right) = 0$$

$$\vec{W} = \eta(T)\left[\vec{\nabla}u + \left(\vec{\nabla}u\right)^T\right].$$

Here, t is the time, ρ is the density, $\vec{u}$ the convective velocity, $\eta(T)$ the dynamic viscosity, T the temperature, p the pressure, g the gravity acceleration, Q the tidal heating, and $\vec{W}$ is the stress tensor. The density dependence on temperature is included only in the buoyancy term, utilizing the Boussinesq approximation. These Navier-Stokes equations are solved concurrently with the heating equation:

$$\rho c_p\left[\frac{\partial T}{\partial t} + \vec{u}\cdot\vec{\nabla}T\right] + K\vec{\nabla}\cdot\vec{\nabla}T = 0, \qquad (1)$$

where c_p is the specific heat capacity and K the thermal conductivity.

The viscosity is modeled using a temperature-dependent law, widely adopted in the literature:

$$\eta = \eta_0 \exp\left[A\left(\frac{T_{melt}}{T} - 1\right)\right], \qquad (2)$$

where η_0 represents a reference viscosity at the zero pressure melting point, A is a constant related to the activation energy, and T_{melt} is the melting temperature.

A 2-D rectangular Cartesian geometry (with a width-to-length ratio of 3:1, even though different ratios will be analyzed in the future) is adopted, following the results of [10], who demonstrated that plane-layer numerical models can be scaled to spherical geometry without introducing significant errors. The assumption of a 2-D Cartesian geometry is further justified by the fact that the ice layer thickness is small compared to the body's radius. Simulations are initialized with a temperature profile consisting of a perturbation of the linear profile—ranging from the base of the crust (275 K) to the surface (100 K)—represented as a single Fourier mode.

Preliminary Results and Conclusions In Fig. 1 we present an example of the results obtained with our model. The frames correspond to a standard case, defined by an ice shell thickness of 20 km, a reference ice viscosity of 10^{12} Pa s, a temperature gradient of 175 K across the shell, and no-slip boundary conditions at the bottom. The first 40 Ma of evolution are shown. What is observed is that convection is weak and affects the ice shell over roughly half of its extent, leaving an overlying conductive layer mostly undisturbed.

Our goal is to explore a range of physical scenarios to constrain both the thickness of the convective ice shell and the overlying conductive lid. The model can also be applied to other icy bodies, such as Enceladus, offering insights into their internal structure.

Future investigations using radar-sounder data will enable the characterization of the thermal structure of Europa's ice shell and help verify the possible presence of solid-state convection [11].

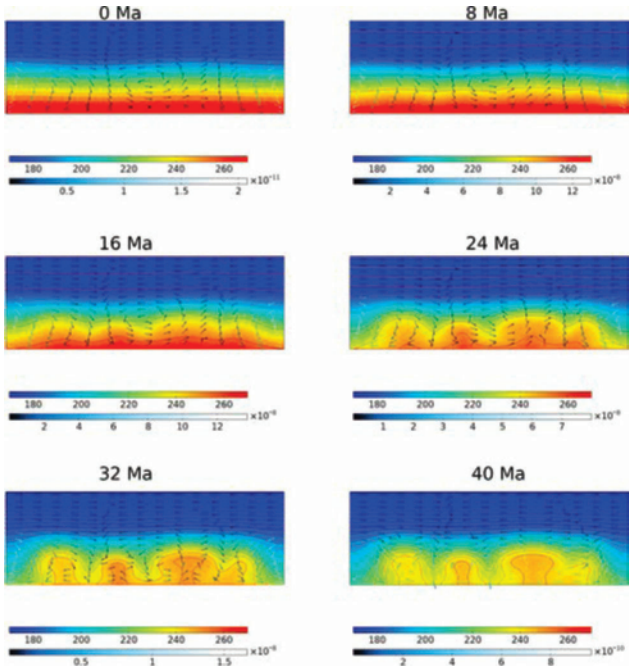


Figure 1: Snapshots of thermal convection for the standard case (reference ice viscosity of 10^{12} Pa s, ice shell size of 20 km, temperature gradient across the shell of 175 K, and no-slip conditions at the bottom). The first 40 Ma are shown. Color scales indicate temperature (in Kelvin) and convective velocity (m/s).

References [1] Andersson et al. 1998, Science 281, 2019-22 [2] Barr & Showman 2009, The University of Arizona space science series ISBN: 9780816528448, p.405 [3] Pappalardo et al. 1998, Nature 391, 365-8 [4] Tobie et al. 2003, JGR Planets 108, E11 [5] Kattenhorn & Prockter 2014, Nature Geoscience 7, 762–767 [6] Sotin et al. 2002, JGR Letters 29, 8 [7] Greenberg & Sack 2014, Earth and Planetary Science Letters 389, 43-51 [8] Mitri & Showman 2005, Icarus 177, 2 [9] Showman & Han 2004, JGR 109, E1 [10] Vangelov & Jarvis 1994, JGR 99, B5 [11] Mitri 2023, Icarus 404, 115648. [12] Formisano et al. 2021, MNRAS 494, 4

Additional Information: This work was supported by the INAF Theory Grant "Thermophysical Modeling of Permanently Shadowed Regions (PSRs) on the Moon and Mercury".

STRIKE-SLIP OR EXTENSIONAL DEFORMATION ON GANYMEDE? KINEMATIC MODELING OF THE SOUTH POLAR ICE SHELL. G. Frasca[1], G. Di Achille[2], T. Kenkmann[3]. [1]IGG-CNR; Torino, 10125, Italy (gianluca.frasca@cnr.it), [2]National Institute for Astrophysics; Teramo, 64100, Italy, [3]University of Freiburg; Freiburg, 79104, Germany.

Introduction: Ganymede, the largest moon in the Solar System and a prime target of ESA's JUICE mission, exhibits a surface composed of two dominant geological units: ancient, heavily cratered dark terrains (~60% of the surface) and younger bright terrains dissected by networks of grooves. These grooves, interpreted as fractures in the icy shell, have been linked to the progressive disruption and separation of the dark terrains [1]. However, the relative contribution of tensional versus lateral-slip deformation in shaping Ganymede's outer shell remains debated, with implications for the mechanical coupling between the surface and the underlying ocean, considered a potential habitat for life [2],[3].

We investigated whether the dominant tectonic regime in Ganymede's south polar region is tensional or lateral-slip by performing a kinematic reconstruction of dark terrains using the open-source plate reconstruction software GPlates. The study focuses on the area between Ptah and Anubis Palimpsests and Mummu Sulci, where relatively high-resolution imagery enables robust geological interpretation [4].

Method: Our reconstruction follows a prioritized, sequential inversion of dark terrain geometries, adopting the most parsimonious model of a polyphase single shell-breaking episode [5]. Dark terrains were considered as rigid continental blocks (following [6]) and extracted from the global geological map of [4]. The procedure of reconstruction follows the approach commonly used on Earth for rift and transform margins [7]. Fitting constraints here relied primarily on terrain boundary geometries and the restoration of dismembered furrows and palimpsest craters. Euler rotation vectors on the spherical surface were solved to minimize boundary misfits, progressively locking the best-constrained terrains and reconstructing subsequent ones relative to them.

Results: The geometry of restored fits and the resulting block kinematics suggest that relative motions among terrains can be best explained by a combination of tensional and lateral-slip deformation, varying locally with boundary orientation. These results indicate an active tectonic regime in the south polar region during an unconstrained epoch more than two billion years ago, consistent with large-scale shell disruption. This reconstruction framework provides a quantitative basis for linking surface tectonics to Ganymede's internal evolution and offers valuable context for forthcoming JUICE mission observations.

References: [1] Parmentier E. et al. (1982) *Nature, 295*, 290–293. [2] Rossi C. et al. (2020) *J. Maps, 16*, 6–16. [3] Pappalardo R. T. et al. (2004) *Jupit. Planet Satell. Magnetos., 2*, 363. [4] Collins G. C. et al. (2013) US Geological Survey, Global Geologic Map of Ganymede. [5] Patterson G. W. et al. (2010) *Icarus, 207*, 845–867. [6] De Marchi F. et al. (2021) *Icarus, 354*, 114003. [7] Frasca G. et al (2021) *Terra Nova, 33*, 573–581.

Serendipitous Lightning Spectroscopy with MAJIS during JUICE Earth Gravity Assist

E. D'Aversa[1], F.Oliva[1], G.Piccioni[1], F.Poulet[2], Y.Langevin[2], I.Kolmasova[3], A.Migliorini[1,] Giuseppe Sindoni[4], Christina Plainaki[4], Marco Giardino[4]

[1]Istituto Nazionale di Astrofisica, INAF-IAPS, Via del Fosso del Cavaliere 100, 00133, Rome, Italy (emiliano.daversa@inaf.it), [2]Institut d'Astrophysique Spatiale, CNRS/Université Paris-Saclay, France, [3]Department of Space Physics, Institute of Atmospheric Physics of the Czech Academy of Sciences, Prague, Czechia, [4]Agenzia Spaziale Italiana.

Introduction: In its travel towards Jupiter, The JUICE spacecraft performed a first-ever gravity assist maneuver at Moon and Earth on August 2024. During the short flyby time, the onboard MAJIS imaging spectrometer acquired a series of observations over West Pacific Ocean, widely covered by several storm systems at that time. In the first data cube, "anomalous" emissions at visible wavelengths have been identified offshore of Sumatra island at nighttime. This serendipitous observation represents the first doubtless space-based spectroscopic measurement of a lightning flash on any planetary atmosphere.

Observations: MAJIS data consist of multispectral images in the 500-5540 nm wavelength range, covered by two channels (VIS-NIR and IR), with a boundary at 2300 nm. No spacecraft depointing was allowed during this gravity assist, so the MAJIS data cubes have been collected by moving the instrument line of sight through the internal mirror. The full spectral range was also acquired in nighttime areas, whose spectra are dominated by telluric thermal emissions. This configuration enabled the serendipitously observation in the VIS-NIR channel of emissions from a maximum of four lightning flashes. The physical interpretation of these emissions is based on the simultaneous presence of spectral signatures of atomic oxygen and nitrogen, whose intensity is diagnostic of emission temperatures of the order of thousands of kelvins (Figure 1). Brightness temperature maps, derived from simultaneous MAJIS IR observations, allow locating the flashes near the edge of a thick thunderstorm cloud.

Results: MAJIS instrument is not optimized for such observations, whose results are biased under several aspects. In particular, we discuss possible correction factors dealing with spectral resolution (emission lines are narrower than MAJIS resolution and sampling) and temporal resolution (lightning flashes lifetimes can be much shorter than the MAJIS integration time). Under these assumptions, we retrieve emission energies quite consistent with average-strength lightning events (0.7-1.3 MJ in the 777 nm O I line). Furthermore, we applied standard techniques based on line intensity ratios to derive emission temperatures. The retrieved values span a broad range of values (5000 to 20000 K), probably reflecting the intrinsic uncertainties of the unresolved dataset. Unfortunately, no coincident detection of the same lightning event is reported by ground-based lightning location networks.

Conclusions: These observations represent a useful benchmark for guiding detection and interpreting possible lightning events on Jupiter, a primary target of the JUICE mission. In this Earth detection, we see a faint Hα signature that may also barely be associated with lightning flashes. On Jupiter, simultaneous H I emissions are expected to be the main diagnostic features for lightning events. Our preliminary extrapolation of the terrestrial case identifies H I emissions near the 650 nm and 1870 nm spectral ranges as the most promising for Jupiter.

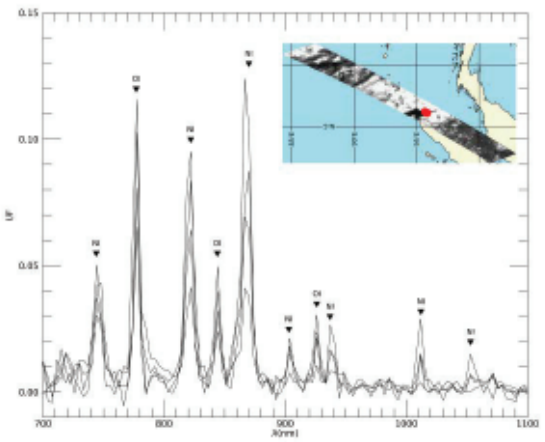


Figure 1: Spectral signatures diagnostic of the presence of high-temperature oxygen and nitrogen neutral atoms. In the inset the location of the VIS-NIR emissions is shown in red over a thermal map at a wavelength of 4610 nm.

Acknowledgements

The Italian participation to JUICE mission is funded by the Italian Space Agency (ASI). In particular, this work has been developed under the ASI-INAF agreement n. 2023-6-HH.0.

AN UPDATED MAPPING OF THE ORIENTALE BASIN (MOON) USING NEWLY DEVELOPED COLOR VISION DEFICIENCY-FRIENDLY COLOR SCALES. Y. Caddeo[1], G. di Achille[1] and G. Nodjoumi[2,3], [1]INAF - Osservatorio Astronomico d'Abruzzo (INAF-OAAB), Teramo, Italy, [2]INAF - Osservatorio Astronomico di Roma (INAF-OAR), Monte Porzio Catone, Italy, [3]School of Science, Constructor University Bremen GmbH, Bremen, Germany.

Introduction: The Orientale Basin is one of the youngest large impact basins on the Moon as well as one of the best preserved multi-ring basins in the Solar System [1, 2]. We already proposed a new, systematic, large-scale (1:200,000) mapping approach for it using a combination of the two main lunar methodologic approaches adopted up to this point [3]. In this work, we present the already existing map updated with a new color-vision deficiency (CVD) color scheme that we designed, in order to increase its accessibility and readability.

Study Area: Centered at ~19°S, ~93°W, this multi-ring basin is one of the most characteristic features on the surface of the Moon. Orientale is located on the western border of the near side of the Moon and is characterized by a structure made up of three concentric rings. The outermost ring is referred to as 'Montes Cordillera' and has a diameter of ~950-930 km, then the Outer Montes Rook have a diameter ranging between ~620 and ~660 km, and finally, the Inner Montes Rook space between ~460 and ~480 km [1, 3, 4].

In addition to this ring system there are some other prominent features that characterize its general morphology. An Inner scarp (d~320 km), a central depression partially infilled by what is known as the 'Mare Orientale', a smooth and dark relatively shallow layer of basalt, and a broad region outside the Montes Cordillera, historically referred to as 'Hevelius Formation', consisting of the basin's ejecta [3, 5].

Orientale is thought to have been formed during the Late Heavy Bombardment and its age, estimated to be ~3.81 Ga, was used to mark the beginning of the Late epoch of the Imbrian period [1, 3, 4].

Color Accessibility: Color-vision deficiency affects ~5% of the global population [6, 7]. More specifically, it is estimated that worldwide 0.5% of women and 8% of men are subject to a CVD and that this phenomenon is significantly higher occurring in populations with a larger fraction of white people (while it reduces to significantly lower fractions in populations from sub-Saharan Africa) [7 and references within].

Although these percentages might not be perceived as strikingly high (albeit in their ratio form they might show better how widespread the phenomenon is), not taking it into account when making use of color in scientific visualization, constitutes something unethical as it hinders the figures' message from spreading [7], especially in the case of maps, where the units and their distribution and association are the message themselves.

Data and Mapping Method: The map was created using the long time stable release of QuantumGIS (QGIS vrs. 3.40) [8] using two main basemaps: the 100 m/px resolution, grayscale mosaic of the Lunar Reconnaissance Orbiter Wide Angle Camera (LROC-WAC) and the 118 m/px elevation model obtained from the Lunar Orbiter Laser Altimeter (LOLA). These two datasets were utilized to characterize the different morphologies and structures found within the basin. Additionally, we also made use of the Clementine UVVIS colored mosaic having a resolution of 200 m/px to add a layer of information regarding differences in composition of apparently visually uniform features (e.g. the mare and the lacūs).

The color scale used for our map was created by making use of the already peer-reviewed open-access Scientific color maps [9] as a starting point. The scale was later also fully tested for accessibility towards people with CVD with the free color blindness simulator Color Oracle (vrs. 1.3) [10].

Our Color Scale: The new color scheme is rooted in the already existing scheme presented inside [5] as we aimed at maintaining the highest possible coherence with the already popularized and standardized products. For example, we maintained a criterion of using lighter hues for younger units and darker hues for older units, as of tradition for the geological criteria of mapping. We also maintained a genesis-based unit differentiation method, by selecting shades of the same hue to indicate units having the same geological process or belonging to the same morphological category.

However, we tried to minimize color combinations scientifically proven to be difficult to perceive by people with CVD like, for example, avoiding the association of red and green colors having similar lightness [7]. We also tried to maintain a general perceptual uniformity, avoiding to make use of bold colors (since they attract the human eye the most, and by making that subtly communicate a higher importance of the data) unless justified by scientifically proven reasons.

Results: Our final product, which to this day represents one of the first examples of CVD-friendly planetary maps, consists of a highly detailed map of the basin. Additionally, when compared with already existing, similar-scale maps, our map appears to be

more detailed and with a higher number of units and sub-units. With the combined approach of detailed mapping and a visually-friendly use of color, we had in mind to design a map capable of improving the general understanding of the complexity of one of the most important lunar structures by clearly identifying and differentiating the various morphologies and terrains making up both the distal and proximal facies of the Orientale Basin.

Our emphasis on creating a rigorous but easy-to-understand product, already presented in [3], has here been elevated by making a map that is accessible to an even higher number of people, coming from both outside and inside the scientific community. With our effort, we hope to establish a precedent for creating a new set of more user-friendly planetary maps.

Future Work: The map, with the current, CVD-friendly color scale, will be submitted for publication in a selected peer-reviewed journal and will be made available in PDF form. We also intend to publicly release the GIS version of our work.

References: [1] Wilhelms, D. E., McCauley, J. F., Trask, N. J. (1987). *U.S. Geological Survey professional paper*, 1348 [2] Spudis, P. D., Martin, D. J. P., Kramer, G. (2014). *Journal of Geophysical Research Planets, 119*. [3] Caddeo, Y., Di Achille, G. (2025). *XX CNSP*. [4] Liu, J., Liu, J., Yue, Z., Zhang, L., Wang, J., Zhu, K. (2022). *Icarus, 378.* [5] Fortezzo, C., Spudis, P. D., Harrel, S. L. (2020). *LI LPSC*. [6] Crameri, F., Shephard, G. E., Heron, P. J. (2020). *Nature Communications, 11*. [7] Crameri, F., Hason, S. (2024). *Patterns, 5*. [8] https://qgis.org/ (last access: 22/11/2025) [9] Crameri, F. (2018). *Zenodo*. [10] https://www.colororacle.org/ (last access: 22/11/2025).

Evaluation of the Moon Mineralogy Mapper reliability in lunar shadowed regions

*G. Massa[1], M. C. De Sanctis[1], F. Altieri[1], A. Raponi[1], S. Besse[2]
[1]INAF Istituto di Astrofisica e Planetologia Spaziali, via Fosso del Cavaliere, 00133 Rome, Italy
[2]ESA/ESAC, Villanueva de la Cañada, Spain
*email: giuseppe.massa@inaf.it.

Introduction:

Permanently shadowed regions (PSRs) of the Moon were suggested to act as cold traps for volatiles [1,2]. The possible presence of water ice in the lunar cold traps may have different origins, both endogenous and exogenous [3]. Endogenous sources include ancient volcanic activity and the slow outgassing from lunar mantle [4], whereas exogenous sources consist of solar wind implantation and impacts by comets, asteroids and micrometeoroids [4].

PSRs receive no direct sunlight and it would not be possible to study their reflectance spectra. However, light scattered or reflected from nearby sunlit terrain (i.e., secondary illumination) makes such observations possible [5].

Several spacecraft have studied the lunar poles over the past thirty years using different instruments [6]. Indirect evidence for the presence of water ice comes from neutron measurements, which indicates localized hydrogen enrichment that, however, cannot be uniquely associated with water ice [7]. Ultraviolet and laser reflectance data, combined with thermal measurements, are consistent with—but not diagnostic of—thin surface frost of about 0.1–2 wt % [8,9].

The LCROSS mission provided the first in situ confirmation of water ice at the lunar south pole measuring approximately 155 ± 12 kg of water, corresponding to 5.6 ± 2.9 wt % H_2O in the regolith at the impact site [3].

Another measurement of water ice comes from the the interpretation of near-infrared spectral analysis of the Moon Mineralogy Mapper (M^3) [10], which revealed absorption of water ice at about 1.25, 1.5, and 2.0 μm in several permanently shadowed craters at both lunar poles. However, latest results based on radiance contrast, obtained by Danuri ShadowCam, [11] show that the ice-bearing areas identified by M^3 exhibit no significant brightness contrast relative to their surroundings, posing the question about the presence of ice in the immediate subsurface.

Aim of this work:

We conducted independent research aimed at studying the presence and characteristics of water ice in the PSRs observed with M3 data.

The M3 data were acquired at very low signal making the ice detection very challenging. For this reason we perfomered a detailed analysis of the M3 data showing the signature of water ice, using a selection method similar to the one applied by Li et al [10]. We were able to reproduce results by [10] but we also identified unexpected water ice signatures in areas where ice is not expected to be stable (non-PSRs). Given that, we investigated the possible source of such ice like features in the M3 spectra, including a possible non-linearity in the instrument response for extremely low level of signal, as those in PSRs and in shadows.

Methods:

To find water ice, we apply a procedure based on the identification of the 1.2, 1.5 and 2.0 um absorption bands with band depth thresholds given by laboratory mixture spectra. To confirm the robustness of the procedure we evaluate it in PSR and on non-PSR regions, that are not expected to contain water ice but show a similar level of DN to the PSR region. Moreover, since we are dealing with very low radiance data with DNs (Digital Numbers) slightly higher, and sometimes even lower, of the dark signal, we evaluated the linearity of the instrument in these low signal pixels and its applicability. Finally, we used a statistical approach to assess whether the percentage of ice detections in the M3 data represents true detections or false positives induced by noise and non-linearity.

Results:

We confirm that, using a method similar to that described in [10], it is possible to select some pixels that, when averaged, show a water ice-like shape of the mean spectrum. However, we found positive detections of water ice in pixels in non-PSR regions (Figure 1), with temperatures higher than those allowed for water ice to remain stable.

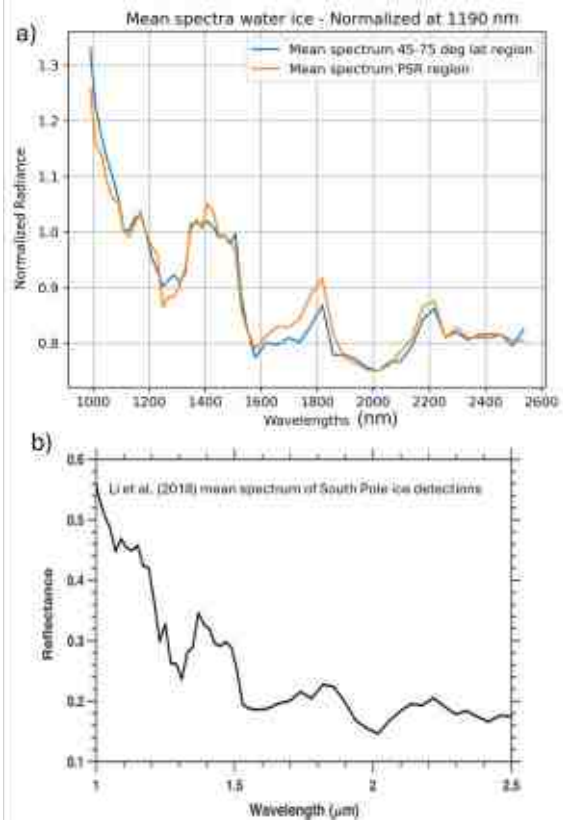


Figure 1: The image a) compares the mean spectra of water ice detections, obtained using the same selection procedure, in two different regions of a single data cube (m3g20090728t171132). The first region spans 45°–75° latitude and the other one is the Shoemaker crater PSR region (a south polar crater). The image b) presents the mean spectrum of positive detections reported by Li et al. (2018) across the entire South Polar region (75°–90° latitude), that include the Shoemaker PSR region.

The mean spectrum of these non-PSRs positive detections is extremely similar to that of the PSRs regions. For these reasons, we conducted a linearity analysis of the data and found that the spectra become distorted when going from high to low radiances. The shape of the distortion is very similar to the Radiance Calibration Coefficient (RCC) used for the calibration of the instrument. We used the spectral shape of the distortion as the continuum of our instrument and propagated the M3 noise obtaining 10^5 simulated spectra. We found that, applying the ice detections procedure, we obtain the same percentage of positive detections and a similar mean spectrum of the positive detected pixels of both the simulated and M3 spectra of shadowed regions (Figure 2).

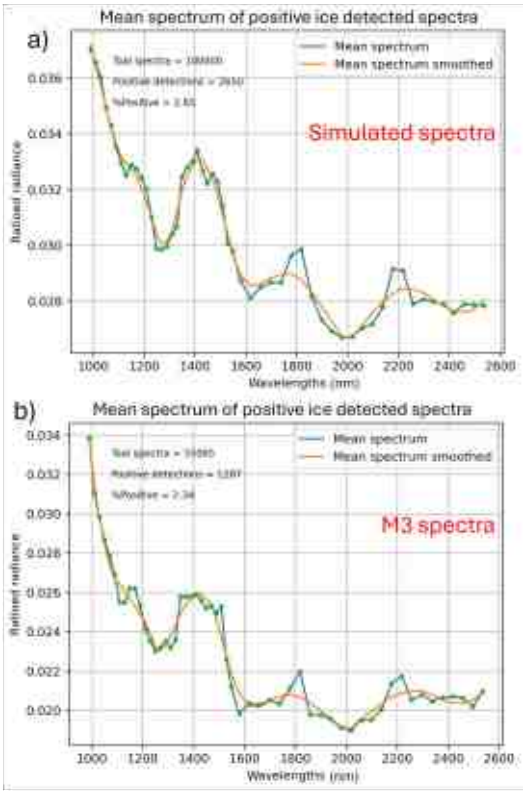


Figure 2: The figures show the mean spectrum of the ice detections on a) simulated and b) M3 spectra and their percentage.

Conclusions:
Our results demonstrate that ice-like spectral features can occur in both PSRs and unexpected lunar regions, and that these detections are more likely due to the M3 instrument response and signal-to-noise limitations than to true water ice signatures. However, this work does not go against the presence of water ice in PSRs, but it shows that M3 data have several limitations. Future in situ missions to the PSRs will directly observe whether there is water ice or not and how it is distributed on the surface.

Aknowledgments:
This work is granted by Accordo ASI – INAF n. 2024-64-HH.0.

References

[1] Watson, K. et al. (1961). *Journal of Geophysical Research, 66*(9), 3033–3045. [2] Urey, H. C. et al. (1952). *Physics Today, 5*(8), 12-12. [3] Colaprete, A. et al. (2010). *Science, 330*(6003), 463-468. [4] Arnold, J. R. (1979). *Journal of Geophysical Research: Solid Earth, 84*(B10), 5659-5668. [5] Mahanti, P. et al. (2024). *The Planetary Science Journal, 5(3), 62*.[6] Lawrence, D. J. (2017). *Journal of Geophysical Research: Planets, 122*(1), 21-52. [7] Feldman, W. C. et al. (1998). *Science, 281*(5382), 1496-1500. [8] Hayne, P. O. et al. (2015). *Icarus, 255*, 58-69. [9] Fisher, E. A. et al. (2017). *Icarus, 292*, 74-85. [10] Li, S. et al. (2018). *Proceedings of the National Academy of Sciences, 115*(36), 8907-8912. [11] Ando, J. et al. (2025). *The Planetary Science Journal, 6*(3), 62.

EMM project: SELENE (Simulated Environment for Lunar Exploration and Natural dynamics Experiments) for lunar dust mobilization experiments. C. Porto[1], G. Franzese[1], G. Mongelluzzo[1], C. I. Popa[1], F. Esposito[1], S. Silvestro[1], I. Donnarumma[2], A. Turchi[2], U. Cortesi[3], F. D'Amico[4], M. Gai[3], A. Argan[4]. [1]Osservatorio Astronomico di Capodimonte, INAF-OACN, Napoli, Italy; [2]Agenzia Spaziale Italiana (ASI), Roma, Italy; [3]Istituto di Fisica Applicata (IFAC-CNR), Firenze, Italy; [4]INAF headquarter, Via del Parco Mellini, Roma, Italy.

Introduction: The Moon is covered by a layer of regolith, which consists of fractured rock and unconsolidated debris, mainly resulting from micrometeorite bombardment. With no magnetosphere and no atmosphere, the regolith is directly exposed to solar wind and the full solar spectrum. As a result, it acquires a charge. On the dayside, the charging is dominated by photoemission from ultraviolet and soft X-ray photons; thus, the surface loses electrons and becomes positively charged. The nightside surface charge instead is determined by the balance between the collection of solar wind protons and electrons. Because of the faster speed of thermal electrons, the surface preferentially collects electrons and becomes negatively charged. Consequently, a plasma sheath develops immediately above the dusty surface, characterized by complex electric field configurations. In this environment, the regolith's finest part, the so-called lunar dust, acquires an electric charge and may exhibit unusual behavior, including levitation and transport across the surface driven by electrostatic forces. The electrostatic interaction between the lofted dust grains and the plasma sheath determines their dynamics.

Several observations indicate the occurrence of such electrostatic processes. The so-called "lunar horizon glow", observed during the Surveyor and Apollo missions, was interpreted to be due to forward-scattered sunlight from dust particles electrostatically lofted above the surface [1]. The Apollo 17 Lunar Ejecta and Meteorites (LEAM) instrument recorded spurious signals close to the terminator passage, which were subsequently interpreted as being due to slow-moving, highly charged dust particles [1], although this interpretation remains debated [2].

Theoretical models have been developed, and several laboratory experiments have been performed to demonstrate dust electrostatic mobilization in plasma environments [1, 3]. Since the first observations, the phenomenon has, indeed, attracted increased attention for its important role in the evolution of the physical and spectral properties of airless body surfaces. Moreover, the lunar dust is regarded nowadays as one of the major technical challenges for future human and robotic exploration on the Moon, especially for long-term human presence. Dust mobilization due to natural mechanisms and/or human activity, indeed, poses a hazard to operations and hardware. Therefore, the behaviour of charged dust needs to be well-characterized to define appropriate operations, design, and mitigation strategies.

We present here the SELENE (Simulated Environment for Lunar Exploration and Natural dynamics Experiment) facility, which is being developed as part of the Earth-Moon-Mars (EMM) project, funded in the framework of the National Recovery and Resilience Plan. This facility has been specifically designed to investigate dust transport and electrostatic dynamics under lunar-like conditions. It has been structured with a high degree of flexibility, allowing a wide range of experiments to be performed under controlled and repeatable conditions that closely reproduce the physical environment at the Moon's surface. Moreover, providing experimental conditions representative of those on the lunar surface, the facility serves as a test platform for sensors or sensor components currently under development within the EMM project.

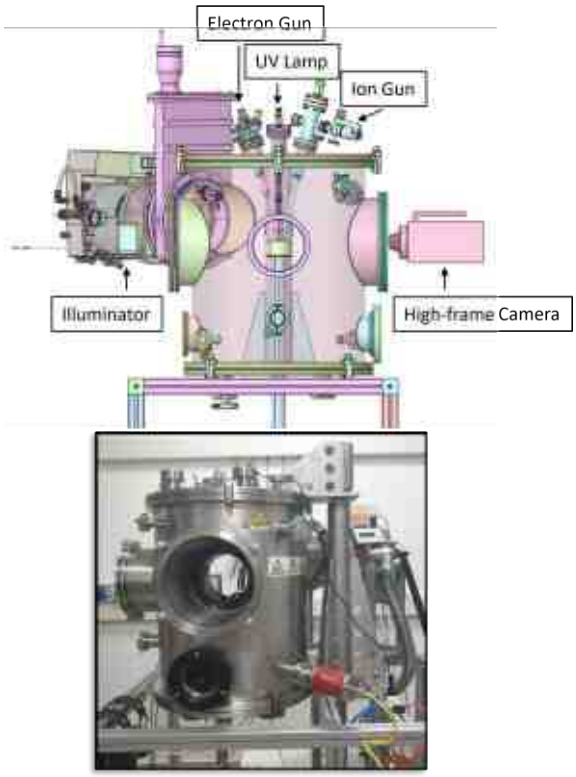


Figure 1: SELENE facility.

SELENE facility: The SELENE facility (see Figure 1) consists of a vacuum chamber 50 cm in diameter and 60 cm in height, capable of reaching a base pressure of 10^{-6} torr. The system is equipped

with several dedicated subsystems that reproduce specific lunar environmental conditions.

Thermal conditions within the experimental chamber are precisely regulated by a temperature control system capable of simulating the extreme thermal excursion observed on the lunar surface (from -150 to +150 °C). Ultraviolet (UV) lamps reproduce UV solar illumination conditions, while electron and ion guns emulate the effects of the solar wind. Electric fields are generated and controlled by a system exploiting high-voltage gridded electrodes and polarizable sample holders, allowing for accurate modulation of field strength and spatial distribution. The sample holders, moreover, are specifically designed to accommodate lunar soil or rock specimens, enabling their exposure to simulated environmental conditions and, thus, the accurate assessment of material responses under well-controlled vacuum, temperature, and radiation conditions.

Environmental sensors and an imaging system, based on a high-frame-rate, high-resolution camera, are employed to monitor the simulated conditions within the chamber.

Lunar dust mobilization experiment: SELENE enables the study of natural dust transport dynamics. To reproduce the lunar environment responsible for dust mobilization, dust particle samples are exposed to three different charging conditions: UV radiation, electron beam, and ion beam. To simulate the UV-induced photoemission, dust grains are illuminated by UV lamps with typical wavelengths of 172 nm and 162 nm. The corresponding photon energies are 7.2 eV and 7.6 eV, respectively, larger than the typical work function of the dusty surface (5.5 eV), thus ensuring the photoelectron emission. To reproduce the Solar wind effect, an electron gun (electron energy range: 10 - 1500 eV) and an H2+ ion gun (H2+ ion energy range: 0 - 3000 eV) are employed to generate, in particular, secondary electron production. As a result of these interactions, the grains are expected to acquire a charge and then to be electrostatically lofted.

The dust movement is recorded with a high-speed video camera equipped with appropriately telecentric and macro lenses. The vacuum chamber is equipped with two opposing inspection flanges, as shown in Figure **1**: one hosts the video-camera, while the other accommodates the illumination system. The video camera provides a pixel resolution of 6.5 μm x 6.5 μm per pixel, with an fps at maximum resolution of 750 images/s. Additional high-speed recording up to 150000 fps can be achieved at reduced resolution. Environmental sensors are employed to monitor the simulated conditions. A Langmuir probe is positioned to directly interact with the plasma generated near the sample holder, allowing the measurement of key plasma parameters such as electron temperature, electron density, and plasma potential during both steady-state and transient operating phases. A Faraday cup is used both to characterize the electron and ion beams and to measure the charge of the lofted dust grains.

The experimental setup enables systematic measurements by varying both the irradiation conditions and the particle size distribution to identify the key parameters influencing dust mobilization dynamics. Furthermore, since the position and orientation of both the sources and the sample holders can be controlled, it is possible to reproduce and investigate terminator-like conditions where illuminated areas are immediately adjacent to shaded areas. This configuration also allows the investigation of electric field effects on the dust transport, as the sample holders can be electrically biased.

Summary: SELENE is a specialized facility designed to simulate lunar surface conditions, thereby supporting lunar exploration research and experimentation. It reproduces key environmental parameters of the Moon's surface, such as vacuum and temperature conditions, UV radiation, solar wind exposure, and regolith-like soil mechanisms. SELENE supports, therefore, the study of the Moon's natural dynamics, including electrostatic dust transport mechanisms. Moreover, it provides a crucial platform for validating hardware performance and operational procedures, thereby mitigating risks for actual lunar missions and contributing to the advancement of lunar surface exploration technologies.

Acknowledgments: The results reported in the article were obtained in the context of the Earth-Moon-Mars (EMM) project, led by INAF in partnership with ASI and CNR, funded under the National Recovery and Resilience Plan (NRRP), Mission 4, Component 2, Investment 3.1: "Fund for the realization of an integrated system of research and innovation infrastructures" - Action 3.1.1 funded by the European Union - NextGenerationEU.

References:

[1] Colwell, J. E., et al. (2007) *Reviews of Geophysics* 45.2.
[2] Grün, Eberhard, and Mihály Horányi. (2013) *Planetary and Space Science* 89: 2-14.
[3] Wang, X., et al. (2016) *Geophysical Research Letters* 43.12: 6103-6110.

CORE AND MANTLE EVOLUTION OF A REDUCED MERCURY. G. Mitri[1] and C. Cioria[1], [1]Dipartimento di Ingegneria e Geologia, Università d'Annunzio di Chieti-Pescara (giuseppe.mitri@unich.it).

Introduction: Mercury's highly reducing formation environment has profoundly influenced its internal structure and long-term evolution. Unlike Earth, Venus, or Mars, characterized by olivine-rich mantles and sulfur-enriched metallic cores, Mercury likely possesses a silicon-enriched metallic core and a mantle rich in pyroxenes. These distinctive properties result from early planetary differentiation under extremely low oxygen fugacities, estimated to lie between 2.6 and 7.3 log units below the iron-wüstite (IW) buffer. Such conditions promote silicon partitioning into the core and stabilize pyroxene phases in the silicate mantle. The primary objective of this study is to investigate how mantle composition, through its control on viscosity, affects heat extraction from the deep interior and governs the timing and extent of inner core solidification.

Model: We developed a coupled numerical model that self-consistently simulates the thermal evolution of Mercury's mantle and core. The mantle model solves conservation equations for mass, momentum, and energy in a two-dimensional Cartesian geometry using a finite-difference method. A non-Newtonian rheology based on dislocation creep is implemented, with flow laws derived from experimental data for dry peridotite and orthopyroxene.

We explored a wide parameter space of pyroxenite content (0-40 wt%) and mantle thickness (300-500 km). The core model, based on an Fe-Si alloy (9 wt% Si in the liquid, 3.8 wt% in the solid), follows an analytical formulation describing the core's thermal, density, and phases' stability evolution, including latent heat and gravitational energy release during inner core crystallization.

Results and discussion: Our results demonstrate that the rheological properties of a pyroxene-rich mantle play a critical role in Mercury's interior evolution. Increased pyroxenite content reduces mantle viscosity, enabling vigorous and long-lasting convection. This enhances heat extraction from the core and favours the progressive growth of a solid inner core over geological timescales. Conversely, a more viscous, peridotite-dominated mantle suppresses convection earlier in planetary history. To evaluate the plausibility of the modelled scenarios, we compute the time evolution of Mercury's normalized moment of inertia, constrained by MESSENGER gravity and rotation data. These data support the presence of a partially molten core, and a mantle mechanically decoupled from a solid inner core.

These findings have implications for the origin and persistence of Mercury's magnetic field. A long-lived outer liquid core may sustain dynamo activity. Moreover, the model-derived histories of radial contraction and internal temperature evolution are consistent with observed tectonic features.

Acknowledgments: GM and CC acknowledge support from the Italian Space Agency (2023-6-HH.0).

FIRST RESULTS FROM A STUDY OF THE PHOTOMETRIC PROPERTIES OF MERCURY'S SURFACE USING MESSENGER-MDIS DATA B. Baschetti[1], G. Filacchione[1], C. Carli[1], F. Capaccioni[1], F. Zambon[1], A. Galiano[1]
[1] Istituto Nazionale di Astrofisica (INAF) – Istituto di Astrofisica e Planetologia Spaziali (IAPS), Roma, Italia.

Introduction and motivation: The reflectance of planetary surfaces, as measured by imaging spectrometers or cameras on spacecrafts, depends not only on the intrinsic albedo and composition of surface materials, but also on illumination conditions and viewing geometry. These effects are quantified and modeled through photometry, which studies how reflectance varies with the phase, incidence, and emission angles. In particular, proper photometric modeling is a necessary step to correct spectral data for geometric effects and to isolate the spectral variability related to composition [1,2].

We investigate the photometric behavior of Mercury's surface using data acquired by the Mercury Dual Imaging System (MDIS) onboard the MESSENGER mission [3]. The study aims to provide a reference framework for the interpretation of future observations from the SIMBIO-SYS VIHI hyperspectral imager from the BepiColombo mission [4]. VIHI will capture images which will fall within a wide range of viewing geometries, thus making photometric correction an indispensable step to retrieve accurate and unbiased spectral information.

Data and methods: We use the data from the MDIS-Wide Angle Camera (WAC) on MESSENGER, a multispectral imager which can provide images in sets of 3, 8, and 11 filters across the visible and near-infrared range (430 – 1020 nm) [5]. Regions of the hermean surface relevant to this study should be covered by a wide range of phase angles (i.e., images acquired at phase angles going from below 30° up to 90°), in at least three filter images. Selected regions currently include areas nearby Nathair Facula (Figure 1, left panel) in the Hokusai quadrangle, Bek crater (Victoria quad.), and Sander crater (Raditladi quad.).

Data cubes are obtained starting from radiometrically calibrated images (CDR) available on the Planetary Data System (PDS). These are processed through the Integrated Software for Imagers and Spectrometers (ISIS), skipping their photometric corrections [6].

The phase curve of a number of regions of interest (ROIs) is derived through an empiric approach, similarly to what has been done on the Moon by [7].

Preliminary results and future work: preliminary results are obtained for the region of the Nathair Facula, where 4 ROIs have been identified. The phase angle of the MDIS-WAC images in this case roughly spans from 25° to 80°. The phase curve of each filter shows an increasing reflectance with smaller phase angles (Figure 1, right panel shows an example of this curve for ROI 1), although a few points have significant deviations from this trend. A possible explanation could be related to the effect of shadows and image resolution. Future work will focus on addressing the issue and on extending the same analysis to the Bek and Sander regions. Finally, an empirical phase curve will be derived from the data.

References:

[1] Filacchione G. et al. (2022) Icarus, 375, 114803. [2] Ciarniello M. et al. (2015) A&A, 583, A31. [3] Solomon S. C. et al. (2001) PSS, 49, 15-15. [4] Cremonese G. et al. (2020) Space Sci. Rev., 216, 75. [5] Hawkins S. E. et al. (2007) Space Sci. Rev., 131, 247–338. [6] Becker K. et al., MESSENGER MDIS Data Users' Workshop 2013 [7] Buratti B. J. et al. (2011) JGR-Planets, 116, E6.

Acknowledgements: This study is supported by the ASI agreement n. 2024-18-HH.0

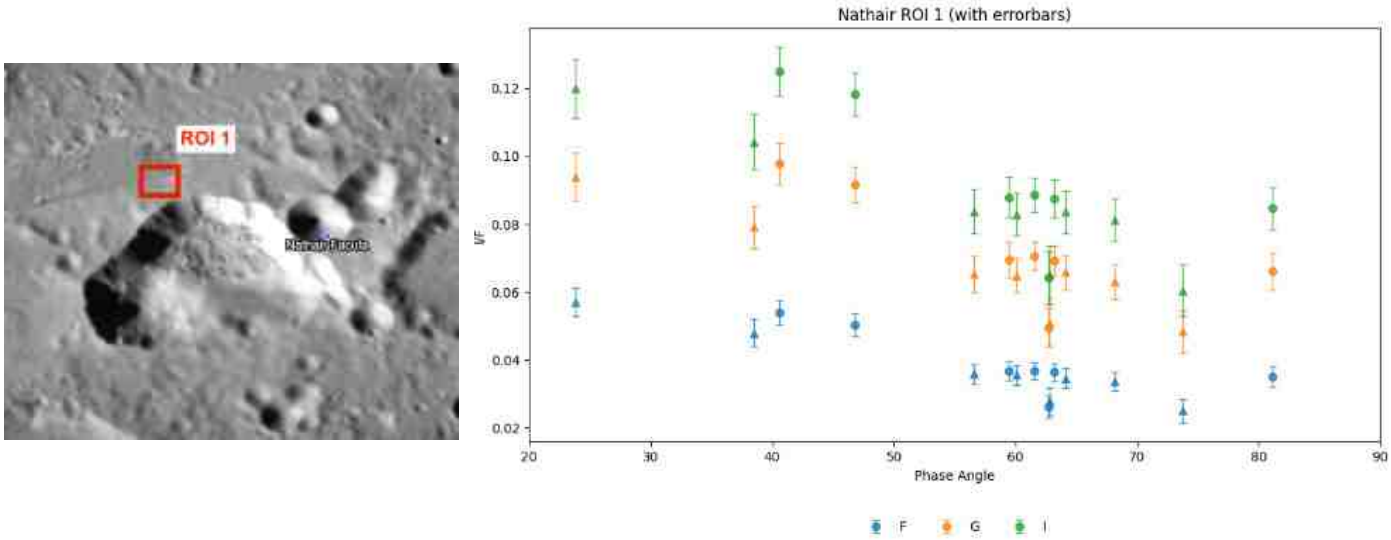


Figure 1: right panel shows the reflectance variations with changing phase angle for the MDIS-WAC filters F, G, and I relative to a small and homogeneous region near Nathair Facula (ROI 1, indicated by the red box in the left panel).

GEOLOGIC MAPPING OF THE BEETHOVEN QUADRANGLE (H07), MERCURY.

L. Guzzetta[1]*, S. Buoninfante[2], L. Giacomini[2], V. Galluzzi[2], A. Lewang[3], H. Hiesinger[3], L. Ferranti[4], P. Palumbo[2]. [1]INAF-Osservatorio Astrofisico di Catania, Catania, Italy; *laura.guzzetta@inaf.it*; [2]INAF-Istituto di Astrofisica e Planetologia Spaziali, Rome, Italy; [3]Institut für Planetologie, Westfälische Wilhelms-Universität, Münster, Germany; [4]DISTAR, Università degli Studi di Napoli Federico II, Naples, Italy.

Introduction: We present the new 1:3,000,000-scale geological map of Mercury's Beethoven quadrangle (H07), compiled using data from NASA's MESSENGER mission. The mapped area is located in the equatorial region of the planet, between latitudes 22.5°N–22.5°S and longitudes 216°–288°E, and covers an area of about 6 million km², representing 7.7% of Mercury's total surface.

Data and Methods: The mapping was primarily carried out using a monochromatic reflectance basemap (BDR – Basemap Reduced Data Record) with a resolution of 166 m per pixel, produced by the MESSENGER team from images acquired by the Narrow-Angle Camera (NAC) and Wide-Angle Camera (WAC) of the Mercury Dual Imaging System (MDIS) instrument [1]. Additional basemaps with different illumination conditions were also consulted, such as the low-incidence-angle mosaic (LOI) and two high-incidence-angle mosaics (≈ 78°) illuminated from the east (HIE) and west (HIW) [1]. These datasets helped reveal surface details in areas shadowed on the BDR mosaic. Three global color mosaics at 665 meters per pixel proved particularly useful for distinguishing volcanic deposits, hollows, and low-reflectance materials. The regional H07 DTM, produced by DLR with a resolution of 222 m [2], and the global DTM, produced by the USGS with a resolution of 665 m [3], were useful to identify tectonic structures and highlight remnants of ancient basin rims. Mapping was performed using ESRI ArcGIS software, where a spatial geodatabase was structured following the USGS – FGDC guidelines [4] to digitize the geological features as vector layers. The final map was produced in Equirectangular projection, using the "IAU Mercury 2015" reference datum with a sphere radius of 2,4394 km.

Geological map: The quadrangle is characterized by three main morphological-stratigraphic plains units: smooth, intermediate and intercrater plains, and by the material of the Tolstojan (~ 4Gyr) Beethoven basin, which partially outcrops in the southwestern region of the quadrangle. The smooth plains are interpreted as products of effusive volcanism and are considered the youngest units on Mercury. The intermediate plains display characteristics intermediate between intercrater and smooth plains and are relatively older than the smooth plains. The intercrater plains represent the oldest and most widespread unit on the planet, with a densely cratered surface.

Craters were distinguished based on their diameter into small ($5 < D > 20$ km), for which only rims were mapped as linear features, and large ($D \geq 20$ km), for which ejecta-related material was mapped as geologic contacts. The crater materials were classified according to a three-class degradation system (C1–C3) that considers the stratigraphic relationships between the craters [5]. For the Beethoven basin, we also distinguished its ejecta as a specific unit, as has been done for other large basins on the planet (e.g., Caloris [6] and Rembrandt [7]). Beethoven has a diameter of about 640 km, making it one of the largest basins on Mercury. The ejecta deposits, defined as hilly and radially lineated material extending outside the subdued rim of the basin, were mapped as **Be** (Beethoven ejecta). The basin floor is covered by volcanic smooth plains formed by later infilling, with an estimated age of 3.7–3.9 Ga [8], which may have buried internal rings. The main tectonic structures within the basin display a concentric pattern, as do those located especially near the western basin rim.

Based on the dominant contractional features affecting Mercury [9], structures in the quadrangle were interpreted as thrusts (low-angle reverse faults), certain or uncertain when they show a marked break in slope and lateral continuity, or as wrinkle ridges (low-relief arches with narrow superposed ridges) when the break is less evident and limited to smooth plains and basin floors.

Finally, features related to explosive volcanism, such as volcanic vents and pitted grounds, were identified and mapped as linear features and surface features, respectively. Pyroclastic deposits, often surrounding volcanic features, and fields of hollows, small rimless depressions formed by volatile loss [10], generally found inside craters, were also mapped as surface features.

This geologic map represents a more detailed cartographic product compared to the previously released 1:5,000,000 map of the quadrangle [11] and will be integrated into the global 1:3 million-scale map of Mercury [12], which is being prepared in support of the ESA/JAXA (European Space Agency, Japan Aerospace Exploration Agency) BepiColombo mission.

References: [1] Denevi B. W. et al. (2018) *Space Sci. Rev., 214*(1*),* 2. [2] Preusker F. et al. (2018) *Planet. Remote Sens. and Mapping*, 149-161. [3] Becker K. J. et al., (2016) *LPSC XLVII,* Abstract #1903. [4] Skinner Jr. J. A. et al., (2022) *PGMP—2022*, USGS N° 11-B13. [5] Galluzzi V. et al. (2016) *J.Maps,* 12(sup1), 227-238. [6] Guzzetta L. et al. (2017) *J. Maps*, 13(2), 227-238. [7] Pegg D. et al. (2021) *J. Maps*, 17(2), 718–729. [8] Massironi et al. (2009) *GRL*, 36, L21204. [9] Byrne P. K. et al. (2014) *Nat. Geosci.,* 7(4), 301–307. [10] Blewett D. T. et al. (2011) *Science,* 333(6051), 1856–1859. [11] King J. S. and Scott D. H. (1990) *USGS Misc. Inv. Ser*., Map I-2048. [12] Galluzzi V. et al. (2024), *Mercury 2024 Conf*., Abstract Booklet.

Funding: We gratefully acknowledge funding from the Italian Space Agency (ASI) under ASI-INAF agreement 2024-18-HH.0

WHY ARE INFILLED CRATERS SO DIVERSE ON MERCURY?: CONSTRAINTS FROM CALCULATED INFILL AND CRUSTAL THICKNESSES

G. W. Schmidt1, V. Galluzzi[1], S. Buoninfante[1], A. Sepe[1,2], and P. Palumbo[1]
[1]INAF, Institute for Space Astrophysics and Planetology, Rome, Italy (gene.schmidt@inaf.it)
[2]University of Naples "Federico II", Department of Earth Sciences, Environment and Resources, Naples, Italy

Introduction: Mercury boasts a variety of volcanically infilled craters with diverse topographies (circular bulges vs. flat) and deformation features (radial, polygonal, and concentric fault patterns) [1]. In some cases, the infill topography forms a central depression which forms from an unknown process. When fault sets are present, they are either a polygonal pattern uniformly across the infill, or are specific to geometric locations within the crater: concentric extensional faults present on budges and the accompanying central depression contains radial or circular extensional faults (i.e. only the center or only on the bulge). Apart from this, the majority of infilled craters have a clear peak ring and central peak present, towering even up to two kilometers over the infill. Since the infilling process is considered to occur from below the center of the craters [2], the different observed topographies may represent buried peak rings, central collapse, or some combination of the two. Furthermore, although various fault set formation mechanisms have been described previously [e.g. 1], a unified global control to explain why some infilled craters form these specific fault sets while others do not, has not been explored.

We present the calculated infill thicknesses of 59 craters grouped by their topographic character, fault patterns, and presence of peak ring (Fig. 1). The crustal thickness below each crater is also measured, which together allow for global comparisons using data not previously realized. We aim to determine the relationship between bulged topography within infill and their more common peak ring topography counterparts. In so doing, we can determine if this infill topography is merely a lava infill which has conformed to a pre-existing peak ring, or the center of the crater has undergone collapse.

Data and Methods: The 59 craters represent a combined catalog of previously determined infilled craters [3, 4] and additions from our own observations. The investigation utilized both MESSENGER topography and gravity data. A Digital Elevation Model (DEM, Fig. 1a) derived from the stereo imagery of the Mercury Dual Imaging System (MDIS) with a resolution of 665 m/px was in combination with image data from the MESSENGER MDIS Global Mosaic (166 m/px). Crustal thickness measurements were obtained from a crustal thickness map derived from MESSENGER gravity data [5]. Infill thickness was calculated using the power law $d = 0.89 \times D^{0.24}$, where d is crater depth and D is crater diameter [6]. The observed elevation of the infill surface was then subtracted from this crater depth to estimate the infill thickness.

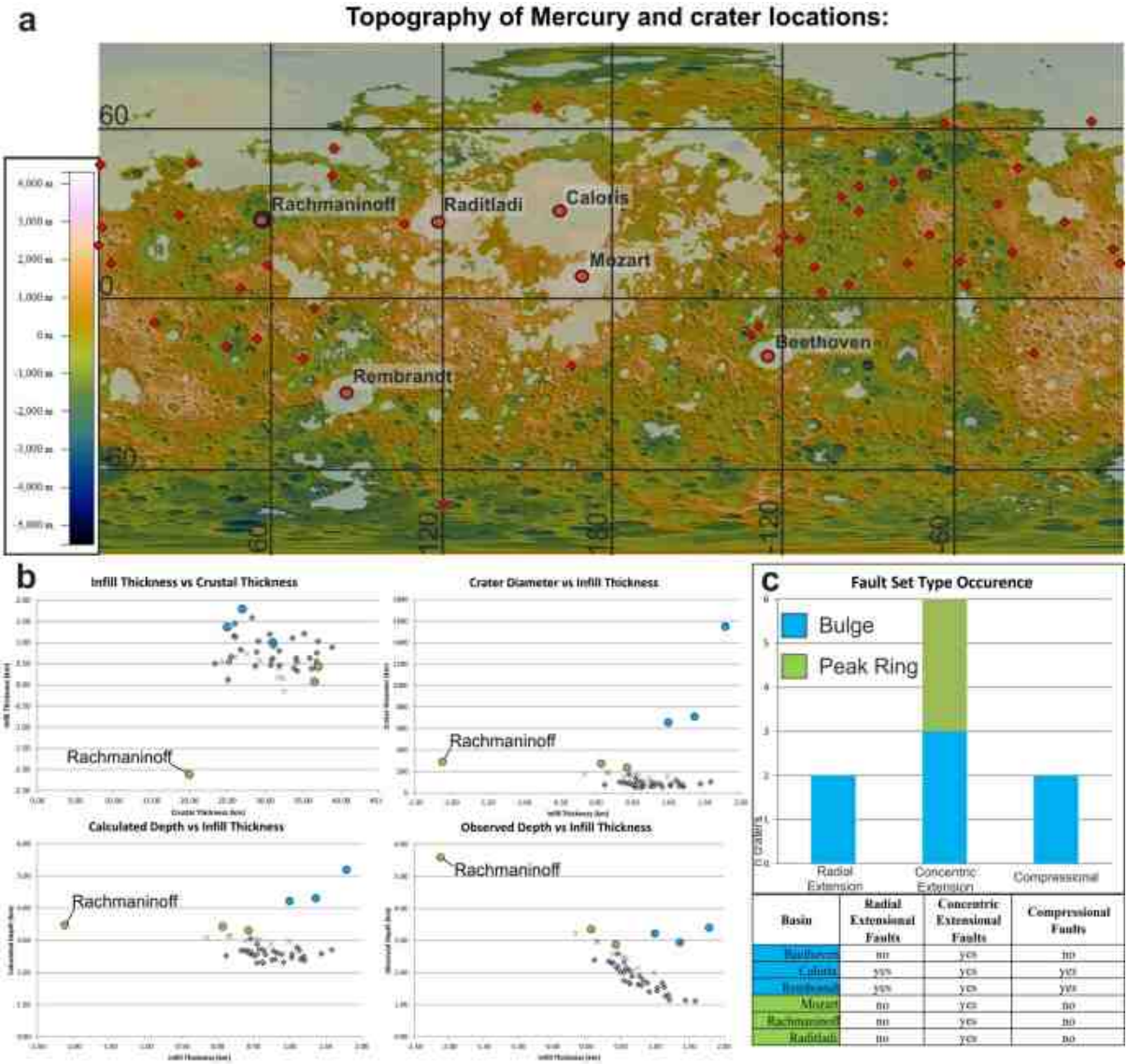
Discussion and Conclusions: The average infill thickness of all 59 craters is 666 m and the average crustal thickness is 30.6 km. Six craters standout from the other 53: Beethoven, Caloris, Rembrandt, Mozart, Rachmaninoff, and Raditladi which all have specific fault patterns (Fig. 1c) and all have diameters greater than 200 km. This may indicate a weight load response, though a cooling effect is still a possibility [1]. The remaining 53 craters were grouped into flat topography and those with peak rings (grey circles and x symbols in Fig. 1b). Within the unique six: 1. Crater diameter, crater depth, and infill thickness are proportional, 2. Craters with bulge topography have thickest infill, 3. Crustal thickness and infill thickness are inversely proportional: infill increases with decreasing crustal thickness.

Rachmoninoff is a major outlier (Fig. 1b), having a negative calculated infill thickness which implies a collapse of 2-3 km. Although Derain, another peak ring basin, has a negative infill thickness too (-0.15 km), it is within the range of other infill thicknesses, which indicates possibly a smaller <0.5 km collapse. The larger collapse of Rachmoninoff is attributed to the measured 20 km crustal thickness below the basin, which is 10 km less than the 30.6 km average of the crustal thickness beneath other basins in this study (Fig.1 b).

The lingering question of infilling rate vs. cooling may well be an overarching control that the current results do not resolve. However, future work on the relative ages between the craters and their compositions is underway. These parameters may further constrain the issuing of timing. Revelations from BepiColombo include higher resolution gravity data, which in turn will provide updated crustal thickness values, as well as the likelihood of more numerous and complex fault patterns.

References: [1] Freed et al. (2012) *JGR: Planets,* 117(E12). [2] Hirata et al. (2022) *Icarus*, 382, 115034. [3] Herrick et al. (2018) *JGR: Planets*, 123(8), 2089-2109. [4] Baker & Head (2013) *Planetary and Space Science,* 86, 91-116. [5] Buoninfante et al. (2023) *Scientific Reports*, 13(1), 19854. [6] Susorney et al. (2018) *Icarus*, 271, 180-193.

Acknowledgements: We gratefully acknowledge funding from the Italian Space Agency (ASI) under ASI-INAF agreement 2024-18-HH.0.



Basin	Radial Extensional Faults	Concentric Extensional Faults	Compressional Faults
Beethoven	no	yes	no
Caloris	yes	yes	yes
Rembrandt	yes	yes	yes
Mozart	no	yes	no
Rachmaninoff	no	yes	no
Raditladi	no	yes	no

Figure 1. a) Locations of all craters measured in this study marked by red dots overlain on the DEM. Shaded grey areas represent smooth plains. The six unique craters Beethoven, Caloris, Rembrandt, Mozart; Rachmaninoff, and Raditladi are labeled. b) Graphs of all 59 measured craters depicting infill thickness vs crustal thickness, crater diameter, and both calculated [6] and observed depth. Rachmaninoff labeled as the outlier from the others. c) The six craters of the 59 to have unique fault patterns. Grouped as bulge topography and those where a peak ring is visible (blue and green respectively). The three fault sets are radial extensional, concentric extensional, and compressional.

ASSESSING THE CRUSTAL DENSITY OF MERCURY THROUGH GRAVITY DATA MODELLING.

S. Buoninfante[1], M. Milano[2], V. Galluzzi[1], L. Ferranti[2,1], M. Fedi[2], G. W. Schmidt[1], P. Palumbo[1], [1]INAF, Istituto di Astrofisica e Planetologia Spaziali, Italy (salvatore.buoninfante@inaf.it), [2]DiSTAR, University of Naples Federico II, Italy.

Introduction: Gravity data have been widely used for modelling the interior of terrestrial planets. NASA's MESSENGER mission provided important advances in understanding Mercury's internal structure. However, the scientific progress achieved since MESSENGER has left open further questions that will be better addressed by the ESA-JAXA BepiColombo mission. Among the main topics concerning Mercury's internal structure is the estimation of lateral crustal density variations. Previous work has shown how admittance and spectral analysis using gravity and topography data can provide useful information on crustal bulk density (e.g., [1, 2]). In this study, we aim to model Mercury's crustal structure using inverse modeling of gravity data. The inversion technique help resolve crustal lateral and vertical density variations in selected areas. The resulting density model offers a valuable basis for further geological and structural interpretations of Mercury.

Methods: We performed a tesseroid-based inversion procedure to retrieve a 3D distribution of densities. To develop and test our inversion method, we first apply it on a synthetic case based on available topography and crust-mantle interface information. We simulated a three-layer crustal structure using tesseroid bodies, adapting the Tesseroids code [3] to Mercury's parameters. We simulated the crustal structure for a region in the Victoria quadrangle of Mercury (295°E-320°E; 45°N-64°N), as one of the highest resolution areas in the gravity field model HgM009 [1].

In an ill-conditioned least-squares problem, multiple substantially different solutions may fit the observed data equally well. To address this ill-posed linear system, we employed a regularized inversion algorithm that incorporates model constraints. Specifically we minimize the following objective function:

$$P^{\mu}(\mathbf{m}) = \min\left\{\sum_{i=1}^{N} \|\mathbf{Am}-\mathbf{d}\|_2^2 + \mu^2 \sum_{k=1}^{M} \frac{w_{zk}^2 m_k^2}{m_k^2+\varepsilon^2}\right\} \quad (1)$$

where **d** is the data vector, **m** is the model to be estimated, and **A** is the sensitivity matrix containing the gravity effect of each tesseroid in the forward model. The parameter μ is the regularization weight, and $\|\mathbf{Am}-\mathbf{d}\|^2$ represents the squared L_2-norm data misfit between the observed data **d** and the model-predicted response **Am**.

The inversion algorithm also incorporates additional constraints, including compactness [4] and a radial weighting function [5]. The compactness constraint is introduced through a compactness function $(1/m_k^2+\varepsilon^2)$, where ε is a small scalar added to avoid singularities, promoting iterative minimization of the 3D source volume. The radial weighting function further guides the solution by imposing depth-dependent constraints.

Results and future work: While spectral analysis reveals interesting bulk-density variations across different regions of the planet, the inversion of gravity data provides detailed information on small-scale structures within specific study areas, though these results remain constrained by the spatial resolution of the available data. Because the resolution in the Southern Hemisphere does not permit reliable interpretation, our investigation focused on the Northern Hemisphere.

A simulated case study was performed to validate and calibrate our approach. We generated a crustal model featuring variable topography and a non-uniform crust–mantle interface, as well as small-scale structures such as intra-crustal intrusions to represent lateral density variations within the crust. Inversion of the forward-modeled gravity response successfully recovered the primary density contrasts of the synthetic model.

We then applied inverse modeling to the observed gravity data. As expected, high densities are concentrated above large impact basin regions, likely influenced by mantle upwelling following the giant impacts. Further investigation is required to determine the origin of both the low- and high-density regions.

As a next step, we will develop a global density distribution using updated gravity models from the BepiColombo mission, which will provide higher-resolution data for the Southern Hemisphere. Additionally, this inversion framework will be highly valuable for reconstructing the internal structure of Ganymede leveraging the updated gravity model from ESA's JUICE mission.

References: [1] Genova A. et al. (2023) *Icarus, 391*. [2] Wieczorek, M. A. (2013) Science, 339, 671-675. [3] Uieda L. et al. (2016). *Geophys., 81, 5*, F41-F48. [4] Last, B. J., and Kubik, K. (1983) *Geophys. 48,* 713–721. [5] Liang et al. (2014) *JGR Planets 119*,1359–1373.

Acknowledgements: We gratefully acknowledge funding from the Italian Space Agency (ASI) under ASI-INAF agreement 2024-18-HH.0. This research is also supported by INAF through RSN3 Mini-Grant “Investigation of Mercury’s Tectonics (iMeT)”.

STRUCTURAL AND TOPOGRAPHIC EVIDENCE FOR A HIDDEN MULTIRING BASIN IN MERCURY'S DISCOVERY QUADRANGLE (H-11)

A. Sepe[1,2], L. Ferranti[2,1], V. Galluzzi[1], G. W. Schmidt[1], S. Buoninfante[1,2], and P. Palumbo[1]
[1]INAF, Institute for Space Astrophysics and Planetology, Rome, Italy (antonio.sepe@inaf.it)
[2]University of Naples "Federico II", Department of Earth Sciences, Environment and Resources, Naples, Italy

Introduction: Basin-forming impacts played a central role in the early evolution of the terrestrial planets, influencing their topography, stratigraphy, and crustal structure [1]. Several basin catalogues have been compiled for Mercury using progressively improved datasets [1-4], yet the total number of basins with diameters D ≥ 300 km (121) remains lower than theoretical expectations (~180 [3]). This discrepancy suggests that a substantial fraction of Mercury's impact basins record may be highly degraded, buried or otherwise difficult to recognize, implying the existence of a population of ancient "hidden" impact basins.

These basins are expected to be pre-Tolstojan in age (> 4 Gy; [1,2]) and to have defined the primordial structural framework that influenced Mercury's subsequent tectonic evolution [2]. Their identification typically relies on three indicators: (1) circular or concentric fault patterns [2]; (2) quasi-circular depressions (QCDs) in topography [5]; (3) circular thin areas (CTAs) in crustal thickness maps [5]. However, robust and quantitative approaches to systematically analyze these signatures are still limited, particularly for highly degraded structures.

Here we propose an integrated workflow for the identification and analysis of hidden impact basins, applied to Mercury's Discovery quadrangle (H-11). This region provides an ideal case study, as it is thought to host at least one ancient, hidden basin (Andal-Coleridge) not visible in image data, hypothesized to represent a multiring basin surrounded by 3-5 concentric rings [2,6].

Data and Methods: To characterize hidden basins, we used the MESSENGER/MDIS basemaps (~166 m/px), the digital elevation model (DEM) of [7], and the crustal thickness map of [8]. We also developed a MATLAB tool (Radial Profiler) that extracts 360 radial profiles (1° spacing) from both topography and crustal thickness, and computes their statistics (min/max, interquartile range, median, mean, etc.). These profiles can also be grouped into user-defined angular sectors (e.g., 90°, 180°, custom) to isolate azimuthal variations in basin-related signals.

Using image and DTM data, we produced a high-resolution structural map of the study region, following the mapping criteria and symbology described in [9,10]. This map reveals a circular arrangement of faults surrounding both a QCD and a CTA (Fig. 1), providing independent evidence for a heavily degraded basin-sized structure. We also performed a beta-analysis [13,14] and concentric deviation analysis [11] to estimate the causative stress-field associated with the mapped faults and to determine its most probable center.

Results show a bimodal stress pattern (Fig. 2). The primary "bull's-eye" distribution is roughly centred in the QCD and is surrounded by circularly aligned scarps, including Discovery Rupes. The secondary distribution is bounded by Adventure Rupes and Resolution Rupes, possibly marking the presence of a smaller and probably older basin.

Following the method of [2], we reconstructed a 5-ring morphology for the Andal-Coleridge basin, exhibiting a maximum diameter of ~1500 km, comparable to the Caloris basin (Fig. 3). The 360 radial profiles support this interpretation, showing an average radius of ~780 km and 5 distinct topographic peaks roughly matching the proposed ring structure. Finally, crustal thickness profiles indicate an excavation depth of ~15 km for the Andal-Coleridge basin-forming impact (Fig. 4), consistent with expectations for a basin of this size [12].

Conclusions and Future Work: Our workflow demonstrates strong potential for identifying and characterizing hidden basins by integrating complementary datasets (imagery, topography, crustal thickness), and by combining manual (structural mapping, beta-analysis) and automated approaches (concentric deviation, radial profiling). Using this approach, we characterize Andal-Coleridge as a 5-ring, ~1500 km-wide hidden basin that excavated Mercury's crust to a depth of ~15 km, and we also identify evidence for an additional older basin in the region.

We plan to apply this workflow systematically to all previously proposed basins (and will extend the analysis to new candidate regions) in order to better assess the contribution of ancient basin-forming impacts to Mercury's present-day tectonic framework.

References: [1] Fassett et al. (2012) *JGR:Planets,* 117(E12). [2] Spudis & Guest (1988) In: *Mercury*, 118-164. [3] Orgel et al. (2020) *JGR:Planets*, 125(8). [4] Szczech et al. (2024) *Icarus*, 442. [5] Edgar (2015) In: *Encyclopedia of Planetary Landforms,* 1675-1678, 298-300. [6] Watters et al. (2001) *Planetary and Space Science*, 49(14-15). [7] Becker et al. (2016) *47th LPSC*, Abstract #1903. [8] Broquet et al. (2025) *JGR:Planets*, 130(9). [9] Galluzzi et al. (2016) *Journal of Maps*, 227-238.

[10] Buoninfante et al. (2025). *Journal of Maps*, 21(1). [11] Karagoz et al. (2024) *JGR:Planets*, 129(1). [12] Wieczorek et al. (1999) *Icarus*, 139(2).

Acknowledgements: We gratefully acknowledge funding from the Italian Space Agency (ASI) under ASI-INAF agreement 2024-18-HH.0. This research is also supported by INAF through RSN3 Mini-Grant "*Investigation of Mercury's Tectonics (iMeT)*"

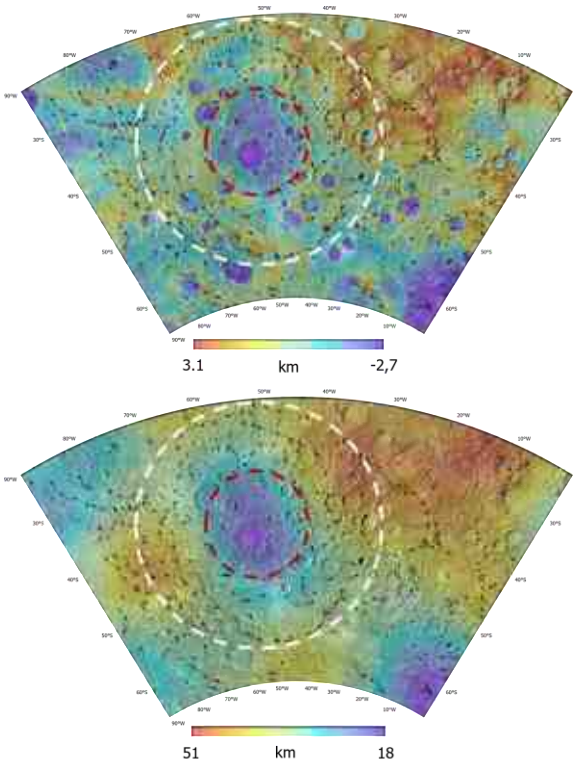


Figure 1 Our structural map for the Discovery quadrangle in LCC projection. White dashed circle outlines the circular arrangement of faults. Red dashed circle outlines the QCD (*top*) and the CTA (*bottom*).

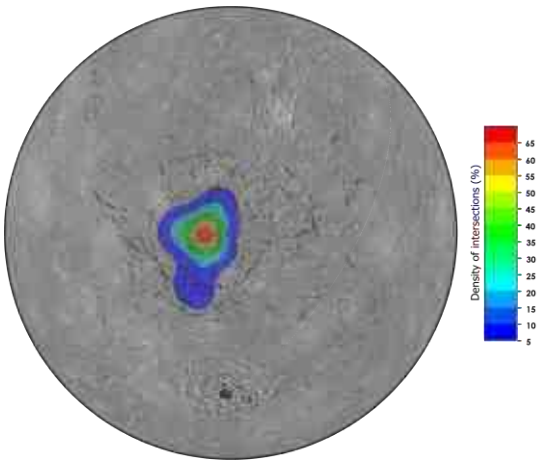


Figure 2 The stress field resulted from the beta-analysis. Orthographic projection centred in 53°W, 42.5°S.

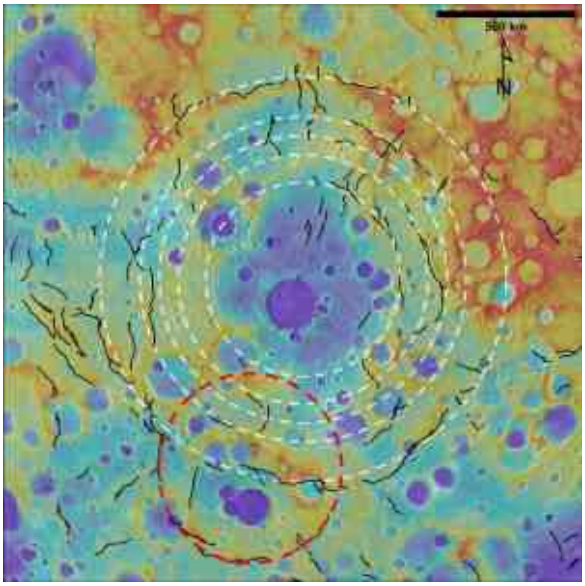


Figure 3 Multiring geometry of the Andal-Coleridge basin inferred from the structural map. White dashed circles indicate rings location. The red dashed circle approximates the extent of the smaller basin.

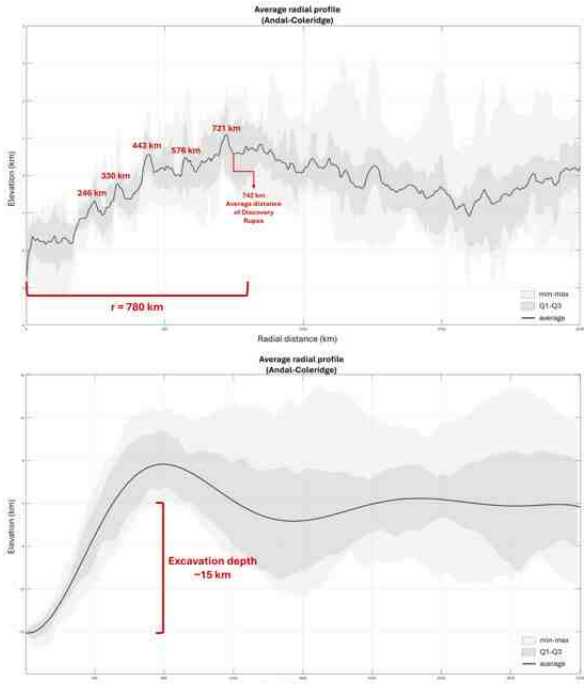


Figure 4 Andal-Coleridge's radial averaged profiles. (top) Average topographic profile (45° spacing) showing the location of the five peaks and the average distance of the Discovery Rupes. (bottom) Average crustal thickness profile corrected for the pre-impact crust-mantle interface (moho). Q1-Q3 refers to the interquartile range.

A NEW VIEW OF MERCURY: IMPROVING GLOBAL MESSENGER MOSAICS WITH GSA PANSHARPENING. A. Tullo[1], C. Re[1], Baschetti B.[2], P. Cambianica[1], Natalia Amanda Vergara Sassarini[1], G. Munaretto[1], S. Bertoli[1] and G. Cremonese[1]. [1]INAF – Astronomical Observatory of Padova, Vicolo dell'Osservatorio 5, 35122 Padova, Italy (adriano.tullo@inaf.it), [2] INAF - IAPS, Rome, Italy.

Introduction: The MESSENGER Mercury Dual Imaging System (MDIS) cameras were a primary instrument that played a critical role in past and present studies of global characterisation of Mercury [1]. The instrument consisted of two cameras: the targeted high-resolution monochromatic Narrow-Angle Camera (NAC) and the multispectral Wide-Angle Camera (WAC), which operated across the visible and near-infrared spectrum (430 nm to 1020 nm) [1]. Several global products have been created from the MDIS WAC and NAC data, with resolutions that vary greatly depending on the acquisition conditions. Due to thermal reasons, the highly elliptical polar orbit reached the closest approach altitudes of ~200 km over the northern hemisphere, but observed the southern hemisphere from a distance ranging from several hundreds to 2000 km [2][3]. Multibands mosaics were resampled at the maximum resolution of 64 pixel per degree (ppd) (665 m/px), despite the effective ground resolution in the southern hemisphere is even reduced due to the higher altitude of the flyover [4]. However, the panchromatic data, which also utilises the higher NAC resolution, compensates for this. The monochromatic MDIS mosaics maintain, in fact, a similar resolution even in the southern hemisphere, and are distributed resampled at 256 ppd (166 m/px) [4].

This study aims to bridge the gap in spatial resolution between multispectral and monochromatic data by utilising data fusion techniques. Pansharpening can, in fact, consistently improve the spatial resolution of available multispectral data by more than four times, resulting in a new set of data that can be used for global studies of Mercury.

Methods: Pansharpening data fusion techniques utilise the information from a reference panchromatic image to enhance the spectral information of a given multi- or hyperspectral image to a higher spatial resolution. Among the many methods that have emerged in recent years, the Gram–Schmidt Adaptive (GSA) method quickly gained popularity due to its reliability, often becoming the standard against which other methods are compared [5][6]. The GSA method builds upon previous GS approach, with which it shares the principles of orthogonalisation, panchromatic substitution, and inverse transformation. Unlike the original, however, it introduces an adaptive mechanism for adjusting the synthetic intensity component in comparison with the reference panchromatic component [7]. This enables it to successfully handle minor registration and alignment errors, making it suitable for managing even large sets of non-orthorectified data. Both products were processed in tiles and then re-mosaicked in order to limit computational costs.

Dataset: The study focused on two different global datasets described by [4]:

- the Map Projected Multispectral Reduced Data Record (MDR) 8-band mosaic generated from WAC,
- The Basemap Enhanced Color Global Mosaic 665m derived from the 430, 750, and 1000 nm bands and places the second principal component, the first principal component, and the 430/1000 ratio in the red, green, and blue channels respectively. This 3-band mosaic emphasises the colour differences in the surface.

The Map-projected low incidence angle basemap reduced data record (LOI), composed of WAC and NAC images captured at low solar incidence angles (up to ~45°), was used as the reference panchromatic data [8]. The low incidence of the LOI helps to emphasise variations in surface albedo. In fact, although previous studies [9] have shown that illumination has relatively little influence on the quality of the results, using low incidence data helps prevent inheriting shadows that could affect the contrast and colour rendering of the images.

Results and conclusions: Both results show a high color fidelity compared to the original cubes, considering the same range and contrast stretch (Fig.1). Several standard performance indicators were adopted for the evaluation, Different standard performance indicators were adopted for the evaluation, investigating both the preservation of spectral information, e.g. using the Spectral Angle Mapper (SAM) and the development of structural characteristics, for example, through the Structural Similarity Index Measure (SSIM). Spectral indicators are used to compare results with the original multispectral data, subsampling the results at the starting resolution, while structural indicators are indicative of the own image stability and the comparison with the reference panchromatic.

The fourfold increase in spatial resolution allows for the observation of numerous smaller-scale features that were previously blurred, such as structural features and medium to large hollows and vents (Fig.2). This increase, while maintaining the original spectral properties, implies extending the usefulness of global data to a broader range of studies and

applications. The methods described are preparatory for the future exploitation of BepiColombo's global data, in particular for the integration of the three channels of the SIMBIO-SYS instrument, HRIC, STC and VIHI [10].

Aknowledgements and data availability: PANCO is released open-source under AGPL-3.0 license at github.com/adritullo/PANCO (10.5281/zenodo.17512026). MESSENGER data are credited to NASA/Johns Hopkins University. This work has been developed under the ASI-INAF agreement n. 2024-40-HH.0.

References: [1] Bedini P. D. (2017) Johns Hopkins APL Tech. Dig., 34. [2] Solomon S. C. et al. (2007) Space Sci. Rev., 131, 3–39.[3] Wright J. et al. (2021) J. Volcanol. Geotherm. Res., 417, 107300. [4] Denevi B. W. et al. (2017) Space Sci. Rev., 214, 2. [5] Dalla Mura M. et al. (2015) IEEE Int. Geosci. Remote Sens. Symp., 37–40. [6] Vivone G. et al. (2021) IEEE Geosci. Remote Sens. Mag., 9, 53–81. [7] Aiazzi, et al. (2007) IEEE TGRS 45, 3230–3239. [8] Murchie S. et al. (2007) J. Geophys. Res., 112, 2006JE002682. [9] Tullo A. et al. (2024) Planet. Space Sci., 254, 105997. [10] Cremonese, G., et al. (2020). Space Sci. Rev. 216, 75.

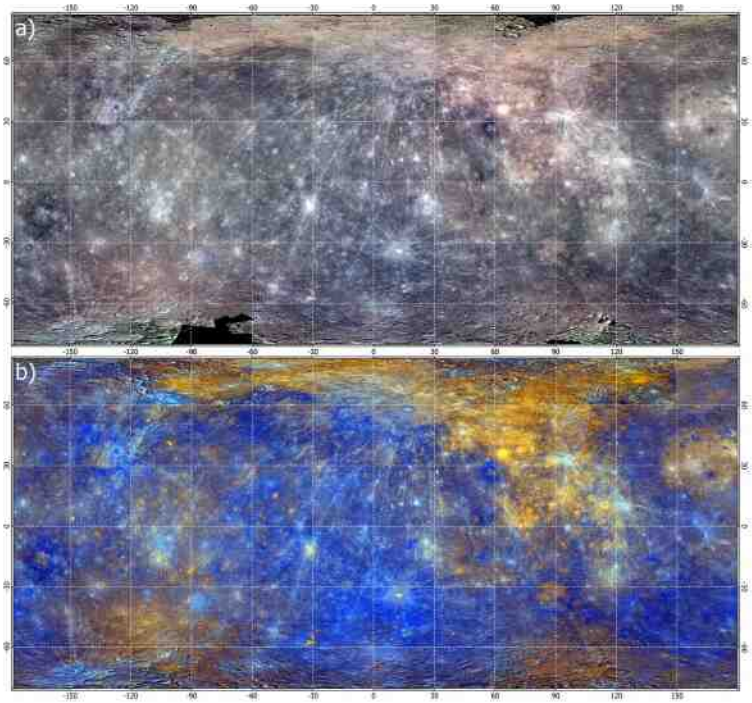


Figure 1 a) the Map Projected Multispectral Reduced Data Record (MDR) 8-band mosaic and b) the Basemap Enhanced Color Global Mosaic enhanced through GSA pansharpening at 166 m/px (256 ppd) from the original 665 m/px (64 ppd).

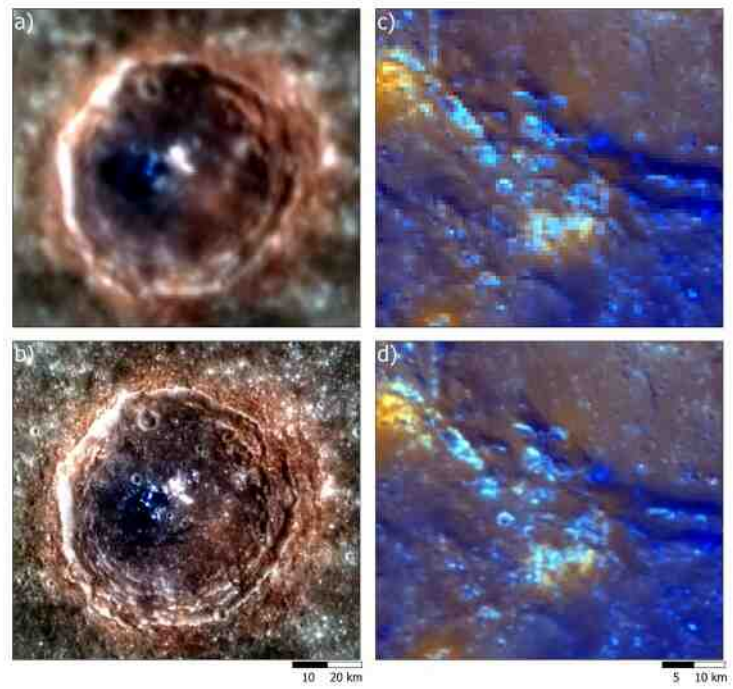


Figure 2 Details of the MDR 8-band mosaic (a, b) and the Basemap Enhanced Color Global Mosaic (c, d) at the original resolution (a, c) and (b, d) enhanced through GSA pansharpening at 166 m/px.

OPTIMISATION OF THE STC COLOUR TARGET ACQUISITION OF THE SURFACE OF MERCURY. Francesco Sala[1], Alberto Avallone[1], Maxence Delorme[2], Cristina Re[3], Emanuele Simioni[3], Adriano Tullo[3], Livio Agostini[3], Gabriele Cremonese[3], Manuel Iori[1]. [1]UNIMORE/DISMI, Reggio Emilia, Italy (253589@studenti.unimore.it), [2]Tilburg University/TiSEM, Tilburg, The Netherlands, [3]INAF/OAPd, Padua, Italy,

Introduction: For decades, the scientific community has devoted considerable efforts to studying Mercury, motivated by its unique position as the closest planet to the sun. The BepiColombo mission [1], a joint European and Japanese endeavor, represents a significant milestone in this exploration. Scheduled to begin the nominal mission in 2027, it will investigate Mercury from multiple scientific perspectives, including its surface as well as its interior and its surrounding environment. Within the European Mercury Planetary Orbiter, the SIMBIO-SYS instrument suite represents an integrated imaging system comprising three distinct yet complementary scientific channels [2]. The Stereo Imaging Channel (STC) is designed to perform global and regional imaging of Mercury's surface through two optical heads to acquire stereo pairs, each including a large panchromatic section and two broad-band colored filters [2]. This configuration enables a comprehensive three-dimensional reconstruction of the planet's surface allowing multispectral surveys of selected regions. The global mapping of the planetary surface will be performed in the first operative phases of the mission (6 Earth months), while the target acquisition with the color filters is scheduled for the second half of the year.

Our work has been focused on the scheduling optimization of the target coverage with the colored filters in this later phase of the mission, by defining an imaging scheduling problem [3] with both optical channels of STC. The goal of this problem is to cover all the identified target areas, each associated with a scientific rank value depending on their importance, with observations performed with all the four broadband filters belonging to both STC channels. The major constraints of such a task are the data volume that can be generated and the number of telecommands (TC) being limited. The data volume produced over the full mission phase is allocated at mission level to each instrument, while TC are operational constraints limiting the number of observations performable in each orbit. Another important driver is the solar incidence angle at acquisition time, which should be kept as low as possible for color acquisitions to obtain high informative observations. Once the observations have been acquired and downlinked back to Earth, image mosaicking will be performed to obtain full target coverage. To improve the mosaicking, the images have to be acquired including an overlap, which is the last of the major operational constraints.

Planning Pipeline: The problem as it is defined can be seen as a weighted Maximal Coverage Problem (MCP). In previous works [4] [5], this same variant of the MCP was solved through mixed integer programming; in our case, although an optimal solution would be desirable, we were more interested in performing a sensitivity analysis over the constraints in a fast and flexible way and, as such, we developed a heuristic approach. We intend to develop a second approach, a matheuristic based on the predict-then-optimize algorithm formulated for the Mars Express mission radar, MARSIS[5], to improve the performance of the heuristic.

The algorithm takes as inputs the frame data shapefiles generated by the Simulator for Operation of Imaging Missions (SOIM) [6], a tool developed within the SYMBIO-SYS team, which simulate the expected instrument pointing at specific time instances for each filter and at a constant minimum interval of one second. It then follows a two-step process: an observation definition phase and an optimization phase.

The observation definition phase follows a three-step pipeline: preprocessing, observation generation phase, and single-camera integration.

Preprocessing: The preprocessing phase takes the raw frame data and filters unneeded frames that are not intersecting any of the targets. We utilized the target convex hull to identify the intersection area between frames and targets; this ensures that there can only be a singular full sequence of frames for each target for every orbit. Finally, we associate each target with a set of points of interest.

Observation identification: The observation identification phase focuses on identifying and generating correct observations from the raw sequences of filtered frames by exploiting the convex hull property [Figure 1]. As the probe will be in an eccentric polar orbit around the planet, there is sizeable variation in the pixel/meter ratio between the frames captured near the poles and the ones captured near the equator. As such, we developed a dynamic filtering mechanism that would allow proper removal of unneeded frames for each observation by identifying the best possible timestep while respecting the overlap constraint.

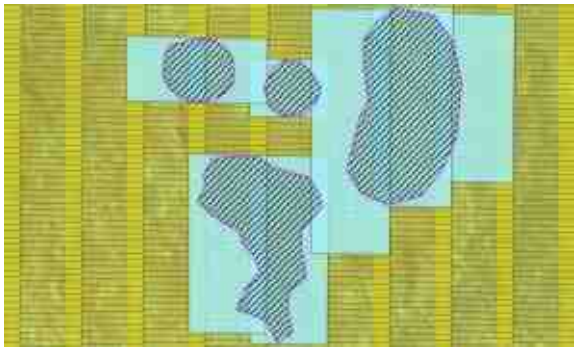


Figure 1: generated feasible observations (cyan) over the raw sequences of frames (yellow).

Single Channel Integration: Each of the optical heads will take observations with both filters at once, which marginally increases data consumption but drastically reduces overall TC requirements to cover the targets. As the shapefiles are generated for each filter separately, the observations need to be merged in pairs belonging to the same channel. Because of the convex hull property, for each filter, there can only be one valid observation of the same target in an orbit. The single channel integration pairs these observations together, generating sets of aggregated observations, one for each optical head.

The optimization phase selects the channel observations to be used by using a two-phase heuristic approach: independent target coverage and target coverage fusion.

Independent target coverage: we identify for each target a greedy coverage solution that can satisfy the active constraints while minimizing data and TC consumption by only selecting observations necessary for full target coverage [Figure 2]. We tag each observation with an "orbit jump" value that contains the orbit index of the first adjacent observation of the same target that it overlaps with for less than the required amount; if an observation is taken, the neighboring observations belonging to orbits within the range identified by the orbit index will be skipped. The targets are sorted by scientific rank, and we select the most relevant observations first. We have two observations sorting modalities: orbit order, which iterates over observations chronologically, starting at the last observation that still covers the first perceivable edge of the target; and point order, which identifies the observation that covers the most target points and then proceeds from there on each side. The algorithm does not use observations that do not add any new points of interest to the overall coverage. Constraints are evaluated against the "true" cost of each observation, meaning the data and TC resources required by the new observation minus the ones of any previously picked redundant observation covered by the newer one. The redundant observations are then discarded from the final selection.



Figure 2: final coverage with 3 observations (dark blue) compared to the original 15 (light blue).

Target coverage fusion: observations covering independent targets within an orbit can be merged together by performing a longer singular observation that covers both of them. This increases data consumption but reduces telecommands as it counts as a singular operation. The observation fusion is performed between the pairs of closest selected observations if the number of telecommands spent exceeds the constraint threshold for an orbit.

Conclusions and future research: Our approach focused on developing an initial heuristic solution to the problem. It has shown itself to be adaptable, has obtained substantial results and does not have high time and computing requirements. This makes it an especially useful tool for gauging the viability of planning strategies for the identified targets. We are currently working to integrate the process into the SIMBIO-SYS planning pipeline which will be nominally used for operational instrument sequences. We are also currently developing exact solution methods for the problem to compare the effectiveness of our heuristic.

References:

[1] J. Benkhoff *et al.*, "BepiColombo - Mission Overview and Science Goals," *Space Sci. Rev.*, vol. 217, no. 8, p. 90, 2021, doi: 10.1007/s11214-021-00861-4.

[2] G. Cremonese *et al.*, "SIMBIO-SYS: Scientific Cameras and Spectrometer for the BepiColombo Mission," *Space Sci. Rev.*, vol. 216, no. 5, p. 75, 2020, doi: 10.1007/s11214-020-00704-8.

[3] B. Ferrari, J.-F. Cordeau, M. Delorme, M. Iori, and R. Orosei, "Satellite Scheduling Problems: A survey of applications in Earth and outer space observation," *Comput. Oper. Res.*, vol. 173, p. 106875, 2025, doi: 10.1016/j.cor.2024.106875.

[4] A. Avallone et al., "Stochastic Optimization of the MARSIS Observation Scheduling Problem using a Predict-then-Optimize Approach," 2025, IWPSS conference, Toulouse.

[5] F. Ferrari et al., "A Predict-then-Optimize Approach for the Research of Underground Water on Mars," 2025, tech. rep. UNIMORE.

[6] E. Simioni et al SOIM User Manual v6.0 10.20371/INAF/TechRep/202 (see ESA page)

Surface and Subsurface Morphometric Evidence for Lava Tubes on Venus. B. De Toffoli[1], R. Pozzobon[1,2,3], L. Carrer[4] and F. Sauro[1]. [1]Department of Geosciences, University of Padova, Padova, Italy (barbara.detoffoli@unipd.it), [2] Department of Physics and Astronomy, University of Padova, Padova, Italy, [3] CISAS - Centro di Ateneo Studi e Attività Spaziali G. Colombo, University of Padova, Padova, Italy, [4]Aresys s.r.l., Via Luigi Cadorna 66a, Vimodrone, 20055 Milano, Italy.

Introduction: The exploration of subsurface cavities in our Solar System has long been a subject of great interest, with lava tubes emerging as particularly intriguing features since they can provide substantial insights into volcanic processes, planetary evolution and will be targets for future exploration [1,2,3]. These underground cavities are well-documented on Earth [4,5], and on Mars and the Moon collapse sinkhole-like morphologies (pits) have been identified in volcanic regions [6,7]. On Venus, the existence of lava tubes has been hypothesized based on observations of pit craters on volcanic slopes [8,9,10,11,12], discontinuous lava channel segments [13], and potential tube-fed lava flows [14]. However, a comprehensive morphometric analysis to definitively link these surface features to subsurface cavities formed by lava flows has not been conducted on Venus until now.

Methods: We utilized the global Magellan synthetic aperture radar left-look mosaic with a 75 m/pixel spatial resolution. The researchers identified and mapped individual pit structures on volcanic edifices larger than 100 km in diameter [15]. Quantitative morphometric analyses were performed, including calculating the minimum bounding geometry for individual pits and entire pit alignments. This process characterized the planform dimensions, overall geometry, and spatial distribution of the pit chains. All mapping was conducted using QGIS open-source software.

For depth estimate at each pit location, this study applies a previously developed methodology to estimate the depth of Venusian pit craters using orbital synthetic aperture radar (SAR) data [16]. The method analyzes radar reflections from pit walls facing the illumination direction.

In the absence of high-resolution digital terrain models, this study used a simplified approach to estimate the volumes of cave collapses and lava tube conduits, based on previous literature [17].

Results:

Surface: Our study identified four potential lava tube collapse chains on Venus, located on the flanks of prominent volcanic edifices: Nyx Mons, Otafuku Tholi, Sif Mons, and Theia Mons. The identified chains, spanning 25 to 65 km in length, comprise 8 to 44 individual collapse features and exhibit sinuous geometry typical of lava tube pit chains. Their mean sinuosity index of 0.79 contrasts with the more linear tectonic collapse alignments (average index 0.98). The pit chains follow the maximum slope of the terrain, consistent with lava flow directions. Their widths remain relatively constant along the chain, distinguishing them from tectonic collapse features. All four instances are located in areas characterized by extensive lava flows and are spatially correlated with surface evidence of volcanic activity visible in SAR imagery.

Subsurface: By examining the relationship between pit width and inferred void depth, a clear distinction emerges between the candidate lava tube collapses and tectonic collapse features. Lava tube pit chains exhibit a more constrained width-to-depth ratio distribution, reflecting the consistent geometry of underlying conduits. In contrast, fault-related tectonic pit chains show a stronger positive correlation between width and depth, signaling the lack of a constrain due to a pre-existing underlyingng cavity [10, 18]. This trend divergence aligns with observations from Earth, Moon, and Mars [17]. Combining surface and subsurface evidence, the study interprets four identified collapse chains as lava tube pit chains. The morphometric characteristics provide a distinctive fingerprint, allowing differentiation between lava tube occurrences and other pit alignments, such as those associated with tectonic structures.

Moreover, despite Venus's Earth-like gravity, these structures exhibit unexpectedly large scales, comparable to lunar lava tubes. The analysis of the linear volume and pit widths suggests an overcrusting formation mechanism for Venusian lava tubes, similar to those found on Earth and Mars [17]. This process typically occurs in lava flows with low viscosity and relatively high, constant effusion rates, indicating extended periods of volcanic activity [19]. An additional unique trend in tube cross-section aspect ratio v. liner volume was identified, suggesting a formation and growth process dominated by lateral spreading of the tube rather than vertical deepening. This unexpected behavior might be attributed to Venus's distinctive surface conditions, which could affect lava flow behavior. The high atmospheric pressure may favor lateral propagation over vertical thickening before crust solidification [20,21].

Conclusion: These findings not only confirm the existence of lava tubes on Venus but also reveal unique characteristics that distinguish them from similar structures on other planets. The research opens new avenues for comparative planetology

studies and enhances our understanding of Venusian volcanic processes.

The discovery of these lava tubes identifies key targets for future missions, particularly the upcoming EnVision mission. Its Subsurface Radar Sounder (SRS) aims to provide crucial information on Venus's geology and potentially unveil more about these subterranean structures. These environments might offer insights into Venus's past climate and possible habitability, contributing to our broader understanding of extreme environments and the potential limits of life in the universe.

References:

[1] Léveillé, R.J. & Datta, S. "Lava tubes and basaltic caves as astrobiological targets on Earth and Mars: a review." Plan. Sp. Sci. 58.4 (2010): 592-598. [2] Sawłowicz, Z. "A short review of pyroducts (lava tubes)." Annales Societatis Geologorum Poloniae. Vol. 90. No. 4. Polskie Towarzystwo Geologiczne, 2020. [3] Titus, T. N., et al. (2021). A roadmap for planetary caves science and exploration. Nature Astronomy, 5(6), 524-525. [4] Bunnell, D. "Caves of fire: Inside America's lava tubes." National Speleological Society, 2008. [5] Tomasi, I., et al. "Inception and evolution of La corona lava tube system (Lanzarote, canary Islands, Spain)." Journal of Geophysical Research: Solid Earth 127.6 (2022). [6] Carr, M.H. "Volcanism on mars." JGR 78.20 (1973): 4049-4062. [7] Carr, M. H., et al. "Some Martian volcanic features as viewed from the Viking orbiters." JGR 82.28 (1977): 3985-4015. [8] Davey, S. C., et al. "Hierarchical clustering of pit crater chains on Venus." Canadian Journal of Earth Sciences 50.1 (2013): 109-126. [9] Sawford, W. C., et al. "Pit Crater chains in the Nyx mons region, Venus." (2015). [10] Wyrick, D. Y., and D. L. Buczkowski. "Pit crater chains across the solar system: evidence for subterranean tectonic caves, porosity and permeability pathways on planetary bodies." JGR Planets 127.12 (2022). [11] Melville, G. P. (1994). Lava tubes and channels of the Earth, Venus, Moon and Mars. [12] Lopez, I., et al., "The volcanology of Idunn Mons, Venus: The complex evolution of a possible active volcano" J. Volc. Geoth. Res., 421, (2022). [13] Lang, N. P., & Hansen, V. L. Venusian channel formation as a subsurface process. JGR-Planets, 111(E4) (2006). [14] Mouginis-Mark, P. Geomorphology and volcanology of Maat Mons, Venus. Icarus, 277, 433-441 (2016). [15] Hahn, R.M., & Byrne, P. "A morphological and spatial analysis of volcanoes on Venus." JGR- Planets 128.4 (2023). [16] Carrer, L. et al. "Assessing the Morphometry of Pit Craters on Venus from Orbital Synthetic Aperture Radar Data." IEEE Tran. Geos. Rem. Sens. (2024). [17] Sauro, F, et al. "Lava tubes on Earth, Moon and Mars: A review on their size and morphology revealed by comparative planetology." Earth-Sci. Rev 209 (2020): 103288. [18] Ferrill, D. A., et al. Coseismic, dilational-fault and extension-fracture related pit chain formation in Iceland: Analog for pit chains on Mars. Lithosphere, 3(2), 133-142. (2011). [19] Dragoni, M., et al. A model for the formation of lava tubes by roofing over a channel. J. Geophys. Res. 100 (B5), 8435–844. (1995). [20] Flynn, I. et al. "Adaptation of a thermorheological lava flow model for Venus conditions." JGRPlanets 128.7 (2023). [21] Filippucci, M et al., "Conditions for crust and tube formation in lava flows with power-law rheology." Bollettino di Geofisica Teorica ed Applicata 52.2 (2011).

Acknowledgment: BDT was supported by the European Union NextGenerationEU programme and the 2023 STARS Grants@Unipd programme "HECATE". FS was supported by the 'The Geosciences for Sustainable Development' project (Budget Ministero dell'Università e della Ricerca–Dipartimenti di Eccellenza 2023–2027 C93C23002690001).

MARTIAN DUST PROPERTIES IN MARS YEARS 34 TO 38: TGO/NOMAD UVIS-LNO NADIR DATA PRELIMINARY RESULTS.

F. Oliva[1,*], E. D'Aversa[1], G. Bellucci[1], F.G. Carrozzo[1], I.R. Thomas[2], L. Ruiz Lozano[6], O. Karatekin[6], F. Altieri[1], F. Daerden[2], B. Ristic[2], M.R. Patel[3], J. Mason[3], Y. Willame[2], M.A. López-Valverde[4], A.C. Vandaele[2] and G. Valentini[5]

[1]*Istituto di Astrofisica e Planetologia Spaziali* (IAPS/INAF), Rome, Italy; [2]*Royal Belgian Institute for Space Aeronomy* (IASB-BIRA), Brussels, Belgium; [3]*School of Physical Sciences, The Open University*, Milton Keynes, U.K; [4]*Instituto de Astrofisica de Andalucia* (IAA), Consejo Superior de Investigaciones Científicas (CSIC), Granada, Spain; [5]*Agenzia Spaziale Italiana* (ASI), Rome, Italy; [6]*Royal Observatory of Belgium*, Brussels, Belgium. *Correspondence: fabrizio.oliva@inaf.it

Nadir and Occultation for MArs Discovery (NOMAD [1]) is a suite of three spectrometers onboard the ESA/Roscosmos Trace Gas Orbiter spacecraft. Its main focus is the study of Martian trace gases, but we exploit it here for the investigation of Martian dust from the top of the atmosphere down to the surface. The nadir datasets of UVIS (200 – 650 nm) and LNO (2200 – 3800 nm) channels provide an extended spectral range that is useful for such a purpose, as demonstrated in [2]. In this study we present the preliminary results on the microphysical properties of dust retrieved from the combined spectra of the two channels. A careful processing has been applied to LNO data to account for issues (likely of electrical origin) in the absolute radiometric calibration [2].

We select spatially and temporally coincident data, in order to reduce potential biases deriving from strong differences in the sampled surface regions. The spectral surface albedo is obtained from clear-sky MEx/OMEGA observations [3] derived through an ad hoc modification of the SAS algorithm [4] which is capable of removing the atmospheric contribution from the data. As a result, we select the range 360 – 590 nm for UVIS data (accounting for the minimum OMEGA wavelength and for known issues longwards of 590 nm) and the range 2200 – 2550 nm for LNO (since approximately devoid of strong gaseous absorptions and hence providing a reliable estimation of the spectral continuum).

At this stage, ice observations are filtered out adopting the same conditions on UV reflectances as in [5]. The MITRA radiative transfer (RT) tool [6,7] is used to perform the retrievals. Dust optical constants by [8] are adopted to cover the composite spectral range (360 – 2550 nm) and, given that grains' shape is still largely unconstrained, spherical scatterers are assumed.

The retrieval on the whole combined UVIS+LNO dataset, encompassing observations from March 2018 (MY34) to May 2025 (MY38), is currently ongoing. Once complete, the results from this analysis will provide valuable information on Martian dust climatology during the different Mars Years.

Acknowledgements

ExoMars is a space mission of the European Space Agency (ESA) and Roscosmos. The NOMAD experiment is led by the Royal Belgian Institute for Space Aeronomy (IASB- BIRA), assisted by Co-PI teams from Spain (IAA-CSIC), Italy (INAF-IAPS), and the United Kingdom (Open University). This project acknowledges funding by the Belgian Science Policy Office (BELSPO), with the financial and contractual coordination by the ESA Prodex Office (PEA 4000103401, 4000121493), by the Spanish MICINN through its Plan Nacional and by European funds under grants PGC2018-101836-B-I00 and ESP2017-87143-R (MINECO/FEDER), as well as by UK Space Agency through grants ST/V002295/1, ST/V005332/1, ST/Y000234/1 and ST/X006549/1 and Italian Space Agency through grant 2018-2-HH.3. The IAA/CSIC team acknowledges financial support from the State Agency for Research of the Spanish MCIU through the 'Center of Excellence Severo Ochoa' award for the Instituto de Astrofísica de Andalucía (SEV-2017-0709). This work was supported by the Belgian Fonds de la Recherche Scientifique – FNRS under grant numbers 30442502 (ET_HOME) and T.0171.16 (CRAMIC) and BELSPO BrainBe SCOOP Project. US investigators were supported by the National Aeronautics and Space Administration. Canadian investigators were supported by the Canada Space Agency.

References

[1] Neefs, E., et al, 2015. Appl. Opt. 54, 28, 8494-8520.
[2] Oliva, F., et al., 2025. EPSC-DPS2025-1416.
[3] Bibring, J.P. et al., 2004. ESA SP-1240.
[4] Geminale, A., et al, 2015. Icarus 253, 51-65.
[5] Wolff, M. et al., 2019. Icarus, 332, 24-29.
[6] Oliva, F., et al, 2018. Icarus 300, 1-11.
[7] D'Aversa, E., Oliva, et al., 2022. Icarus, 371, 114702.
[8] Wolff, M.J., et al, 2010. Icarus, 208.

Geomorphological evidence of ice activity on Mars surface at mid-latitude

Marco Moro [1], Adriano Nardi [1], Matteo Albano [1], Monica Pondrelli [2], Antonio Piersanti [1], Michele Saroli [1,3], Beatrice Baschetti [4,5], Erica Luzzi [6], Lucia Marinangeli [7] and Nicola Bonora [3]

1) Istituto Nazionale di Geofisica e Vulcanologia, Via di Vigna Murata 605, 00143, Rome, Italy
2) Dipartimento di Ingegneria e Geologia International Research School of Planetary Sciences, Università d'Annunzio, viale Pindaro 42, 65127 Pescara, Italy
3) Dipartimento di Ingegneria Civile e Meccanica, Università degli Studi di Cassino e del Lazio meridionale, via G. di Biasio 43, 03043 Cassino, FR, Italy
4) Istituto Nazionale di Astrofisica (INAF) - IAPS, Via del Fosso del Cavaliere 100, 00133, Rome, Italy
5) Dipartimento di Geoscienze, Università degli Studi di Padova, Via G. Gradenigo 6, 35131, Padua, Italy
6) Mississippi Mineral Resources Institute, The University of Mississippi, University, MS, USA
7) Dipartimento di Scienze Centro Ud'A Terra-Mare, Università d'Annunzio, Via Vestini 31, 66013, Chieti, Italy

Introduction: The presence of water ice (permafrost) at mid and low latitudes on Mars is widely supported by radar investigations (e.g., SHARAD [1-4]), spectrometric data [5-8], and paleoclimate models [9-11]. However, the exact composition, age, and potential current activity of these deposits remain poorly constrained. In the Ismenius Lacus area (lat ≈ 34°N), the presence of permafrost and glacial forms has been hypothesized [12], but the dynamics are still debated. This study presents new geomorphological evidence, based on high-resolution stereoscopic (3D) analysis (HiRISE and CTX imagery), that indicates active plastic glacial activity in the Ariguani Delta system (Fig.1), within Ismenius Cavus.

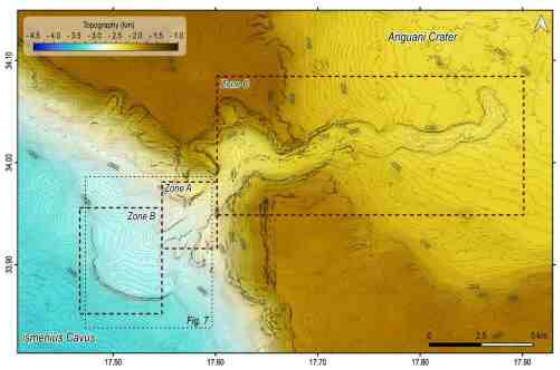


Figure 1. *The Ariguani delta system is subdivided into three study areas: A, B, and C. They are named, from right to left, Feed, Flow, and Expansion Zones.*

Method: geomorphological analyses were conducted using a digital stereoscope to study very high resolution (25 cm per pixel) stereoscopic pairs derived from the HiRise/MRO dataset. Local pressure and temperature variations were compared on an annual time scale using TES/MGS dataset.

Geomorphological Evidence: The stereoscopic analysis revealed a distinctive set of surface morphologies that are incompatible with a fluvial origin but are diagnostic of glacial flow.

Sharp-Edged Polyhedra (SEP): The entire area, including the delta surface, does not exhibit a "pitted" texture as previously suggested, but is characterized by convex, sharp-edged polyhedra (SEP). These features, ranging from 10 to 100 m in size, are interpreted as the surface expression of an underlying glacial mass (Fig. 2c).

Evidence of Plastic Flow: In the feeder channel area (Zone A), the SEPs are arranged in "chevron patterns". This geometry is clear evidence of differential flow, typical of glaciers, where velocity is maximum at the center and minimum at the edges due to friction with the canyon walls (Fig. 2a).

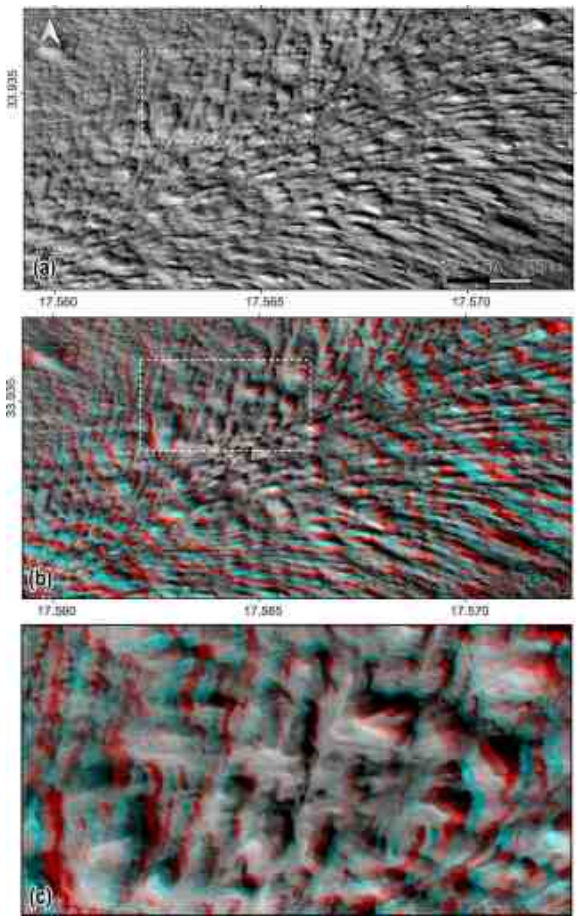


Figure 2. *Chevron pattern composed of SEP structures. (a) 2D image; (b) 3D image; (c) enlargement of the area highlighted with dashed rectangle. To observe anaglyphs B and C, special glasses with red and blue lenses are required. (Credits: HiRISE, NASA/JPL/University of Arizona)*

Evidence of Recent Activity: On the right flank of the canyon (Zone A), we identified open en-echelon fractures. The fact that these fractures are "open" and not filled by aeolian deposits (which are ubiquitous in the area) suggests very recent and likely ongoing dynamics (Fig. 3).
Feeder Zone Morphology: Zone C, the system's feeder area, shows a sapping morphology but is not fluvial. There is no point source; instead, flows appear to originate perpendicularly from the lateral escarpments, suggesting diffuse feeding from the walls.

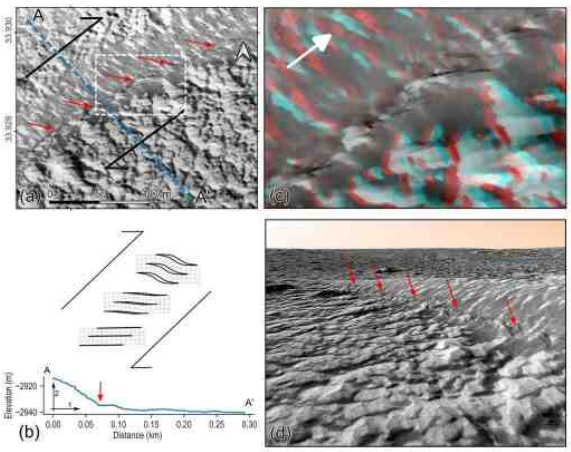


Figure 3. *En-echelon fractures (red arrows): (a) raw image. Black arrows show the sliding direction according to the scheme of figure (c); (b) cinematic scheme and cross-sectional profiles A-A' (dashed blue line); (c) anaglyph of the area indicated in panel (a) with the dashed white rectangle. White arrow indicates the light direction; (d) 3D view. This area is located on the right side of Ariguani canyon (A zone of Fig.1). (Credits: HiRISE, NASA/JPL/University of Arizona).*

Mechanism and Discussion: We analyzed Mars Global Surveyor (TES) temperature and pressure data for the study area. The results show that current environmental conditions are compatible with the year-round stability of water ice (H_2O). Average values are 6.87 mbar and 264.31 K; only in summer can the temperature touch the triple point. We propose a non-meteorological (unlike terrestrial glaciers), endogenous feeding mechanism. The lithostatic pressure ($P_L = \rho \cdot g \cdot h$), combined with the geothermal gradient, is sufficient to induce partial melting of permafrost at estimated depths of 50 to 100 m. This deep, plastic/liquefied layer is "squeezed" and ascends along the escarpments, generating neo-glacial flows that actively feed the glacial tongue in Zones A and C (Fig. 1). This same mechanism (deep melting due to pressure) can also explain other regional morphologies observed: (i) subsidence of U-shaped valleys: endorheic (closed) basins that we interpret as subsidence due to the emptying of melted permafrost at depth; (ii)"ring-mold" craters: impact craters that appear "filled" by SEPs, indicating that the plastic flow has invaded the depression; (iii) Deep-seated Gravitational Slope Deformations (DGSDs): large-scale slides favored by the presence of a weak, plastic layer (melting permafrost) at depth.

Conclusions: Our high-resolution stereoscopic observations provide strong evidence for active and recent glacial dynamics at Martian mid-low latitudes (Ismenius Lacus). The entire Ariguani Delta system is reinterpreted as a glacial environment.
The proposed feeding mechanism is not atmospheric but linked to permafrost melting induced by lithostatic pressure, which generates ice flows from the escarpments.
We propose the Sharp-Edged Polyhedra (SEP) as a new diagnostic marker for identifying ongoing glacial dynamics on Mars, potentially usable for future automated detection approaches.

References:
[1] Bramson A.M. et al. (2015) *Geophys. Res. Lett.*, 42, 6566–6574, https://doi.org/10.1002/2015GL064844.
[2] Petersen E.I.; et al. (2018) *Geophys. Res. Lett.*, 45, 11595–11604, https://doi.org/10.1029/2018GL079759.
[3] Plaut J.J.; et. al. (2009) *Geophys. Res. Lett.*, 36, L02203, https://doi.org/10.1029/2008GL036379.
[4] Xu X. et al. (2025) *JGR Planets*, 130, e2023JE008145, https://doi.org/10.1029/2023JE008145.
[5] Feldman W.C. et al. (2002) *Science*, 297, 75–78, https://www.doi.org/10.1126/science.1073541.
[6] Pathare A.V. et al. (2018) *Icarus*, 301, 97–116, https://doi.org/10.1016/j.icarus.2017.09.031.
[7] Murchie S. et al. (2007) *J. Geophys. Res.*, 112, E05S03, https://doi.org/10.1029/2006JE002682.
[8] Christensen P.R. et al. (2001) *J. Geophys. Res.*, 106, 23823–23871, https://doi.org/10.1029/2000JE001370.
[9] Madeleine J.B. et al. (2009) *Icarus*, 203, 390–405, https://doi.org/10.1016/j.icarus.2009.04.037.
[10] Head J.W. (2003) *Nature*, 426, 797–802, https://doi.org/10.1038/nature02114.
[11] Vincendon M. et al. (2010) *J. Geophys. Res.*, 115, E10001, https://doi.org/10.1029/2010JE003584.
[12] Dehouck E. et al. (2010) *Planet. Space Sci.*, 58, 941–946, https://doi.org/10.1016/j.pss.2010.02.005.

ANALYIS AND MITIGATION OF INTERFERENCES IN MARSIS RADARGRAMS: A COMPUTER VISION APPROACH

Alessandro Piombini[1], R. Orosei[2], [1]Alma Mater Studiorum – Università di Bologna, alessandro.piombini8@gmail.com, [2]Istituto di Radioastronomia – Istituto Nazionale di Astrofisica (IRA-INAF) (Via Piero Gobetti 101, 40129 Bologna, Italy, roberto.orosei@inaf.it)

Introduction: MARSIS is a radar mounted on board the Mars Express spacecraft. Its primary goal is to map the distribution of water, both in liquid and solid form, in the Martian subsurface.

The data were acquired by transmitting radio pulses centered at 1.8, 3, 4, or 5 MHz, each with a bandwidth of 1 MHz [1]. The raw data produced by the radar, corresponding to a single orbit, consist of a matrix of echoes, in which the columns represent the individual echoes.

If necessary, a reduced amount of data can be saved in a flash memory and sent to Earth still in raw form, where they undergo a processing operation.

Nevertheless, the data, both raw and processed, remain strongly affected by various noise sources, including interference generated by onboard electronics, local plasma resonances, attenuation and dispersion introduced by the ionosphere, and echoes originating from distant regions of the surface.

It has been hypothesized that, once the echo matrix is projected into the Fourier frequency space through a two-dimensional transform, the effects described above become more easily recognizable and separable. The result is a representation that we will call the "Doppler–frequency diagram."

After examining a large amount of samples, three main types of interference were classified, each with its own characteristic appearance, while it was observed that the useful part of the signal is concentrated in a very narrow vertical band which, in the raw data, aligns along the Doppler frequency caused by the spacecraft's vertical motion.

It is hypothesized that it may be possible to use computer vision techniques to automatically identify the interference in order to create a systematic catalog, facilitating statistical analysis.

The algorithms were developed in Python using the OpenCV library.

The YOLO (You Only Look Once) algorithm [2] was tested for the identification of the last type.

The second part of the work focused on filtering the processed data using statistical criteria based on the median values of the columns of the Doppler–frequency diagram.

Interferences detection: The data analyzed for this thesis work concern approximately 5,800 orbits. After examining a large portion of images, it was possible to identify three types of interference differing in morphology and frequency.

The first type appears as a set of horizontal lines of varying intensity extending across the entire image.

The developed algorithm, after converting the image to grayscale and applying equalization to enhance contrast, calculates the average brightness for each row and defines a threshold at the 20th percentile to identify anomalous rows; finally, the peaks exceeding the threshold are detected using SciPy's find_peaks() function (Figure 1).

The second type appears as a series of bright peaks arranged diagonally in a regular pattern, almost forming a "constellation."

The detection algorithm in this case involves a combination of filtering, to reduce noise while preserving edges, and binarization, producing a black-and-white image based on a specifically chosen threshold to retain only the brightest parts. Using the DBSCAN clustering algorithm [3], nearby points are grouped into a single cluster, and the centroid of each cluster is calculated. The obtained centroids are then input into the iterative RANSAC method [4], which allows estimating the parameters of a model from a dataset containing outliers, i.e., anomalous or noisy values (Figure 2).

The last type occurs less frequently than the previous ones and appears as an isolated bright peak, usually near the center of the image. For automatic detection of this interference, YOLO, a widely used real-time object detection algorithm [2], was employed. YOLO is a pre-trained model on large generic datasets; however, it is necessary to adapt it to the problem domain, in this case the recognition of third-type interferences.

A dataset was thus created, divided into training, validation, and test sets, on which the model was then trained, achieving more than satisfactory performance (Figure 3).

Data filtering: As mentioned, it was observed that, after projecting the echo matrix into the Fourier frequency domain, the useful part of the signal, that is, the echo from the surface and subsurface, is concentrated in a very bright, narrow vertical band.

It is therefore hypothesized that, instead of mitigating noise by removing the interferences, the signal can be improved by eliminating everything outside this band.

The algorithm, this time developed in MATLAB, is based on calculating the median of each column, obtaining a one-dimensional representation of the spectrogram with peaks corresponding to the portion

of the useful part of the signal, as it is usually the brightest part of the image (Figure 4).
Then, to decide a threshold below which the median values are set to zero, Otsu's binarization method was used, which automatically calculates the threshold by minimizing intra-class variance, assuming the image contains only two classes.
Once the filtering is performed, it is sufficient to calculate the inverse transform and compare the signal-to-noise ratio before and after the cleaning operation (Figure 5). On 25 filtered orbits, an average increase of ~16 dB was observed.

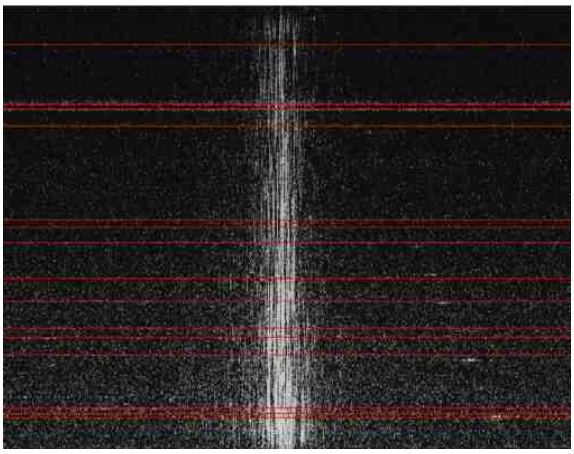


Fig. 1 – First type, the red lines represent the detected interferences

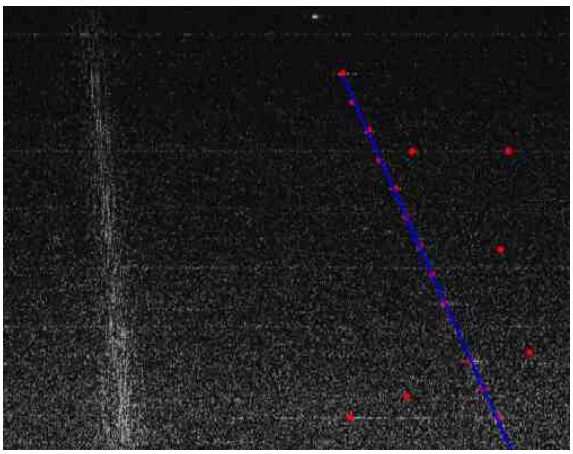


Fig. 2 – Second type, the red dots represent the centroids of the clusters, the blue line is the interefence detected

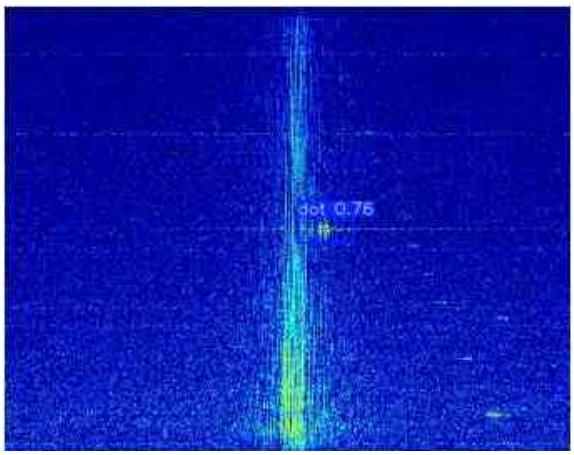


Fig. 3 – Third type, output of the inference of the fine-tuned YOLO model on unseen data

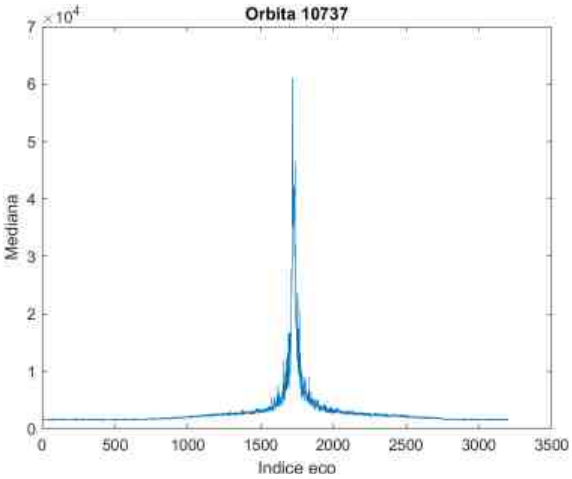


Figura 4 - Median of the values in the Doppler–frequency diagram

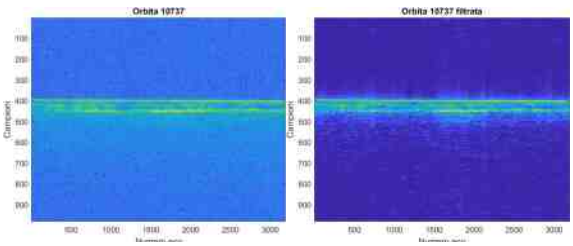


Figura 5 - Echo matrix before and after filtering

References:

[1] R. Orosei, R. Huff, A. Ivanov, R. Noschese, ESA Technical Report MARSIS ICD (2017). [2] J. Redmon, S. Divvala, R. Girshick, A. Farhadi, arXiv:1506.02640 (2015). [3] M. Ester, H.-P. Kriegel, J. Sander, X. Xu, KDD, 226–231 (1996). [4] M. A. Fischler, R. C. Bolles, Commun. ACM 24, 381–395 (1981). [5] N. Otsu, IEEE Trans. Syst. Man Cybern. 9, 62–66 (1979).

MOSTO: a 3D virtual reality hyperspectral analysis application for CRISM MTRDR data

M. Baroni[1] and M. di Mambro[1], M. Mariotti[1], A. Pisello[1], M. Petrelli[1], D. Perugini[1]

[1]Università degli Studi di Perugia, Dipartimento di Fisica e Geologia FISGEO, Perugia, Italy

Introduction: Hyperspectral data are essential for investigating the composition of planetary surfaces and have been a pivotal tool to understand the geological history of many planetary bodies. On Mars, the highest resolution hyperspectral data were gathered by the Compact Reconnaissance Imaging Spectrometer for Mars (CRISM), onboard the Mars Reconnaissance Orbiter (MRO). CRISD collected hyperspectral datacubes with a spatial resolution of up to 18.4 m/px and a spectral resolution of 6.55 nm within a spectral range between 362 nm and 3920 nm [1]. CRISM datacubes are usually analyzed by means of various softwares (ENVI©, Python), by creating RGB maps using the spectral parameters datacube do derive summary information about the scene [2] and then selecting regions of interest (ROIs) from which to extract the spectral information to derive a main composition of that area. However, 2D compositional maps inherently decouple the spectral information from the 3D geometry and topography of the scene, obstructing a more complete and intuitive understanding of the geology of the area under study. To overcome this intrinsic limitation, we present an application called MOSTO (Mars Orbital Spectroscopical and Topographical Odissey) written in Python and Unity 6© that allows CRISM data to be explored in Virtual Reality (VR), mimicking a geological field experience.



Figure 1: example of 3D object of Kai crater (Meridiani Planum, CRISM ID: FRT00009B5A) with false color CRISM map coregistered on top. Height is exaggerated by a factor of 2.

Dataset and methods: At the moment, our pipeline can ingest only Map Projected Target Reduced Data Records (MTRDR) of CRISM, that are the most advanced data formats in which CRISM data can be found. Each MTRDR datacube consists of various components, on which we focused on three: the spectral reflectance datacube, the summary parameters datacubes and the geometry datacube. The first one provides the spectral information of the Martian surface, the second one the spectral parameters defined by [2], and the third one provides useful ancillary information about the terrain geometry, including the elevation per pixel. Using this last one, we were able to create in Python, with the aid of the package PyVista [4], a 3D model of the scene and, by applying the spectral parameters to create RGB maps accordingly with [2], we were able to map them onto the 3D model, obtaining so a 3D representation of the scene (see figure 1). By importing this model alongside all the RGB maps and spectral parameters in Unity 6©, we created an application to then interact with the scene directly and immersively, with the user capable of live changing the texture (RGB map), as well as extracting spectra from ROIs by drawing them using polygons. Then, the spectra corresponding to the pixels that lies inside the polygon are extracted from the spectral reflectance datacube, to be finally analyzed by a secondary Python pipeline to retrieve the mean spectrum encompassed by the polygon. This mean spectrum can then be normalized/continuum removed by various means: convex hull, neutral spectrum selection [5] and another method we called all-map, that functions by using as neutral spectrum the median spectrum of all the black pixels in the RGB map. Lastly, the obtained products can be exported in a selected format along with all the relevant metadata (i.e. polygon position, height, phase angle etc).

Discussion and Conclusions: We constructed an application for VR compositional mapping of CRISM data that will enable more geologically meaningful and intuitive selection of ROIs than conventional mapping, such as was already proven regarding morphological analysis on digital outcrops [6,7]. Indeed, by combining CRISM compositional maps with high-resolution topography in VR, we can directly link mineral assemblages to slopes, landforms and stratigraphic contacts, sharpening geomorphological/geological interpretation and potential site of interest assessment in a way similar to Martian VR environments built from stereo DTMs [8]. Lastly, the developed application could also be beneficial for teaching and training purposes, in line with immersive virtual fieldwork studies that highlight the potential of such environments to reproduce key learning outcomes and improve accessibility [9].

Aknowledgments: Fondazione ICSC, Spoke 3 Astrophysics and Cosmos Observations. National Recovery and Resilience Plan (Piano Nazionale di Ripresa e Resilienza, PNRR) Project ID CN_00000013 "Italian Research Center on High-Performance Computing, Big Data and Quantum Computing" funded by MUR Missione 4 Componente 2 Investimento 1.4: Potenziamento strutture di ricerca e creazione di "campioni nazionali di R&S (M4C2-19)" - Next Generation EU (NGEU) - Progetto AI-VISIO-LAB (PI: Maurizio Petrelli). Agreement ASI-UniPG N. 2019-2-HH.0. The authors also acknowledge the support from MUR in the framework of SUPER-C, `Dipartimento di Eccellenza 2023-2027'.

References: [1] Murchie, S. et al. (2007). JGR Planets 112, E05S03. [2] C. E. Viviano-Beck et al. (2014), JGR Planets, 119, 1403-1431. [3] F. P. Seelos et al. (2016), LPSC XXXXVII, Abstract #1783. [4] Sullivan et al. (2019). JOSS, 4(37), 1450, [5] K. Seelos et al. (2012) CRISM 2012 Data Users' Workshop.http://crism.jhuapl.edu/data/CRISM_workshop_2012/agenda.php. [6] Caravaca et al. (2020) PSS 182, 104808 [7] Zhao et al. (2019) GSIS, *22*(4), 237–250. [8] J-R. Kim et al. (2012) C&G, Volume 44, Pages 184-195, [9] L. Guillaume et al. (2023) JGE, 71(4), 462–475.

Predict-then-optimize stochastic planning for MARSIS raw data acquisition A. Avallone[1], B. Ferrari[1], A. Cicchetti[2], M. Delorme[3], M. Iori[1], M. Lippi[4], and R. Orosei[5], [1]UNIMORE/DISMI, Reggio Emilia, Italy (alberto.avallone@unimore.it), [2]INAF/IAPS, Rome, Italy, [3]Tilburg University/TiSEM, Tilburg, The Netherlands, [4]UNIFI/DINFO, Firenze, Italy, [5]INAF/IRA, Bologna, Italy.

Introduction: The Mars Advanced Radar for Subsurface and Ionosphere Sounding (MARSIS) onboard Mars Express is a radar sounder and altimeter designed to investigate the structure of the subsurface of Mars. It operates during a 30-minute observation window around perihelion, collecting and storing up to 134 seconds of raw echoes per day in its flash memory [1]. The quality of data acquisitions is quantified by the Signal To Noise Ratio (SNR) of the echo received by MARSIS. Data quality is affected by instrument interference and environmental conditions, such as the Total Electron Content (TEC) of the ionosphere, illumination condition, intensity of solar activity, and ground topography.

To support MARSIS observations, which led to the discovery of water on Mars [2], we developed an automated and optimized planning approach to be integrated into the MARSIS Operation Center (MOC) [3]. Building on previous solutions [4], we deployed a predict-then-optimize approach [5], using machine learning and mathematical programming to enhance expected SNR in a stochastic environment interfering with MARSIS operations. We do not consider the scheduling of downlink [6] and assume that sufficient memory is available for acquisitions.

Planning Pipeline: To optimize the generation of observation plans, we built upon our previous approach [3][7][8], which used a sequential approach that integrates a Machine Learning (ML) phase with an optimization phase based on Mathematical Programming (MP) [9].

In the ML phase, the quality of future observations is predicted based on their relationship with several known environmental and instrumental features by using a neural network. The result values are classified into distinct quality levels and serve as inputs for the subsequent optimization phase.

In the optimization phase, we consider the current level of coverage of the planet and the data quality reached through past observations as a starting point. We formalized the planning problem through an MP model based on the maximal covering location problem, focusing on the South Pole of Mars. We also developed a matheuritic, which iteratively invokes smaller MP models.

In the current work, we introduce a more sophisticated and realistic formulation, that tackles the same problem but in a stochastic environment. The resulting methodology has been tested on the whole surface of Mars and can produce solutions for high-discretization instances of the problem.

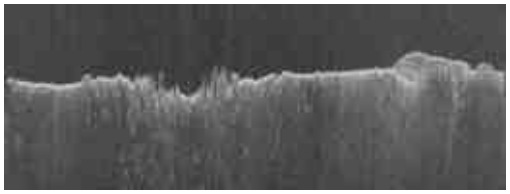
Stochastic Methodology: Our current work focuses on adapting the proposed planning pipeline to the dynamic and stochastic nature of the space environment. This includes accounting for factors such as extraordinary solar activity, which can disrupt radar operations or result in consistent data loss.

To address the dynamic aspects of the MARSIS planning problem, we employ a Dynamic Optimization (DO) in a rolling horizon framework [9], firstly solving an MP model periodically (e.g., once a month), and then allowing each solution to adapt by integrating updated information.

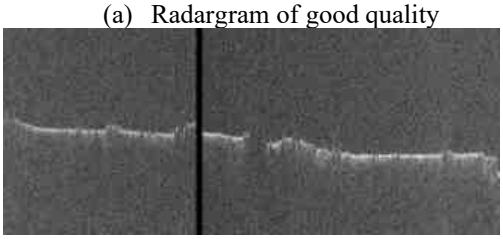
Potential disruptions and data loss may be included in the MP model by using stochastic information extracted from the historical mission dataset. To this aim we are developing a Scenario-Based Planning Approach [10], Incorporating stochastic elements into the optimization process facilitates the generation of more robust solutions, minimizing the need for significant adjustments by the MOC team.

Each scenario is realized by considering the different environmental features impacting the observation quality, as shown in Figure 1. An instrument-dependent error in the collection, storage, or transmission of data will cause the resulting radargram to have one or multiple black narrow strips (Figure 1b). This type of failure has a fairly random occurrence rate. Differently, an intense solar event may partially (Figure 1c) or totally (Figure 1d) interfere with the collection of data. This is caused by the ionosphere of Mars, whose high TEC during solar events blocks signal transmission [11]. The occurrence of events varies during an 11-year cycle, peaking in the middle, and each one consist a solar emission of energy (e.g., solar flares) or matter (e.g., interplanetary coronal mass ejection), which leads to higher probability of a total or partial blackout [12].

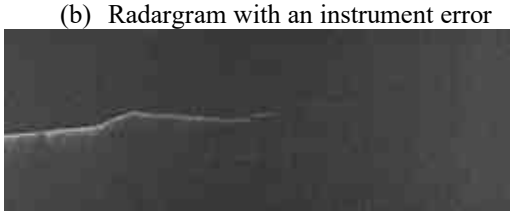
Results and Implementation: The mathematical model were implemented in Python using GUROBI as MP solver. They efficiently solved small-size instances of the problem but failed to solve large ones. This was expected due to the complexity of the problem and the need to consider a sufficiently large number of scenarios (30 or more), thus increasing the number of variables and constraints of the model. We could find optimal solutions for low-discretization instances within a few seconds. For higher-discretization instances, the matheuristic algorithm efficiently generates feasible schedules within one hour of computing time.



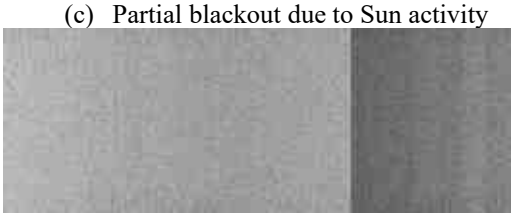
(a) Radargram of good quality



(b) Radargram with an instrument error



(c) Partial blackout due to Sun activity



(d) Total blackout due to Sun activity

Figure 1:. Classification of raw data radargrams acquired by MARSIS, following the classification proposed in [12]

We are now integrating planning into a Decision Support System (DSS) [14] to help the MOC's planning process. The DSS will provide daily recommendations for acquisitions, initially considering a horizon of a single month. Each recommended acquisition will include key performance indicators, such as ML-based quality predictions and coverage rates. These metrics will enable MOC planners to make informed decisions, balancing immediate objectives with long-term goals.

Conclusion and Future Research: This research focuses on the optimization of the raw data acquisition plan of MARSIS. The current methodology enhances the three key outcomes of our previous work [3]. First, the optimization algorithms allow to quickly produce a short-term and long-term observation plan. Second, ML predictions are a valuable standalone resource, supporting decisions on observation prioritization and trade-off evaluations. Third, our stochastic algorithms yield positive results under the high uncertainty of future observation.

We are now integrating our optimization tools into a user-friendly interface that will allow the MOC team to quickly make decisions supported by medium-term predictions and optimal covering solutions. We also plan to include in the DSS the option of automatically recognizing interesting features from the collected data, building on a computer vision approach [13]. Currently, we are exploring the application of similar methodologies to other instruments and missions, such as the BepiColombo mission.

Acknowledgments: This research was supported by the Italian Government and the Next Generation EU program, Mission 4, Component 1, project "Combining mAchine Learning and optImization for Planetary remote Sensing missiOns" (CALIPSO), Unique Project Code C53D23010010001. The authors gratefully acknowledge support from the Italian Space Agency (ASI) through contract 2024-40-HH.0 and operations of the Mars Express spacecraft by the European Space Agency (ESA).

References: [1] Jordan R. et al.*"The Mars express MARSIS sounder instrument"*, 2009, *PSS, 57* [2] Orosei R. et al., *"Radar evidence of subglacial liquid water on Mars"*, 2018, *Science, 361* [3] Ferrari B. et al., *"Dynamic optimization of the MARSIS raw data acquisition plan with machine learning and mathematical programming",* 2025, *CNSP XX.* [4] Ferrari B. et al. "*Satellite Scheduling Problems: A survey of applications in Earth and outer space observation"*, 2024, *Computers & Operations Research, 173* [5] Sadana, U., et al. *"A Survey of Contextual Optimization Methods for Decision Making under Uncertainty"*, 2024, *European Journal of Operational Research.* [6] Righini G. and Tresoldi E. *"A mathematical programming solution to the Mars Express memory dumping problem"*, 2009, *IEEE Transactions on Systems, Man, and Cybernetics, Part C, 40* [7] A. Avallone et al.*, "Stochastic Optimization of the MARSIS Observation Scheduling Problem using a Predict-then-Optimize Approach,",* 2025*, IWPSS conference, Toulouse.* [8] Ferrari B. et al. *"A Predict-then-Optimize Approach for the Research of Underground Water on Mars"*, 2024, technical report. [9] Glomb L. et al., *"A rolling-horizon approach for multi-period optimization"*, 2022, *European Journal of Operational Research,* 300 [10] King A.J. and Wallace S.W., *"Modeling with Stochastic Programming",* 2012, *Modeling with stochastic programming*. [11] Cartacci, M. et al., *"Improved estimation of mars ionosphere total electron content"*, 2017, *Icarus, 299* [12] Lester, M., et al., "The Impact of Energetic Particles on the Martian Ionosphere During a Full Solar Cycle of Radar Observations: Radar Blackouts", 2022, *JGR Space Physics, 127* [13] Pierau R.E. et al., *"Detection of Subsurface Layer Instances on Radargrams from Mars through Hyper-Spectral Image Construction"*, 2025, *CNSP XX*.

The application of σ-FORUM radiative transfer code to the Martian atmosphere

L. Buriola[1,2], E. Papandrea[2], T. Maestri[1], G. Liuzzi[3]

[1] Department of Physics and Astronomy "Augusto Righi", University of Bologna, Bologna, Italy
[2] National Research Council (CNR), Institute of Atmospheric Sciences and Climate (ISAC), Bologna, Italy
[3] Department of Engineering, University of Basilicata, Potenza, Italy

Introduction: Mars is the most studied planet after Earth because of its proximity, with the purpose of understanding its evolution, searching for life, and preparing for future human exploration. For these reasons, in the past years, a significant number of measurements have been collected through various satellite missions. These observations have provided valuable insights into the composition, structure, and dynamics of the Martian atmosphere, helping scientists better characterize the climate of the "Red Planet".

In the framework of the project "Earth Moon Mars" (EMM)[†], this study aims to create a new tool for the fast and accurate analysis of legacy and future Mars datasets, enhancing our understanding of the Martian atmosphere. Adopting a comparative planetology approach, this work also contributes to a broader understanding of the atmospheres of the Earth and other planetary bodies. The focus of the project is a forward model (FM), dedicated to simulating Martian spectra in the longwave region. It is foreseen that in the final pipeline, a retrieval module will be included for the inversion of radiance measurements and retrieve atmospheric parameters (see *Figure 1*). Building upon the flexibility and capabilities of the recently developed forward model σ-FORUM (also referred to as σ-IASI/F2N) [1], this project seeks to extend its application to the study of the Martian atmosphere.

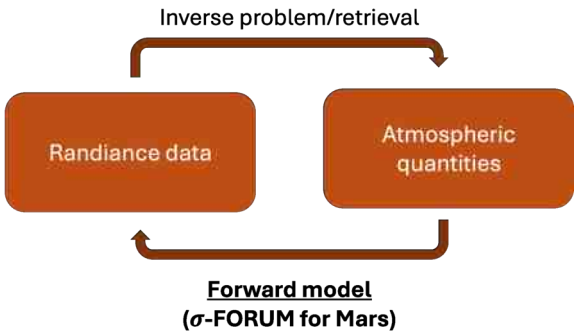


Figure 1: Scheme of the complete tool for the analysis of Martian data. Note that σ-FORUM is the FM.

The forward model: σ-FORUM is a high-performance and multipurpose radiative transfer code, originally developed for the study Earth's atmospheric radiation in the longwave region under nadir-viewing geometry. It generates high-resolution spectra (with a default spectral resolution of 10^{-2} cm^{-1}) while maintaining computational efficiency by using parametrized gas optical depths (ODs) that are precomputed and stored in lookup tables. As illustrated in *Figure 2*, the code requires as input the state of the atmosphere, including temperature and gas profiles, surface temperature and emissivity, clouds and dust parameters. Internally, it employs stored gas optical depths, cloud and aerosol properties and collision induced absorption (CIA) coefficients to compute the output radiance and associated Jacobians.

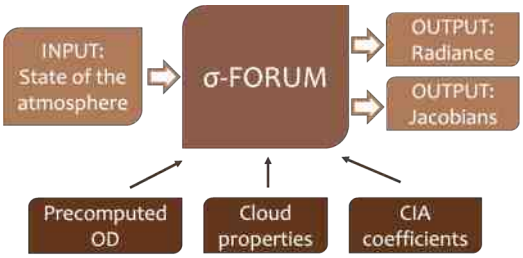


Figure 2: Scheme of the structure of σ-FORUM.

It is important to note that the code can simulate cloudy and dusty atmospheric conditions, which are particularly common on Mars. Multiple scattering is accounted for by means of scaling methods, namely the Chou scaling approximation [2] and the Tang correction [3]. σ-FORUM allows the computation of fast analytical derivatives of the radiance with respect to atmospheric properties and clouds, thus being suitable for the application in fast retrieval of infrared instruments.

Optical depths computation: To adapt σ-FORUM for use in Martian atmospheric studies, the code has been appropriately tuned to simulate the unique characteristics of the "Red Planet". New pressure levels have been chosen to discretize the atmosphere, properly accounting for the high variability of the surface pressure of the planet.

High resolution ODs for the most abundant and active gas species have been computed employing a line-by-line radiative transfer code, the Planetary Spectrum Generator (PSG) by NASA [4]. In *Table 1* information about the simulation parameters are summarized. The spectroscopic line parameters are gathered from HITRAN2020 [5] while the atmospheric quantities were derived from version 5.3 of the Mars Climate Database (MCDv5.3) [6]. The spectroscopic resolution used is very high (10^{-4} cm^{-1}) to account for the presence of extremely narrow lines due to the low pressures on Mars, and only later binned down to the default resolution of σ-FORUM.

[†] Part of the research activities described in this paper were carried out with contribution of the Next Generation EU funds within the National Recovery and Resilience Plan (PNRR), Mission 4 - Education and Research, Component 2 - From Research to Business (M4C2), Investment Line 3.1 - Strengthening and creation of Research Infrastructures, Project IR0000038 – "Earth Moon Mars (EMM)". EMM is led by INAF in partnership with ASI and CNR.

Gasses	CO_2, CO, H_2O, O_3, HCl, HDO
Spectroscopic Database	HITRAN2020
Frequency range	100-3000 cm^{-1}
Frequency resolution	10^{-4} cm^{-1}
Atmospheric Database	MCDv5.3
Atmospheric Layering	Custom, fixed pressure grid

Table 1: Summary of the chosen parameters for the computation of ODs.

Gas optical depths are computed for each gas g, for each pressure level l and for each wavenumber ν for a custom mean atmospheric state (see *Figure 3*). The same procedure is then repeated by modifying the temperature profile in increments of ±10 K, covering the range from −60 K to +60 K, in order to obtain optical depths as a function of temperature. Finally, the ODs are parametrized as a cubic polynomial function of ΔT.

$$\tau_{g,l,\nu} = \frac{\rho_{g,l}}{\rho_{0\,g,l}}\left(C_{0\,l,g,\nu} + C_{1\,l,g,\nu}\Delta T_l + C_{2\,l,g,\nu}\Delta T_l^2 + C_{3\,l,g,\nu}\Delta T_l^3\right)$$

The coefficient C_0, C_1, C_2, C_3 are saved in lookup tables to be red by σ-FORUM.

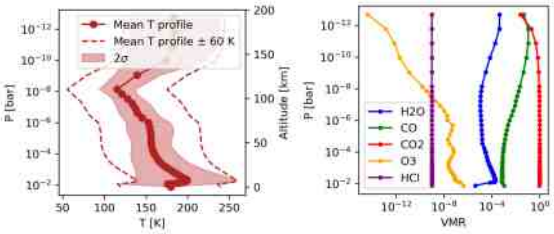


Figure 3: Mean temperature and gas volume mixing ratio profiles

Continuum absorption coefficients. For the continuum part of the spectrum a new subroutine has been included in σ-FORUM for accounting the CIA formalism [7]. Given that the Martian atmosphere is composed predominantly of CO_2, the only CIA process detectable within this spectral range arises from CO_2 self-interaction (see *Figure 4*).

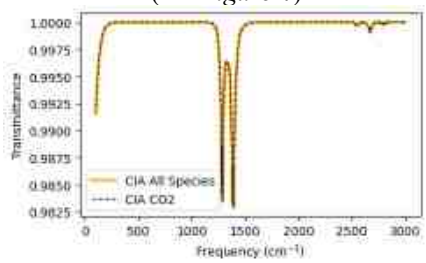


Figure 4: CIA transmittance comparison on Mars between all species and only self-CO2

Code performance tests: To evaluate the accuracy of the code, two different tests were performed. The first test consists of a comparison between the ODs reconstructed from the polynomial coefficients and the reference ODs computed by PSG. This assessment allows identification of potential issues related to the selected polynomial degree and highlights the spectral regions that are more challenging to fit accurately. We tested the goodness of fit for the different gasses at each wavenumber and altitude, showing the advantages of using a cubic polynomial for the fitting procedure instead of a quadratic one, as previously used on the Earth.

The second, and most significant test, involves a direct comparison of the radiances simulated by σ-FORUM with those obtained from the reference code PSG (*Figure 5*). This evaluation is essential for assessing the behavior of the FM, the good parameterization of the ODs and the sensitivity of the code to variations in the atmospheric state. We successfully compared the high-resolution spectra from the two codes for different atmospheric scenarios and including the CIA continuum. For future real data analysis, instrumental response functions were implemented for two different instruments, ACS-TIRVIM, on board the ExoMars-TGO [8], and the EMIRS on board the Emirate Mars Mission [9], that sounded the Martian atmosphere in the infrared region.

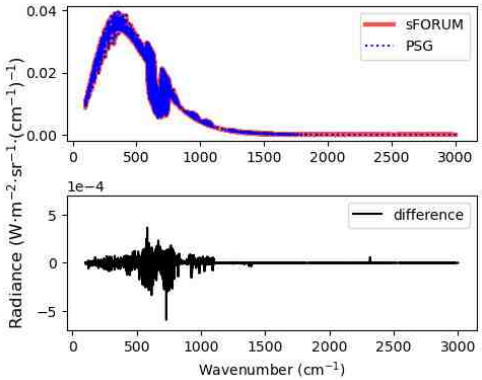


Figure 5: Example of comparison between high resolution radiance from the two codes.

Next steps: Two major goals will be fulfilled in the future. The first is the simulation of dusty condition, which is essential to face the real atmospheric condition of Mars. New lookup tables of Martian dust need to be built and included in the code. Secondly, following the completion of the forward model, the simulated spectra will be compared to some real data obtained by satellite missions.

References:

[1] Masiello G. et al. (2024) *JQSRT, 312,* 108814, DOI: 10.1016/j.jqsrt.2023.108814.
[2] Chou M.-D. et al. (1999) *Journal of Cimate*, 12 (1), pp.159-169, DOI: 10.1175/1520-0442-12.1.159
[3] Tang G. et al. (2018) *Journal of Atmospheric Science*, 75 (7), pp. 2217 - 2233, DOI: 10.1175/JAS-D-18-0014.1
[4] Villanueva G. L. et al. (2018) *JQSRT, 217,* pp 86-104, DOI: 10.1016/j.jqsrt.2018.05.023.
[5] Gordon I. E. et al. (2022) *JQSRT*, 277, 107949. DOI: 10.1016/j.jqsrt.2021.107949
[6] Millour E. et al. (2018) *From Mars Express to ExoMars*, 68, p. 68.
[7] Terragni J. et al (2025), *JQSRT,* 347, 109631, DOI: 10.1016/j.jqsrt.2025.109631.
[8] Vlasov P.V. et al. (2023) *Sol Syst Res, 57*, 516–532. DOI: 10.1134/S0038094623060084
[9] Edwards C.S. et al. (2021) *Space Sci Rev, 217*, 77 DOI: 10.1007/s11214-021-00848-1

TOWARDS A THREE-DIMENSIONAL INTERIOR MODEL INVERSION FRAMEWORK

A. Genova[1*], M. Ciambellini[1], G. Boccacci[1], A. M. Gargiulo[1], M. Paris[2,3], A. Ghirotto[4], E. Del Vecchio[1], T. Torrini[1], and S. Andolfo[1]. [1]Department of Mechanical and Aerospace Engineering, Sapienza University of Rome, via Eudossiana 18, Rome, Italy, [2]INAF, IAPS, Roma, Italy, [3]Dipartimento di Fisica, Sapienza University of Rome, Italy,[4]ETH, Zurich, Switzerland. *antonio.genova@uniroma1.it

Introduction: The characterization of the interior of planetary bodies is a key science objective of deep-space missions aimed at addressing fundamental questions on the formation and evolution of the solar system [1]. To enable a thorough determination of internal structure and properties, geodetic and geophysical quantities are measured through dedicated onboard instrumentation, yielding key constraints, such as the body's moment of inertia (MoI), tidal response, and orientation. By combining these observations with complementary assumptions based on geochemistry and composition, model inversion techniques are used to constrain the properties of the internal structure.

Building on the limitations of state-of-the-art interior modeling inversion frameworks, we present improvements to our approach to enable a more comprehensive characterization of planetary body's interior, including constraints on lateral variations derived from the estimation of geophysical maps.

Limitations of current interior model inversion: The determination of internal structure and properties on the global scale is primarily based on defining the internal layering through one-dimensional (1D) radial modeling. This assumption forms the foundation of inversion frameworks that rely on geophysical measurements such as moment of inertia and mass. Because the match between the modeled mass and the prescribed internal layering is performed in 1-D, spherical shells are adopted, constraining the interior to a sphere whose outer boundary is fixed at the body's mean radius. A common limitation of this approach is that the resulting volume of the proposed models is often inconsistent with the observed mass and radius due to the imposed spherical geometry.

A 1-D formulation is also widely used to represent the tidal response of a planetary body. By assuming a rheological model for the internal layers, tidal Love numbers k_2, h_2, and l_2 are computed to match the observations. The spherical geometry adopted in these models prevents the investigation of local variations in rheological properties, thereby limiting the interpretation of the tidal response.

The orientation of a planetary body is similarly affected by deviations from spherical geometry, particularly when the outer layers, such as icy shells in icy moons or the crust and mantle in terrestrial planets, are decoupled from the deep interior. Gravitational torques resulting from shape asymmetries significantly influence the longitudinal librations of the outer layers. An elliptical representation of the internal layering is therefore essential to enable an accurate computation of the orientation parameters predicted by interior models.

A 1-D interior description also prevents the incorporation of gravity, topography, and magnetic field maps as observations in the inversion process. Accounting for these key datasets requires a transition to a three-dimensional interior modeling approach, and this study introduces a preliminary solution to address this requirement.

The methodology presented here is based on a Bayesian inference framework employing Markov Chain Monte Carlo (MCMC) techniques, extended first to an ellipsoidal interior representation to incorporate accurate modeling of planetary orientation, and subsequently to a full 3D representation to accommodate lateral variations in gravity and topography.

Ellipsoidal upgrade to account for orientation constraints: The extension of the inversion framework from a 1D to an ellipsoidal interior representation addresses a fundamental limitation of spherical interior models: their inability to capture the rotational dynamics driven by internal asymmetries and the decoupling between layers. To represent these effects, the internal structure is still parameterized through concentric layers of constant density, but their interfaces are described as triaxial ellipsoids in hydrostatic equilibrium. The principal axes of each ellipsoid are computed using the fourth-order formulation [2], enforcing the equipotential condition on the combined rotational, tidal, and gravitational potentials. This approach enables a self-consistent description of the body's shape and the gravitational torques responsible for its orientation behavior.

Within this formulation, the inversion incorporates orientation data through the forced longitudinal librations of synchronously rotating icy moons. These librations arise from the periodic misalignment between the tidal bulge and the direction to the parent body due to orbital eccentricity. Their amplitude depends sensitively on the distribution of inertia within the outer layers, and particularly on the presence of a global ocean, which dynamically decouples the outer layers from the deeper interior.

To model this behavior, the inversion framework implements the elastic-librational formulation [3]. The model accounts for the main torques acting on the system: those generated by the planet acting on the static and periodic tidal bulges, the gravitational

coupling between misaligned internal layers, and the pressure forces transmitted across the liquid ocean. The resulting equations describe the angular motion of a differentiated body in which the shell and interior may librate with different amplitudes depending on the strength of internal coupling.

By incorporating libration amplitude as an observable, this inversion reduces the degeneracy that characterizes radial models, where mass and moment of inertia alone constrain only the total thickness of the hydrosphere. The librational response provides an independent probe of the mechanical structure of the outer layers, allowing the inversion to distinguish between the contributions of the ice shell and the underlying ocean. This upgrade therefore enables the use of orientation dynamics as a geophysical constraint, marking a critical step toward the development of a full three-dimensional inversion framework. Figure 1 shows preliminary results for interior model inversion of Enceladus using measured mass, MoI and libration amplitude as constraints.

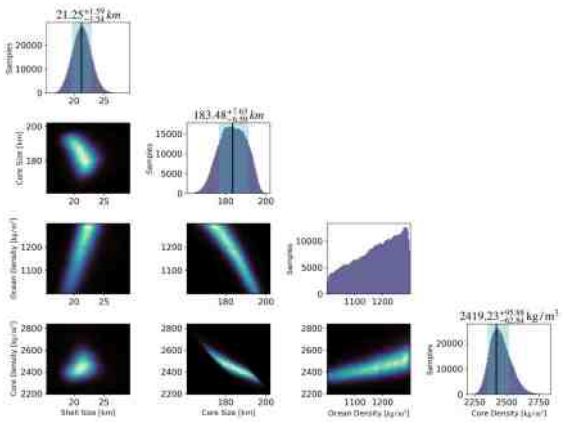


Figure 1 Corner plot showing the posterior distribution of Enceladus' interior properties obtained from an inversion constrained by mass, MoI, and libration amplitude.

Three-dimensional preliminary implementation: The transition from one-dimensional and ellipsoidal interior representations to a fully 3D formulation represents a major step toward characterizing bodies with irregular shapes and laterally varying properties. The framework was extended to treat bodies with lateral variations, with Enceladus selected as an initial test case due to its pronounced shape irregularities and small size. The key challenge arises from the computational cost inherent to MCMC methods, which require generating and evaluating at least hundreds of thousands of models, making finite-element or fluid-dynamical simulations impractical for routine sampling. To address this limitation, the internal structure is represented as a perturbation of a reference sphere, in which deviations encode the 3D variability of properties such as ice-shell thickness. This parameterization captures the essential geometry of an irregular body while avoiding the numerical overhead associated with voxel-based 3D descriptions.

Within this formulation, mass and moment of inertia are computed for the irregular, laterally varying model and incorporated directly into the MCMC algorithm. This approach enables the estimation of lateral variations of properties constrained by gravity and topography, including shell thickness and its associated uncertainty at each latitude and longitude, providing a probabilistic mapping of these variations within a Bayesian inversion framework. Preliminary results were obtained for Enceladus by using the observed mass, C_{20}, C_{22}, and C_{30} as constraints instead of MoI. The 3D interior model inversion converged to results consistent with those from 1D modeling, while additionally providing maps of ice-shell thickness and the corresponding gravity field, as shown in Figure 2.

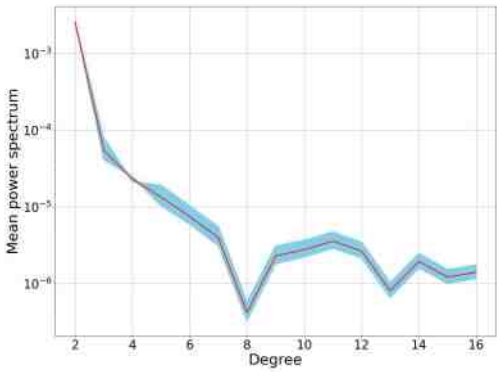


Figure 2 Gravity spectrum of the interior models resulting from the inversion that accounts for 3D modeling (**shaded cyan area**), together with their mean value (**red**).

Summary: This study extends interior model inversion beyond standard one-dimensional approaches by introducing a ellipsoidal interior formulation that incorporates orientation constraints through forced librations, and a preliminary three-dimensional implementation capable of handling irregular shapes and lateral variations. Using a Bayesian MCMC framework, the upgraded methods enable the estimation of spatially varying internal properties, such as ice-shell thickness, while maintaining computational efficiency. These developments represent an initial step toward a fully 3D inversion capability for planetary interiors.

Acknowledgments: AG acknowledges acknowledge funding from the Italian Space Agency (ASI) grant n. 2023-60-HH.0

References: [1] Genova A. et al. (2021) *Space Sci. Rev.*, 217(2), 31. [2] Tricarico P. (2014) *Astroph. J.*, 782(2), 99. [3] Van Hoolst T. et al. (2013), *Icarus*, 226(1), 299-315.

CAN WE RELY ON OUR NETWORK? UNCOVERING HUMAN-FACTOR SIGNATURES IN BOULDER MAPPING WITH THE CARE-ON PROJECT. S. Rossato[1], L. Criscuolo[1], C. Da Lio[1], G. Dal Sasso[1], G. Frasca[1], V.M. Rossi[1], G. Vivaldo[1], L. Zaggia[1] , M. Pajola[2], F. Tusberti[2], [1]Institute of Geosciences and Earth Resources, National Research Council of Italy, [2]INAF-Astronomical Observatory of Padova.

Introduction: Manual identification of geological features, such as craters or boulders, often requires long, repetitive tasks to unravel their geological significance. This challenge is amplified in planetary science, where ground truthing is limited and the interpretation of features must rely heavily on remote sensing data. Machine learning offers powerful tools to process large volumes of high-resolution imagery: for example, the OSIRIS-REx mission applied machine learning to map and analyse boulder distributions on Bennu [1], and the Lunar Reconnaissance Orbiter uses AI to support comprehensive crater mapping and age-dating of lunar terrains [2].

Despite these advancements, manual or visual identification by trained observers remains indispensable in the research pipeline (e.g., [3], [4]). Uncertainties arise from multiple sources, including human error, individual biases, fatigue, and differences in expertise [5]. The subjective nature of visual interpretation may lead to divergent results among observers analysing the same dataset [6]. Additionally, limitations in image resolution and quality can hinder reliable discrimination of features. Establishing standardized identification and classification procedures is therefore essential to ensure consistency, accuracy, and reproducibility.

The CARE-ON project (https://care-on.cnr.it/) is positioned within this framework. Its goal is to explore the role of the human factor in the identification of boulders on the lunar surface, where similar mapping provided interesting results (e.g., [7]). It evaluates how observer bias, expertise, and fatigue influence feature recognition, with particular attention to ambiguous cases. By systematically assessing human-related uncertainties, the project aims at informing best practices for manual mapping, provide statistically grounded metrics for result reliability, and lay the groundwork for larger participatory initiatives that can support expert researchers in routine yet demanding analytical tasks (e.g., [8]).

Study area and participants: The study focuses on two sample areas in Mare Crisium, east of the Luna 24 landing site, adjacent to a fresh ~1-km Copernican crater. These locations were selected for their high-resolution imagery (pixel size ~0.5 m) and for the relative simplicity of geological processes in mare regions, minimising the superimposition of multiple boulder-forming phenomena.

Two groups of participants contributed to the mapping effort, distinguished by platform and presumed expertise.

- Group 1: 26 attendees of the 2025 Geologic & Planetary Mapping Winter School (https://www.planetarymapping.eu/). Participants had prior familiarity with planetary geology and GIS tools, providing an intermediate level of proficiency aligned with the CARE-ON objectives.
- Group 2: 65 Italian amateur astronomers affiliated with local astronomical clubs. Although knowledgeable in basic astronomy, they were generally unfamiliar with planetary surface analysis or GIS workflows. Their contributions were collected through Zooniverse (https://www.zooniverse.org/), the world's largest citizen-science platform.

Both groups received theoretical training on boulder identification and hands-on orientation on the respective mapping platforms. Each participant independently mapped two areas with different boulder densities over the following months.

Preliminary results: Participant datasets were compared with a benchmark mapping produced and cross-validated by three expert researchers. Initial analyses reveal spatial and observer-dependent trends in feature identification, including both consistent patterns and notable discrepancies within and between the two participant groups, as well as relative to the expert benchmark. The detailed results will be presented at the conference.

By integrating academic expertise with volunteer contributions, CARE-ON aims to develop robust protocols for feature detection and to openly share workflows that enhance reproducibility in planetary mapping. The project also evaluates the long-term viability of citizen participation in supporting scientific research on planetary surface processes.

References: [1] Rizos, J. L. et al. (2021) *Icarus, 364*, 114467. [2] Fairweather, J. H. et al. (2022). *Earth and Space Science, 9(7)*, e2021EA002177. [3] Burke, K. N. et al. (2021) *Remote Sensing, 13(7)*, 1315. [4] Kawashima, O. et al (2022) *Icarus, 378*, 114938. [5] Petronijevic, J. et al. (2019) *Computers & Industrial Engineering, 127*, 665-676. [6] Hodgson, D. (2023) *Rock Art Research: The Journal of the Australian Rock Art Research Association (AURA), 40(2)*, 159-185. [7] Pajola, M. et al. (2019) *Planetary and Space Science, 165*, 99-109.. [8] Holwerda, B.W. et al (2025) *Publications of the Astronomical Society of Australia, 41:e115*.

PLUMES WITH SMOOTHED PARTICLE HYDRODYNAMICS: FROM ENCELADUS TO EUROPA AND BEYOND. M. Teodori[1], L. Maggioni[1,2], M. Formisano[1], G. Magni[1], M. C. De Sanctis[1], F. Altieri[1], E. D'Aversa[1], M. Ciarniello[1] and G. Piccioni[1], [1]INAF-IAPS, Via del Fosso del Cavaliere, 100, Roma 00133, Italy, email: matteo.teodori@inaf.it, [2]Department of Physics, University of Rome Tor Vergata, Via della Ricerca Scientifica, 1, Roma 00133, Italy.

Introduction: The emission of volatiles from planetary objects offers a fundamental tool to investigate ongoing and past processes involving surfaces and interiors, pushing the search for biologically relevant compounds in our Solar System. In particular, plume emission on icy satellites, as observed on Enceladus [1-9] and suspected for Europa [10,11], provide a unique opportunity to study the interior of such objects and their origin, strongly thought to be a salty subsurface ocean beneath the icy crust [12]. On Enceladus, these cryovolcanic eruptions release in space water vapor, icy grains, organics, salts and other gases [9], a material outgassing from surface fractures [1,2]. On Europa, a similar activity may occur, although the emission mechanisms are not constrained and the plume activity is elusive. Here we present the main results of a plume emission model through a Smoothed Particle Hydrodynamics (SPH) approach [13-15], applied to Enceladus. We then focus on the application of the model to Europa as well as to the release of volatiles from other objects.

Simulations of Enceladus plumes: Our SPH model for Enceladus' plumes accounts for several physical processes and is described in details in [16].

The SPH model: We numerically solve the hydrodynamic equations ruling the temporal and spatial evolution of density, velocity and thermo-kinetic energy of a multi-component fluid. We initially set a reservoir of water vapor at saturated conditions and at triple point, that simulates the ocean evaporation at the base of a surface fracture (5 km deep, section of 200 m^2). During evolution we account for phase transitions, that is, the deposition of water vapor into icy grains and their possible sublimation. This yields a two-fluid plume with a gaseous (water vapor) and a solid (icy grains) component, whose viscous interaction in different regimes is considered. The phase change can occur both during flight and due to thermal interaction with the cold icy surface. The surface temperature is estimated by observations and according to illumination conditions. In addition, the effect of the solar radiation and radiative equilibrium, the gravitational attraction and tidal limitations are considered.

Results: Our simulations characterizes the spatial, kinematical and thermal properties of the plume particles as they move through space and time. In our work, we focus on the differences between simulations assuming 1.0 and 100 micron sized icy grains, respectively, as this parameter affect multiple physical processes. We simulate 120 s of evolution, that is the time after which > 90% of the reservoir is released into space for the simulation with smaller grains. After this time, the simulation with a larger grain size has still half of the total material within the fracture. Indeed, a higher grain size reduces the vapor-ice viscous coupling efficiency within the fracture, producing a lower average velocity. At the end of the simulations, the vapor is more spatially distributed for the case with smaller grains, due to the different release time. Conversely, the behavior of the ice component is also altered by the viscous coupling. For smaller grains, the vapor accelerates the ice efficiently on the top of the emitting region, where the density is still high enough. Afterwards, ice dynamics becomes ballistic and remarks the earlier acceleration, which is almost isotropic (Fig. 1).

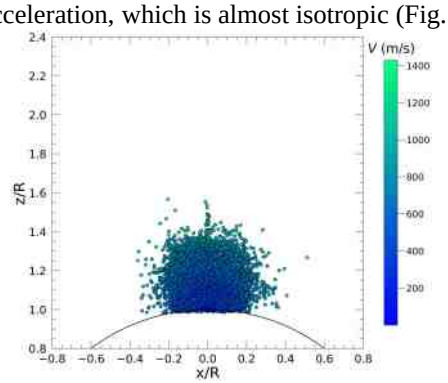


Figure 1: ice velocity distribution in the x-z plane after 120 s for a grain size of 1.0 micron.

On the contrary, larger grains are less affected by the viscous coupling after release and we see an higher collimation (Figure 2).

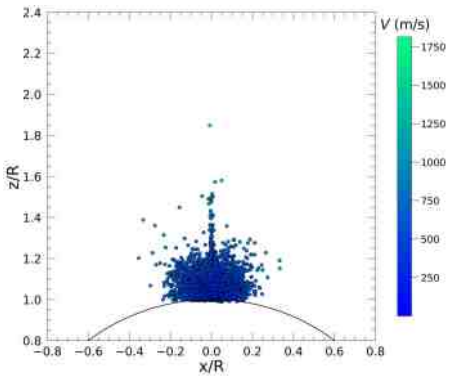


Figure 2: ice velocity distribution in the x-z plane after 120 s with 100 micron sized icy grains.

The thermal interaction with the cold surface of Enceladus favors the surface deposition of ice in

both simulations. In particular, the surface density of accumulated ice results symmetrical around the emitting ares. Thus, we evaluate the accumulation rate in mm/yr as a function of the projected radial distance from the fracture at different times (Figure 3a and 3b).

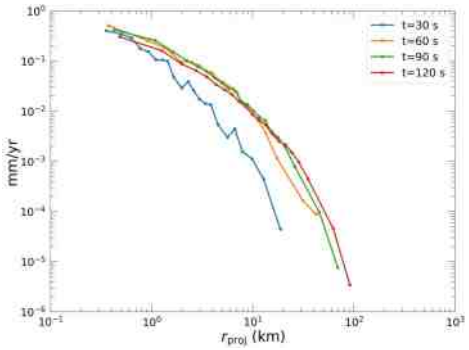


Figure 3a: projected radial profile of the rate of surface accumulated ice at different times for the simulation with a grain size of 1.0 micron.

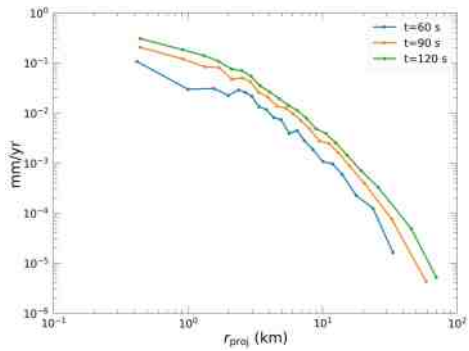


Figure 3b: projected radial profile of the rate of surface accumulated ice at different times for the simulation with a grain size of 100 micron.

We obtain that the area around the source reaches values consistent with estimates from the literature obtained with other methods [4]. The two simulations yield similar estimates of the deposited material, with differences associated to the amount of released material at the end of the simulation. Furthermore, the accumulated ice results stable to sublimation.

Europa plumes and beyond: The application of the SPH model to Enceladus plumes is compatible with the existing knowledge and sustains the validity of the model. However, some aspects need improvements to increase the robustness of the approach. In addition, the adaptation to volatile release from other targets needs further development, to consistently account for different initial and boundary conditions, as well as physical processes.

In particular, our model can be applied to the possible cryovolcanic activity on Europa [10,11]. Here, the emission mechanisms are not constrained and the oceanic source is only one of the possibilities [17]. In this case, it is important to asses the key parameters and processes, such as the role of the jovian plasma environment in altering the plume properties. Furthermore, the poor knowledge on the icy shell thickness reflects on the location of the liquid source for an oceanic plume. In addition, in the perspective of different source mechanisms like near-surface liquid inclusion, the extent of the liquid reservoir is highly uncertain. Moreover, it is not clear the temporal modulation of plume activity on Europa. As a consequence, we aim at identifying and explore the physical parameters that leave a detectable effect on the plume properties, in the perspective of interpreting the future observations of Europa Clipper and JUICE missions.

Finally, we can apply our SPH model to other volatile emissions, such as cometary activity [18], drilling-induced release of volatile-dust mixtures on Mars [19-21] and sublimation and/or deposition from and within Permanently Shadowed Regions [22]. We introduce the ongoing development and challenges, also concerning the joint work with surface and subsurface modeling [23,24] as well as atmosphere modeling.

References:

[1] Hansen et al. 2006, Science 311, 1422.
[2] Waite et al. 2006, Science 311, 1419.
[3] Schmidt et al. 2008, Nature, 451, 685.
[4] Kempf et al. 2010, Icarus, 206, 446-457.
[5] Dong et al. 2011, J. Geophys. Res., 116.
[6] Ingersoll & Ewald 2011, Icarus, 216, 492.
[7] Yeoh et al. 2017, Icarus, 281, 357.
[8] Teolis et al 2017, Astrobiology, 17, 9.
[9] Postberg et al. 2018, Nature, 558, 564.
[10] Roth et al. 2014, Science, 343, 171.
[11] Sparks et al. 2016, ApJ, 829, 121.
[12] Spencer & Nimmo 2013, Annu. Rev. Earth Planet. Sci. 41, 693.
[13] Gingold & Monaghan 1977, MNRAS, 181, 375.
[14] Lucy 1977, AJ, 82, 1013.
[15] Monaghan 2005, Rep. Prog. Phys. 68, 1703.
[16] M. Teodori et al. 2026, Icarus, 443, 116765.
[17] A. Vorburger & P Wurz, JGR Space Physics, 126, e2021JA029690.
[18] G. Rinaldi et al. 2025, EPSC-DPS2025-1556.
[19] L. Maggioni et al. 2025, MNRAS, 543, 3310.
[20] L. Maggioni et al. 2025, EPSC-DPS2025-613.
[21] L. Maggioni et al. 2025, PSS, under review.
[22] M. Teodori et al. 2025, EPSC-DPS2025-323.
[23] M. Formisano et al. 2018, J. Geophys. Res., 123, 2445.
[24] M. Formisano et al. 2024, PSS, 251, 105969.

Additional Information: This work is supported by INAF within the Minigrant “PLUMES” and “JUICE mission”.

NEW PARAMETRIZATIONS OF NON-LTE EFFECTS FOR ATMOSPHERIC STUDIES AND APPLICATIONS TO SATELLITE IR OBSERVATIONS.

Lorenzo Cassini[1,2], Guido Masiello[2], Sergio De-Souza Machado[3,6], Manuel López-Puertas[4], Larrabe Strow[3], Giuliano Liuzzi[2], Christopher Hepplewhite[6], Tiziano Maestri[5], Michele Martinazzo[5], Carmine Serio[2], Pamela Pasquariello[2], Marco D'Emilio[2], Rocco Giosa[2], Federico Donat[7,5], Elisa Fabbri[5], Marco Falda[5], Raffaele Inglese[2], Fabrizio Masin[5], Giorgia Proietti Pelliccia[5]; [1]University La Sapienza, Department of Civil, Building and Environmental Engineering, Via Eudossiana 18, 00184, Rome, Italy (lorenzo.cassini@uniroma1.it or cassinilorenzo03@gmail.com); [2]University of Basilicata, Department of Engineering, Viale dell'Ateneo Lucano, 10, 85100, Potenza, Italy; [3]University of Maryland, Baltimore County, Department of Physics, 1000 Hilltop Circle, Baltimore, MD, 21250, USA; [4]Instituto de Astrofísica de Andalucía, CSIC, Glorieta de la Astronomía, s/n, 18008, Granada, Spain; [5]University of Bologna, Department of Physics and Astronomy Augusto Righi, Via Irnerio, 46, Bologna, 40126, Italy; [6]Goddard Earth Sciences Technology and Research (GODARD II), Research Park Drive 5523, Baltimore, MD 21228,USA; [7]University of Trento, Department of Physics, via Sommarive 14, Povo, 38123, Italy.

Introduction: Infrared hyperspectral radiance measurements have been extensively used in recent years thanks to the outstanding performances of new instruments such as the Infrared Atmospheric Sounder Interferometer (IASI), the Atmospheric InfraRed Sounders (AIRS), and the Cross-track Infrared Sounder (CrIS). Assimilation of the radiance data by Numerical Weather Prediction models has led to significant improvements in meteorological forecasts (Collard & McNally, [1]). A new generation of the IASI instrument, namely IASI-NG, is incoming together with a new generation of the SEVIRI instrument on board of the third generation of Meteosat satellite. In recent years, the European Space Agency (ESA) and the American National Aeronautics and Space Administration (NASA) have additionally developed new missions to measure the far infrared section of the spectra of Earth atmosphere, one example being the Far-Infrared Outgoing Radiation Understanding and Monitoring mission (FORUM, Palchetti et al., [2]) launching in 2027 from ESA. This is the context where the new version of the radiative transfer code σ-IASI/F2N has been developed (Masiello et al., [3]) showing good results in reproducing both far and near infrared spectra in clear sky and cloudy sky conditions. Different upgrades have been implemented in this new version, including an enhanced description of the scattering processes from suspended particles thanks to an improved scaling methodology for the optical properties and the addition of the Tang correction, essential for a correct description of clouds interaction with IR radiation especially in the far infrared (Martinazzo et al., 2021 [4]). Still, some systematic inaccuracies occur with this fast radiative transfer code for daytime radiance simulations. This is particularly evident approaching the CO ν vibrational band, situated around 4.3 μm, where non-Local Thermodynamic Equilibrium (NLTE) phenomena appears, which are very common across several planetary atmospheres. This particular condition shows up as an excess in the observed radiance induced by the excess over the average kinetic temperature of the vibrational temperatures of the emitting states of the CO. Different phenomena are responsible for this effect but the main trigger can be identified in the absorption of sunlight by CO. Usually, molecules tend to redistribute excess energy through collisions between atmospheric species in the same layer, but this primarily occurs only in the troposphere and in the lower stratosphere. At lower pressures in the higher altitudes, collisions start becoming infrequent, up to a point where the population of vibrational levels have excitation temperatures way bigger than the average kinetic temperature. The NLTE effect mainly occurs where radiation is sensitive to the lower mesospheric and upper stratospheric temperatures, but there are non-zero effects in some lower temperature sounding channels. NLTE radiances can be computed using line by line models, such as the Line By Line Radiative Transfer Model (LBLRTM, Clough et al., [5]) and kCARTA (DeSouza- Machado et al., [6]), provided they are supplied with the non-LTE vibrational temperatures of the emitting levels corresponding to the atmospheric state (kinetic temperature and composition) of the scene. Unfortunately, these line-by-line calculation (as well as the supplied vibrational temperatures) are computationally intensive and thus too slow to be used for daily operational purposes. For this reason, during these past years, much work has been done to find an optimal method to reproduce this effect in an effective, accurate and faster way, designed to work with fast radiative transfer models such as SARTA and RTTOV (DeSouza-Machado et al., [6]; Matricardi et al., [7]). This work adapts the fast model methods into σ-IASI/F2N. To do so, we opted for an approach similar to other fast radiative transfer codes such as RTTOV or SARTA which both rely on a multilinear fit with a fixed set of predictors. The goal is to maintain a similar accuracy as line-by-line models compared to the SARTA and RTTOV fast models, which have already proven to be very effective in the accounting of NLTE, but with a new set of predictors. This new approach includes multiple terms linked directly to the CO amount in the atmosphere making the algorithm more flexible, allowing for a better description of different scenarios of climatological interest, both forward and backward in time. Assuming the radiance that reaches the top of atmosphere

as a sum of two terms, one related to the classical LTE radiative transfer and another one due to the presence of NLTE emission, it is possible to define the residuals between LTE and NLTE as follow: $\Delta R_i = R^{NLTE}{}_i - R^{LTE}{}_i$ where ΔR_i is the contribution due to the presence of NLTE, *i* represent the spectral variability, whereas R^{NLTE} represents the radiance computed with the NLTE enhancement and R^{LTE} represents the simulation in LTE condition. Once all the ΔR_i for all the different configurations (349 profiles x 6 scan angles x 10 solar zenith angles x 3 CO_2 mixing ratios profiles) are computed, we can express the excess radiance due to deviation from thermodynamic equilibrium at each spectral point as:

$$\Delta R_i = A_{i,j}\, x_j$$

where $A_{i,j}$ is a matrix containing all the weights computed through multivariable linear regression, *i* represent the spectral channel and *j* is an index that scales with the number of predictors, the vector x_j is a vector containing all the predictors for the specific profile. The predicotrs selected for our parametrization preserves most of the information coming from the solar radiation ($\cos(\theta_{sun})$ where θ_{sun} is the solar zenith angle) since this is the main driver of the solar pumping. The dependency with respect to the observer zenith angle is also included allowing for a better description for off nadir geometries ($\sec(\theta_{sat})$ where θ_{sat} is the observer zenith angle). Two variables combine the information about the vertical distribution of temperature with the solar zenith angle ($\langle T\rangle_1 \cos\theta_{sun}$ and $\langle T\rangle_2 \cos\theta_{sun}$). Our set of predictors includes also three new terms directly related to the CO vertical distribution profile ($CO_{2,surf}$, $\langle CO_2\rangle_1 \cos\theta_{sun}$ and $\langle CO_2\rangle_2 \cos\theta_{sun}$). With this selection we now retain some information coming from the temperature profile which is directly related to both latitudinal, longitudinal and seasonal variations while also allowing the inclusion of CO_2 dependency. There are multiple reasons for this choice: first, this approach allows more flexibility in the choice of the vertical distribution of the carbon dioxide allowing for a better description of climatological data both backward and forward in time. Plus this new variability can potentially be exploited in a retrieval scheme allowing to retrieve all the information available in the 4.3 μm band, which spans the range 2230-2390 cm^{-1}.

The radiances from which we have developed and tested the new linearization approach have been generated using the line by line model LBLRTM v12.17 together with an improved set of CO vibrational temperatures. This set has been generated for a sample of 349 pressure/temperature and composition profiles with an improved description above 80 km compared to the previous database. Also, a new version of the non-LTE model, the Generic RAdiative traNsfer AnD non-LTE population Algorithm (GRANADA, Funke et al., [8]) has been utilized with an improved description of the excitation by O(1D) as well as other non-LTE parameters (see Guarino et al., [9]). First we computed a huge set of vibrational temperature profiles utilizing the GRANADA algorithm, across multiple configuration (349 atmospheric profiles, 12 solar zenith angle, 3 different CO_2 concentration and 57 possible transitions). All these vibrational temperatures profiles have been utilized in LBLRTM simulations across multiple observation angles (from 0° to 50°) in order to produce a huge set of ΔR_i to be utilized both for the fiting process as well as a test set for the linerarization. In particular, we simulated a total of 64,820 different scenatios (between changing in the atmospheric composition or observation geometry); these simulations have been computed both in LTE and NLTE configuration. Later the set has been split in two part: the first 16.000 profiles have been utilized to fit the NLTE effect, the remaining 44,000 have been utilized as test set. Once the parametrization has been tested, the computation of NLTE contribution has been added directly into the fast radiative transfer code σ-IASI/F2N. The new and improved version of the σ-IASI code has been tested against IASI daytime observations over sea to verify the agreement between simulations and real data. In this work, we will present such results, and show the way forward in this work and possible adaptations of general interest for the planetary science community.

References:

[1] Collard, A.D. and McNally, A.P. (2009), The assimilation of Infrared Atmospheric Sounding Interferometer radiances at ECMWF. Q.J.R. Meteorol. Soc., 135: 1044-1058. https://doi.org/10.1002/qj.410 Booth, N. and Smith, A. S., [Infrared Detectors], Goodwin House Publishers, New York & Boston, 241-248 (1997);

[2] Palchetti, L., et al. (2020), FORUM: Unique Far-Infrared Satellite Observations to Better Understand How Earth Radiates Energy to Space. *Bull. Amer. Meteor Soc.*, 101, E2030–E2046, https://doi.org/10.1175/BAMS-D-19-0322.1;

[3] Masiello G., et al. (2024), The new σ-IASI code for all sky radiative transfer calculations in the spectral range 10 to 2760 cm-1: σ-IASI/F2N, Journal of Quantitative Spectroscopy and Radiative Transfer, Volume 312, 2024, 108814, ISSN 0022-4073, https://doi.org/10.1016/j.jqsrt.2023.108814;

[4] Martinazzo M., et al. (2021), Assessment of the accuracy of scaling methods for radiance simulations at far and mid infrared wavelengths, Journal of Quantitative Spectroscopy and Radiative Transfer, Volume

271, 107739, ISSN 0022-4073, https://doi.org/10.1016/j.jqsrt.2021.107739;

[5] Clough S.A., et al. (2005), Atmospheric radiative transfer modeling: a summary of the AER codes, Journal of Quantitative Spectroscopy and Radiative Transfer, Volume 91, Issue 2, 2005, Pages 233-244, ISSN 0022-4073, https://doi.org/10.1016/j.jqsrt.2004.05.058;

[6] DeSouza-Machado, S. G., et al. (2007), Fast forward radiative transfer modeling of 4.3 μm nonlocal thermodynamic equilibrium effects for infrared temperature sounders, *Geophys. Res. Lett.*, 34, L01802, doi:10.1029/2006GL026684;

[7] , Modeling of nonlocal thermodynamic equilibrium effects in the classical and principal component-based version of the RTTOV fast radiative transfer model. *Journal of Geophysical Research:Atmospheres*, 123, 5741–5761, https://doi.org/10.1029/2018JD028657;

[8] B. Funke, et al. (2012), GRANADA: A Generic RAdiative traNsfer AnD non-LTE population algorithm, Journal of Quantitative Spectroscopy and Radiative Transfer, Volume 113, Issue 14, Pages 1771-1817, ISSN 0022-4073, https://doi.org/10.1016/j.jqsrt.2012.05.001;

[9] Guarino, M.-V., et al. (2024), A Novel Gravity Wave Transport Parametrization for Global Chemistry Climate Models: Description and Validation, Journal of Advances in Modeling Earth Systems, 16, 2024, e2023MS003938, https://doi.org/10.1029/2023MS003938;

A COMPREHENSIVE PICTURE ABOUT JOVIAN CLOUDS AND HAZES FROM JUNO/JIRAM INFRARED SPECTRAL DATA

F. Biagiotti[1], D. Grassi[2], T. Guillot[3], L. N. Fletcher[4], S. Atreya[5], G. Liuzzi[6], G. Villanueva[7], P. Rannou[8], G. Piccioni[2], A. Mura[2], F. Tosi[2], S. Bolton[9], and the entire Juno/JIRAM team. [1]University of Rome La Sapienza, Physics, Italy, [2]INAF – Istituto di Astrofisica e Planetologia Spaziali (INAF-IAPS), [3]Observatoire de la Côte d'Azur, UniCA, Lagrange CNRS, [4]School of Physics and Astronomy, University of Leicester, [5]Department of Climate and Space Sciences and Engineering, University of Michigan, [6]Università degli Studi della Basilicata, Potenza, Italy, [7]NASA Goddard Space Flight Center, Greenbelt, MD, USA, [8]Université de Reims, GSMA, Reims, France, [9]Southwest Research Institute.

Introduction: Jupiter, the solar system's largest planet, serves as a crucial reference for understanding **gaseous exoplanets** and their atmospheres. While the chemical composition of its upper troposphere is well-known, the precise **nature and structure of its clouds** remain poorly understood. Addressing this challenge relies on both theoretical models and remote sensing data. Traditional equilibrium chemistry condensation models (ECCM) are sensitive to input parameters, but advanced models [1] offer more realistic predictions of cloud properties. Predicted tropospheric layers include upper **ammonia ice** (~0.7 bar) and **ammonium hydrosulfide** (~2 bar) clouds [2], though their spectral detection has been limited to small, dynamically active regions (<2% of the disk) [3, 4]. Remote sensing, coupled with multiple scattering atmospheric retrieval, can help determine cloud properties and test theoretical predictions, despite the process being computationally demanding due to high degeneracy.

Methods: This study utilizes averaged **JIRAM/Juno data** from the first perijove passage [5] to investigate Jovian clouds and aerosols, focusing on viewing conditions relevant to future exoplanet missions. Preliminary radiative transfer simulations (using **PSG** [6]) indicated that aerosol signatures are most prominent in the **2.6−2.8 μm** and **4.5−5 μm** high gas transmittance windows. The low gas opacity in these windows allows JIRAM to observe aerosol contributions through the reflection of incident solar radiation (2.6−2.8 μm) and the attenuation of thermal black body radiation from the planet (4.5−5 μm). The observed solar reflection specifically necessitates a **vertically extended tropospheric haze layer**, consistent with previous observations [7] and Titan-adapted microphysical models [8, 9], suggesting **stratospheric formation via methane photochemistry** [10].

Retrievals across the full **2−5 μm JIRAM range** were performed using the Planetary Spectrum Generator [6] and a MCMC framework, varying cloud/haze parameters and gas mixing ratios. The model employed a **single haze layer** and **two cloud layers** (main and deep). Three compositions were tested for the main cloud: pure ammonia ice, tholins [11], and **"Jupiter-adapted" tholins** (tholins [11] data with the 4.7 μm feature removed). The haze and deep cloud were modeled as reflecting and grey absorbers, respectively.

Results: The retrieval results confirm the **necessity of a haze layer** and successfully constrain its size and density. The **"Adapted" tholins** provided the best spectral fit for the main cloud composition, see **Fig. 1**. Further findings include: (1) **Main Cloud Densities:** Retrieved main cloud densities were significantly **lower** than both ECCM and advanced model [1] predictions, with particle radii measured around **2−3 μm**; (2) **Deep Cloud Densities:** Deep cloud densities were found to align well with the predicted top of the **ammonium hydrosulfide cloud**. These results suggest that **photochemistry** may play a major role, combined with classic condensation, in shaping Jupiter's aerosol layers. Given the observation of photochemistry in cold gaseous exoplanets like GJ-1214b [12], Jupiter's troposphere represents a highly accessible laboratory for detailed investigation of these processes up close.

Discussion: We propose two options for the creation of the best-fit **"adapted" tholins**: (1) **Coagulation Scenario:** The tholins result from the successful coagulation of small haze hydrocarbon particles and products of gaseous ammonia photolysis at pressures between 0.2 and 0.7 bar. Further work is needed to test the efficiency of this process in creating large particles around 3 μm; (2) **UV Dissociation Scenario:** Alternatively, tholins may be produced at the top of freshly generated ammonia ice clouds. Here, UV radiation could dissociate larger ice particles, which subsequently react with hydrocarbons and gaseous ammonia photolysis products. This scenario is particularly compelling as it aligns with the so-called **"chromophore model"** [13]. More **accurate chemical models** and **laboratory measurements** are required to verify these hypotheses regarding the formation and composition of Jupiter's cloud and aerosol layers.

References: [1] Ackerman A. S., Marley M. S., 2001, ApJ, 556, 872. [2] Atreya S. K., Wong M. H., Owen T. C., Mahaffy P. R., Niemann H. B., dePater I., Drossart P., Encrenaz T., 1999, Planet. Space Sci., 47, 1243. [3] Baines K. H., Carlson R. W., Kamp L. W., 2002, Icarus, 159, 74. [4] Biagiotti, F., Grassi, D., Liuzzi, G., et al. 2025, Monthly Notices of the

Royal Astronomical Society, staf38. [5] Adriani, A., Filacchione, G., Di Iorio, T., et al. 2017, Space Sci. Rev., 213, 393. [6] Villanueva G. L., Smith M. D., Protopapa S., Faggi S., Mandell A. M., 2018, Quant. Spec. Radiat. Transfer, 217, 86. [7] Dahl E. K. et al., 2021, Planet. Sci. J., 2, 16. [8] McKay, C. P., Pollack, J. B., & Courtin, R. (1989). Icarus, 80(1), 23–53. [9] Rannou, P., McKay, C. P., & Lorenz, R. D. (2003). Planetary and Space Science, 51(14–15), 963–976. [10] Moses, J. I., Fouchet, T., Bézard, B., et al. 2005, JGRE, 110, E08001. [11] Imanaka H., Cruikshank D. P., Khare B. N., McKay C. P., 2012, Icarus, 218, 247. [12] Kreidberg L. et al., 2014, Nature, 505, 69. [13] Baines K. H., Sromovsky L. A., Carlson R. W., Momary T. W., Fry P. M., 2019, Icarus, 330, 217

Acknowledgements: This work is supported by the Italian Space Agency (ASI) under agreement 2016-23-H.0

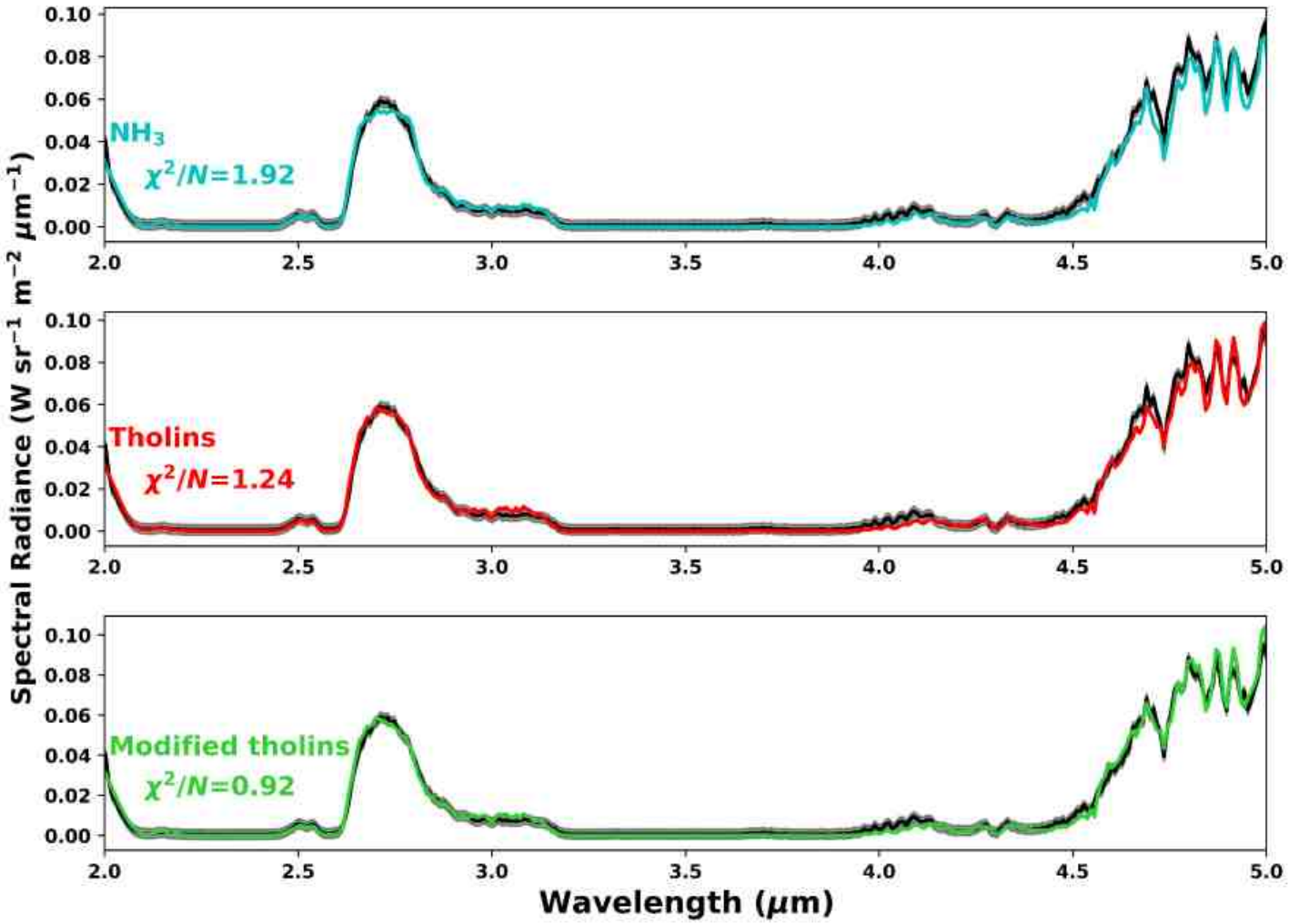


Fig. 1: Best-fitting PSG retrievals

Integration of Exomercat 2.0 into ExoplAn3T for Extended Exoclimate Simulations

Francesca Manni[1,2], Angelo Zinzi[3], Eleonora Alei[4,5], Laura Silva[6], Michele Maris[7]
[1]Department of Physics, University of "Tor Vergata" – Rome, [2]INAF – Turin Astrophysical Observatory, [3]Agenzia Spaziale Italiana - Roma, [4]NASA Goddard Space Flight Center - USA, [5]ETH Zurich, Inst. f. Teilchen- und Astrophysik - Zurich, [6]INAF – Trieste, [7]INAF – Rome.

Introduction: The ExoMerCat catalogue is going to update and integrate into the ExoplAn3T tool following the revision of the parameters presented in Table B.4 of [3]. In addition, we implemented new error-handling routines to improve the stability and reliability of catalogue queries.
The aim of this work is to enhance the identification of Earth-like exoplanets and to improve their climate characterisation through ARTECS simulations. The updated set of parameters—covering semi-major axis, eccentricity, planetary radius, and atmospheric composition—broadens the range of physical and orbital scenarios that can be modelled. Using ARTECS, we performed climate simulations varying FO (ocean fraction), GEO (geography), SMA (semi-major axis), and ECC (eccentricity), and produced seasonal temperature cycles and latitudinal temperature distributions for selected exoplanets.
Compared to previous analysis not using ExoMerCat, the expanded catalogue and improved modelling capabilities allowed us to identify a larger number of potentially Earth-like planets and to simulate them more comprehensively with ARTECS.

Analysis: We analyzed a set of Earth-like exoplanets selected via a targeted query and and evaluated their climate conditions using the ARTECS climate models database. The resulting climatological maps show systematic thermal distribution trends linked to variations in FO, GEO, ECC and SMA. The cross-planetary trends could be classified as:

- equatorial heating: FO$\geq$0.5, GEO$\leq$1, ECC$\leq$0.2;
- edge or polar heating: FO$\leq$0.4, GEO$\geq$2, ECC$\geq$0.3;
- seasonal asymmetry (e.g. heating only in 0–0.2 yr and 0.8–1.0 yr) is strongly linked to: High ECC ($\geq$0.3), Low FO ($\leq$0.4).

Specifically, the characteristics of each climatological map of the planets, along with the selected simulation parameters, are presented in the Table 1.

Low FO (0.1–0.4) tends to produce localized heating at the extremes of the year (e.g., 0–0.2 yr and 0.8–1.0 yr). Heat is often concentrated at the edges of the planet (latitudinally).
Kepler-1052 c (FO=0.1, 0.3) has equatorial band at 305 K or heating only at the edges. Kepler-401 d (FO=0.1) has strong edge heating, up to 400 K. Kepler-289 e (FO=0.4) has equatorial heating with seasonal peaks.
High FO (0.6–0.8) promotes more uniform heat distribution, especially along the equator or tropical bands. In some cases, heat shifts toward polar regions or specific longitudinal bands due to the large heat capacity of water, which buffers temperature variations. Kepler-69 c, Kepler-311 d, Tau Ceti f have equatorial or polar-focused heating. HD-20794 f (FO=0.8) has delayed heating in the second half of the year.

For GEO equal to 0 (uniform geography with a constant ocean fraction at all latitudes) heat patterns are more symmetric and latitudinally zoned, and often shows clear equatorial bands or edge heating. Kepler-1090 b, Kepler-1126 c, Kepler-69 c have equatorial or edge-focused heat.
GEO $\geq$ 2 (asymmetric Earth-like, equatorial or polar continental distributions) introduces asymmetries and localized heating zones, often tied to specific longitudes. Heat may appear in patches or shifted zones. Kepler-1052 c (GEO=2,3) has equatorial or edge heating depending on ECC. Tau Ceti f (GEO=4 realistic Earth-like latitude-dependent ocean fractions) has polar or longitudinally confined heating.

For SMA equal to 0.9 AU most planets in this range show moderate to high temperatures (300–400 K). Heating is often seasonal, with stronger variation in high-ECC or low-FO cases. Kepler-1052 c, Kepler-69 c, Kepler-401 d have strong seasonal or edge heating. For SMA $\geq$ 1 AU climates are generally cooler (180–260 K), with delayed heating toward the end of the year. Heat is often confined to equatorial or tropical bands. Kepler-311 d, Kepler-289 e, HD-20794 f have cooler, more stable patterns.

For ECC equal to 0–0.1 (circular orbits) produces stable, symmetric heating — often equatorial and only weak seasonal variations. Kepler-1052 c (ECC=0) maintains a persistent equatorial warm band. Tau Ceti f (ECC=0.1) has mild seasonal peaks.
ECC $\geq$ 0.3 (eccentric orbits) leads to strong seasonal heating, often at the start and end of the year. Heat may be confined to specific longitudes or shifted toward poles. Kepler-401 d (ECC=0.5) has extreme heating at 0–0.2 and 0.9–1.0 yr. Kepler-289 e (ECC=0.6) has strong heating in specific longitudinal bands.

Conclusions and future works: Based on our climatological simulations and the parameters provided, the planet that most closely resembles Earth-like climate

behavior is Tau Ceti f (Figure 1), specifically in the configuration FO=0.8, GEO=3, SMA=1.1, ECC=0.4 (ID 11335). A high ocean fraction enhances the redistribution of heat, promoting relatively uniform temperatures across low and mid-latitudes. The asymmetric continental configuration introduces localized thermal contrasts, while the high orbital eccentricity drives strong seasonal variations linked to the changing stellar flux. Despite an average insolation similar to Earth's, the eccentric orbit produces a brief but intense heating event near periastron. This occurs between 0.9 and 1.0 yr, where temperatures rapidly rise—especially between latitudes −20° and −80°—reaching values up to ~380 K. Outside this narrow interval, the planet remains within a temperate, non-glaciated regime across nearly all latitudes, consistent with an Earth-like, seasonally variable climate.
Other candidates like Kepler-289 e (ID 27829) and Kepler-311 d (ID 27829) show similar equatorial heating, but their temperatures are generally lower or more variable.
The next step will be to enable a quantitative classification of climates favorable to habitability, identifying which simulations of real exoplanetary systems are most similar to terrestrial climatology. This approach could open new perspectives in the study of the Galactic habitable zone and the search for complex life.

PLANETS	ID	FO	GEO	SMA	ECC
Kepler 1052 c	3103	0.1	0	0.9	0
	4703	0.3	0	0.9	0
	5268	0.3	0	0.9	0.3
	1561	0.8	2	0.9	0.2
	10821	0.8	3	0.9	0.1
kepler-1090 b	6787	0.5	0	0.9	0.3
	10821	0.8	3	0.9	0.1
Kepler-1126 c	6409	0.5	0	0.9	0.1
	1561	0.8	2	0.9	0.2
Kepler-69 c	27974	0.4	0	0.9	0.2
	10821	0.8	3	0.9	0.1
	28277	0.4	0	0.9	0.3
	1561	0.8	2	0.9	0.2
Kepler-311 d	27829	0.4	0	1	0.1
	27978	0.4	0	1	0.2
	1564	0.8	2	1	0.2
	11470	0.8	3	1	0.5
Kepler-401 d	3287	0.1	0	0.9	0.1
	4003	0.1	0	0.9	0.3
	25341	0.6	0	0.9	0.1
	21973	0.1	4	0.9	0.2
HD-20794 f	27981	0.4	0	1.1	0.2
	2833	0.4	0	1.5	0.4
	110033	0.8	3	1.1	0.2
	11351	0.8	3	1.5	0.4
Kepler-289 e	27829	0.4	0	1	0.1
	28462	0.4	0	1	0.5
	10996	0.8	3	1	0.2
	11603	0.4	0	1	0.6
TauCet f	6416	0.5	0	1.1	0.1
	21983	0.6	4	1.1	0.2
	1457	0.8	2	1.1	0.1
	11335*	0.8	3	1.1	0.4

Table 1: reference models to analyse parameter variability and observe temperature trends throughout the year. (*) we show the map of the model.

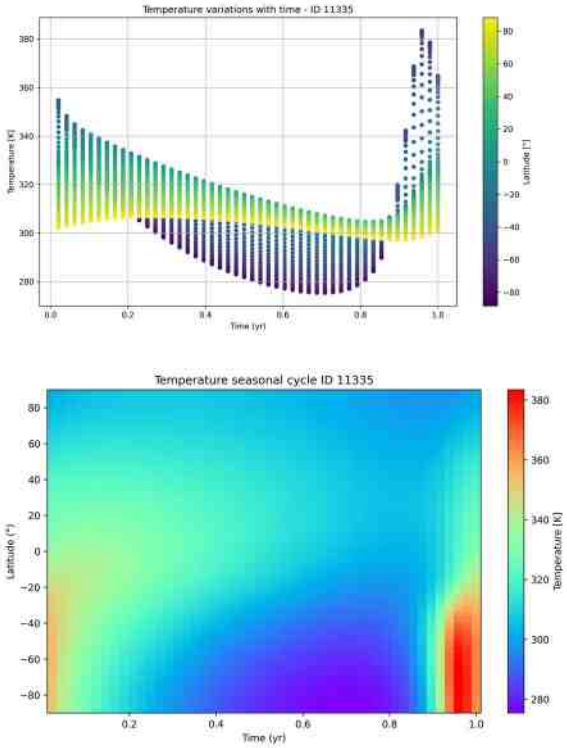


Figure 1: Tau Ceti f (ID 11335) *Top panel:* The plot highlights the strong asymmetric seasonal response driven by the eccentric orbit: a smooth temperature decline toward apastron followed by a sharp rise near periastron. While the planet maintains Earth-like temperate conditions for most of its orbit, a short-lived overheating phase occurs at mid-to-high southern latitudes. *Bottom panel*: The heatmap shows the evolution of surface temperature as a function of latitude and orbital phase. The planet remains mostly temperate throughout the year, but due to the high orbital eccentricity a short, intense seasonal heating event occurs near periastron, producing temperatures up to ~380 K in the southern hemisphere. Outside this brief interval, temperatures remain within a temperate, non-glaciated regime across most latitudes.

References: [1] Vladilo, Giovanni, et al. "Modeling the surface temperature of earth-like planets."The Astrophysical Journal 804.1 (2015): 50.
[2] Silva, Laura, et al. "From climate models to planetary habitability: temperature constraints for complex life."International Journal of Astrobiology 16.3 (2017): 244-265.
[3] Alei, Eleonora, et al. "Exo-MerCat v2. 0.0: Updates and open-source release of the Exoplanet Merged Catalog software." *Astronomy and Computing* 51 (2025): 100936.

SPECTROSCOPY RESULTS FROM THE NEAR-EARTH OBJECTS PHYSICAL OBSERVATIONS AND PROPERTIES SIMULATIONS (NEOPOPS) PROGRAM: WHAT WE HAVE LEARNED SO FAR

S. Ieva[1], J. Bourdelle de Micas[1], E. Dotto[1], M. Lazzarin[2], D. Perna[1], E. Mazzotta Epifani[1], F. Ferri[3], F. La Forgia[2], A. Farina[2], A. C. Mura[2,4] and the NEOPOPS team

[1]INAF - Osservatorio Astronomico di Roma, Via Frascati 33, 00078, Monteporzio Catone (Roma), Italy
[2]Dipartimento di Fisica e Astronomia "Galileo Galilei", Università di Padova, vicolo dell'Osservatorio 3, 35122, Padova, Italy
[3]Centro di Studi e Attività Spaziali "Giuseppe Colombo" (CISAS), Università di Padova, via Venezia 1, 35122, Padova, Italy
[4]INAF - Osservatorio Astronomico di Padova, Vicolo dell'Osservatorio 5, 35122, Padova, Italy

Introduction: The study of Near-Earth Objects (NEO) is of fundamental importance for several reasons. First, these objects are the keys to understand the origin and the evolution of the early Solar System, as they likely played a role in delivering organic materials and water to primitive Earth [1,2]. Moreover, their study is crucial for planetary protection purposes. Major catastrophic impacts – like the K-Pg event 65 million years ago, when an asteroid of 10km impacted on what today is the gulf of Mexico – can cause mass extinction and they happen statistically once every hundred million years [3 and Fig. 1]. However, recent events have highlighted that threats can originate even from much smaller objects. The fall of the 20m-Chelyabinsk meteor over the homonym Russian city in 2013 led to no casualties and 15 billions of € in damages. More recently, the detection of 2024 YR4 - a NEO with an impact probability of 3% at its discovery – caught the attention of the scientific community and the general public. The impact in 2032 was subsequently excluded thanks to multiple ground-based observations [4], but it highlighted how much work still needs to be done.

Indeed, small NEOs (D < 140 m) are the ones with the higher statistical significance to impact Earth, due to their overall abundance in the NEO population [5], and the ones that can cause regional catastrophes. Current discoveries of NEOs are in the order of 40,000 objects. However, while we have discovered more than 95% of NEOs with a diameter larger than 1 km, we currently know ~30% of the smaller 100m-range population [6]. In addition, physical characterization for NEOs (photometry, spectroscopy, light-curves, polarimetry, albedo…) is missing for a large part of the small ones. This is mainly due because they become bright enough to be observed only for a very limited time, typically on the order of a few weeks after their discovery. If not characterized by then, their chance to be studied in detail could be lost forever.

The NEOPOPS program: In order to keep the physical characterization up with the NEO discoveries, the Near-Earth Objects Physical Observations and Properties Simulations (NEOPOPS) was approved by the EU and implemented by ESA. The project, started in February 2025, will be completed by August 2028, and it is built upon the legacy of prior large programs financed by the EU commission (NEOShield-2, NEOROCKS) devoted to the comprehension and the physical characterization of the NEO population. Those past surveys have made clear that only a joint effort is able to address the current major issues related to NEO impact monitoring and mitigation.

Within the NEOPOPS program, INAF is in charge of the WP1 (Project Office), WP4 (Spectroscopy) and WP6 (Rapid Response). In particular, WP4 is responsible for conducting spectroscopic observations of high-profile NEOs (e.g. potential impactors, target of space missions and small-sized recently discovered NEOs). Using the 8.2m VLT (Paranal, Chile), the 3.58m TNG (La Palma, Spain) and other stations around the world, our goal is to characterize the mineralogical surface composition and the taxonomy of observed objects.

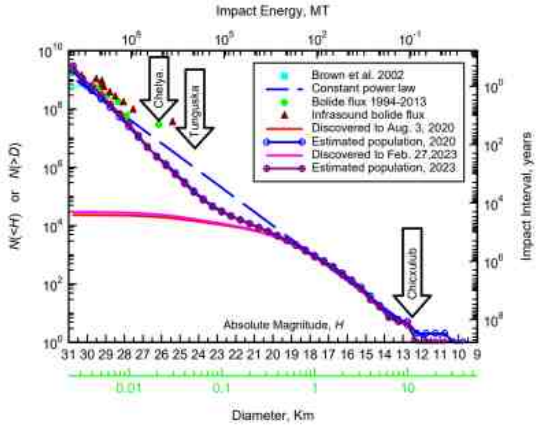


Fig. 1 - The estimated NEO population, according to their estimated size. Taken from [3].

These observations will be conducted in the visible to near-infrared range. Within this wavelength range, we can identify spectroscopic features, such as absorption bands, associated with specific minerals. The compositional characterization, combined with meteorite comparison, will help constrain the Yarkovsky effect [6], which represents the major uncertainty on the orbital evolution in the next century for these objects.

Spectroscopic observations will be integrated with additional datasets provided by collaborators in the NEOPOPS program (lightcurves, color indexes, polarimetry), contributing to a continuously updated monthly database maintained by the European Space Agency (ESA). We will focus on the spectroscopic

observation component of the project (WP4). We will present examples of the methodology (spectra, parameters computation, estimation of the taxonomy, meteorite comparison), based on data obtained during the first year of the project.

References: [1] Morbidelli et al. (2000), M&PS, 35, 1309. [2] Marty et al. (2016), E&PSL, 441, 91. [3] Harris & Chodas (2023), ACM 2023, 2851, 2519. [4] Devogele et al. (2025), JAsSc 72, 59. [5] Perna et al. (2015), PSS, 118, 311. [6] Mainzer et al. (2017), JGRE, 122, 789. [7] Farnocchia et al. (2013), Icarus, 224, 1.

Acknowledgements: The NEOPOPS observations contract is funded by the Horizon Europe Programme of the European Union and implemented by ESA (agreement No. 4000147191/25/D/MRP).

ROUGHNESS OF PLANETARY SURFACES: STATISTICAL MULTI-FACET APPROACH COMBINING HAPKE AND FRACTAL THEORIES. Andrea Raponi[1] (andrea.raponi@inaf.it), Mauro Ciarniello[1], Michelangelo Formisano[1], Alessandro Frigeri[1], Gianrico Filacchione[1], Fabrizio Capaccioni[1], Maria Cristina De Sanctis[1]. [1]INAF-IAPS (Via Fosso del Cavaliere, 100, 00133, Rome-Italy).

Introduction: The characterization of surface roughness on planetary bodies is crucial for improving the accuracy of photometric and thermophysical models [1]. It also offers important insights into geological and physical processes, and it is key in engineering contexts such as the identification of safe landing sites. Although numerous planetary missions have collected remote (spectral) imagery of surface features, these datasets are constrained by their spatial resolution. However, many surface phenomena, especially those influencing light scattering and thermal behavior, usually take place at scales smaller than a single spatial pixel.

To investigate roughness at unresolved scales, physically based photometric models such as Hapke's theory [2] are commonly employed. This analytical framework represents a rough surface as an ensemble of facets, each characterized by a slope angle, and describes the macroscopic roughness into a single parameter: the mean slope angle (θ). Despite its usefulness, Hapke's model often requires estimating several photometric parameters simultaneously, which demands substantial amounts of data to avoid degeneracies in the solutions.

Method: Here we propose a novel method to isolate and estimate surface roughness using Hapke's theory under specific conditions. By comparing the reflectance from adjacent terrain regions that share the same photometric properties (including composition) and have low albedo (dark surfaces), under the condition that they are observed at nearly identical phase angles, the ratio of their reflectances becomes a function of viewing geometry and roughness alone. These conditions occur in the (spectral) imaging datasets returned from many space missions.

To overcome the aforementioned limitations of the analytical Hapke formulation, we introduce the Statistical Multi-Facet Algorithm (SMFA) [3], a numerical modeling approach that simulates reflectance from complex surface geometries. SMFA is more accurate when modeling facets with high slopes, and it allows to simulate polydisperse slope populations, resulting in a substantial improvement of the model fits. In particular, SMFA can handle nested roughness structures, i.e. cases in which each facet has its own internal roughness (intrafacet).

Furthermore, we take advantage of the fractal theory to estimate the degree of fractality of the modeled terrain in terms of the Hurst exponent used as indicator. Previous works [4] already estimated this parameter for planetary surfaces thanks to laser-altimeter data, and/or high-resolution imaging from landers. Here, as a novel method, we estimate this indicator with the use of the SMFA methodology.

Data: The SMFA has been tested on two high-resolution (100 m/px) acquisitions in VIS and IR channels of the VIR instrument onboard the Dawn spacecraft [5], targeting the floor of the crater Ezinu on Ceres (43.2° north latitude and 195.7° east longitude). We averaged reflectances across spectral bands spanning over 0.6 μm for both channels. For the VIS channel, the range taken into account is 0.35-0.95, i.e., almost all spectral range covered by the channel (0.25 -1.05 μm), excluding the extremes, which are affected by higher noise due to the low responsivity of the detector. For the IR channel, we have taken into account the 2.7-3.3 μm range to maximize the distance from the VIS range (avoiding the range affected by thermal emissivity), to provide a significantly different case for the two acquisitions. Then, we grouped data by incidence and emission angles, providing several bins for each acquisition. Lastly, reflectance ratios were computed and normalized.

Results: The normalized reflectances were compared against SMFA-generated profiles. As best fit, we obtained two levels of roughness at different scales, with the smaller size being rougher, as expected for a natural self-affine terrain.

We take into account the spatially-resolved roughness at a 100 m scale as a reference value. Furthermore, we consider the roughness at the smallest scale as generated by the smallest asperities capable of casting shadows in geometric optics regime, i.e., of the order of 100λ (from Fresnel number definition: $F = a^2 / \lambda z >> 1$, , where a is the size of the asperities, z is the distance between the asperity and the casted shadow, and assuming $F = a^2 / \lambda z \geq 10$, and $z \sim 10a$).

The two acquisitions (VIS and IR) correspond to two significantly different viewing geometries (other than different wavelengths), yet they give very similar results in terms of the retrieved Hurst exponent (see the figure below), demonstrating that the method is robust.

The vertical amplitude of the asperities (σ) retrieved is ~0.2 m at 1 m window size. This is compatible, with the presence of boulders 10–50 cm high, and fractured or cratered terrain on a decimeter scale.

Overall, we obtain an estimation of the physical size of the asperities making up the rough surface, spanning scales over ~7 order of magnitudes.

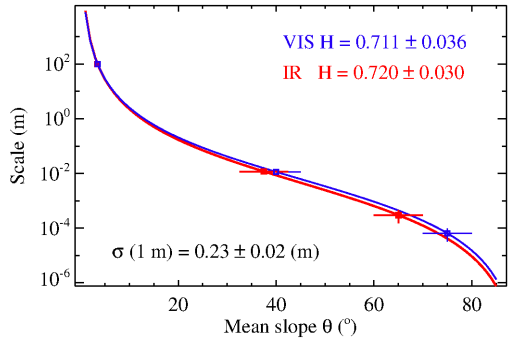


Figure. Points with errors indicate the retrieved mean slope parameters as derived from VIS (in blue) and IR (in red) observations. The point at larger scale indicate the topographic roughness. The resulting Hurst exponent (H) and the amplitude (σ) are indicated.

Applications: Given the possibility of retrieving the roughness with virtually a single high-resolution image, possible future applications of the method proposed here include the mapping of roughness at any given scale of interest over the global surface of a target body. The large datasets from recent space missions allow for their exploitation in this aim. Furthermore, a better constraint of the roughness would improve the reliability of previous and future thermal and photometric models.

References: [1] Formisano, M. et al., (2025), *MNRAS*, 543, 4187-4197. [2] Hapke B. (1993) *Theory of Reflectance and Emittance Spectroscopy*. [3] Raponi A. et al., (2020) *14th EPSC 2020*, abstract 761. [4] Otto K.A. et al., *MNRAS*, 500, 3178-3193. [5] De Sanctis M. C. (2011) et al., *SSR, 163,* 329-369.

THE EVOLVING ACTIVITY OF THE HYPERBOLIC COMET C/2024 E1 (WIERZCHOS): A "PROXY TARGET" FOR THE ESA COMET INTERCEPTOR SPACE MISSION Elena Mazzotta Epifani[(1)], Cecilia Tubiana[(2)], Ivano Bertini[(3)], Vincenzo Della Corte[(4)], Alessandra Rotundi[(3)], Laura Inno[(3)], Aurélie Guilbert-Lepoutre[(5)], Colin Snodgrass[(6)], Matthew M. Knight[(7)], Rosita Kokotanekova[(8)], Carrie E. Holt[(9)]. [1]INAF-Osservatorio Astronomico di Roma, Via Frascati 33, Monte Porzio Catone (RM), Italy (elena.mazzottaepifani@inaf.it); [2]IAPS – Istituto di Astrofisica e Planetologia Spaziale, Via Fosso del Cavaliere, Roma, Italy; [3]Dep. Science and Technology, Parthenope University of Naples, CDN-IC4 Napoli, Italy; [4]INAF - Osservatorio Astronomico di Napoli, Via Moiariello, Napoli, Italy; [5]LGL-TPE, UMR 5276 CNRS, Université Lyon 1, ENS, Villeurbanne, France; [6]Institute for Astronomy, University of Edinburgh, Royal Observatory, Edinburgh EH19 3HJ, UK; [7]Physics Department, United States Naval Academy, 572C Holloway Road, Annapolis, MD 21402, USA; [8]IANAO, Sofia, Bulgaria; [9]LCO, Goleta, USA

Introduction: Only a handful of comets have been visited in-situ by space missions, and they are all Short Period Comets (SPCs) (with the only exception of the Halley-type 1P): 19P, 9P, 81P, 103P and most of all 67P, the target of the successful Rosetta mission. SPCs (with orbital periods of ~6 years for Jupiter family comets like the Rosetta target), and even the 76-years-period 1P, have encountered the Sun many times, with significant evolution of the visible surface with each perihelion passage.

The Rosetta mission showed that each perihelion passage erodes some of the nucleus away as ice sublimates, and that the evolution of the surface layers of the nucleus can be different despite indications that the nucleus formed from relatively homogeneous building blocks. Thus, to understand the greater complexities of planet-building in our disk [1][2], it is mandatory to investigate comets while inbound, still distant, before they can evolve, and study their first-time evolution towards inner regions of the solar system.

In particular, dynamically new comets incoming for the first time from the Oort Cloud provide the best testbed to constrain mechanisms and models of planetesimals formation and evolution, and ice distribution in the proto-planetary disk. They are believed to be the least processed (although not perfectly pristine) bodies observable in our Solar System.

The ESA Comet Interceptor mission: The new ESA mission, Comet Interceptor (CI) [3], aims to investigate, for the first time ever, the environment of a long period comet, possibly dynamically new, or even an interstellar comet, i.e. a visitor coming from extrasolar planetary systems as 1I/`Oumuamua and 2I/Borisov. These targets will likely be less evolved, more primordial objects than SPCs. The CI mission is being designed and will be very likely launched before its target is discovered. CI will wait in a parking orbit around the Sun-Earth L2 point, where it can station-keep with very little fuel, until a reachable target is found. The spacecraft will depart L2 to encounter the comet at a distance from the Sun of ~1 au, following a cruise period of up to 3 years. Even with this technique, the target comet must be discovered inbound at a relatively large distance, in order to give sufficient time to characterize its orbit and activity levels, and for the spacecraft to reach the encounter position. This would have been impossible a decade ago, when dynamically new comets were typically discovered only a few au from the Sun, less than a year from their perihelion passage. In the near future, powerful sky surveys such as the Vera Rubin Observatory's LSST (starting in 2026) will be able to find many comets on their incoming orbital branch, at unprecedented large distances well beyond 10 au from the Sun.

The comet C/2024 E1 (Wierzchos): Up to now, few comets have been discovered with activity when very far from the Sun, still on their inbound orbital branch. Comets C/2010 U3 (Boattini) and C/2017 K2 (PANSTARRS) were discovered at 18.4 au and 16 au, while pre-discovery observations show that they were already active at 25.8 and 23.7 au, respectively [4][5]. Comet C/2014 UN271 (Bernardinelli-Bernstein) is presently at $r_h \sim 15$ au, and has shown variable activity from ~ 26 au [6][7]. None of these comets have perihelion distance $q < 1.2$ au, which would have been required for CI to reach them if CI was already in its parking orbit at their discovery.

Actually, inbound discovery of comets with distant activity and a low q is quite rare. Comet C/2024 E1 (Wierzchos) is a rare exception, discovered when it was on its inbound orbital branch at $r_h \sim 8.3$ au [8]. Its very close perihelion distance is $q = 0.56$ au (January 2026). For the first time ever, C/2024 E1 offered the opportunity to start the investigation of the properties of a long period comet's coma when far from the Sun and to monitor the evolution of the coma itself up to a very short heliocentric distance. The evolution of cometary activity drivers from more volatile gases (CO2, CO, at large r_h) to water (close to the Sun) is still poorly understood, as well as the relation between distant activity and fundamental nucleus properties.

For all these reasons, comet C/2024 E1 represents an important "proxy" for a future CI target, for which it will be pivotal to understand how observed

activity levels at very large distances are related to nucleus properties, how they evolve in transition regimes, and how distant outgassing and dust production rates could allow accurate predictions about a target's environment at the time of the mission encounter, around 1 au.

TNG monitoring campaign: We will present the results obtained during our multi-epoch, multi-filter observing campaign of comet C/2024 E1 (Wierzchos) performed with the Telescopio Nazionale Galileo (TNG, La Palma) while the comet was on its inbound orbital branch. The campaign started with awarded DDT in July 2024, when the comet was at r_h ~7 au, and continued with regular proposals, with multi-epoch observations while it is approaching perihelion. The evolution of the dust environment of the comet (see Figure 1) will be presented, and its properties discussed also in comparison with those of other long-period comets and comets pertaining to other groups and families.

References: [1] J. Blum et al., 2017, MNRAS 469, S755. [2] G. Filacchione et al., 2024, in Comets III, Univ. of Arizona Press. [3] G. Jones, C. Snodgrass, C. Tubiana et al., 2024, SSR 220, 1, id.9. [4] M.-T. Hui, D. Farnocchia & M. Micheli, 2019, AJ 157, 4, 162. [5] X. L. Zhang, D. Jewitt & M. T. Hui, 2019, MNRAS, 487, 2, 2919. [6] T.L. Farnham, M.S.P. Kelley & J.M. Bauer, 2021, PSJ, 2, 6, 236. [7] M.S.P. Kelley, R. Kokotanekova, C.E. Holt et al., 2022, ApJL 933, 2, L44. [8] K.W. Wierzchos, 2024, MPEC 2024-E102

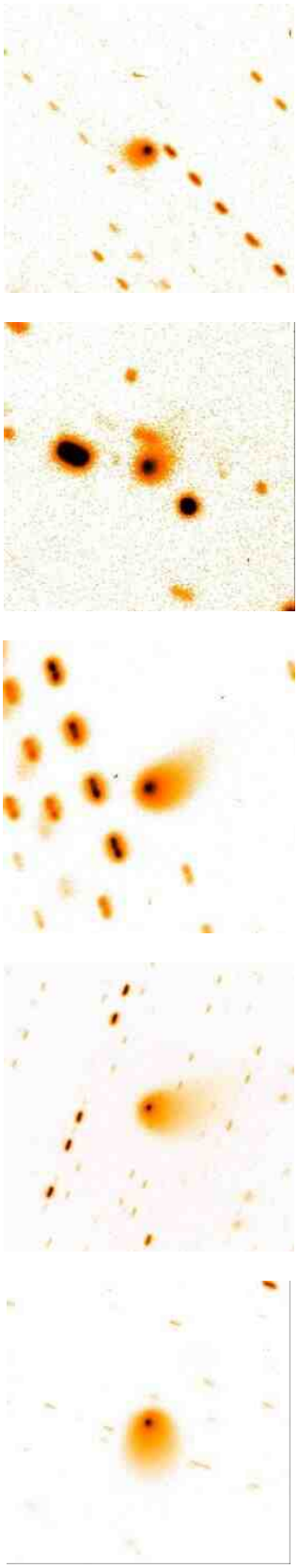


Figure 1 – From top to botton, TNG image in the R filter of comet C/2024 E1 (Wierzchos), obtained in the observing slot of July 2024, February, March, April and June 2025, respectively. Linear scale: 2.3 × 10^5 km. N is up, E is left.

NEW INSIGHTS INTO THE DIDYMOS SURFACE: GEOLOGICAL MAP USING BOTH DART/DRACO AND UNEXPLORED LICIACUBE/LUKE IMAGES. Tusberti Filippo[1], Pajola Maurizio[1], Penasa Luca[1], Lucchetti Alice[1], Beccarelli Joel[2,1], Munaretto Giovanni[1], Rossi Costanza[1], DART and LICIACube team. [1]INAF-OAPD Astronomical Observatory of Padova, vicolo dell'osservatorio, 5, 35142, Padova, Italy (filippo.tusberti@inaf.it); [2]Centro di Ateneo di Studi e Attività Spaziali – Giuseppe Colombo (CISAS), Padova, via Venezia 15, 35131 Padova, Italy.

Introduction: (65803) Didymos is a stony/Sq-Type binary system [1] recently visited by the NASA Double Asteroid Redirection Test (DART) spacecraft [2]. Didymos is the primary member and has a maximum diameter of 819 m, while its moonlet Dimorphos is 177 m across [3]. The ASI Light Italian Cubesat for Imaging of Asteroids (LICIACube) is a CubeSat that was deployed on 11 September 2022 to acquire images of the DART spacecraft while impacting on the Dimorphos surface [4]. Images were obtained through two instruments: the LICIACube Explorer Imaging for Asteroid (LEIA) which resulted out of focus and is therefore not presented here, and the LICIACube Unit Key Explorer (LUKE) [5]. The scientific phase of LUKE started 29 s after the impact, acquiring triplets of images with different exposure times. During this phase, and in particular right after closest approach, LUKE acquired several images of the southern pole of Didymos, which was not previously observed by Didymos Reconnaissance and Asteroid Camera for Optical Navigation (DRACO) [6]. Such dataset has never been used before to complement previous studies and investigate the surface morphology of Didymos.

In this work, we exploit such images to present an improved version of the geologic map of Didymos previously published by [1] including also the areas covered by the LUKE images. Our findings highlight a potential new crater that has not been previously detected, as well as an improved boulder Size Frequency Distribution (SFD) of Didymos.

Data and Methods: To conduct this work we made extensive use of both DRACO and LUKE images. We selected four LUKE images (liciacube_luke_l2_1664234225_00002_01; liciacube_luke_l2_1664234227_01003_01; liciacube_luke_l2_1664234229_00005_01; liciacube_luke_l2_1664234234_00002_01) with a pixel scale of 2.6 m/px to better interpret the geology of the studied area. We also used DRACO data to extend the study area as much as possible and to have a continuity with the first released geologic map [1]. In particular, we chose the image dart_0401929842_42894_02_iof because of its extensive coverage and its pixel scale of 6.34 m/pixel.

All these images have been analyzed both on Qgis and Small Body Mapping Tool (SBMT) [7], which we used to project the images on the 3D model of Didymos. This was pivotal to have a better understanding of the three-dimensional perspective of the body and, therefore, of the geological unit distribution. Afterwards, we used the tools of SBMT to acquire high-resolution snapshots of the 3D model of Didymos overlaid by the DRACO and LUKE images. We acquired the snapshot from four different viewpoints (Fig. 1) starting from the [1] perspective (Fig. 1A) and then rotating the model toward the southern pole of Didymos(Fig. 1B, C, D). Therefore, we prepared four distinct, but spatially-connected, geological maps in order to give a three-dimensional perspective of the products.

To prepare the geologic maps we followed established methodologies [8] and used the Qgis *mappy* plugin [9]. To discriminate between different geological units, we used the abundance of visible boulders present on the studied surfaces. Areas containing a higher number of visible boulders appear rougher and more irregular, while areas with few or no visible boulders display smoother surfaces. We then defined three distinct units described below:

- ***Rough unit:*** encompasses areas characterized by the presence of boulders larger than 15 m, which are also visible at the DTM scale. These areas exhibit a highly rough and hummocky appearance.
- ***Intermediate unit:*** includes areas that appear smoother than the *rough* unit, although boulders larger than 15 m are still visible at the scale of LUKE and DRACO images.
- ***Smooth unit:*** includes areas that do not show any boulders both at the scale of the DTM, LUKE, nor DRACO images. We highlight that these regions may exhibit a non-flat topography but still appear smooth and not bumpy.

The "*not mapped*" areas are those with low resolution, distorted images, or missing data, which prevented a correct interpretation of the surface geology.

Results and Discussions: The four geological maps show Didymos as a body mainly characterised by a rough surface. Indeed, of the total area analysed, the most extensive unit is the *Rough* one, which covers about 71% of the mapped area, followed by the *Intermediate* (23%) unit and the *Smooth* unit (6%). This roughness is most likely due to the extensive presence of large boulders across the majority of the surface of Didymos. On the other hand, some regions show smoother terrains, likely reflecting the absence of large boulders. These areas are completely circled by the *rough* regions, which

extend through the vast majority of the studied surface.

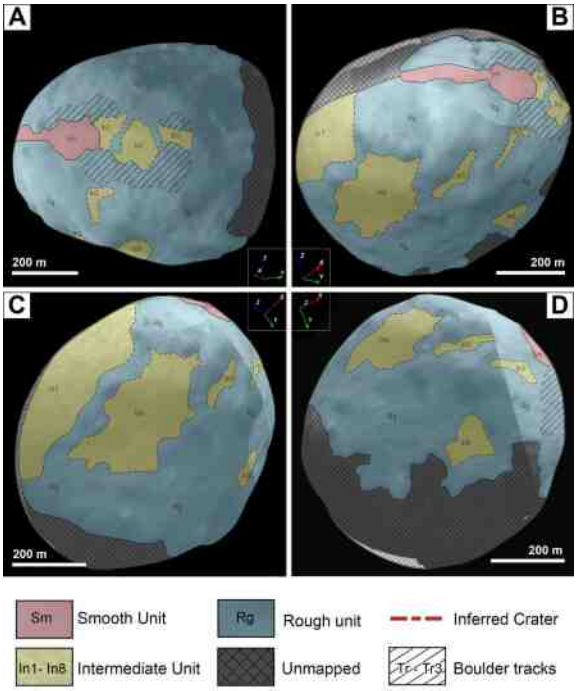


Fig. 1: The geologic map of Didymos seen from four different points of views: A) geologic map overlying the DRACO image oriented with the north up (Z+); B) geologic map overlying the LUKE and DRACO images combined; C) and D) geologic maps of the southern pole overlying the LUKE images.

The unique *Smooth* region is located in the equatorial region between 60W and 5E. It is ~400 m long and ~30-50 m wide, displaying an irregular linear-like shape. This specific shape can be due to regolith mass movement effects [1] linked to the dynamics of the equatorial region also supported by the presence of potential boulder tracks [10]. Nevertheless, our investigation is limited by a pixel scale of 2.5-6 m/px. Therefore, it is probable that these regions are characterized by accumulations of boulders with smaller sizes, not identifiable with the available images resolution.

In addition, a potential crater has been found in the area between ~50-160°W and ~10-70°S (Fig. 2). This feature is 520 m long, 286 m wide and its elevation profile shows an elongated ellipsoidal shape with a depth of ~60 m (Fig. 2). It is characterized by a smoother floor with the presence of very few boulders or bumps at the scale of the image. This wide depression is circled by raised rims mostly composed of large boulders and mounds arranged in an ellipsoidal shape. These properties suggest that this feature could be a crater. However, it might also just be a topographic depression, since its large size implies that some morphologic features should be more pronounced, and the lack of any high-resolution images currently prevents a definitive interpretation. The Hera mission will reach the (65803) Didymos system at the end of 2026, and will conduct high-resolution imaging of the surface of Didymos. The higher resolution data expected from the mission will reveal the composition of these uncertain regions.

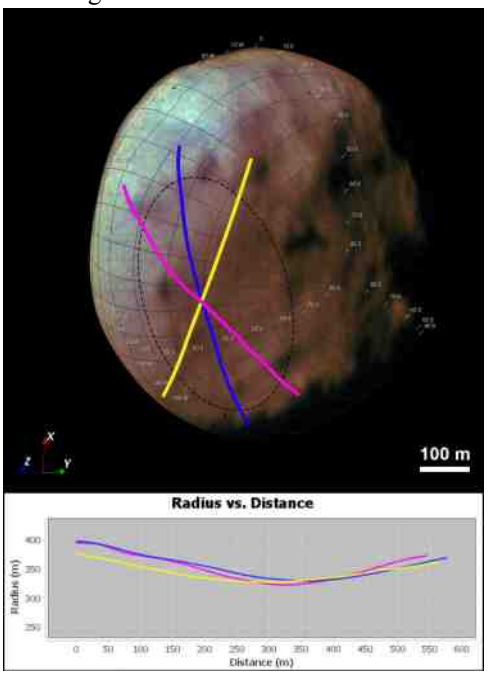


Fig. 2: Potential crater located close to the southern pole marked with dashed black line. The colored lines correspond to the elevation profiles reported at the bottom.

Future work: The next step will be to analyze the boulder Size Frequency Distribution of Didymos, improving the first results of [11] by adding to these statistics also the boulders identified with the LUKE images. The updated version of this work including the results of this analysis will be presented at the conference.

Acknowledgements: This work was supported by the Istituto Nazionale di Astrofisica (INAF) with the mini grant project 2024 "*Unveiling the Secrets of NEAs and Their Parent Bodies: A Surface Lithological Analysis*"; and HERA project (ASI-INAF agreement n. 2022-8-HH.0).

References: [1] Barnouin, et al. (2024) *Nature Commu.,* 15(1), 6202. [2] Rivkin, A., et al. (2021). *PSJ*, *2*(5), 173. [3] Ieva, S., et al. (2022). *PSJ*, *3*(8), 183. [4] Dotto, E., et al. (2024). *Nature*, *627*(8004), 505-509. [5] Dotto, E., et al. (2021). *PSS*, *199*, 105185. [6] Fletcher Z.. J., et al. (2018) Space Telescopes and Instrumentation [7] Ernst, C. M., et al. (2018) LPSC 49, abstract no. 1043. [8] Tusberti, F., et al. (2025) *Icarus*, 116744. [9] Penasa, L., et al. (2020) EPSC2020-1057. [10] Bigot, J., et al. (2024) *Nature Commu.*, *15*(1), 6204. [11 Pajola et al. (2024) *Nature Commu.*

NEOPOPS – How to characterize a potential threat with ground-based observations? J. Bourdelle de Micas[1], S. Ieva[1], E. Dotto[1], E. Mazzotta Epifani[1], P. Pravec[2], M. Lazzarin[3], S. Bagnulo[4], M.A. Barucci[5], M. Birlan[6,7], J. L. Cano[8], M. Devogèle[9], A. Farina[3], P. Fatka[2], F. Ferri[3], M. Fulchignoni[5], F. La Forgia[3], M. Micheli[6], A. Mura[3], D. Perna[1], and M. Siciliano[10], [1]INAF – Osservatorio Astronomico di Roma, via Frascati 33, Monte Porzio Catone, Italy, jules.bourdelledemicas@inaf.it, [2]Astronomical Institute of the Academy of Sciences of the Czech Republic, Fričova 298, Ondřejov, CZ-25165, Czech Republic, [3]Department of Physics and Astronomy "Galileo Galilei", University of Padova, Vicolo dell'Osservatorio 3, 35122, Padova, Italy, [4]Armagh Observatory & Planetarium, College Hill, BT61 9DB, Armagh, Northern Ireland, UK, [5]LIRA, Observatoire de Paris, Université PSL, Sorbonne Université, Université Paris-Cité, CY Cergy Paris Université, CNRS, 5 place Jules Janssen, 92195, Meudon, France, [6]Astronomical Institute of Romanian Academy, 5 - Cutitul de Argint, Bucharest, Roumaine, [7]LTE, Observatoire de Paris, 77 avenue Denfert-Rochereau, 75014 Paris Cedex, France, [8]Planetary Defense Office, ESA ESOC, Robert-Bosh-Strasse 5, 64293 Darmstadt, Germany, [9]ESA NEO Coordination Centre, European Space Agency, Largo Galileo Galilei 1, Frascati, 00044, Roma, Italy, [10]Resolvo S.r.l, via di Novoli 91/S ,50127 Firenze, Italy.

Introduction: The study of Near-Earth Objects (NEOs) has become a crucial component of planetary defense and of research into the early Solar System. Their proximity to Earth makes them accessible to ground-based observations, and also a potential significant threat to our civilization. For example, this population played a major role in the K-Pg impact event 65 million years ago, which led to the extinction of the dinosaurs. More recent cases, such as the Chelyabinsk meteor in February 2013, which caused substantial material damages, and the alert triggered by 2024 YR4 [1], highlight the threat posed by objects sized from 20 to 50 m in diameter, capable of causing regional-scale damage [2]. It is, therefore, essential to characterize these potential hazards by providing key information to support civil protection and mitigation efforts.

To address these operational challenges, the NEOPOPS project (NEO Physical Observations and Properties Simulation) was initiated and funded by the European Space Agency (ESA). In this presentation, we focus on the Rapid Response activities (WP6) carried out within the framework of this project.

Methods: The Rapid-Response work package of NEOPOPS aims to comprehensive characterization of objects that may pose a threat. Based on alerts issued by the European Space Agency, we conduct observations of potentially hazardous objects, either by following our scheduled observing plan or by requesting a Director's Discretionary Time (DDT) on various telescopes. This need for rapid observations stems from the short observability window of NEOs after their discovery. Their small sizes (typically in the range of 10-100m in diameter) mean that they remain bright enough for detailed observations only for very limited time spans, typically on the order of a few weeks. After this period, they usually become unobservable until shortly before their predicted close approach or impact date.

The characterization of these potential threats includes astrometric follow-up, spectroscopic, photometric, and polarimetric observations. Our primary facilities include the 3.58m Telescopio Nazionale Galileo (La Palma, Spain), the 1.54m Danish Telescope (La Silla, Chile), the 8.2m Very Large Telescope (Cerro Paranal, Chile), and the 1.2m Galileo Telescopio (Asiago, Italy). The information obtained from these observations is essential for enabling potential mitigation measures if the impact risk is real.

Examples: To date, we have received four different alerts during the year 2025, concerning 2024 YR4, 2025 FA22, 2025 SC5, and 2025 VP2. Most of these objects were assigned a Torino Scale [3] level of 1 (or up to 3 in the case of 2024 YR4). We took advantage of these "real-case scenarios" to apply our Rapid-Response procedures, obtaining key information such as albedo estimates, rotational period determinations, and insights into surface composition and shape of the body. In particular, the observations of 2025 FA22 were conducted as part of a dedicated IAWN campaign. These parameters are essential for defining potential mitigation measures. Additional information on 2024 YR4 has been published in [1].

Conclusions: This ability to carry out timely physical characterization of an imminent impactor is a key requirement for developing a rapid-response system for civil protection purposes. Thanks to several alerts issued in 2025, we were able to perform observations within the limited observability windows of these potential hazardous NEOs, enabling us to obtain both dynamical and physical characterization. Through the various work packages of the NEOPOPS project, we were able to mobilize our monthly observing time at multiple telescopes around the globe to focus on these "high-priority" objects. In addition, we successfully obtained DDT, when necessary, to deliver crucial information required for assessing potential mitigation strategies.

References: [1] Devogèle et al. (2025), arXiv:2511.09405, https://arxiv.org/abs/2511.09405.

[2] Perna et al. (2015), *P&SS*, 118, p.311-317, https://doi.org/10.1016/j.pss.2015.07.006. [3] Binzel et al. (2000), P&SS, 48-4, 297-303, https://doi.org/10.1016/S0032-0633(00)00006-4.

Acknowledgments: The NEOPOPS observations contract is funded by the Horizon Europe Programme of the European Union and implemented by ESA (agreement No.4000147191/25/D/MRP).

NEAs Global Boulder Size Frequency Distribution: what to Expect for (99942) Apophis?

M. Pajola[1], A. Lucchetti[1], L. Penasa[1], F. Tusberti[1], J. Beccarelli[1,2], G. Poggiali[3], J.B. Vincent[4]

[1]INAF-Astronomical Observatory of Padova, Vic. Osservatorio 5, 35122 Padova, Italy (maurizio.pajola@inaf.it); [2]CISAS, Center of Studies and Activities for Space, CISAS, G. Colombo, University of Padova, via Venezia 15, 35131 Padova, Italy; [3]INAF-Osservatorio Astrofisico di Arcetri, Largo Enrico Fermi 5, 50125 Firenze, Italy; [4]Deutsches Zentrum für Luft- und Raumfahrt (DLR), Rutherfordstraße, 2, 12489 Berlin, Germany.

Images of NEAs acquired by space missions have enabled the most detailed boulder analyses ever obtained on small bodies [1–6]. In particular, the investigation of boulder SFDs obtained from size range between few centimeters to hundreds of meters, were found to commonly follow power-law fits [1-3,5–8]. From a formative perspective, this means that these boulders have been generated by a sudden fragmentation, as an impact event, and leading to a distribution of remnants characterized by fractals [8,6]. Such a result, coupled with both the extremely blocky nature of the observed surfaces and the presence of the largest boulders that are usually ~1/10 the NEAs' diameters, support an impact scenario for the boulders, whether from craters' emplacement or from the progenitor catastrophic disruption [8]. The power-law indexes obtained on global counts for C-complex asteroids (henceforth called carbonaceous asteroids) (162173) Ryugu and (101955) Bennu are −2.65 ± 0.05 for boulders with sizes 5–160 m (hereafter, all size-ranges indicated show the maximum boulder size identified for each mentioned NEA) and −2.5 ± 0.1 for boulders with sizes 0.2–100 m, respectively. These values indicate that such bodies are rubble piles dominated by impact processes [5,6,9]. On the other hand, the global boulder distribution of the S-complex (henceforth called stony) NEA (25143) Itokawa has a power-law index of −3.05 ± 0.14 for boulders 5–50 m, although on specific areas of the asteroid the boulder SFD was fit by broken power-law curves [7]. Stony NEAs (433) Eros and (4179) Toutatis have a SFD with a power-law index of −3.25 ± 0.14 for boulders 10–140 m and of −4.4 ± 0.1 for boulders 20–61 m, respectively [1,3,7,10]. The (65803) Didymos-Dimorphos stony binary system is also characterised by the ubiquitous presence of boulders. In particular, Didymos boulder SFD is fit by a power-law curve with index -3.6 ± 0.7 for sizes ≥ 22.8 ± 2.3 m, while Dimorphos boulder ≥ 5 m SFD is fit by a power-law curve with index of -3.4 ± 1.2 [11]. As for the carbonaceous counterpart, such trends are reflective of a rubble pile origin as a result of a progenitor catastrophic disruption (with Eros being a possible single shard fractured exception, later modified by multiple impacts [12,13]). Nevertheless, the power-law index is higher on stony asteroids than on carbonaceous asteroids. This suggests that on the former, more of their surface mass is contained in smaller boulders rather than on the latter [6], hence reflecting how distinct materials respond differently to meteoroid bombardment and thermal cracking [14].

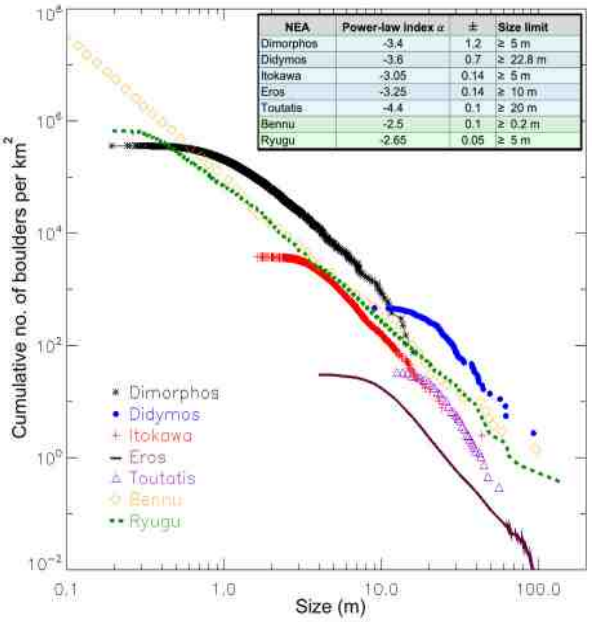


Figure 1. Comparative plot showing all global boulder SFD obtained for the visited NEAs [11]. Stony NEAs are highlighted in light blue in the superimposed table, while carbonaceous ones are highlighted in green.

Stony Asteroid (99942) Apophis has a size of 450 × 170 m. Its dimensions suggest that such NEA is a non-monolithic aggregate made of numerous boulders inherited from catastrophically disrupted parent bodies, which later coalesced under the influence of gravity [15, 16]. In this context, the future analysis of its boulder SFD and its maximum boulder size with respect to the largest dimension of the body will enable us to investigate the evolution and collisional history of its parent body, shedding light on the geomorphological processes that shape the rubble piles surfaces [17, 18, 8] and contextualizing it within the NEA stony versus carbonaceous framework. Moreover, the future analysis of Apophis surface and structure will have wide implications on the planetary defense strategy needed to deviate such objects.

Acknowledgments: This research was supported by the Italian Space Agency within the HERA project (ASI-INAF agreement n. 2022-8-HH.0).

References: [1] Thomas, P.C. et al. Shoemaker crater as the source of most ejecta blocks of the asteroid 433 Eros. Nature 413, 394–396 (2001). [2] Michikami, T. et al. Size-frequency statistics of boulders on global surface of asteroid 25143 Itokawa. Earth Planets Space 60, 13–20 (2008). [3] Jiang, Y. et al. The distribution and source of boulders on asteroid 4179 Toutatis. Proc. IAU Symp. 10, 153–155 (2016). [4] Mazrouei, S., et al. Block distributions on Itokawa. Icarus 229, 181–189 (2014). [5] Michikami, T. et al. Boulder size and shape distributions on asteroid Ryugu. Icarus 331, 179–191 (2019). [6] Burke, K. N. et al. Particle size-frequency distributions of the OSIRIS Rex candidate sample sites on asteroid (101955) Bennu. Remote Sens. 13, 1315 (2021). [7] Tancredi, G., et al. Distribution of boulders and the gravity potential on asteroid Itokawa. Icarus 247, 279–290 (2015). [8] Pajola, M. et al. Anticipated geological assessment of the (65803) Didymos-Dimorphos system target of the DART-LICIACube mission. Planet. Sci. J. 3, 210 (2022). [9] Beitz, E., et al. The collisional evolution of undifferentiated asteroids and the formation of chondritic meteoroids. ApJ 824, 12 (2016). [10] Michikami, T. & Hagermann, A. Boulder sizes and shapes on asteroids: a comparative study of Eros, Itokawa and Ryugu. Icarus 357, 114282 (2021). [11] Pajola, M. et al. Evidence for multi-fragmentation and mass shedding of boulders on rubble-pile binary asteroid system (65803) Didymos. Nat Commun 15, 6205 (2024). [12] Buczkowski, D. L., et al. 433 Eros lineaments: Global mapping and analysis. Icarus 193, 39–52 (2008). [13] Housen, K. Cumulative damage in strength-dominated collisions of rocky asteroids: rubble piles and brick piles. Plant. Sp. Sci. 57, 142–153 (2009). [14] Cambioni, S. et al. Fine-regolith production on asteroids controlled by rock porosity. Nature 598, 49–52 (2021). [15] Campo Bagatin, A. et al. How many rubble piles are in the asteroid belt? Icarus 149, 198–209 (2001). [16] Davis, D. R., et al. Collisional evolution of small-body populations. Asteroid III Ch 4, 545–558 (2002). [17] DellaGiustina, D. N. et al. Properties of rubble-pile asteroid (101955) Bennu from OSIRIS-Rex imaging and thermal analysis. Nat. Astron. 3, 341–350 (2019). [18] Schröder, S. E. et al. The boulder population of asteroid 4 Vesta: size-frequency distribution and survival time. Earth Space Sci. 8, e00941 (2020).

First year of NEAs Spectroscopic Observations within the NEOPOPS Project at Asiago Observatory

F. La Forgia[1], M. Lazzarin[1], A. Farina[1], A. C. Mura[1], F. Ferri[2], S. Ieva[3], J. Bourdelle de Micas[3], E. Dotto[3], D. Perna[3], E. Mazzotta Epifani[3] and the NEOPOPS team
[1]Dipartimento di Fisica e Astronomia "Galileo Galilei", Università di Padova, vicolo dell'Osservatorio 3, 35122, Padova, Italy
[2]Centro di Studi e Attività Spaziali "Giuseppe Colombo" (CISAS), Università di Padova, via Venezia 1, 35122, Padova, Italy
[3]INAF - Osservatorio Astronomico di Roma, Via Frascati 33, 00078, Monteporzio Catone (Roma), Italy

Introduction: Near Earth Asteroids (NEAs) play an important role in planetary defense and in the study of the early Solar System. NEAs are asteroids with perihelion distances smaller than 1.3 AU and represent a valuable source of information on primitive Solar System material. After long periods of dynamical evolution driven by gravitational interactions with the planets, many of these objects reach the inner Solar System. Their study helps us understand the evolution of small bodies, the possible delivery of water and organic molecules to the early Earth, and the processes that shaped the formation of the Solar System. NEAs are also relevant because they may become useful mining resources in the future, and they are essential for evaluating impact risks. A specific group of NEAs, called Potentially Hazardous Asteroids (PHAs), follows orbits that can pass close to the Earth and they have sizes large enough to produce significant damage in the event of an impact. At present, about 2500 PHAs are known, including objects such as Didymos and Apophis. Understanding their dynamical and physical properties (for example size, structure, composition, density, velocity and impact geometry) is necessary to evaluate the risks linked to close approaches and to design realistic mitigation strategies. For these reasons, the detailed study of NEAs, and especially PHAs, remains a priority. Improving our knowledge of these objects gives the information needed to model their behaviour, assess their possible hazard and prepare effective responses in case of a future impact threat.

NEOPOPS Project: While several space missions have been planned to study specific NEAs in detail, observations from the ground remain the main method for investigating these objects. Ground-based observations are the best for giving numerous and fast information on NEA that requires a rapid characterization, such as potential threats or recently discovered objects. Ground-based characterization of NEAs that will be visited by future missions is also essential to optimise the instruments on board and to prepare the scientific analysis of the targets.

As of November 2025, 40,000 NEAs are known (https://www.esa.int/Space_Safety/Planetary_Defence/40_000_near-Earth_asteroids_discovered), with an average of about 3,000 new discoveries per year, roughly eight per night. The NEO Physical Observations and Properties Simulation project (NEOPOPS) is funded by the Horizon Europe Programme of the European Union, implemented by ESA and led by INAF–OAR (Observatory of Rome) [see presentation by Dotto et al. SISP 2025]. Its goal is the physical characterization of Near Earth Objects. The project began in February 2025 and will continue until August 2028. It builds on the results of previous large programmes supported by the European Commission, such as NEOShield-2 and NEOROCKS, which focused on understanding the properties of the NEO population. These earlier efforts showed that only a coordinated approach can address the main challenges related to NEO impact monitoring and mitigation. The current need is to improve our knowledge of the physical nature of small NEOs, which have the highest statistical probability of impacting the Earth in the next centuries, and to reduce the risk of unexpected events. Moreover, as these objects become unobservable soon after their discovery, the current need is for a very rapid response as soon as they are discovered. This helps significantly in reducing the risk of unexpected events.
NEOPOPS aims to match the physical characterization rate of NEAs with the discovery rate, using complementary techniques such as photometry, spectroscopy and polarimetry and providing rapid responses. The team will also identify high-priority NEAs, including recently discovered objects and potential impactors, working in coordination with space agencies and international institutions involved in Solar System science and planetary defense.

Observations: In this work we present the first year preliminary results of our spectroscopic survey of NEAs carried out at the Asiago Observatory as part of Work Package 4 (Spectroscopy) [see presentation by Ieva et al. SISP 2025] and 6 (Rapid Response) of the NEOPOPS project. These work packages focus on the acquisition and analysis of data for newly discovered small objects, including possible PHAs.

Our observations are obtained with the 1.22 m Galileo Telescope equipped with the Boller & Chivens spectrograph and with the 1.82 m Copernico Telescope equipped with AFOSC (Asiago Faint Object Spectrograph and Camera). Both telescopes are located at the Asiago Observatory in Italy. The covered spectral range extends from about 0.4 to 1.0 microns. Observing NEAs is challenging because these objects are generally faint with a visual magnitude about 18 and move quickly across the sky, requiring short exposure times and careful planning.

Since the beginning of the project, we have observed about thirty NEAs, including several recently discovered bodies with estimated sizes between 30 and 900 meters. We also carried out observations of particularly interesting asteroids, such as the binary 1999 HF1, and PHA 2025 FA22, which appeared near the top of the ESA NEO Coordination Centre risk list in May 2025 due to a possible impact scenario in 2089.

Results: The analysis includes a taxonomic classification, which can be done sometimes also including complementary data, such as spectra of the same objects in the NIR, based on the system of DeMeo et al. (2009), which allows us to place NEAs into groups according to their spectral properties and possible mineralogical composition.
We also compare asteroid spectra with meteorite data collected on Earth, usually considered using laboratory meteorite spectra from the RELAB database. This step is important to test the links between asteroids and meteorite analogs and to understand their composition and origin. Comparing the two datasets also helps us investigate the processes that shaped these bodies and preserved material

from the early Solar System. In addition, we study the spectral slope to examine the overall shape of the spectra and obtain information on surface properties. Particular attention is given to absorption features, which allow the identification of specific minerals present on the surface.

Most of the objects we observed and analysed have a missing or uncertain taxonomic classification in the literature.

For the binary asteroid 1999 HF1 we covered two full rotations, allowing us to study not only its taxonomic and meteoritic type but also how the spectral slope changes along its rotational phase. We performed a simple geometric analysis to investigate possible differences between the surface of the primary and secondary components.

We also obtained twelve spectra of the PHA 2025 FA22 sampling about 2.3 hours of its rotation (about 13h). For this object, we analysed the variation of the spectral slope with rotational phase and compared each spectrum with taxonomic and meteoritic templates.

Conclusions: The observations carried out so far confirm the value of regular ground-based monitoring for the characterization of newly discovered NEAs. The data collected as part of the NEOPOPS project already provide useful information on the taxonomic class, surface properties and rotational behaviour of several NEAs and PHAs. Expanding this survey will improve our knowledge of these objects and support future studies related to Solar System science and planetary defense.

Acknowledgment: The NEOPOPS observations contract is funded by the Horizon Europe Programme of the European Union and implemented by ESA (agreement No.4000147191/25/D/MRP).

3D Reconstruction of DART Ejecta at Dimorphos Highlights An Anisotropic, Filamentary Structure

J. D. P. Deshapriya[1], P. H. Hasselmann[1], Elisabetta Dotto[1], Igor Gai[2], A. Zinzi[3] & LICIACube team
[1]INAF - Osservatorio Astronomico di Roma , Via Frascati 33, 00078 Monte Porzio Catone (Rome), Italy
[2]Università di Bologna, Bologna, Italy
[3]Agenzia Spaziale Italiana, Roma, Italy

Introduction: The NASA Double Asteroid Redirection Test (DART) mission demonstrated planetary defense through a kinetic impact on Dimorphos, the smaller component of the Didymos binary asteroid system, on September 26, 2022. The mission aimed to validate kinetic impact as a viable strategy for asteroid deflection. The impact successfully reduced Dimorphos's orbital period by 33 ± 1 minutes [1], exceeding the mission's primary objective.

A key metric of the impact efficiency, the momentum enhancement factor (β), which quantifies momentum transferred through ejecta recoil, was estimated to range between 2.2 and 4.9 [2]. These values indicate a momentum transfer significantly greater than that of a perfectly inelastic collision (β = 1). Without the contribution of ejecta, the orbital period change would have been only about 7 minutes, consistent with pre-impact simulations.

Analysis of the ejecta distribution using data acquired by the LICIACube spacecraft [3, 4] revealed an ejecta cone with an elliptical base, characterized by half-angles of 69° and 51° [5]. These findings underscore the crucial role of ejecta in enhancing momentum transfer and further confirm the effectiveness of kinetic impact as a method for asteroid deflection.

Although the ejecta curtain can be approximated by a cone, the real physical structure is more complex than a cone, as evident from LUKE image data returned by LICIACube. As seen from Fig. 1, on both face-on and side-on views of the ejecta obtained during the flyby, it is clear that the ejecta curtain is a debris field that is characterized by extended features originating from and around the impact location on Dimorphos. A critical understanding of the spatial distribution of these features in three dimensional space is required (a) to better understand how the momentum was distributed among escaping ejecta; (b) to constrain the ejection velocities of particles that are part of these structures; (3) to better estimate the mass of the ejecta, following radiative transfer calculations coupled with observed optical depths of features. As such, in this work we attempt to reconstruct the distribution of these features using LUKE data.

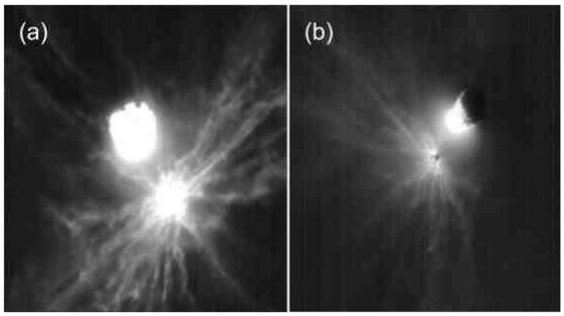


Figure 1: (a) A face-on view of the ejecta field during the approach phase of the flyby, 149 seconds after the impact, from a distance of 127.7 km from Dimorphos (b) an oblique view of the ejecta field during the final phase of the flyby, 189 seconds after the impact, from a distance of 144.3 km from Dimorphos.

Methods and Results:

In order to accurately identify the extended features in both face-on and side-on/oblique images of the ejecta field, we first enhanced the images to highlight the details of the ejecta field using python scikit-image library [6]. Then we cropped the images to 400x400 px frames, centred on Dimorphos. These were then compiled to make short video clips thus enabling us to track the features in consecutive images.

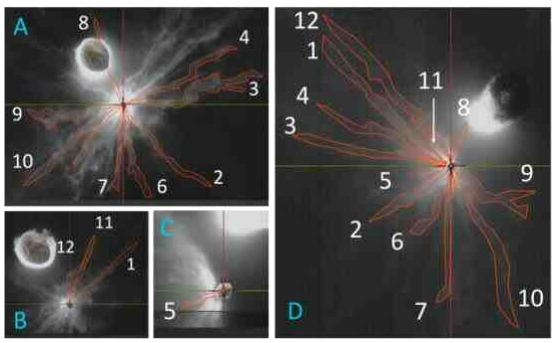


Figure 2: Identified 12 features in both front, side and oblique viewing geometries.

Upon successful identification of 12 features (Fig. 2) , using the 3D animation software Blender (version 3.5), we trace out delimiters around each of the features in both face-on and side-on images.

Next, we populate homogenous and evenly spaced cubic particles around Dimorphos inside a cube of 2km a side, and capture the particles that are inside the aforementioned delimiters of a given feature (Fig. 3) in face-on image (we use cubic particles of 50m per a side, comparable to the spatial resolutions of several LUKE pixels during the flyby). Next we switch to the simulation of the side-on view/ oblique view of the ejecta and populate the restricted particles from the previous step. Then, using the delimiters of the same feature in this different observing geometry we further restrict the volume in space that corresponds to the feature in question. Similarly we iterate over other features and obtain the 3D orientations and span of all the identified features. Transformations among different LUKE camera orientations are performed using NAIF/SPICE[7] package offered by Python3 package spiceypy[8].

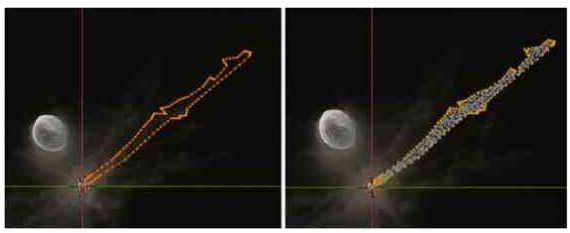


Figure 3: An example of an identified feature and how its delimitation is used to constrain the particles that are along the line of sight of this feature, in this case of a face-on image, superposed over a simulation of the observation. The origin of the coordinate system is at the centre of Dimorphos

In Fig. 4, can be visualized the simulation of the ejecta field observation along with a LUKE image.

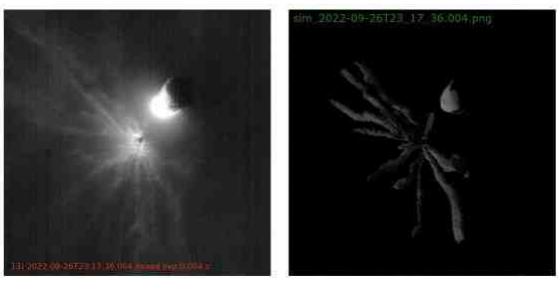


Figure 4. Left – LUKE image featuring the ejecta field observed with an oblique geometry as LICIACube was leaving the Didymos system following the closest approach. Right – Simulation of the ejecta field at the same time and geometry using the ejecta features retrieved using our method.

We then used images with longer exposure times to estimate the extends of ejecta features and thereby derive lower limits for ejecta velocities. Out of the features we used for this estimation, we found velocity ranges in the range of 30-70 m/s.

We quantified each feature by fitting a representative vector to its voxel cloud and comparing it with the corresponding cone wall vector, revealing that most features lie close to the cone (±10°), while some show coherent azimuth-locked deviations up to 20° (Fig. 5). Azimuthal occupancy analysis indicates uneven voxel distribution, with preferred sectors aligned with bright LUKE filaments, confirming that deviations from the cone are directionally structured rather than random. Features with both large radial extent and high voxel population tend to cluster near the cone wall, indicating that a substantial fraction of optically dominant ejecta resides close to the cone boundary. We will present the final results and discuss the implications at the congress.

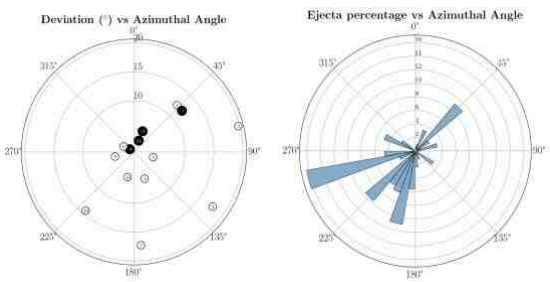


Figure 5. Quantified deviations of the ejecta distribution from an elliptical cone model.

Acknowledgments: The LICIACube team acknowledges financial support from Agenzia Spaziale Italiana (ASI, contract No. 2019-31-HH.0 CUP F84I190012600).

References:

[1] Thomas et al. (2023), Nature, 616, 448
[2] Cheng et al. (2023), Nature, 616, 457
[3] Dotto et al., (2011), PSJ, 199, 105185
[4] Impresario et al., (2025), Acta Astronautica, 231, 223-234
[5] Deshapriya et al. (2023), PSJ, 4:231
[6] van der Walt et al. (2014), PeerJ 2:e453
[7] Acton, C. H. (1996), P&SS, 44, 65
[8] Annex, A., Pearson, B., Seignovert, B., et al. (2020), JOSS, 5, 2050

SPECTROSCOPIC MEASUREMENTS OF HEXAHYDRITE RELEVANT FOR THE JOVIAN ICY MOONS

F. Furnari[1,2], G. Piccioni [1], S. Rubino[1], S. Stefani[1], S. De Angelis[1], F. Tosi[1], C. Carli[1], M. Ferrari[1]
1 *Istituto di Astrofisica e Planetologia Spaziali (IAPS), Istituto Nazionale di Astrofisica (INAF), Via del Fosso del Cavaliere 100, 00133 Rome, Italy,* 2 *Dipartimento di Fisica, Sapienza Università di Roma, Rome, Italy*
francesca.furnari@inaf.it

Introduction: The surfaces of Jupiter's icy moons, as Europa and Ganymede, feature mixtures of water ice with various non-ice materials. Among these, hydrated minerals can mimic the 1.5 and 2.0 μm water ice absorption bands. In particular, the presence of hydrated magnesium sulfate, such as hexahydrite ($MgSO_4 \cdot 6H_2O$), was first suggested on the surface of these icy bodies based on Galileo/NIMS data, possibly indicating remnant of past extrusion of liquid water from an ocean below [1]. Although other compounds, particularly chloride salts, have subsequently been proposed to explain spectral signatures observed by NIMS, the key interest for future close exploration is to understand whether these non-water ice materials are distinguishable in mixtures with water ice, and whether they are of exogenic or endogenic origins. Characterizing such minerals under environmental conditions as much as possible similar to those found on the icy moons' surfaces is therefore crucial, especially considering the link between the presence of hydrated salts on Solar System bodies and geological processes that occurred in the presence of liquid water, with potential implications for the establishment of a habitable environment.
This work is also important in supporting upcoming observations of the MAJIS (Moons and Jupiter Imaging Spectrometer) instrument [2,3] onboard the ESA's JUICE mission as well as NASA's Europa Clipper mission [4]. Although similar work on hexahydrite was carried out previously [5,6,7], the MAJIS spectral sampling, which is 3.6 nm from 0.50 to 2.35 μm and 6.5 nm from 2.25 to 5.54 μm, as well as its spectral range and the emerging physical processes at play, motivate performing new laboratory measurements at higher spectral resolution and different physical-chemical conditions.

Experimental procedure: We prepared powders of hexahydrite at different grain sizes, ranging from 50 to 500 μm, to investigate the variation of the spectral features in the infrared and visible spectral ranges under different environmental conditions. Reflectance spectra and visible images were acquired using a microscope coupled to a FTIR spectrometer and a cryogenic cell (Figure 1), which can be filled with different gases, capable of reaching pressures down to 10^{-3} mbar and temperatures as low as 40 K.



Figure 1*: Micro-IR setup, composed of a FTIR spectrometer coupled to a microscope and a cryogenic cell, which allows the acquisition of both the visible imaging and the VIS-IR reflectance spectra of the surface of the sample.*

Samples of different grain sizes were placed in the cryogenic cell using a custom sample holder, allowing for sequential measurements during a single session of different samples. Spectra were collected as the pressure was gradually reduced, with a stabilization time for each pressure of a few minutes.

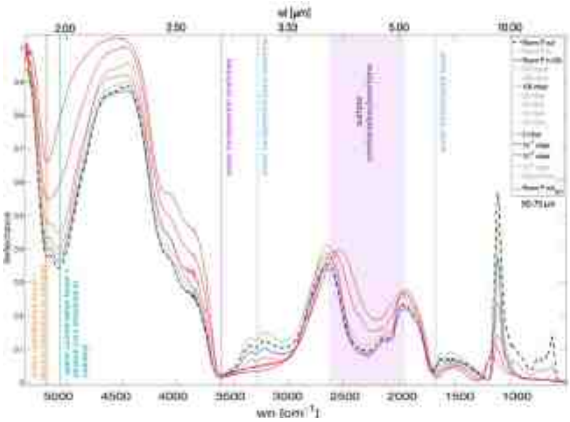


Figure 2*: Hexahydrite IR reflectance spectra acquired at room temperature (300K), ranging from room pressure to 10^{-3} mbar and then exposing the sample back to air. For clarity, only a limited number of spectra are displayed, while the legend show all the measured pressures.*

Results and conclusions: The results (partially displayed in Figure 2) show that the material undergoes structural changes at specific pressure thresholds, which vary depending on grain size, suggesting a complex interaction between physical properties and environmental conditions, with water playing a major role in the processes.
These measures highlight the correlation between the spectral features of this kind of planetary analogs for the icy satellites, their physical properties, and the environment. One of the most interesting aspects we came across is a change in the lattice structure of this sample, which seems incompatible in its crystalline and hydrated form (hexahydrite) at the extremely low pressure on the surface of the icy moons (10^{-8}-10^{-12} mbar). Preliminary laboratory measurements show that the process of amorphization and dehydration with vacuum occurs in a timescale of tens of minutes at room temperature. If these results are confirmed at low temperature, the existence of hexahydrite on the surface of the icy satellites would require a continuous replenishment or could be ephemeral, sustaining the subsurface liquid water as a possible source. On the other hand, this hydrated salt could eventually be preserved thanks to some mechanism that involves the rapid emplacement in simultaneous surface conditions of low temperatures and ultra-high vacuum. In this regard, new measurements at cryogenic temperatures are scheduled to better constrain the spectral behaviour and the processes of this sample at environmental conditions closer to the jovian icy moons' surface. Moreover, we are performing similar measurements starting from a pure N_2 atmosphere inside the cryocell, with the aim of discriminating whether the structural change of hexahydrite is due to the pressure itself or the amount of water vapour in the atmosphere inside the chamber.
These results are of paramount importance to avoid any ambiguity in the determination of the surface composition of the icy moons, also in view of the MAJIS data to come.

References:

[1] T.B. McCord et al., *Icarus*, **209,** 639-650 (2010)
[2] G. Piccioni et al., *IEEE 5th International Workshop on Metrology for AeroSpace*, 318-323 (2019)
[3] F. Poulet et al., *Space Sci Rev*, **27,** 220 (2024)
[4] R.T. Pappalardo et al., *Space Sci Rev*, **220,** 40 (2024)
[5] T.B. McCord et al., *JGR*, **104,** 11827-11851 (1999)
[6] J.B. Dalton et al., *Icarus*, **177,** 472-490 (2005)
[7] S. DeAngelis et al., *Icarus*, **281,** 444-458 (2017)

Acknowledgments: *This work has been developed under the ASI-INAF agreement n. 2023-6-HH.0. This work is supported by EU and Regione Campania with FESR 2007/2013 O.O.2.1*

EMM project: The PLATA laboratory facility for the martian boundary layer research

G. Franzese[1], G. Mongelluzzo[1], C. Porto[1], S. Silvestro[1], C. I. Popa[1], F. Esposito[1], Sofia Grusovin[2], Loris Todesco[2], Paolo Vagliasindi[2], Rolando Parmesani[2], U. Cortesi[3], I. Donnarumma[4], A. Turchi[4], F. D'Amico[5], M. Gai[3], A. Argan[4]. [1]Osservatorio Astronomico di Capodimonte, INAF-OACN, Napoli, Italy; [2]ASSE srl – Via Cicerone n. 11, Trieste, Italy, [3]Istituto di Fisica Applicata (IFAC-CNR), Firenze, [4]Agenzia Spaziale Italiana (ASI), Roma, Italy; Italy; [5]INAF headquarter, Via del Parco Mellini, Roma, Italy.

Introduction:

PLATA (PLanetary images, LAboratory experiment and Terrestrial Analogues) is a novel infrastructure under development at the INAF Astronomical Observatory of Capodimonte for a comprehensive study of sand and dust mobilization phenomena in planetary environment, with particular focus on the martian one, using a multi-pronged approach. As suggested by the name, PLATA is divided into three main parts: a planetary images analysis center, a laboratory facility and field studies of terrestrial analogues. This peculiar combination will allow to study the topic using the direct data of the planetary surfaces, the data reproduced in laboratory and the data acquired on field in analogue sites on Earth. The activity is part of Earth-Mars-Moon (EMM), which is an INAF, CNR and ASI joint project funded by the PNRR European recovery funds.

In this work we present the laboratory component of PLATA, that is currently under development and commissioning at the premises of Capodimonte, in collaboration with Asse s.r.l.. The activity foresees the upgrade of the vacuum chamber already present in our planetology laboratory, to reproduce the martian environment in a wide range of atmospheric conditions, so to perform extensive experiments on the grain mobilization processes.

The scientific community has focused on building planetary-environment simulation facilities since the early stages of space exploration, and many low-pressure simulation chambers with different capabilities exist around the world. However, most of them are dedicated to simulation in still atmosphere, and the low pressure wind tunnels are still scarce. The NASA Mars Wind Tunnel (MarsWIT) [1] represents one of the earliest, being active since the middle of 70s and still reliable operating up to now. Nowadays, one of the most advanced tunnels is the Aarhus Mars Simulation Wind Tunnel Simulator (AWTSII) [2]. Our facility takes inspiration from the AWTSII, but on a smaller scale, combining the aeolian studies with the capacity to simulate the atmospheric electric field, in a similar manner to what suggested by Farrell et al. 2015 [3]. In addition, we also aim to reproduce the conditions of the planetary boundary layer in terms of solar radiation and temperature with a representative regolith bed. The sum of all these factors will allow to simulate the martian boundary layer conditions from clear sky to heavy dust weather, in different seasons, wind regimes and light exposure, allowing both to test the space mission instrument and perform experiments in a large plethora of scenarios.

Facility Description:

The planetary laboratory of Capodimonte is equipped with a cylindrical vacuum chamber of 2.3 m · 1.3 m able to reach pressures of 10^{-2} mbar. The chamber, previously used to simulate the martian CO_2 still atmosphere, is under upgrade with a new series of subsystems including [4]:

a) a low pressure wind tunnel (WT) for speeds up to 15 m/s, able to reproduce the martian boundary layer;
b) a nitrogen thermally regulated plate at the bottom of the tunnel frame, to simulate martian polar and night conditions down to -80°;
c) two vertical electrodes, with adjustable distance, to generate an electric field (E-field) up to ±150 kV/m;
d) a solar radiation simulator, made by a system of UV lamps to induce photoelectric grain charging;
e) a dust injection system, to regulate the grain velocity and concentration in the tunnel;
f) a monitoring system, involving a series of environmental sensors:
   - an imaging system, to record the grain trajectories using a backlight configuration and high resolution and fps cameras;
   - a Faraday cup, to measure the grain charges;
   - a Langmuir probe, for the induced plasma;
   - pitot tubes and temperature sensors to characterize the wind profile;
   - an electric field mill to monitor the induced E-field between the vertical electrodes.

The base frame that will host the system is depicted in black in *Figure 1*, it can be inserted inside the vacuum chamber (in light-blue) sliding on the tailor-made binaries. All the systems are designed to be modular to maintain maximum flexibility. *Figure 2* shows the final realized model outside and inside the vacuum chamber.

The martian wind tunnel is designed as an open-circuit. The main flow blows inside a rectangular frame of ∼1.34 m · 0.5 m · 0.5 m, centered on the chamber. This frame hosts the test section of ∼ 1 m · 0.4 m, i.e. the region where the wind achieves the logarithmic profile of the boundary layer. The rectangular frame is preceded by an inlet, to shape the flow, and followed by an outlet where an aspiring vertical fan is located. This leads the total length of

the wind tunnel to ~ 1.94 m. The remaining volume of the vacuum chamber, external to the rectangular frame, represents the return flow section. The tunnel is designed to achieve a laminar flow speed up to 15 m/s.



Figure 1: PLATA laboratory facility.



Figure 2: The wind tunnel frame, before and after its insertion in the vacuum chamber

The bottom of the frame performs multiple functions: it is thermally controlled, but also host the lower electrodes of the E-field generator and can act as a sample holder. The upper electrode has instead a circular 150 mm shape and is connected through a movement system to a flange on the top of the chamber, in order to regulate its height. The lower electrode can also be raised by a fixed amount in correspondence with the upper electrode, using a cylinder of the same diameter. Both electrodes are connected to a high-voltage generator, and can be independently powered in the range ± 8 kV. The electrodes distance and ΔV can therefore be tuned to achieve the desired vertical E-field value, up to ±150 kV/m. Due to the low atmospheric breakdown of the martian conditions, the E-field induced by the electrodes or the grains motion can potentially lead to electric discharges. For this reason, the chamber is equipped with a Languir probe to characterize the plasma.

The UV solar radiation is simulated by means of an excimer and a deuterium lamp that can be focused in different points within the chamber. The Faraday cup can also be placed in different spots and orientations to characterize the amount of charge of the grains set in motion, both in horizontal or vertical trajectores.

One of the core components of the facility is its monitoring system to characterize the grain dynamics. We tuned an high fps imaging system to the geometrical constraints of the chamber and its flanges to use it on a wide range of sizes from 10 μm dust to over 100 μm sand.

Application and Potentiality:

Due to its wide range of potential simulated conditions, the facility represents an excellent tool for testing and calibrating the instrumentation to be landed on Mars and other planetary surfaces, facing most of the expected situations of their operative cycle.

However, despite its technological capabilities, the laboratory facility is designed primarily with scientific purposes in mind. As clear from its description, the PLATA facility puts equal efforts into the study of the wind flow and of the atmospheric E-field, because the main aim of the simulation chamber is the characterization of the sand and dust mobilization phenomena. Indeed, during the lifting process the grains are electrically charged, hence it is fundamental to study both the contribution of the wind shear and of electric forces to characterize the lifting. The charging is related both to the UV radiation, that can charge the grains when they are still resting on the surface, and to mutual and with surface collisions during the motion, which triboelectrically charge the grains.

The authors aim to perform an extensive experimental campaign for studying the sand and dust mobilization and lifting threshold, by varyng the radiation and electric conditions. The tests will start with monodisperse samples and will then increase in complexity using more representative simulants. We hope to shed light on the grain electrification process and on the interconnected feedback between saltation dynamics, aeodynamic stress, and electric forces.

Acknowledgments: The results reported in the article were obtained in the context of the Earth-Moon-Mars (EMM) project, led by INAF in partnership with ASI and CNR, funded under the National Recovery and Resilience Plan (PNRR), Mission 4, Component 2, Investment 3.1 - Action 3.1.1 funded by the EU- NextGenerationEU.

References:

[1] Greeley, R. "The Martian Surface Wind Tunnel (MARSWIT)." Bulletin of the American Astronomical Society, Vol. 9, p. 448. Vol. 9. 1977.

[2] Holstein-Rathlou, C., et al. "An environmental wind tunnel facility for testing meteorological sensor systems." Journal of atmospheric and oceanic technology 31.2 (2014): 447-457.

[3] Farrell, William M., et al. "Is the electron avalanche process in a martian dust devil self-quenching?." Icarus 254 (2015): 333-337.

[4] Franzese, Gabriele, et al. "PLATA Martian Facility for Sand and Dust Mobilization Experiments (EMM Project)." *2025 IEEE 12th International Workshop on Metrology for AeroSpace (MetroAeroSpace)*. IEEE, 2025.

Experimental petrology approaches to lunar volcanism: the case study of Lunar Sinuous Rilles (LSR)

G. Scognamiglio[1], A. Pisello[1], M. Fastelli[1], A. Zinzi[2] and D. Perugini[1], [1] Department of Physics and Geology, University of Perugia, gabriele.scognamiglio@dottorandi.unipg.it, [2]ASI Space Science Data Center (ASI-SSDC), Roma.

Introduction:

The Moon has been shaped over time by many different processes, some of which have left evident features on its surface, such as impact craters, mare basins, and lunar sinuous rilles (LSRs). LSRs, meandering channel-like structures created by turbulent, low-viscosity lava flows [1], have recently gained interest—together with lava tubes—as possible sheltering sites for future human habitats [2]. The processes that formed these features also influenced the distribution of minerals and elements on the lunar surface, making their study essential for future lunar exploration and *in situ* resource utilization [3]. Since the acquisition and interpretation of spectral data is very common in planetary surface studies, one of the main objectives of this project is to create a solid reference database of silicate glasses with different Moon-like compositions, to support future efforts in interpreting the Moon's surface. Additional objectives include the rheological characterization of these lunar simulants and the implementation of numerical modelling of lava flows and erosion patterns under lunar environmental constraints.

Materials and Methods:

The first step has been the creation of laboratory-made igneous analogues with the compositions of four different lunar products: Apollo 11 high-Ti mare basalt (renamed MB), Apollo 15 low-Ti basalt (LTB), Apollo 15 KREEP basalt (KB), and Apollo 15 Green Glass (GG). These compositions were taken from Taylor (1982) [4] and were selected to provide a preliminary dataset that offers a degree of chemical variability among the basalt-like compositions observed on the Moon. The preparation of the synthetic silicate glasses involved mixing pre-weighed oxides (by planetary mill, using agate jar and balls) and melting them in a Nabertherm furnace at 1400 °C, with an average high-temperature homogenization time of 3–4 hours for each sample. After this procedure the melts were quenched to obtain homogeneous amorphous samples (glasses). Each sample was then ground and melted twice to achieve better homogenization. XRPD (X-Rays Powder Diffraction) analysis were performed to verify the amorphous nature of these simulants. After producing the four analogues, 10 grams of each sample were ground and sieved into four granulometric classes (0–38 µm, 38–63 µm, 63–106 µm, 106–150 µm). These four classes (for a total of 16 samples) were analyzed with FTIR (Fourier Transform Infrared) spectroscopy (Bruker). The preliminary spectral dataset was studied in the VNIR (Visible-Near Infrared) and MIR (Mid-Infrared) ranges, since these are the most commonly observed in planetary science.

In parallel with the spectral analysis, the four samples were melted again in a GERO furnace at 1400 °C to measure their viscosities with a viscometer (Anton Paar Rheometer) using the Concentric Cylinders method. The experimental apparatus is also composed by a rotating cylindrical platinum spindle connected to the rheometer. The liquidus temperature of the samples was modelled with MELTS [5], while the viscosities were modelled using the equations from Giordano et al., (2008) [6].

Results:

The XRPD analysis showed that all the samples were amorphous except for MB, that showed crystallization of ilmenite and Fe-Ti spinels, despite all the high temperature procedures and the rapid quenching.

The spectral analysis (Fig. 1) showed a clear dependence of the reflectance from the grain size. Generally it shows an increase in reflectance values as the grain size increases. In the MIR region was possible to detect the presence of the CF (Christensen Feature) at a wavelength of ~8.0 µm and RB_{peak} (Reststrahlen band) at ~10.0 µm. It was more difficult to detect the TF (Transparency Feature), typically associated with finer grain size. In the VNIR region were observed two absorption bands at ~1.1 µm and ~1.9 µm. The flat spectra observed for MB are related to the spread micro-crystallization previously reported.

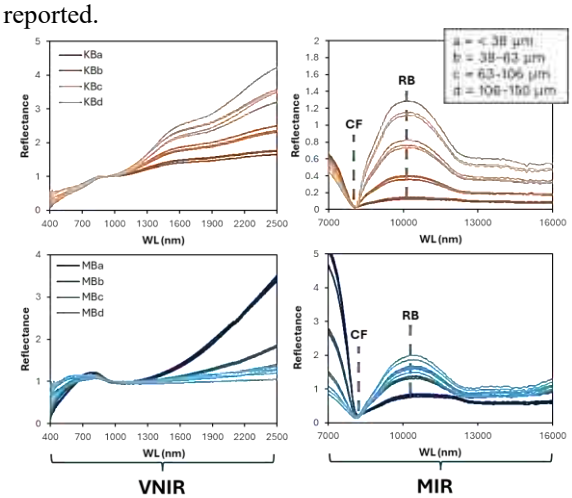


Fig.1: VNIR and MIR spectra of KB samples (orange curves) and MB samples (blue curves).

Regarding the rheological characterization, the viscosities measured so far are comprised between 10 and 10^2 Pa s, approximately one order of magnitude lower than those of common terrestrial basalts. These values seems to be half to one order of magnitude higher than the values modelled with the Giordano et al., (2008) formula (Fig. 2). The experiments were conducted by varying the shear rate between 1 and 10 s^{-1}, but the viscosity values measured at the same temperature did not show significant variations.

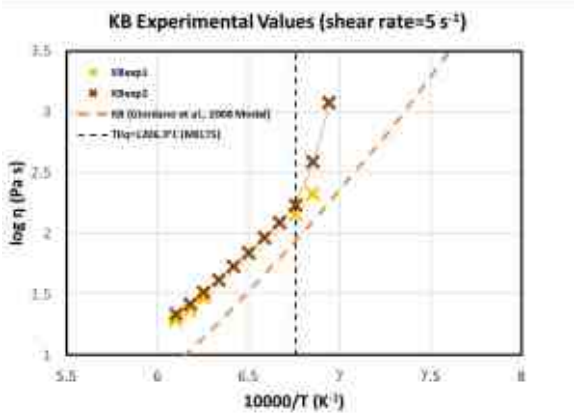


Fig. 2: logη vs 10^4/T diagram for the sample KB at a shear rate=5 s^{-1}, where η is the viscosity and T the temperature in Kelvin. Yellow and brown crosses refer to two different experimental runs.

Final considerations and further perspectives:

These preliminary results demonstrate the feasibility of producing lunar analogue glasses with controlled compositions and grain sizes, and highlight the importance of environmental conditions in preventing unwanted crystallization. Ongoing vacuum-furnace experiments and extended rheological and spectral measurements will further refine the reference database and improve future interpretations of lunar surface materials. An extension of the dataset is also planned through the production of new simulants covering a broader range of compositions, as well as it is planned to make use of analytical techniques that have not yet been investigated to study these samples.

Acknowledgements:

We acknowledge the support of ASI under the ASI–UniPG agreement 2019-2-HH.0.

References:

[1] Wilson, L., and Head, J. W. (2023). The Planetary Science Journal, 4(11), 210. [2] Kalita, H., et al. (2021). *Earth and Space 2021*. 2021. 944-957. [3] Glotch, T., D., et al. (2021). *The Planetary Science Journal* 2.4 (2021): 136. [4] Taylor, S. R. (1982). *Planetary science: A lunar perspective* (Vol. 3303). Houston: Lunar and Planetary Institute. [5] Ghiorso, M. S. and Sack, R.O. (1995). *Contribution to Mineralogy and Petrology* ***119****, 197-212.* [6] Giordano, D., Russell, J. K., and Dingwell, D. B. (2008). *Earth and Planetary Science Letters*, *271*(1-4), 123-134.

INSIGHTS ON MERCURY'S CRUSTAL COMPOSITIONS BY COMBINING THERMODYNAMIC MODELLING AND SPECTRAL ANALYSES OF GLINKA CRATER

C. Cioria[1,2], M. Ianiri[1,2], and G. Mitri[1,2], *[1]Dipartimento di Ingegneria e Geologia, Università d'Annunzio (camilla.cioria@unich.it), [2]International Research School of Planetary Sciences, Dipartimento di Ingegneria e Geologia, Università d'Annunzio.*

Introduction: Mercury'surface has been revealed to be characterized by diverse compositions by MESSENGER spectral data [1]. Overall, the main mineralogy retrieved from elementary information suggests a volcanic composition with variable abundance of plagioclase, olivine and pyroxene (e.g., [2]). This suggests that the hermean regolith could be mainly characterized by rocks similar to terrestrial magnesian basalts, komatiite or boninite (e.g., [3–4]) with a lower iron abundance (<1%, e.g., [5]) and a relatively higher albite content in plagioclase. Laboratory studies have attempted to constrain the spectral response of these low-Fe minerals (e.g., olivine, [6]). However, the specific nature of Mercury's crust remains uncertain. Finally, reduced Mercury-like mantles dominated by enstatite and clinopyroxene have been consistently predicted by thermodynamic models and recent EH-derived melting experiments [7]; [8]. Therefore, a novel investigation of the possible crustal mineralogies, directly constrained to those mantellic, is necessary, also in light of the growing importance of pyroxenes as planetary'surfaces component [9].

Relevant constrains for understanding both the composition and evolution of planetary surfaces could be provided by the study of ejecta, particularly from fresh craters, as Glinka crater (located in the Bee thoven quadrangle (H-07)) [10]. We selected this crater as test- area because it exposes spectral- heterogeneous terrains and includes units whose spectral behaviour has been linked to fresh ejecta and possible pyroclastic products [10], [11] and hollows [12][13].

Objectives: Our ongoing investigation of the crustal composition of Mercury aims to integrate thermodynamic modeling, high-pressure and high-temperature experiments, and remote sensing analyses in order to provide a comprehensive framework to understand chemical- reduced crusts.

Methods: We use the reduced mantles modelled in [7] as parental sources to compute, using Perple_X software [14], S-free crustal compositions through a two-step batch melting–crystallization approach. The same bulk compositions used for thermodynamic simulations will be used to prepare novel synthetic samples to perform Paris-Edinburgh press novel experiments, following the approach in [15]. The mineralogy of run- products will be compared to the thermodynamically predicted ones and to investigated properties of selected units of Glinka [10].

Results and Discussions: Our mineralogical models provide concrete predictions for BepiColombo's future measurements: ultra-magnesian, Fe-free crusts should display high-wavenumber Christiansen Features and subdued Reststrahlen bands in the 7–14 μm region, consistent with Mg-rich, Fe-poor silicates [e.g., 16]. Conversely, more evolved vent-related materials should exhibit lower CF positions and stronger band contrasts. These diagnostics will help evaluate whether Glinka samples multiple crustal levels consistent with the end-member diversity recently identified at Caloris [17]. Although a direct comparison between Glinka's hybrid spectral units and our crustal mineralogies is still ongoing, the marked spectral diversity observed at Glinka, compared to the compositional homogeneity expected from simple batch melting, suggests that additional processes such as fractional crystallization [17] or mantle-source variations may be required [4].

Acknowledgement: G.M., C.C. and M.I. acknowledge support from the Italian Space Agency (2022-16-HH.1-2024).

References: [1] Weider, S. Z. et al. (2015). *EPSL*, 416, 109-120.[2] Namur, O. et al. (2017). *Nat. Geosci.* 10, 9–13. [3] Stockstill-Cahill, K.R. et al. (2012). *J. Geophys. Res.* 117, E00L15. [4] Charlier, B. et al. (2013). *EPSL*, 363, 50-60. [5] Weider, S.Z., et al., (2014). *Icarus*, 235, 170–186. [6] Anzures, B. A., et al. (2025). *Am. Min.*, 110(4), 570-581. [7] Cioria, C. et al. (2024). *JGR:Planets*. 129(7). [8] Boujibar, A. et al. (2025). *Icarus*. 437 , 116602. [9] Rider-Stokes, B. G., et al. (2025). *Icarus*, 116713.[10] Ianiri, M. et al. (2025) EPSC-DPS2025-1503. https://doi.org/10.5194/epsc-dps2025-1503. [11] Thomas R. J. et al. (2014) *Icarus* 229, 221-235.[12] De Toffoli B. et al. (2024) *Earth Space Sci.* 11. [13] Bickel, V. Tet al. (2025). *JGR: Machine Learning and Computation*, *2*(1), e2024JH000431. [14] Connolly J.A.D. (1990). *Am.J.Sci.* 290(6). [15] Cioria, C., et al. (2025)(EPSC-DPS2025 -507)https://doi.org/10.5194/epsc-dps2025-507 [16] Morlok, A., et al. (2024). *Icarus*, 415, 116078. [17] Hirata, K. et al. (2025). *JGR:Planets*.130(4).

Quantifying Ammonium in Two-Component Mineral Mixtures Using IR Reflectance: Influence of Matrix Albedo

E. La Francesca[1], S. De Angelis[1], M.C. De Sanctis[1], M. Ferrari[1], E. Ammannito[2], M. Ciarniello[1], G. Filacchione[1], A. Raponi[1]
[1]Institute for Space Astrophysics and Planetology, IAPS-INAF, Via Fosso del Cavaliere, 100, 00133, Rome, Italy, [2]Italian Space Agency, ASI, Via del Politecnico snc, 00133, Rome, Italy

Introduction: Recent planetary missions have revealed the widespread presence of hydrated and ammonium-bearing materials on several Solar System bodies, highlighting the importance of characterizing NH_4^+ spectral features in laboratory analogues [1-6].

Based on these findings, ammoniated materials may also be present on objects within the outer Main Belt. In this context, the MIST-A [7-9] (Mwir Imaging Spectrometer for Target-Asteroids) instrument on board the EMA (Emirates Mission to the Asteroid Belt), which will conduct close-up observations of seven main belt asteroids, will provide valuable data to investigate the occurrence and distribution of these compounds.

To support the interpretation of such observations, laboratory studies of NH_4^+ spectral behavior are essential. In this work, we present mid-infrared (1.4–11.5 μm) reflectance measurements of controlled two-component mixtures combining synthetic ammonium salts with mineral matrices of varying albedo. Three ammonium salts were studied—ammonium sulfate, ammonium chloride, and monoammonium phosphate—while the matrix endmember was chosen for its spectral flatness in regions corresponding to ammonium absorption bands. Previous analyses [10] focused on bright (Glencoe rhyolite) and dark (magnetite) matrices, revealing two distinct regimes: (i) linear scaling of band parameters with NH_4^+ abundance for rhyolite mixtures, and (ii) non-linear, exponential trends for magnetite mixtures. The different trends observed in the band parameters can be explained by the combined effect of albedo and multiple scattering contribution. In this study, we extend the investigation by introducing a new set of mixtures using an Etna lava sample (Etna Crateri Silvestri, ECS3), whose reflectance is intermediate between rhyolite and magnetite in the <5 μm spectral region. ECS3-based mixtures were prepared with the same ammonium salts and weight proportions as before, enabling a systematic comparison across matrices of different brightness.

These laboratory measurements provide a useful framework for interpreting data.

Experimental setup and Samples: Measurements were performed in the 1.4÷11.5 μm range using the CAPSULA setup in use at IAPS CLAB [10,11]. A Bruker's FTIR spectrometer, INVENIO model, equipped with a liquid nitrogen cooled MCT (Mercury Cadmium Telluride) detector, is used to reach a spectral sampling 0.13 nm. The illumination source is the internal FTIR SiC emitter suitable for measurements up to the mid IR. The FTIR was coupled with a TVC chamber trough a CaF_2 viewport. The sample was illuminated end reflected light was acquired by a system of mirrors inside the chamber. Observation geometry was: i=45° and e=0°.

The prepared mixtures and their corresponding endmembers, along with their weight proportions, are summarized in Table 1, which provides a complete overview of all two-component mixtures considered in this study.

Table 1: Endmembers of mixtures under analysis

Mixtures	Endmember 1	Endmember 2
Mix 1	Rhyolite	$(NH_4)_2SO_4$
Mix 2	Rhyolite	NH_4Cl
Mix 3	Rhyolite	$NH_4H_2PO_4$
Mix 4	Magnetite	$(NH_4)_2SO_4$
Mix 5	Magnetite	NH_4Cl
Mix 6	Magnetite	$NH_4H_2PO_4$
Mix 7	ECS3	$(NH_4)_2SO_4$
Mix 8	ECS3	NH_4Cl
Mix 9	ECS3	$NH_4H_2PO_4$

The mixtures are realized with the weight criteria according to percentage reported in Table 2 and Table 3. For the magnetite mixtures, we extended the series with additional steps—down to 5% magnetite and 95% salt—to explore the low-albedo regime more finely.

Table 2: Endmembers and mixstures percentages of Mix 1-3 (Rhyolite + Ammonium Salts), Mix 7-9 (ECS + Ammonium Salts)

Mix n	Endmember 1 (Rhyolite/ECS) wt%	Endmember 2 (NH_4^+-Salt) wt%
End_1	100%	0%
Mix n-A	80%	20%
Mix n-B	60%	40%
Mix n-C	40%	60%
Mix n-D	20%	80%
End_2	0%	100%

Table 3:Endmembers and mixtures percentages of Mix 4-6 (Magnetite + Ammonium Salts).

Mix n	Endmember 1 Magnetite wt%	Endmember 2 (NH_4^+-Salt) wt%
End_1	100%	0%
Mix n-A	80%	20%
Mix n-B	60%	40%
Mix n-C	40%	60%
Mix n-α	30%	70%
Mix1-D	20%	80%
Mix n-β	15%	85%
Mix n-δ	10%	90%
Mix n-γ	5%	95%
End_2	0%	100%

Results: Figure 1 shows the mid-infrared reflectance spectra of the selected endmembers—Glencoe rhyolite, magnetite, and ECS3 lava—measured in air at ambient temperature over the spectral range of 1.4–11.5 µm.

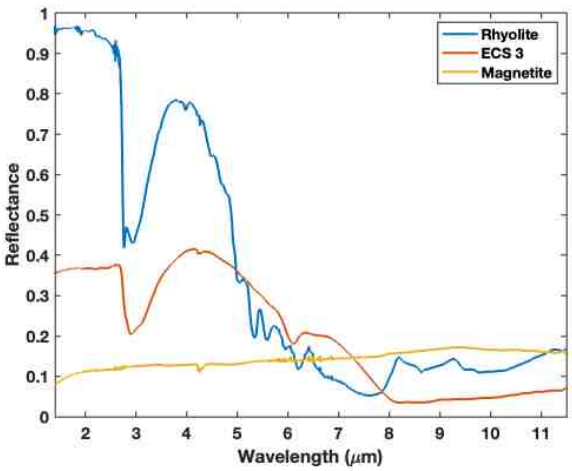


Figure 1: Spectra of selected endmebers, in air at ambient temperature, in the spectral range of observation (1.4-11.5 μm).

These spectra highlight the differences in overall reflectance and spectral features among the three materials, with rhyolite exhibiting the highest brightness, magnetite the lowest, and ECS3 displaying intermediate reflectance.

Figure 2 presents the continuum-removed spectra of a mixture of ECS3 and monoammonium phosphate, measured in air. The top panel highlights the 1.6-µm absorption feature, corresponding to the $2\nu_3$ vibrational mode of NH_4^+, while the bottom panel shows the 2.1 µm absorption, associated with the $\nu_2 + \nu_3$ and $\nu_3 + \nu_4$ vibrational modes [12,13].

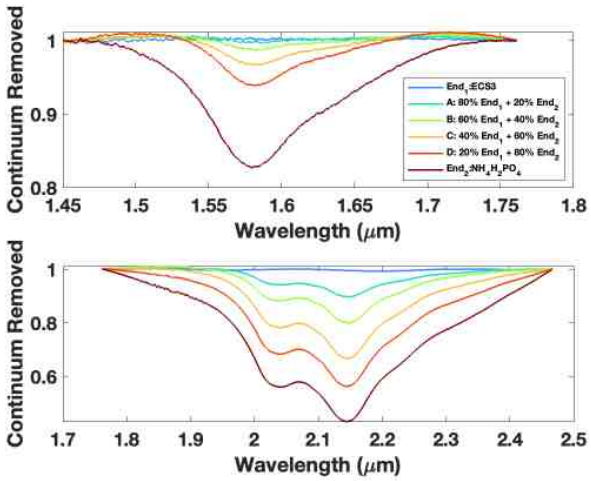


Figure 2:Continuum removed spectra of mixture of ECS3 and Monoammonium Phosphate, in air. Top panel: 1.6-μm absorption due to NH_4^+ vibrational modes $2\nu_3$; bottom panel: 2.1-μm absorption due to $\nu_2 + \nu_3$ and $\nu_3 + \nu_4$ vibrational modes [12,13]

Future work: Additional mixtures to be considered and analyzed will include a non-Fe-bearing dark phase (e.g. a carbon phase) to disentangle from the behavior of Fe-bearing dark components such as magnetite. All mixtures will also be analysed in vacuum and heated to high temperature for volatile analysis by mass spectrometry. This process can be useful, particularly at 3 µm, to distinguish the contribution of water from that of ammonia.

References: [1] De Sanctis M.C. et al., Nature Letter 528, 241-244, 2015. [2] Kitazato K., et al.,Science, 364, 272-275, 2019. [3] Hamilton V.E., et al., Nature Astronomy, 2019. [4] Cook J.C., et al., Icarus 315 (2018) 30–45. [5] Cruikshank D.P. ,et al., 201, Icarus, 330, 155-168. [6] Cartwright R.J. et al., The Planetary Science Journal, 4:42 (28pp), 2023. [7] Filacchione, G., et al., EPSC-DPS2025-978. Copernicus Meetings, 2025.[8]Filacchione G., et al., ACM 2023 (LPI Contrib. No. 2851)). [9] Al Mazmi et al., 2024, COSPAR, b1.1-0036. [10] La Francesca, Eliana, et al. No. EPSC-DPS2025-1581. Copernicus Meetings, 2025. [11]De Angelis S., et al. (2022): *16, EPSC2022-540.* [12] De Angelis S., et al., Memorie S.A.It, vol.95, Issue 4, 91-102, 2024. [13] Fastelli M., et al., Icarus 382 (2022) 105055. [14] Busigny V. et al., American Mineralogist, Volume 89, pages 1625-1630 (2004).

Acknowledgments: This work has been funded by mini-Grant AMMONHIA (Abundance Mass spectrometry Measurements Of NH In Analogues materials) “Bando Ricerca Fondamentale INAF 2023”.The experimental setup used has been funded in the framework of the Agreement ASI-INAF n.2018-16-HH.0.

THE ARCETRI ASTROBIOLOGY LABORATORY: EXPLORING THE SOLAR SYSTEM WITHIN INTERNATIONAL SPACE AGENCIES PROGRAMS, LOOKING FOR TRACES OF LIFE AND POTENTIAL SIGN OF ASTROBIOLOGICAL PROCESSES.

J. R. Brucato[1], T. Fornaro[1], A. Meneghin[1], C. García-Florentino[1], G. Poggiali[1], M. Battistuzzi[1], A. Roussel[1], A. Alberini[1,2], C. Lorenz[1], S. Biancalani[4,5,6,1], S. Pagnoscin[1,2,7], F. Renzi[1,2], T. Guidetti[1], J. Ferro[1]

[1]INAF- Astrophysical Observatory of Arcetri, L.go E. Fermi 5, 50125 Firenze, Italy (john.brucato@inaf.it); [2]Department of Physics and Astronomy, University of Florence, Via Giovanni Sansone 1, 50019 Sesto Fiorentino, Florence; [4]Department of Physics, University of Trento, Via Sommarive 14, 38123 Povo, Trento, Italy; [5]Italian Space Angency (ASI), viale del Politecnico snc, 00133, Rome, Italy; [6]Department of Earth Sciences, University of Florence, via G. La Pira 4, 50121, Florence, Italy; [7]Istituto di Geoscienze e Georisorse del CNR, Via Moruzzi 1, 56124 Pisa, Italy.

Introduction: The progress of planetary sciences and astrobiology is mainly driven by space missions and technological innovation. Since mission data are often complex and influenced by multiple factors, laboratory simulations are essential for testing hypotheses, interpreting remote and in-situ observations, and reducing ambiguity in data analysis. By recreating planetary or cosmic environmental conditions and isolating key variables, laboratory work bridges the gap between theory and exploration. This enables the development of new detection strategies and improves our ability to identify biosignatures and understand complex processes.

Hence, the Arcetri Astrobiology Laboratory (INAF – Astrophysical observatory of Arcetri, Florence) focuses on a multidisciplinary approach, integrating tools and protocols from scientific fields like astrophysics, geology, engineering, chemistry and biology. Its main activities range from support to Mars exploration to icy moons modelling, small bodies characterization, prebiotic chemistry, biomarkers' investigations and protocol development in the context of planetary protection. These activities have been possible thanks to the collaborations with NASA, ESA, ASI and JAXA agencies.

Laboratory facilities: In the laboratory, protocols making and optimization is focused on the preparation of analog samples, both in dry conditions and in an aqueous environments, aiming for simulating as many extraterrestrial contexts as possible: from the Martian surface (both present Mars and its past wet-phase) to asteroid regoliths and icy moons environments. The procedures for preparing analog samples include selecting different grain-size, adsorbing organic molecules through controlled spike or kinetic processes on powders or pressed pellets. To ensure reproducibility of the preparations, samples are characterized before and after treatment using optical and IR microscopy, together with UV spectroscopic analysis. This approach not only allows for the simulation of planetary conditions with a high degree of realism, but also enables the controlled monitoring of relevant physical and chemical transformations.

The characterization of samples and monitoring of their changes during experimental treatments are carried out with a dedicated suite of instruments. The main analytical techniques are infrared (IR), deep UV Raman spectroscopy, chromatography. For IR analyses, a Bruker VERTEX 70v FTIR interferometer is used, configured in both Diffuse Reflectance Infrared Fourier Transform (DRIFT) mode, using a Harrick Praying Mantis™ accessory to obtain spectral information representative of the entire sample, and in microscopy using the HYPERION 1000 µ-FTIR system equipped with a 64×64 pixel Focal-Plane Array (FPA) detector that allows a spatial resolution of approximately 2 µm and processing such as cluster analysis. For DUV Raman and fluorescence analyses, the laboratory is equipped with the DUV Raman/PL 200, a compact spectrometer provided with a 248.6 nm randomly polarized laser source. Its design enables mapping of surfaces using both Raman scattering and photoluminescence, making it suitable for detecting trace organics, molecular structures and mineral phases with strong UV responsivity. The system can scan areas up to 50 × 50 mm with 100 or 50 µm spatial resolution, offering complementary information to the µ-FTIR maps, thus providing insight into the chemical and structural characteristics of heterogeneous samples. In addition, the laboratory has a Liquid Chromatography - Mass Spectrometry (LC-MS) system and an ultra-high vacuum chamber dedicated to Mass Spectrometry (GC-MS), which enable the identification, quantification, and tracking of complex organic molecule transformations during experiments.

The laboratory facility provides also simulated conditions relevant to space, applying thermal control, ranging from cryogenic temperatures to high values, together with in situ UV irradiation. The combination of these tools and techniques allows for systematic, multi-scale monitoring of the effects of physical and chemical processes on samples, contributing significantly to the interpretation of data from space missions.

Main laboratory results:

Mars. Laboratory experiments have evaluated the photostability of organic molecules under simulated Martian UV radiation, focusing on how minerals affect their preservation or degradation [1]. Data from Jezero crater (NASA Mars 2020 Perseverance mission) indicate a spatial association between organics and sulfate minerals [2], and comparison with laboratory spectra of multiple candidate organic compounds shows the closest match with PAHs [3]. Experiments confirm that magnesium sulfate can protect organics such as carboxylic acids and PAHs from UV-driven degradation [4][5]. Similar studies on clays show their preservation potential is

variable and depends on environmental factors such as pH, which affects molecular adsorption and stability [6][7][8]. Ongoing measurements on analogue materials for ESA ExoMars mission aim to improve the interpretation of future in situ observations.

Small bodies. The interpretation of Martian moons origin is one of the main object of the laboratory. Spectroscopic data collected from orbital observations and ground-based telescopes are analyzed and compared with laboratory analog samples. Mineralogical mixtures, meteorites and dark components such as space-weathered materials, are analyzed under controlled conditions to best reproduce the surface properties of the satellites [9][10]. Comparison between laboratory results and orbital data has identified spectral signatures most compatible with observations, indicating that the surfaces of Phobos and Deimos are likely dominated by dark materials – such as amorphous carbon and phases containing FeO and FeS. This work provide an important interpretative framework for future JAXA Martian Moons eXploration (MMX) mission, improving the ability to analyze and compare the data that will be collected in situ and from samples brought back to Earth.

Icy Moons. The oceans hidden beneath the icy shells of Solar System's Icy Moons are investigated with numerical models focused on the fluid dynamical processes. Simulations showed that km-scale convective plumes within the subsurface oceans play a major role in transporting heat from the seafloor to the water-ice interface [11]. Results further revealed pronounced spatial variability in basal melting and freezing, which can in turn induce heterogeneities in ice-shell thickness and create surface "hotspots," i.e., regions where the surface lies closer to the hidden ocean, thereby promoting transient connections and upwelling of endogenous material. Identifying these regions is crucial, as they may represent priority targets for future missions (such as ESA's JUICE), where chemical signatures of the ocean – or even potential indicators of habitability – could be more accessible and detectable.

Prebiotic chemistry. The laboratory also investigates prebiotic chemistry, studying how simple interstellar molecules evolve into more complex compounds. Experiments simulating interstellar environments showed that ethanolamine-rich ices are UV-resistant and can remain trapped on dust grain analogues up to high temperatures, and that their UV irradiation produces more complex species, suggesting a potential role in early chemical evolution pathways [12].

Astrobiology biomarkers. Studies on the lichen Xanthoria parietina and its pigment parietin showed their significant UV resistance under simulated space and Mars-like conditions. The lichen was able to reactivate performing photosynthesis after treatments. Spectroscopic analyses of parietin revealed IR features preservation under UV radiation, highlighting parietin as a potential UV shielding and biologically relevant marker for astrobiology [13][14]. Detectability and survivability studies on different microorganisms are instead being carried on within project AnoxyMars. The aim is that of characterizing the microorganisms (or the molecules derived from their degradation) after exposure to a Martian superficial and subsuperficial radiative environment (UV, ionizing radiation), missed or not with a martian regolith simulant. The characterization will be done with instrumentation analog to that on board of the ExoMars' rover and will provide reference data to interpret the future mission findings.

Instrument development. The laboratory is also involved in the development of new methodologies and payloads for space mission able to analyse liquid samples in situ. New lab-on-chip technologies are designed and built to investigate the presence of organics and biomarkers in samples from planetary surfaces. Several project are ongoing on this topic with the support of ASI, such as participation to SpaceIt-Up! project.

Planetary protection. Exploring the Solar System comes with clear scientific and ethical responsibilities, which form the basis of planetary protection: the effort to prevent biological and organic contamination between Earth and other celestial bodies. In this framework, the laboratory contributed to PPOSS, a European platform that brings together researchers, engineers, industry stakeholders and policy makers to develop shared guidelines for planetary protection.

Conclusion: Laboratory simulation is proving effective in interpreting planetary processes and reducing uncertainty in remote observations. The integration of knowledge from different fields of research and investigative techniques is showing to be an efficacious way of addressing complex astrobiological and planetary issues. Finally, the return and ongoing analysis of samples from the asteroids Bennu and Ryugu, together with future sample return programs from Mars, represent an important, perhaps crucial, step forward. These samples will directly link experimental simulation with authentic extraterrestrial materials, allowing for rigorous validation of hypotheses about the chemical evolution and potential habitability of the Solar System.

References: [1] Fornaro, T., Steele, A., & Brucato, J. R. (2018) Life, 8(4), 56; [2] Sharma, S. et al. (2023) Nature, 619, 724–732; [3] Fornaro, T. et al. (2025) Nat. Astron., 1–14; [4] Alberini, A. et al. (2024) Sci. Rep., 14, 15945; [5] Alberini, A. et al. (2025) Sci. Rep., 15, 40484; [6] Kopacz, N. et al. (2023) Icarus, 394, 115437; [7] McIntosh, O. et al. (2024) Astrobiology, 24, 518–537; [8] García-Florentino, C. et al. (2025) Icarus, 116757; [9] Poggiali, G. et al. (2022) MNRAS, 516, 465–476; [10] Poggiali, G. et al. (2025) EPSC-DPS, Abstract 1606; [11] Pagnoscin, S. et al. (2025) Icarus, 116875; [12] Biancalani, S. et al. (2024) A&A, 691, A256; [13] Lorenz, C., Bianchi, E., Poggiali, G. et al. (2023) Sci Rep, 13, 4893; [14] Lorenz, C., Arena, C., Vitale, E. et al. (2024) Planta, 259, 25.

Acknowledgements: ASI/INAF Agreement 2023-3-HH.

PVRG ROCKS SPECTRA CATALOGUE: INSIGHTS INTO NATURAL VOLCANIC ROCKS IN THE EFFECT OF THE CRYSTALLINE-AMORPHOUS RATIO ON THE VNIR AND MIR SPECTRA

M. Fastelli,[1*] A. Pisello[1], E. Scricciolo[1], M. Baroni[1], A. Zucchini[1], A. Zinzi[2,3], D. Perugini[1] and P. Comodi[1]
[1]Department of Physics and Geology, University of Perugia, Perugia, Italy (*maximiliano.fastelli@unipg.it)
[2]Agenzia Spaziale Italiana (ASI), Via del Politecnico snc, 00133 Rome, Italy
[3]ASI-Space Science Data Center, Via del Politecnico, snc, 00133, Rome, Italy

Introduction: Remote determination of the surface composition of rocky planets is a major goal in planetary science, as it provides essential insights into their geological evolution and the history of rocky bodies in the Solar System, starting with Mars. Among geological processes, volcanism is particularly relevant, as it extensively shapes the surfaces of Earth and other terrestrial planets. Mars, the best-studied planet after Earth, exhibits a high mineralogical diversity, revealed by imaging spectrometers such as OMEGA on Mars Express [1] and CRISM [2] on the Mars Reconnaissance Orbiter. Ongoing and upcoming missions continue to advance this field: NASA's Mars 2020 rover carries the SuperCam infrared spectrometer (IRS) [3], while ESA's ExoMars mission will perform subsurface NIR investigations using the Ma_MISS point spectrometer integrated into the drill system [4]. Early surface Mars characterisation was performed assuming a surface composed of oxidised basaltic or ultramafic rocks and relative alteration products [5], and more recently, studies were able to identify large zones of Mars where volcanism deeply shaped the morphology of the planet [6]. As is well known, terrestrial volcanic rocks show significant variability in both chemistry and texture, different crystal sizes and crystal-to-amorphous ratios, sometimes with the same bulk chemistry, depending mainly on the cooling rate. To understand how these chemical and textural features of volcanic rocks influence the VIS-NIR spectra, in this work, 12 volcanic rocks having a wide range of chemical and mineralogical composition were selected. This collection brings together a set of rocks that have been reported elsewhere in the Solar System and particularly on Mars. Samples were characterised by means of different analytical techniques, that are X-ray fluorescence (XRF), scanning electron microscopy (SEM) and X-ray powder diffraction (XRPD). Reflectance spectra were collected in the VNIR (0.4-2.5 μm) and MIR (7-13 μm) range at room temperature (R*T*). Quantitative phase analyses (QPA) using the Rietveld method were performed to evaluate the crystal-to-amorphous ratio. In addition, the influence of grain size was examined by analysing spectra from powdered samples with four distinct grain size ranges. The collected data will be used to develop a spectral database of volcanic rocks, both natural and synthetic, to investigate how crystalline and amorphous components interact and to what extent they influence the spectral response of rocks and terrains. This integrated analysis will provide a valuable reference for a more detailed interpretation of the observations from ESA-Roscosmos ExoMars and NASA Mars 2020 missions.

Materials and Methods: Twelve natural volcanic rock samples were selected to cover a compositional range representative of the chemical and mineralogical variability of these products, from basaltic (silica-poor) to rhyolitic (silica-rich) compositions. The selected rocks are: basalt, alkaline basalt, andesitic basalt, leucitite, melilite, andesite, trachy-leucitite, trachy-rhyolite, and two rhyolites.

Major element chemistry was determined using XRF Thermo Scientific Quant'X equipped with Thermo Scientific™ UniQuant Software, while qualitative mineralogical composition was assessed through SEM imaging (COXEM CX-200 PLUS) with Energy Dispersive X-ray Spectroscopy (EDS) system (Oxford Xplore 15 EDS) and XRPD Bruker D8 Advance equipped with a Lynxeye XE-T position sensitive detector and Cu Kα radiation. QPA was carried out using the Rietveld refinement method [7], with the addition of an internal standard for the quantification of the amorphous phase. The FT-IR apparatus consists of a Bruker Invenio-X spectrometer coupled with Harrick Praying Mantis™ for Diffuse Reflectance. The interferometer is equipped with three detectors and optical elements that allow investigation in the wavelength range 0.35–17 μm.

Results: Figure 1 presents an example of the characterization and the corresponding reflectance spectra for one of the samples included in the work.

The results of the XRF and XRPD analyses show that the samples analysed have a low silica (SiO_2) content (~41–51.8 wt%) and are characterized by plagioclase, pyroxene, and olivine as the dominant mineralogical phases. The leucitite sample is enriched in feldpatoid minerals (leucite/nepheline). The samples with intermediate SiO_2 content (54 – 61.4 wt%) are characterised by the presence of feldspar and minor contents of pyroxene and amphibole. Finally, high-silica samples (> 68 wt%) display assemblages consisting of alkali feldspar, plagioclase, and quartz, accompanied by minor phases such as amphibole.

The quantification of the amorphous fraction is currently being finalised, and preliminary results indicate the presence of an amorphous portion ranging from a few percent up to a maximum of ~45 wt%.

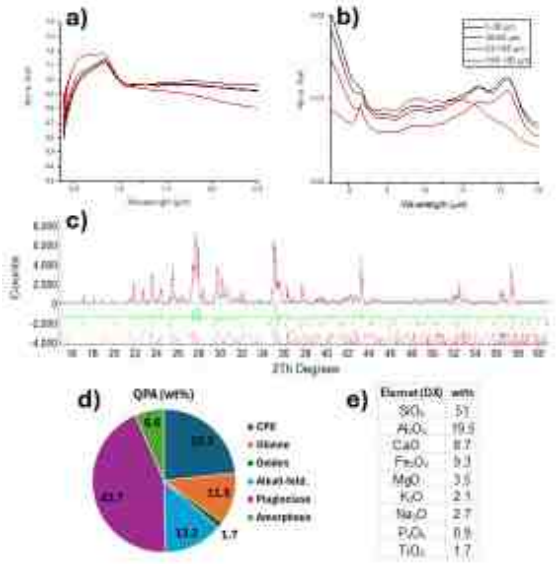


Figure 1: characterisation of the basalt rock sample: VNIR and MIR reflectance spectra (a-b), XRPD Rietveld refinements (c), QPA results (d) and XRF data (e).

Regarding the VNIR spectral range, the spectral shape of all samples is characterised by a generally positive slope and absorption at ca 1.1 μm, and a second absorption at ca. 1.9 μm. These features are the usual ones observed for silicate rocks and are linked to the presence of Fe-O bonds [9]. The spectral slope in our sample set varies in relation to the oxide content (e.g. magnetite) and as the content increases, the slope becames flat. In this spectral range, it is difficult to clearly identify spectral features related to the mineralogical species identified, like plagioclase or feldspar, with respect to the amorphous component.

Regarding MIR region, the spectra are dominated by the fundamental Si-O vibrational modes of silicate minerals and glass. The broad absorption between ~8 and ~13 μm corresponds to the Si-O stretching and O-Si-O bending modes associated with pyroxene or olivine [10].

The position and shape of these bands vary systematically with the bulk silica content and the degree of polymerization of the silicate network: (i) in basaltic compositions, the main Reststrahlen band occurs at longer wavelengths (9.5–10.5 μm), consistent with a less polymerized, chain- or framework-deficient structure; (ii) in rhyolitic samples, the absorption shifts toward shorter wavelengths (8.5–9.3 μm), reflecting the higher Si–O bond strength and a more polymerized framework.

However, investigations are currently in progress to determine how the different mineralogical compositions may affect the position and type of these bands.

All spectra show a local negative peak at ~8 μm that can be recognised as the Christiansen Feature (CF), a local minimum which appears on both amorphous and crystalline materials, and that is often used as a diagnostic feature for igneous products [11]. Moreover, the presence of fine material produces a transparency feature at ca. 12 μm occurring when a large surface/volume ratio determines a larger ratio of scattered/absorbed light [11].

Considerations and future perspectives:

All these spectra will be made available on PVRG rock spectra catalogue on the SSDC-ASI portal (https://www.ssdc.asi.it/rockspectra/) [12], and the use of these spectra as reference material will be important for the interpretation of data observed by observations from ESA-Roscosmos ExoMars and NASA Mars 2020 missions. This multi-parametric study aims to provide a comprehensive understanding of the spectral characteristics of volcanic rocks, with particular attention to the role of the amorphous *vs* mineral phases in shaping their spectral features. The ongoing characterisation of the natural rock samples included in this work will enable the quantification of amorphous phases and clarify how, and to what extent, amorphous and crystalline components interact in determining the spectral signature of volcanic materials.

Acknowledgements:

Part of this work was supported by the Ministero dell'Istruzione dell'Università e della Ricerca (MUR) through the program "Dipartimenti di Eccellenza 2023-2027" (Grant SUPER-C) and was also carried out thanks to ASI-UniPG agreement 2019-2-HH.0.

References: [1] Murchie S. L. et al. (2009) *JGR: Planets*, 2009, 114.E2. [2] Mustard J. F. et al. (2008) *Nature*, *454*(7202), 305-309. [3] Maurice S. et al. (2021) *Space Sci. Rev. 217(3), 47.* [4] De Sanctis M. C. et al. (2017) *Astrobiology*, *17*(6-7), 612-620. [5] Singer R. B. et al. (1979) *JGR: Solid Earth*, 1979, 84.B14: 8415-8426. [6] Platz T. et al. (2015) *Geol. Soc. Spec. Publ.*, 401 (2015), pp. 1-56. [7] Rietveld H. M. (1969) *Appl. Cryst* 2.2: 65-71 [8] De la Torre A. G. (2001) *Appl. Cryst.*, 34(2), 196-202. [9] Adams, J. B. (1974). *JGR*, *79*(32), 4829-4836. [10] Morlok A. et al. (2024) *Icarus*, 415, 116078. [11] Pisello A. et al. (2023) *Minerals*, *13*(2), 170. [12] Pisello A. et al. (2022) (No. EPSC2022-539). Copernicus Meetings.

Laboratory IR Spectroscopic Study of Asteroid (269) Justitia Analogues for EMA Mission. S. De Angelis[1], M. Ferrari[1], G. Filacchione[1], M. Ciarniello[1], F. Capaccioni[1], M.C. De Sanctis[1], M. Formisano[1], A. Raponi[1], E. La Francesca[1], A. Galiano[1], C. Cencia[1]. [1]INAF-IAPS (Via Fosso del Cavaliere, 100, 00133, Rome-Italy). (simone.deangelis@inaf.it).

Introduction: The (269) Justitia asteroid is, among the seven targets planned for the EMA (Emirates Mission to the Asteroid Belt) mission, the last to be visited in 2034 [1]. Justitia spectrum is characterized by a very red slope and almost featureless shape in the VIS-NIR region, denoting a similarity with TNOs and Outer Solar System objects [2,3]. However, the origin of Justitia as a TNO or Main Belt object is currently uncertain and debated [2,3,4]. The reddening of reflectance spectra of airless bodies such as asteroids or satellites is attributed to space weathering acting over timescales of thousands of years and more [2,3]. While the VIS-NIR reflectance spectrum of Justitia is characterized by extreme reddening and the near absence of absorption bands [2,3], IR telescopic observations of Justitia with the IRTF facility [4] have revealed a 2-4 μm spectrum showing the presence of hydration (partial 2.7-2.8-μm band) and aliphatic compounds (3.4-3.5-μm band). Based on the IR 2-4-μm spectrum, a CM-like composition has been supposed for this asteroid [4].

According to the migration hypothesis, Justitia might have formed in the TNOs region beyond the snow line of volatile organic materials, and then it migrated in the Main Belt [3]. However, in this scenario, the observed aqueous alteration remains to be explained. Alternatively, Justitia might have formed directly in the Main Belt, yet leaving open the question of its very red slope [4].

With the aim of getting clues about the Justitia surface composition and processes, and to build a laboratory spectral dataset that will be useful for the interpretation of future data acquired by the MIST-A IR spectrometer [5] onboard EMA, we started a VIS-MIR spectral investigation of different possible analogue materials and mixtures to be used as simulants.

Experimental Methods: In our study, we investigated a set of ternary mineral mixtures made of (i) primary silicates, (ii) a carbon-bearing compound, and (iii) a phyllosilicate/hydrated silicate. Two different mixtures were prepared by changing the relative amounts of the single components and were spectrally analyzed in the VIS-NIR-MIR spectral range. The Mix-J1 is composed of pyroxene (augite), serpentine (lizardite), and carbon in equal relative proportions (33 wt%). Mix-J2 is composed of pyroxene (augite, 30 wt%), carbon (40 wt%), and serpentinite (POL1, 30 wt%). The serpentinite sample is itself a rock composed mainly of lizardite with some amounts of chlorite, clinopyroxene, and magnetite.

For both mixtures, carbon DECS19 is used.

Spectral measurements were performed in the IR 1-12 μm range, which largely encompass the MIST-A spectral range (2-5 μm), using the CAPSULA laboratory facility [6] available at INAF-IAPS. Measurements on both the separate endmembers and mixtures J1-J2 were taken first at ambient conditions (room P-T) and then at various increasing levels of high vacuum, to better characterize the 2-4 μm spectral region without the disturbing absorption features due to ambient H_2O and CO_2.

Results: We present preliminary results of our experiments in the NIR-MIR range. In Fig.1, the spectra of MIX-J1 are shown for the region 2-4.5 μm. The red line spectrum has been acquired in air conditions, and for this reason, the 2.6-3.6-μm region is dominated by the water absorption features. The orange to yellow lines spectra have been measured instead in High Vacuum (HV); finally, the green line one has been obtained in HV with the sample cooled at 80 K. Data are compared with the telescopic spectrum of Justitia from Rivkin et al. [4, black dots]. In spite of the higher noise in the telescopic spectrum and the lack of data in the 2.6-2.7 μm window (due to atmospheric absorption), we find a good match with laboratory data. The spectrum of Justitia seems to be less hydrated, and there is a similarity between the 3.4-3.5 μm band in both datasets. Given the gap at 2.7 μm is still not possible to make a more precise comparison with laboratory data for the identification of a plausible candidate phyllosilicate.

In Fig. 2, measurements taken on the second mixture (MIX-J2-A) are shown. Spectra have been taken again in air and then in high vacuum. The Justitia spectrum (black dots) appears similar in the 2.8-3.1 μm region with laboratory spectra acquired in high vacuum, which produced dehydration of the sample. The positions of several absorption bands, as indicated by dashed lines, are compatible with the organic aliphatic compounds (features of CH_2 and CH_3 at 3.25, 3.32, 3.40, 3.48 μm). Anyway, the amount of the aliphatic component in the measured mixture must be considerably decreased to better reproduce the shallower intensity (smaller band depth) of the observed C-H band. Other weak features in the Justitia spectrum occurring at ~2.31 and 3.66 μm appear to match well with corresponding features in laboratory spectra, although the bands in the telescopic spectrum are quite noisy and could be dubious.

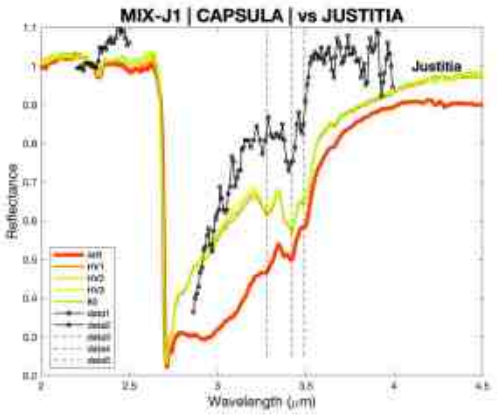


Fig.1. IR Spectra of MIX-J1 measured in air and at different levels of vacuum. The black dot spectrum refers to Justitia spectrum [4].

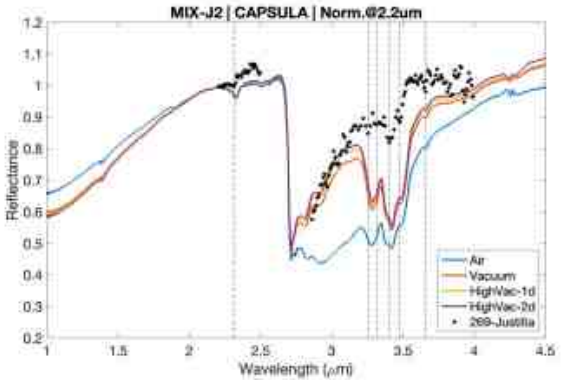


Fig.2. IR Spectra of MIX-J2-A measured in air and at different levels of vacuum. The black dot spectrum refers to Justitia spectrum [4].

Conclusions and Future Work: The spectra of mixtures presented in this work well reproduce some portions of the Justitia telescopic spectrum, for what concerns the IR 2-4 μm range, particularly the band positions of several CH_2-CH_3 absorption features and the hydration feature near 2.7-3 μm. Nevertheless, much work needs to be done taking into account other effects that might modify the spectral features. Many factors could be responsible for the Justitia red slope and featureless spectrum, among these, the space weathering, collisional history, and thermal evolution are believed to have likely modified the surface features of this object. For this reason, the processing of the mineral mixtures and analogue meteorite samples with different space weathering techniques (heating, irradiation, bombardment) will be crucial to study the composition of primordial material on asteroid surfaces.

Acknowledgements. MIST-A science, calibrations, operations, and data processing responsibilities are in INAF/IAPS, Rome. The MIST-A program is managed by the Italian Space Agency (ASI) as leading funding agency. We wish to thank Dr Vassilissa Vinogradoff from University of Marseille for supplying the DECS19 carbon sample.

References:

[1] Al Mazmi et al., 2024, COSPAR, B1.1-0036; [2] Hasegawa et al., 2021, ApJ L., 916, L6; [3] Hasegawa et al., 2022, ApJ L., 939, L9; [4] Rivkin et al., 2023, ACM, #2302; [5] Filacchione G., et al., COSPAR, abstract B1.1-0037-24, 2024; [6] De Angelis S., et al., Mem. S.A.It., Vol.95, 91, 2024.

VENOM: VENTURE THE EXTRACTION OF ORGANIC MOLECULES – MAINFRAME DESIGN AND SUBSYSTEM RECONFIGURATION.

T. Troise [1,2], G. Colombatti [1,2], J.R. Brucato [3], A. Aboudan [2], C. Bettanini [1,2], F. Ferri [2], N. Trabacchin [2], I. Terlizzi [2], A. Meneghin [3], G. Valentini [4], F. Ferranti [4] and the VENOM TEAM [1,2]
[1] DII - Università degli Studi di Padova, 35131 Via Venezia 1, Padova, Italy (giacomo.colombatti@unipd.it),
[2] CISAS "Giuseppe Colombo" – Università degli Studi di Padova, 35131 Via Venezia 15, Padova, Italy,
[3] INAF Arcetri- FI, [4] ASI - Rome

Introduction: The VENOM (Venture the ExtractioN of Organic Molecules) instrument employs advanced detection methods to identify a wide range of biogenic compounds, from small molecules to cellular structures. Our goal is to create a miniaturized, multi-functional lab-on-a-chip platform capable of detecting, identifying, and quantifying biogenic compounds with high sensitivity (parts per billion) through immunological and enzymatic assays. This platform must be robust enough to withstand sterilization, mission conditions, and waste management requirements, while fully adhering to planetary protection protocols.

This paper presents the work carried out to adapt the preliminary design, studied last year, to the mission conditions proposed identified by the Project; combining custom components, designed and dimensioned internally with commercial components to increase the reliability of the instrument and reduce design times.

Subsystem:

Mainframe Assembly: it has been redesigned following the original idea of creating two linear guides that allow to insert easily the mounting base for all components, while having a structural function. To do this, blind holes were created in the mainframe to mount the linear guides. The carriage is mounted on the slides that run on the linear guides. The trolley consists mainly of two rigidly connected structural rings that reduce the deformation of the mainframe when it is under pressure, thus ensuring the seals remain intact and the module survives the cosmic vacuum. The holders for the remaining subsystems are then mounted on this structure. Below is a detailed list of components to better describe the assembly and the materials used in their production.

Mainframe	
component	material
External case	EN AW 7075
Lid	EN AW 7075
Carriage structure	EN AW 7075
Ring nut SKF KMK 6	Stainless steel
gasket	Indium wire
Threaded interface	EN AW 7075

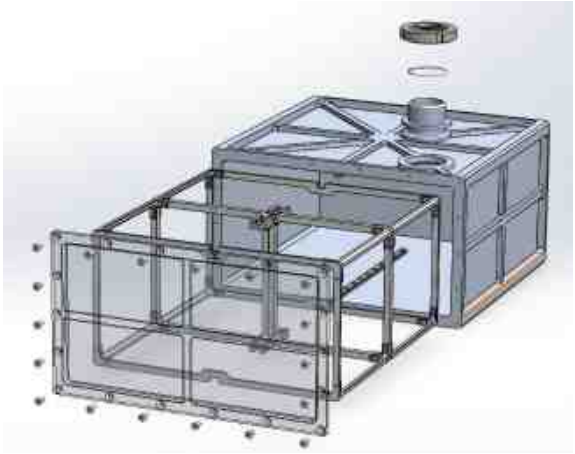


Figure 1: Mainframe Assembly

A preliminary FEM study was carried out using SolidWorks Simulation to verify the proposed design.
The simulation was performed by constraining the mainframe on the lower surface and imposing a differential pressure of 2 atmospheres on the inner faces of the mainframe. The simulation considers the rail and carriage that stiffen the structure in the most stressed area, the center of the lower and upper faces. The maximum deformation detected is on the rear face, equal to 0,342 mm.
This face does not have the reinforcement flange required for the umbilical power line, which will increase its rigidity.

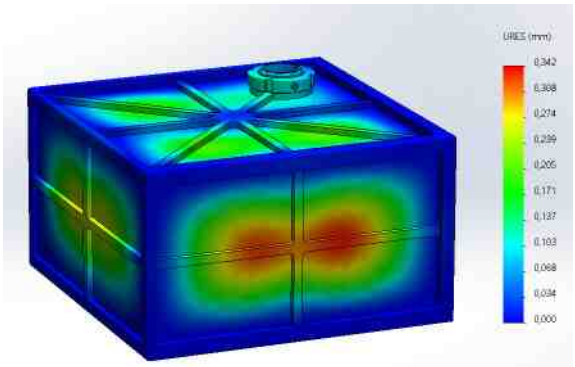


Figure 2: Max deformation at a pressure of 2 atm

The simulation gives us an FOS of 1.22. Considering that a pressure of 2 atmospheres is an unforeseen situation and not the working condition, which is at ambient pressure, we can be satisfied with the preliminary simulation.



Figure 3: FOS of the external case

Acquisition Mechanism: To ensure a reliable mechanism, a commercial high-vacuum gate valve (VAT 01.2 mini gate valve [4]) was chosen and its operation modified from a normally open valve to a normally closed valve. To do this, a mechanism was designed that uses two linear actuators by Actuonix [5] and a compression spring that works in opposition to ensure the compression of the commercial valve seals.

All dimensioning has been carried out, and the FOS complies with the chosen values.

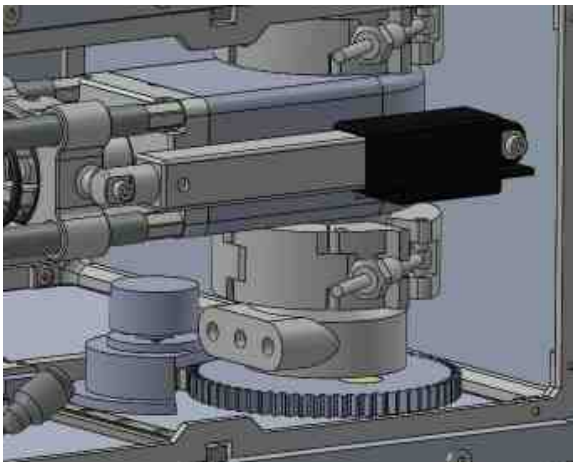
Below is a list of the components of the acquisition mechanism:

Acquisition mechanism:	
component	material
Upper bracket	EN AW 6082
Carriage	EN AW 6082
Rods	EN AW 6082
Compression Spring	EN 10270-1
VAT Mini Gate Valve	EN AW 6082



Figure 4: Acquisition mechanism Assembly

MagMixer: To ensure the hermetic seal of the acquisition module and allow the sample to be mixed with the solvents, it was necessary to design a mechanism that did not require through shafts. The system consists of a motor connected to a speed reducer with a magnetic bipole, while inside the acquisition module there is a magnetic rod. Once the motor is activated, the magnetic rod will begin to mix the sample with the solvent.



Conclusions: This paper presents the current status of various subsystems that have been designed and dimensioned, ready to be manufactured by the various production companies, once the final adjustments have been made and the electronics have been produced.

Once all the components have been acquired, Venom will be assembled and ready for the test campaign.

Acknowledgements:

"Venture the ExtractioN of Organic Molecules (VENOM)" is a project selected by the Italian Space Agency ASI Astrobiology call: "Attività relative al supporto allo sviluppo di progetti/esperimenti scientifici nell'ambito dell'Astrobiologia" (prot.n. DC-DSR-UVS-2022-231) and funded through the contract ASI N.2023-8-U.0.

References:

[1] BRUCATO, John Robert et al. AstroBio CubeSat a new tool for astrobiology experiments in Medium Earth Orbit. In: AAS Division of Planetary Science meeting #52, id. 001.03. Bulletin of the American Astronomical Society, 2020, Vol. 52, No. 6 e-id 2020n6i001p03

[2] NASCETTI, Augusto, et al. In-orbit Characterization of a Lab-on-Chip Payload with Integrated Thin-Film Photosensors for Chemiluminescent Immunoassays aboard the AstroBio CubeSat Mission. In: 2023 9th International Workshop on Advances in Sensors and Interfaces (IWASI). IEEE, 2023. p. 246-250.

[3] CALABRIA, Donato, et al. AstroBio-CubeSat: A lab-in-space for chemiluminescence- based astrobiology experiments. Biosensors and Bioelectronics, 2023, 226: 115110.

[4] VAT Mini Gate Valve https://www.vat-group.com/series/mini-vacuum-gate-valve/01228-KA06 (Accessed November 2025)

[5] Actuonix https://www.actuonix.com/l12-50-210-12-i (Accessed November 2025)

IN SITU PLANETARY EXPLORATION: FROM TITAN (HUYGENS-HASI), TO MARS (EXOMARS-AMELIA/DREAMS) AND BACK TO THE OUTER SOLAR SYSTEM.

F. Ferri[1], B. Saggin[1,2], A. Aboudan[1], G. Colombatti[1,2], C. Bettanini[1,2], E. Dolejsi[1]
[1]Università degli Studi di Padova – Centro di Ateneo per Studi e Attività Spaziali 'Giuseppe Colombo' CISAS
[2]Dipartimento di Ingegneria Industriale DII via Venezia 1 35131 Padova francesca.ferri@unipd.it ,.

Introduction: Direct, contact measurements provide key information for the *in situ* exploration of planetary bodies visited by spacecrafts. The *in situ* characterization is essential for the interpretation of the local context and environment in order to interpret remote sensing observations and to support data analysis.We will discuss *in situ* measurements by multi sensor packages aimed at investigating physical properties of atmosphere, surface, soil and subsoil of planetary bodies and to monitor the environmental conditions. The possible instrument concepts derive from experience gained with past experiments flown in space missions of Solar System exploration.

***In situ* science packages:** *In situ* exploration missions foresee entry probes and landers; measurements could be performed during the approaching phase (i.e. entry, descent and landing – EDL) to the planetary body. Once reached the target body, sampling devices, landers, surface platforms, rovers and automated ultra-light vehicles could be deployed to stand, roving around and flying over the surface. Different sensors could be accommodated on different mission elements, at different sites in order to explore the atmosphere, soil and subsoil and to monitor the environmental conditions at the surface.

EDL science and Atmospheric Structure Instruments (ASI): The Entry, Descent Landing System (EDLS) of an atmospheric probe or lander requires measurements in order to trigger the events of the descent sequence. These measurements besides being aimed to guarantee a safe landing, could provide essential information of the study of planetary atmosphere. Few planetary in situ probes have entered the atmosphere of planetary bodies such as Mars, Venus, Jupiter and Titan, the largest moon of Saturn carrying onboard scientific instrumentations.

On 14 January 2005, ESA's Huygens probe entered the atmosphere of Titan at some 6 km/s. The Huygens Atmospheric Structure Instrument (HASI) [1] started to be operative during the high-speed entry and continued to make *in situ* measurements during the descent phase under parachute and at the impact with ground. HASI data allowed reconstructing not only the atmospheric vertical profiles [2, 3], but also the trajectory and attitude of the Huygens probe [4] providing a reference for all other Huygens data.

The experience and the lessons learned in the framework of the Huygens project have been put forward in the definition of requirements and specifications for other atmospheric entry vehicles in the context of missions of *in situ* planetary exploration.

The entry, descent and landing of the ExoMars descent module (EDM), offered a rare (once-per-mission) opportunity for *in situ* investigations of the martian environment over a wide altitude range. The aim of the ExoMars AMELIA experiment was to exploit the Entry, Descent and Landing System (EDLS) engineering measurements for scientific investigations of Mars' atmosphere and surface [5]. While the DREAMS on Schiaparelli would have monitored the meteorological and environmental conditions at the surface for 4 sols [6]. Despite the ultimate failure of Schiaparelli to safely land, sufficient EDL data were returned to reconstruct the trajectory and attitude of the EDM and to retrieve atmospheric profiles over the altitude range from 105 to 3 km above the surface [7]. Similar experiments (e.g. AMELIA) and measurements (e.g. PACIS-MarsTEM) will be performed on ExoMars Rosalind Franklin mission in 2028 (recovery of the ExoMars2022 mission suspended because of the war).



Fig. 1 Cassini-Huygens probe mission at Titan



Fig. 2 The ESA ExoMars Programme

On the heritage of HASI, the concept for *in situ* measurements have been developed for atmospheric entry probes for the exploration of Titan, Venus, giant planets, and the ice giants: Uranus and Neptune [8] in the framework of several ESA and international mission proposals and studies.

Surface/Environmental packages: Surface packages are devoted to analysis and measurements for local characterization of surface, soil and subsoil, and monitoring the environmental conditions.
This type of instruments could be applicable both for planetary bodies with an atmosphere (as Huygens SSP at Titan [9], and ExoMars-DREAMS at Mars [6]), and for airless bodies (i.e. the Moon, Mercury, icy moons, asteroids, and comets). Beside meteorological parameters, such as pressure, temperature, wind, also dust and electrical properties could be measured to monitor the conditions at the surface, investigate the meterology and atmospheric boundary layer or exosphere and to assess the environment and therefore also the potential risk and hazard for robotic and manned missions.
Sensors deployed on, in contact, or near the surface or within the soil are proposed for determine mechanical, thermal and electrical properties of the surface, regolith, soil and subsoil; these measurements can also complement sample return by the local characterization of the sampling context.

The instrument concepts of surface/environment package have been designed in the framework of International and ESA Cosmic Vision / Voyage2050 future mission proposals and studies for complementing sample return from asteroid (e.g. MarcoPolo-R the ESA CV M3 candidate), for *in situ* investigation of the Moon (ASI White Paper, ASI Moon-ROMULUS study), icy moons (e.g. ESA-NASA Titan Saturn System Mission [10], ESA CV M* Ice Giants mission, NASA Uranus *Flagship* UOP) and comets (e.g. ORIGO ESA CV M7 proposal).

Conclusions:

The experience acquired with Huygens-HASI have been put into perspective for Entry, Descent and Landing science (e.g. ExoMars and RFM 2028) and for new opportunity for *in situ* measurements and ASI/MET instrumentation on board future entry probe and *in situ* missions (e.g. landers, rovers). We are looking forward to applying know-how and lessons learned for future missions to the outer Solar System (e.g. Ice Giants and ESA L4 mission to Saturn's system) possibly in the framework of an outstanding international cooperation like the NASA/ESA/ASI Cassini-Huygens mission.

References:

[1] Ferri F. et al. (2002) *Acta Astro. Jou.l*, **50**, 249-255.
[2] Fulchignoni M. et al. (2005) *Nature*, **438**, 785-791, doi:10.103038/nature04314.
[3] Colombatti G. et al (2008) *Planet Space Scie* **56**, 586-600
[4] Aboudan A. et al. (2008) *Planet Space Scie* **56**, 573-585
[5] Ferri F. et al. (2019) *Space Scie Rev* **215**: 8. https://doi.org/10.1007/s11214-019-0578-x
[6] Esposito F. et al (2018) *Space Scie Rev* **214**, 103, doi: 10.1007/s11214-018-0535-0
Bettanini C. et al. (2018). *Measurement*, doi: 10.1016/j.measurement.2018.01.019
[7] Aboudan A. et al (2018) *Space Scie Rev* **214**, 97, doi: 10.1007/s11214-018-0532-3.
[8] Ferri F. et al. (2020) *Space Scie Reviews* **216**, 118 https://doi.org/10.1007/s11214-020-00749-9
[9] Zarnecki J.C. et al. (2002) *Space Science Rev* **104**: 593–611.
[10] Coustenis A. et al. (2009) *Exp Astron* DOI 10.1007/s10686-008-9103-z

Aknowledgements: We acknowledge the support of ASI (Italian Space Agency) for the design, development and implementation of the Huygens HASI, ExoMars DREAMS and AMELIA experiments in the past and at present (AMELIA RFM2028 ASI-CISAS n.2025-9-HH.0 and NASA Uranus Flagship ASI n. 2024-5-HH.0) that grant us the knowledge and experience to develop new instrument concepts for future *in situ* exploration mission.

DEVELOPING A NEO-RADAR CAPABILITY IN EUROPE: UPGRADE PROPOSAL FOR DSS-63

G. Pupillo[1], A. Margheri[2], R. Orosei[1], S. Righini[1], A. Virkki[3], [1]INAF-IRA (Via Gobetti 101, 40129 Bologna, Italy) - giuseppe.pupillo@inaf.it, [2]Università di Trento (Via Sommarive 14, 38123 Trento, Italy), [3]University of Helsinki (Gustaf Hällströmin katu 2, FI-00014, Helsinki, Finland)

Introduction: Ground-based planetary radar is a uniquely powerful tool for the physical and dynamical characterization of near-Earth objects (NEOs). Radar observations offer unmatched astrometric precision and constraints on size, shape, rotation, surface properties and the presence of satellites, providing key information for science, planetary defense and mission planning [1-2]. Currently, more than 1160 NEAs and 138 main-belt asteroids have been observed using radar. However, since the collapse of Arecibo, global radar capacity has become critically dependent on the 70-m DSS-14 antenna at Goldstone, which currently hosts the world's only dedicated planetary radar transmitter. Its planned shutdown for upgrade from mid-August 2026 to October 2028 would leave the international community without operational radar coverage for over two years, underscoring the urgency of expanding worldwide capabilities.

In parallel, the DSS-43 antenna at Canberra has been performing planetary-radar experiments since 2015 [3], although using a non-dedicated transmitter.

In this context, equipping the 70-m DSS-63 antenna at Madrid DSCC with a high-power transmitter, analogous to the Goldstone Solar System Radar (GSSR), represents a timely and strategic opportunity for Europe.

Recent European NEO Radar Observations: In the last years, we have successfully carried out several radar observations of NEOs in Europe, coordinated by the INAF NEO-Radar group in collaboration with NASA-JPL. These experiments made use of the INAF radio telescopes (the "Grueff" 32-m dish at Medicina and the 64-m Sardinia Radio Telescope/SDSA) together with other European antennas that were used as receivers in bistatic and multistatic radar configurations. As transmitters, the experiments employed the 70-m DSS-14 (Goldstone) and DSS-63 (Madrid) antennas.

Here, we present a brief overview of selected NEO radar observations - 2005 LW3 (23 Nov. 2022), 2006 WB (25-26 Nov. 2024), and 2025 FA22 (18 Sep. 2025) - in which DSS-63 was used as the transmitter, even with its modest current maximum output of 20 kW. As an example of the obtained results, we report the detection of the satellite of the binary asteroid 2005 LW3 and the reconstruction of the primary body's shape derived from Doppler-only radar spectra (see Fig. 1).

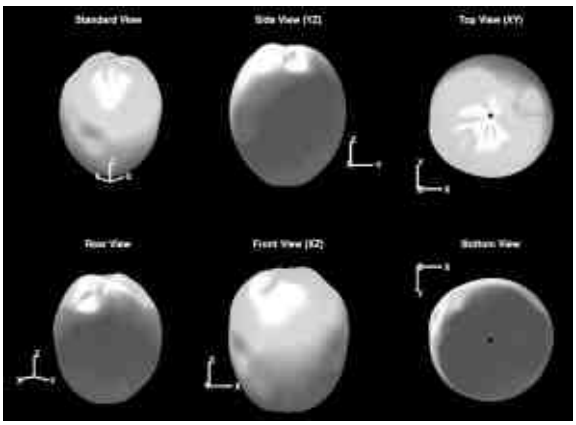


Figure 1 – Different views of the 2005 LW3 shape model obtained by Doppler only radar observations performed on 23 Nov. 2022, (Margheri et al., in preparation).

The results of our radar campaigns highlight Europe's operational expertise in radar-based NEO characterization and astrometry, even without a dedicated transmitter, and demonstrate the high scientific return accessible once a full radar system becomes available.

ESA Pilot Project: Within the ESA-funded pilot project (SSA P3-NEO-XXII, "NEO Observation Concepts for Radar Systems"), we assessed the performance and limitations of existing European infrastructures for planetary radar. The study revealed that Europe already possesses strong receiving capabilities and advanced data-analysis expertise, but lacks a dedicated high-power transmitter, which remains the principal critical point preventing independent NEO radar observations.

In the same project, we carried out a preliminary analysis of the potential performance of future European radar systems through simulations. By varying the antenna diameter, transmitter power, frequency band, mean weather conditons, and observing geometry, we estimated the number of NEOs detectable annually with an SNR/track≥30, which is sufficient for accurate astrometric and physical characterization measurements (see Fig. 2).

The results of these simulations indicate that a 70-m class antenna - such as DSS-63 - equipped with a proper X-band high-power transmitter could potentially observe from several dozens to more than one hundred NEOs per year, significantly enhancing global radar coverage and contributing substantially both to asteroid characterization and planetary defense.

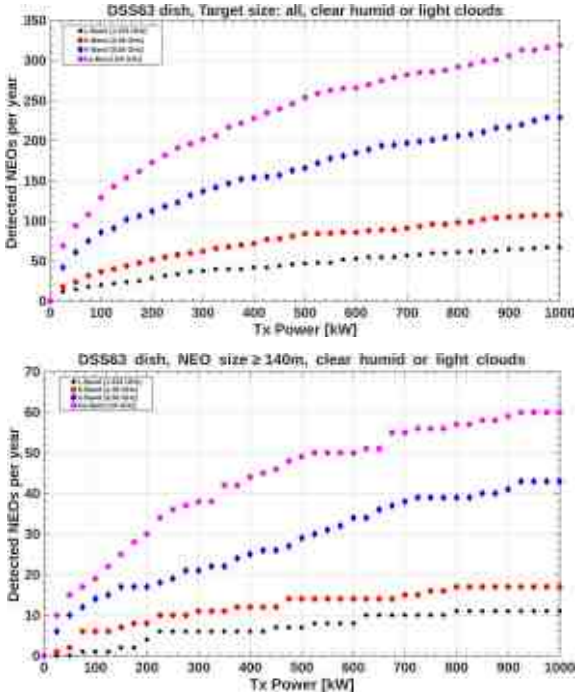


Figure 2 – Expected yearly number of asteroids for all sizes (upper plot) and for diameters ≥ 140 m (lower plot), detectable by the DSS-63 antenna as a function of the transmitted power, assuming a 5-day response readiness after discovery.

The main findings of this project, including several radar experiments, are published in [4].

Proposed Upgrade of the DSS-63 Antenna: The DSS-63 Madrid antenna (see Fig. 3) is mechanically and structurally identical to the DSS-14 Goldstone dish. It also has an unused transmitter cone, reserved for the host country (Spain), providing a unique opportunity for hosting a planetary radar system. It should be stressed that, as the DSS-63 is owned by NASA and operated by INTA (Instituto Nacional de Técnica Aeroespacial) under JPL coordination, upgrading this dish would require a formal agreement among JPL/NASA, ESA and Spain.



Figure 3 – The DSS-63 antenna at the Madrid Deep Space Communications Complex.

Equipping this cone with a transmitter similar to the GSSR minimizes technical risk, as well as development effort and costs compared with other frequency bands, such as Ka-band, or with alternative solutions (e.g., transmitting array). The GSSR operates at ~8560 MHz with a nominal 450 kW CW output, produced by two klystrons of ~250 kW each. It supports multiple waveform modes: continuous-wave (CW) for Doppler measurements, linear frequency-modulated chirp (LFM) and binary phase code (BPC) for ranging and delay-Doppler imaging. In the latter mode, the GSSR is capable of reaching resolutions down to 3.75 m per delay cell. The system can operate in monostatic, bistatic, and multistatic configuration, with real-time Tx waveform modulation designed to precompensate for Doppler shifts of the signal at the receiver [5].

A dedicated feasibility study is now required to address all relevant aspects of such an upgrade at DSS-63, including hardware, software and subsystem architecture, electromagnetic compatibility and safety, power and cooling infrastructure and overall system integration. Such a study will also be essential to establish indicative development, implementation, operational, and maintenance costs.

References: [1] Ostro S.J et al. (2002), *Asteroid Radar Astronomy* in Asteroids III, 151-168. [2] Naidu S. et al. (2016), *AJ*, 152, 1-9. [3] Benson G. et al. (2017), *Radio Sci.* 2017, 52, 1344-1351. [4] Pupillo G. et al. (2024) *Remote Sens., 90,* 1151–1154. [5] Rodriguez-Alvarez N. et al. (2019), *Goldstone Solar System Radar (GSSR) Learning Manual*, NASA/JPL.

Acknowledgments: Part of this work has been carried out within the project SSA P3-NEO-XXII – NEO Observation Concepts For Radar Systems, ESA contract n. 4000130252/20/D/CT.
We thank L.A. Benner and M. Brozovic at Goldstone and J. Lazio at Caltech/JPL for their assistance with the observations.

THERMOPHYSICAL MODELING IN THE SSDC SOLAR SYSTEM EXPLORATION FRAMEWORK: TOWARDS FUTURE MISSIONS AND PLANETARY DEFENSE

E. Rognini[1], A. Zinzi[2], V. Camplone[1], G. Nodjoumi[1,3], M. Giardino[2], A. Chessa[2]
[1]INAF-OAR Osservatorio Astronomico di Roma, Via Frascati 33, 00078, Monte Porzio Catone (RM), Italy
[2]Agenzia Spaziale Italiana (ASI), Via del Politecnico snc, 00133, Rome, Italy
[3]School of Science, Constructor University Bremen gGmbH, Bremen, DE

Introduction: Thermophysical modeling is important in determining the physical structure of airless bodies, providing information on the solar system evolution. Surface features may be also useful to determine the landing area of a spacecraft, establishing an engineering requirement. Furthermore, the thermal inertia causes the Yarkovsky effect, so thermophysical modeling is also useful in planetary defense.

Methods: A thermophysical model computes the surface and sub-surface temperature of an airless body under realistic assumptions on thermal conductivity, density and specific heat. Our code solves the 1D heat equation with a finite difference approach, by taking into account the illumination conditions; the shape of the target is approximated by a shape model, that is a set of triangular facets, and every facet can be or not illuminated depending on the solar direction in the body frame and the topography. If a facet is illuminated, the incoming solar flux is a combination of cosine of incidence angle and heliocentric distance, and these informations are retrieved with the SPICE kernels or from orbital and rotational parameters. The output of the running is the temperature as function of time and depth, and IR flux seen by an observer can be also calculated once the thermal map and observational conditions are given. Temperature and/or IR flux can be compared with the observations, and the fitting procedure allows to retrieve or constrain the thermophysical properties.

Results and future work: The model here described has been already used for the analysis of data provided by the Dawn mission for Vesta and Ceres [1, 2, 3] and for a sensitivity test of the link between surface temperature and sodium content of the exosphere of Mercury has been done [4]. We are currently defining and testing a new approach aiming at the calculation of thermal conductivity of a polydisperse soil, in order to simulate rubble-pile asteroids [5]; optical images show that the surface of these bodies is covered with boulders of different sizes. We employ the thermal data of Bennu and Ryugu for the comparison with the model.

A version of the code of Mercury and Ceres is available on MATISSE [6], the ASI-SSDC scientific webtool devoted to the analysis and visualization of the data provided by the spatial missions. The development and the use of the model is a part of the new SSDC plans. A version of the code is also being written and improved for the Moon; it will be used for the work of the CLEVER team, that is one of the five selected as part of SSERVI project of NASA, whose purpose is the future exploration of the Moon. In general, the thermal features of the soil are a requirement for the selection of landing sites for the Moon exploration.

As stated above, the thermal parameters determine how the Yarkovsky effect is important; we want to study the case of 99942 Apophis, that will have a close encounter with the Earth on 13 April 2029.

In the very next future we are planning to optimize the model for a parallelization, thus being ready to be used with the HPC of the ASI-SSDC and loaded into MATISSE. Hence a huge set of points of a target selected by the user can be simulated in a reasonable time. The code is being modified in order to be modular, so new targets can be added and simulated without modification to the main code. Finally, the use of geological tool will allow the selection by geological features and not only by simple geographical coordinates.

References:

[1] M. T. Capria et al. (2014), *GRL*, **41**, 1438-1443
[2] E. Rognini et al. (2020), *JGR: Planets*, **125**, e2018JE005733
[3] E. Rognini et al. (2021), *Planetary and Space Science*, **205**, 105285
[4] E. Rognini et al. (2022), *Planetary and Space Science*, **212**, 105397
[5] A. Ryan et al. (2020), *Journal of Geophysical Research: Planets*, **125**, 06100
[6] A. Zinzi et al. (2016), *Astronomy and Computing*, **15**, 16-28

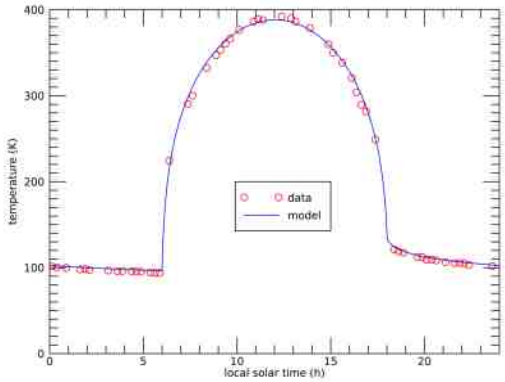


Figure 1: Example of comparison between observed and calculated temperature of the Moon. Longitude = 8.25°, latitude = 13.25.°

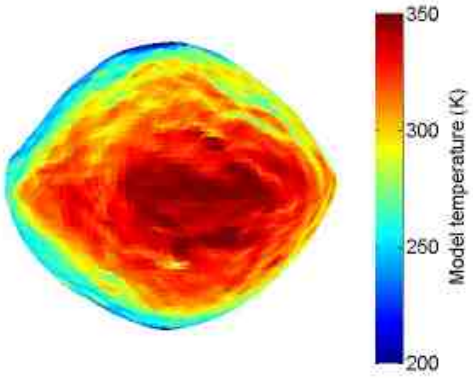


Figure 2: Bennu thermal map derived from data by Approach Phase of the Osiris Rex mission. Figure from https://www.asteroidmission.org/bennu2/

EXPLORING THE LUNAR SOUTH POLAR REGIONS WITH MOONIS, THE ITALIAN SPECTROMETER ON RASHID 3 ROVER. De Sanctis[1] M.C., F. Altieri[1], D. Biondi[1], S. De Angelis[1], L. Rossi[1], M. Ciarniello[1], M. Ferrari[1], G. Filacchione[1], M. Formisano[1], A. Frigeri[1], V. Galluzzi[1], G. Massa[1], A. Raponi[1], E. Ammannito[2], R. Pepe[3], J. Regolini[4], [1]INAF/IAPS, Via Del Fosso Del Cavaliere 100, 00133, Rome, Italy (mariacristina.desanctis@inaf.it), [2]Agenzia Spaziale Italiana, Via del Politecnico snc 00133 Rome Italy, [3] Agenzia Spaziale Italiana, Località Terlecchia 75100 Matera, Italia, [4] Leonardo Company, Via Delle Officine Galileo, 1, 50013 Campi Bisenzio FI.

Introduction: The Emirates Lunar Mission of the Mohammed Bin Rashid Space Centre (MBRSC) Rashid Rover 3 is part of the MBRSC lunar exploration program. The program involves the development and launch of the series of "Rashid" lunar rovers. The MoonIS instrument is a VIS-IR spectrometer onboard the 3rd rover, that will explore the lunar South Pole region, with the main objectives of:

- Analyzing the geological characteristics of the lunar South Pole, examining the surface properties and composition of the soil.
- Exploring a Permanent Shadowed Region (PSR) in the lunar South Pole.
- Studying the presence of water in the southern polar region, identifying ice and hydroxyl on the surface and under the surface.

MoonIS spectrometer, a heritage of the Ma_MISS instrument on board the Rosalind Franklin rover of the ESA ExoMars mission [1], is part of the scientific payload on board the Rashid lunar rover. The instrument will be integrated in the Leonardo company (Campi Bisenzio, Florence) premises. The launch of the mission is scheduled for 2028.

Lunar PSRs and water ice: Permanently shadowed regions on the Moon and other Solar System bodies (e.g., Mercury and Ceres) act as cold traps for the accumulation of water ice and other volatiles, which are thought to have been released over time by impacts of comets, asteroids, or even possible outgassing and interaction of the surface with the solar wind. The lunar PSRs are expected to host large quantities of water-ice, which are key for sustainable exploration of the Moon [2-4]. However, only limited information is available about fine-scale geomorphology and the distribution of ice within PSRs because the orbital imagery obtained to date lacks sufficient resolution and/or signal. Furthermore, it is not clear how much water ice on the Moon is exposed, since from a morphological point of view, it does not present the expected characteristics.

Characterizing water ice in the PSRs is a primary goal of lunar science and exploration, and it is the objective of several lunar missions. The origin of water ice in the PSRs through the Solar System is not clear, and the study of lunar PSRs could help understanding the history of volatiles on the lunar surface and on other planetary bodies. In situ investigations are therefore essential to better understand the nature of the ice and its amount. For this reason, several space agencies are planning to send rovers to better investigate water-ice and overall surface composition within PSRs and pave the way for human exploration.

The MoonIS instrument: The MoonIS instrument is designed to obtain spectra of the lunar surface in the 0.4-2.4 μm range. The MoonIS spectrometer is inherited from the Ma_MISS instrument aboard the ESA's ExoMars Rosalind Franklin Rover with substantial changes in the optical head, calibration target, thermomechanical, and electronics design. Differently from Ma_MISS, MoonIS Optical Heads (OHs) will be mounted on the rover mast and connected through optical fibers to the spectrometer, housed on the rover (Fig. 1). Each fiber is coupled to a dedicated optical element (OH) to allow to observe the scene while the other end is coupled to the spectrometer's slit. The present design foresees 3 Optical Heads. This configuration allows to disperse the signal of each fiber across multiple pixels on a detector. The resulting hyperspectral image consists of the same number of "spots" on the detector as the number of fibers and OHs.

An external Calibration target for radiometric and spectral calibration of the MoonIS instrument is also foreseen. MoonIS will be equipped with a redundant illumination system, capable to illuminate the region of interest in the PSRs.

The area in front and surrounding the rover is scanned with the rover mast, that will allow to investigate the entire region of interest. Using this concept, MoonIS will be able to acquire consecutive or not consecutive images of multiple "pseudo-pixels", thanks to the mast and rover movements.

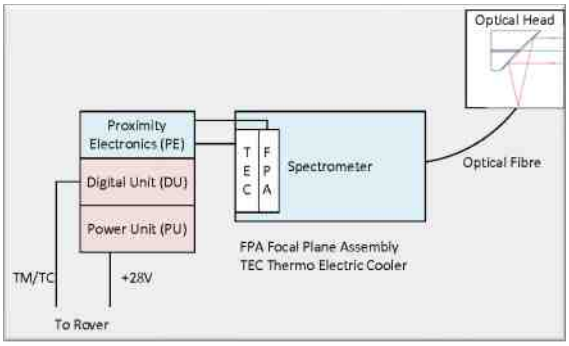


Figure 1: Schematic view of the MoonIS instrument.

Main scientific objectives: The mission payload is mainly devoted to the identification and characterization of lunar ice. MoonIS is designed to achieve high-quality spectral data, focusing on the identification, distribution, and analysis of water ice. Moreover, the instrument will give key results in the characterization of the mineralogy of the lunar surface at the south polar region. The main MoonIS goals can be summarized as follows:

- identify and distinguish H_2O and OH in the PSR ;
- evaluate the amount of H_2O and OH and their distribution;
- recognize the main class of lunar rocks;
- identify and quantify different minerals (e.g., pyroxenes, olivines, feldspars, spinels, etc.);
- identify different mixtures and determine their spatial distribution;
- study the ice distribution and its relation with minerals.

MoonIS characteristics (see Table 1) in terms of S/N, spectral resolution, range, and spatial resolution are suitable to achieve the above-mentioned goals both in the Sun-illuminated regions and in the PSR, the primary focus of the mission.

MoonIS	
Spectral range	0.4-2.4 µm
Spot size at ground	About 2 cm
Spectral resolution	<21 nm in the range 1-2.3 µm < 35 nm in the range 0.4-1 µm
Spectral channels	364
Spectral Sampling	≤ 5 nm
Focal plane	HgCdTe Sofradir detector Window: 256 × 500 pixel

Table 1: MoonIS main characteristics

At the end of the integration phase, the Moonis instrument will be fully characterized in the INAF-IAPS calibration facility by using a dedicated optical setup with the aim to determine the spectral, spatial and radiometric responses of each OHs. These measurements will be executed in a range of instrument's temperatures representative of the operative conditions expected on the lunar environment. Further functional tests will be executed after the instrument will be integrated onboard the Rashid rover to verify the imaging performances of the OHs mounted on the rover's mast.

Acknowledgments: This work is granted by Accordo ASI – INAF n. 2024-64-HH.0. The instrument is funded by ASI and manufactured by Leonardo S.p.A. (Italy).

References: [1] De Sanctis et al. (2017): *Astrobiology 17*, 6, 7. [2] McCubbin et al. (2015) *American Mineralogist 100*: 1668-1707. [3] Honniball et al. (2021) *Nature Astronomy 5*: 121-127. [4] Pieters et al. (2009) *Science*, 326, 568–572.

RADIOMETRIC PERFORMANCE MODEL FOR A NOTIONAL IMAGING SPECTROMETER AS PART OF THE "URANUS FLAGSHIP" MISSION. B. Gorga[1,2], F. Tosi[2], G. Piccioni[2], F. Camilloni[2], D. Grassi[2], F. Zambon[2], and P. Tortora[3], [1]Sapienza University of Rome, Piazzale Aldo Moro 5, 00185, Rome, Italy (beatrice.gorga@uniroma1.it), [2]INAF-IAPS, Via del Fosso del Cavaliere 100, 00133, Rome, Italy (beatrice.gorga@inaf.it), [3]University of Bologna, Via Zamboni 33, 40126, Bologna, Italy.

Introduction: Although every planet in our Solar System has been visited at least once by spacecraft, Uranus remains one of the least explored. The only close-up observations of the planet were obtained during Voyager 2's flyby in 1986, leaving many fundamental questions about its atmosphere, interior, magnetosphere, rings, and satellites unresolved. Remote observations from HST and JWST have provided new insights into the Uranian system, yet many mysteries persist. Recognizing this gap, the 2023-2032 Planetary Science Decadal Survey has prioritized the Uranus Orbiter and Probe (UOP) as NASA's top Flagship mission concept for the coming decade [1]. The proposed mission will deploy an atmospheric probe into Uranus's upper layers and conduct a multi-year orbital campaign to investigate the planet's complex system in unprecedented detail [2].

Recent data, obtained from both ground-based and space-based telescopic facilities, reveal that Uranus's five classical icy satellites (Miranda, Ariel, Umbriel, Titania, and Oberon) exhibit neutral to slightly reddish slopes in the ~0.3-1.3 μm range [3]. In the 1.4-2.5 μm region, their spectra transition toward a bluish slope, consistent with the presence of water ice intimately mixed with varying amounts of optically dark, non-ice materials such as organics and silicates.

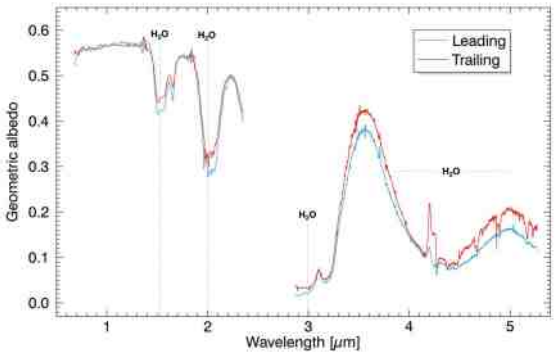


***Fig. 1*:** Geometric albedo spectra of Ariel's leading (blue) and trailing (red) hemispheres obtained by combining two different datasets: IRTF/SpeX (~0.8-2.5 μm) and JWST/NIRSpec (2.87-5.25 μm).

The geometric albedo spectra presented in Fig. 1 are dominated by water ice absorption bands at 1.52, 2.02, 3, and 4.5 μm. The feature at 1.65 μm and the Fresnel peak at 3.1 μm are indicative of the presence of crystalline H_2O ice. The trailing hemisphere of Ariel displays distinct CO_2 ice combination and overtone bands between 1.9 and 2.2 μm (see Fig. 4 in [4]), which are absent on the leading hemisphere [4]. This hemispherical asymmetry may result from charged particle bombardment within Uranus's magnetosphere, contributing to surface reddening [5,6]. Additionally, spectral signatures detected on Ariel in the 3.87-5.25 μm range (Fig. 2) may arise from hydrocarbons, nitriles, and carbonates [7]. The presence of CO_2 ice is further supported by a broad scattering peak centred at 4.2 μm, flanked by an absorption band at 4.27 μm [7].

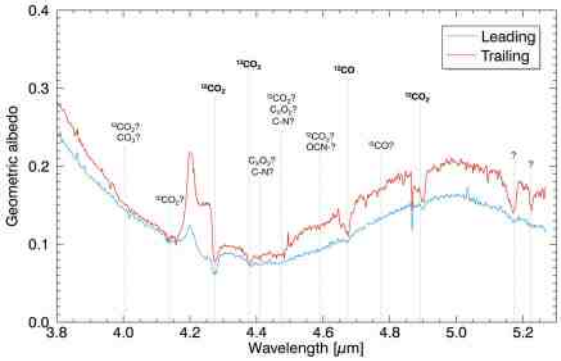


***Fig. 2*:** Zoom of the same albedo spectra in the 3.8-5.25 μm range. Confirmed absorption bands are shown in bold, whereas suggested constituents are followed by a question mark [7].

Radiometric model: The payload of the UOP mission includes remote sensing instruments, including an imaging spectrometer, designed to investigate and map the surface composition of Uranus' major moons in the VIS/NIR range (0.8-5.2 μm). Such an instrument, with a range extended towards visible wavelengths, would also be key to investigating the atmosphere of Uranus [8]. The goal of a radiometric performance model is to simulate the instrument's response under realistic observational conditions by computing the expected signal, the contributions of the different sources of noise, and hence the signal-to-noise ratio (SNR) of the selected target.

The current implementation of the model includes simulations of fundamental parameters such as detector quantum efficiency, filter transmittance, grating efficiency, reflectance of coating materials, and primary noise sources (e.g. shot noise, readout noise, and dark current).

The input for this model is Ariel's radiance spectrum (Fig. 3) in units of $W/m^2/\mu m/sr$, calculated by

multiplying the geometric albedo by the solar flux scaled by the square of Uranus' heliocentric distance (~19 AU).

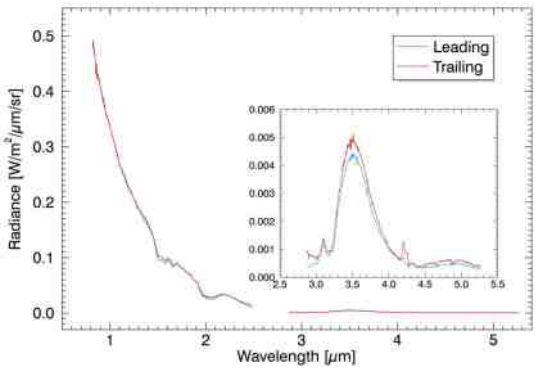


***Fig. 3*:** Radiance spectra of Ariel's leading (blue) and trailing (red) hemispheres. The inset shows a zoom of the same radiance spectra in the region between 2.87 and 5.25 μm.

The radiance entering the spectrometer is reflected by mirrors inside the instrument and directed onto the grating, where it is diffracted. The model thus simulates the reflectance and transmittance of these optical components (including any coating materials), taking into account potential photon losses. After passing through the optical system, the photons reach the detector, where they are converted into photoelectrons and then into a digital signal. The conversion probability is closely linked to the quantum efficiency and the structure of the detector, which in this case consists of three components: a linear variable filter (LVF), a sapphire window, and the detector itself. LVFs are particularly effective as order-sorting filters, designed to suppress higher diffraction orders produced by the gratings. The sapphire window serves as a protective barrier for the detector, shielding it from external contaminants (dust, moisture, and mechanical impacts).

Preliminary results: The SNR represents one of the most critical outputs of the radiometric model, as it provides a direct measure of the instrument's response to a given input radiance. In particular, the SNR serves as a diagnostic tool to identify spectral regions where the instrument performs optimally, as well as those where signal degradation may occur due to noise dominance.

In this study, the SNR is initially calculated by considering only the shot noise, which arises from the statistical nature of photon arrival. This idealized scenario provides an upper bound on the instrument's performance, representing the best-case detection capabilities. Assuming a Teledyne HgCdTe H1RG detector as a representative case, the readout noise is incorporated, revealing how electronic noise introduced during signal digitalization affects the detectability of low radiance features. Finally, noise related to the dark current was added, which is the signal generated inside the detector in the absence of light. This signal is caused by the thermal agitation of charge carriers and therefore strongly depends on the detector's operating temperature. As shown in Fig. 4, the inclusion of these sources of noise leads to a noticeable degradation in SNR, especially in spectral regions where the signal is weak.

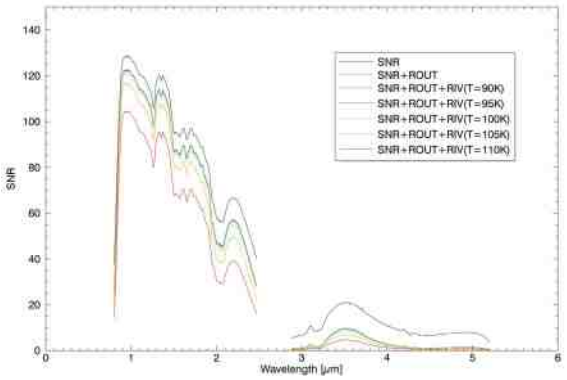


***Fig. 4*:** SNR calculated over an exposure time of 1 s for Ariel, considering only the shot noise (black), then adding the readout noise (grey) and at least the dark current at different temperatures (90-110 K).

Conclusions: The radiometric modelling presented in this study provides a robust framework for evaluating the performance of imaging spectrometers under realistic observational conditions at Uranus. These insights are critical for guiding instrument design choices and observation strategies for the UOP mission.

Acknowledgements: We acknowledge support from the "*Studio preliminare dei payloads per la missione URANUS flagship di NASA*", funded by the Italian Space Agency (ASI) under contract n. 2024-5-HH.0 - CUP n. F33C24000160005.

References: [1] National Academies (2023) *Origins, Worlds, and Life: A Decadal Strategy for Planetary Science and Astrobiology 2023-2032,* NAS, Press. [2] Simon A. et al. (2021) *Uranus Orbiter and Probe: Planetary Mission Concept Study for the 2023-2032 Decadal Survey.* [3] Karkoschka E. (2001) *Icarus*, 151, 51-68. [4] Cartwright R. J. et al. (2015) *Icarus*, 257, 428-456. [5] Cartwright R. J. et al. (2018) *Icarus*, 314, 210-231. [6] Cartwright R. J. et al. (2020) *ApJL*, 898, L22. [7] Cartwright R. J. et al. (2024) *ApJL*, 970, L29. [8] Camilloni F. et al. (2026), CNSP, this conference.

The Lunar Earth Temperature Observatory (LETO) instruments on the Moon: Extending FORUM Climate Datasets with Disk-Integrated Far-Infrared Observations

S. Menci, G. Di Natale, L. Palchetti, CNR-INO (National Institute of Optics), Via Madonna del Piano, 10, 50019, Sesto Fiorentino, Florence, Italy, simone.menci@ino.cnr.it.

Introduction: The Earth-Moon-Mars (EMM) project has been recently selected under the Italian National Recovery and Resilience Plan (PNRR). The initiative, led by the Italian National Institute of Astrophysics (INAF) in collaboration with the Italian Space Agency (ASI) and the National Research Council (CNR), includes among its objectives the realization of an infrastructure to be deployed on the lunar surface. This infrastructure will host several modules. Within this framework, CNR is contributing to the development of an Earth-observing system called Lunar Earth Temperature Observatory (LETO), which comprises a Fourier transform spectro-radiometer (LETO-FTS) and an imager (LETO-IMG). These two instruments, conceptually similar to those onboard the FORUM mission [1], will provide continuous monitoring of the Earth's entire disk measuring both the brightness temperature and the outgoing longwave (OLR) flux.

In particular, the LETO spectro-radiometer will record the spectral radiance emitted by the full Earth disk across the far-infrared (FIR) and mid-infrared (MIR) spectral regions, approximately between 100 and 1600 cm^{-1} (corresponding to wavelengths from 6 to 100 μm). The accompanying imaging system will enable the identification of thermal anomalies associated with extreme events — such as wildfires, volcano eruptions, and other large-scale phenomena — that could influence the overall Earth brightness temperature measured by the FTS.

LETO Instruments:



Figure 1: Engineering Model of LETO-FTS in laboratory.

We built a prototype of LETO-FTS (Figure 1) with an interferometric layout with double-input and double-output ports in Mach-Zehnder configuration. It has a 3D structure to optimize optical performance with a constrained size and weight. It is foreseen the definitive instrument will have a shutter for protection during possible passage of the Sun in the FOV, which is 2° to cover all Earth's disk.

Visibility in the Moon-based Earth observation: Given the requirement, for such instruments, to have an unobstructed line of sight to make the measurements, we carried out a study to understand if, and to what extent, the coordinates of the landing site affect the visible percentage of the Earth's disk and the measurement time window. A software tool, based on JPL SPICE Toolkit [2], was produced and carefully configured to carry out this task: simulations show that limited latitude and longitude for the selenographic LETO coordinates are required in order for the instruments to reach the maximum scientific performances. Locations impact performance differently in terms of geometric visibility, terrain orography, thermal excursion and floating dust.

Three lunar sites have been considered at different latitudes: 0° (equator), -70° (south region) and -90° (south pole). Only the first 2 scenarios allow a continuous observation of the full Earth disk and, in the end, the mid-south hemisphere seems the best tradeoff for the project (Figure 2).

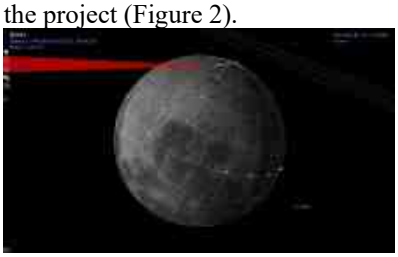


Figure 2: LETO FOV at -70° (south region).

Earth-Moon motion and radiance contribution computation:

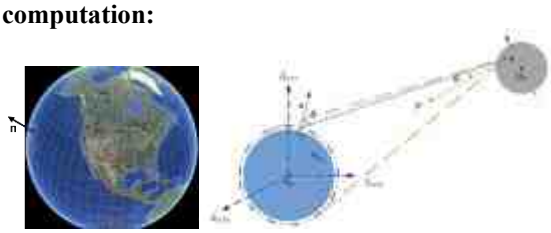


Figure 3: Earth grid and orbital geometry.

The orbital simulator computes, for each time step, which Earth sectors are visible from the Moon. Normal unit vector **n** is used for each sector of the grid to compute θ angle with respect to the line of sight connecting the lunar site. $cos(\theta)$ is the factor of radiative transfer needed to compute the spectral radiance contribution from each visible sector of the grid to the LETO location.

Simulation of the average spectral radiance: Simulations of the average spectral radiance emitted by

the inhomogeneous Earth's disk, as a function of time and of the Moon-Earth position, have been performed by using specific radiative transfer models able to account for the presence of both ice/liquid clouds, aerosols in the Earth's atmosphere. The Earth's atmospheric and surface properties, such as vertical profiles, surface temperature, emissivity and sea, cloud and vegetation cover, needed for the radiative transfer computations, have been extracted from ECMWF Reanalysis v5 (ERA5) database [3]; soil spectral emissivity down to the FIR band from Huang et al. 2016 database. A final integration of the contributions of all Earth's disk produces the desired average spectral radiance.

Example results:

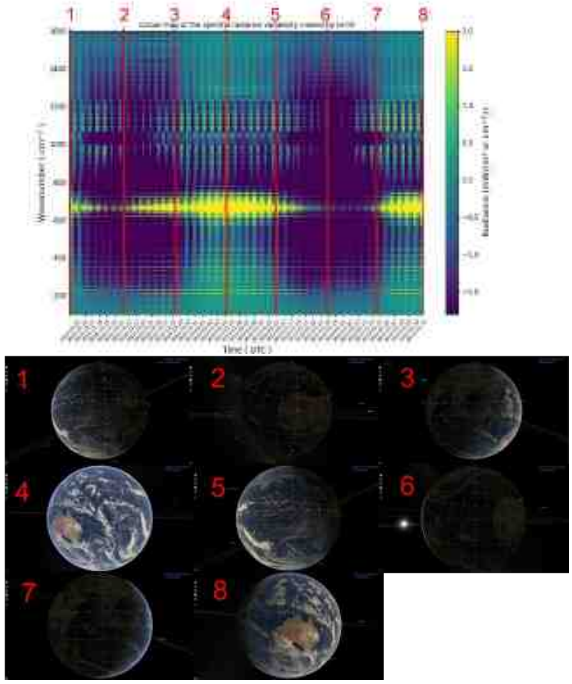


Figure 4: Hourly variability over 1 month in Jan 2019.

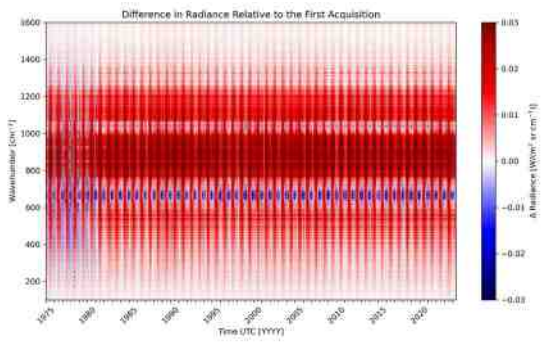


Figure 5: Weekly variability over 50 years with Earth's disk centered in the middle of the Pacific Ocean.

Figure 4 shows the correlation, simulated over 1 month (January 2019) between the illumination state of the Earth's disk as seen by LETO and the simulated radiance arriving at the spectrometer, which is also correlated with the specific visible portion of Earth surface (as an example, ground and ocean emit differently).

Figure 5 shows the weekly variability over 50 years with Earth's disk centered in the middle of the Pacific Ocean, in which Earth's disk is nearly totally oceanic; this exalts the contribution of the atmosphere, which we can see has increased in the last 50 years as an effect of climatic alterations.

Figure 6 shows the simulated average spectra over 50 years (1975-2025), as seen by LETO, differentiated for season of interest, with summer's emissions appropriately higher than winter ones.

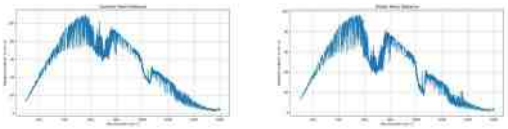


Figure 6: Seasonal LETO average spectra over 50 years since 1975 (summer and winter).

We are interested in the creation of a large dataset, available to the reasearch community, of the spectral radiances of the Earth's disc over a long period from the past to the future.

The sensitivity of the measured spectral radiance to the Earth's parameters such as the average temperature, the cloud cover, the ice and vegetation cover, etc., is currently under study with the aim to assess the tradeoff between the requirements for the measurement and its capability to monitor the time evolution of the Earth's geophysical parameters with given accuracy. We are also interested in testing the capability to identify from these simulations the climatological trend through the comparison with climate models.

Summary: LETO will be deployed on the Moon within the framework of the PNRR EMM project. The simulated radiances will be used to reproduce the measurements, which will be collected every 1–2 minutes to minimize the impact of the Earth's rotation on the observed scene. The temporal variations of the signal will enable us to track the global mean temperature trend and, potentially, to monitor changes in the overall coverage of clouds, ice, and vegetation.

Acknowledgements: We thank the EMM (Earth-Moon-Mars) project funded under the National Recovery and Resilience Plan (NRRP), Mission 4, Component 2, Investment 3.1, Action 3.1.1, funded by the European Union - NextGenerationEU.

References:

[1] – FORUM Website.
[2] – JPL SPICE Toolkit.
[3] – ECMWF Reanalysis v5 (ERA5) database.

OBSERVATION STRATEGY AND PERFORMANCE ANALYSIS OF MIST-A ONBOARD THE EMIRATES MISSION TO THE ASTEROID BELT M. Ciarniello[1], G. Filacchione[1], A. Raponi[1], M. C. De Sanctis[1], F. Capaccioni[1], S. De Angelis[1], M. Ferrari[1], M. Formisano[1], D. Biondi[1], A. Boccaccini[1], S. Stefani[1], E. La Francesca[1], A. Galiano[1], C. Cencia[1], G. Piccioni[1], A. Mura[1], M. Galinier[1], A. Tiberia[2], E. Ammannito[2], A. Olivieri[2], B. Negri[2], C. Bartolo[3], E. Borgato[3], L. Bucciantini[3], G. Carbone[3], G. A. Cossu[1,3], M. Dami[3], M. Galli[4], T. Giorgi[3], P. Inglese[3], M. Iuzzolino[3], S. Nencioni[3], A. Nicola[3], V. Pagliazzi[3], A. Ristori[3], C. Spagnesi[3], M. Santoni[3], L. Tommasi[1,3], L. Toni[5].

[1]INAF-IAPS, Institute for Astrophysics and Planetology from Space, via del Fosso del Cavaliere, 100, 00133, Rome, Italy (mauro.ciarniello@inaf.it; gianrico.filacchione@inaf.it), [2]ASI Italian Space Agency, via del Politecnico snc, 00133, Rome, Italy, [3]Leonardo, via delle Officine Galileo, 1, 50013, Campi Bisenzio, Florence, Italy, [4]Ad Maiorem Italia S.r.l, via Alfredo Campanini 4, 20124 Milano; [5]ALTEN Italia, via Gaetano Crespi 12, 20134 Milano, Italy.

Introduction: The Emirates Mission to the Asteroid Belt (EMA) is a multi-asteroid mission, aimed at investigating the formation and evolution of water-rich targets [1]. EMA will be launched in March 2028, and it will perform flybys of six asteroids from 2030 to 2033, before completing its tour of the main belt with a rendezvous with (269) Justitia in 2034 and the deployment of a demonstrative lander. The flyby targets (10253 Westerwald, 623 Chimaera, 13294 Rockox, 88055 Ghaf, 23871 Ousha, and 59980 Moza) are from different spectral types, most of them likely being primitive objects and/or members of collisional families.

The main target of the mission, (269) Justitia, is one of the two reddest asteroids in the main belt, along with (203) Pompeja. The peculiar color of Justitia, comparable to red-colored trans-Neptunian objects [2], might suggest a possible origin in the outer Solar System, while raising the question of how this spectral feature has survived collisional, space weathering, and thermal processing [3].

The remote sensing payload of EMA includes the camera suite EMACS (composed of a visible color narrow angle camera and an infrared camera), the thermal IR spectrometer (EMBIRS) and the Italian-contributed Mid-wave Infrared Spectrometer for Target-Asteroids (MIST-A, [4]).

MIST-A is a slit hyperspectral imager operating in the 2-5 μm spectral interval, with a sampling of <10 nm. Thanks to the selected wavelength range, it will investigate and map the surface composition of EMA targets, characterizing different classes of compounds, including organics, carbonates, ammonium salts, hydrated silicates, and water ice.

MIST-A is equipped with a scanning mirror, allowing to observe a composite field of view (FOV) of 3.52°X12° with an instantaneous field of view (IFOV) of 238 μrad, corresponding to a spatial sampling of 24 m from 100-km distance. The instrument operates with the spectrometer's slit parallel to the spacecraft's velocity direction, thus the observation scene is built thanks to the movement of the scanning mirror in the across-slit direction, as a collection of hyperspectral images of the target through the slit (so-called lines).

Here we present the status of MIST-A observation planning at Justitia and during the flybys, including anticipated mapping coverage and data volume, and the expected instrument performances in terms of SNR.

Observations of Justitia: the EMA spacecraft (MBR Explorer), will spend about seven months around Justitia, including the 14-weeks-long primary science phase. During Primary Science Orbits (PSO), MBR will be stabilized on nearly polar circular orbits, with a period of ~12-21 h (depending on the asteroid gravitational field), orbital radius of ~91-97 km (~65-71 km altitude, corresponding to MIST-A spatial sampling of ~15-16 m/pix), and β angle ~30°-45°.

In the nominal scenario MIST-A will operate during the dayside part of the orbits with a typical repetition time of 2 s (acquisition cadence of consecutive lines, including 0.8 s for exposure and 1.2 s for detector readout). This value is smaller than the expected dwell-time of ~4-7 s, thus preserving spatial resolution. A full across-slit scan over the maximum 12° FOV would require the acquisition of ~870 contiguous lines, taking approximately 29 minutes. Depending on the orbital period and corresponding ground-track velocity, the scan extent (i.e. duration) and cadence can be adjusted to avoid gaps and ensure desired overlap between consecutive scans along the same track.

Operating with a duty cycle of 3 days per week, as per planned mission constraints, and depending on the orbital scenario, MIST-A will be able to map 50% of Justitia's surface in a maximum of 4-6 weeks, with near-complete coverage (>90%) achievable during the span of the PSO.

By means of MIST-A radiometric model and spectrophotometric simulations of Justitia's reflected and thermal radiance, we computed the expected SNR at Justitia. This occurs to be larger than 100

over most of the investigated spectral range for observations encompassing the equatorial belt up to mid-latitudes with the nominal 0.8 s exposure time.

Strategies for further optimization of the coverage, redundancy, data-volume, and SNR are under development.

Flybys: During the 6 asteroids flybys, MIST-A observations will be primarily conducted at ±2 hr around the Closest Approach (CA), during which the spacecraft Tracking and Autonomous Landing Onboard Navigation System (TALONS) will ensure continuous pointing of the instrument's boresight towards the asteroid's photometric center. Also in this scenario, MIST-A will operate by scanning the scene in the across-track direction, and the extent of the scan will be adjusted as a function of the target distance to match the apparent size of the asteroid and to accommodate spacecraft's pointing errors.

By simulating the expected signal for observations of the different targets, we find that at minimum phase angle (typically within a few minutes from the closest approach) MIST-A will achieve average SNRs between a few to several hundred for wavelengths below 3.5 μm, and >50 (up to a few hundred) at longer wavelengths, with a nominal exposure time of up to 0.8 s (repetition of 2 s).

We are currently investigating further optimization of exposure and repetition times for each flyby, with the objective of maximizing the SNR across the entire science phase by accounting for the targets' reflectance properties, varying observation geometries, and distances, while simultaneously preventing saturation and minimizing pixel smearing. By adapting the exposure time, we anticipate extending observations throughout the full flyby science windows (CA-10 hr to CA+2 hr), which will include the acquisition of subpixel images.

References:

[1] Al Mazmi et al., 2024, COSPAR, b1.1-0036; [2] Hasegawa et al., 2021, ApJ L., 916, L6; [3] Bottke et al., 2023, ACM Conference 2023 (LPI Contrib. No. 2851); [4] Filacchione et al., 2024, COSPAR, b1.1-0037.

Acknowledgements: MIST-A science, calibrations, operations, and data processing responsibilities are in INAF/IAPS, Rome. The MIST-A program is managed by the Italian Space Agency (ASI) as leading funding agency. Leonardo (Campi Bisenzio, Florence) is the primary industrial contractor (ASI contract n. 2025-33-I.0). Funding for the Emirates Mission to Explore the Asteroid Belt is provided by the United Arab Emirates Space Agency, in collaboration with its knowledge partner, the Laboratory for Atmospheric and Space Physics at the University of Colorado Boulder.

A Multiband Imaging Camera for the Exploration of the Uranian Planetary System: Design and Expected Performance

P. Fraccaroli[1,2], A. Lucchetti[2], G. Naletto[3], M. Pajola[2], L. Penasa[2]; [1]Alma Mater Studiorum - Università di Bologna, Italy (pietro.fraccaroli2@unibo.it); [2]INAF-OAPD Astronomical Observatory of Padova, Italy; [3]University of Padova, Department of Physics and Astronomy, Italy.

Introduction: The Uranian system, identified as the highest-priority target for the next flagship mission by the Planetary Science and Astrobiology Decadal Survey 2023–2032 [1,2], provides a unique opportunity to investigate the formation and evolution of ice giant planets and their satellites. Knowledge of Uranus's major moons, Ariel, Umbriel, Titania, Oberon, and Miranda, remains largely based on Voyager 2 flyby observations [3], which revealed geologically diverse terrains but left major questions regarding their composition, internal structure, and evolutionary history unresolved. Achieving the scientific objectives defined for a future Uranus flagship mission [4] requires advanced multispectral imaging systems capable of acquiring data across a broad spectral range at high spatial resolution, enabling the detection of spectral signatures of ices, minerals, and volatiles, as well as monitoring atmospheric phenomena such as cloud motions and auroral emissions. Recent advances in detector technology now enable high-performance imaging across the full VIS–SWIR range (400–2400 nm) using a single focal plane, eliminating the need for dual-channel architectures. This capability supports a compact and unified imaging system with reduced complexity and improved scientific efficiency. This work presents the conceptual design of a compact, high-resolution multispectral camera operating from 400 to 2400 nm, developed to address the key scientific requirements of a dedicated mission to the Uranian system.

Design and optimization: the instrument is based on an unobscured Three Mirror Anastigmat (TMA) telescope configuration, featuring a 200 mm entrance pupil diameter (EPD), a 1.14° × 1.14° field of view (FOV), and an instantaneous field of view (IFOV) of 10 µrad across the 400–2400 nm spectral range. The selected detector is the 2k × 2k pixel CHROMA-D sensor from Teledyne e2v [5].

Specification	*Value*
EPD	*200 mm*
EFL	*1800 mm*
F/#	*9*
FOV	*1.14° x 1.14°*
Detector format	*2k x 2k pixel*
Pixel size	*18 µm*
IFOV	*10 µrad*
Spectral range	*400 – 2400 nm*

Tab.1: *Optical Specifications.*

Its 18 µm pixel pitch, combined with an effective focal length (EFL) of 1800 mm, yields a ground sampling distance of 1 m/pixel at a target distance of 100 km. The resulting system operates at an F-number of F/9. *Tab.1* summarizes the main optical parameters of the conceived camera system.

Beyond the instrument level requirements, the optical system must also satisfy several geometrical constraints. An accessible intermediate focal plane is needed to accommodate a field stop for stray light mitigation. Similarly, the exit pupil must be accessible to enable the integration of two filter wheels and a cold stop. A minimum back focal distance equal to the separation between the primary and secondary mirrors is required to provide sufficient space for positioning the filter wheels between the tertiary mirror and the focal plane. To simplify Assembly, Integration, and Testing (AIT) activities and reduce integration costs, the separation between mirrors M1 and M2 was intentionally set equal to the distance between M2 and M3 (see *Fig.1*).

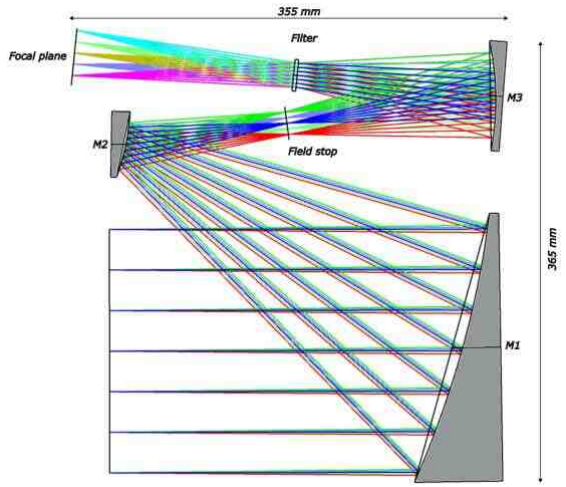


Fig.1*: Raytrace diagram. The colors represent different fields. Key elements, such as the mirrors, intermediate focus, filter, and focal plane, are highlighted. The exit pupil is located at the filter position.*

During the optimization design process, multiple configurations met the instrument's constraints. Therefore, a trade-off analysis was conducted in order to identify the most suitable configuration based on the following criteria:

- ➢ maximizing optical performance in terms of spot diagram and MTF, ensuring optimal imaging quality;
- ➢ minimizing dimensions and bulks to reduce the payload's mass and overall size;

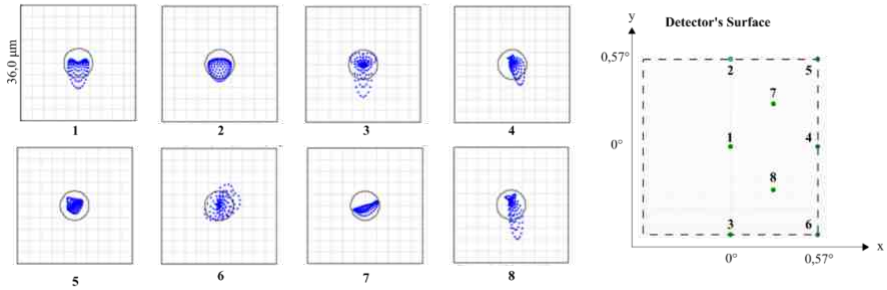


Fig.2: Spot Diagram evaluated in 8 different fields (listed on the right side). The circles in the Spot diagram represent the Airy disk at 400 nm

- ➢ maximizing the available space around the intermediate focus and exit pupil, facilitating the design and integration of the field stop, filter wheels and cold stop;
- ➢ minimizing the exit pupil diameter to reduce the required filter size and minimize the filter wheels dimensions.

Performances: This all-reflective configuration is an optimal solution, given the wide spectral range over which it operates, with the filter representing the only source of chromatic aberration. *Fig.2* shows the spot diagrams generated in Zemax OpticStudio. The square box corresponds to a 2 × 2 pixel region (36 µm × 36 µm), while the circle indicates the Airy disk at the shortest wavelength, 400 nm, with an Airy radius of 4.5 µm. At the shortest wavelengths the system is limited by the pixels, but for wavelengths longer than 1600 nm, where the Airy disk has the same size of the pixel, the system is diffraction-limited. *Fig.3* shows the polychromatic diffraction MTF of the optical elements for the whole spectral range 400 - 2400 nm, in the eight fields considered. The maximum spatial frequency considered is relative to the Nyquist frequency, which is:

$$MTF_{nyq} = \frac{1}{2 \times pixel_{size}} = \frac{1}{2 \times 18\,\mu m} 10^3 = 27.7\ \frac{cycles}{mm}$$

The designed system achieves MTF values ranging from 0.543 to 0.596, depending on the field.

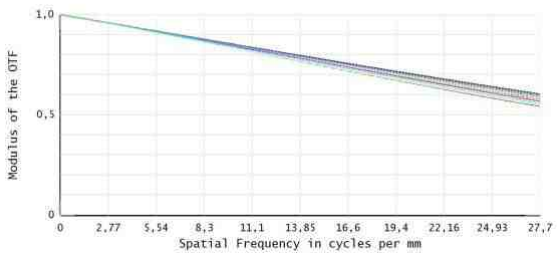


Fig.3: Polychromatic diffraction MTF (computed as the modulus of the Optical Transfer Function) in the whole frequency range up to Nyquist frequency, computed in several points of the field of view as per spot diagram in Fig.2.

The MTF is always above 54% over the whole field of view for frequencies smaller than 27.7 cycles/mm. To assess the expected post-alignment performance, a Monte Carlo analysis with 1000 iterations was performed, accounting for tolerances on all key parameters, including optical element positioning and surface irregularities. The quality of each perturbed optical configuration was evaluated using a performance criterion based on the RMS wavefront error, with a threshold of 70 nm (λ/14 at 1000 nm), in accordance with the Marechal criterion [6]. The results highlight the need for particularly stringent tolerances in the alignment of the primary mirror. To partially compensate for misalignments and reduce overall wavefront degradation, decentering of the secondary mirror was introduced as a compensator.
The instrument is designed to acquire narrowband images across the VIS-SWIR (400 - 2400 nm) spectral ranges, using a set of 22 narrowband and broadband filters selected according to the mission's scientific requirements. The filter assembly consists of two coupled wheels, each accommodating 11 filters plus one empty position. During the optical optimization process, the exit pupil diameter, where the filters are placed, was reduced to 20 mm to limit the filter dimensions and maintain a compact and manageable wheel design.

Conclusion: this work presents the preliminary design of an unobstructed Three Mirror Anastigmat (TMA) telescope developed for a dedicated mission to the Uranian system. The instrument provides multiband imaging through a single optical channel, spanning a wide spectral range from 400 to 2400 nm. The telescope has a polychromatic MTF consistently exceeding 54% over the full FOV. The system includes a set of custom multiband filters specifically selected to fulfill the mission's scientific measurement objectives.

Acknowledgements: This activity has been developed under the ASI/UniBo-CIRI agreement n. 2024-5-HH.0.

References

[1] National Academies of Sciences, Engineering, and Medicine, "Origins, Worlds, and Life: A Decadal Strategy for Planetary Science and Astrobiology 2023–2032", Washington, DC: The National Academies Press, 2023.
[2] Simon, A. Nimmo, F. Anderson, R. C. (7 June 2021). "Journey to an Ice Giant System: Uranus Orbiter and Probe". Planetary Mission Concept for the 2023–2032 Planetary Science Decadal Survey.
[3] Stone, E. C., et al. (1986). The Voyager 2 encounter with the Uranian system. Science, 233(4759), 39–43.
[4] Lucchetti, A et al. (2023) Surface Characterization of the Uranian Moons from Visible-Near Infrared (Vis-NIR) Multiband Imaging. Uranus Flagship Workshop July 25–27, 2023
[5]https://www.teledynespaceimaging.com/en-us/Products_/Pages/infrared-hgcdte-chroma-d.aspx
[6] Born, M., & Wolf, E. (1999). Principles of Optics

SPATIAL SAMPLING IN GEOLOGIC INVESTIGATIONS WITH GPR IN PLANETARY EXPLORATION

Caterina Rossi[1], Alessandro Frigeri[1], Francesca Altieri[1] and Maria Cristina De Sanctis[1].
[1]Istituto di Astrofisica e Planetologia Spaziali (IAPS), Istituto Nazionale di Astrofisica (INAF), Roma, Italy (Caterina.Rossi@inaf.it);

Introduction: Ground Penetrating Radar (GPR) uses electromagnetic waves to image subsurface features non-destructively [1]. Developed for mining and then applied to geology and archaeology on Earth, GPR is now part of the planetary exploration, for example in missions looking for traces of life on missions Mars, with experiments like RIMFAX on NASA/Mars2020 [2] and WISDOM on ESA/Rosalind Franklin [3].

GPRs are commonly operated on moving carts or sleds on Earth and rovers in space mission, so that echo returns frames (A-scan) can be arranged into bi-dimensional radargrams (B-scan).

The knowledge of the rover's geospatial position (considering the geographic coordinates and the topography) at each acquisition point of its path is key to correctly associate radar traces with surface locations and apply geometric corrections in data processing.

In particular, the distance between GPR traces is essential for scientific investigation and a correct geologic interpretation. The spacing between traces must be adequate to ensure that the sampling is unaliased, while also ensuring that there is sufficient distance between acquisitions to prevent over-sampling.

The Nyquist theorem offers a way to determine the minimum spacing required between acquisitions in order to guarantee correct sampling of the subsurface.

To investigate the importance of geospatial positions of radar traces, we examined data from the Radar Imager for Mars' subsurface experiment (RIMFAX) [2].

Data and methods: RIMFAX data are available from NASA's Planetary Data System (PDS) Geosciences Node [4]. The archive includes calibrated RIMFAX datasets, stored in accordance with the Planetary Data System version 4 (PDS4). Rover coordinates in terms of latitude, longitude and radius were extracted and converted to Cartesian coordinates.

Once the path on the surface along which the rover traveled has been determined, we compute the distance between the traces and make considerations based on Nyquist's theorem [5] providing the fundamental criterion for correctly digitizing and reconstructing transmitted and received signals. To preserve all information carried by the radar signals, the sampling frequency must be at least twice the highest frequency component, or more commonly in radar practice, twice the signal bandwidth after.

The conventional application of the theorem concerns the time domain of each A-scan, and for GPR data this corresponds to sampling along the dimension of the profile in the direction of depth. Each GPR trace records the temporal evolution of the electromagnetic echo reflected in the subsurface, and this temporal signal is discretized into samples representing the amplitude of echo returns along the depth.

Besides that, in GPR, spatial sampling is also relevant. It refers to the spatial separation at which a trace is acquired at different location along the rover path. Previous work [6] applied the Nyquist theorem to the case of a two-dimensional GPR profile, concluding that spacing equal to a quarter of the signal wavelength should be used. Sampling the surface at a greater distance reduces the horizontal resolution and generates aliasing phenomena. It is also important to avoid acquiring traces that are too close together.

At very short distances, the gain in scientifically relevant information diminishes, while data volume increases. The additional information may not outweigh the trade-off with the increase in data rate and the resources required to store, transmit and process the data.

Results: On sol 202, the Mars2020 rover covered a distance of 44.69 m, during which the radar performed 1485 soundings. The distance between acquisitions is shown in Figure 1. The mean distance over this interval has also been determined and it is equal to 3.01 cm (orange line in Figure 1). Figure 2 shows the histogram of the data presented in Figure 1.

To apply Nyquist's theorem, the wavelength of the

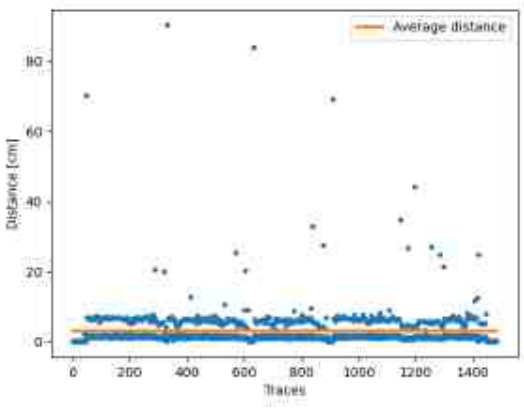


Figure 1: Spacing between traces of Mars2020/RIMFAX data acquired during sol 202.

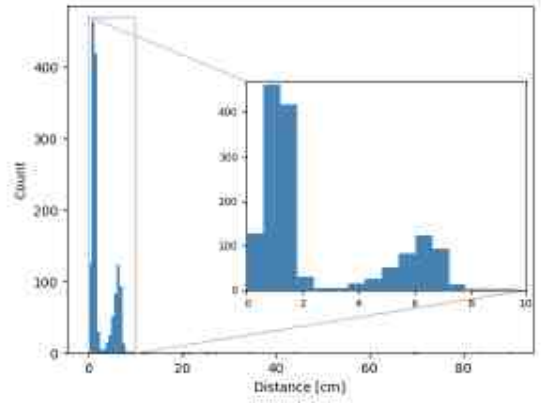


Figure 2: Histogram of the distribution of distances. The zoom in the figure highlights a bimodal trend of the Gaussian distribution.

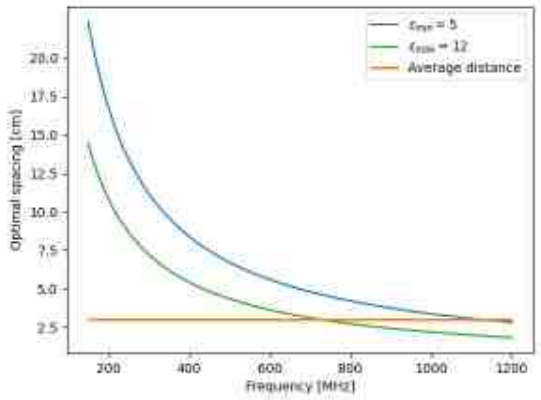


Figure 3: Optimal distances bewteen traces for RIMFAX according to the Nyquist theorem. The average distance value is the one shown in Figure 1.

signal in the medium under investigation must be calculated. The dielectric constant values adopted in this study are based on previous estimates reported in the literature [7], which derived the permittivity of the Martian subsurface through the analysis of diffraction hyperbolas identified in RIMFAX radargrams. We adopted the range of dielectric constant values for sedimentary deposits reported in the study [7]. The RIMFAX operating frequency range of 150-1200 MHz was used to compute the optimal trace spacing according to Nyquist, with the resulting trend shown in Figure 3. In the most conservative scenario, considering the maximum signal frequency, the optimal distance for RIMFAX acquisitions is slightly below 2.5 cm.

Discussion: We assessed that RIMFAX GPR data acquires data with the optimality criterion by comparing the spatial acquisition of traces with the theoretical minimum spacing required to avoid aliasing, as determined by Nyquist's sampling theorem. On average, the mean trace spacing is comparable with the optimal value. At the upper end of the radar's operating frequency range, slightly denser spacing would be needed to fully prevent aliasing, while for the lower frequencies in the range, the condition is satisfied. However, at the higher end of the frequency range, the system is less efficient because the terrain acts as a low-pass filter, attenuating the upper portion of the spectrum [7]. The data volume generated is reasonable relative to its scientific return, with no significant loss of information on average.

Conclusions: As GPR signals are typically in the MHz range, high sampling frequencies are necessary for the effective recording of the A-scan in the time domain, thus generating a significant amount of data. The same consideration extends to the B-scan where it is essential to know the position at the time of acquisition and compute the distance between successive acquisitions. This ensures adequate spatial–temporal resolution for structure identification.

This study demonstrates the importance of geospatial positioning of GPR radar frames and its relationship with aliasing and data volume. This impacts the quantity and the quality of scientific information returned which is critical for the final geologic interpretation of the data.

These aspects are relevant for a wide range of application: from data analysis, to field data acquisition, to the development of new instruments.

References: **[1]** J. L. Davis and A. P. Annan. en. In: *Geophysical Prospecting* 37.5 (July 1989), pp. 531–551. **[2]** S.-E. Hamran et al. In: *2015 8th International Workshop on Advanced Ground Penetrating Radar (IWAGPR)*. IEEE, July 2015, pp. 1–4. **[3]** V. Ciarletti et al. In: *Astrobiology* 17.6–7 (July 2017), pp. 565–584. **[4]** S.-E. Hamran and D. A. Paige. en. **[5]** H. Nyquist. In: *Transactions of the American Institute of Electrical Engineers* 47.2 (Apr. 1928), pp. 617–644. **[6]** M. Grasmueck et al. en. In: *GEOPHYSICS* 70.1 (Jan. 2005), K12–K19. **[7]** D. A. Paige et al. en. In: *Science Advances* 10.4 (Jan. 2024), eadi8339.

DEVELOPMENT OF AN ADDITIVELY MANUFACTURED TEMPERATURE SENSOR FOR MARTIAN ATMOSPHERIC MEASUREMENTS. E. Dolejsi[1], B. Saggin[1,2], F. Ferri[1], A. Aboudan[1], C. Bettanini[1,2], G. Colombatti[1,2], [1]CISAS "Giuseppe Colombo" – Centre of Studies and Activities for Space, University of Padua, Via Venezia 1, 35131 Padova PD, Italy, elisabetta.dolejsi@unipd.it [2] DII – Department of industrial engineering, University of Padua, Via Venezia 1, 35131 Padova PD, Italy.

Introduction: For preparing better future missions to Mars, accurate atmosphere temperature measurements are fundamental, to better understand Martian atmospheric dynamics, climate variability, and boundary layer physics. It is also crucial to provide accurate and effective thermal control that is capable of handling the challenges posed by future human missions. Within the Space It Up program, a consortium funded by the Italian Space Agency (ASI) and the Ministry of University and Research (MUR), a specific research project is focused on the "Development of prototypes for analysis of the external environment of potential extraterrestrial habitats". In this context, a temperature sensor is being developed to collect measurements of the Martian atmosphere.

The extreme environment (140–250 K, 70-1400 Pa, surface wind speeds 0–50 m/s, pervasive dust, composed of 95% CO_2) [1,2] presents unprecedented challenges to sensor design and operation. Heritage missions have demonstrated critical limitations in current technology for direct temperature measurement, such as thermal drift exceeding 0.1 K due to dust deposition [3], and high time constants [4] limiting measurement cadence.

This work presents a novel approach combining: (1) dual-element RTD (Resistive Temperature Detector) design, (2) Additive Manufacturing (AM) support structure for optimized thermal response and mass reduction, and (3) comprehensive rarefied gas heat transfer modeling. The sensor achieves a 1.5× improvements in time constant and accuracy compared to heritage sensors (MarsTem/DREAMS) [4], positioning it as a viable platform for future Mars atmospheric exploration.

Sensor Architecture: The temperature sensor is a dual-element platinum wire RTD consisting of a fine element (50 μm diameter) and a coarse element (60 μm diameter insulated wire). The fine element is the most important part of the sensor, allowing for precision measurements, while the coarse element provides a backup measurement. It is a development of earlier instruments such as MarsTem from the ExoMars 2016 DREAMS package [4] and HASI TEM (Huygens Atmospheric Structure Instrument) from the Huygens mission [5].

The support structure (Fig.1) is produced in a high performance nanoceramic resin, which minimizes heat conduction and permits the production of complex geometries. The mass reduction was 75% less compared to the version previously produced with Ti-6Al-4V. In the future it is planned to design a package to protect the instrument from dust vortex and other extreme atmospheric events.



Fig. 1: Design of the support structure of the novel temperature sensor.

Heat transfer in rarefied CO_2 atmosphere: The Martian atmosphere presents extreme rarefaction compared to Earth, leading to unique heat transfer conditions. For the thermophysical properties, the following atmospheric characteristics have been calculated, assuming a model only with the presence of CO_2, with surface pressure p = 600 Pa and characteristic temperatures between 150 and 300 K:

- Thermal conductivity: k = 0.0092-0.0167 W/(m·K).
- Dynamic viscosity: μ = 9.0-15.0 μPa·s.
- Prandtl number: Pr ≈ 0.75-0.77.

The mean free path is calculated from kinetic theory [6], yielding to λ =6-20 μm across the altitude range 0–10 km.

For our 50 μm diameter RTD wire element, this produces a Knudsen number Kn = λ/d in the range 0.14–0.34, falling within the transitional regime, where neither continuum nor free-molecular flow assumptions apply. In the transitional regime, convective heat transfer coefficients are modeled using slip flow corrections [7] with thermal accommodation effects [8], since standard continuum-based Nusselt correlations (Churchill-Bernstein, Hilpert) are invalid.

Conclusions: The sensor under development combines transitional flow heat-transfer physics, additive manufacturing innovation, and dual-element architecture, resulting in a comprehensive design for

a next-generation Mars temperature sensor. Despite the challenges, especially for the transitional heat-transfer model, the faster response time and mass reduction justify the development effort for next-generation Mars atmospheric platforms. The sensor achieves improvements in resolution, accuracy, and especially in response time compared to heritage DREAMS/MarsTEM.

Acknowledgment: This study was carried out within the Space It Up project funded by the Italian Space Agency, ASI, and the Ministry of University and Research, MUR, under contract n. 2024-5-E.0 - CUP n. I53D24000060005.

References:

[1] F. Forget, F. Hourdin, R. Fournier, C. Hourdin, O. Talagrand, M. Collins, S. R. Lewis, P. L. Read, and J.-P. Huot, Improved general circulation models of the Martian atmosphere from the surface to above 80 km, J. Geophys. Res., 104(E10), 24155–24175 (1999), https://doi.org/10.1029/1999JE001025.

[2] E. Millour, F. Forget, A. Spiga, T. Pierron, A. Bierjon, L. Montabone, M. Vals, F. Lefèvre, J.-Y. Chaufray, M. Lopez-Valverde, F. Gonzalez-Galindo, S. Lewis, P. Read, M.-C. Desjean, and F. Cipriani, and the MCD Team, The Mars Climate Database (Version 6.1), Europlanet Science Congress 2022, Granada, Spain, 18–23 Sep 2022, EPSC2022-786 (2022), https://doi.org/10.5194/epsc2022-786.

[3] Giacomo Colombatti, Carlo Bettanini, Alessio Aboudan, Stefano Debei, Francesca Esposito, Cesare Molfese, Anselmo Cecere, John Merrison, Jens Jacob Iversen, MarsTEM sensor simulations in Martian dust environment, *Measurement*, Volume 122, 2018, Pages 453-458, ISSN 0263-2241, https://doi.org/10.1016/j.measurement.2017.12.043.

[4] G. Colombatti *et al.*, "MarsTEM: The temperature sensor of the DREAMS package onboard Exomars2016," *2014 IEEE Metrology for Aerospace (MetroAeroSpace)*, Benevento, Italy, 2014, pp. 249-254, doi: 10.1109/MetroAeroSpace.2014.6865929.

[5] M. Fulchignoni, Ferri F., Angrilli F., et al., The characterisation of Titan's atmospheric physical properties by the Huygens Atmospheric Structure Instrument (HASI), *Space Science Reviews 104*, 395–431 (2002), https://doi.org/10.1023/A:1023688607077.

[6] Kunze, S., Groll, R., Besser, B. *et al.* Molecular diameters of rarefied gases. *Sci Rep* **12**, 2057 (2022). https://doi.org/10.1038/s41598-022-05871-y

[7] Lilian Peinado, Victor Muntean, Isabel Pérez-Grande, A free convection heat transfer correlation for very thin horizontal wires in rarefied atmospheres, *Experimental Thermal and Fluid Science*, Volume 122, 2021, 110295, ISSN 0894-1777, https://doi.org/10.1016/j.expthermflusci.2020.110295

[8] V. Vesovic and W.A Wakeham, G.A. Olchowy and J.V. Sengers, J.T.R. Watson, J. Millat, The Transport Properties of Carbon Dioxide, J. Phys. Chem. Ref. Data, Vol. 19, No. 3, 1990

SIMULATION, PLANNING AND VISUALIZATION OF MOONIS OPERATIONS

Lorenzo Rossi[1,2], M. C. De Sanctis[1], F. Altieri[1], D. Biondi[1], S. De Angelis[1], M. Ciarniello[1], M. Ferrari[1], G. Filacchione[1], M. Formisano[1], A. Frigeri[1], V. Galluzzi[1], G. Massa[1], A. Raponi[1], E. Ammannito[3], R. Pepe[4], J. Regolini[5]

[1]INAF-IAPS, Via del Fosso del Cavaliere 100, Rome, Italy (lorenzo.rossi@inaf.it); [2]Politecnico di Milano, Via Giuseppe La Masa 34, Milan, Italy; [3]Agenzia Spaziale Italiana, Via del Politecnico snc, Rome, Italy; [4]Agenzia Spaziale Italiana, Località Terlecchia, Matera, Italy; [5]Leonardo S.p.A., Via Delle Officine Galileo 1, Campi Bisenzio (FI), Italy.

Introduction: MoonIS is a VIS–IR spectrometer onboard Rashid Rover 3, which is part of the Emirates Lunar Mission (ELM) programme led by the Mohammed bin Rashid Space Centre (MBRSC). Rashid Rover 3, planned for launch in 2028, will land near the lunar south pole to study surface geology and investigate the presence of water ice and other cold-trapped volatiles within permanently shadowed regions (PSRs) [1]. To maximise the scientific return of MoonIS in this constrained operational environment, we are developing a dedicated software tool to simulate, plan, and visualise MoonIS operations.

The MoonIS Instrument: MoonIS will acquire reflectance spectra of the lunar surface in the 0.4-2.3 μm wavelength range, with the goal of characterizing water ice and overall surface composition in and around PSRs [2]. The instrument design builds on the heritage of Ma_MISS, the spectrometer on board ESA's ExoMars Rosalind Franklin rover [3]. It features a modular architecture comprising two main units: a spectrometer and electronics box housed inside the rover body, and an optical head unit (OHU) mounted on the rover mast.

Light collected by the OHU is relayed to the spectrometer through optical fibres. The OHU is co-located on the mast with CAM-25, a multispectral camera, and NavCam, a stereo camera pair used for navigation. It comprises three individual off-axis parabolic mirrors (OAPs) that collect light and couple it into three separate fibres. MoonIS therefore acquires three spectra simultaneously, one for each OAP, corresponding to three instantaneous fields of view (IFOVs) on the surface. Pointing is controlled by actuating the mast azimuth and elevation joints.

MoonIS Operations: In addition to single-point acquisitions, MoonIS will perform scan sequences in which the mast sequentially points to a grid of positions while the rover remains stationary. At each mast pose, MoonIS acquires three spectra from three small spots on the ground, corresponding to the FOV footprints of the three OAPs. A scan sequence thus produces a "pseudo hyperspectral image" of the scanned region of interest, whose (non-regular) ground sampling distance (GSD) and spatial resolution are determined by the mast pointing geometry and the chosen scan grid spacing (i.e. the distance between consecutive acquisitions). Operations inside PSRs are strongly constrained by energy and thermal limits, which restrict the total time available for science activities. A trade-off between spatial coverage and sampling, signal-to-noise ratio (SNR), and overall sequence duration is therefore required.

Simulating MoonIS Operations: To support the definition and optimization of MoonIS operations we are developing a dedicated software tool to simulate observation geometry, estimate sequence durations and assist in planning optimised MoonIS operations. While the tool is still in early stages of development, we already implemented some basic functionalities, summarised below.

Rover and Mast Kinematics: The pointing of MoonIS and the mast-mounted cameras (CAM-25 and NavCam) is controlled via two mast joints, providing azimuth and elevation control. To compute and visualise the instrument and camera footprints for arbitrary rover attitudes and mast configurations, we implemented a simple kinematic model of the rover and mast. For each component, we define a reference frame describing its position and orientation. The mast is modelled as a rigid-body serial kinematic chain. Overall, the system model has eight degrees of freedom (DoF): six describe the rover position and attitude with respect to a local "world" frame, and two correspond to the mast azimuth and elevation angles. For most MoonIS operations the rover is assumed to be stationary, so scan sequences are executed by varying only the two mast DoFs. The kinematic model is

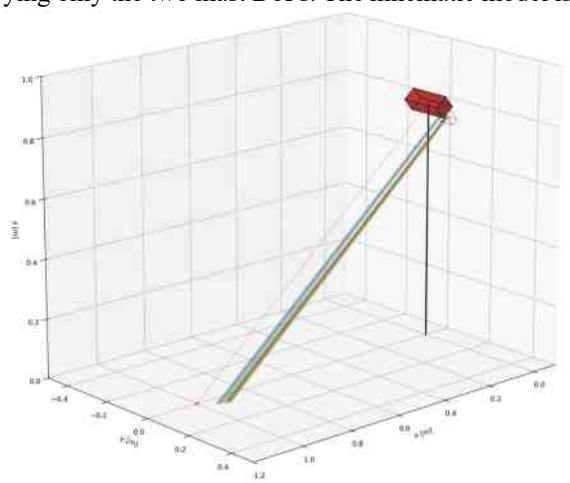


Figure 1. Example of 3D observation geometry visualisation. The red cuboid represents the mast head unit, on which CAM-25, NavCam and MoonIS OHU are mounted. In the configuration shown here, CAM-25 boresight (dashed red line) is pointed at a target on the ground 1 m ahead of the rover.

used to perform forward kinematics and visualise the 3D observation geometry (FOVs and ground footprints of both MoonIS and the mast-mounted cameras) in function of rover attitude and mast joint angles. In addition, we implemented an inverse kinematics solver to compute the mast azimuth and elevation angles required to point the instrument's boresight towards a selected target.

Footprint Geometry: To model the MoonIS field of view, the acceptance cone of each OAP is represented as a conical frustum whose shape and size are derived from ray-tracing simulations. The ground footprint is computed as the intersection between each frustum and a surface representing the terrain. A simplified schematic representation of the observation geometry is shown in Figure 1. Here, the conical frusta representing the FOVs of the three OAPs are shown in different colours. In the current implementation, the ground is modelled as a plane (optionally tilted with respect to the rover). Future versions will employ a mesh-based description of the terrain, enabling the simulation of more realistic surface geometries, including slopes, roughness, boulders and pits.

Scan Sequence Planning: A key functionality of the tool is the planning of MoonIS scan sequences. The user specifies the size and position of the region of interest and the scan grid spacing. Smaller grid spacing yields finer spatial sampling and a larger number of acquired spectra, at the cost of increased sequence duration. The tool then generates a sequence of mast pointing configurations that covers the selected area with the desired sampling. For each mast pose, the corresponding MoonIS ground footprints are computed, and the full scan pattern is visualized in a 3D environment and in camera projections, as show in Figure 2.

Duration estimation: Once a scan sequence has been defined, the tool estimates its total execution time. The duration model takes into account the duration of each MoonIS acquisition as well as the time required to slew the mast between subsequent acquisitions. The duration of individual MoonIS acquisitions is computed as a function of user-supplied acquisition parameters, such as the integration time and the number of averaged frames per acquisition.

Camera Projection: Images from CAM-25 and NavCam will provide context information to MoonIS measurements. To make the most out of the combined information provided by MoonIS and the cameras, it is essential to locate MoonIS measurement on camera images. To predict how MoonIS footprints will appear in these images, we used a simple pinhole camera model for CAM-25 and NavCam. The 3D coordinates of the footprint boundary points are projected into the camera image plane, providing an estimation of the location, shape and size of MoonIS footprints in image coordinates. An example of camera projection of MoonIS footprints is displayed in the top panel of Figure 2, which shows how the ground footprints of a MoonIS scan sequence would look like in a CAM-25 image. The scan sequence shown here comprises MoonIS acquisitions at 90 different mast poses, for a total of 270 individual spectra.

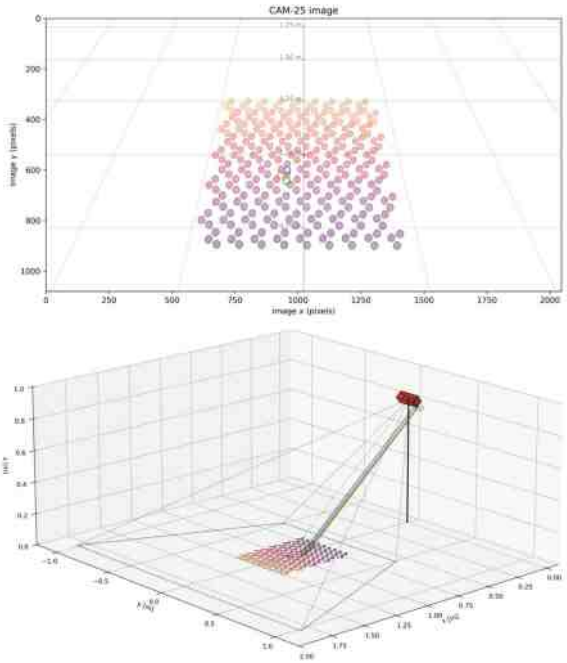


Figure 2. Top: Example of camera projection of the ground footprints of a scan sequence. Bottom: 3D view of the same scene, where CAM-25's field of view and ground footprint are shown in dashed grey lines.

Conclusion: The MoonIS operations simulation tool will provide an integrated environment to model observation geometry, plan scan sequences, and estimate the duration of MoonIS operations. We started developing its core functionalities, which we present in this work.

Ongoing and future work focuses on extending the functionalities of the toolkit, implementing realistic terrain models to simulate complex surface geometries, and implementing automated optimization of scan sequences under user-defined time constraints. The tool will support both pre-landing planning and, in the future, the analysis and refinement of operations during the active mission phase.

Acknowledgements: This work is supported by Accordo ASI – INAF n. 2024-64-HH.0. The MoonIS instrument is funded by ASI and manufactured by Leonardo S.p.A. (Italy).

References:

[1] Almatroushi H. et al. (2025) EPSC-DPS2025-13, https://doi.org/10.5194/epsc-dps2025-13.
[2] De Sanctis M.C et al. (2025) EPSC-DPS2025-587, https://doi.org/10.5194/epsc-dps2025-587.
[3] De Sanctis M.C: et al (2022) *Planet. Sci. J.* 3 142, https://doi.org/10.3847/PSJ/ac694f.

DAEDALUSCAM: MEASURING LAVA TUBES TO COMPARE THE EFFECTIVENESS OF ROBOTIC EXPLORATION. J. E. Suarez-Valencia[1], M. Massironi[1], B. Casarotto1, K. Toyokawa[2], R. Pozzobon[1], C. A. De Donno[3], M. Mucci Beltrami[3], C. Pernechele[4], E. Simioni[4], D. Scaccabarozzi[5], and the DaedalusCAM Team.1University of Padova (javier.suarez@unipd.it), 2University of Tokyo, 3Planetek Italia S. r. l., 4 INAF-OAPD, 5Politecnico di Milano.

Introduction: The DaedalusCAM is an infrastructure intended to acquire, process, and visualize data during the exploration of lava tubes, with a focus on lunar exploration [1]. The main instrument to perform this task is an hyper hemispheric camera, which has the capability of capturing information in a 360° degrees above the horizontal level (**Figure 1**). This extensive range of acquisition make DaedalusCAM ideal to survey the collapses or pits that serve as entrance to lava tubes, which are usually semi-closed environments [2]. A mission concept with this technology would involve the descent of the DaedalusCAM through the pit and into the first meters of a lava tube, so the qualities of the camera would be essential for navigation and for collecting scientific information about the pit walls. In this work we designed a methodology to measure the effectiveness of DaedalusCAM as a tool to recognize geological features, by comparing it to other techniques that are usually applied in terrestrial environments.

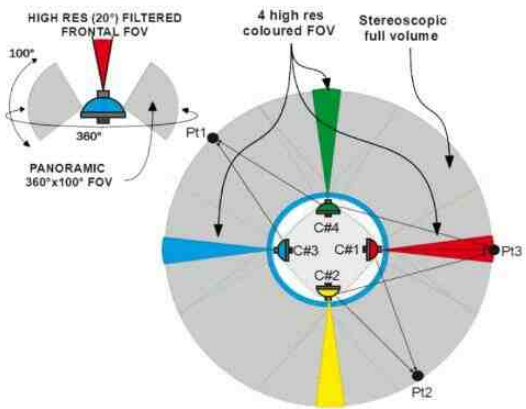


Figure 1: Configuration DaedalusCAM [1].

Methodology: To perform the desired comparison we will analyze three types of datasets: measurements from digital models obtained by a ground laser scanner, drone flights, and hyperspectral cameras; measurements obtained from the digital models reconstructed from DaedalusCAM; and direct measurements taken on the field. At this point of the project, we are performing the first set of analysis.

The information for the first dataset comes from two field campaigns done to Lanzarote in the Canary Islands, and to Mount Etna in Sicily earlier this year. From Lanzarote we collected information from "Jameo de la Gente", a collapse leading into La Corona tube, the biggest one on Earth; and from Etna we collected info from the collapses of the Tre Livelli and Intraleo tubes, and the Cisternazza crater. We reconstructed 3D models for these locations using Cyclone, CloudCompare; hyperclouds using Blender and Python; and we performed our measurements in the VRGS software. We obtained an initial acquisition with DaedalusCAM during the Etna campaign, but the final acquisition will be performed during the first semester of 2026, we will follow a similar workflow to create the 3D models, and also do the measurements in VRGS [3]. As for the on-site measurements, they will be carried out simultaneously during the final acquisition, using common field techniques like scanlines.

Results: The 3D models for the locations were successfully reconstructed (**Figure 2, Figure 3**). The original point clouds were processed in CloudCompare to generate 3d meshes. To include hyperspectral information, we recreated the scene positions in Blender and then used the Hylite python Pacakge to create hyperclouds [4].

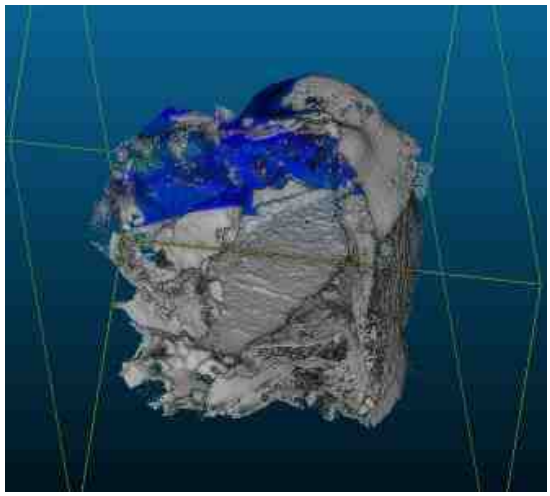


Figure 2: Initial hypercloud of the Tre Livelli colapse.

We then developed a table with 23 features to measure in the three datasets that we defined (**Table 1).** These features can be group in three categories: structural, morphological, and cavity. For the structural component we focused on fractures, striations, and grooves, which give information about how the

lava tube formed and its internal dynamic. The second components is about identifying typical morphologies that form inside and near the entrance of the tube. And the final one is about the volume and size of the explored cavity.

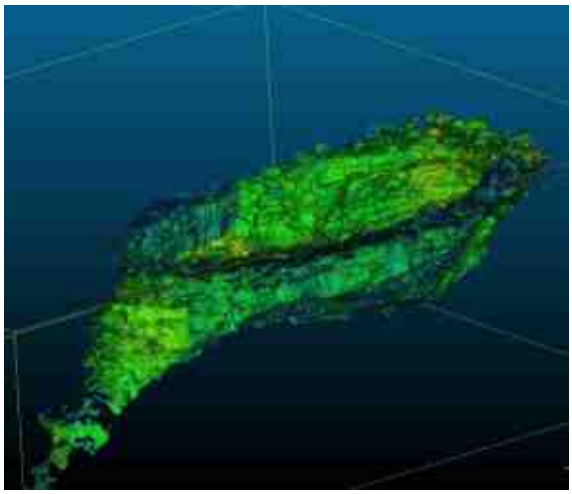


Figure 3: 3D model of Jameo de la Gente.

Type	Structure	Measurements
Structural	Fractures	Amount of fractures in a scanline.
		Presistence, orientation, aperture.
	Striation	Orientation: azimuth and dip. Quantity.
	Grooves	Orientation: azimuth and dip. Quantity.
Morhplogical	Flow ledges	Lateral extension of the ledge from the wall.
		Vertical extension of the ledge.
	Stalactites and stalacmites	Quantity of structures identified.
		Length of the structures.
	Rolling-overs	Diameter of the coiled structure.
		Curvature of the foil.
	Lining walls	Presence of absence of the structure.
Cavity	Cavity/Outcrop	Measurements of the long and short diameters.
		Measurement of the area of the pit.
	Cave/Outcrop	Measurement of the volume of the pit or structure.

Table 1: Measurements made in the three datasets.

These parameters were measured in the VRGS software, and we made comparison with initial results from DaedalusCAM.

Discussion and conclusions: The 3D models constructed with the ground laser scanner are particularly sensitive to the distance of acquisition. The smaller and more confined locations like Tre Livelli and Intraleo retained great details, allowing the identification of internal morphologies like lining walls and roll-overs; while the ones in Cisternazza and Jameo de la Gente did not, allowing mainly general measurements of the lava layers and big fractures. The hyperspectral information is consistent with the expected basaltic composition, but the sites are too homogeneous to catch meaningful spectral variations.

Finally, from the initial comparison with the Daedalus images we found that there is again a limitation with the distance to the target, but also with the illumination. In open locations like Cisternazza the resolution of the camera is a limitation, and poor illuminated collapses like Tre Livelli also showed poor results. However, in closed and well illuminated locations like Intraleo, the images of DaedalusCAM have enough resolution to resolve major fractures, record lava layers, and shoe changes in composition.

References: [1] E. Simioni, C. Pernechele, R. Pozzobon, M. Massironi, V. Della Corte, M. Landoni, B. Saggin, and D. Scaccabarozzi, "*The Daedalus CAM: The immersive and stereoscopic way for lunar lava tubes exploration*," on behalf of the Daedalus CAM team, INAF Padova; University of Padova; INAF IASP (Roma); INAF Brera (Milano); Polytechnic University of Milano.

[2] F. Sauro, R. Pozzobon, M. Massironi, P. De Berardinis, T. Santagata, and J. De Waele, "Lava tubes on Earth, Moon and Mars: A review on their size and morphology revealed by comparative planetology," *Earth-Science Reviews*, vol. 209, Art. no. 103288, 2020, doi: 10.1016/j.earscirev.2020.103288.

[3] D. Hodgetts, R. L. Gawthorpe, P. Wilson, and F. Rarity, "Integrating digital and traditional field techniques using Virtual Reality Geological Studio (VRGS)," in *69th EAGE Conference & Exhibition incorporating SPE EUROPEC 2007*, London, UK, 11-14 June 2007. European Association of Geoscientists & Engineers, 2007. doi: 10.3997/2214-4609.201401718.

[4] S. T. Thiele, S. Lorenz, M. Kirsch, R. Gloaguen, et al., "Multi-scale, multi-sensor data integration for automated 3-D geological mapping using hylite," *Ore Geology Reviews*, vol. 136, art. no. 104252, 2021, doi: 10.1016/j.oregeorev.2021.104252.

A FEASIBILITY STUDY FOR AN OPTICAL-IR SPECTROMETER FOR A FUTURE URANUS MISSION: THE ATMOSPHERIC SCIENCE CASE

F.Camilloni[1], D. Grassi[1,2], F. Biagiotti[3,1], C. Castagnoli[1,6], A. Mura[1], G. Piccioni[1], A. Migliorini[1], C. Plainaki[2,4], G. Sindoni[4], P. Tortora[5], and F. Tosi[1]

[1]IAPS-INAF (francesco.camilloni@inaf.it), [2]Max Planck Institute for Solar System Research, [3]Sapienza Univ. di Roma, [4]ASI, [5]Alma Mater Studiorum – Università di Bologna, [6]CNR-ISAC, Bologna

Introduction. We present a study of the performance of a visible-infrared spectrometer proposed by the Italian Space Agency (ASI) for the upcoming NASA-led mission Uranus Orbiter and Probe (UOP). One of the main scientific goal of the mission is studying the atmosphere of Uranus, which we characterize by solving the atmospheric retrieval problem.

Physics of the problem. An extensive analysis of the optical properties of the Uranus atmosphere was performed by [1] in the visible band. They inferred an atmospheric structure made by three layers: (1) one first deeper layer ($p > 5 - 7$ bar) primarily composed of H_2S and possibly also by NH_3 clouds (2) an optically thick aerosol layer made by condensed CH_4 clouds around 1 bar. (3) a third upper layer made by a thin haze made of submicron particles extending to upper altitudes. We adopted this physical scenario for our analysis.

Methods: To solve the atmospheric retrieval problem, we simulated the visible and infrared Uranus spectra with the code ARS (Атмосфера, Радиация,Спектр - Atmosphere, Radiation, Spectrum) [2]. ARS employs the correlated-k formalism and databases such as EXOMOL [3] and HITRAN [4], providing a simulated spectrum as output. Beside solving the radiative transfer problem for multiple scattering, in our modeling we considered also the contribution from Rayleigh scattering and Collision-Induced Absorption (CIA). The first step was computing the Jacobian Matrix, modifying the input parameters of the simulation and storing the information on how the spectra in output change (i.e numerical differentiation). After estimating the covariance and noise matrices, with the formalism described in [5], we were able to estimate the retrieval capability of the instrument. This is quantified with the retrieval error, which should be efficiently minimized.

Results: starting from the physical scenario described above, we modeled our problem including three aerosols components (a1, a2, a3) and three gases (CH_4, NH_3 and H_2S). We first solved the retrieval problem in the visible range, using the atmospheric profiles derived by [1]. In the visible band, we obtained quite satisfactory results (Fig. 1), with the a2 aerosol layer and CH_4 showing the strongest response (i.e lowest retrieval error). However, the analysis in the infrared band turned out to be much more challenging, given the very low radiance of Uranus for wavelengths greater than 2 μm (Fig. 2).

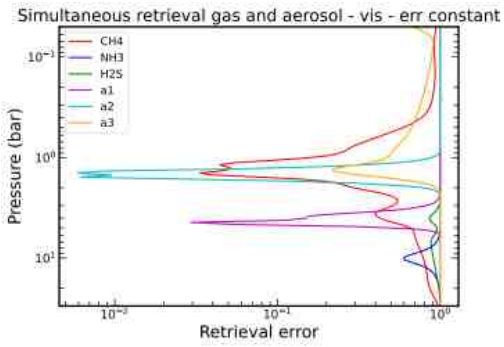


Fig. 1. Retrieval error in visible band.

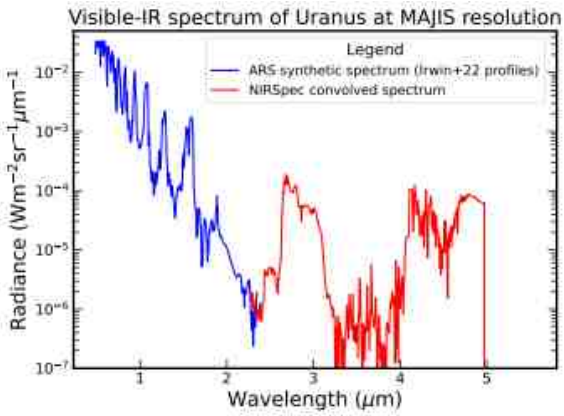


Fig. 2. Spectra of Uranus at the spectral resolution of a MAJIS-like instrument. The visible spectrum (blue) is obtained with ARS using the atmospheric profiles from [1], while the IR one (red) is the original JWST spectrum convolved to the MAJIS resolution.

Therefore, we first analyzed the Cycle 1 data (proposal ID 01248, P.I. L. Fletcher) obtained with the NIRSpec camera of the James Webb Space Telescope (JWST). We plotted the datacube in two bands (Fig. 3), initially focusing our attention on the auroral emission. As a first step, we convolved the original spectra at the resolution of MAJIS (Moons and Jupiter Imaging Spectrometer) [6], in order to replicate the observational condition of a state-of-the-art

spectro-imager. Using the h3ppy code [7], we fitted the auroral emission between 3.3-4 μm (Fig. 4), obtaining as temperatures T_1 = 406 ± 5 K, T_2 = 393 ± 10 K and T_3 = 428 ± 28 K, respectively for the three regions indicated in Fig.3.

Further developments: to estimate the retrieval error also in IR band, we first needed to find a best fit for the spectra at the spectral resolution of MAJIS. The parameters of the fit are the effective cross-section Σ, the single scattering albedo ω_0 and the g factor of the Heyney-Greenstein phase function. Since this problem is highly degenerate, we developed a fitting algorithm based on the Markov Chain Monte Carlo (MCMC) technique. Currently, our work is focused on obtaining meaningful constraints from the IR spectra. From these constraints, we want to derive the atmospheric profiles of the three aerosols and gas species. These profiles are needed to calculate the Jacobian matrix and to estimate the retrieval error also in the IR band, completing the characterization of the instrument.

References: [1] Irwin, P. G. J., Teanby, N.A., Fletcher,L. N., et al.(2022) JGRE, 127, e07189 [2] Ignatiev, N. I., Grassi, D., & Zasova, L. V. (2005) P&SS, 53, 1035-1042 [3] Tennyson, J., & Yurchenko, S. N. (2012) MNRAS, 425, 21-33 [4] I. E. Gordon, L. S. Rothman, R. J. Hargreaves, R. Hashemi, E. V. Karlovets, F. M. Skinner, *et al.*, *J. Quant. Spectrosc. Radiat. Transfer* **277**, 107949 (2022) [5] Grassi et al. 2010, P&SS, 58, 1265-1278. [6] Poulet, F., Piccioni, G., Langevin, Y., et al., 2024, Space Science Review, 220, 3, 27 [7] Melin, H., *et al. Nat Astron* **9**, 666–671 (2025).

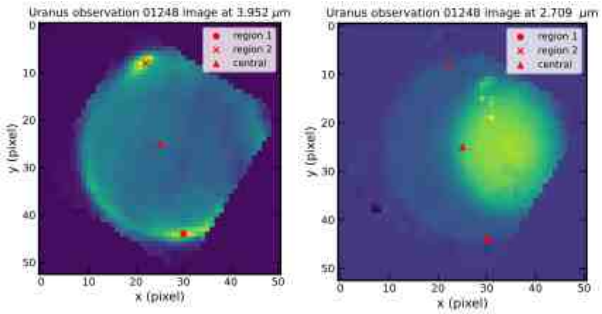


Fig 3. JWST data plotted a 3.952 μm and 2.709 μm bands, which highlight the auroral and aerosol polar cap emission, respectively.

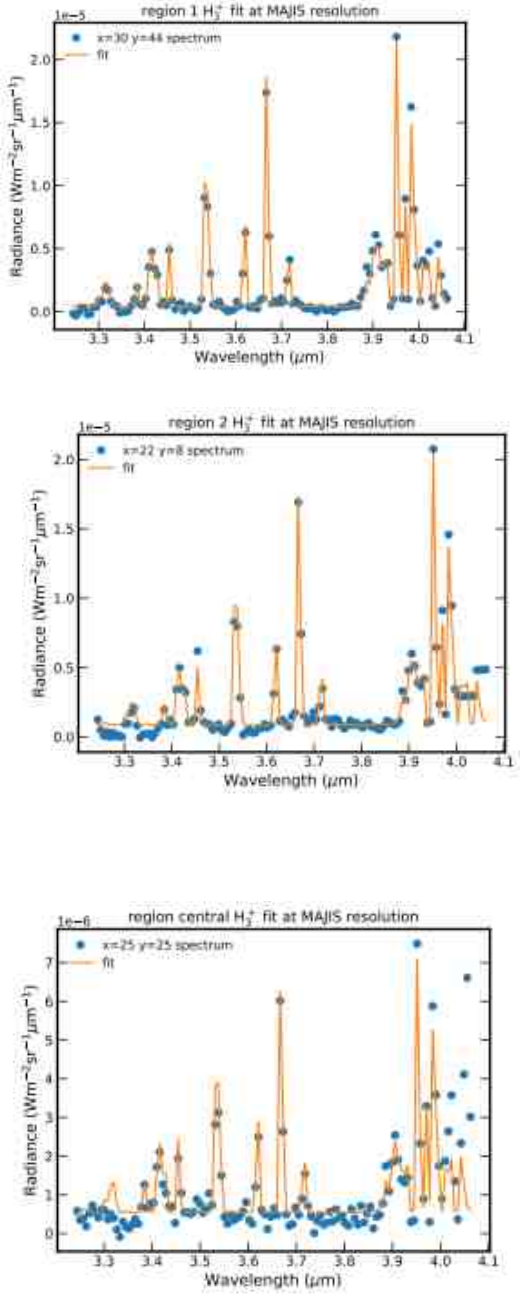


Fig 4. JWST data convolved at the MAJIS resolution fitted with h3ppy code

Acknowledgments: This work is supported by ASI through the agreement ASI/UniBo-CIRI n. 2024-5-HH.0. We also gratefully acknowledge Dr. N. Ignatiev of IKI-RAS, Moscow, Russia, for granting permission to use his ARS code in this project